



prosthesis

Special Issue Reprint

Recent Advances in Foot Prosthesis and Orthosis

Edited by
Arnab Chanda

mdpi.com/journal/prosthesis



Recent Advances in Foot Prosthesis and Orthosis

Recent Advances in Foot Prosthesis and Orthosis

Guest Editor

Arnab Chanda



Basel • Beijing • Wuhan • Barcelona • Belgrade • Novi Sad • Cluj • Manchester

Guest Editor

Arnab Chanda
Centre for Biomedical
Engineering
Indian Institute of Technology
Delhi (IIT Delhi)
New Delhi
India

Editorial Office

MDPI AG
Grosspeteranlage 5
4052 Basel, Switzerland

This is a reprint of the Special Issue, published open access by the journal *Prosthesis* (ISSN 2673-1592), freely accessible at: https://www.mdpi.com/journal/prosthesis/special_issues/4VP3191S89.

For citation purposes, cite each article independently as indicated on the article page online and as indicated below:

Lastname, A.A.; Lastname, B.B. Article Title. <i>Journal Name</i> Year , Volume Number, Page Range.
--

ISBN 978-3-7258-4081-6 (Hbk)

ISBN 978-3-7258-4082-3 (PDF)

<https://doi.org/10.3390/books978-3-7258-4082-3>

Cover image courtesy of Arnab Chanda

© 2025 by the authors. Articles in this book are Open Access and distributed under the Creative Commons Attribution (CC BY) license. The book as a whole is distributed by MDPI under the terms and conditions of the Creative Commons Attribution-NonCommercial-NoDerivs (CC BY-NC-ND) license.

Contents

About the Editor	vii
----------------------------	-----

Salman Shaikh, Bhakti Jamdade and Arnab Chanda Effects of Customized 3D-Printed Insoles in Patients with Foot-Related Musculoskeletal Ailments— A Survey-Based Study Reprinted from: <i>Prosthesis</i> 2023 , 5, 38, https://doi.org/10.3390/prosthesis5020038	1
--	---

Silvia Faccioli, Giulia Tonini, Elena Vinante, Alessandro Ehsani, Eleonora Pellarin, Giuliano Cassanelli, et al. The Role of Ankle–Foot Orthoses in Improving Gait in Children and Adolescents with Neuromotor Disability: A Systematic Review and Meta-Analysis Reprinted from: <i>Prosthesis</i> 2025 , 7, 13, https://doi.org/10.3390/prosthesis7010013	13
--	----

Komal Chhikara, Sarabjeet Singh Sidhu, Shubham Gupta, Sakshi Saharawat, Chitra Kataria and Arnab Chanda Development and Effectiveness Testing of a Novel 3D-Printed Multi-Material Orthosis in Nurses with Plantar Foot Pain Reprinted from: <i>Prosthesis</i> 2023 , 5, 6, https://doi.org/10.3390/prosthesis5010006	35
---	----

Jesus Alejandro Serrato-Pedrosa, Guillermo Urriolagoitia-Sosa, Beatriz Romero-Ángeles, Francisco Carrasco-Hernández, Francisco Javier Gallegos-Funes, Alfonso Trejo-Enriquez, et al. Numerical Analysis of the Plantar Pressure Points during the Stance Phases for the Design of a 3D-Printable Patient-Specific Insole Reprinted from: <i>Prosthesis</i> 2024 , 6, 32, https://doi.org/10.3390/prosthesis6030032	50
--	----

Ali F. Abdulkareem, Auns Q. Al-Neami, Tariq J. Mohammed and Hayder R. Al-Omairi The Design and Application of an Advanced System for the Diagnosis and Treatment of Flatfoot Based on Infrared Thermography and a Smart-Memory-Alloy-Reinforced Insole Reprinted from: <i>Prosthesis</i> 2024 , 6, 108, https://doi.org/10.3390/prosthesis6060108	78
---	----

Hasan Mhd Nazha, Muhsen Adrah, Thaer Osman, Mohammad Issa, Ahmed Imran, Yicha Zhang and Daniel Juhre Investigating Material Performance in Artificial Ankle Joints: A Biomechanical Study Reprinted from: <i>Prosthesis</i> 2024 , 6, 36, https://doi.org/10.3390/prosthesis6030036	97
---	----

Anna Pace, James Gardiner and David Howard Simulation-Based Design of a Cam-Driven Hydraulic Prosthetic Ankle Reprinted from: <i>Prosthesis</i> 2025 , 7, 14, https://doi.org/10.3390/prosthesis7010014	116
---	-----

Karen E. Rodriguez Hernandez, Jurriaan H. de Groot, Eveline R. M. Grootendorst-Heemskerck, Frank Baas, Marjon Stijntjes, Sven K. Schiemanck, et al. Compensating the Symptomatic Increase in Plantarflexion Torque and Mechanical Work for Dorsiflexion in Patients with Spastic Paresis Using the “Hermes” Ankle–Foot Orthosis Reprinted from: <i>Prosthesis</i> 2025 , 7, 12, https://doi.org/10.3390/prosthesis7010012	130
---	-----

Marco Leopaldi, Tommaso Maria Brugo, Johnnidel Tabucol and Andrea Zucchelli Parametric Design of an Advanced Multi-Axial Energy-Storing-and-Releasing Ankle–Foot Prosthesis Reprinted from: <i>Prosthesis</i> 2024 , 6, 51, https://doi.org/10.3390/prosthesis6040051	146
---	-----

Michael J. Greene, Ivan Fischman Ekman Simões, Preston R. Lewis, Kieran M. Nichols and Peter G. Adamczyk Non-Backdrivable Wedge Cam Mechanism for a Semi-Active Two-Axis Prosthetic Ankle Reprinted from: <i>Prosthesis</i> 2024 , 6, 49, https://doi.org/10.3390/prosthesis6030049	164
Peter Dabnichki and Toh Yen Pang User-Centered Design Framework for Personalized Ankle–Foot Orthoses Reprinted from: <i>Prosthesis</i> 2025 , 7, 11, https://doi.org/10.3390/prosthesis7010011	189
Muhammad Khafidh, Donny Suryawan, Lilis Kistriyani, Muhammad Naufal and Rifky Ismail Friction Optimization of Talc Powder-Reinforced Elastomers for Prosthetic Foot Application Reprinted from: <i>Prosthesis</i> 2023 , 5, 7, https://doi.org/10.3390/prosthesis5010007	205
Rubén Sánchez-Gómez, Juan Manuel López-Alcorocho, Almudena Núñez-Fernández, María Luz González Fernández, Carlos Martínez-Sebastián, Ismael Ortuño-Soriano, et al. Morton’s Extension on Hallux Rigidus Pathology Reprinted from: <i>Prosthesis</i> 2023 , 5, 19, https://doi.org/10.3390/prosthesis5010019	217
Susmita Das, Dalia Nandi and Biswarup Neogi Design Analysis of Prosthetic Unilateral Transtibial Lower Limb with Gait Coordination Reprinted from: <i>Prosthesis</i> 2023 , 5, 40, https://doi.org/10.3390/prosthesis5020040	230
Omar A. Gonzales-Huisa, Gonzalo Oshiro, Victoria E. Abarca, Jorge G. Chavez-Echajaya and Dante A. Elias EMG and IMU Data Fusion for Locomotion Mode Classification in Transtibial Amputees Reprinted from: <i>Prosthesis</i> 2023 , 5, 85, https://doi.org/10.3390/prosthesis5040085	242

About the Editor

Arnab Chanda

Prof. Arnab Chanda is an Associate Professor in the Centre for Biomedical Engineering, IIT Delhi, and a joint faculty at the Department of Biomedical Engineering, AIIMS, Delhi. He is also the founder of a start-up company, BIOFIT Technologies LLC, USA. He earned his PhD from the University of Alabama, USA, and has also been a Postdoctoral Researcher at the University of Pittsburgh, USA. Dr. Chanda is an expert in the area of “Biomechanics”, especially in Tissue Mimicking (Artificial Tissues) and Characterization, finite element modeling (FEM), robotics and wearable device development, and entrepreneurship. To date, he has received the Young Researcher Award and Early Career Award from ASME, MHRD, and AO Spine International-Singapore, and Top-Cited Paper Awards from IOP Publishing and Wiley. He holds and has filed 10+ US and Indian Patents, authored 6 Books and 100+ articles in reputed international journals. Dr. Chanda is in the list of top 2% scientists worldwide as per Scopus Elsevier and Stanford University databases in both years 2023 and 2024. He also teaches two successful Executive Programs: “Executive Program in Healthcare Entrepreneurship and Management” and “Executive Program in Robotics”, and multiple Swayam/NPTEL courses to engineers, doctors, and management professionals. Dr. Chanda is serving as the editor for ‘Biomedical Materials for Multi-functional Applications’, a book series published by Springer Nature, editorial board member for Nature Scientific Reports, and guest editor for several journals such as Engineering Research Express, IOP Publishing.

Article

Effects of Customized 3D-Printed Insoles in Patients with Foot-Related Musculoskeletal Ailments—A Survey-Based Study

Salman Shaikh ¹, Bhakti Jamdade ² and Arnab Chanda ^{3,*}¹ Biomechanics Research Cell, Metafix Ortho (P) Ltd., Pune 411005, India; salman@metafix.io² Application and Clinical Research, Metafix Ortho (P) Ltd., Pune 411005, India; bhakti@metafix.io³ Center for Biomedical Engineering, Indian Institute of Technology, Delhi 110016, India

* Correspondence: arnab.chanda@cbme.iitd.ac.in; Tel.: +91-11-2659-1086

Abstract: The prevalence of individuals with flat feet and high arches is very high (between 15% to 37%), which can often lead to other orthopedic complications. Three-dimensional-printed insoles are being studied and validated for their effects in correcting these highly prevalent foot disorders. Highly customizable parameters while printing the insole allows for precise correction of foot biomechanics. In this study, 200 patients suffering from various foot-related problems and joint pain were given 3d-printed insoles (designed using plantar pressure systems and clinical practitioner's assessment) to use in their footwear. Tested activities included standing, walking, running, sports, and gym workout. Customization of insoles included custom density, heel cup, heel rise, medial arch height, and lateral wedge. Based on the patient history, additional podiatry elements were provided for patients with diabetes. Each insole was designed as per the insole profile of the shoe with a comfortable fit. These insoles were found to be effective in alleviating pain for more than 90% of the patients and provided a longer life cycle with effective orthotic correction (for >16 months of daily use). This paper presents the post-use effects (6–18 months) of custom 3D-printed insoles.

Keywords: foot orthosis; flat foot; 3D printing; insoles

Citation: Shaikh, S.; Jamdade, B.; Chanda, A. Effects of Customized 3D-Printed Insoles in Patients with Foot-Related Musculoskeletal Ailments—A Survey-Based Study. *Prosthesis* **2023**, *5*, 550–561. <https://doi.org/10.3390/prosthesis5020038>

Academic Editor: Jeroen Bergmann

Received: 24 April 2023

Revised: 26 May 2023

Accepted: 31 May 2023

Published: 7 June 2023



Copyright: © 2023 by the authors. Licensee MDPI, Basel, Switzerland. This article is an open access article distributed under the terms and conditions of the Creative Commons Attribution (CC BY) license (<https://creativecommons.org/licenses/by/4.0/>).

1. Introduction

Flat foot and high arch problems are very common and have a high prevalence rate. These foot disorders are mainly congenital or hereditary in nature, with other causes being injuries (acquired or acute), rheumatoid arthritis, diabetes, or Achilles tendon injury. These fallen arches often tend to affect the bones and joints of the foot and ankle complex, resulting in pain and discomfort. While for athletes, Achilles tendinopathy and plantar fasciitis were amongst the most common injuries suffered [1]. With growing age, this pain can be observed at the ankle joint, midfoot, knee joint, hip joint as well as lower back of the patient. Increased foot pronation/supination, overweight, intrinsic muscle weakness, and improper footwear alter foot biomechanics. These risk factors cause repetitive tensile stresses on the fascia resulting in microtrauma at its origin, pain, and functional disability [2]. This associated pain has a detrimental impact on health and limits the ability to participate in physical activity and affects productivity. While congenital flat feet or high arches cannot be cured completely, orthoses have been found useful to “correct” foot biomechanics and delay the above-mentioned problems that can arise over time. For patients with diabetic/neuropathic feet, podiatry elements of the insoles, such as a metatarsal bar, metatarsal pad, and weight off-loader rings are useful in the prevention as well as curing of foot ulceration [3]. Orthotic insoles have been prescribed over the years and were made up of cork, leather, rubber, and various types and densities of foam material but have the shortcomings of high labor and time costs. Moreover, customization via digital technology can rarely be achieved in the conventional way of orthosis design. Advanced

rapid prototyping technology allows precise and effective solutions, such as 3d-printed insoles. Fused Deposition Modeling (FDM) technology was found useful in designing full contact and orthopedic insoles that provide custom density, allowing excellent shock absorption for the prevention of injury. Foot orthoses with shock absorption were found to provide a 28% reduction in the risk of developing an overall injury and a 41% reduction in the risk of developing a lower limb stress fracture [1]. For designing a custom insole, various parameters need to be taken into account, of which plantar pressure data (for flat foot/high arch as well as patients with diabetic foot) is the most crucial. This data provides static as well as dynamic reports that need to be considered while designing a customized insole. Plantar pressure relief is sensitive to orthotic design decisions that can be achieved in 3d-printed insoles by selecting different densities referring to plantar pressure mapping [3]. Materials such as Polyurethane (including PORON[®]), polyethylene (including Plastazote[®]), and Ethylene Vinyl Acetate (EVA) reduce peak pressure beneath varying regions of the foot. Materials were found to influence plantar pressures affecting force and contact area (dependent on the hardness, density, thickness, and ability to contour to the foot) [4]. Three-dimensional-printed insoles designed for this study used variable density in the base insole (Thermoplastic Polyurethane (TPU) material) and top layers of PORON and EVA to combine its effects. Anatomical 3D-printed insoles can be total contact, podiatric, or orthopedic in nature. Being in direct contact with the foot, it supports the body weight, thereby correcting the biomechanical force distribution. Figure 1 shows a plantar pressure scan of one of the subjects involved in this study. It can be seen that the weight distribution in the static position is slightly unbalanced: 48% on the left foot and 52% on the right. On the left foot, the weight distribution is concentrated in the heel, the metatarsal, and, to a lesser extent, the toe. Any weight-bearing excessive physical activity of such individuals can cause extreme discomfort and pain over time. Incorrect support may lead to injuries in the long term, also resulting in osteoarthritis [5].

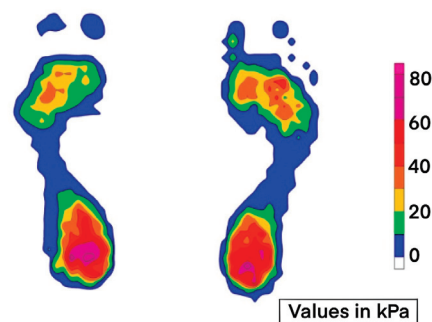


Figure 1. Plantar pressure scan. Values indicating ground reactive forces in static test. These values can be acquired for various gait events in static as well as dynamic conditions. They help in understanding the altered biomechanics of foot due to foot disorders.

Porous (or mesh) structures were used in the design of the insole as the effective Young's modulus of TPU alone is beyond the demand of alleviating plantar pressure [6]. Porous structures in the insole can be designed using CAD modeling, or advanced slicing features can be used to add areas of different densities and rigidity for shock absorption and support. This helps reduce the effective modulus, which is necessary for diabetic insoles. For the case in Figure 1, an elevation in the heel area (termed “heel rise”) will improve its midfoot contact area, thereby reducing fatigue and pain in static conditions. In dynamic conditions of the above case, better stability is achieved with heel rise provided in the insole [7]. The pattern and infill percentage affect the tensile strength, hardness, and flexure of the insole [8]. This needs to be customized for every individual by referring to their plantar pressure scans. The shore hardness value of the TPU decides the value of the infill percentage. This ultimately affects the printing time and cost of the insole. The time and cost are not only associated with the design and 3D printing but are also affected by the availability of the plantar pressure systems for data acquisition. The lack

of portability of these systems restricts the tests to laboratory or clinical environments [9]. The acquisition is also affected by the “foot targeting effect”, where the users alter their natural gait pattern in order to correctly place the foot on the platform. For designing 3D-printed insoles without any plantar pressure scan, total contact insoles are prescribed. These are developed by acquiring a 3D scan of the foot in a non-weight-bearing condition. This is digitally “corrected” using mesh tools in CAD, and a total contact insole is designed. This method is preferred mainly in patients with diabetes [10,11]. Additional podiatric elements such as metatarsal bars/pads or off-loaders can be added depending on each respective case.

This study involved designing custom 3d-printed insoles for 200 subjects (flat foot/high arch/diabetic foot and those suffering from joint pain). Using a 3D-printed insole was found to improve comfort score and foot function in individuals [12,13]. The above research findings were taken into consideration while designing these insoles for the subject. The orthoses developed included all three types: orthopedic insole (neutral correction and high arch), podiatric insoles, and total contact insoles.

2. Materials and Methods

For this study, scanning (2D and 3D), modeling, and FDM 3D-printing techniques were used. For data acquisition, 2D pressure plantar system (with 3000 and 5000 sensors) and a 3D scanner (Occipital Structure Sensor) were used. This study is based on the previous (undocumented) part of research work on the interdisciplinary design aspects of custom 3d-printed insoles using plantar pressure mapping. It consisted of 10 patients (a mix of flat foot/diabetic foot ulcer and joint pain) as subjects. After a 6-month follow-up and various trials and validation, the same study was scaled up to include a larger number of subjects to understand the commercial viability and potential of FDM as a low-cost solution in foot orthoses. This study was carried out at a leading orthopedic and rehabilitation hospital in Pune, India.

2.1. Participant Requirement

As a succession to the unpublished research work mentioned above, this study was targeted toward users with foot-related disorders, users who experienced pain in ankle, knee, hip, and lower back joints, and patients with diabetic foot conditions. This research study required 2D plantar pressure scans with patient history and, in some cases (diabetic foot/ulcers/corns, etc.), 3D scanning. Users were briefed about the research aspect and were informed about the follow-up procedure that was needed for further documentation and analysis.

2.2. Insole Design and Development

The most important part of customized 3d-printed insole design is the acquisition of the data for reference design (Figure 2). This data can be qualitative as well as quantitative.

2.2.1. Foot Scan and Acquisition

Plantar pressure measurements were recorded for each patient for static and dynamic analysis. Stabilometry test data was also recorded as a part of static foot pressure analysis. This data forms the quantitative feedback for insole design. Plantar pressure measurement was taken for all 200 users. Foot health practitioners provided clinical assessment data. Figure 3 shows the 2D scan for patients. For patients with diabetic foot ulcers, additional 3D scan was required and is must for developing total contact insoles. (A total contact insole is a Boolean subtraction of the 3D foot scan and arch support insole).

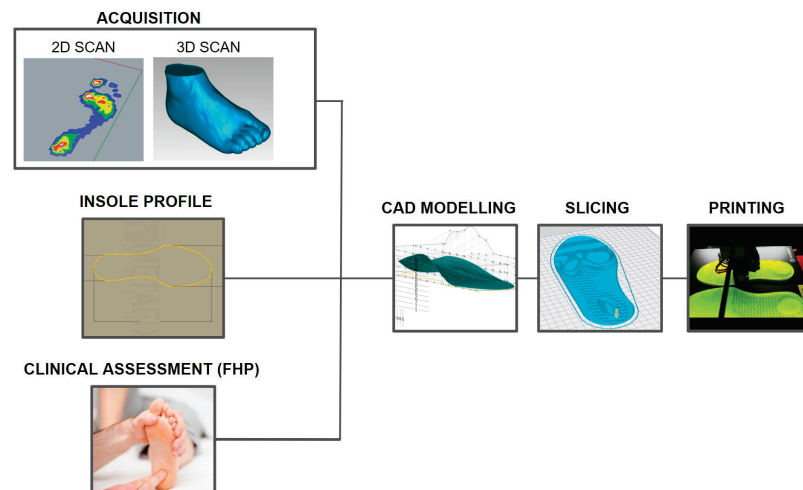


Figure 2. Manufacturing workflow for designing customized 3d-printed insoles.

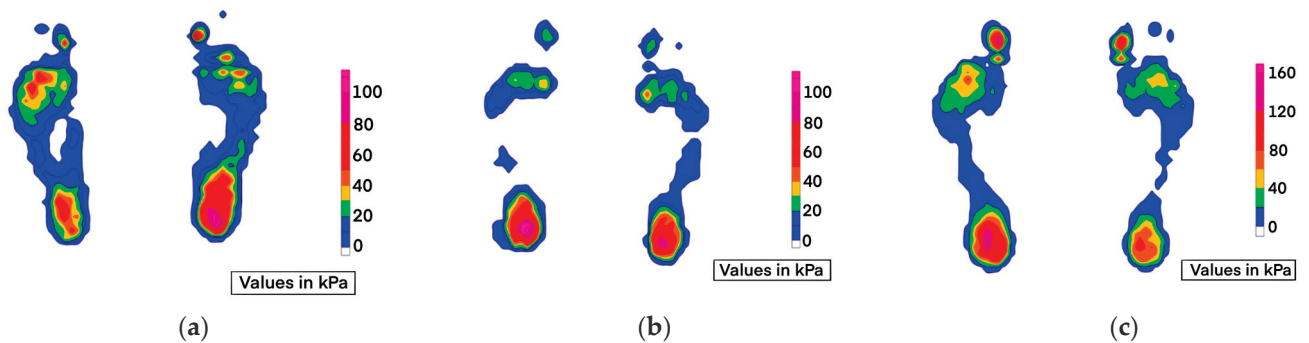


Figure 3. Static scan <age–gender–diagnosis–Body Mass Index> (a) 38Y–F–Overpronation–Arthritis (BMI 20); (b) 14Y–F–Overpronation–Knee Hyperextension–Flexible Flat Foot (BMI 28); (c) 28Y–M–Acquired Flat Foot–Badminton Player (BMI 21).

Apart from the static data, the dynamic data also provide important information about the gait parameters, as shown in Figure 4. Dynamic data is required when designing insoles for sports people or athletes who often come across high ground reactive forces (GRF). Figure 5 shows the gait response while walking. Abnormality can be clearly seen in weight-loading forces.

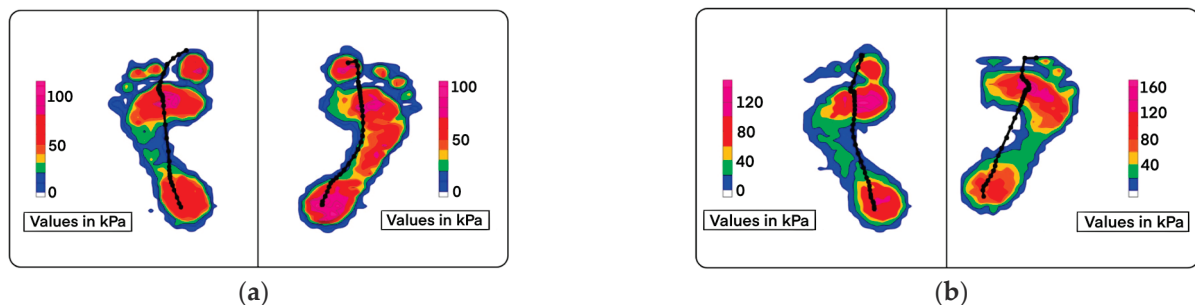


Figure 4. Dynamic scan <age–gender–diagnosis–Body Mass Index> (a) 44Y–M–Rigid Flat Foot (BMI 27); (b) 35Y–M–Overpronation (BMI 25).

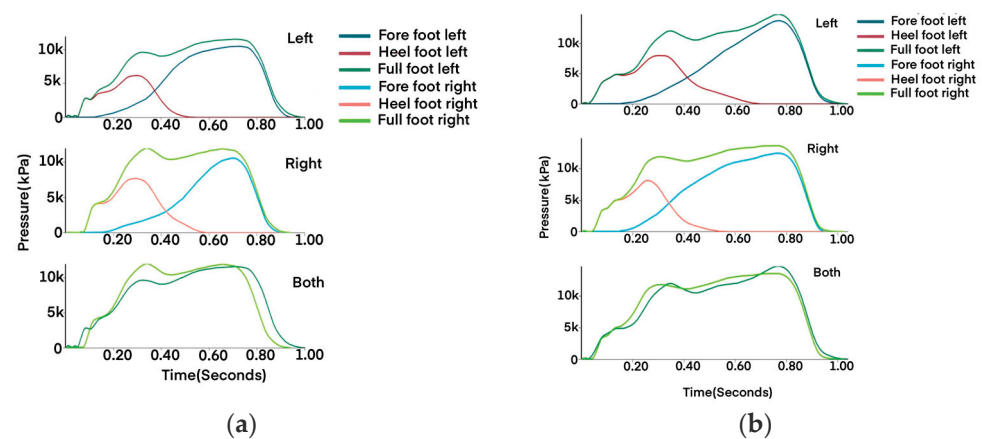


Figure 5. Weight-loading curve for dynamic scan in Figure 4. (a) 44Y-M-Rigid Flat Foot (BMI 27); (b) 35Y-M-Overpronation (BMI 25). In both cases, lower load values at heel contact are seen as a natural response of the body to overcome heel pain (resulting from static conditions).

2.2.2. Insole Design

For designing a custom 3d-printed insole, five key parameters are taken into consideration: heel cup, medial arch height, lateral wedge height, density, and heel raise. These parameters can be applied when designing orthopedic and podiatric insoles. Total contact insole does not require this level of customization at this stage (CAD design) but is modified during the “slicing” phase of file conversion. CAD software (SolidWorks 2020, Dassault Systemes, Vélizy-Villacoublay, France), was used for designing.

For custom fit, shoe insole is required to make the base profile. For patients with over-pronation, “neutral” correction insoles are recommended. Based on the previous study, it was found that over-pronated patients experience pain in static conditions such as standing when natural correction is provided. (Neutral correction is the term that we have used that reflects 75–80% of the natural correction height for medial arch support.) Figure 6 shows the CAD design parameters of foot contour profile for neutral correction at medial arch but elevated lateral wedge support.

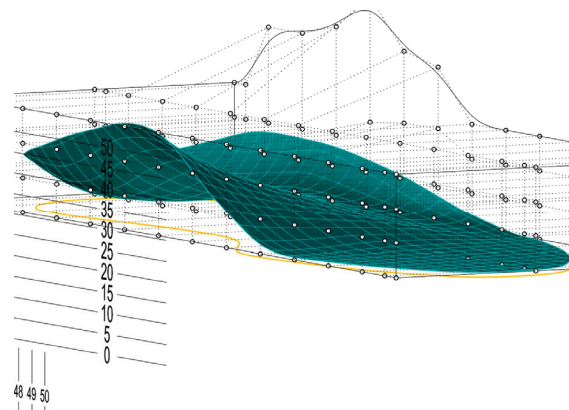


Figure 6. CAD modeling: Parametric modeling is used to define the insole form. Focus is on the design of mid-foot and hind-foot anatomical structure support. Bounding box pattern allows for contour adjustment of the profile (the numbers represent the scale in millimeters used as a reference for design and modification).

2.2.3. Slicing

This is the last stage in the manufacturing flow. Slicing is a process where a graphical layer-by-layer code format is generated for the CAD design. This software slices the object model into multiple layers that can be 3D printed. Slicing parameters provide the flexibility

of adjusting the “Density” of the insole, which can be mono-pattern or have multi-patterns in the final print. The density does not depend alone on the slicer settings but also on various other factors (nature of the foot problem, Body Mass Index (BMI), type of filament, and type of the insole). This directly affects the printing time and cost of the insole. TPU material is very difficult to print; hence, the topology of the printer plays an important role in achieving successful printing. Figure 7 shows the “parameters” that are important in customization.

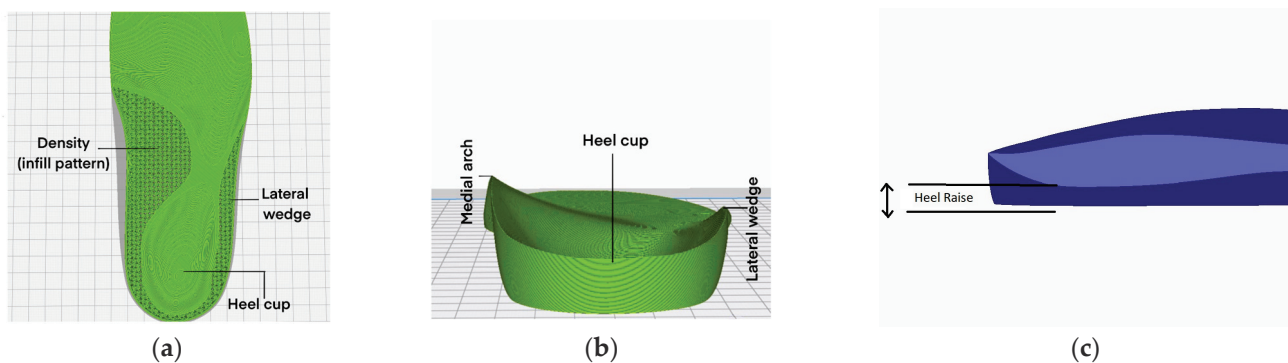


Figure 7. (a) Insole slicing profile showing the infill pattern; (b) the podiatric parameters in insole design (back view); (c) heel raise (X-Ray side view of the hind part).

For orthopedic insoles, it is of utmost importance to maintain the smooth contour shape of the insole. This reduces any discomfort that may otherwise result while wearing an orthosis. Figure 8 shows the contour analysis (zebra lines) that shows the smooth transition of the podiatric elements.



Figure 8. Contour profile for orthopedic insoles. In neutral correction insoles, metatarsal bars/pads are not provided.

2.2.4. Three-Dimensional Printing and Post-Processing

Every user was given a customized 3D-printed insole for trial and validation. The diagnosis and data acquisition were carried out as explained in the above sections. Six 3D printers, FDM (JGmaker, Ultimaker, and Raise3D printers), Cartesian, and Core-XY topology, were used for printing 200 insoles. In Core-XY system, the belt moves the print head along X and Y coordinates, reducing the moving mass while printing the object, whereas in Cartesian, the print bed moves, making it less stable mechanism. As TPU material is difficult to print, direct extrusion printers can be considered for printing. Two types of TPU material were used for printing the insoles of 90A and 95A shore hardness. The prints from the TPU filament diameter of 1.75 and 2.85 were similar and showed no or little difference. There was more post-processing for the Cartesian style printers compared to finer finished Core-XY print. Post-processing involved grinding, buffing, and pasting of padding sheets as a top layer of the insole. The padding sheet used was of EVA sheet (1 mm and 2 mm thick) and PORON sheet (2 mm thick). These materials combined with

the correct slicing parameters showed excellent durability and satisfactory improvement rate of over 95% of the validated trials [14]. In few users, as a special request, suede leather was used as a padding material. Every insole was post-processed and fitted in shoes of the users by certified prosthetist and orthotist.

2.3. Tools and Procedure

For the analysis of the conditions post use of these 3d-printed insoles, the standard American Orthopaedic Foot and Ankle Society (AOFAS) Ankle-Hindfoot score was used. This scale includes 9 items that are further divided into 3 sub-scales of pain, function, and alignment. Having patient-reported and physician-reported parts, it is assessed on the final score for the user, ranging from 0 to 100. Lower score indicates severe pain and impairment, while a high score indicates no pain symptoms or impairment. The pain subscale consists of maximum of 40 points, indicating no pain. Functionality is assessed over seven items, with a maximum score of 50 points. Alignment subscale has a maximum score of 10 points.

3. Results

This study was carried out on 200 subjects with varying foot-related problems, and customized 3d-printed insoles were fitted into their daily use footwear (this study is restricted to the use of 3d-printed insoles fitted in the “shoe” and not sandals, as the shoe provides ankle and navicular stability that is required for patients with the overpronated flat foot condition). The designed insoles and fitment for this study are shown in Figure 9.

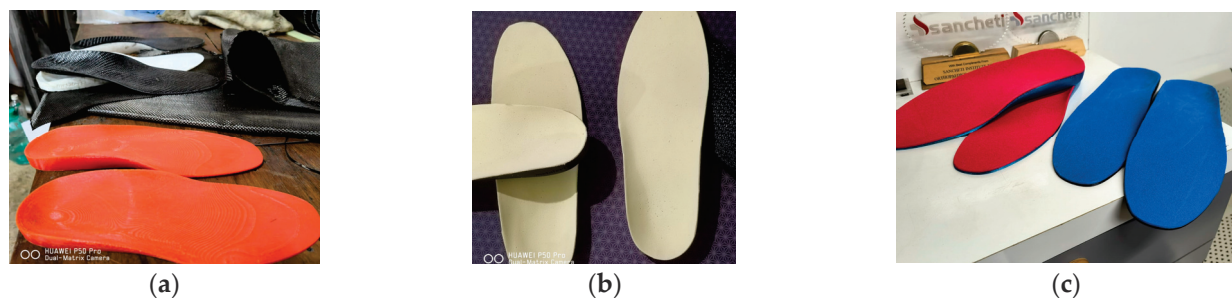


Figure 9. Customized insoles: (a) raw 3d-printed insoles; (b) EVA foam-padded insoles; (c) PORON foam-padded insoles.

The following section describes the insole fitting and results post usage for the subjects. The data covers the feedback score for custom 3D-printed insoles after a minimum of 6 months of daily usage. Telephone follow-up was conducted every month for the first six months. As a continuation of this research study, a follow-up clinical examination after every four months was carried out. These subjects were evaluated based on the AOFAS Ankle-Hindfoot scale. A descriptive statistical analysis is made on the findings of this research study.

3.1. Flat Foot, High Arch

Out of the 200 users, 166 were diagnosed with a flat foot condition (overpronation, flexible flatfoot, rigid flatfoot, or hallux valgus), and 16 were diagnosed with a high arch. This included users from the age group of 12 years to 77 years. Many complained about some or another sort of joint pain, and some were advised by doctors for orthoses. Qualitative and quantitative analysis diagnosed them with flat foot and high arch problems. The navicular drop was the most common problem seen in patients with hyperlaxity. Hallux valgus was persistent in more than 90% of patients with overpronation. The lateral wedge in the insole was found to be the most efficient and comfortable as it provided stability and correction for navicular drop [15,16]. High-ankle shoes with 3D-printed insoles were prescribed to these patients. Shoes with wider toe boxes and rigid medial and lateral

supports were prescribed. Cloth material/cotton slip-ons were strictly not recommended for any of the patients.

3.2. Diabetic/Neuropathic Foot

Diabetic-specific 3d-printed insoles were fitted to 18 users. This included patients from the 38–69 years age group. A study based on the Finite Element (FE) approach used soft plugs in areas with high plantar pressure (in patients with diabetes) and tested it for various Young's moduli [17]. Slicing options in 3D printing allow variable density printing, thereby avoiding the need to use any extra material for diabetic insole fabrication. Elements for corn pressure relief, metatarsal bar, and pads were included in the insole design. The top layer of the PORON sheet helps reduce peak pressure points. This padding increases the durability of the insoles and can be replaced if needed. Abandonment was found in two patients, and both had three ulcers and lived with obesity.

3.3. Patients with Joint Pain

Altered biomechanics of the foot and ankle complex can lead to joint pain (ankle, midfoot, knee, hip, and lower back pain). Of the 200 subjects in this study, 126 patients had visited the doctor to address the joint pain they suffered, totally unaware of their foot condition. This shows unawareness about foot and ankle problems, as joint pains are often seen and treated as orthopedic problems, totally ignoring the foot diagnosis. The effects of 3D-printed insoles on this set of users who already faced joint pain are presented separately in the results section.

Table 1 shows the AOFAS score of the patients. The scores assessment showed that more than 90% of the patients experienced pain, discomfort, and limited functionality.

Table 1. AOFAS Ankle-Hindfoot score before use of insole.

Type	Number	Score			
		A (>90)	B (75–90)	C (50–75)	D (<50)
Flexible Flat Foot	96	3	62	29	2
Rigid Flat Foot	29	1	13	8	7
Overpronated	41	6	20	6	9
High Arch	16	2	8	3	3
Diabetic (with corn/ulcers)	12	0	5	6	1
Diabetic (without ulcers)	6	1	3	2	0
Total	200	13	111	54	22

AOFAS Ankle-Hindfoot score: A (Excellent), B (Good), C (Poor), and D (Bad).

Overall, 22 subjects showed poor scores, a maximum from rigid flat foot and overpronated foot problems. The clinical examination followed up post six months showed much-improved scores on the AOFAS scale. Table 2 shows the scores after a minimum of 6 months of usage.

A substantial improvement in the scores was observed after using the customized 3D-printed insoles. For a flexible flat foot, the height of the medial arch was kept at 100% of the expected correction. The medial arch infill was selected at the lowest possible acceptable rigidity value. A total of 93% of the AOFAS scores for this group were found to be excellent and good, compared to 65% before the use of the insoles. In the case of rigid and overpronated cases, 75% of the expected correction height was provided for the medial arch, with semi-rigid support. This approach helped improve the AOFAS “Excellent” score from 14% to 65%.

For patients suffering from joint pain due to foot problems, insoles were designed specifically for their physical activities.

Table 2. AOFAS Ankle-Hindfoot score after use of insole for minimum of six months.

Type	Number	Score			
		A (>90)	B (75–90)	C (50–75)	D (<50)
Flexible Flat Foot	96	69	20	7	0
Rigid Flat Foot	29	17	8	2	2
Overpronated	41	28	11	1	1
High Arch	16	9	7	0	0
Diabetic (with corn/ulcers)	12	6	4	1	1
Diabetic (without ulcers)	6	3	3	0	0
Total	200	132	53	11	4

AOFAS Ankle-Hindfoot score: A (Excellent), B (Good), C (Poor), and D (Bad).

Table 3 shows AOFAS scores for subjects with persistent pain. Many complained about their restricted ability to participate in activities (few subjects involved in high GRF sports).

Table 3. AOFAS Ankle-Hindfoot score before use of insole, for subjects with persistent pain.

Type	Number	Score			
		A (>90)	B (75–90)	C (50–75)	D (<50)
Midfoot Pain	48	10	26	11	1
Ankle Pain	36	6	13	14	3
Knee Pain	32	3	8	20	1
Hip and Lower Back Pain	10	0	6	2	2
Total	126	19	53	47	7

AOFAS Ankle-Hindfoot score: A (Excellent), B (Good), C (Poor), and D (Bad).

Table 4 shows the scores after the use of insoles. While the scores improved, activities that involved jumps and high values of GRF witnessed instability while using the insoles.

Table 4. AOFAS Ankle-Hindfoot score after use of insole for minimum of six months, for subjects with persistent pain.

Type	Number	Score			
		A (>90)	B (75–90)	C (50–75)	D (<50)
Midfoot Pain	48	30	18	0	0
Ankle Pain	36	25	8	1	2
Knee Pain	32	22	8	1	1
Hip and Lower Back Pain	10	6	3	1	0
Total	126	83	37	3	3

AOFAS Ankle-Hindfoot score: A (Excellent), B (Good), C (Poor), and D (Bad).

Around 96% of the subjects reported relief from joint pain post use of insoles. Overall improvement of 93% was observed with patients using the insole for more than 5 h (average weight-bearing time), while 5% (suffering from ankle, knee, and lower back pain) reported a slight improvement in their conditions. Hallux valgus cases showed substantial improvement post 2 months of usage of the insoles and prescribed footwear. Among the 200 subjects, 17 subjects wanted softer insoles, while many expressed their desire to have an insole that can fit multiple shoes. There were two cases of abandonment of insoles observed, both amongst patients with diabetic foot ulcers. Four insoles were replaced in the first month's post fitting due to design-level errors. Three-dimensional-printed insoles customized and developed following the above procedure (plantar pressure assessment, different levels of customization and design, and use of TPU and PORON) have been found to be effective, durable as well as affordable. After the follow-up clinical

examination (6 months), the curative effects of customized 3d-printed insoles are found to be satisfactory with promising results and should soon surpass the traditional insole manufacturing process.

4. Discussion

In this research study, customized insoles were designed, developed, tested, and validated to treat foot-related musculoskeletal ailments in patients, as well as patients with diabetic foot problems. A detailed process from assessment, data acquisition, CAD design, slicing, and printing was optimized to develop these insoles. The reason for post-processing techniques was to enhance durability, flexibility, and comfort for the end user. The methodology explains the FDM technique for 3D printing, but the customized insoles can be manufactured via various 3D printing techniques. FDM is effective for the insoles to be used in daily routine life. They are found to be effective in alleviating pain arising from static weight-bearing activity as well as walking. The SLS method is preferred for high GRF activities where the design of the insole is of “extrusion” type. The extrusion type of insole is primarily a 2–3 mm thick foot profile contour (similar to Figure 6 with added thickness). This mechanical form helps provide support to the arch as well as store and release energy during the gait cycle. The static, as well as dynamic, assessment can help in further customizing the 3D-printed insole for activity-specific use. High variations in foot pressure distribution were observed in the users, with higher plantar pressure in patients with diabetes compared to healthy, non-diabetic patients with foot problems. This signifies the prevalence of foot ulcer problems in patients with diabetes. A research study based on an in-shoe pressure measurement device reported a similar finding [18]. These devices can be used to assess the forces acting at the interface of the plantar fascia and the 3D-printed insole and understand the cause of corns and ulcers in diabetic patients. Custom 3d-printed insoles can, thus, be prescribed to treat a variety of foot problems that may lead to musculoskeletal ailments in healthy public as well as in patients with diabetic foot.

4.1. Limitations

While extrusion-type insoles can universally fit in footwear, the TPU-based solid insole has its limitations. It is a universal problem as various shoe manufacturers have different shoe sole profiles. Any dimensional tolerance of more than 3 mm inside the shoe will make it uncomfortable for the user. It is important to note that none of the footwear prescribed or fitted with insole during this study had a ready arch support or a very narrow midfoot insole profile. The reason behind not prescribing narrow midfoot sports shoes is that the insoles are not able to provide the required vertical support, as narrower midfoot means the arch structure becomes unstable and ultimately collapses on the sidewalls of the shoe.

4.2. Conclusions

The custom 3D-printed insoles designed and prescribed to the users provided biomechanical correction and were found to be useful in alleviating pain caused by foot problems. The durability of 3D-printed insoles can be exceptionally good with certain precautionary measures taken by the users. TPU insoles must not be exposed to water, as it will affect their elasticity performance; moreover, the internal infill structures will not work as expected. Few of the subjects from the above study tend to use these insoles (21 months since the beginning of the study in June 2021), and no visible deformation is seen (except in two cases where the shoes got wet; TPU can attract moisture resulting in temporary deformation of the shape). For subjects with higher BMI, it is advised to replace the insoles after 18 months of regular use. The scope of this paper was limited to FDM printed insoles, but a similar flow can be used to design insoles using SLA, PolyJET, and SLS technology.

Author Contributions: Conceptualization, Validation, Design, Printing: S.S.; Analysis, Investigation, Assessments, and Comparative Analysis: S.S. and B.J.; Writing, Review, Editing, Supervision: S.S. and A.C. All authors have read and agreed to the published version of the manuscript.

Funding: This research received no external funding.

Institutional Review Board Statement: This study was approved by the Research Review Committee (Ethical Clearance (Non-Invasive-Survey based trials)) by Vikalp Rehabilitation Center (Application: APR_0221/5 April 2021).

Informed Consent Statement: Informed consent was obtained from all subjects involved in the validation.

Data Availability Statement: Data for the conducted trials can be obtained via email at 3drs@metafix.io. The data is made available upon request and only for research and academic use.

Acknowledgments: This study was largely supported by Rahul Saroj and Sushant Raut, experienced prosthetists and orthotists whose help made the trials be conducted in the given time. Shalini Balgude and Hrishikesh Garud, biomedical engineers with a specialization in Biomechanics, provided design and printing support.

Conflicts of Interest: The authors declare no conflict of interest.

References

1. Bonanno, D.; Landorf, K.B.; Munteanu, S.; Murley, G.S.; Menz, H. Effectiveness of foot orthoses and shock-absorbing insoles for the prevention of injury: A systematic review and meta-analysis. *Br. J. Sports Med.* **2017**, *51*, 86–96. [CrossRef] [PubMed]
2. Yildiz, S.; Sumer, E.; Zengin, H.Y.; Bek, N. Intensive physiotherapy versus home-based exercise and custom-made orthotic insoles in patients with plantar fasciitis: Pilot study. *Foot* **2022**, *51*, 101906. [CrossRef] [PubMed]
3. Martinez-Santos, A.; Preece, S.; Nester, C.J. Evaluation of orthotic insoles for people with diabetes who are at-risk of first ulceration. *J. Foot Ankle Res.* **2019**, *12*, 35. [CrossRef] [PubMed]
4. Gerrard, J.M.; Bonanno, D.R.; Whittaker, G.A.; Landorf, K.B. Effect of different orthotic materials on plantar pressures: A systematic review. *J. Foot Ankle Res.* **2020**, *13*, 35. [CrossRef] [PubMed]
5. Davia-Aracil, M.; Hinojo-Pérez, J.J.; Jimeno-Morenilla, A.; Mora-Mora, H. 3D printing of functional anatomical insoles. *Comput. Ind.* **2018**, *95*, 38–53. [CrossRef]
6. Ma, Z.; Lin, J.; Xu, X.; Ma, Z.; Tang, L.; Sun, C.; Li, D.; Liu, C.; Zhong, Y.; Wang, L. Design and 3D printing of adjustable modulus porous structures for customized diabetic foot insoles. *Int. J. Lightweight Mater. Manuf.* **2019**, *2*, 57–63. [CrossRef]
7. Jin, H.; Xu, R.; Wang, S.; Wang, J. Use of 3D-Printed Heel Support Insoles Based on Arch Lift Improves Foot Pressure Distribution in Healthy People. *Experiment* **2019**, *25*, 7175–7181. [CrossRef] [PubMed]
8. Yarwindran, M.; Sa'aban, N.A.; Ibrahim, M.; Periyasamy, R. Thermoplastic elastomer infill pattern impact on mechanical properties 3D printed customized orthotic insole. *ARPN J. Eng. Appl. Sci.* **2016**, *11*, 6519–6524.
9. Leal-Junior, A.G.; Díaz, C.R.; Marques, C.; Pontes, M.J.; Frizzera, A. 3D-printed POF insole: Development and applications of a low-cost, highly customizable device for plantar pressure and ground reaction forces monitoring. *Opt. Laser Technol.* **2019**, *116*, 256–264. [CrossRef]
10. Zuñiga, J.; Moscoso, M.; Padilla-Huamantínco, P.G.; Lazo-Porras, M.; Tenorio-Mucha, J.; Padilla-Huamantínco, W.; Tincopa, J.P. Development of 3D-Printed Orthopedic Insoles for Patients with Diabetes and Evaluation with Electronic Pressure Sensors. *Designs* **2022**, *6*, 95. [CrossRef]
11. Singh, S.; Mali, H.S. 3D printed orthotic insoles for foot rehabilitation. In *3D Printing in Podiatric Medicine*, 1st ed.; Sandhu, K., Singh, S., Eds.; Academic Press: Cambridge, MA, USA, 2023; pp. 211–219. [CrossRef]
12. Daryabor, A.; Kobayashi, T.; Saeedi, H.; Lyons, S.M.; Maeda, N.; Naimi, S.S. Effect of 3D printed insoles for people with flatfeet: A systematic review. *Assist. Technol.* **2022**, *35*, 169–179. [CrossRef] [PubMed]
13. Jin, H.; Xu, R.; Wang, J. The Effects of Short-Term Wearing of Customized 3D Printed Single-Sided Lateral Wedge Insoles on Lower Limbs in Healthy Males: A Randomized Controlled Trial. *Experiment* **2019**, *25*, 7720–7727. [CrossRef] [PubMed]
14. Wang, Y.; Jiang, W.; Gan, Y.; Yu, Y.; Dai, K. Clinical Observation of 3D Printing Technology in Insoles for Flexible Flatfoot Patients. *J. Shanghai Jiaotong Univ. Sci.* **2021**, *26*, 398–403. [CrossRef]
15. Jandova, S.; Mendricky, R. Benefits of 3D Printed and Customized Anatomical Footwear Insoles for Plantar Pressure Distribution. *3D Print. Addit. Manuf.* **2022**, *9*, 547–556. [CrossRef] [PubMed]
16. Hsu, C.Y.; Wang, C.S.; Lin, K.W.; Chien, M.J.; Wei, S.H.; Chen, C.S. Biomechanical Analysis of the FlatFoot with Different 3D-Printed Insoles on the Lower Extremities. *Bioengineering* **2022**, *9*, 563. [CrossRef] [PubMed]

17. Geiger, F.; Kebbach, M.; Vogel, D.; Weissmann, V.; Bader, R. Efficient Computer-Based Method for Adjusting the Stiffness of Subject-Specific 3D-Printed Insoles during Walking. *Appl. Sci.* **2023**, *13*, 3854. [CrossRef]
18. Gupta, S.; Jayaraman, R.; Sidhu, S.S.; Malviya, A.; Chatterjee, S.; Chhikara, K.; Singh, G.; Chanda, A. Diabot: Development of a Diabetic Foot Pressure Tracking Device. *J* **2023**, *6*, 32–47. [CrossRef]

Disclaimer/Publisher’s Note: The statements, opinions and data contained in all publications are solely those of the individual author(s) and contributor(s) and not of MDPI and/or the editor(s). MDPI and/or the editor(s) disclaim responsibility for any injury to people or property resulting from any ideas, methods, instructions or products referred to in the content.

Systematic Review

The Role of Ankle–Foot Orthoses in Improving Gait in Children and Adolescents with Neuromotor Disability: A Systematic Review and Meta-Analysis

Silvia Faccioli ^{1,*}, Giulia Tonini ², Elena Vinante ³, Alessandro Ehsani ⁴, Eleonora Pellarin ⁵, Giuliano Cassanelli ⁶, Francesca Malvicini ⁶, Silvia Perazza ¹, Francesco Venturelli ⁷, Andrea Guida ^{7,8} and Silvia Sassi ¹

- ¹ Pediatric Rehabilitation Unit, Azienda Unità Sanitaria Locale IRCCS of Reggio Emilia, 42122 Reggio Emilia, Italy; silvia.perazza@ausl.re.it (S.P.); silvia.sassi@ausl.re.it (S.S.)
- ² Department of Biomedical and Neuromotor Sciences, Alma Mater Studiorum, University of Bologna, 40126 Bologna, Italy; giulia.tonini@studio.unibo.it
- ³ Pediatric Rehabilitation Unit IAFC ULSS 2 of Treviso, 31100 Treviso, Italy; elena.vinante@aulss2.veneto.it
- ⁴ Physical Medicine and Rehabilitation Unit, Sant'Andrea Hospital, Sapienza University of Rome, 00189 Rome, Italy; alessandro.ehsani@uniroma1.it
- ⁵ Physical Medicine and Rehabilitation Unit, Policlinico San Marco, 30173 Venezia, Italy; eleonorapellarin@gmail.com
- ⁶ Department of Mental Health and Pathological Addictions, Azienda Unità Sanitaria Locale of Piacenza, 29121 Piacenza, Italy; g.cassanelli@ausl.pc.it (G.C.); f.malvicini@ausl.pc.it (F.M.)
- ⁷ Epidemiology Unit, Azienda Unità Sanitaria Locale IRCCS of Reggio Emilia, 42122 Reggio Emilia, Italy; francesco.venturelli@ausl.re.it (F.V.); andrea.guida@ausl.re.it (A.G.)
- ⁸ Medical Specialization School of Hygiene and Preventive Medicine, University of Florence, 50121 Florence, Italy
- * Correspondence: silvia.faccioli@ausl.re.it or silviaeffe73@gmail.com; Tel.: +39-0522-296208

Abstract: Background/Objectives: International guidelines recommend the use of orthoses in subjects with cerebral palsy (CP), even though there is limited evidence of their effectiveness. Little is known about their effectiveness in children and adolescents with other types of neuromotor disability. **Methods:** The review protocol was recorded on the PROSPERO register (CRD42024509165) and conformed to the PRISMA guidelines. The inclusion criteria were any type of ankle–foot orthoses (AFOs); pediatric subjects with any non-acquired neuromotor disease; any type of outcome measure regarding gait performance; controlled studies; and those in the English language. Screening, selection, risk of bias assessment, and data extraction were performed by a group of independent researchers. **Results:** Fifty-seven reports were included, with most regarding CP; three involved subjects with Charcot–Marie–Tooth disease or Duchenne dystrophy. Nine were RCTs. A meta-analysis was performed for studies including subjects with CP. The meta-analysis demonstrated the effectiveness of AFOs in increasing stride length (MD −10.21 [−13.92, −6.51]), ankle dorsiflexion at IC (MD 9.66 [7.05, 12.27]), and peak ankle DF in stance (MD 5.72 [2.34, 9.09]) while reducing cadence (MD 0.13 [0.06, 0.17]) and the energy cost of walking (MD −0.02 [−0.03, −0.00]). The peak ankle power generated at push-off was significantly increased with flexible AFOs compared to rigid AFOs (MD 0.38 [0.30, 0.46]), but it decreased with both compared to walking barefoot or with shoes (MD −0.35 [−0.49, −0.22]). Evidence regarding DMD and CMT was limited but suggested opting for individualized flexible AFOs, which preserved peak ankle power generation. **Conclusions:** AFOs improve gait performance in CP. Flexible AFOs are preferable because they preserve the peak ankle power generated at push-off compared to rigid AFOs.

Academic Editor: Arnab Chanda

Received: 1 December 2024

Revised: 11 January 2025

Accepted: 15 January 2025

Published: 28 January 2025

Citation: Faccioli, S.; Tonini, G.; Vinante, E.; Ehsani, A.; Pellarin, E.; Cassanelli, G.; Malvicini, F.; Perazza, S.; Venturelli, F.; Guida, A.; et al. The Role of Ankle–Foot Orthoses in Improving Gait in Children and Adolescents with Neuromotor Disability: A Systematic Review and Meta-Analysis. *Prosthesis* **2025**, *7*, 13. <https://doi.org/10.3390/prosthesis7010013>

Copyright: © 2025 by the authors. Licensee MDPI, Basel, Switzerland. This article is an open access article distributed under the terms and conditions of the Creative Commons Attribution (CC BY) license (<https://creativecommons.org/licenses/by/4.0/>).

Keywords: orthotic device; walking; gait analysis; rehabilitation; cerebral palsy; gait disorders; neurologic; neuromuscular diseases; muscular dystrophies; hereditary sensory and motor neuropathy; foot orthoses

1. Introduction

Australian CPG [1] guidelines and Italian care pathways [2] recommend the use of orthoses (either functional or positional) in patients with cerebral palsy, even though both declare that there is limited evidence of their effectiveness. Previous systematic reviews (SRs) have explored the role of orthoses in improving gait and gross motor performance in patients with cerebral palsy. Aboutarabi et al. [3] reviewed studies on gait improvement in patients with cerebral palsy walking with ankle–foot orthoses (AFOs), but the search was limited to 2007–2015. Lintanf et al. [4] extended the search to 2018 and reported significant improvements in spatial–temporal parameters (speed, step length, and cadence) and ankle dorsiflexion at initial contact and in the swing phase. Betancourt et al. [5] reviewed only prospective controlled studies published between 2001 and 2016, restricted to a minimum sample of 20 patients for non-randomized and 10 patients for randomized trials. The interventions were limited to rigid or articulated AFOs versus barefoot or shoes only as a control condition.

A recent SR by Miccinilli et al. [6] studied the literature published in 2006–2022, focusing on randomized controlled trials regarding ankle–foot or knee–ankle–foot orthoses in pediatric patients with cerebral palsy. Nonetheless, the authors included among the outcomes several outcomes beyond gait, such as trunk control, balance, the prevention of muscle contractures, and quality of life. Furthermore, most of the included studies used orthoses combined with other treatments.

In general, improvements in spatial–temporal parameters and energy expenditure are reported, but evidence specifically relating to the influence of AFOs on gait parameters needs to be updated. Furthermore, we were interested in extending this SR to other neurologic disorders limiting walking performance in children and adolescents. Similar biomechanic problems and gait patterns might occur in different pathologies, which might, hence, share the same type of orthotic approach. For this reason, we were interested in studying the role of AFOs not limited to CP and were open to the possibility of finding studies with mixed health conditions. Therefore, we performed an SR inquiring about the role of any type of ankle–foot orthoses in modifying gait performance in children or adolescents diagnosed with a neurological disease inducing motor disability.

2. Materials and Methods

The present study is a systematic review of primary studies performed according to the reporting guidelines of the PRISMA statement [7] and Cochrane’s methodological recommendation [8]. The review protocol was recorded on the PROSPERO public online register (CRD42024509165). This study was conducted according to the pre-specified protocol, except for the inclusion–exclusion criteria that were modified, limiting inclusion to controlled studies (retrospective or prospective) and excluding any other type of study; in addition, a meta-analysis was performed.

The scope of this systematic review was structured according to the PICO (patients, intervention, control, outcome) framework for intervention:

- P: children and adolescents (age 0–18 years) with neurological disease such as cerebral palsy or neuromuscular disease or spina bifida (excluding orthopedic diseases, cancer, and acquired brain injuries);

- I: the use of any type of functional ankle–foot orthoses (solid, hinged, carbon leaf, etc.);
- C: no treatment or any other treatment;
- O: a change in walking performance, measured by means of any gait parameter or outcome measure to assess gait improvement after intervention, such as velocity, stride length, or any other three-dimensional gait analysis parameter, 6 min walk test (6 MWT), or 10 m walk test (10 MWT).

The search procedures are described in Supplementary Table S1. A literature search was performed on 11 August 2023 in the following databases: PubMed, Scopus, and Cinahl. Articles were searched without limits on the year of publication, age, or language. A limit was introduced regarding the type of study, with systematic reviews, guidelines, and animal studies being excluded. Non-controlled studies, publications with samples involving adult patients, and papers in languages other than English or Italian were also excluded. Other articles were also obtained from the reference lists of the papers identified through the primary search in the databases.

According to these inclusion and exclusion criteria, all the studies were screened firstly by title/abstract and then by full text by two independent authors (SF, EV, EP, GC, FM, GT, IT, and AE). Any disagreement was resolved through discussion among the authors. Non-retrieved papers and ongoing studies were just recorded as not retrieved.

2.1. Data Extraction

Two authors independently completed the data extraction (SF, GT, IT, and AE). The authors extracted data about the study design and methodology, participant characteristics, protocol details, outcome measures, and results of the studies. Any disagreement among the authors was discussed and resolved by consensus.

2.2. Risk of Bias Assessment

The risk of bias (RoB) was assessed with a domain-based approach using the Risk of Bias in Non-randomized Studies of Interventions (ROBINS-I) [9,10] tool in controlled studies and using version 2 of the Cochrane risk-of-bias (ROB2) tool for RCTs (specific for a cross-over design) [11,12]. Two independent reviewers (SF, GT, IT, and AE) assessed the methodological quality and risk of bias of all the included studies. Any disagreement was resolved through discussion among the authors. The assessment of the RoB did not provide criteria for excluding articles but allowed for stratifying them.

2.3. Meta-Analysis

A meta-analysis was performed to pool studies reporting comparable outcomes.

Each type of ankle–foot orthosis (AFO) was compared to the control condition (bare-foot or shoes), except for the outcome “peak ankle power in pre-swing”, where an additional comparison between rigid and flexible AFOs was carried out. The heterogeneity was investigated using the I^2 test. The source of heterogeneity was investigated when appropriate. For continuous outcomes, mean differences (MDs) and their 95% confidence intervals (CIs) were calculated using the inverse variance method according to a random-effects model. For the outcomes stride length and energy cost at self-selected speed, the data were converted to a uniform unit of measurement. The pooled estimates are presented as overall and stratified by AFO type (rigid and flexible). Statistical analyses were conducted using Stata 18 software [13].

3. Results

After full text analysis, 57 studies were finally included in the review [14–70]. Figure 1 provides details about the study identification and selection (PRISMA flow diagram).

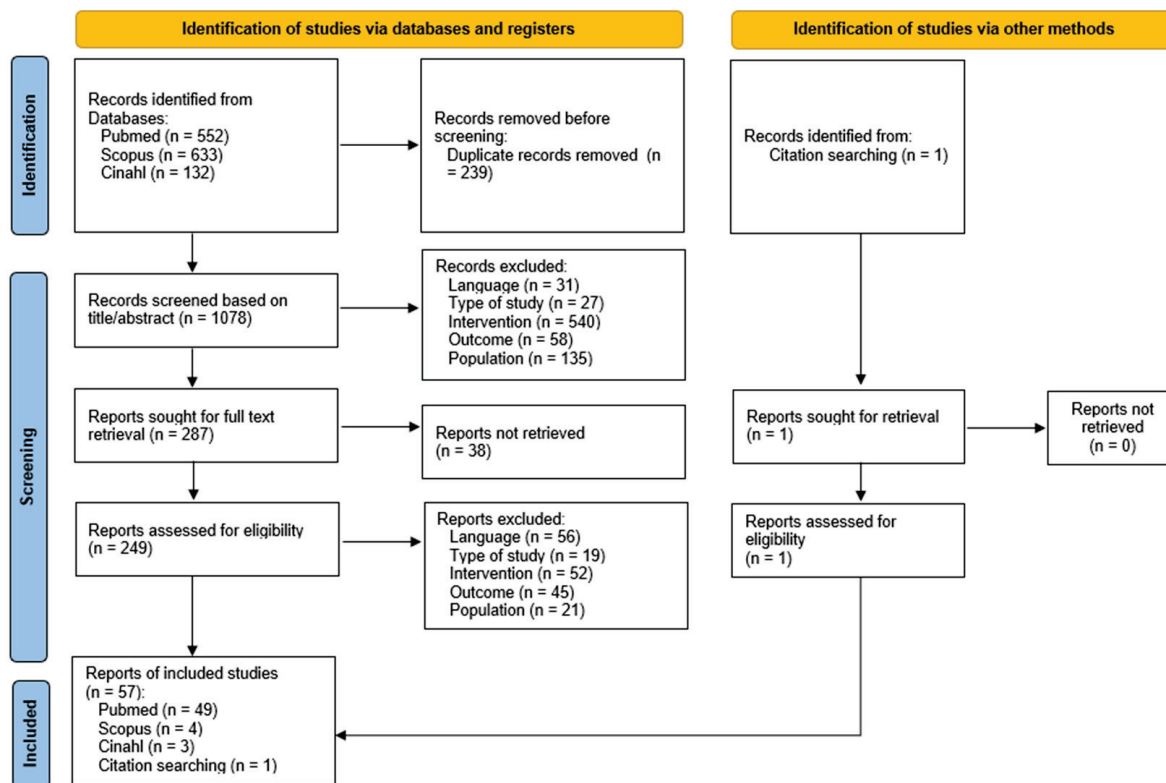


Figure 1. PRISMA flow diagram.

3.1. Risk of Bias of Included Studies

An overall synthesis of the RoB of the included studies is represented in Figures 2 and 3. Samples including a wide age range, mixed gross motor functioning levels, mixed diagnoses, and combined interventions were considered to have confounding factors. Furthermore, a lack of time interval between the gait analysis assessment in different conditions was included as a possible confounding aspect, because of the possibility of fatigue influencing the second assessment. The overall quality of non-randomized studies was low, while only some concerns were attributed to RCTs. The study by Meins et al. [67] presents bias in the selection of the reported results because the authors describe secondary results of a previously published RCT [66].

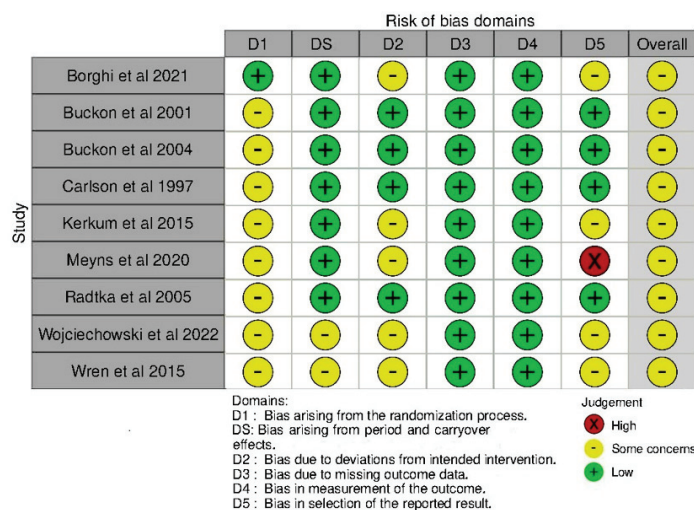


Figure 2. Risk of bias of RCT intervention studies: ROB2 plot [62–70].

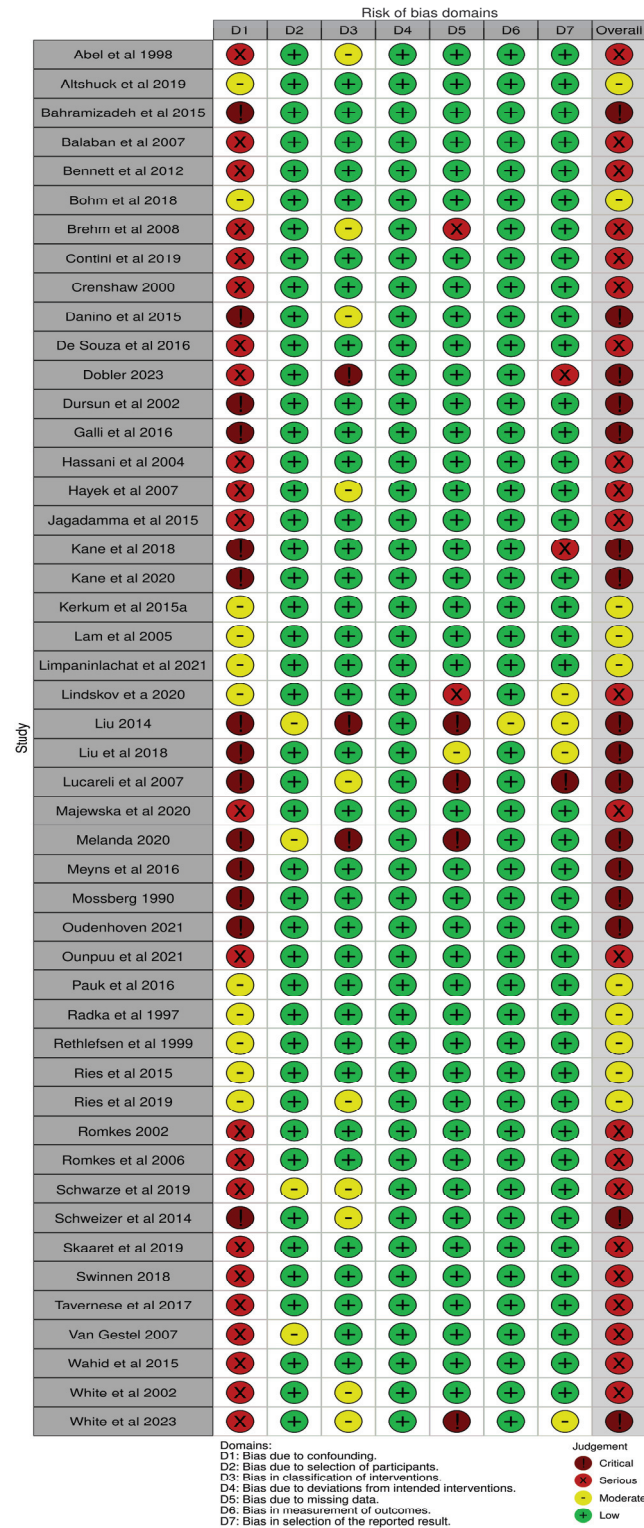


Figure 3. Risk of bias of non-controlled studies: ROBINS-I plot [14–61].

3.2. Evidence Synthesis

Several types of AFO were explored in the included studies. Solid or fixed AFOs [18,20,21,23,31,32,35,37,38,45,47–50,57,59–61,63,64,68] and rigid ventral shell AFOs (vAFOs) [33,66,67] were described as solid AFOs (SAFOs). Furthermore, different types of flexible AFOs were proposed: dynamic AFO (DAFO) [23,27,28,34,47,51,53,70]; hinged ankle–foot orthosis (HAFO) [17,18,21–23,27,28,31,35,37,38,41,42,44,45,48,49,51,52,54,55,60–64,68]; hinged ankle–foot orthosis with a contoured footplate (HAFOc) [36]; hinged ankle–

foot orthosis with a flatter, unmodified footplate (HAFO) [36]; adjustable dynamic response AFO (ADRAFO) [70]; carbon-composite ankle-foot orthoses (c-AFO) [15]; carbon modular orthosis (CAMO) [31,57]; carbon-fiber AFO Ankle Seven (CAFO) [62]; dual carbon fiber spring AFO (CFO) [58]; DAFO with dynamic, elastic shank adaptation (DESA) [53]; tone reducing AFO (TRAFO) [22]; stiff and flexible vAFO [66,67]; ground (or floor) reaction force ankle-foot orthosis (GRAFO) [19,39,45,50,53,55]; modified GRAFO (mGRAFO) [16]; instantaneously adjustable alignment ankle-foot orthosis (iAA-AFO) [32]; orthosis with the dorsal part containing 11 sleeves (Orteams®) [58]; posterior leaf spring (PLS) [20,23,31,40,44,45,49,56,58,63,64]; supramalleolar orthosis (SMO) [22,31,37,38,65]. Multiple comparisons were performed either between different types of AFO or with walking barefoot or with shoes.

Most of the studies focused on patients with cerebral palsy, except three.

The only study that investigated children with DMD (20 subjects, aged 4–12 years) compared two groups walking with shoes or with AFOs [24]. Furthermore, five children were re-assessed after a 6-month period of night-time AFO use. The results are limited by the small sample and non-randomized protocol. The authors interestingly suggested that both daytime and night-time use of AFOs minimized typical compensations to equinus observed in the DMD gait pattern. Nonetheless, daytime AFOs reduced the ankle power generation at pre swing.

Two studies assessed the role of AFOs in patients affected by Charcot–Marie–Tooth (CMT) disease. An RCT [69] involved 12 children with mixed CMT types (types 1A, 1E, 2, 2D, 4, and X3) and mixed foot deformities (cavovarus, neutral, and planovalgus). The authors compared the effectiveness of mixed types of traditional or 3D-printed AFOs (PLF, HAFO, and SAFO) with shoes only. All the types of AFOs restored the DF at initial contact and maximum ankle plantarflexion moment in stance, reduced the peak pressure beneath the foot, and resulted in similar scores in the Client Satisfaction with Device module of the Orthotics and Prosthetics Users' Survey. Compared to traditional AFOs, 3D-printed redesigned AFOs increased the maximum ankle plantarflexion at push-off because of their improved flexibility. A non-randomized cross-over study [45] involved 15 children with mixed-type CMT (1, 2, 4E, and unknown) and compared the gait performance with individualized AFOs (PLF, HAFO, and SAFO) and barefoot. Like in the previous RCT, improvements were observed in patients with increased equinus in swing, but the AFOs did not provide enough support in patients with increased dorsiflexion in the terminal stance.

The age range was generally wide within most of the studies, extending from children to young adults: this was considered to pose an RoB.

The outcome measures, related to gait performance, included three-dimensional gait analysis (3DGA) parameters, such as kinematics; kinetics; electromyography (EMG); spatial-temporal parameters (STPs); derived indexes, such as the gait variability index (GVI), gait deviation index (GDI), and gait profile index (GPI); and energy cost.

The characteristics of the included RCTs and non-randomized prospective or retrospective studies are represented in Table 1 and Supplementary Table S2, respectively. The outcome measures are described, but only statistically significant results are reported. The level of significance was 5% for all the studies ($p < 0.05$), except for the study by Swinnen et al. (2018) [56], where the authors considered a level of significance of 10% ($p < 0.10$).

Table 1. Characteristics of included randomized controlled trials.

References	Study Design	Population	Mean Age	Diagnosis	Level of Functioning	Usage Period	Comparisons	Outcomes	Results
Borghi C. et al., 2021 [62]	RCT crossover	10 (5 M, 5 F)	11.5 ± 4	DCP	GMFCS: II	4 wk	HAFO vs. CAFO	3DGA: ankle pw generation, KEn in St	Energy produced (J/kg): HAFO 6.9 IQR 5, CAFO 9.5 IQR 7.8 Energy absorbed (J/kg): HAFO 17.4 IQR 7.4, CAFO 13.8 IQR 8.3 DF at IC (°): SAFO 2 ± 4, HAFO 3 ± 4, PLS −0.2 ± 5, BF −11 ± 6 Peak DF in ST (°): HAFO 16 ± 6, SAFO 11 ± 5, PLS 13 ± 7, BF 6 ± 5 Dynamic ankle range (°): HAFO 16 ± 4, SAFO 11 ± 3, PLS 15 ± 4, BF 26 ± 7 Peak ankle pw in ST (W/kg): SAFO 0.88 ± 0.30, HAFO 1.24 ± 0.35, PLS 1.15 ± 0.29, BF 1.41 ± 0.51 sl (m): HAFO 0.57 ± 0.09, SAFO 0.57 ± 0.10, PLS 0.59 ± 0.09, BF 0.50 ± 0.10 SL (m): HAFO 1.18 ± 0.17, SAFO 1.14 ± 0.17, PLS 1.19 ± 0.15, BF 1.01 ± 0.18 Cad (steps/min): HAFO 117 ± 14, SAFO 117 ± 12, PLS 119 ± 16, BF 127 ± 17 WEC self-selected ws (J/kg): SAFO 0.258 ± 0.05, HAFO 0.257 ± 0.07, PLS 0.264 ± 0.05, BF 0.276 ± 0.05 WEC fast walking (J/kg): SAFO 0.259 ± 0.05, HAFO 0.250 ± 0.07, PLS 0.264 ± 0.06, BF 0.279 ± 0.05
Buckton CE et al., 2001 [63]	RCT crossover	30, 21 M and 9 F	9.4 range 5–15 yrs	HCP	Unsp	3 mo no AFO – 3 random sequences of SAFO/HAFO/PLS, for 3 mo each	BF vs. SAFO vs. HAFO vs. PLS	3DGA: kinematics, kinetics, STP; oxygen consumption, WEC; BOTMP; GMFM, PEDI	

Table 1. Cont.

References	Study Design	Population	Mean Age	Diagnosis	Level of Functioning	Usage Period	Comparisons	Outcomes	Results
Buckton CE et al., 2004 [64]	RCT crossover	16, 10 M and 6 F	8.4 ± 2.4 yrs	SDCP	GMCFs: I (4 pt)–II (12 pt)	3 mo no AFO – 3 random sequences of SAFO/HIAFO/PLS, for 3 mo each	BF vs. SAFO vs. HIAFO vs. PLS	3DGA: kinematics, kinetics, STP; oxygen consumption, WEC; BOTMP, GMFM, PEDI	<p>Minimum pelvic tilt (°): HAFO 13.5 ± 7, PLS 16 ± 6.9, SAFO 13.4 ± 6.9, BF 14.7 ± 4.3</p> <p>Minimum HF (°): HAFO 0.5 ± 7.6, PLS 3.1 ± 8.6, SAFO −0.7 ± 9.7, BF 2.6 ± 9.4</p> <p>DF at IC (°): HAFO 5.4 ± 3.9, PLS 4.8 ± 4.6, SAFO 5 ± 4.5, BF −7.2 ± 13</p> <p>Peak DF in ST (°): HAFO 18.6 ± 8.3, PLS 14.8 ± 7.3, SAFO 12.5 ± 5.3°, BF 5.7 ± 12.9</p> <p>Peak DF time (%): HAFO 46 ± 5, PLS 38 ± 13, SAFO 36 ± 13, BF 27 ± 14</p> <p>Peak DF in SW (°): HAFO 8.3 ± 5.5, PLS 6.9 ± 4.6, SAFO 7.2 ± 5.6, BF −3.6 ± 13.9</p> <p>Peak KE moment early stance (Nm/kg): HAFO 0.54 ± 0.28, BF 0.33 ± 0.32</p> <p>Peak DF moment early ST (Nm/kg): HAFO −0.11 ± 0.09, PLS −0.13 ± 0.12, SAFO −0.11 ± 0.09, BF 0.01 ± 0.03</p> <p>Peak ankle pw in ST (W/kg): HAFO 1.18 ± 0.31, PLS 1.23 ± 0.45, SAFO 0.83 ± 0.17, BF 1.59 ± 0.51</p> <p>sl (m): HAFO 0.50 ± 0.10, PLS 0.54 ± 0.08, SAFO 0.51 ± 0.10, BF 0.45 ± 0.08</p> <p>SL (m): HAFO 0.99 ± 0.18, PLS 1.05 ± 0.15, SAFO 1.02 ± 0.18, BF 0.91 ± 0.15</p> <p>Cad (steps/min): HAFO 118 ± 14, PLS 127 ± 22, SAFO 124 ± 15, BF 142 ± 23</p> <p>WEC self-selected ws (mLO₂/Kg/m): HAFO 0.363 ± 0.09, PLS 0.368 ± 0.08, SAFO 0.353 ± 0.09, BF 0.417 ± 0.11</p> <p>WEC fast ws (mLO₂/Kg/m): HAFO 0.360 ± 0.08, PLS 0.352 ± 0.08, SAFO 0.338 ± 0.07, BF 0.398 ± 0.10</p> <p>BOTMP UL coordination: HAFO 13.5 ± 5.4, PLS 13.9 ± 5.7, SAFO 14.9 ± 4.4, BF 11.9 ± 5.6</p> <p>BOTMP UL speed&dexterity: HAFO 28 ± 10.1, PLS 28.1 ± 10.7, SAFO 28.0 ± 8.8, BF 26.2 ± 9.1</p> <p>GMFM walking/running/jumping: HAFO 61 ± 10.9, PLS 60.8 ± 10.3, SAFO 60.6 ± 10.5, BF 57.1 ± 12</p>

Table 1. Cont.

References	Study Design	Population	Mean Age	Diagnosis	Level of Functioning	Usage Period	Comparisons	Outcomes	Results
Carlson WE et al., 1997 [65]	RCT crossover	11, 6 M and 5 F	6.9 ± 2.19 yrs	SDCP	Unsp	1 mo no AFO – 1 mo AFO or SMO – 1 mo no AFO – 1 mo AFO or SMO	AFO vs. SMO vs. BF	3DGA: kinematics, kinetics, STP	Sagittal ankle ROM (°): 1st baseline 26.1 ± 6.6, AFO 11.9 ± 3.4, 2nd baseline 24.6 ± 4.4, SMO 25.4 ± 6.4 Peak DF at IC (°): 1st baseline 3.8 ± 6.6, AFO 10 ± 6, 2nd baseline 1.8 ± 6.7, SMO 3.3 ± 7 Peak ankle PF moment (Nm/kg): 1st baseline 0.85 ± 0.13, AFO 1.02 ± 0.19, 2nd baseline 0.87 ± 0.12, SMO 0.94 ± 0.11 Peak ankle pw in pSW (W/kg): 1st baseline 1.35 ± 0.35, AFO 1.05 ± 0.37, 2nd baseline 1.50 ± 0.54, SMO 1.64 ± 0.61 Speed (m/s): rigid 1.07, stiff 1.00, flexible 1.05, shoes 1.09 Peak KE in MSt (°): rigid 16.7 ± 10.0, stiff 18.1 ± 8.6, flexible 18.4 ± 9.3, shoes 22.7 ± 8.7 Peak KE moment in MSt (Nm/kg): rigid –0.15 ± 0.17, stiff –0.12 ± 0.15, flexible –0.07 ± 0.16, shoes 0.08 ± 0.15 Ankle RoM in stride (°): rigid 7.0 ± 2.4, stiff 15.4 ± 4.3, flexible 19.5 ± 3.9, shoes 35.4 ± 8.1 DF at IC (°): rigid 3.7 ± 2.2, stiff 2.3 ± 5.9, flexible 1.0 ± 6.1, shoes –2.6 ± 7.6 DF in MSt (°): rigid 7.9 ± 2.6, stiff 9.1 ± 5.1, flexible 9.4 ± 6.1, shoes 11.4 ± 8.4 Peak PF ankle moment in ST (Nm/kg): rigid 1.21 ± 0.18, stiff 1.21 ± 0.18, flexible 1.19 ± 0.19, shoes 0.95 ± 0.21 CoP excursion in step (mm): rigid 189 ± 38, stiff 174 ± 43, flexible 181 ± 27, shoes 126 ± 35 Ankle pw generation (W/kg): rigid 0.73, stiff 1.21 ± 0.43, flexible 1.43 ± 0.53, shoes 1.49 ± 0.71 WEC (J/Kg/m): rigid 5.5 ± 1.1, stiff 5.4 ± 1.2, flexible 5.6 ± 1.5, shoes 6.1 ± 1.7
Kerkum YL et al., 2015b [66]	RCT crossover AFO-CP trial	15, 11 M, 4 F	10 ± 2 yrs, range 6–14 yrs	SCP	GMFCS: 2 level I, 11 level II, 2 level III	acclimatization period of 4 wk for each level of stiffness	Three level of stiffness (flexible, stiff, rigid) vAFO vs. shoes	3DGA: kinematics, kinetics, STP, WEC	

Table 1. Cont.

References	Study Design	Population	Mean Age	Diagnosis	Level of Functioning	Usage Period	Comparisons	Outcomes	Results
Meyns P et al., 2020 [67]	RCT crossover AFO-CP trial	15, 11 M, 4 F	10 ± 2 yrs, range 6–14 yrs	SCP	GMFCS: 2 level I, 11 level II, 2 level III	acclimatization period of 4–6 wk for each level of stiffness	Three level of stiffness (flexible, stiff, rigid) vAFO vs. shoes	3DGA: trunk kinematics, STP, gait stability (MoS)	Trunk Rot ROM (°): rigid 18.4 ± 4.9, stiff 15 ± 6.2, flexible 13.4 ± 5.9, shoes 11.9 ± 4.4 Trunk Lat ROM (°): rigid 20.5 ± 7.9, stiff 21.9 ± 8.5, flexible 22.6 ± 7.8, shoes 16.7 ± 6 ML_MoS (m): rigid 0.011 ± 0.019 m vs. 0.016 ± 0.021 sdML_MoS (m): rigid 0.026 ± 0.014 m vs. shoes 0.018 ± 0.011 Pearson's correlation between netEC and Trunk ROM: tilt ROM flexible vAFO 0.68, stiff vAFO 0.69; lateroflexion ROM flexible vAFO 0.78, stiff AFO 0.81, rigid AFO 0.78; sdML_MoS flexible vAFO 0.57, rigid vAFO 0.76
Radtko SA et al., 2005 [68]	RCT crossover	12, 6 M and 6 F	7.5 ± 3.83 yrs, range 4–16 yrs	DCP	GMFCS I/II (10 pt)–III (2 pt)	SAFO (9 pt), HAFO (3 pt) (worn for ≥1 yr) – 2 wk no AFO – 1 mo SAFO – 2 wk no AFO – 1 mo HAFO	SAFO and HAFO vs. BF	3DGA: kinematics, kinetics, STP; sEMG (muscle timing in ST)	DF in MSt (°): SAFO 10.59 ± 4.93, HAFO 11.67 ± 7, shoes 0.69 ± 4.3 DF in Tst (°): SAFO 11.50 ± 4.28, HAFO 16.13 ± 6.17, shoes –1.30 ± 6.59 Peak ankle moment at Tst (Nm/kg): SAFO 0.96 ± 0.2, HAFO 0.94 ± 0.25, shoes 0.69 ± 0.14 Peak ankle pw at Tst (W/kg): SAFO 0.24, HAFO –0.87 ± 0.42, shoes –0.26 ± 0.33 Peak ankle pw at pSW (W/kg): SAFO 1.16 ± 0.39, HAFO 1.07 ± 0.46, shoes 1.16 ± 0.39 Peak PF at pSW (°): AFO –4.3 ± 2.5, 3DprintedAFO –5.1 ± 3.3, shoes –15.6 ± 10.9 DF at IC (°): AFO 0 ± 3.5, 3DprintedAFO –0.6 ± 3.7, shoes –5.9 ± 7.6 Peak DF moment in LR (Nm/kg): AFO –0.3 ± 0.1, 3DprintedAFO –0.3 ± 0.1, shoes –0.1 ± 0.1 Peak PF moment in ST (Nm/kg): AFO 1.1 ± 0.3, 3DprintedAFO 1.1 ± 0.3, shoes 0.9 ± 0.3 ↓ weight (–35.2%), ↓ material (–24.4%) vs. traditional AFO
Wojciechowski EA et al., 2022 [69]	RCT crossover	12 (6 M, 6 F)	11.2 ± 3.6 range 5–16 yrs	CMT	Unsp	Unsp	AFO, 3D printed AFO, BF	3DGA: kinematics, kinetics, STP, AFO's features	

Table 1. Cont.

References	Study Design	Population	Mean Age	Diagnosis	Level of Functioning	Usage Period	Comparisons	Outcomes	Results
Wren T et al., 2015 [70]	RCT crossover	10 (6 M, 4 F)	4–12	5 HCP, 5 DCP	GMFCS: I–III	4 wk	DAFO, ADRAFO, BF	3DGA: kinematics, kinetics, STP; OPUS, PODCI, WA	SL (m): BF 0.69 ± 0.21 , DAFO 0.79 ± 0.23 , ADRAFO 0.85 ± 0.2 HE ST (°): BF 7.6 ± 10.4 , DAFO 5 ± 9.9 , ADRAFO 3.8 ± 11 DF ST (°): BF -4.3 ± 11.4 , DAFO 8.9 ± 4.4 , ADRAFO -0.4 ± 8.5 DF Sw (°): BF -11.4 ± 11.5 , DAFO 5.5 ± 4.9 , ADRAFO -4.2 ± 7.2 KE ST (°): BF 10.9 ± 9.7 , DAFO 12.5 ± 12.1 , ADRAFO 7.1 ± 13.7 Peak ankle pw at pSW (W/kg): BF -1.36 ± 0.74 , DAFO 0.74 ± 0.36 , ADRAFO 1.06 ± 0.5 WA (steps/day): DAFO 5952, ADRAFO 5224

Legend—3DGA: 3D gait analysis; AFO: ankle foot orthoses; ADRAFO: adjustable dynamic response AFO; BF: barefoot; BOTMP: Bruininks-Oseretsky Test of Motor Proficiency; Cad: cadence; Ca.M.O: carbon modular orthosis; d: day / days; DAFO: dynamic ankle foot orthosis; DF: dorsiflexion, (+) value denotes dorsiflexion, (−) value denotes plantar flexion; DCP: diplegic cerebral palsy; DS: double support; FL: flexion; GMFM: gross motor functional measure; HAFO: hinged ankle-foot orthosis; HCP: hemiplegic cerebral palsy; HF: hip flexion; HE: hip extension; IC: initial contact; ISw: initial swing; KF: knee flexion; KE: knee extension; LR: loading response; ML_MoS: medio-lateral margin of stability; Mo: month; MST: mid stance; MSw: mid swing; netEC: net energy cost; OPUS: Orthotics and Prosthetics Users' Survey; PEDI: Pediatric Evaluation of Disability Inventory; PF: plantarflexion; PLS: Posterior leaf spring; PODCI: Pediatric Outcomes Data Collection Instrument; PROM: passive range of motion; PSw: pre-swing; Pw: power; pt: patient/patients; SAFO: solid (or fixed) ankle-foot orthosis; SDGP: spastic diplegic cp; sdML_MoS: standard deviation medio-lateral margin of stability; sl: step length; SL: stride length; SMO: supra malleolar orthoses; ST: stance phase; STP: spatio-temporal parameters; SW: stride width; Sw: swing phase; TA: tibialis anterior; TS: terminal stance; TSw: terminal swing; Unsp: unspecified; vAFO: ventral shell spring-hinged AFO; WA: walking activity; WEC: walking energy cost; wk: week/ weeks; ws: walking speed; yrs: years; M: Male; F: Female; ↓: decrease.

3.3. Meta-Analysis Results

Five RCTs involving children with CP were included in the meta-analysis [63–66,68]. To compare the results, we decided to group solid (SAFO) or fixed AFO [63–65,68] and rigid ventral shell AFO (vAFO) [66] as rigid AFO. Similarly, the following different types of orthoses were clustered as flexible AFO, because they all left flexibility at the ankle: HAFO [63,64,68], stiff and flexible vAFO [66], SMO [65], and PLS [63,64]. The results of the meta-analysis are represented in Figures 4–10.

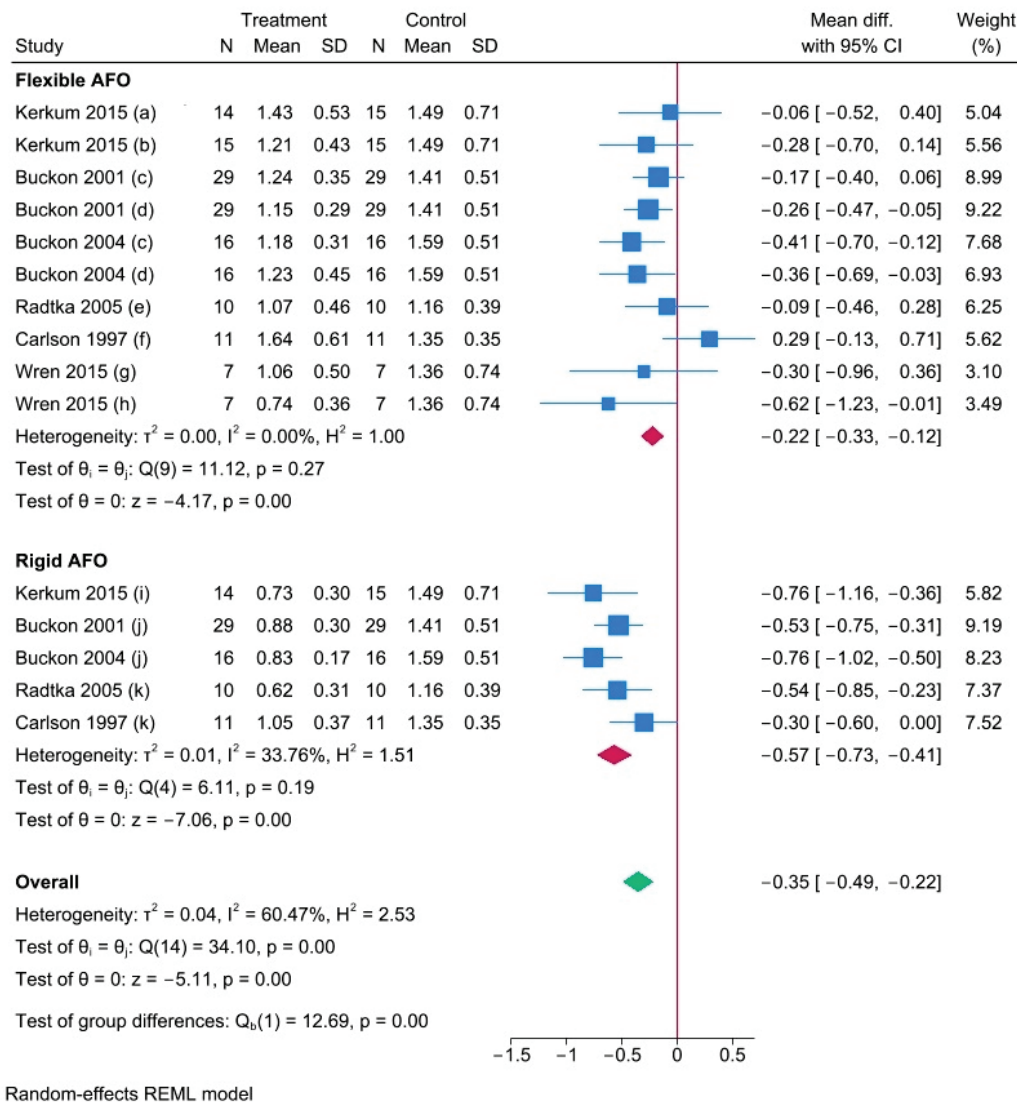


Figure 4. Forest plot showing the meta-analysis of the effectiveness of rigid ankle-foot orthoses (Rigid AFOs) and flexible ankle-foot orthoses (Flexible AFOs) vs. barefoot/shoes on the peak ankle power in pre-swing in children with cerebral palsy. The outcomes are expressed as mean differences (Mean Diff.) in W/Kg. Comparisons: (a) Flexible vAFO vs. shoes; (b) Stiff vAFO vs. shoes; (c) HAFO vs. barefoot; (d) PLS vs. barefoot; (e) HAFO vs. shoes; (f) SMO vs. shoes; (g) ADR-AFO vs. barefoot; (h) DAFO vs. barefoot; (i) Rigid vAFO vs. shoes; (j) SAFO vs. barefoot; (k) SAFO vs. shoes. In blue, effect estimate and associated 95% confidence interval from each included study. In red, pooled estimate from studies included in each subgroup. In green, overall pooled estimate from all included studies [33,63–65,68,70].

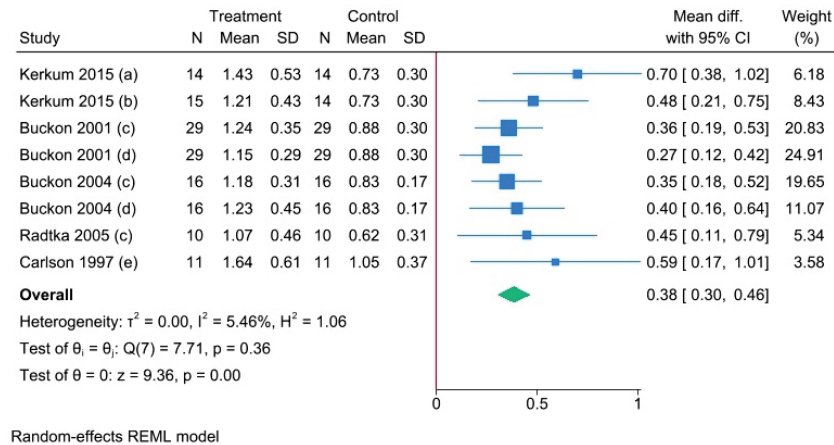


Figure 5. Forest plot showing the meta-analysis of the effectiveness of flexible ankle-foot orthoses (Flexible AFOs) vs. rigid ankle-foot orthoses (Rigid AFOs) on the peak ankle power in pre swing in children with cerebral palsy. The outcomes are expressed as mean differences (Mean Diff.) in W/Kg. Comparisons: (a) Flexible vAFO vs. rigid vAFO; (b) Stiff vAFO vs. rigid vAFO; (c) HAFO vs. SAFO; (d) PLS vs. SAFO; (e) SMO vs. SAFO. In blue, effect estimate and associated 95% confidence interval from each included study. In green, overall pooled estimate from all included studies [33,63–65,68].

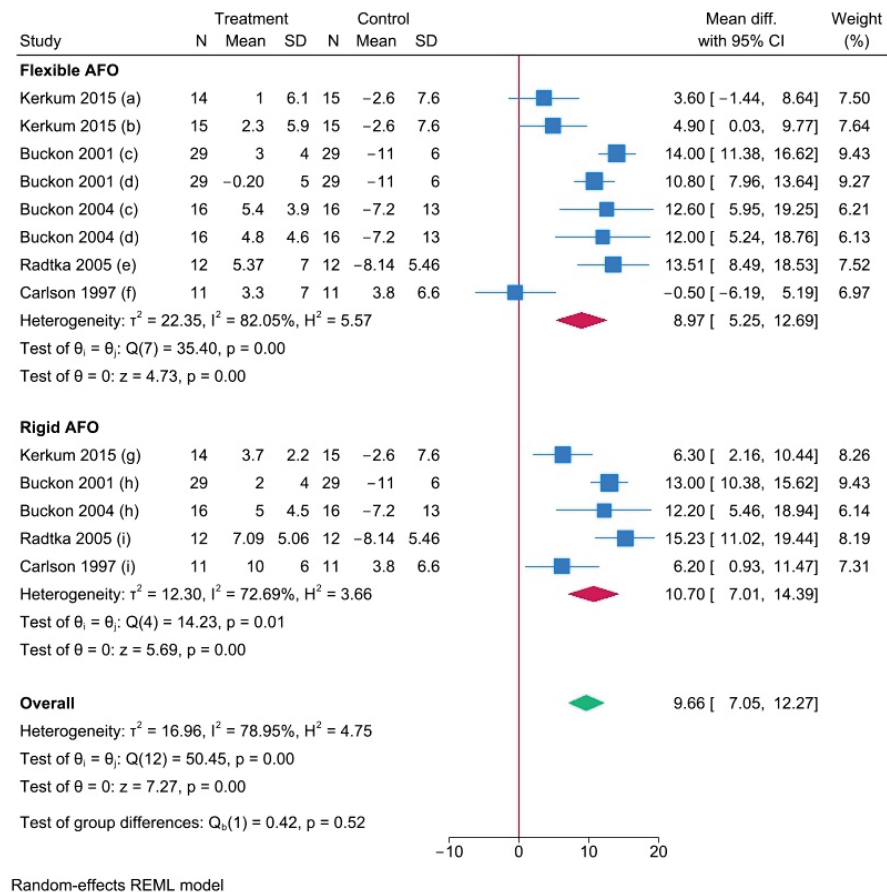


Figure 6. Forest plot showing the meta-analysis of the effectiveness of rigid ankle-foot orthoses (Rigid AFOs) and flexible ankle-foot orthoses (Flexible AFOs) vs. barefoot/shoes on the dorsiflexion at initial contact in children with cerebral palsy. The outcomes are expressed as mean differences (Mean Diff.) in degrees. Comparisons: (a) Flexible vAFO vs. shoes; (b) Stiff vAFO vs. shoes; (c) HAFO vs. barefoot; (d) PLS vs. barefoot; (e) HAFO vs. shoes; (f) SMO vs. shoes; (g) Rigid vAFO vs. shoes; (h) SAFO vs. barefoot; (i) SAFO vs. shoes. In blue, effect estimate and associated 95% confidence interval from each included study. In red, pooled estimate from studies included in each subgroup. In green, overall pooled estimate from all included studies [33,63–65,68].

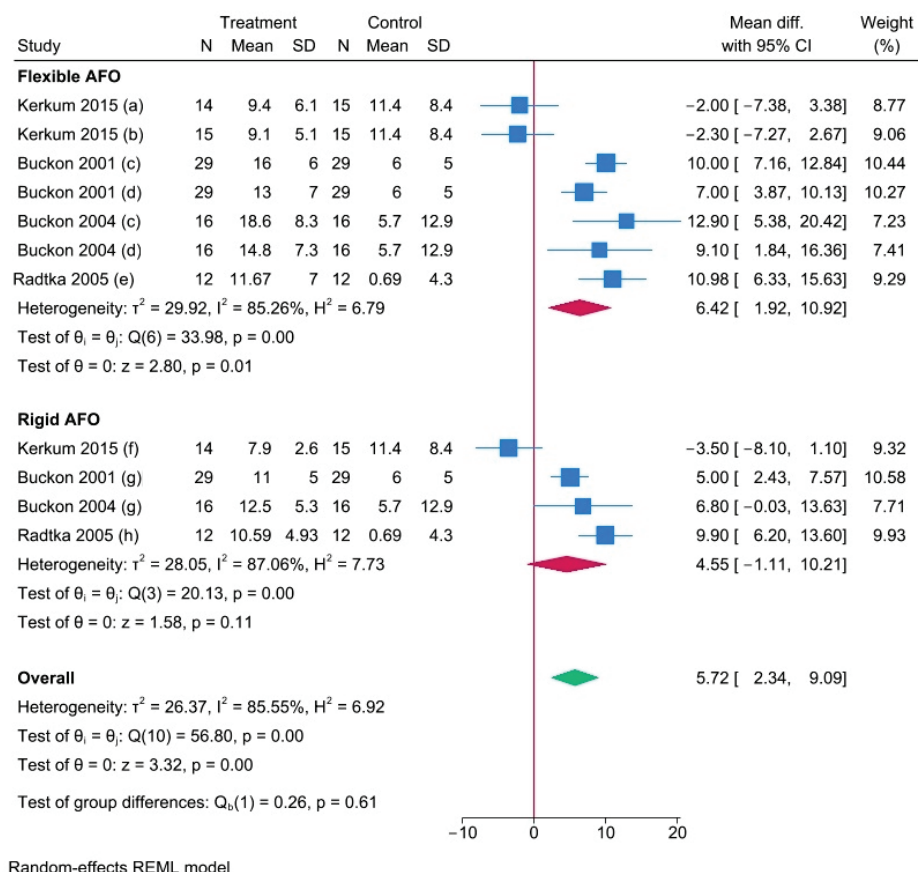


Figure 7. Forest plot showing the meta-analysis of the effectiveness of rigid ankle-foot orthoses (Rigid AFOs) and flexible ankle-foot orthoses (Flexible AFOs) vs. barefoot/shoes on the peak dorsiflexion in stance in children with cerebral palsy. The outcomes are expressed as mean differences (Mean Diff.) in degrees. Comparisons: (a) Flexible vAFO vs. shoes; (b) Stiff vAFO vs. shoes; (c) HAFO vs. barefoot; (d) PLS vs. barefoot; (e) HAFO vs. shoes; (f) Rigid vAFO shoes; (g) SAFO vs. barefoot; (h) SAFO vs. shoes. In blue, effect estimate and associated 95% confidence interval from each included study. In red, pooled estimate from studies included in each subgroup. In green, overall pooled estimate from all included studies [33,63,64,68].

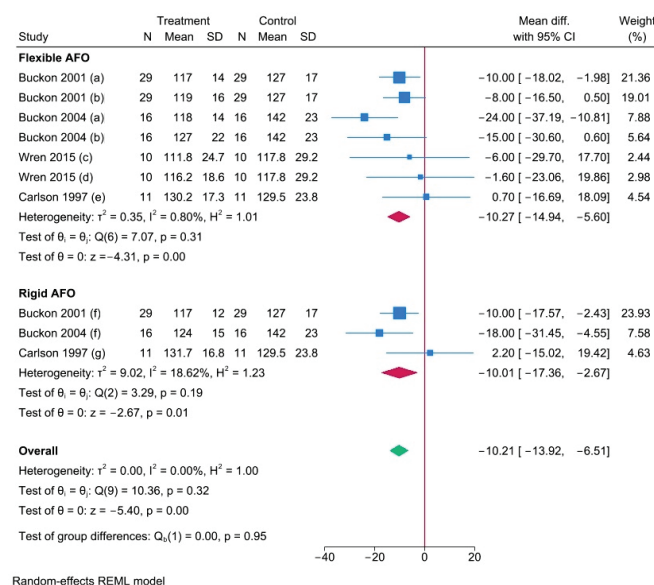


Figure 8. Forest plot showing the meta-analysis of the effectiveness of rigid ankle-foot orthoses (Rigid AFOs) and flexible ankle-foot orthoses (Flexible AFOs) vs. barefoot/shoes on cadence in children with

cerebral palsy. The outcomes are expressed as mean differences (Mean Diff.) in steps per minute. Comparisons: (a) HAFO vs. barefoot; (b) PLS vs. barefoot; (c) DAFO vs. barefoot; (d) ADR-AFO vs. barefoot; (e) SMO vs. shoes; (f) SAFO vs. barefoot; (g) SAFO vs. shoes. In blue, effect estimate and associated 95% confidence interval from each included study. In red, pooled estimate from studies included in each subgroup. In green, overall pooled estimate from all included studies [63–65,70].

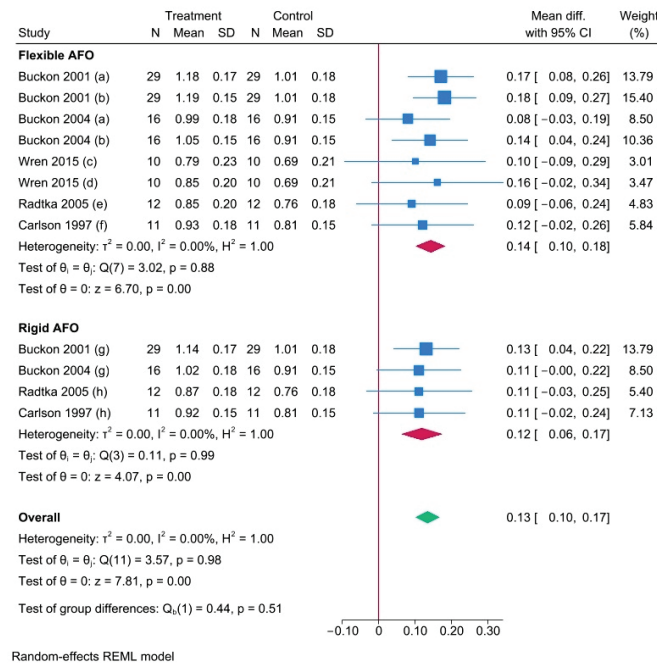


Figure 9. Forest plot showing the meta-analysis of the effectiveness of rigid ankle-foot orthoses (Rigid AFOs) and flexible ankle-foot orthoses (Flexible AFOs) vs. barefoot/shoes on stride length in children with cerebral palsy. The outcomes are expressed as mean differences (Mean Diff.) in meters. Comparisons: (a) HAFO vs. barefoot; (b) PLS vs. barefoot; (c) DAFO vs. barefoot; (d) ADR-AFO vs. barefoot; (e) HAFO vs. shoes; (f) SMO vs. shoes; (g) SAFO vs. barefoot; (h) SAFO vs. shoes. In blue, effect estimate and associated 95% confidence interval from each included study. In red, pooled estimate from studies included in each subgroup. In green, overall pooled estimate from all included studies [63–65,68,70].

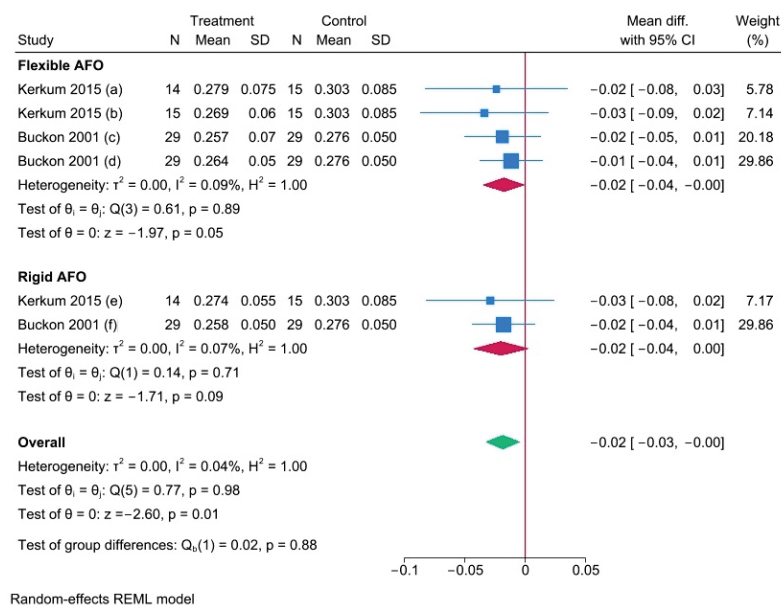


Figure 10. Forest plot showing the meta-analysis of the effectiveness of rigid ankle-foot orthoses (Rigid AFOs) and flexible ankle-foot orthoses (Flexible AFOs) vs. barefoot/shoes on energy cost at

self-selected speed in children with cerebral palsy. The outcomes are expressed as mean differences (Mean Diff.) in mL O₂/Kg/meter. Comparisons: (a) Flexible vAFO vs. shoes; (b) Stiff vAFO vs. shoes; (c) HAFO vs. barefoot; (d) PLS vs. barefoot; (e) Rigid vAFO vs. shoes; (f) SAFO vs. barefoot. In blue, effect estimate and associated 95% confidence interval from each included study. In red, pooled estimate from studies included in each subgroup. In green, overall pooled estimate from all included studies [33,63].

3.4. Undesirable Effects

No undesirable effects were reported except in the study by Kerkum et al. (2015b) [66], in which the authors declared that one child refused to wear the rigid vAFO, and another child could not acclimatize to the flexible vAFO because of pressure marks.

4. Discussion

Interesting data emerged from the meta-analysis of studies involving patients with CP. In general, solid or flexible AFOs reduce the peak ankle power in pre-swing compared to walking barefoot or with only shoes. Nonetheless, the results are heterogeneous, mainly due to findings from flexible AFOs, which are closer to those for controls. This is linked to the reduction in the range of motion (ROM) at the ankle: the ROM is the most limited in rigid AFO, and the moment and power are the lowest at the ankle. The ankle push-off contributes to leg swing and to center of mass acceleration [71]; thus, ankle power should be preserved to improve gait efficiency. Interestingly, the peak ankle power tends to increase compared to control when using SMO [65], which does not limit the ankle sagittal ROM but impedes excessive valgus-pronation, optimizing the action of plantar flexors at push-off. Comparing flexible versus rigid AFO, a significant overall effectiveness regarding peak ankle power in pre swing is confirmed, and results are homogeneous. Based on this, flexible AFOs might be preferable to rigid ones.

On the contrary, excessive flexibility might reduce the effectiveness in promoting dorsiflexion at initial contact. As shown in Figure 6, an overall positive result was achieved considering all types of AFO compared to barefoot or shoes, but the heterogeneity was high mainly due to SMO and flexible vAFO. Dorsiflexion at initial contact allows for “landing” on the heel, as in a typical gait, and precedes reaching plantar support in the stance. Furthermore, it promotes a higher step and stride length.

The meta-analysis demonstrated a significant increase in stride length and a reduction in cadence when comparing all types of AFO versus barefoot/shoes, with no overall heterogeneity. These parameters indicate a more efficient gait.

As a confirmation, an overall reduction in energy cost was demonstrated while walking with AFO at self-selected speed compared to barefoot/shoes. The heterogeneity was almost null. This outcome was measured for a 31 m [63,64] or 6 min walk [66]. Over longer distances, the advantage might be amplified and reduce fatigue; therefore, AFO might promote mobility in ecological contexts.

An overall significant increase in peak ankle dorsiflexion (DF) was observed when comparing AFO versus barefoot/shoes (Figure 7). The results were heterogeneous, mainly due to the study by Kerkum et al. [66]. This might be due to the population included in the study, which presented excessive knee flexion (at least 10°) in the midstance phase. One objective of the proposed AFOs was counteracting excessive knee flexion, therefore reducing ankle dorsiflexion in stance. In general, a proper ankle DF ROM allows for the anterior roll of the tibia relative to the foot during the midstance phase of gait, which contributes to forward movement of the body. A limitation of peak ankle DF affects ground reaction forces and the torque of the lower extremity joints; it reduces the ankle plantar flexor moment and may induce foot external rotation as compensation to allow progression of the tibia [72]. Based on the results of a study on adult normal gait, if the

peak ankle dorsiflexion angle is less than 9.03° , the lower limb movement pattern changes significantly [73]. On the contrary, when ankle dorsiflexion in stance is persistent and/or excessive, as the plantar flexors cannot decelerate the progression of the tibia, the ground reaction force is posterior to the knee, creating a flexion moment on the knee, leading to progressively inefficient crouch gait [74].

Non-randomized controlled studies (Supplementary Table S2), involving subjects with CP, substantially confirmed the results of the meta-analysis. The methodological limitations (Figure 3) of these studies do not permit us to draw reliable conclusions on other aspects. Nonetheless, interesting findings are reported regarding the effect of AFOs on trunk displacement [42,56], which is increased on either the transverse or the frontal plane. Similar changes are reported in typically developing children wearing orthoses that limit the ankle ROM [75]. This must be taken into account when considering the introduction of AFOs in subjects with CP, particularly in the presence of trunk asymmetry such as scoliosis.

Walking performance may be conditioned by several factors such as body mass index (BMI); spasticity; recent surgery; concurrent physiotherapy or medications (particularly those to treat spasticity); and the use of assistive devices such as crutches, canes, or a walker. The patient's weight and height are usually considered in computed gait analysis and in the individually customized AFOs, but only two studies have declared it [66,67]. None systematically explored the role of BMI while comparing walking with or without AFOs. Only Ratdka et al. [68] measured spasticity using the Ashworth Scale. Most of the studies explicitly excluded recent surgery [62–64,66–68], but two studies [65,70] did not specify it. Only Borghi et al. [62] reported recent botulinum injections among the exclusion criteria. No one reported whether the patients underwent physiotherapy. Additionally, the studies compared gait without and with orthoses during the same assessment session or after a short accommodation period (usually 4–6 weeks). Therefore, major changes due to BMI or clinical modifications were not believed to have influenced the comparison. All the included subjects were community ambulators, mostly at levels I and II of GMFCS. A few patients at GMFCS level III used assistive devices during the assessment [68,70]. In the studies by Kerkum et al. [66] and Meyns et al. [67], they were included only if they were able to walk independently for at least 15 m, and to perform the gait analysis without external supports.

The limited evidence regarding neuromuscular diseases (CMT and DMD) suggests that, as in CP, AFOs are effective in reducing equinus in swing and improving DF at initial contact, but reduce ankle power generation at pre-swing, unless there is individual adaptation to preserve AFOs' flexibility. Limiting the ankle ROM is critical in patients who incur progressive weakness and usually develop compensatory movements at the trunk.

Limitations

The present systematic review focused on gait performance as the outcome. Many reports were found regarding the effectiveness of AFOs on the gait performance of subjects with CP. Nonetheless, as clinicians, we outline the need for more specific indications to guide the choice of AFO. The studies tended to select samples based on the diagnosis, hemiplegic and/or diplegic CP, but these may include different patterns of gait. Furthermore, several types of AFOs are described as having specific characteristics. The choice to categorize them as flexible or rigid AFOs was functional in the meta-analysis but is a simplification. The meta-analysis was performed after considering the appropriateness of a cross-over design for trials comparing the effect of different AFOs in children with CP and considering that no carry-over effect or period effect was expected. Given the available data, in this meta-analysis, all the measurements from intervention and control periods were analyzed as if the included studies were randomized parallel trials. It should

be considered that this approach may have introduced a unit-of-analysis error with the possible consequence of masking clinical heterogeneity, even if this analysis was deemed conservative, according to the Cochrane handbook [76]. As Degelaen [77] affirmed, there are several difficulties “in comparing the evidence related to two distinct orthoses that target different problems in different children”. Future studies should focus on specific gait pattern alterations, to compare the effects of different types of AFOs. At the same time, the rebound on other segments (i.e., the trunk) must be considered.

As Morris C. [78] declared, the cross-over design “may overcome the difficulty of the heterogeneity of the cerebral palsies by making each child their own control”, but it “does not provide information on the long-term benefits or harm of using different designs of orthoses”. Nonetheless, studying the long term effect of AFOs is challenging because of the influence of several factors such as BMI and concurrent treatments (i.e., surgery, spasticity treatment, and physiotherapy). Perhaps innovative multicenter trials involving artificial intelligence will enable the exploration of big data over time and studying the reciprocal relationships between all these factors.

The present study did not consider the children’s and adolescents’ satisfaction and the effectiveness of AFOs in improving their participation. However, in clinical practice, we experience that the compliance and satisfaction of the “client” mostly influence the use of the orthoses in an ecological context. As Kane et al. [79] recommend based on a recent focus group involving clinicians in Canada to improve AFO prescription, future research should “develop valid and reliable measures of gait quality and participation specific to orthotic evaluation” and “examine parent and child perceptions of AFO intervention in order to understand what is meaningful to clients, and identify the most effective targets for evaluation”.

5. Conclusions

The present meta-analysis demonstrates the effectiveness of AFOs in increasing stride length, ankle dorsiflexion at IC, and peak ankle DF in stance, as well as reducing cadence and the energy cost of walking, in children and adolescents with CP. Flexible AFOs are preferable because they preserve the peak ankle power generated at push-off compared to rigid AFOs. The evidence regarding DMD and CMT is limited but suggests opting for flexible AFOs, which partially preserve ankle power generation and, thus, plantar flexors’ activity. Nonetheless, further studies should select samples based on specific pathological patterns rather than on the diagnosis, to compare the effects of different types of AFOs and draw more specific indications. Furthermore, the compliance and satisfaction of the users should be considered as outcomes, to include the effectiveness at the participation level of ICF.

Supplementary Materials: The following supporting information can be downloaded at <https://www.mdpi.com/article/10.3390/prosthesis7010013/s1>: Table S1: Search procedures. Table S2: Characteristics of included non-randomized studies.

Author Contributions: Conceptualization, S.F. and S.P.; methodology, S.F. and F.V.; formal analysis, S.F., E.V., E.P., F.M., G.C., G.T., A.E., A.G. and F.V.; investigation, S.F., E.V., E.P., F.M., G.C., G.T. and A.E.; data curation, S.F.; writing—original draft preparation, S.F. and F.V.; writing—review and editing, S.F., E.V., E.P., F.M., G.C., G.T., A.E., A.G., F.V., S.P. and S.S.; supervision, S.S.; project administration, S.F. All authors have read and agreed to the published version of the manuscript.

Funding: This research received no external funding.

Institutional Review Board Statement: Not applicable.

Informed Consent Statement: Not applicable.

Data Availability Statement: The original contributions presented in this study are included in the article/Supplementary Materials. Further inquiries can be directed to the corresponding author.

Acknowledgments: We acknowledge Chiara Cavicchi, Clinical Medicine Library of the University of Bologna, for her support in the searching procedures.

Conflicts of Interest: The authors declare no conflicts of interest.

References

1. Management of Cerebral Palsy in Children: A Guide for Allied Health Professionals. Available online: <http://www.health.nsw.gov.au/kidsfamilies/> (accessed on 6 August 2021).
2. Faccioli, S.; Sassi, S.; Pagliano, E.; Maghini, C.; Perazza, S.; Siani, M.F.; Sgherri, G.; Farella, G.M.; Foscan, M.; Viganò, M.; et al. Care Pathways in Rehabilitation for Children and Adolescents with Cerebral Palsy: Distinctiveness of the Adaptation to the Italian Context. *Children* **2024**, *11*, 852. [CrossRef] [PubMed]
3. Aboutorabi, A.; Arazpour, M.; Bani, M.A.; Saeedi, H.; Head, J.S. Efficacy of ankle foot orthoses types on walking in children with cerebral palsy: A systematic review. *Ann. Phys. Rehabil. Med.* **2017**, *60*, 393–402. [CrossRef] [PubMed]
4. Lintanf, M.; Bourseul, J.-S.; Houx, L.; Lempereur, M.; Brochard, S.; Pons, C. Effect of ankle-foot orthoses on gait, balance and gross motor function in children with cerebral palsy: A systematic review and meta-analysis. *Clin. Rehabil.* **2018**, *32*, 1175–1188. [CrossRef] [PubMed]
5. Betancourt, J.P.; Eleeh, P.; Stark, S.; Jain, N.B. Impact of Ankle-Foot Orthosis on Gait Efficiency in Ambulatory Children with Cerebral Palsy: A Systematic Review and Meta-Analysis. *Am. J. Phys. Med. Rehabil.* **2019**, *98*, 759–770. [CrossRef]
6. Miccinilli, S.; Santacaterina, F.; Della Rocca, R.; Sterzi, S.; Bressi, F.; Bravi, M. Efficacy of Lower Limb Orthoses in the Rehabilitation of Children Affected by Cerebral Palsy: A Systematic Review. *Children* **2024**, *11*, 212. [CrossRef]
7. Page, M.J.; Moher, D.; Bossuyt, P.M.; Boutron, I.; Hoffmann, T.C.; Mulrow, C.D.; Shamseer, L.; Tetzlaff, J.M.; Akl, E.A.; Brennan, S.E.; et al. PRISMA 2020 explanation and elaboration: Updated guidance and exemplars for reporting systematic reviews. *BMJ* **2021**, *372*, n160. [CrossRef]
8. Higgins, J.P.; Thomas, J.; Chandler, J.; Cumpston, M.; Li, T.; Page, M.J.; Welch, V.A. (Eds.) *Cochrane Handbook for Systematic Reviews of Interventions*, 2nd ed.; John Wiley & Sons: Chichester, UK, 2019.
9. Sterne, J.A.C.; Hernán, M.A.; Reeves, B.C.; Savović, J.; Berkman, N.D.; Viswanathan, M.; Henry, D.; Altman, D.G.; Ansari, M.T.; Boutron, I.; et al. ROBINS-I: A tool for assessing risk of bias in non-randomized studies of interventions. *BMJ* **2016**, *355*, i4919. [CrossRef]
10. Available online: <https://sites.google.com/site/riskofbiastool/welcome/home?authuser=0> (accessed on 28 February 2024).
11. Sterne, J.A.C.; Savović, J.; Page, M.J.; Elbers, R.G.; Blencowe, N.S.; Boutron, I.; Cates, C.J.; Cheng, H.Y.; Corbett, M.S.; Eldridge, S.M.; et al. RoB 2: A revised tool for assessing risk of bias in randomised trials. *BMJ* **2019**, *366*, l4898. [CrossRef]
12. Available online: <https://www.riskofbias.info/welcome/rob-2-0-tool/rob-2-for-crossover-trials> (accessed on 28 February 2024).
13. StataCorp. *Stata Statistical Software*, Release 18; StataCorp LLC: College Station, TX, USA, 2023.
14. Abel, M.F.; Juhl, G.A.; Vaughan, C.L.; Damiano, D.L. Gait assessment of fixed ankle-foot orthoses in children with spastic diplegia. *Arch. Phys. Med. Rehabil.* **1998**, *79*, 126–133. [CrossRef]
15. Altschuck, N.; Bauer, C.; Nehring, I.; Böhm, H.; Jakobeit, M.; Schröder, A.S.; Mall, V.; Jung, N.H. Efficacy of prefabricated carbon-composite ankle foot orthoses for children with unilateral spastic cerebral palsy exhibiting a drop foot pattern. *J. Pediatr. Rehabil. Med.* **2019**, *12*, 171–180. [CrossRef]
16. Bahramizadeh, M.; Arazpour, M.; Hutchins, S. The Effect of Modified Floor Reaction Ankle Foot Orthoses on Walking Abilities in Children with Cerebral Palsy. *Iran. Rehabil. J.* **2015**, *13*, 95–101.
17. Balaban, B.; Yasar, E.; Dal, U.; Yazicioglu, K.; Mohur, H.; Kalyon, T.A. The effect of hinged ankle-foot orthosis on gait and energy expenditure in spastic hemiplegic cerebral palsy. *Disabil. Rehabil.* **2007**, *29*, 139–144. [CrossRef] [PubMed]
18. Bennett, B.C.; Russell, S.D.; Abel, M.F. The Effects of Ankle Foot Orthoses on Energy Recovery and Work During Gait in Children with Cerebral Palsy. *Clin. Biomech.* **2012**, *27*, 287–291. [CrossRef] [PubMed]
19. Böhm, H.; Matthias, H.; Braatz, F.; Döderlein, L. Effect of floor reaction ankle-foot orthosis on crouch gait in patients with cerebral palsy: What can be expected? *Prosthet. Orthot. Int.* **2018**, *42*, 245–253. [CrossRef]
20. Brehm, M.; Harlaar, J.; Schwartz, M. Effect of ankle-foot orthoses on walking efficiency and gait in children with cerebral palsy. *J. Rehabil. Med.* **2008**, *40*, 529–534. [CrossRef]
21. Contini, B.G.; Bergamini, E.; Alvini, M.; Di Stanislao, E.; Di Rosa, G.; Castelli, E.; Vannozzi, G.; Camomilla, V. A wearable gait analysis protocol to support the choice of the appropriate ankle-foot orthosis: A comparative assessment in children with Cerebral Palsy. *Clin. Biomech.* **2019**, *70*, 177–185. [CrossRef]
22. Crenshaw, S.; Herzog, R.; Castagno, P.; Richards, J.; Miller, F.; Michaloski, G.; Moran, E. The Efficacy of Tone-Reducing Features in Orthotics on the Gait of Children with Spastic Diplegic Cerebral Palsy. *J. Pediatr. Orthop.* **2000**, *20*, 210–216. [CrossRef]

23. Danino, B.; Erel, S.; Kfir, M.; Khamis, S.; Batt, R.; Hemo, Y.; Wientroub, S.; Hayek, S. Influence of orthosis on the foot progression angle in children with spastic cerebral palsy. *Gait Posture* **2015**, *42*, 518–522. [CrossRef]
24. de Souza, M.A.; Figueiredo, M.M.L.; de Baptista, C.R.d.J.A.; Aldaves, R.D.; Mattiello-Sverzut, A.C. Beneficial effects of ankle-foot orthosis daytime use on the gait of Duchenne muscular dystrophy patients. *Clin. Biomech.* **2016**, *35*, 102–110. [CrossRef]
25. Dobler, F.; Cip, J.; Lengnick, H.; Alexander, N. Effects of ankle-foot orthoses on different gait patterns in children with spastic cerebral palsy: A statistical parametric mapping study. *Prosthet. Orthot. Int.* **2023**, *47*, 449–456. [CrossRef]
26. Dursun, E.; Dursun, N.; Alican, D. Ankle-foot orthoses: Effect on gait in children with cerebral palsy. *Disabil. Rehabil.* **2002**, *24*, 345–347. [CrossRef] [PubMed]
27. Galli, M.; Cimolin, V.; Rigoldi, C.; Albertini, G. Quantitative Evaluation of the Effects of Ankle Foot Orthosis on Gait in Children with Cerebral Palsy Using the Gait Profile Score and Gait Variable Scores. *J. Dev. Phys. Disabil.* **2016**, *28*, 367–379. [CrossRef]
28. Hassani, S.; Roh, J.; Ferdjallah, M.; Reiners, K.; Kuo, K.; Smith, P.; Harris, G. Rehabilitative orthotics evaluation in children with diplegic cerebral palsy: Kinematics and kinetics. In Proceedings of the 26th Annual International Conference of the IEEE Engineering in Medicine and Biology Society, San Francisco, CA, USA, 1–5 September 2004; pp. 4874–4876. [CrossRef]
29. Hayek, S.; Hemo, Y.; Chamis, S.; Bat, R.; Segev, E.; Wientroub, S.; Yzhar, Z. The effect of community-prescribed ankle-foot orthoses on gait parameters in children with spastic cerebral palsy. *J. Child. Orthop.* **2007**, *1*, 325–332. [CrossRef] [PubMed]
30. Jagadamma, K.C.; Coutts, F.J.; Mercer, T.H.; Herman, J.; Yirrell, J.; Forbes, L.; van der Linden, M.L. Optimising the effects of rigid ankle foot orthoses on the gait of children with cerebral palsy (CP)—An exploratory trial. *Disabil. Rehabil. Assist. Technol.* **2015**, *10*, 445–451. [CrossRef]
31. Kane, K.; Musselman, K.; Lanovaz, J. O 063—Individualizing the ankle angle in an ankle-foot orthosis: Effects at the knee for children with cerebral palsy and equinus. *Gait Posture* **2018**, *65*, 128–129. [CrossRef]
32. Kane, K.; Musselman, K.; Lanovaz, J. Comparison of dorsiflexion motion allowed by solid and flexible ankle-foot orthoses during gait for children with cerebral palsy and equinus. *Gait Posture* **2020**, *81*, 176–177. [CrossRef]
33. Kerkum, Y.L.; Brehm, M.-A.; van Hutten, K.; Noort, J.C.v.D.; Harlaar, J.; Becher, J.G.; Buizer, A.I. Acclimatization of the gait pattern to wearing an ankle-foot orthosis in children with spastic cerebral palsy. *Clin. Biomech.* **2015**, *30*, 617–622. [CrossRef]
34. Lam, W.K.; Leong, J.C.Y.; Li, Y.H.; Hu, Y.; Lu, W.W. Biomechanical and electromyographic evaluation of ankle foot orthosis and dynamic ankle foot orthosis in spastic cerebral palsy. *Gait Posture* **2005**, *22*, 189–197. [CrossRef]
35. Limpaninlach, S.P.; Prasertsukdee, S.; Palisano, R.J.P.; Burns, J.; Kaewkungwal, J.; Inthachom, R. Multidimensional Effects of Solid and Hinged Ankle-Foot Orthosis in Children with Cerebral Palsy. *Pediatr. Phys. Ther.* **2021**, *33*, 227–235. [CrossRef]
36. Lindskov, L.; Huse, A.-B.; Johansson, M.; Nygård, S. Muscle activity in children with spastic unilateral cerebral palsy when walking with ankle-foot orthoses: An explorative study. *Gait Posture* **2020**, *80*, 31–36. [CrossRef]
37. Liu, X.-C.; Embrey, D.; Tassone, C.; Klingbeil, F.; Marquez-Barrientos, C.; Brandsma, B.; Lyon, R.; Schwab, J.; Tarima, S.; Thometz, J. Foot and ankle joint movements inside orthoses for children with spastic CP. *J. Orthop. Res.* **2014**, *32*, 531–536. [CrossRef] [PubMed]
38. Liu, X.-C.; Embrey, D.; Tassone, C.; Zvara, K.; Brandsma, B.; Lyon, R.; Goodfriend, K.; Tarima, S.; Thometz, J. Long-Term Effects of Orthoses Use on the Changes of Foot and Ankle Joint Motions of Children with Spastic Cerebral Palsy. *PM&R* **2018**, *10*, 269–275. [CrossRef]
39. Lucareli, P.R.G.; Lima, M.d.O.; Lucarelli, J.G.d.A.; Lima, F.P.S. Changes in joint kinematics in children with cerebral palsy while walking with and without a floor reaction ankle-foot orthosis. *Clinics* **2007**, *62*, 63–68. [CrossRef] [PubMed]
40. Joanna, M.; Magdalena, S.; Katarzyna, B.-M.; Daniel, S.; Ewa, L.-D. The Utility of Gait Deviation Index (GDI) and Gait Variability Index (GVI) in Detecting Gait Changes in Spastic Hemiplegic Cerebral Palsy Children Using Ankle-Foot Orthoses (AFO). *Children* **2020**, *7*, 149. [CrossRef]
41. Melanda, A.G.; Pauleto, A.C.; Iucksch, D.D.; Cunha, R.F.M.D.; Smaili, S.M. Results of Orthoses Used on Ambulatory Patients with Bilateral Cerebral Palsy. *Acta Ortop. Bras.* **2020**, *28*, 137–141. [CrossRef]
42. Meyns, P.; Kerkum, Y.; Buizer, A.; Becher, J.; Brehm, M.-A.; Harlaar, J. The effect of ankle foot orthosis stiffness on trunk movement and walking energy cost in cerebral palsy. *Gait Posture* **2016**, *49*, 2. [CrossRef]
43. Mossberg, K.A.; Linton, K.A.; Friske, K. Ankle-foot orthoses: Effect on energy expenditure of gait in spastic diplegic children. *Arch. Phys. Med. Rehabil.* **1990**, *71*, 490–494.
44. Oudenhoven, L.M.; Kerkum, Y.L.; Buizer, A.I.; van der Krogt, M.M. How does a systematic tuning protocol for ankle foot orthosis-footwear combinations affect gait in children in cerebral palsy? *Disabil. Rehabil.* **2021**, *44*, 6867–6877. [CrossRef]
45. Öunpuu, S.; Garibay, E.; Acsadi, G.; Brimacombe, M.; Pierz, K. The impact of orthoses on gait in children with Charcot-Marie-Tooth disease. *Gait Posture* **2021**, *85*, 198–204. [CrossRef]
46. Pauk, J.; Ihnatouski, M.; Daunoraviciene, K.; Laskhousky, U.; Griskevicius, J. Research of the spatial-temporal gait parameters and pressure characteristic in spastic diplegia children. *Acta Bioeng. Biomech.* **2016**, *18*, 121–129.
47. Radtka, S.A.; Skinner, S.R.; Dixon, D.M.; Johanson, M.E. A comparison of gait with solid, dynamic, and no ankle-foot orthoses in children with spastic cerebral palsy. *Phys. Ther.* **1997**, *77*, 395–409. [CrossRef] [PubMed]

48. Rethlefsen, S.; Kay, R.; Dennis, S.; Forstein, M.; Tolo, V. The effects of fixed and articulated ankle-foot orthoses on gait patterns in subjects with cerebral palsy. *J. Pediatr. Orthop.* **1999**, *19*, 470–474. [CrossRef] [PubMed]
49. Ries, A.J.; Novacheck, T.F.; Schwartz, M.H. The Efficacy of Ankle-Foot Orthoses on Improving the Gait of Children with Diplegic Cerebral Palsy: A Multiple Outcome Analysis. *PM&R* **2015**, *7*, 922–929. [CrossRef]
50. Ries, A.J.; Schwartz, M.H. Ground reaction and solid ankle-foot orthoses are equivalent for the correction of crouch gait in children with cerebral palsy. *Dev. Med. Child Neurol.* **2019**, *61*, 219–2255. [CrossRef]
51. Romkes, J.; Brunner, R. Comparison of a dynamic and a hinged ankle-foot orthosis by gait analysis in patients with hemiplegic cerebral palsy. *Gait Posture* **2002**, *15*, 18–24. [CrossRef]
52. Romkes, J.; Hell, A.K.; Brunner, R. Changes in muscle activity in children with hemiplegic cerebral palsy while walking with and without ankle-foot orthoses. *Gait Posture* **2006**, *24*, 467–474. [CrossRef]
53. Schwarze, M.; Block, J.; Kunz, T.; Alimusaj, M.; Heitzmann, D.W.W.; Putz, C.; Dreher, T.; Wolf, S.I. The added value of orthotic management in the context of multi-level surgery in children with cerebral palsy. *Gait Posture* **2019**, *68*, 525–530. [CrossRef]
54. Schweizer, K.; Brunner, R.; Romkes, J. Upper body movements in children with hemiplegic cerebral palsy walking with and without an ankle-foot orthosis. *Clin. Biomech.* **2014**, *29*, 387–394. [CrossRef]
55. Skaaret, I.; Steen, H.; Terjesen, T.; Holm, I. Impact of ankle-foot orthoses on gait 1 year after lower limb surgery in children with bilateral cerebral palsy. *Prosthet. Orthot. Int.* **2019**, *43*, 12–20. [CrossRef]
56. Swinnen, E.; Baeyens, J.-P.; Van Mulders, B.; Verspecht, J.; Degelaen, M. The influence of the use of ankle-foot orthoses on thorax, spine, and pelvis kinematics during walking in children with cerebral palsy. *Prosthet. Orthot. Int.* **2018**, *42*, 208–213. [CrossRef]
57. Tavernese, E.; Petrarca, M.; Rosellini, G.; Di Stanislao, E.; Pisano, A.; Di Rosa, G.; Castelli, E. Carbon Modular Orthosis (Ca.M.O.): An innovative hybrid modular ankle-foot orthosis to tune the variable rehabilitation needs in hemiplegic cerebral palsy. *NeuroRehabilitation* **2017**, *40*, 447–457. [CrossRef] [PubMed]
58. Van Gestel, L.; Molenaers, G.; Huenaerts, C.; Seyler, J.; Desloovere, K. Effect of dynamic orthoses on gait: A retrospective control study in children with hemiplegia. *Dev. Med. Child Neurol.* **2008**, *50*, 63–67. [CrossRef] [PubMed]
59. Wahid, F.; Begg, R.; Sangeux, M.; Halgamuge, S.; Ackland, D.C. The effects of an ankle foot orthosis on cerebral palsy gait: A multiple regression analysis. In Proceedings of the 37th Annual International Conference of the IEEE Engineering in Medicine and Biology Society, Milan, Italy, 25–29 August 2015; pp. 5509–5512. [CrossRef]
60. White, H.; Barney, B.; Augsburg, S.; Miller, E.; Iwinski, H. AFOs Improve Stride Length and Gait Velocity but Not Motor Function for Most with Mild Cerebral Palsy. *Sensors* **2023**, *23*, 569. [CrossRef]
61. White, H.; Jenkins, J.; Neace, W.P.; Tylkowski, C.; Walker, J. Clinically prescribed orthoses demonstrate an increase in velocity of gait in children with cerebral palsy: A retrospective study. *Dev. Med. Child Neurol.* **2002**, *44*, 227–232. [CrossRef]
62. Borghi, C.; Costi, S.; Formisano, D.; Neviani, R.; Pandarese, D.; Ferrari, A. Effectiveness comparison between carbon spring and hinged ankle-foot orthoses in crouch gait treatment of children with diplegic cerebral palsy: A randomized crossover trial. *Eur. J. Phys. Rehabil. Med.* **2021**, *57*, 577–584. [CrossRef]
63. Buckon, C.E.; Thomas, S.S.; Jakobson-Huston, S.; Sussman, M.; Aiona, M. Comparison of three ankle-foot orthosis configurations for children with spastic hemiplegia. *Dev. Med. Child Neurol.* **2001**, *43*, 371–378. [CrossRef]
64. Buckon, C.E.; Thomas, S.S.; Jakobson-Huston, S.; Moor, M.; Sussman, M.; Aiona, M. Comparison of three ankle-foot orthosis configurations for children with spastic diplegia. *Dev. Med. Child Neurol.* **2004**, *46*, 590–598. [CrossRef]
65. Carlson, W.E.; Vaughan, C.L.; Damiano, D.L.; Abel, M.F. Orthotic management of gait in spastic diplegia. *Am. J. Phys. Med. Rehabil.* **1997**, *76*, 219–225. [CrossRef]
66. Kerkum, Y.L.; Buizer, A.I.; Van Den Noort, J.C.; Becher, J.G.; Harlaar, J.; Brehm, M.-A. The Effects of Varying Ankle Foot Orthosis Stiffness on Gait in Children with Spastic Cerebral Palsy Who Walk with Excessive Knee Flexion. *PLoS ONE* **2015**, *10*, e0142878. [CrossRef]
67. Meyns, P.; Kerkum, Y.L.; Brehm, M.A.; Becher, J.G.; Buizer, A.I.; Harlaar, J. Ankle foot orthoses in cerebral palsy: Effects of ankle stiffness on trunk kinematics, gait stability and energy cost of walking. *Eur. J. Paediatr. Neurol.* **2020**, *26*, 68–74. [CrossRef]
68. Radtka, S.A.; Skinner, S.R.; Johanson, M.E. A comparison of gait with solid and hinged ankle-foot orthoses in children with spastic diplegic cerebral palsy. *Gait Posture* **2005**, *21*, 303–310. [CrossRef] [PubMed]
69. Wojciechowski, E.A.; Cheng, T.L.; Hogan, S.M.; Mudge, A.J.; Balassone, D.; Menezes, M.P.; Little, D.G.; Dwan, L.N.; Burns, J. Replicating and redesigning ankle-foot orthoses with 3D printing for children with Charcot-Marie-Tooth disease. *Gait Posture* **2022**, *96*, 73–80. [CrossRef] [PubMed]
70. Wren, T.A.L.; Dryden, J.W.; Mueske, N.M.; Dennis, S.W.; Healy, B.S.; Rethlefsen, S.A. Comparison of 2 Orthotic Approaches in Children With Cerebral Palsy. *Pediatr. Phys. Ther.* **2015**, *27*, 218–226. [CrossRef] [PubMed]
71. Zelik, K.E.; Adamczyk, P.G. A unified perspective on ankle push-off in human walking. *J. Exp. Biol.* **2016**, *219 Pt 23*, 3676–3683. [CrossRef]
72. Aquino, M.R.C.; Resende, R.A.; Kirkwood, R.N.; Souza, T.R.; Fonseca, S.T.; Ocarino, J.M. Spatial-temporal parameters, pelvic and lower limb movements during gait in individuals with reduced passive ankle dorsiflexion. *Gait Posture* **2022**, *93*, 32–38. [CrossRef]

73. Gao, T.; Ma, Z.; Yang, N.; Zhang, S.; Shi, H.; Zhang, H.; Ren, S.; Huang, H. The relationship of peak ankle dorsiflexion angle with lower extremity biomechanics during walking. *J. Foot Ankle Res.* **2024**, *17*, e12027. [CrossRef]
74. Brunner, R.; Frigo, C.A. Control of Tibial Advancement by the Plantar Flexors during the Stance Phase of Gait Depends on Knee Flexion with Respect to the Ground Reaction Force. *Bioengineering* **2023**, *11*, 41. [CrossRef]
75. Degelean, M.; De Borre, L.; Salvia, P.; Pelc, K.; Kerckhofs, E.; De Meirleir, L.; Cheron, G.; Dan, B. Effect of ankle-foot orthoses on trunk sway and lower limb intersegmental coordination in children with bilateral cerebral palsy. *J. Pediatr. Rehabil. Med.* **2012**, *5*, 171–179. [CrossRef]
76. Higgins, J.P.T.; Eldridge, S.; Li, T. Chapter 23: Including Variants on Randomized Trials. Cochrane Handbook. Available online: <https://training.cochrane.org/handbook/current/chapter-23#section-23-2> (accessed on 10 January 2025).
77. Degelaen, M. Effect of ankle-foot orthoses on motor performance in cerebral palsy. *Dev. Med. Child Neurol.* **2019**, *61*, 119–120. [CrossRef]
78. Morris, C. A review of the efficacy of lower-limb orthoses used for cerebral palsy. *Dev. Med. Child Neurol.* **2002**, *44*, 205–211. [CrossRef]
79. Kane, K.; Manns, P.; Lanovaz, J.; Musselman, K. Clinician perspectives and experiences in the prescription of ankle-foot orthoses for children with cerebral palsy. *Physiother. Theory Pract.* **2019**, *35*, 148–156. [CrossRef]

Disclaimer/Publisher’s Note: The statements, opinions and data contained in all publications are solely those of the individual author(s) and contributor(s) and not of MDPI and/or the editor(s). MDPI and/or the editor(s) disclaim responsibility for any injury to people or property resulting from any ideas, methods, instructions or products referred to in the content.



Article

Development and Effectiveness Testing of a Novel 3D-Printed Multi-Material Orthosis in Nurses with Plantar Foot Pain

Komal Chhikara ¹, Sarabjeet Singh Sidhu ², Shubham Gupta ¹, Sakshi Saharawat ³, Chitra Kataria ³ and Arnab Chanda ^{1,4,*}

¹ Centre for Biomedical Engineering, Indian Institute of Technology (IIT), Delhi 110016, India

² Mechanical Engineering Department, Sardar Beant Singh State University, Gurdaspur 143521, India

³ Indian Spinal Injuries Center-Institute of Rehabilitation Sciences, New Delhi 110070, India

⁴ Department of Biomedical Engineering, All India Institute of Medical Science (AIIMS), Delhi 110016, India

* Correspondence: arnab.chanda@cbme.iitd.ac.in

Abstract: Plantar foot pain is one of the most common musculoskeletal conditions affecting the foot. It is regularly experienced by the population with occupations that require prolonged standing hours, especially in nurses. The etiology of plantar foot pain remains unclear, but it is likely to be multi-factorial, with many associated risk factors including increased hours of standing. Orthoses and insoles are often recommended to plantar foot pain patients, however with minimal scientific advancements and limited customizations. In this study, a novel 3D-printed multi-material customized foot orthosis was developed, and its effectiveness on plantar foot pain reduction and functional ability improvement was studied in the nursing population. A total of thirty-six subjects were recruited and were randomized into two groups. The experimental group received the novel 3D-printed multi-material customized foot orthosis, whereas the control group received the standard-of-care (or traditional) intervention. Pre-test and the post-test scores of pains, functional ability and plantar pressure were observed using SPSS software. Improvements were observed in both of the groups; however, better improvements were seen in the experimental group. Overall, the novel 3D printing-based customized foot orthosis showed significant efficacy in reducing plantar foot pain and pressure, and also in increasing functional ability in the nursing population as compared to the traditional method.

Keywords: plantar pain; foot orthosis; 3D printing; custom insoles; nurses

Citation: Chhikara, K.; Sidhu, S.S.; Gupta, S.; Saharawat, S.; Kataria, C.; Chanda, A. Development and Effectiveness Testing of a Novel 3D-Printed Multi-Material Orthosis in Nurses with Plantar Foot Pain. *Prosthesis* **2023**, *5*, 73–87. <https://doi.org/10.3390/prosthesis5010006>

Academic Editor: Marco Cicciu

Received: 18 November 2022

Revised: 30 December 2022

Accepted: 5 January 2023

Published: 11 January 2023



Copyright: © 2023 by the authors. Licensee MDPI, Basel, Switzerland. This article is an open access article distributed under the terms and conditions of the Creative Commons Attribution (CC BY) license (<https://creativecommons.org/licenses/by/4.0/>).

1. Introduction

Plantar foot pain is a common condition that affects the musculoskeletal system, particularly for the population that requires hours of prolonged standing in their occupations [1]. Several causes that lead to plantar foot pain include prolonged standing hours, bad posture, deteriorated gait cycle, increased weight, increased age, weak musculature, etc. [2]. The normal foot anatomy includes fourteen phalanges, five metatarsals and seven tarsals, where the foot structure is commonly divided into three subcategories, i.e., forefoot, midfoot and hindfoot [3,4]. This structure is generally affected by several musculoskeletal disorders that cause foot pain, such as hallux valgus, metatarsalgia in the forefoot; and plantar fasciitis, Achilles tendinopathy, heel fat pad atrophy, calcaneal stress fractures, tarsal tunnel syndrome, and retrocalcaneal bursitis in the mid- and hindfoot [5]. These disorders may or may not be caused by prolonged standing [1,5]. During clinical diagnosis, plantar foot pain is the most commonly reported sign by the affected population [6–8]. As per the literature [9,10], nurses have comparatively increased hours of standing, and require innumerable physical endurance in their jobs. Due to these reasons, foot pain is found to be one of the most frequent complications faced by the nursing population.

Generally, the occurrence of plantar foot pain is indicated by sharp, burning, shock-like, shooting, radiating and localized, and sometimes dull aching pain [6,11]. These

complications can be managed through conservative management techniques which involve modified shoes, over-the-counter orthoses, customized insoles, rest and steroid injections. Choosing amongst these management options is generally based on several factors such as non-invasiveness, affordability, economical acceptability, ease of use, and comfortability [12]. The use of orthotic insoles manages to comprise all of these features, when compared to other management options. The use of orthotic insoles has shown to be effective, and is the most prescribed option for plantar pain management [13].

Orthotic insoles can either be prefabricated or customized according to the subject's measurements. Pain relief and comfort are achieved through customizing the fit and using materials that are soft and adaptable to the foot [14]. There are a variety of materials and fabrication techniques that can be used to fabricate these customized orthotic insoles. A variety of materials, such as evazote, plastazote, polyurethane, leather and P-lite, can be used in fabrication [15,16]. The fabrication techniques can vary from the traditional techniques to recently popular additive manufacturing. The traditional techniques are mostly based on approximation rather than accuracy. Accuracy and precision can be achieved with the use of additive manufacturing techniques. This production technique allows for point-to-point precision, and for the manufacturer to fabricate insoles using a 3D scan of the subject's foot [17]. The digital scans provide exact measurements, and allow for the creation of a replica of the subject's foot [18,19].

The scope of shock absorption and cushioning is usually limited to the available standard insole materials, which may or may not alleviate foot pain in subjects prescribed with them [20–22]. There is some evidence which suggests that customized orthoses are effective in altering plantar heel pain and functional ability in prolonged standing occupations. However, there are limited findings regarding the effect of these orthoses in nursing populations with plantar foot pain [23–25]. Thus, the purpose of this study was to develop and conduct effectiveness testing of a novel 3D printing-based multi-material customized orthosis for reducing the pain, and improving functional ability in nurses with plantar foot pain.

2. Materials and Methods

2.1. Demographics

This study was conducted on the nursing population employed in the Indian Spinal Injuries Center, Delhi, India. Subject recruitment was based on the inclusion criteria, such as female nurses, subjects who experienced pain for more than 6 months, a pain (VAS (Visual Analog Scale)) score between 3–7, a BMI (Body Mass Index) between 19–25 kg/m², normal range of motion in the hip, knee, and ankle, and subjects having pain during walking. The basis of exclusion for the subjects were subjects with chronic pain more than 8 on the 0–10 VAS, a lower extremity injury in the past 6 months, subjects with a history of hip, knee, or ankle surgery, and those receiving a plantar steroid injection within the previous 3 months. The thirty-six subjects who met the inclusion criteria received an informed consent form, and were recruited after they agreed. The mean and standard deviations of age, height, weight and BMI are shown in Table 1.

The baseline characteristics of all of the subjects were approximately the same in both groups. The subjects were randomly divided into two groups; the experimental group 1 received the 3D printing-based customized insoles, and the control group 2 received the standard-of-care insoles, which are usually prescribed in the hospital (Figure 1). A similar body mass index for both groups was observed, which was calculated by weight in kilograms and height in centimeters.

Table 1. Demographic data of all the recruited subjects.

	Group	Number of Subjects	Mean	Standard Deviation	Standard Error Mean
Age *	1	18	26.66	4.22	0.99
	2	18	26.16	4.24	1.00
Height *	1	18	156.83	10.28	2.42
	2	18	156.33	5.25	1.23
Weight *	1	18	59.00	10.14	2.39
	2	18	58.22	12.99	3.06
BMI *	1	18	21.62	2.28	0.88
	2	18	21.73	1.43	0.23

Note: * Indicates a 95% confidence interval.

**Figure 1.** Standard-of-care insole used in the study.

2.2. Design and Fabrication of Orthosis

Compared to over-the-counter orthoses which consist of fixed geometries to fit the foot arch and other areas, our study included actual foot geometries of the subjects. Firstly, the foot regions of all subjects were scanned using a 3D scanner (3D Systemes, Stone Mountain, SC, USA). The scanned files were exported in STL format (stereolithography format). The artifacts and scanned deformities were smoothened using a mesh editing software, Meshmixer (Autodesk, Mill Valley, CA, USA). Other minor additions such as heel alignment and correction in the arches of the foot were carried out to obtain the corrected foot model. Figure 1 represents the scanned and smoothened model of one of the subjects. The scanned model was then imported to 3D CAD software (SolidWorks 2020, Dassault Systemes, Vélizy-Villacoublay, France). Based on the foot geometries, a negative mold was prepared for casting polyurethane as the hard and flexible base. The mold was 3D-printed using a 3D printer (Creality Ender 3, Shenzhen, China) with polylactic acid (PLA) material. The design of the insole included 4 layers of different materials used for fabrication. The first layer was made of plastazote with a 2 mm dimension; the second layer of evazote had a 5 mm dimension; the third layer was of made of rexine, a layering fabric 1mm in dimension; the most distal or base part comprised the 3D printing-based polyurethane (PU) layer, which was designed subject-specifically using 3D printing. The second layer of evazote had the cut-out for pouring silicone, as per the subject's requirement.

The insoles were fabricated using a combination of both conventional and 3D printing. The fabrication procedure began with scanning and tracing of the subject's foot (Figure 2).

The scan was captured using a 3D scanner (3D systems, USA), and a stereolithography (STL) file was modified using Autodesk Meshmixer software.

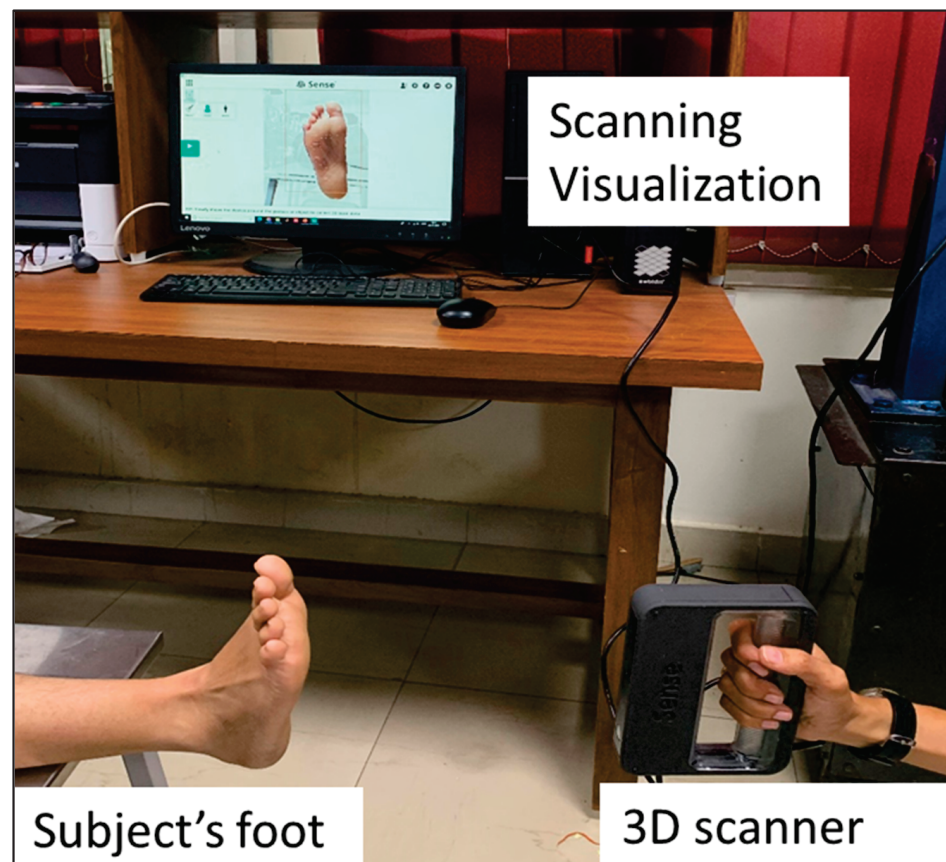


Figure 2. 3D scanning of the subject.

The foot model terminated just below the metatarsals. The STL file was then transformed into a CAD file. It was reversed, and a negative CAD file was obtained using Solidworks software. A 3D-printed solid mold was obtained using PLA (polylactic acid) material with a fused deposition modelling technique (FDM) after 3D printing with a Creality Ender 3 (Shenzhen, China) printer [25]. PU with shore 40A was used as the pouring material in the PLA mold to obtain the base layer. The basis for selecting PU 40 was from its characteristic of rigidity for motion control [26]. The aim to provide the rigid base was to accommodate the deformities and application of the corrections within the foot [27]. The PU material was left for 24 hours to cure, and then it was taken out from the PLA mold.

The trace of the patient's foot was used as a reference for the cutout of three other layers. These layers were fabricated with the prominently used materials in many lower extremity orthotic devices. The materials included evazote, plastazote and rexine [10,28,29]. These cutouts were then grinded for a smoother structure. The plastazote layer was just a simple cut-out as per the trace taken; it was used as the base layer of the evazote layer. The evazote layer was given grinded grooves for pouring the silicone material, due to its extra cushioning and shock absorption properties. The location of the grooves was decided as per the pressure measurements of each patient. The evazote and plastazote layers were then stuck together using adhesive. After the complete adhesive drying process, silicone polymer was poured, and was left to cure for the next 6–8 hours. After the curing process was complete, the last layer of rexine material was applied using adhesive. The uppermost layer consisted of anti-fungal and perspiration absorption properties, thus making it most suitable for the layer that was directly in contact with the skin. The PU layer was then applied to the base of the fabricated insole using adhesive, and was left to dry. The fabricated insole was then grinded and smoothened overall to make it even.

It was made sure that no unevenness was present, as this could exaggerate the pain and discomfort, thereby affecting the subject's functionality. The plantar surface of the foot and the uppermost layer of the fabricated insole had to have an even topology for better adaptation, and to placate the subject's specificity [30] (Figure 3).

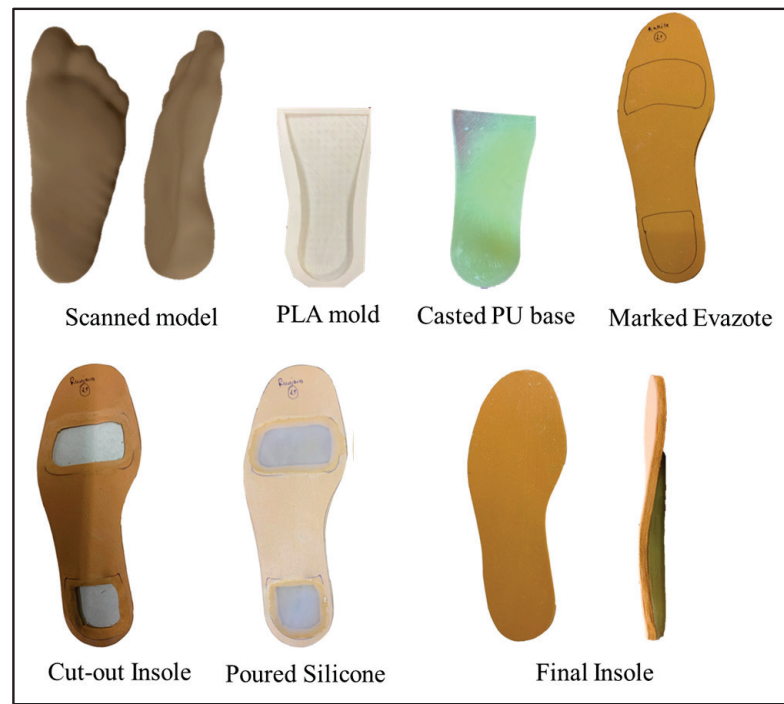


Figure 3. Fabrication procedure of the insole.

2.3. Material Selection

The materials were selected due to their performance and physical properties, as shown in the literature. PU was used as the rigid base layer, with the purpose of motion control, heel alignment and arch support in the foot. Several studies from the literature have shown the use of PU with a shore hardness of 40 to 70A as being effective for foot orthoses [31]. The rationale for selection of evazote and plastazote were for their cushioning effects [29,30]. The patented silicone simulants were implemented into the insole, depending on the requirement for each patient. The location of the silicone groove in the evazote layer was decided based on pain location and pressure distribution in the subject's foot. The shore hardness of the silicone polymer was varied as per the subject's need, and the shore hardness of silicone polymer ranged between 5A to 30A, where the softness decreased with increasing shore hardness. However, the hardness of the silicone polymer with shore 30A was softer when compared to the plantar region of the skin [32].

2.4. Validation

A pressure sensor-based smart insole was used to obtain the pressure values for objective assessment of the 3D-printed insoles. This device was used to calculate the pressure prior to insole application, and after the insole application across the considered groups. The pressure measurements were taken for both standing and walking conditions. The subject was allowed to stand for 60 s, and subjects were asked to walk for 5 min after a break of 5 min (Figure 4). An array consisting of 114 pressure values were extracted from the device every 5 milliseconds.



Figure 4. Subject walking with the smart insole.

2.5. Measures

The subjective and objective data were collected for all of the subjects recruited in the study. For subjective data collection, pain and functional ability were assessed using the visual analog scale (VAS) [33] and foot and ankle ability measure (FAAM) [34] questionnaires, respectively. The VAS questionnaire contains a 10 cm line, where one end demonstrates no pain, and the other extreme end denotes worst pain. The subject must mark the level of pain felt on the line ranging from no pain to worst pain in this questionnaire. The FAAM questionnaire assesses the foot and ankle ability to perform the activities conducted by the subjects. The scale is broadly divided into two sections, where one section has several questions to assess daily activities through the FAAM activities and daily living subscale, whereas the sports activities of the subjects are assessed using the FAAM sports subscale. These questionnaires are widely accepted as the standard measures to quantify the pain and functional ability. The nursing occupation requires long standing hours which affect plantar pressures, and lead to elevations in these pressure values. Therefore, the pressure values were calculated for standing as well as during walking. The objective data were collected using pressure measurements in the plantar foot region while standing and walking.

2.6. Data Analysis

The statistical analysis was performed using SPSS statistics 26.0. An independent *t*-test was used to analyze the results obtained from both of the insole groups. Both of the insoles were compared according to their performance on the VAS and FAAM questionnaires, at p -value < 0.5 . The data were analyzed using SPSS software. Mean and standard deviation were computed for each study variable. An independent *t*-test was used to analyze the post-test data within the insole groups. The hypothesis was tested at a significance level of p -value < 0.5 and confidence interval of 95%.

3. Results

This section deals with the results obtained after the data analysis of the outcome values from the objective and subjective assessments. The following sections discuss each measure with respect to values obtained before the implication of the orthotic intervention, and after the application of the orthotic intervention for four weeks. A thorough follow up was carried out each week to observe the progression of the insoles on plantar pain mitigation. The baseline scores were taken as pre-test and post-test values, for all of the measures. Subjects from each group were assessed for pain, functionality, standing and

walking plantar pressures. These scores were analyzed using SPSS software for the paired sample t-test within group results, which are discussed below.

3.1. Pain

The nursing population requires a lot of physical endurance and muscular strength for standing and running between wards as part of their daily routine. In this study, pain was assessed using the VAS questionnaire, where the subjects marked their pain values from 0 to 10 on the VAS scale. The results were compared between the pre-test and post-test data of both groups, with and without the 3D-printed foot orthosis. The pretest pain scores were 3.94 ± 1.76 , and the post-test scores were 1.22 ± 0.87 in the experimental group, representing a reduction of approximately 69% in the pain level scores [35,36] in subjects using the 3D-printed insoles. The pain scores for group 2, i.e., the control group with the standard-of-care insole, were also assessed at the same confidence interval and *p*-value. The pre-test score obtained was 4.16 ± 1.91 , and the post-test score was 2.66 ± 1.78 , representing an approximately 36% reduction. The comparison of pre-test and post-test data for the experimental and control group is shown in Figure 5.

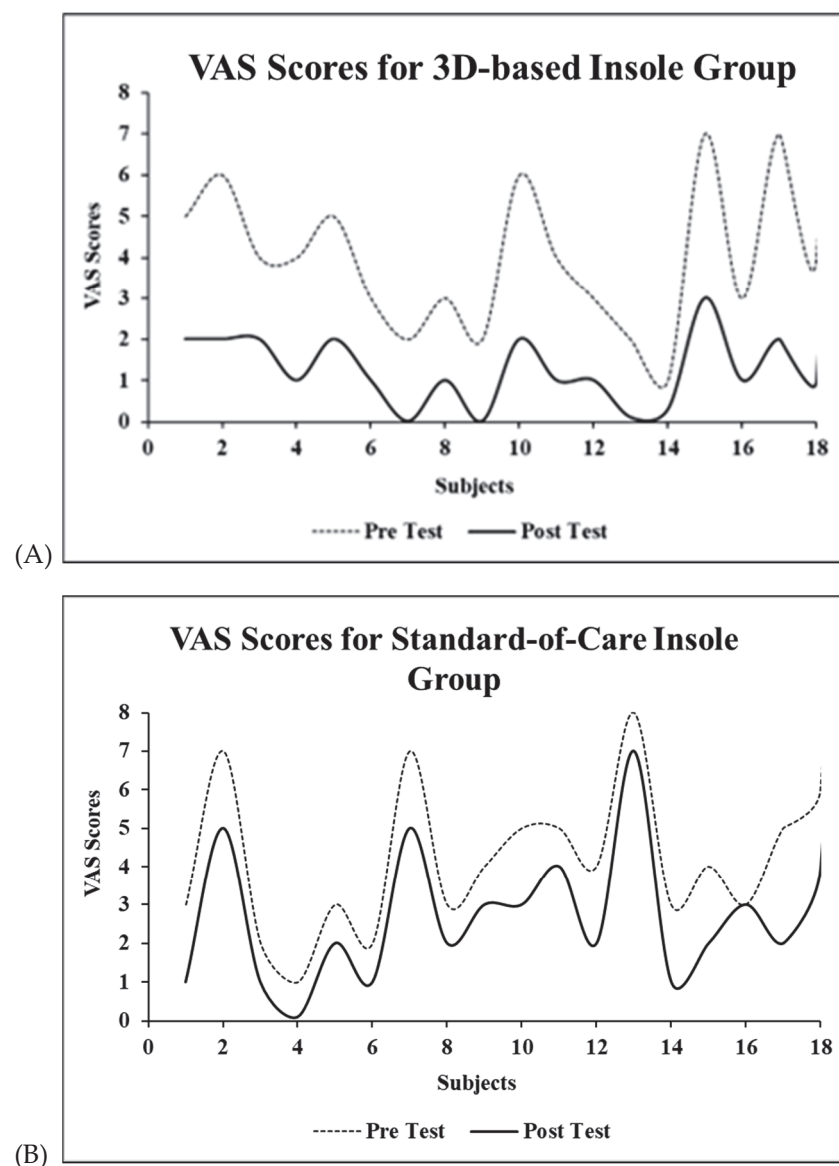


Figure 5. Pre-test and post-test values of VAS for pain in groups wearing (A) 3D printing-based customized and (B) standard-of-care insoles.

The post-test values of both groups were compared using the paired sample *t*-test with SPSS. This comparison could provide better evidence regarding the efficacy of the 3D printing-based customized insole group. The paired *t*-test result demonstrated that the reduction in the pain scores of 3D printing-based group 1 was 2.72 ± 1.01 , whereas in standard-of-care insole group 2, the reduction was just 1.50 ± 0.70 . These results demonstrate the better effectiveness of the 3D printing-based multi-material customized insole, as a greater reduction in pain scores was observed. This pain score reduction is possibly due to customization of the 3D-printed insole. The rectified pain areas of each patient were provided with soft silicone cushioning for pressure reduction and shock absorption. Since all of the pain areas were cushioned for shock absorption, therefore a reduction in the pain scores was observed (Figure 5) in the 3D printing-based insole group.

3.2. Functionality

Prolonged standing hours are known to affect the functionality of the nurses, affecting their activities of daily living. The FAAM questionnaire was used to assess the functional ability of the subjects of the experimental group prescribed with the 3D-printing-based customized insole. The pre-test score obtained was 55.80 ± 20.84 , and the post-test value was 76.19 ± 14.46 , representing an increase of approximately 37% in the functional level scores [35,36]. The same functional assessment was conducted in the control group, i.e., group 2 with standard-of-care insole. The pre-test value obtained was 54.88 ± 20.12 , and the post-test value was 66.11 ± 17 , representing an approximately 20% increase. The scores obtained are described in graphical form in Figure 6.

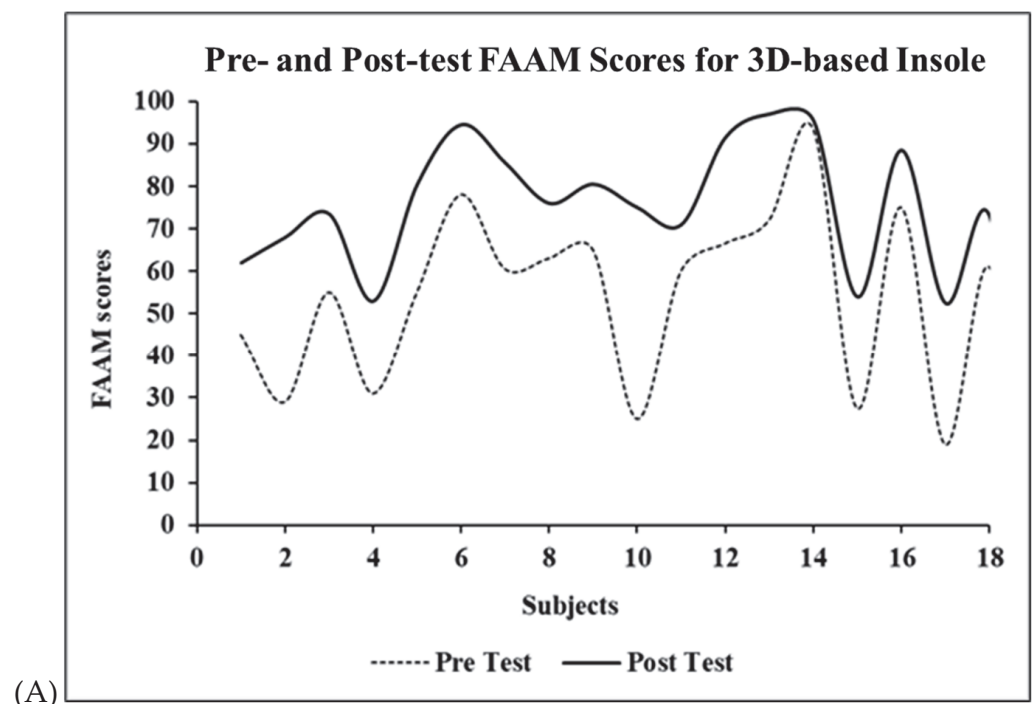


Figure 6. Cont.

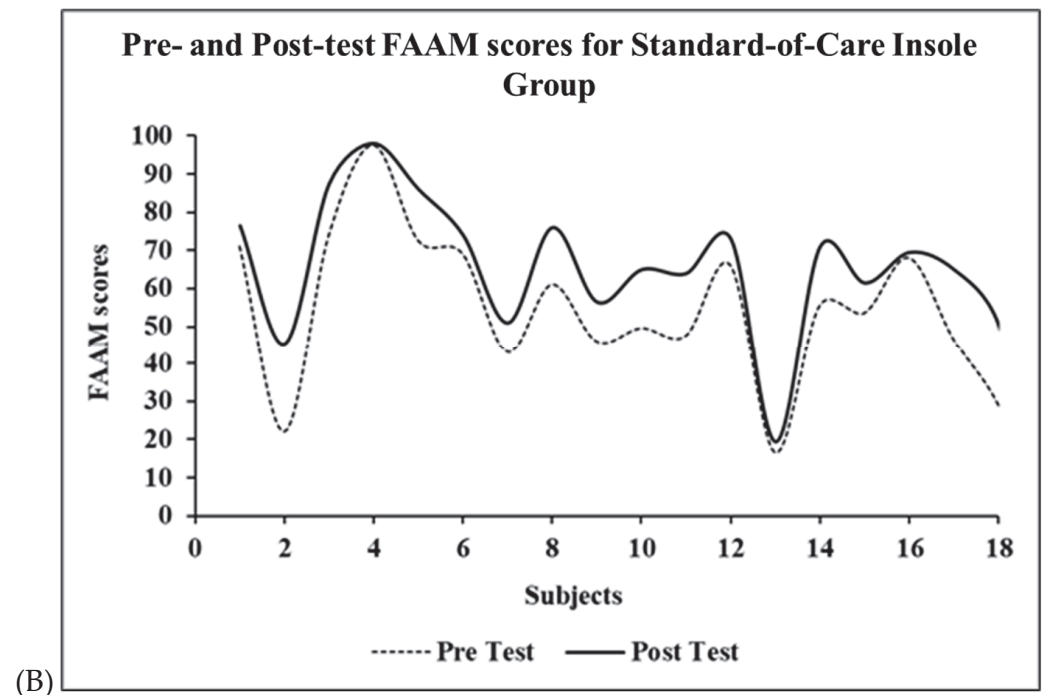


Figure 6. Pre-test and post-test functionality scores of subjects wearing (A) 3D-printing-based customized and (B) standard-of-care insoles.

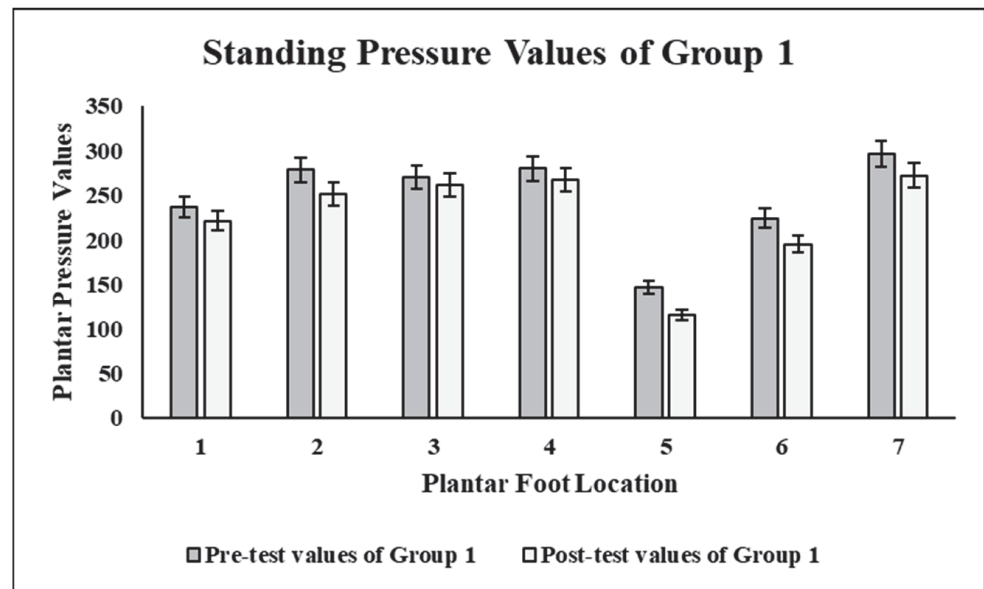
The post-test values of functional ability for both groups were compared using the paired sample *t*-test with SPSS. The comparative post-test functional ability could provide better evidence of the efficacy regarding the 3D-printing-based customized insole group. The paired *t*-test result demonstrated that the improvements in the functional scores of groups 1 was 21.69 ± 11.23 , whereas in group 2 it was 11.22 ± 6.80 . This result demonstrated the prominence of the 3D-printing-based customized insole, as a greater improvement in functional ability scores was observed.

3.3. Plantar Pressure

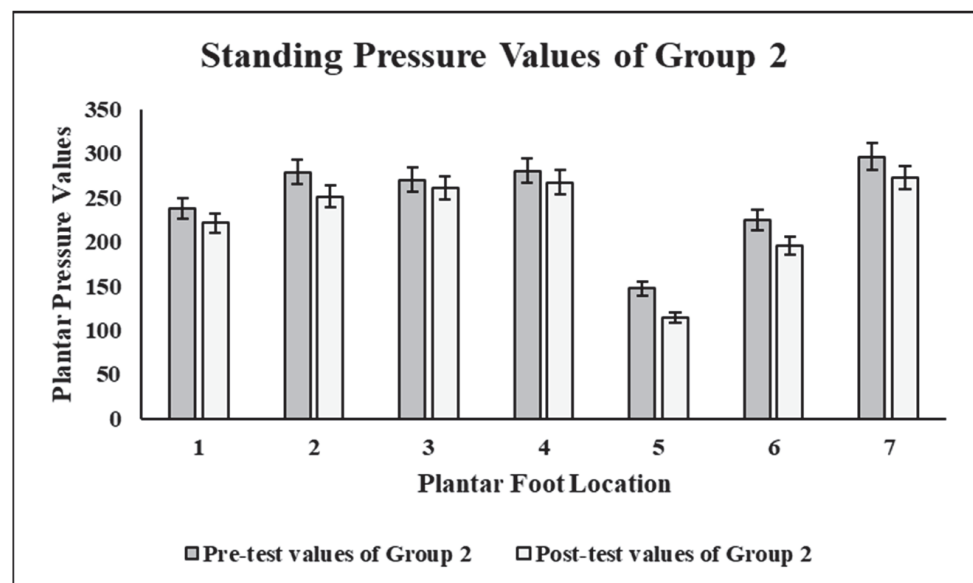
Plantar pressure was observed throughout the plantar areas of the foot. The pressure values were obtained for seven different locations in the plantar region of the foot, i.e., hallux, first metatarsal, third metatarsal, fifth metatarsal, medial midfoot, lateral midfoot and heel.

3.3.1. Standing

The mean pre-test plantar pressure values for standing in group 1 at the aforementioned locations were 238.16 kPa, 278.61 kPa, 273.55 kPa, 282.55 kPa, 143.66 kPa, 222.83 kPa and 293.83 kPa, respectively (Figure 7A). The post-test means values obtained after application of the insole for four weeks were 197.61 kPa, 222.44 kPa, 222.22 kPa, 226.55 kPa, 98.94 kPa, 137.72 kPa and 237 kPa, respectively. The pressure values for group 2 are demonstrated in Figure 7B. The mean pre-test plantar pressure values at the same seven locations were 237.38 kPa, 278.94 kPa, 270.22 kPa, 280.22 kPa, 147.05 kPa, 224.50 kPa and 296.38 kPa, respectively. The mean post-test pressure values were 221.55 kPa, 251.50 kPa, 261.50 kPa, 267.44 kPa, 115.00 kPa, 195.33 kPa and 272.50 kPa, respectively. Both the pre-test and post-test values are shown in Figure 7.



(A)



(B)

Figure 7. Pressure values taken in standing position in 3D-printing-based group 1 (A) and standard-of-care insole group 2 (B) at seven different locations in the plantar region, 1: hallux, 2: first metatarsal, 3: third metatarsal, 4: fifth metatarsal, 5: medial mid-foot, 6: lateral mid-foot and 7: heel, for (A) experimental group and (B) control group.

The distribution of the standing plantar pressure is represented in Figure 8 for both the experimental as well as the control group. In the case of the experimental group, the peak values ranged from 98.94 to 237 kPa, whereas in the control group, the peak values ranged from 115.00 to 272.50 kPa.

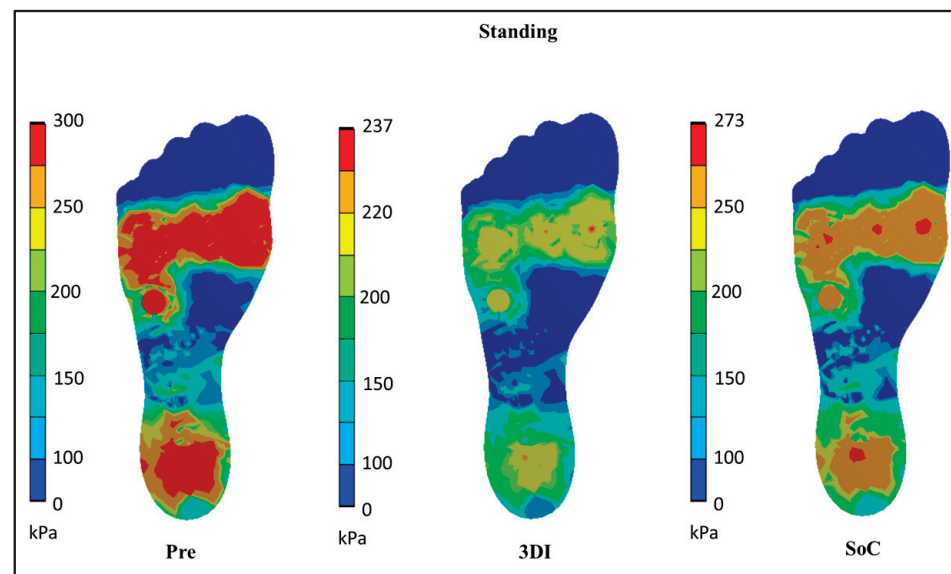
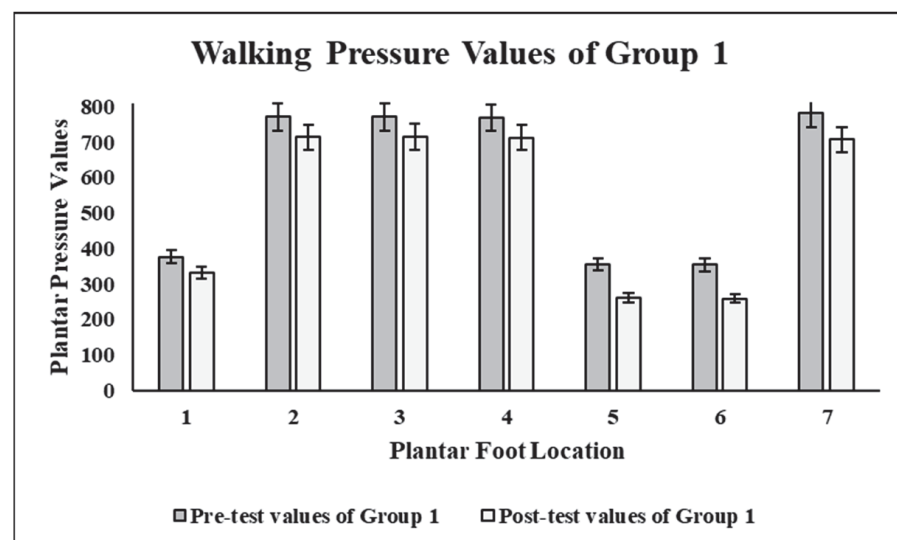


Figure 8. Standing plantar pressure distributions across the experimental (3DI) and control (SoC) groups.

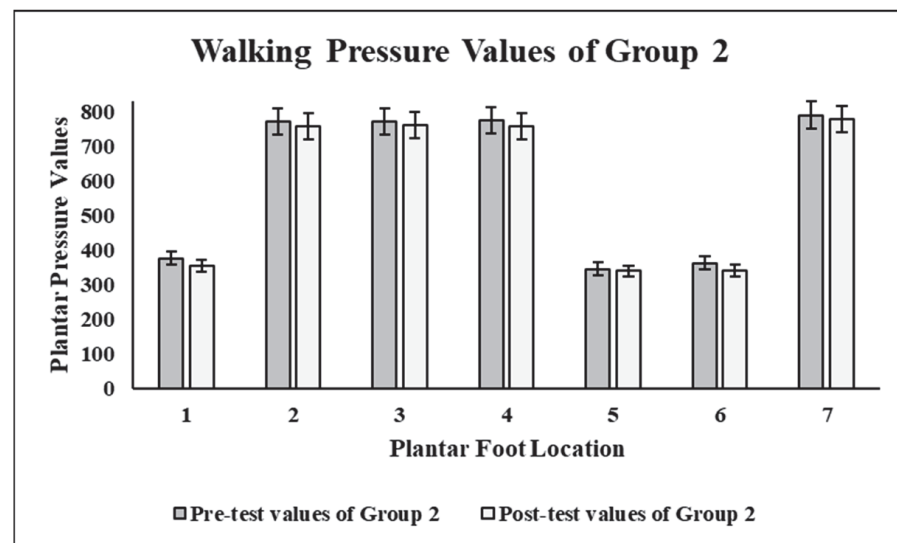
3.3.2. Walking

The pressure values were taken in the walking phase as well. The mean pre-test values for walking with the application of the 3D printing-based insole obtained were 376.33 kPa, 770.61 kPa, 770.38 kPa, 768.38 kPa, 354.88 kPa, 354.50 kPa and 782.05 kPa at the hallux, first metatarsal, third metatarsal, fifth metatarsal, medial mid-foot, lateral mid-foot and heel, respectively. The post-test values obtained for the same group were 332.55 kPa, 714.38 kPa, 714.66 kPa, 712.05 kPa, 260.94 kPa, 259.33 kPa and 707.66 kPa, respectively. The walking pressures for group 2 were also assessed, and the mean pre-test values obtained were 374.72 kPa, 769.50 kPa, 770.33 kPa, 773.55, 345.16, 362.38 and 788.05, respectively. The post-test values obtained were 354.94, 757.94, 758.50, 757.00, 338.44, 339.11 and 776.66 kPa, respectively. Both sets of values obtained were tested using the paired sample *t*-test at 95% confidence interval. The values are demonstrated in Figure 9.



(A)

Figure 9. Cont.



(B)

Figure 9. Pressure values taken in the walking position in 3D-printing-based group 1 (A) and standard-of-care insole group 2 (B) at seven different locations in the plantar region, 1: hallux, 2: first metatarsal, 3: third metatarsal, 4: fifth metatarsal, 5: medial mid-foot, 6: lateral mid-foot and 7: heel.

The distributions of the walking plantar pressure are represented in Figure 10 for both the experimental as well as the control group. In the case of the experimental group, the peak values ranged from 259.33 to 714.66 kPa, whereas in the control group the values ranged from 338.44 to 776.66 kPa. Better improvements in the plantar pressures could be observed in the post-test scores of standing and walking plantar pressures in the 3D-printing-based customized insole group. The figures demonstrating the plantar pressure distribution also show evidence of these improvements.

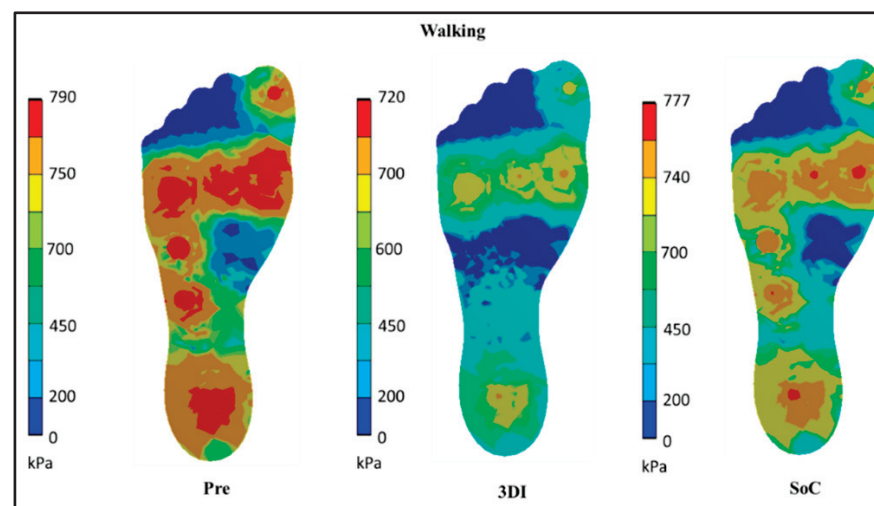


Figure 10. Walking plantar pressure distributions across the experimental (3DI) and control (SoC) groups.

4. Discussion

The current study demonstrated the fabrication of a 3D-printed customized orthosis for subjects with plantar foot pain. The target population chosen was subjects with an occupation of long-standing and walking hours, specifically the nursing population. The experimental group was compared with a control group that was prescribed a traditional standard-of-care insole. The foot of the subjects was scanned using a 3D scanner, and

using 3D printing and other manufacturing techniques, a novel multi-material customized insole was developed. The insole was prescribed to the subjects for an intervention period of four weeks. The data of the groups were assessed using SPSS based on the values obtained using certain measures for the pain, functionality and pressure in the plantar region of the foot. The developed customized orthoses were found to be more effective in alleviating the plantar pain amongst nurses as compared to the standard treatment which were earlier provided.

The results demonstrated the efficacy of both insoles in the experimental and the control groups. However, the differences in all the measures, pain using VAS, functional ability using FAAM, and pressures using a validation device with pressure sensors, were higher in the experimental group when compared to the control group. While the pre-test values of both groups seemed to be similar, when the post-test values were compared, a more significant improvement was seen in the 3D-printing-based customized insole group. Peak foot pressures were found to correlate and provide an objective measure of pain. The VAS and FAAM values shown in this study represented a significant difference between the groups, with and without the 3D-printed foot orthosis, and greater improvement in functional ability of the 3D-printed insole group. These differences in scores could be considered significant, and in line with literature studies reporting similar significant differences [35,36].

The maximum pain and pressures were observed in the heel and the metatarsal regions. This may be possible evidence of the fact that the maximum weight is borne on these two plantar regions prominently. The physical properties of shock absorption and cushioning offered by the silicone material were tuned to maximize cushioning in these regions. The reduction in pain and pressure improved the functional activity of the subjects, hence improving their work performance. The subjects reported that they were able to improve their work productivity after wearing the customized insoles, thereby confirming the efficacy of the 3D-printing-based customized insoles.

A few limitations of this study should be reported. Although the developed insole was found to produce significant reduction in plantar pain, increased thickness led to the replacement of the already pasted insoles which came with the footwear. Finding ways of minimizing the thickness of the insoles while providing the same amount of cushioning will be beneficial for future studies. Secondly, the population size was moderate; for further testing, a larger sample size needs to be recruited.

5. Conclusions

This study found that the novel 3D-printing-based multi-material customized insole could be a better possible line of conservative management for subjects with plantar foot pain. The efficacy of the insole was tested by prescribing it to a nursing population, and observing its effect on an occupation with maximum standing hours. The results showed significant reductions in the pain and pressure scores; moreover, there was an increased functional level in all of the subjects. Therefore, it can be concluded that these novel insoles can help subjects with prolonged standing occupations to improve their job performance. Further testing of this insole on individuals with other standing occupations such as teachers, guards, etc., is anticipated to help better understand the improvements required for commercialization.

Author Contributions: K.C.: methodology, validation, investigation, formal analysis, writing—original draft and writing—review and editing. S.S.S.: methodology, investigation, formal analysis. S.G.: methodology, data curation, formal analysis and investigation. S.S.: data curation, investigation and formal analysis. C.K.: data curation, investigation and formal analysis. A.C.: conceptualization, methodology, formal analysis, supervision, and writing—review and editing. All authors have read and agreed to the published version of the manuscript.

Funding: No funding was received for this study.

Institutional Review Board Statement: The study was conducted according to the guidelines of the Declaration of Helsinki, and approved by Ethical Committee of Indian Spinal Injuries Centre, New Delhi (protocol code New Delhi ISIC/RP/2022/023 and date of approval was 13 July 2022).

Informed Consent Statement: The subject provided a signed consent form before the study was conducted.

Data Availability Statement: The datasets generated during and/or analyzed during the current study are not publicly available, due to being large datasets; however, data are available from the corresponding author on reasonable request.

Conflicts of Interest: The authors declare no conflict of interest.

References

1. Rao, S.; Riskowski, J.L.; Hannan, M.T. Musculoskeletal conditions of the foot and ankle: Assessments and treatment options. *Best Pract. Res.* **2012**, *26*, 345–368. [CrossRef] [PubMed]
2. Porter, K.B. Plantar Heel Pain. In *Physical Therapy: Treatment of Common Orthopedic Conditions*; JP Medical Ltd.: London, UK, 2016; pp. 382–412. [CrossRef]
3. Chan, C.W.; Rudins, A. Foot Biomechanics During Walking and Running. *Mayo Clin. Proc.* **1994**, *69*, 448–461. [CrossRef] [PubMed]
4. Choo, Y.J.; Park, C.H.; Chang, M.C. Rearfoot disorders and conservative treatment: A narrative review. *Ann. Palliat. Med.* **2020**, *9*, 3546–3552. [CrossRef] [PubMed]
5. Badlissi, F.; Dunn, J.E.; Link, C.L.; Keysor, J.J.; McKinlay, J.B.; Felson, D.T. Foot musculoskeletal disorders, pain, and foot-related functional limitation in older persons. *J. Am. Geriatr. Soc.* **2005**, *53*, 1029–1033. [CrossRef] [PubMed]
6. Alshami, A.M.; Souvlis, T.; Coppieters, M.W. A review of plantar heel pain of neural origin: Differential diagnosis and management. *Man. Ther.* **2008**, *13*, 103–111. [CrossRef]
7. Gutteck, N.; Schilde, S.; Delank, K.S. Pain on the Plantar Surface of the Foot. *Dtsch. Arztebl. International.* **2019**, *116*, 83–88. [CrossRef]
8. Chia, J.K.; Suresh, S.; Kuah, A.; Ong, J.L.; Phua, J.M.; Seah, A.L. Comparative trial of the foot pressure patterns between corrective orthotics, formthotics, bone spur pads and flat insoles in patients with chronic plantar fasciitis. *Ann. Acad. Med. Singapore.* **2009**, *38*, 869. [CrossRef]
9. Soylar, P. Evaluation of the prevalence of musculoskeletal disorders in nurses: A systematic review. *Artic. Med. Sci. Int. Med. J.* **2018**, *7*, 479–485. [CrossRef]
10. Waters, T.R.; Dick, R.B. Evidence of health risks associated with prolonged standing at work and intervention effectiveness. *Rehabil. Nurs.* **2015**, *40*, 148–165. [CrossRef]
11. Goecker, R.M.; Banks, A.S. Analysis of release of the first branch of the lateral plantar nerve. *J. Am. Podiatr. Med. Assoc.* **2000**, *90*, 281–286. [CrossRef]
12. Landorf, K.B.; Keenan, A.M.; Herbert, R.D. Effectiveness of Foot Orthoses to Treat Plantar Fasciitis: A Randomized Trial. *Arch. Intern. Med.* **2006**, *166*, 1305–1310. [CrossRef]
13. Elattar, O.; Smith, T.; Ferguson, A.; Farber, D.; Wapner, K. Uses of Braces and Orthotics for Conservative Management of Foot and Ankle Disorders. *Foot Ankle Orthop.* **2018**, *3*. [CrossRef]
14. Hawke, F.; Burns, J.; Radford, J.A.; Toit, V.D. Custom-made foot orthoses for the treatment of foot pain. *Cochrane Database Syst. Rev.* **2008**, *3*. [CrossRef]
15. Healy, A.; Dunning, D.N.; Chockalingam, N. Materials used for footwear orthoses: A review. *Footwear Sci.* **2010**, *2*, 93–110. [CrossRef]
16. Bus, S.A.; Ulbrecht, J.S.; Cavanagh, P.R. Pressure relief and load redistribution by custom-made insoles in diabetic patients with neuropathy and foot deformity. *Clin. Biomech.* **2004**, *19*, 629–638. [CrossRef]
17. Chhikara, K.; Singh, G.; Gupta, S.; Chanda, A. Progress of Additive Manufacturing in Fabrication of Foot Orthoses for Diabetic Patients: A Review. *Ann. 3D Print. Med.* **2022**, *8*, 100085. [CrossRef]
18. Telfer, S.; Woodburn, J. The use of 3D surface scanning for the measurement and assessment of the human foot. *J. Foot Ankle Res.* **2010**, *3*, 1–9. [CrossRef]
19. Hale, L.; Linley, E.; Kalaskar, D.M. A digital workflow for design and fabrication of bespoke orthoses using 3D scanning and 3D printing, a patient-based case study. *Sci. Rep.* **2020**, *101*, 1–7. [CrossRef]
20. Chanda, A.; Unnikrishnan, V. Novel insole design for diabetic foot ulcer management. *Proc. Inst. Mech. Eng. Part H J. Eng. Med.* **2018**, *232*, 1182–1195. [CrossRef]
21. Chanda, A.; McClain, S. Mechanical Modeling of Healthy and Diseased Calcaneal Fat Pad Surrogates. *Biomimetics* **2019**, *4*, 1. [CrossRef]
22. Chanda, A.; Unnikrishnan, V. Customized Insoles for Diabetic and Pressure Ulcers. US Patent US20180008000A1, 2017.
23. Stolt, M.; Suhonen, R.; Virolainen, P.; Leino-Kilpi, H. Lower extremity musculoskeletal disorders in nurses: A narrative literature review. *Scand. J. Public Health* **2016**, *44*, 106–115. [CrossRef] [PubMed]
24. Ajibade, B.L.; Alao, M. Prevalence of musculo-skeletal disorders among nurses in Osun State, Nigeria. *J. Biol. Agric. Healthc.* **2013**, *3*, 170–175. Available online: <https://www.iiste.org/Journals/index.php/JBAH/article/view/6331> (accessed on 4 January 2023).

25. Chatterjee, S.; Chanda, A. Development of a Tribofidelic Human Heel Surrogate for Barefoot Slip Testing. *J. Bionic Eng.* **2022**, *192*, 429–439. [CrossRef]
26. Chhikara, K.; Gupta, S.; Chanda, A. Development of a novel foot orthosis for plantar pain reduction. *Mater. Today Proc.* **2022**, *62*, 3532–3537. [CrossRef]
27. Yick, K.L.; Tse, C.Y. Textiles and other materials for orthopaedic footwear insoles. In *Handbook of Footwear Design and Manufacture*; Woodhead Publishing: Sawston, UK, 2013; pp. 341–371. [CrossRef]
28. Mulligan, E. Lower Leg, Ankle, and Foot Rehabilitation. *Phys. Rehabil. Inj. Athl.* **2012**, *4*, 426–463. [CrossRef]
29. Nicolopoulos, C.S.; Black, J.; Anderson, E.G. Foot orthoses materials. *Foot* **2000**, *10*, 1–3. [CrossRef]
30. Brückner, K.; Odenwald, S.; Schwanitz, S.; Heidenfelder, J.; Milani, T. Polyurethane-foam midsoles in running shoes-impact energy and damping. *Procedia Eng.* **2010**, *2*, 2789–2793. [CrossRef]
31. Gerrard, J.M.; Bonanno, D.R.; Bonanno, D.R.; Whittaker, G.A.; Landorf, K.B. Effect of different orthotic materials on plantar pressures: A systematic review. *J. Foot Ankle Res.* **2020**, *13*, 1–11. [CrossRef]
32. Akambase, J.A.; Kokoreva, T.V.; Gurova, O.A.; Akambase, J.A. The effect of body positions on foot types: Considering body weight. *Transl. Res. Anat.* **2019**, *16*, 100048. [CrossRef]
33. Fähndrich, E.; Linden, M. Reliability and validity of the Visual Analogue Scale (VAS). *Pharmacopsychiatry* **1982**, *15*, 90–94. [CrossRef]
34. Martin, R.L.; Irrgang, J.J.; Burdett, R.G.; Conti, S.F.; Van Swearingen, J.M. Evidence of Validity for the Foot and Ankle Ability Measure (FAAM). *Foot Ankle Int.* **2005**, *26*, 968–983. [CrossRef]
35. Karami, E.; Kashani, R.V.; Bani, M.A.; Daryabor, A. Effect of Prefabricated Insole with Shock Absorb Canal and Custom-Molded Insole on Pain and Function in Subjects with Plantar Fasciitis: A Pilot Study. *J. Clin. Physiother. Res.* **2020**, *5*, e25. [CrossRef]
36. Chung, C.L.; Paquette, M.R.; DiAngelo, D.J. Impact of a dynamic ankle orthosis on acute pain and function in patients with mechanical foot and ankle pain. *Clin. Biomech.* **2021**, *83*, 105281. [CrossRef]

Disclaimer/Publisher’s Note: The statements, opinions and data contained in all publications are solely those of the individual author(s) and contributor(s) and not of MDPI and/or the editor(s). MDPI and/or the editor(s) disclaim responsibility for any injury to people or property resulting from any ideas, methods, instructions or products referred to in the content.

Article

Numerical Analysis of the Plantar Pressure Points during the Stance Phases for the Design of a 3D-Printable Patient-Specific Insole

Jesús Alejandro Serrato-Pedrosa ^{1,*}, Guillermo Urriolagoitia-Sosa ^{1,*}, Beatriz Romero-Ángeles ^{1,*}, Francisco Carrasco-Hernández ², Francisco Javier Gallegos-Funes ¹, Alfonso Trejo-Enriquez ¹, Alfredo Carbajal-López ¹, Jorge Alberto Gómez-Niebla ¹, Martín Ivan Correa-Corona ¹ and Guillermo Manuel Urriolagoitia-Calderón ¹

- ¹ Instituto Politécnico Nacional, Escuela Superior de Ingeniería Mecánica y Eléctrica, Sección de Estudios de Posgrado e Investigación, Unidad Profesional Adolfo López Mateos, Edificio 5, 2do, Piso, Biomechanics Group, Col. Lindavista, Del. Gustavo A. Madero, Ciudad de México 07320, Mexico; fgalegosf@ipn.mx (F.J.G.-F.); atrejoe@ipn.mx (A.T.-E.); alcarbajal97@gmail.com (A.C.-L.); george7gomez@gmail.com (J.A.G.-N.); mcorreac1000@alumno.ipn.mx (M.I.C.-C.); urrio332@hotmail.com (G.M.U.-C.)
- ² Universidad Tecnológica de Durango, Departamento Académico de Mecatrónica y Energías Renovables, Carretera Durango—Mezquitlan km 4.5 s/n, Gabino Santillán, Durango C.P. 34308, Mexico; francisco.carrasco@utd.edu.mx
- * Correspondence: alejandroserrato@live.com.mx (J.A.S.-P.); guiurri@hotmail.com (G.U.-S.); romerobeatriz97@hotmail.com (B.R.-Á.)

Citation: Serrato-Pedrosa, J.A.; Urriolagoitia-Sosa, G.; Romero-Ángeles, B.; Carrasco-Hernández, F.; Gallegos-Funes, F.J.; Trejo-Enriquez, A.; Carbajal-López, A.; Gómez-Niebla, J.A.; Correa-Corona, M.I.; Urriolagoitia-Calderón, G.M. Numerical Analysis of the Plantar Pressure Points during the Stance Phases for the Design of a 3D-Printable Patient-Specific Insole. *Prosthesis* **2024**, *6*, 429–456. <https://doi.org/10.3390/prosthesis6030032>

Academic Editors: Arnab Chanda and Marco Cicciu

Received: 2 March 2024

Revised: 18 April 2024

Accepted: 22 April 2024

Published: 26 April 2024



Copyright: © 2024 by the authors. Licensee MDPI, Basel, Switzerland. This article is an open access article distributed under the terms and conditions of the Creative Commons Attribution (CC BY) license (<https://creativecommons.org/licenses/by/4.0/>).

Abstract: The study of the phenomena occurring in the plantar region is remarkably intriguing, especially when performing a normal gait cycle where the foot is under loading conditions. The effects presented in the foot while walking provide relevant indicators regarding clinical means for enhancing regular performance or rehabilitation therapies. Nevertheless, more than traditional methods are needed to biomechanically evaluate foot structural conditions, leading to an incomplete database for determining the patient's needs so that advanced methodologies provide detailed medical assessment. Therefore, it is necessary to employ technological engineering tools to optimize biomechanical plantar pressure evaluations to reach suitable personalized treatments. This research initially evaluated numerically the pressure points in the foot sole region in each one of the five stance phases in a normal gait cycle. Medical imaging techniques were utilized to construct an anatomically accurate biomodel of the soft tissues of the right foot. The Finite Element Method was employed to predict peak plantar pressure in barefoot conditions for all stance phases; results from this case study presented a close alignment with gait experimental testing implemented to analyze the feasibility and validation of all mechanical considerations for the numerical analyses. Hence, having a solid foundation in the biomechanical behavior from the first case study close estimates, a 3D-printable patient-specific insole was designed and numerically analyzed to observe the mechanical response in the plantar critical zones utilizing a personalized orthotic device. Results from the second case study notably demonstrated a crucial decrement in excessive pressure values. Employing morphological customization orthopedics modeling combined with 3D-printable materials is revolutionizing assistive device design and fabrication techniques. The fundamental contribution of this research relies on deepening the knowledge of foot biomechanics from an interdisciplinary approach by numerically analyzing pressure distribution in critical regions for all five stances phases; thus, based on the methods employed, the results obtained contribute to the advances of patient-specific foot orthopedics.

Keywords: stance phases; finite element method; patient-specific foot orthopedics; plantar pressure; 3D-printable materials; gait cycle

1. Introduction

Accurately identifying plantar contact and pressure distribution is of great interest to clinicians and researchers in evaluating foot functions, human movement, and posture, which is considered indispensable to understanding its effects on the gait of the human body [1–4]. Human gait is considered an essential physiological activity for every individual, to the point of being compared to breathing or sleeping [5]. Briefly explained, the gait cycle is divided into two phases: the stance and swing phases, representing 60% and 40% of the total human gait, respectively. The stance phase is subdivided into five different stages. When the foot initially has contact with the ground, it is known as the heel strike phase. Once it has made contact, the foot progressively descends towards the ground to have a foot flat, which is the loading response stage. Next is the mid-stance position, where the body tilts forward, with the ankle joint as the pivot and the hip joint on top. Heel rise occurs when the forefoot area comes into contact directly to propel the body. Finally, when part of the toes is the only area in contact with the ground, the end of the stance phase is commonly referred to as toe-off or pre-swing [6–9]. The analysis of the distribution of pressure points in the foot under this activity facilitates the understanding of its functionality and the ability of the foot to adapt to different surfaces and conditions. The comprehension of how a foot distributes pressure and adjusts to each step provides valuable insights into a primary data source in gait and posture analysis; foot pressure reveals the otherwise challenging to analyze biomechanical effects occurring at the interface between the foot and the supporting surface, enabling the evaluation of underlying musculoskeletal behavior [10–12].

From a biomechanical approach, stresses and strains generated in each position and movement during normal walking set the standard for predicting a possible tendency to develop foot pathologies [13–17]. The employment of numerical simulations marks a turning point in analyzing human anatomy behavior in various scenarios and the prosthetic and orthotic design [18–21]. Regarding foot healthcare and footwear production, this shift promises a future where efficiency and cost-optimization reign supreme over conventional experimental testing to meet truly personalized insole construction demands [22,23]. In addition, an increasing technological trend is guiding the path toward a more sustainable and innovative production of foot orthotics by implementing additive manufacturing [24–26].

Foot orthoses have always been a mainstay in podiatric treatment and have conventionally been manufactured using a cast-and-mold approach. However, recent advancements in 3D printing technology offer the potential for patient-specific, customizable insoles. The study and research of foot insole construction through additive manufacturing materials are of great interest to the scientific community to replicate and enhance the mechanical behavior of standard orthoses [27–29]. Throughout the literature, different 3D-printable material testing has been conducted to compare the mechanical behavior to reproduce shock-absorbing effects, polymers such as polylactic acid (PLA), acrylonitrile butadiene styrene (ABS), polyamide filaments (NYLON), polyamide (PA), and thermoplastic polyurethane (TPU) are the printing materials most studied and employed for footwear purposes [30–32]. An optimized mechanical response along with the highest standard for comfort are the main aims of current 3D-printing technologies for foot insole design; a combination of novel approaches in infill percentages, infill matrix patterns, combined material structures, and numerical analyses [33–38] have improved traditional hand-made workflows in orthopedic devices. Another crucial aspect of the recent advancements in 3D-printed patient-specific insoles is 3D scanning technology, which allows the acquisition of more precise anthropometric data, resulting in advantages in time and accuracy to obtain a detailed three-dimensional copy that meets the actual morphology of such a complex geometry of the human body [39–41] over traditional foot plaster models and conventional measurement techniques that lack data consistency due to utilizing diverse procedures and different measurement instruments for foot dimension evaluation [42–44]. These increasingly technological methods have revolutionized the ergonomics and footwear industry and have significantly impacted clinical applications since they provide cutting-edge ad-

vancements in tangible solutions to musculoskeletal disorders [45–48]. The capability of 3D modeling and printing of foot orthoses have provided promising prospects for improving patient care of all ages, conditions, and activities. Clinical studies investigating 3D-printed insoles in specific applications are being developed more frequently, with promising results emerging in sports performance enhancement, elderly populations, children’s feet, and pathological feet. These studies have promoted the understanding, diagnosis, and treatment of specific musculoskeletal conditions by applying engineering principles, such as reverse engineering [49–54].

Therefore, a comprehensive study that accurately quantifies peak plantar pressure during a normal gait cycle performing all stance phases is crucial to deepening into weight bearing and pressure distribution foot functions, revolutionizing a worldwide approach to foot health management and enabling further precise interventions to individual needs. Consequently, this leads to personalized foot health care flourishing and fully customized foot orthotic devices based on the accurate morphology of the individual [55–57]. Through the Finite Element Method, it is possible to obtain and analyze plantar distribution numerically in detail during the different stance phases of the gait cycle. This multifaceted approach promises to significantly advance the understanding of foot pressure points while performing all stance phases during a normal gait, aiming to develop more effective and personalized plantar orthoses.

This study seeks to delve deeper into the interactions among foot soft tissues, pressure points, and orthosis-relieving properties. To employ Finite Element analyses, a 3D anatomical model with high-fidelity detail is generated through established medical imaging techniques [19]. Such models offer the distinct advantage of capturing the complex geometrical features of human biological systems, enabling detailed analysis and insights not readily achievable through traditional 2D representations. This current research is focused on numerically analyzing stance phases for barefoot plantar pressure validated with experimental testing to design a fully customized foot orthosis for numerically evaluating the biomechanical effects in the sole region utilizing the orthopedic device, where the level of complexity to understanding foot-insole plantar effects challenges experimental testing, which commonly yields to insufficient and poorly explained data for accurate foot function diagnosis. Likewise, this manuscript can provide a different innovative approach to gait patterns, optimize foot health, and enhance the quality of life for individuals requiring plantar support.

2. Materials and Methods

2.1. Biomodel Construction

The 3D foot model was developed on a 30-year-old male Mexican adult exhibiting apparent health status through a computed tomography (CT) scan. Additionally, the patient presented a standard body mass index and foot morphology (Figure 1a). Subsequently, image acquisition, visualization, and segmentation of the DICOM data for 3D model construction were conducted. The biomodel reconstruction process corresponds to a previous study conducted [58]. The segmentation process mainly focused on reconstructing two critical soft tissue structures, the intrinsic foot muscles and the skin, and profoundly comprehending the biomechanical analysis of pressure points on the plantar surface. Intrinsic foot musculature contributes to postural maintenance and shock absorption functions by employing its stabilizing actions [59]. Due to the high concentration of multiple tissue layers and the anatomical variance within the intrinsic muscle group, the modeling approach was represented as a unified encapsulated body.

The segmentation process was initially performed utilizing the medical software Simpleware ScanIP® (version 3.2 Build 1) (Figure 1b). Once this process has been appropriately conducted, solidification and smoothing of elements created were applied to the biological model to optimize its complex geometry, hence acquiring a more realistic morphology. A re-meshing was also generated in the biomodel, resulting in a computationally efficient

mesh structure better suited for further discretization. All computational procedures were conducted within the Materialise 3-Matic® software (version 21.0) (Figure 1c).

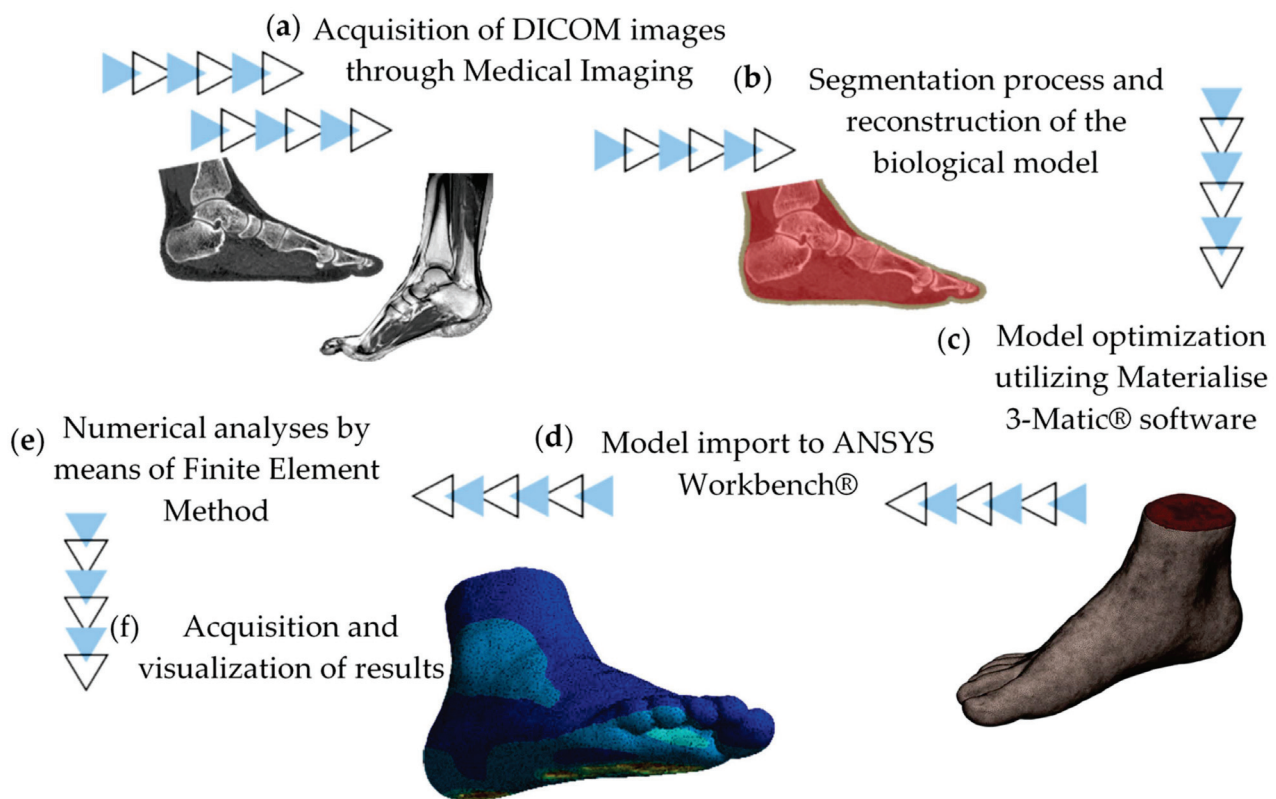


Figure 1. 3D foot biomodel reconstruction and analysis methods. (a) Medical imaging study. (b) Segmentation process. (c) Model optimization process. (d) Model optimization process. (e) Numerical analyses. (f) Analysis and interpretation of results.

The complex biomodel was finally exported to Finite Element Analysis software ANSYS Workbench® (version 2021 R1 student) (Figure 1d), where the type of mechanical analysis to be developed was defined, the mechanical properties of the biological elements were applied, the geometries were discretized, and boundary conditions and the application of external agents were established (Figure 1e).

As mentioned above, the steps explained correspond to the Finite Element software preprocessing stage, which, once completed, generates a convergence of the partial differential equations towards a result to obtain the solution of the biomodel and finally visualize the mechanical behavior obtained (Figure 1f).

2.2. Gait Experimental Baropodometric Testing

The present study employed the FreeSTEP® software (version v.1.4.01) and the Professional 180 cm × 50 cm Platform baropodometer for quantifying pressure points during a gait cycle analysis. This pressure-measuring device utilizes a matrix of resistive sensors equipped with 24 K gold conductors and an insulating coating capable of registering data at a frequency of up to 500 Hz. Notably, the system captures three pressure traces per complete step, enhancing the resolution and depth of information regarding the impact of ground reaction forces in the plantar region. This high data acquisition rate enabled the capture of approximately 400 frames per second, dynamically adapting to the patient's walking rhythm or speed throughout the study. The patient walked barefoot several times at a comfortable and average pace to obtain a representative regular gait pattern. The program automatically divided the pressure zone on the soles of the feet. Feet were sectioned into eight anatomical regions, mainly separating the rearfoot, midfoot, and forefoot. Auto-

matic sectioning allowed the adequate limit of each stance phase to define the boundary conditions for the numerical analysis. A baropodometric platform system was selected to perform experimental testing over in-shoe systems since they provide accurate fundamental data to evaluate barefoot pressure distribution conditions, guiding to adequate insole design. In addition, in-shoe systems may lead to discomfort, alter gait patterns due to the sensors, and change foot pressure profile effects. Also, sensor size limitations can affect spatial resolution [17,60–63].

2.3. Finite Element Analyses Simulating the Stance Phases of the Gait Cycle

2.3.1. First Case Study

The assignment of mechanical properties to the model corresponds to valuable insights found in biomechanical literature by Luboz for the muscle-encapsulated tissue and skin mechanical properties [64]. Moreover, ground reaction forces in the plantar region were produced by employing a rigid plate [65]. The mechanical properties values can be seen in Table 1. To achieve high fidelity in results, the Finite Element model discretization was employed with high-order 3D solid elements with 20 nodes per element. The analysis encompasses three distinct regions: skin, encapsulated muscle mass, and plate. Through a combination of fine and semi-controlled meshing techniques, a total of 371,120 elements and 196,576 nodes were generated.

Table 1. Mechanical properties of the elements [64,65].

Material	Young's Modulus (MPa)	Poisson's Ratio
Foot skin	0.2	0.485
Foot muscles	0.06	0.495
Plate support	210,000	0.3

To numerically study the gait using the biological model of the patient utilizing the Finite Element Method, five different numerical studies corresponding to the five stance phases that the foot undergoes during a normal gait are considered.

Once the angles and orientation of the foot were determined for each stance phase according to the experimental analysis, the boundary conditions for foot position were assigned according to the position the foot took for each one of the phases. Furthermore, the model incorporates embedded regions in the upper and medial-lateral zones to ensure realistic biomechanical behavior. These embedded regions are surrounded by constraint regions, simulated by 2-mm-wide tapes relative to the foot dimensions. This approach prevents unrealistic lateral displacement during load application. Similarly, constraints in the instep and toe area restrict excessive vertical loading transfer. These boundary embedding conditions were considered since no bony tissues were re-constructed to focus more on soft tissue mechanical behavior. Likewise, these constraint considerations provide structural integrity in the model, replicating osseous tissue function, thus avoiding unrealistic deformations in the model. Applying this mechanical approach has successfully evaluated plantar pressure distribution in a previous study [58].

As an external agent, the rigid plate was set to apply a vertical displacement that simulates the effects of ground reaction forces on the plantar surface. According to the medical-experimental literature, it is recorded that between 1–2 mm of additional displacement is generated in the skin of the foot sole according to the degree of dorsiflexion and plantar flexion [66]. On the other hand, another study showed a similar displacement of 1–3 mm in the forefoot in the dorsiflexion of the toes during the pre-swing phase [67]. Even in different investigations, ranges between 6 and 10 mm were used as indentation elements on the forefoot side to evaluate the heel response [68]; a range between 10 and 14 mm [69] was also tested. Using ultrasound and ultrasound scans, stretching on the skin of the sole up to 10 mm was appreciated in the areas of contact of the foot with the ground during walking [70]. Therefore, according to these considerations from experimental literature, vertical displacements between 5.5 and 8.5 mm were applied for the respective stance

phases. Once the parameters necessary to determine the application of the external agent for each stance phase were analyzed, a vertical displacement of 6 mm was used to simulate the effects of the ground reaction forces. Likewise, the position and orientation of the foot in that phase obtained from the experimental analysis were used. Figure 2a represents the loading and boundary conditions for which the numerical solution was developed for the heel strike stance phase. The same constraints were used to assign boundary conditions for the loading response stage; a vertical displacement of 7 mm was implemented to analyze this stance phase (Figure 2b). A vertical displacement of 5.5 mm was employed as an external agent for the mid-stance position (Figure 2c). The assignment for the external agent corresponds to a vertical displacement of 8 mm to analyze the heel rise phase. Likewise, the constraints previously used were also considered (Figure 2d). To simulate the pre-swing phase, which is where most plantar pressure is generated, a vertical displacement of 8.5 mm was applied (Figure 2e). Furthermore, a coefficient of friction of 0.6 between the foot and ground was included, complementing loading and boundary conditions parameters [71].

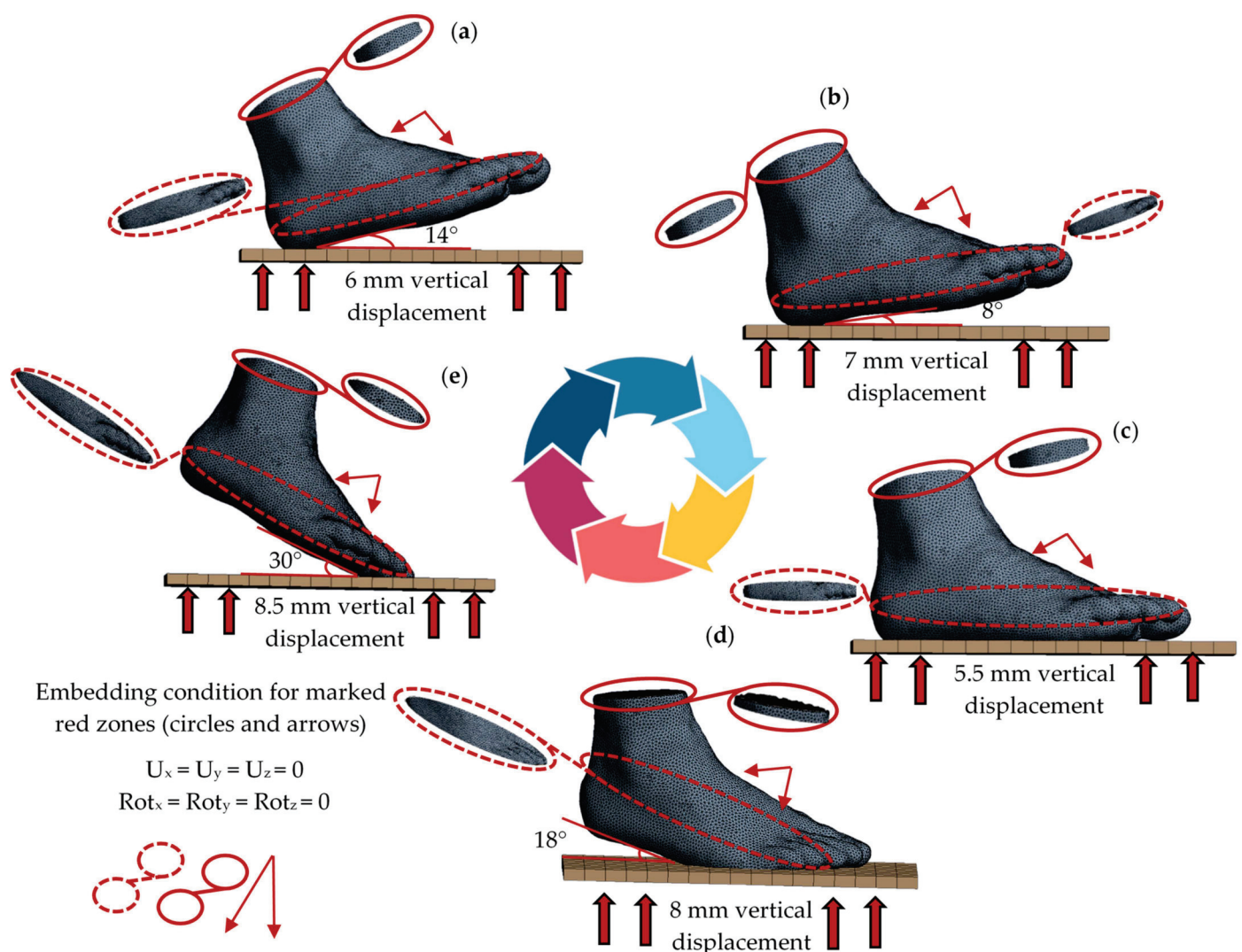


Figure 2. Loading and boundary condition free body diagrams for all stance phases. (a) Heel strike. (b) Loading response. (c) Mid-stance. (d) Heel rise. (e) Pre-swing.

2.3.2. Second Case Study

A personalized 3D-designed full-length total contact insole assigned with thermoplastic polyurethane (TPU) properties was employed to analyze the biomechanical behavior and attenuation effects of peak plantar pressure contact points within patient-specific

orthopedic footwear under identical anatomical positioning and mechanical principles, simulating all five stance phases of the gait cycle. This inclusion reflects the common practice of orthotic devices, where the insole's cushioning properties absorb a significant portion of ground reaction forces [72]. The medical foundation on the plantar region studies shows that parametrically modeled insoles demonstrably influence optimal biomechanical behavior [73,74].

Therefore, the selection of TPU as the insole material was considered after analyzing various research highlighting its advantageous characteristics. Notably, its printability through fused deposition modeling (FDM) aligns with the principles of additive manufacturing [75,76], offering cost-effective and customizable 3D-printed solutions [77]. Furthermore, TPU boasts ideal mechanical strength conducive to outstanding cushioning effects and excessive pressure relief. An extensive review of existing methodologies was conducted to create the 3D-designed orthotic insole; the methodology was mainly focused on the patient's specific right foot geometry. The employment of accurate foot morphology from the re-constructed biomodel provided unique data to meet absolute customization in the design process; SpaceClaim® CAD software (version 2021 R1 student) was utilized for the custom foot orthotic design.

The acquisition of foot morphology as the establishment for the design of personalized footwear principals has been used and stated in various research as a crucial parameter to optimize insole design [58,78–80]. Personalized insole design process workflow is represented in Figure 3.

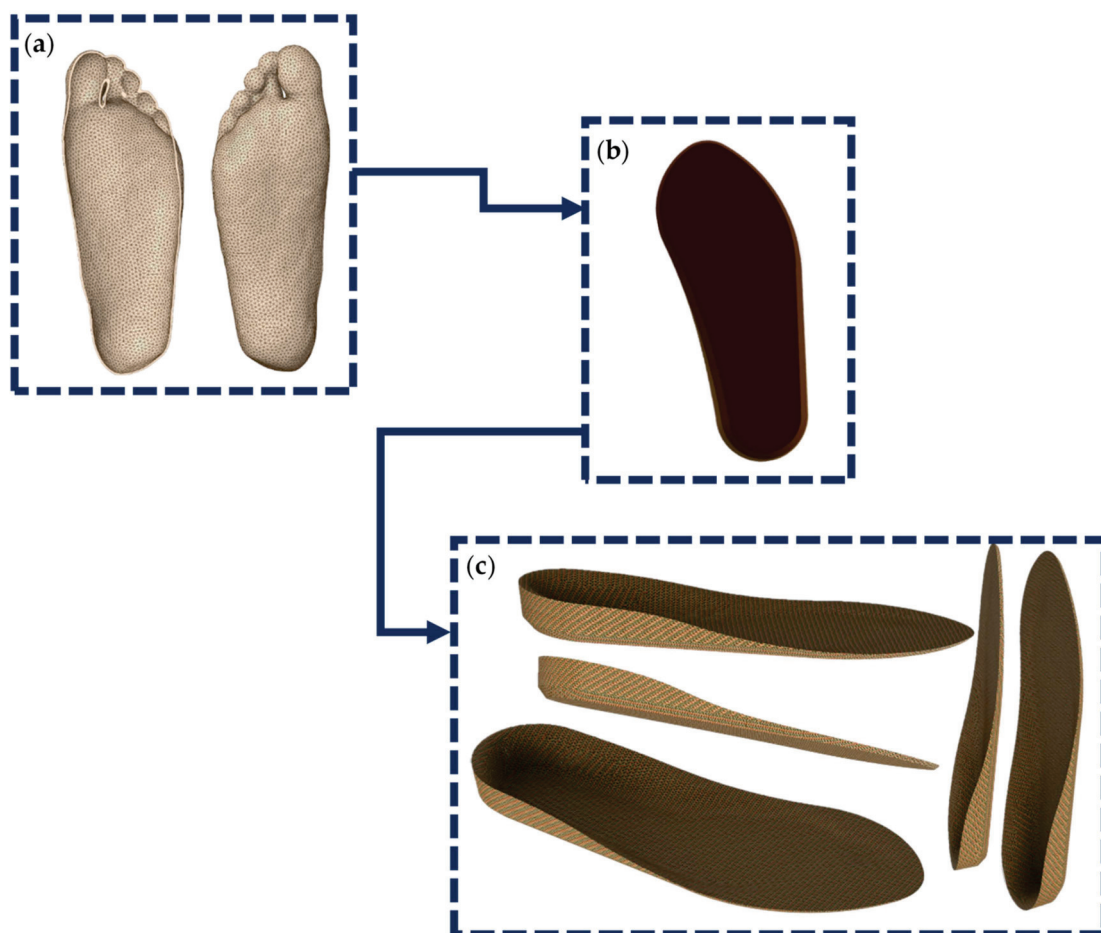


Figure 3. Workflow of the design process of a patient-specific 3D-printable foot orthosis. (a) Foot morphology's mold. (b) Insole base. (c) Personalized 3D-printable insole.

Likewise, the right foot biomodel, a re-meshing of elements, was performed on the customized insole, computationally optimizing the discretization process for numerical analysis needs with uniform elements. Discretization was employed in a semi-controlled manner utilizing high-order elements. This process generated a total of 62,065 nodes and 34,816 elements. It is noteworthy to mention that for both study cases, the convergence of Finite Element Analyses was computationally efficient due to uniform discretization, accurate assignment of loading and boundary conditions, and appropriate hardware and software utilized (Intel Core i9-12900H, 16 GB RAM, and GeForce RTX 3070 TI); this allowed us to obtain results within a short period of 10 min. The personalized foot insole based on patient morphology was defined with TPU material properties from the literature (Table 2) [81–83]. Moreover, a coefficient of friction of 0.5 was implemented for the interaction between the foot and the orthotic insole [84].

Table 2. Mechanical properties of TPU insole [81–83].

Material	Young's Modulus (MPa)	Poisson's Ratio
Thermoplastic Polyurethane (TPU)	11	0.45

3. Results

3.1. Results Gait Experimental Baropodometric Testing

The results and general clinical assessments of the experimental analysis are shown in Figure 4. This result provided a general idea of the behavior and distribution of plantar pressure under typical conditions in the transition of stance phases during the gait cycle. Despite tending to relapse and stance mainly on the left foot, the behavior of the right foot is completely normal. Significant support in the forefoot area over the rearfoot (about 72 and 28%, respectively) was exhibited, which physiologically is considered minimally abnormal; however, this is not detrimental to its performance. Thus, it was obtained that a higher percentage of the total load is concentrated in the forefoot area, mainly in the central part over the second and third metatarsal heads, about 27.12%. This percentage was followed by a concentration of 17.12% on the fourth and fifth metatarsal heads, and finally, 10.65% on the first head.

To numerically study the gait using the biological model of the patient utilizing the Finite Element Method, five different numerical studies corresponding to the five stance phases that the foot undergoes during a normal gait are considered. During the experimental analysis of the gait cycle, the evolution of the contact zones of the foot with the ground was obtained visually; these zones correspond to an average of the number of frames per millisecond taken in 831 ms (milliseconds). Twenty-nine frames of the path of the right foot were recorded over a surface of 118 cm² (Figures 5 and 6).

Based on the contact phases recorded in the baropodometric study, a graph was made between the information collected by the software and the contact area of the plantar zone concerning the frame recorded to determine the precise contact angle between the foot and the ground (Figure 7). The relationship between the contact between the rearfoot and the ground was taken with a positive angle as it was the beginning of the registration during gait. Therefore, the first stance phase (heel strike) was recorded in the second frame (frame 1) with an angle of 14°, and the loading response phase had an angle of 8° and was recorded in frame number 5. The mid-stance phase was recorded in frame 10, where the angle was 0°, and the foot was fully supported on the ground. As soon as the forefoot area connected with the ground, the angle was assumed to have a minus value since it passed through a 0 and acquired values with the opposite sign. Heel rise had an angle with the ground of −18° and was recorded in frame 17. Finally, the pre-swing phase was presented in the 25th frame with an angle of −30°. Negative-valued angles are only for reference, considering that the recording of the contacts began in the rearfoot area and ended with the forefoot at the tip of the hallux.

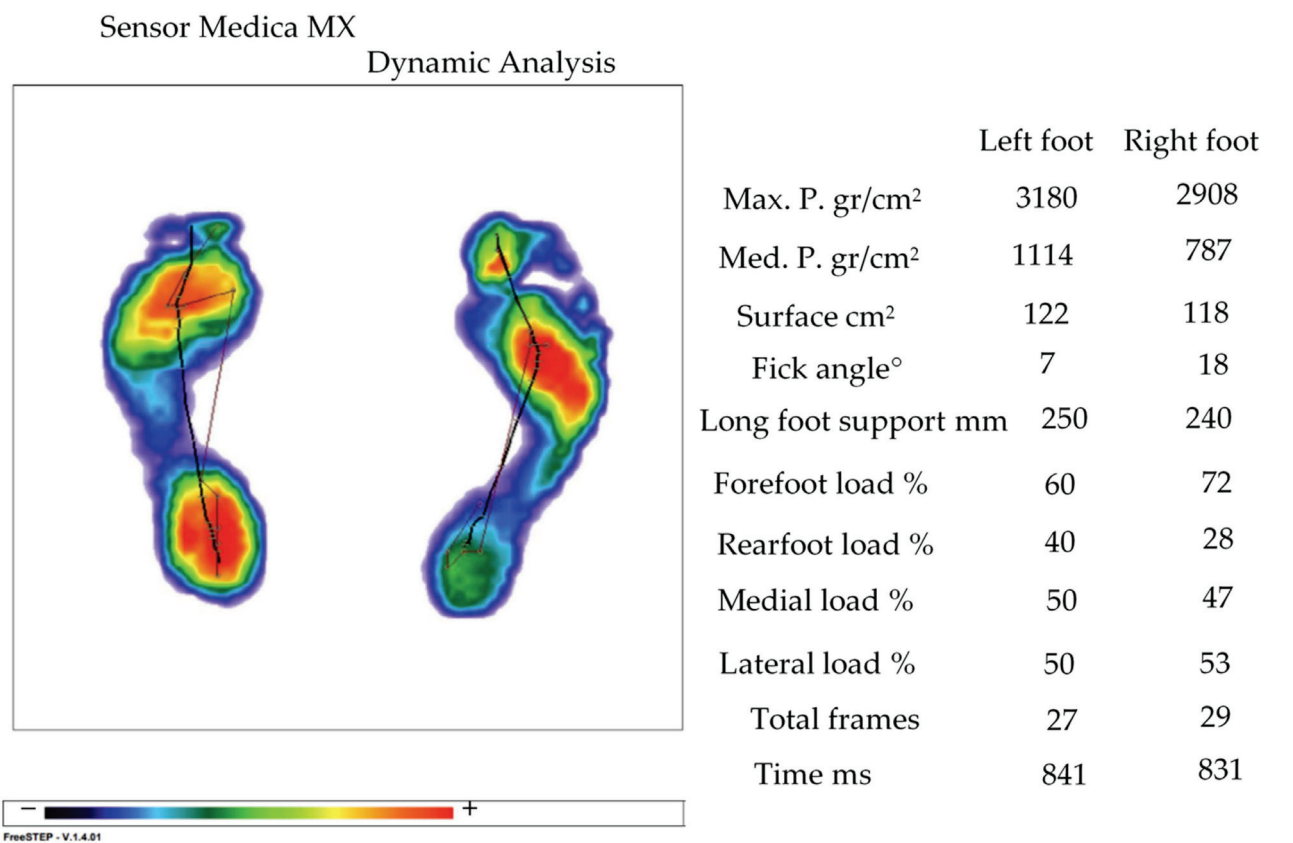


Figure 4. General clinical assessment of dynamic analysis.

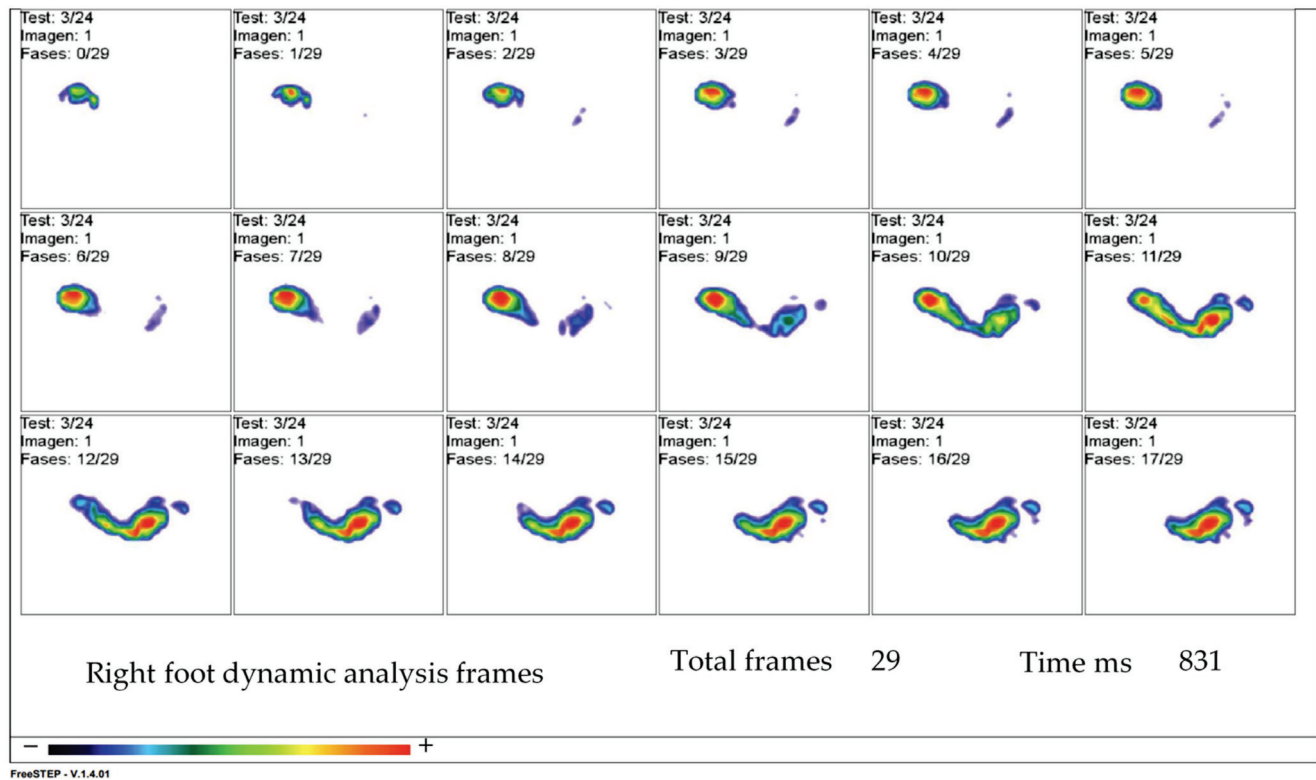


Figure 5. Initial gait cycle frame evolution.

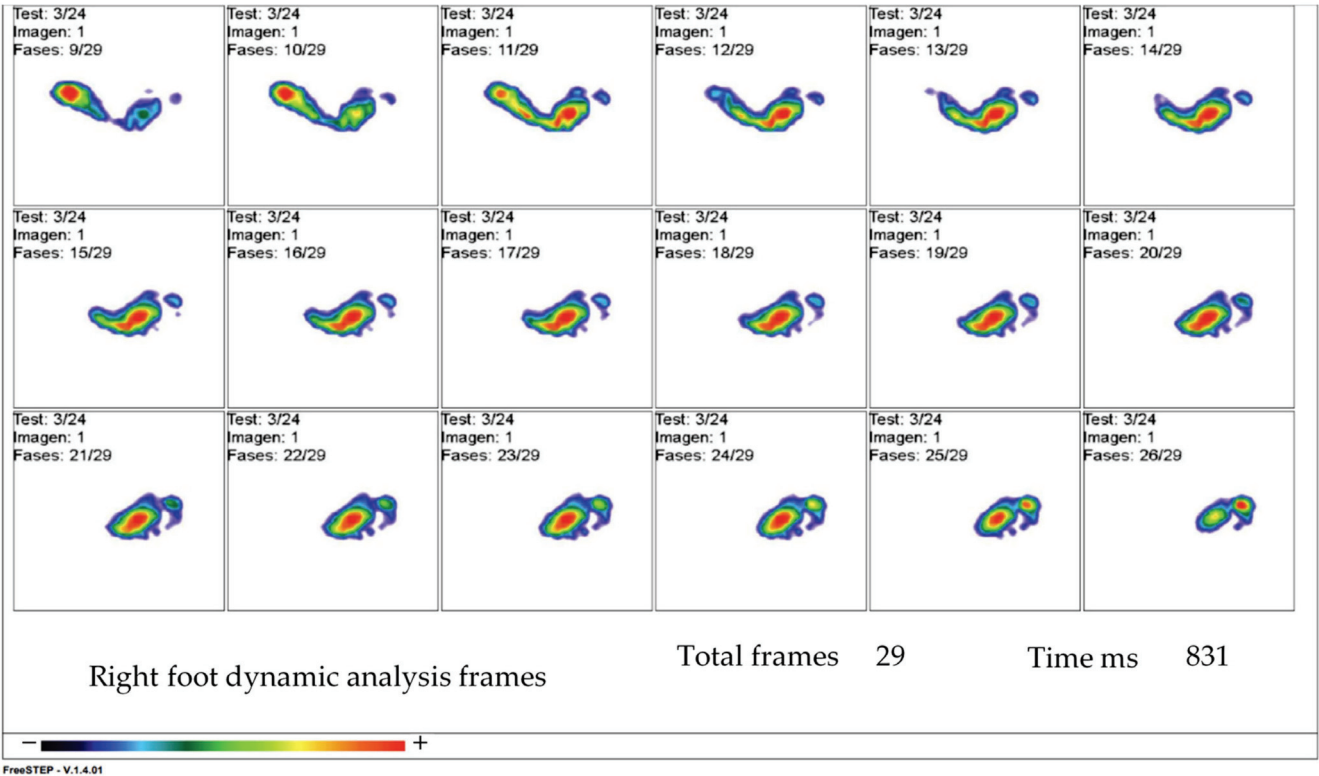


Figure 6. Final gait cycle frame evolution.

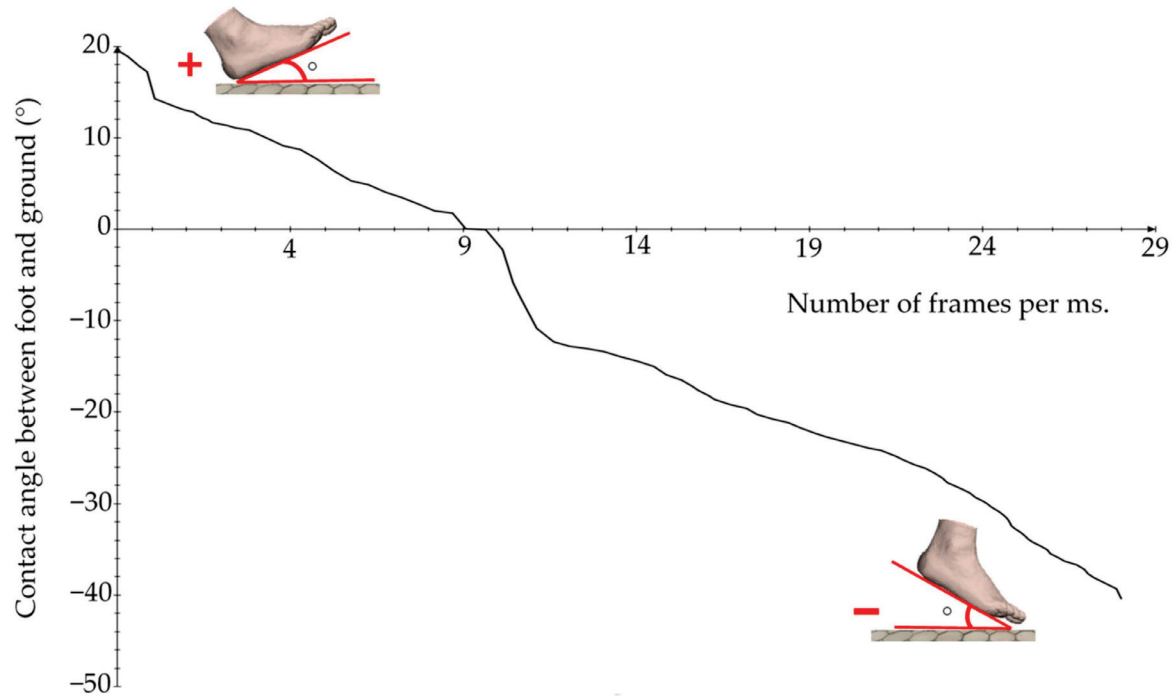


Figure 7. Graph between the angle of foot contact with the ground and the recording of frames per milliseconds during the experimental analysis.

Furthermore, not only was the accurate definition of the contact angle between the foot and the ground known, but also the direction and orientation of the foot were given through the experimental analysis by recording a Fick angle at the foot of 18° , which records an entirely normal angle of external rotation of the midline of the body [85]. Considering this parameter, it is understood that the right foot tends to perform a slight normal adduction in the forefoot part during gait.

The gait experimental testing results were graphed according to the total number of frames taken and the maximum plantar pressure values exerted for each one of the stance phases. Figure 8 shows the results and specific behavior of the three crucial plantar regions: forefoot, midfoot, and rearfoot. The maximum pressure measurement was initiated by analyzing the rearfoot region from the heel strike phase to the pre-swing phase in the forefoot and toes region.

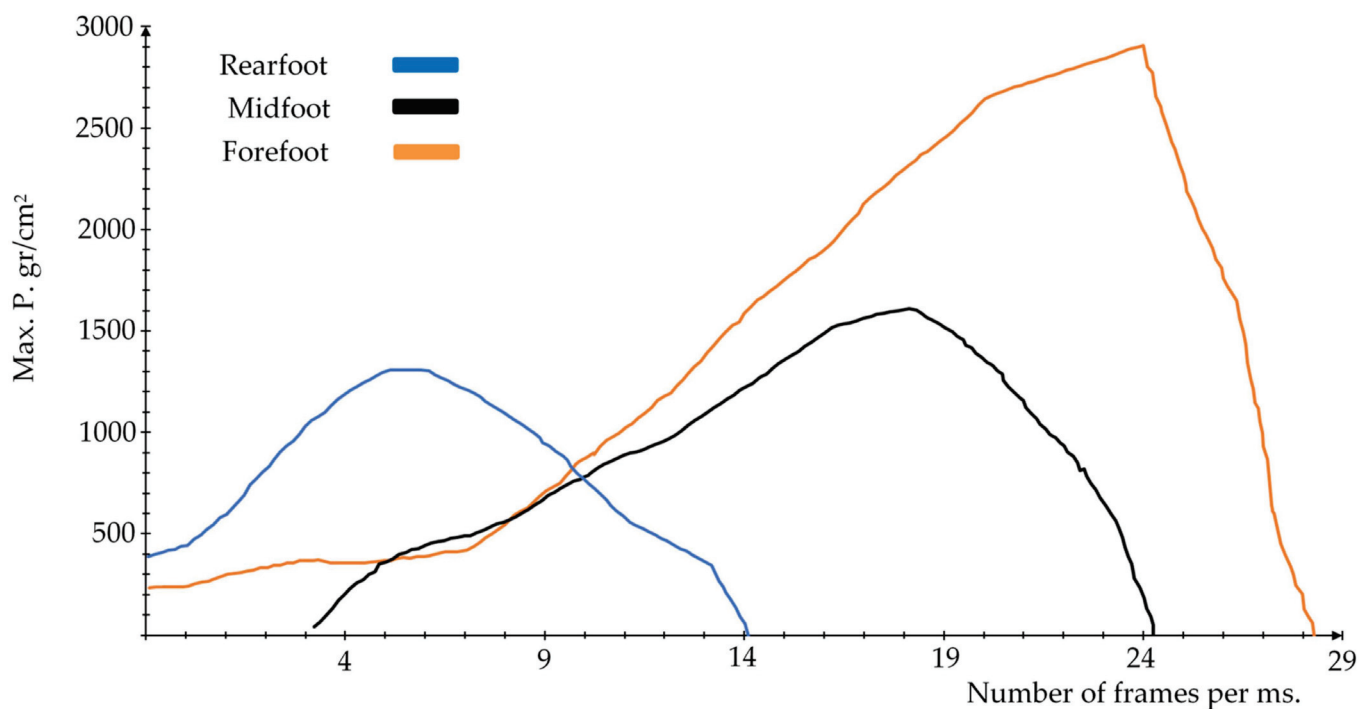


Figure 8. Results of the maximum foot pressure registered and the recording of frames per millisecond during the experimental analysis.

3.2. Results of the First Case Study of Finite Element Analyses Simulating the Stance Phases of the Gait Cycle

The convergence of the numerical analysis equations allowed the acquisition of accurate predictive pressure results; von Mises stress failure theory was priorly employed due to its ability to provide valuable estimation data in the biomechanical behavior of the foot sole, employing the result of different types of stresses in all axis and planes. Therefore, it is ideal to evaluate the biomodel (tensile) ductile properties and the complex conditions of the plantar region under the gait cycle. Figures 9–13 represent the predicted pressure for each one of the stance phases. For Figures 9–13, stance phases were shortened to H.S. for heel strike, L.R. for loading response, M.S. for mid-stance, H.R. for heel rise, and P.S. for pre-swing. Detailed numerical data, including maximum and minimum values, are provided in Appendix A and Tables A1 and A2.

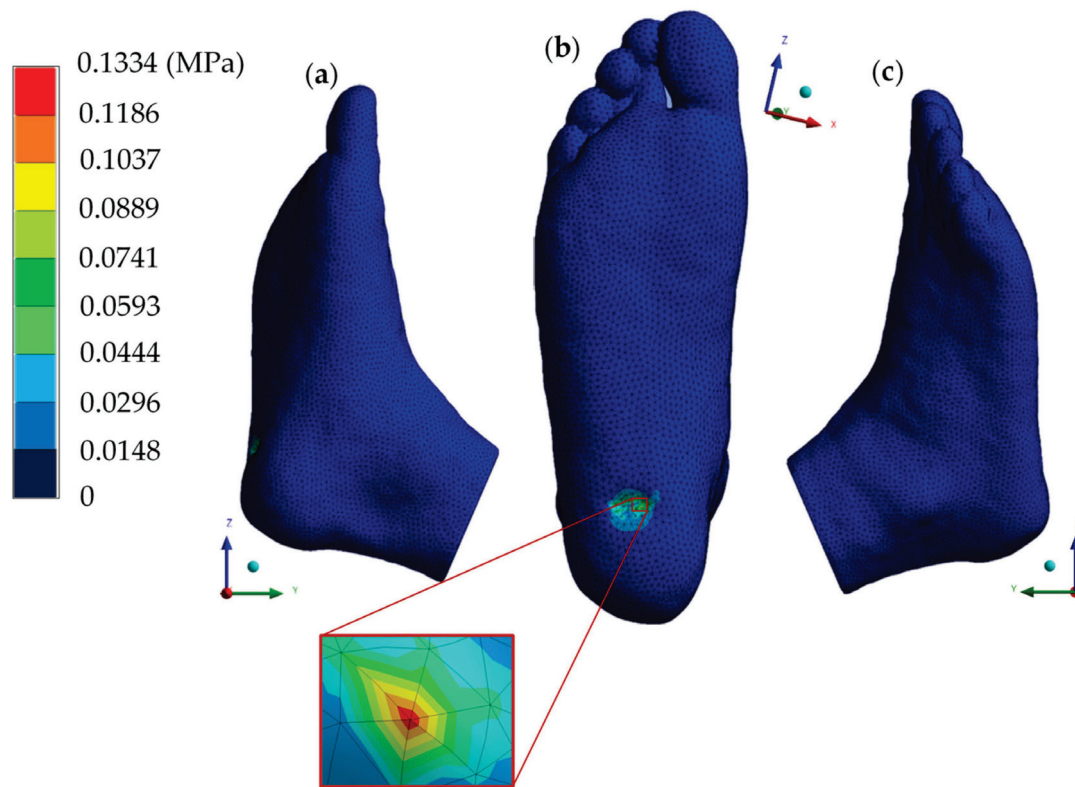


Figure 9. von Mises stress (H.S.). (a) Left side view. (b) Plantar region. (c) Right side view.

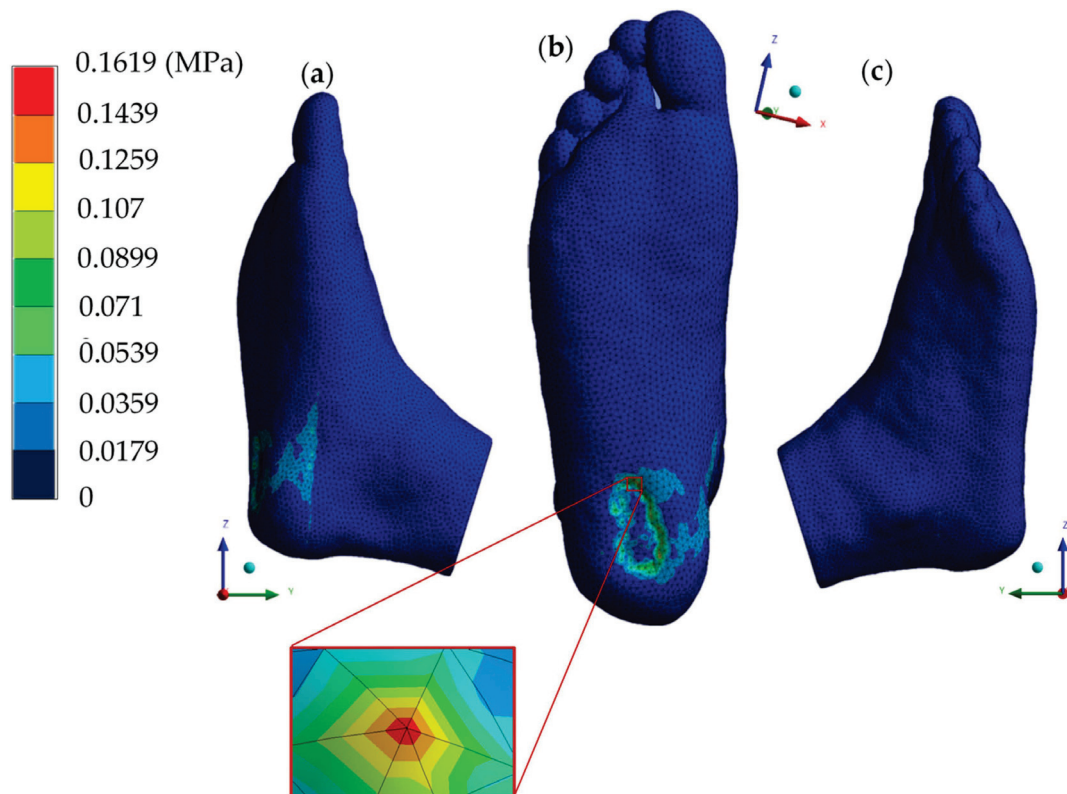


Figure 10. von Mises stress (L.R.). (a) Left side view. (b) Plantar region. (c) Right side view.

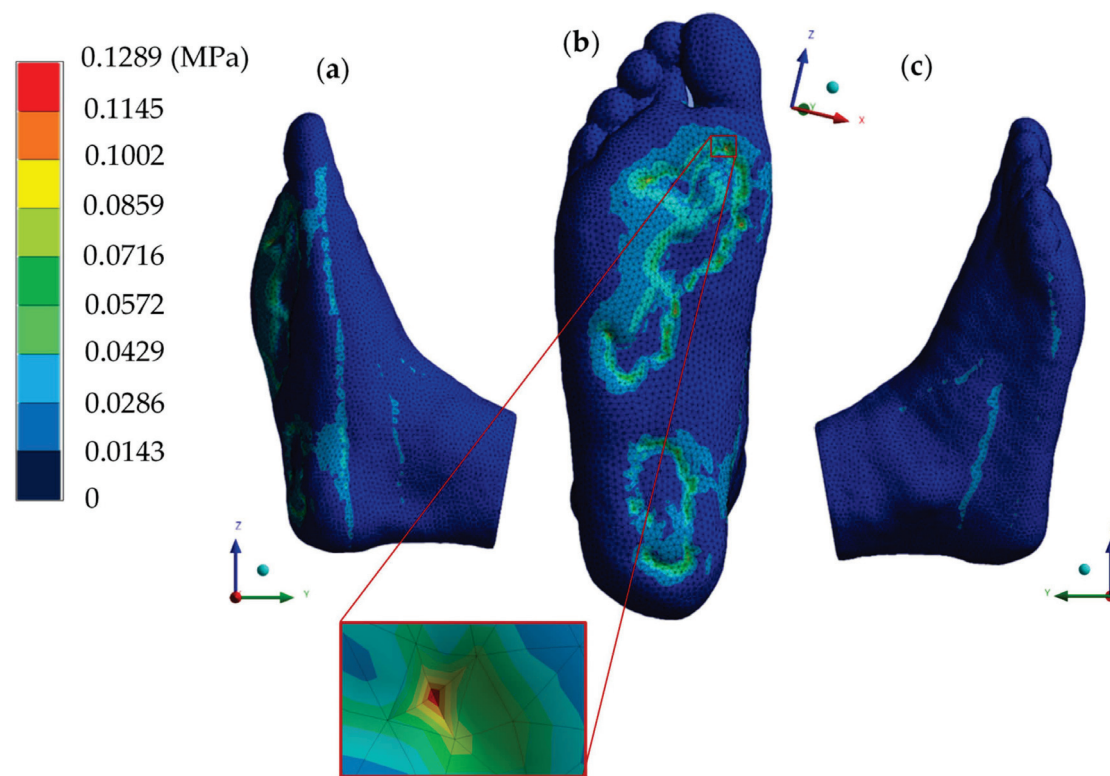


Figure 11. von Mises stress (M.S.). (a) Left side view. (b) Plantar region. (c) Right side view.

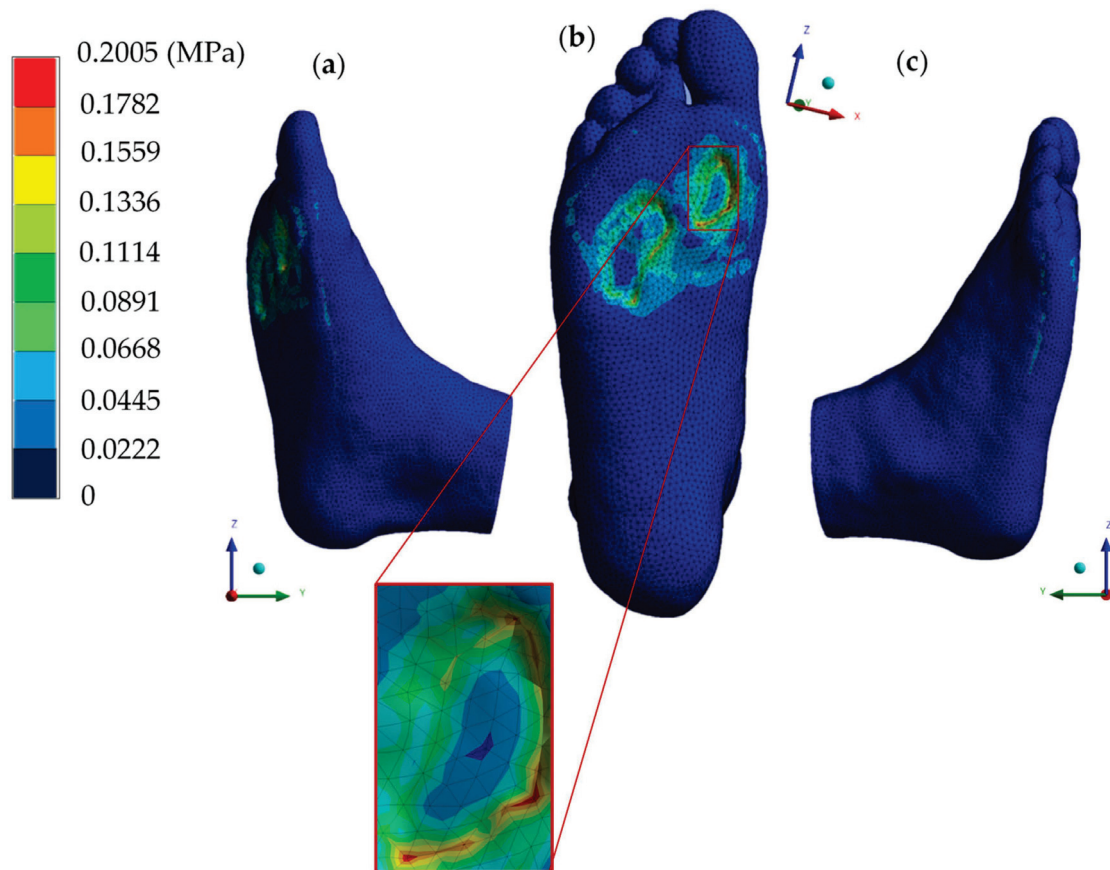


Figure 12. von Mises stress (H.R.). (a) Left side view. (b) Plantar region. (c) Right side view.

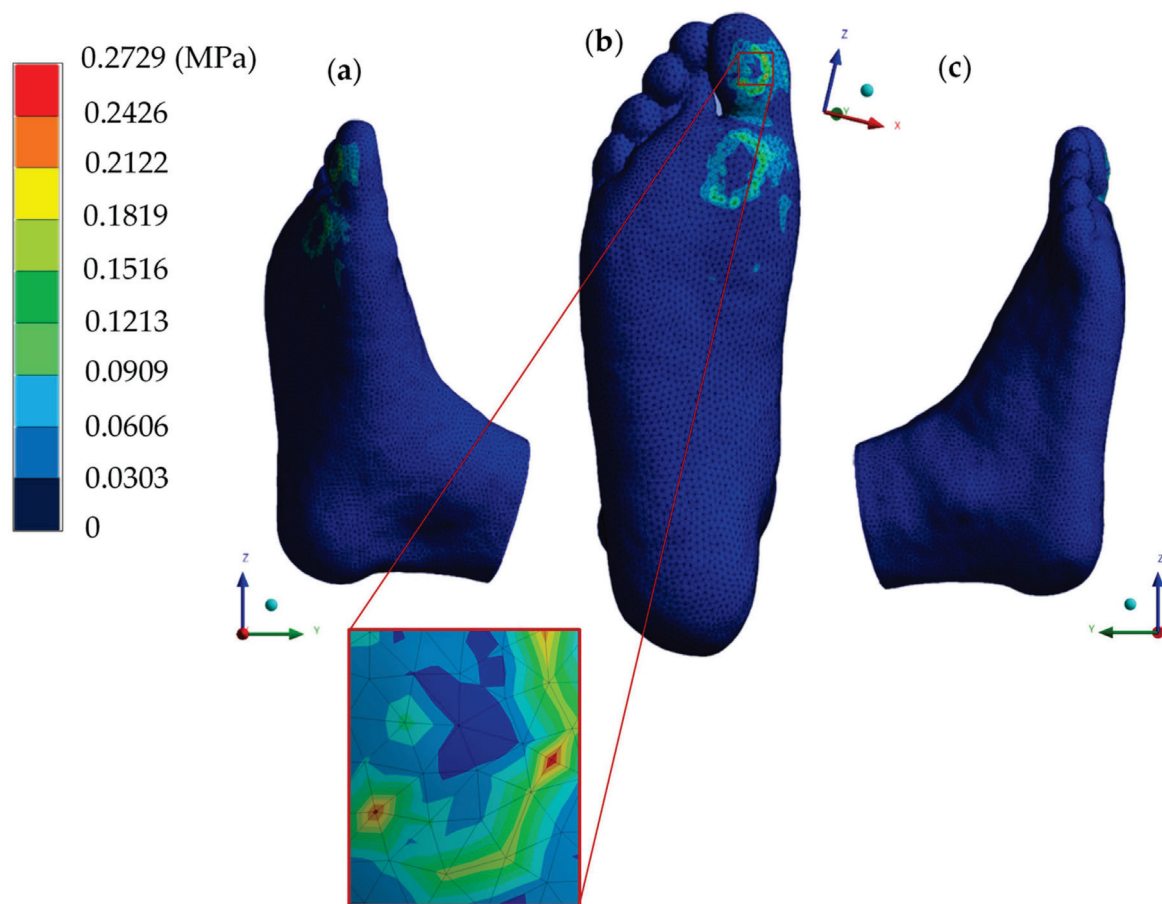


Figure 13. von Mises stress (PS.). (a) Left side view. (b) Plantar region. (c) Right side view.

3.3. Validation and Comparison to First Case Study Results with Experimental Gait Cycle Testing Results

For the validation process, the considerations taken to obtain the results numerically and the maximum plantar pressure values in each of the five stance phases were compared with those acquired in the baropodometric gait study. The von Mises stress distribution was used since it is ideal for evaluating soft tissues and musculoskeletal conditions in biomechanical applications. Based on the graph in Figure 8, a comparison was made between the experimental and numerical results of maximum plantar pressure (Figures 14–16). In the heel strike phase corresponding to frame 1, a 596 gr/cm^2 pressure was recorded, equating to 0.05844 MPa. The plantar pressure prediction using the Finite Element Method provided a value of around 0.0444–0.0593 MPa according to the color scale presented (Figure 14). For the loading response phase, a 1297 g/cm^2 pressure value corresponding to 0.12719 MPa was experimentally acquired (frame 5). Numerically, in this stance phase, the values oscillated from 0.0719–0.1619 MPa. However, in some zones, a value closer to the experimental one of 0.1259 MPa was obtained (Figure 14).

Through the Finite Element Method, values of 0.0572–0.0716 MPa were obtained, where in some points, there were stress concentrators that increased foot sole pressure to 0.1289 MPa due to the contact between the plate and the plantar zone (Figure 15). The mid-stance phase had a plantar pressure of 797 g/cm^2 , equal to 0.07815 MPa, according to the baropodometric study (photogram 10).

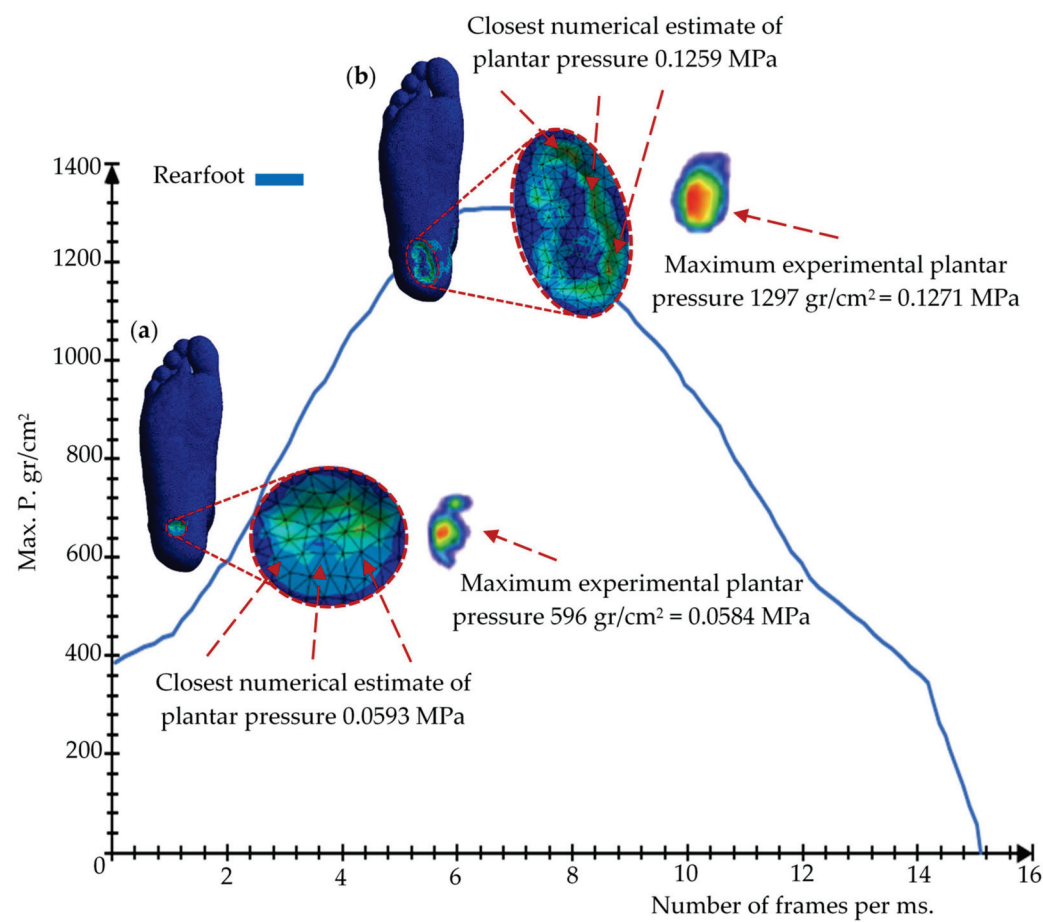


Figure 14. Comparison of experimental and numerical results. (a) Heel strike phase. (b) Loading response phase.

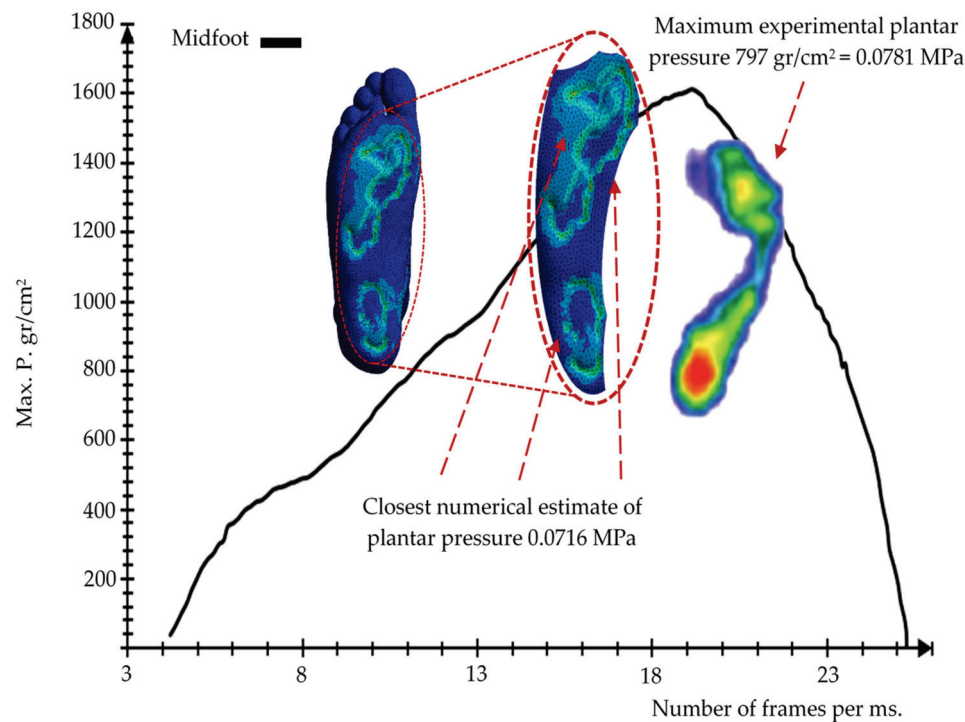


Figure 15. Comparison of experimental and numerical results of the mid-stance phase.

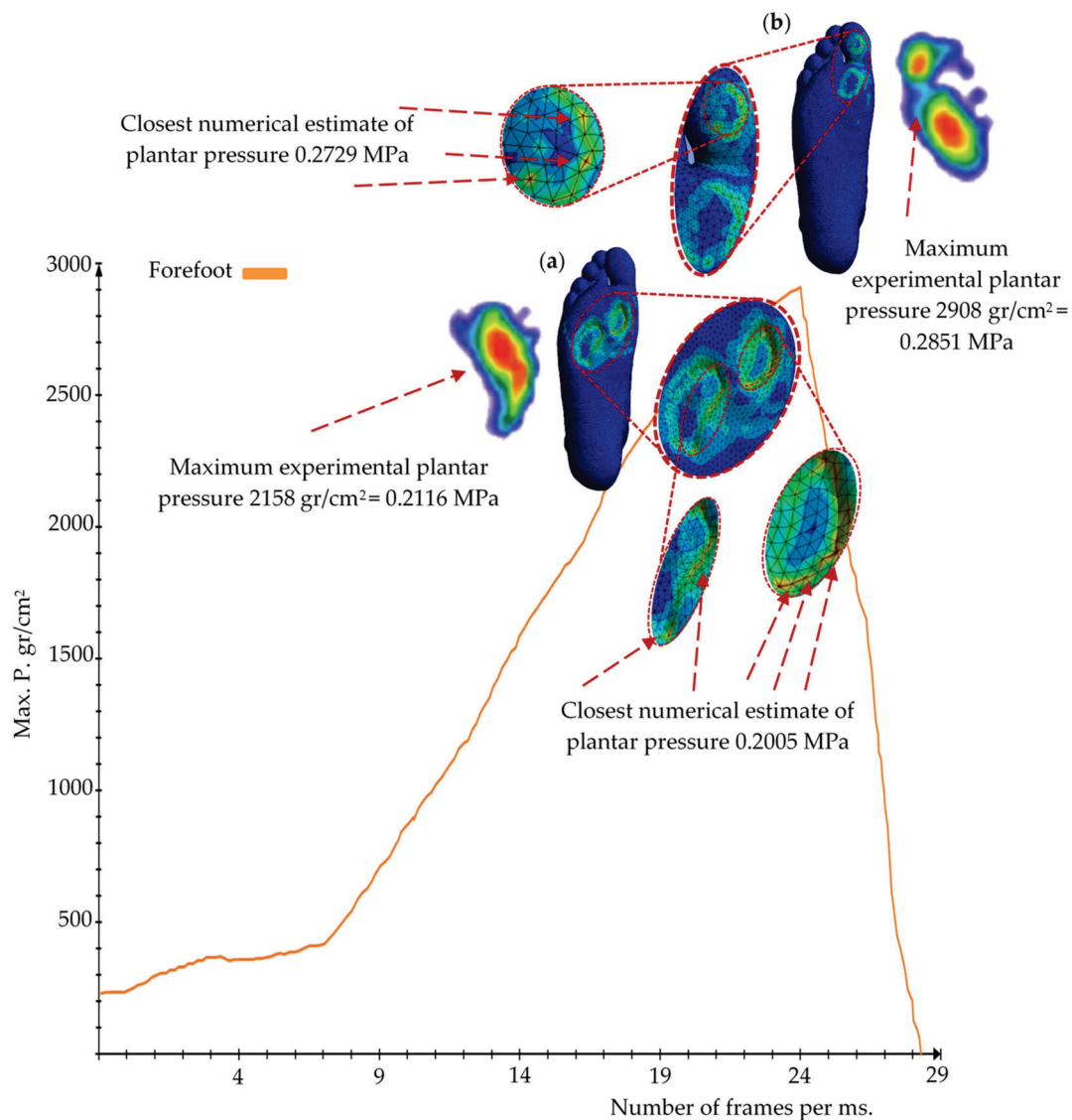


Figure 16. Comparison of experimental and numerical results. (a) Heel rise. (b) Pre-swing phase.

In the heel rise phase, the plantar pressure rose to 2158 gr/cm², corresponding to 0.21162 MPa (frame 17). For the numerical analysis corresponding to this phase, a continuous section under the first metatarsal head was predicted and came closest to the experimental result with a value of 0.2005 MPa (Figure 16). Finally, the baropodometric result generated a plantar pressure of 2908 gr/cm² for the pre-swing phase, equal to 0.28517 MPa (frame 25). The numerical simulation obtained values of 0.2729 MPa in the hallux areas, where, anatomically, there was a higher pressure concentration for this gait stance phase (Figure 16).

3.4. Results of the Second Case Study of Finite Element Analyses Simulating the Stance Phases of the Gait Cycle

Plantar pressure results utilizing the patient-specific insole simulating all five stance phases are shown in Figures 17–21. These Finite Element results allow us to visualize the pressure redistribution on the foot sole, highlighting the insole's shock-absorbing and relieving capabilities. Detailed numerical data, including maximum and minimum values, are provided in Appendix A and Tables A3 and A4. In Figure 22, the von Mises stress distribution fields for all stance phases in the plantar region of the customized insole are depicted.

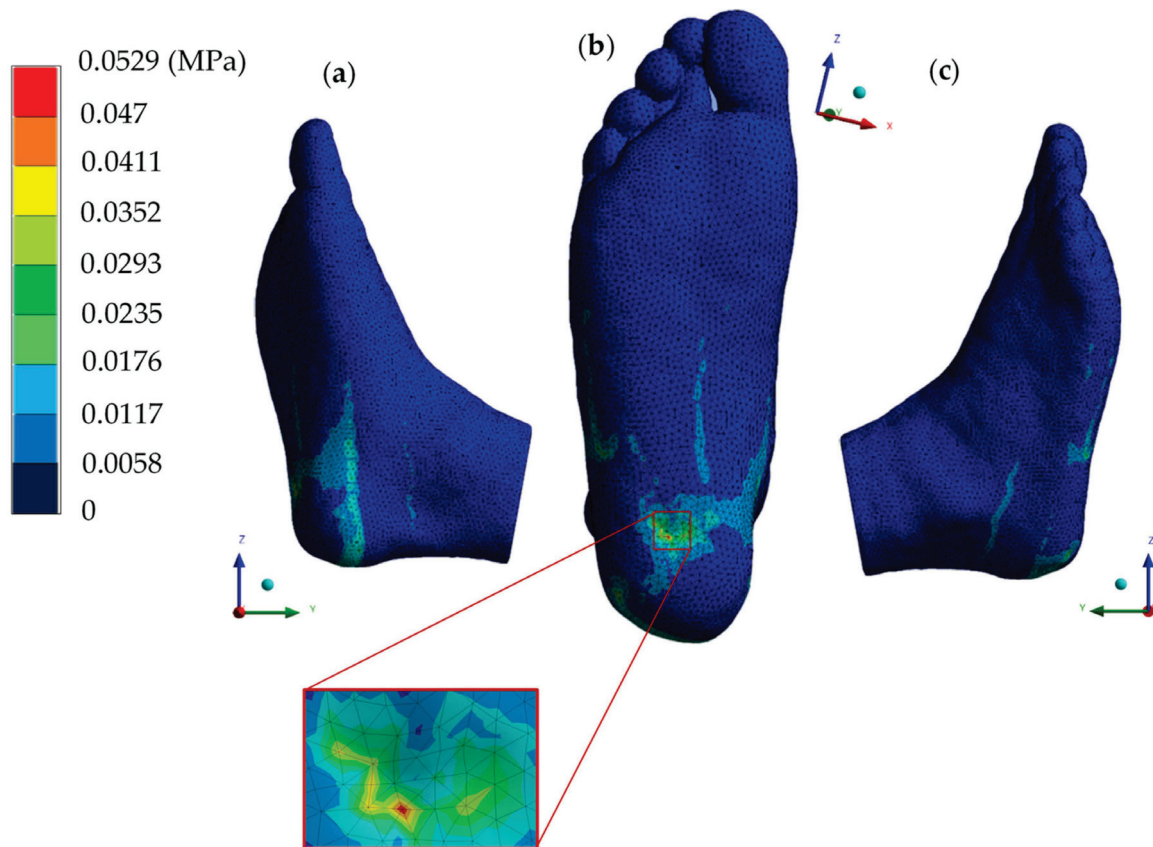


Figure 17. von Mises stress with patient-specific foot orthosis (H.S.). (a) Left side view. (b) Plantar region. (c) Right side view.

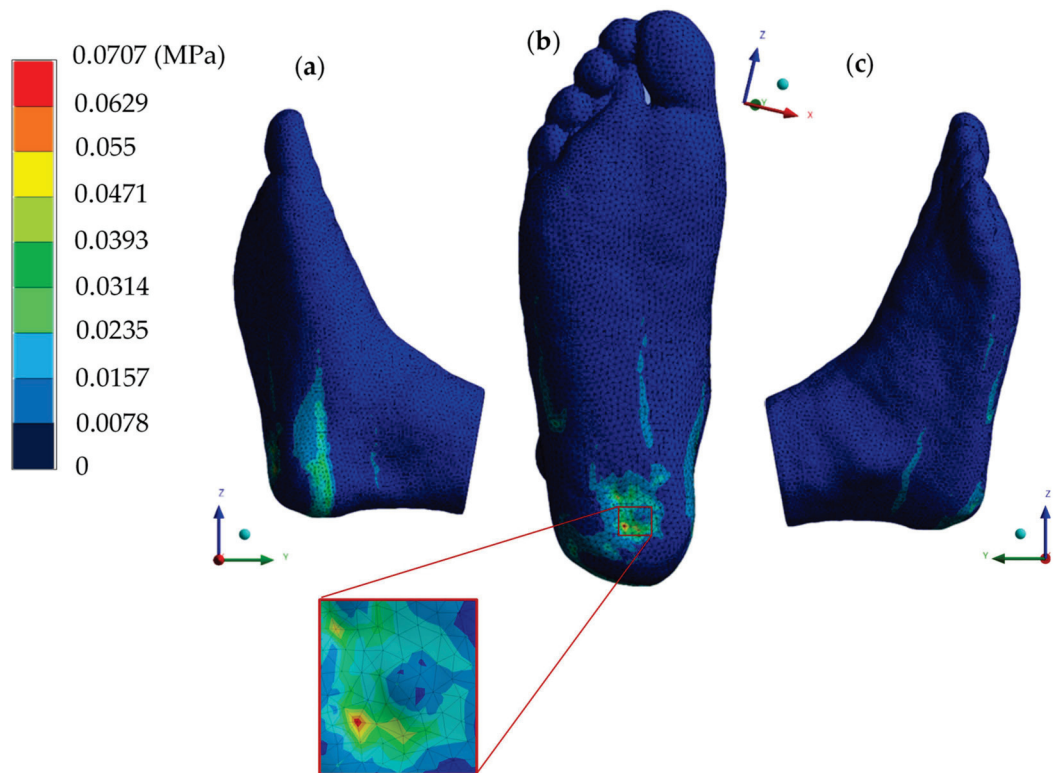


Figure 18. von Mises stress with patient-specific foot orthosis (L.R.). (a) Left side view. (b) Plantar region. (c) Right side view.

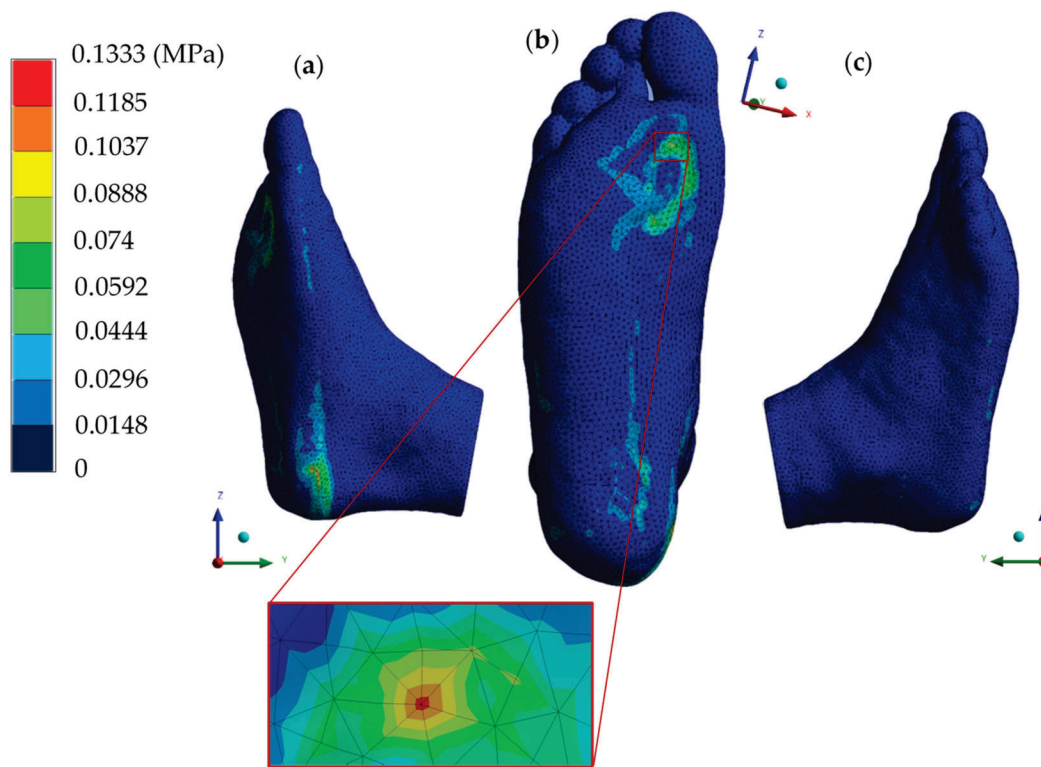


Figure 19. von Mises stress with patient-specific foot orthosis (M.S.). (a) Left side view. (b) Plantar region. (c) Right side view.

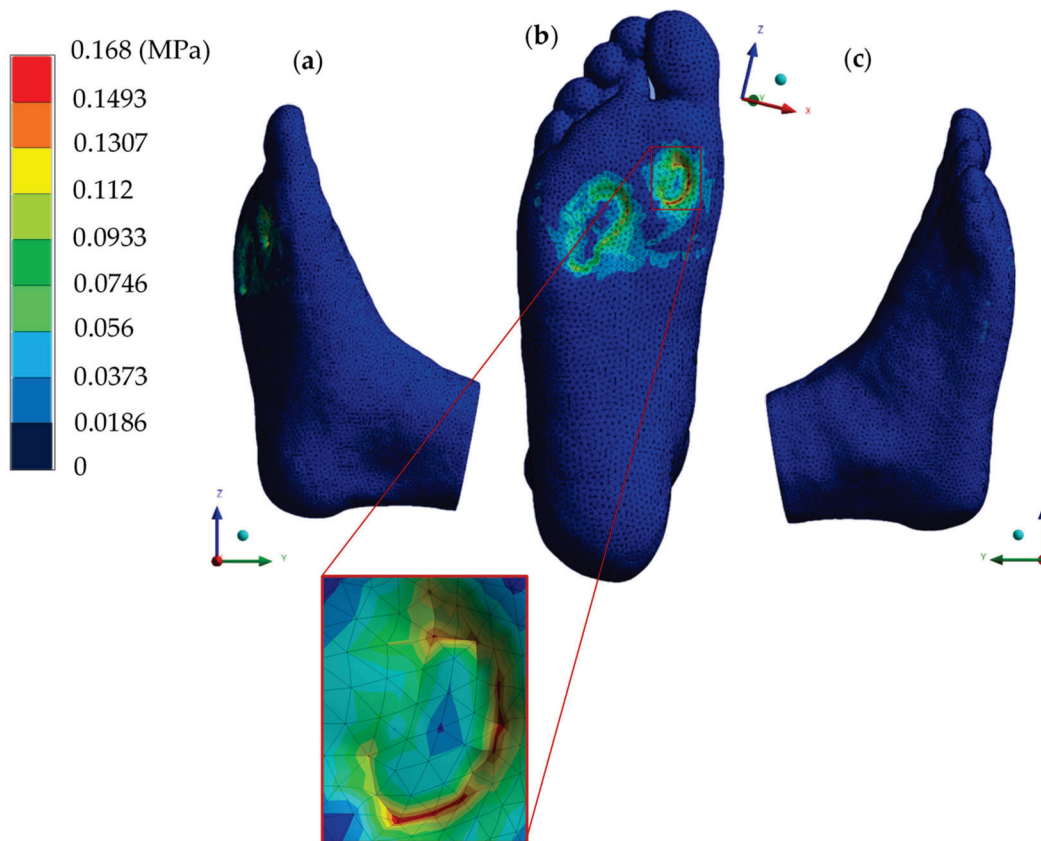


Figure 20. von Mises stress with patient-specific foot orthosis (H.R.). (a) Left side view. (b) Plantar region. (c) Right side view.

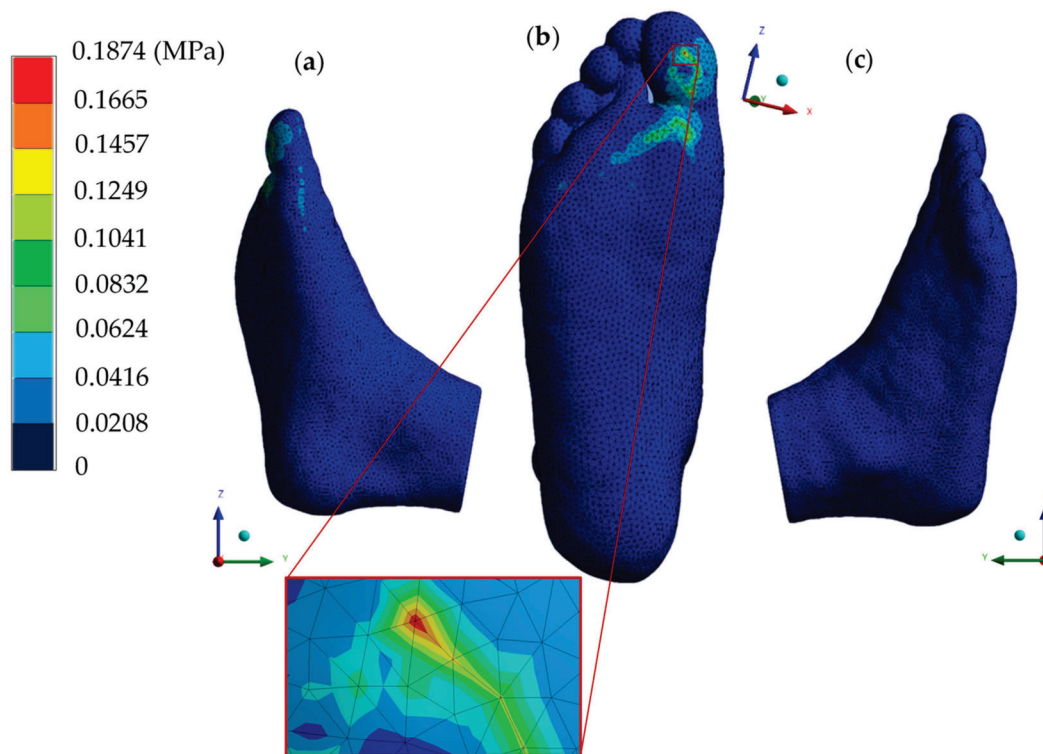


Figure 21. von Mises stress with patient-specific foot orthosis (P.S.). (a) Left side view. (b) Plantar region. (c) Right side view.

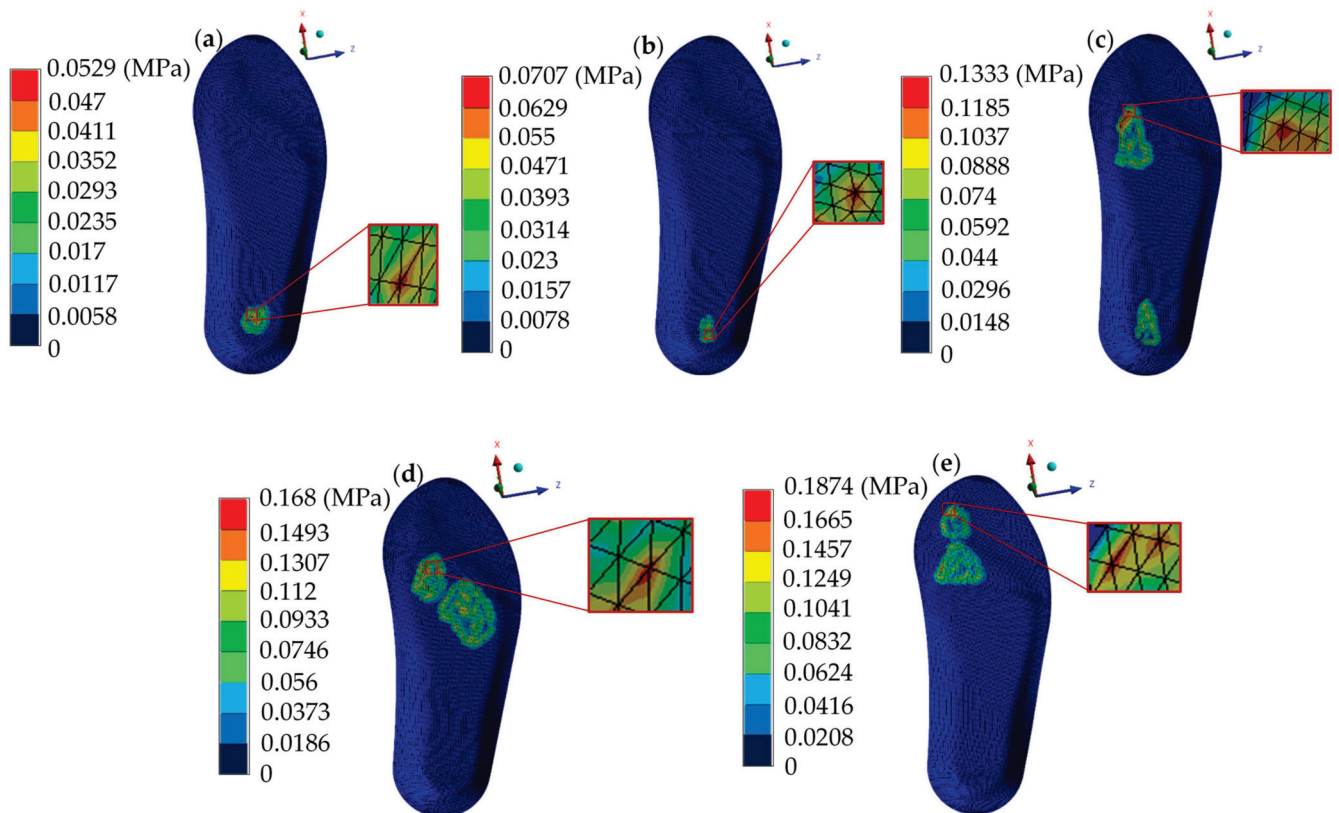


Figure 22. von Mises stress in the plantar region of the patient-specific insole for all stance phases. (a) Heel strike. (b) Loading response. (c) Mid-stance. (d) Heel rise. (e) Pre-swing.

4. Discussion

The current research employed a high-complexity biological model of the right foot focused on segmenting soft tissues, intrinsic muscles, and skin. In contrast to most foot Finite Element Analyses that employ bony tissues, this research presents a novel and different approach to analyzing the plantar surface with a yet-defined 3D detailed model development. Both numerical and experimental testing were conducted to biomechanically evaluate the behavior of pressure distribution on the foot sole region during all five stance phases in a normal gait cycle to design a 3D-printable personalized foot insole based on the patient's unique morphology for evaluating the complex behavior of foot-insole effects presented in the plantar zone. The assignment of loading and boundary conditions presented in the Finite Element Analysis showed an innovative and unconventional method to employ new mechanical considerations to analyze soft tissues; utilizing a displacement as an external agent allowed the development of accurate effects.

Numerical results indicated that the highest concentrations of von Mises stress fields are found in the pre-swing phase in the forefoot, specifically at the hallux, as well as in the values of the experimental analysis. These Finite Element Method results, particularly the stress distribution (ring-shaped), should be interpreted within the context of the model's construction and considerations, specifically using only soft tissue. The contact between the ground tends to displace the tissue due to its high ductility, resulting in a higher stress concentration in the contour and not in the center. Despite this limitation, the agreement with experimental data regarding pressure spectrum, peak plantar pressure, and average pressure suggests that the model offers valuable insights into soft tissue pressure distribution biomechanical behavior during foot-ground contact. Furthermore, previous research reported this ring-shaped or gap stress distribution field, stating that the mentioned effect occurs only by analyzing soft tissue [86]. Thus, the plantar pressure distribution showed agreement with the two types of analysis, which validates numerical analyses as both had similar behavior and patterns, having an average error range in the five stance phases of less than 5% in the maximum pressure points of the numerical simulation compared to the experimental one.

On the other hand, most of the analyses showed a uniform stress distribution, commonly green shades in the isochromatic scale, with values between 0.055 and 0.08 MPa, corresponding to the general average pressure. The baropodometric test registered a result of 787 gr/cm², equal to 0.0771 MPa. This study evaluated the effects caused on the foot sole for each one of the stance phases from a statically mechanical study, representing the exact moment when the foot is in contact with the ground, disregarding dynamic considerations, which enables this method to optimize and simplify dynamic analysis. The high fidelity of the results obtained in the experimental testing and the first case study indicate that despite any modeling and dynamic simplifications previously mentioned, the principles and parameters utilized in the Finite Element Analysis were accurate and appropriate to simulate the stance phases of a normal gait cycle. Furthermore, the findings of this study are consistent with observations previously reported in the literature of Finite Element Analyses focused on the gait cycle. Despite methodological differences, numerical results align closely with the observations reported by the cited research [87] for the mid-stance, heel rise, and pre-swing values along the plantar zone; the loading response also shows good agreement in the heel lateral region. Similar stress distribution and values presented in this research for the heel rise phase replicate the findings from different investigation groups [88,89]. Results obtained in the hallux when evaluating the pre-swing phase are in solid concordance with results reported in a numerical study in the first ray [90]. The total elastic strain values in Appendix A tables show consistent behavior with an analysis of the strain effects in the plantar region skin [91].

The comprehension of the biomechanical behavior of the model under gait cycle stance phases provided essential insights to design a 3D-printable patient-specific insole. Numerical results for the second case study supported the insole's material selection and the accurate parametric design to considerably attenuate peak plantar pressure, specifically

in critical stance phases, such as heel strike and pre-swing. The prediction of pressure points during the performance of daily activities through Finite Element analyses facilitates novel approaches that seek high-biofidelity methods to analyze and understand dynamics in real-life biomechanics, aiming to enhance current customization principles for orthotic and prosthetic devices, contributing innovative scientific solutions to the medical field.

The presented research is categorized as a presentation of a method for presenting a distinctive approach with innovative mechanical considerations to analyze pressure points in a healthy patient, which also brings certain limitations for the methods implemented. The need to employ the proposed methods in various healthy patients before testing them in pathological foot cases is worth mentioning. Methods employed have a relevant impact in providing proper knowledge and general guidelines in the study of pressure points and their re-distribution towards designing fully customized foot orthopedic devices. Further approaches in pathological and specific-condition cases can potentially be achieved using the described methods; for example, future research focused on the elderly, children, or athletes.

5. Limitations

The interpretation of the findings presented in the current study and their applicability requires careful consideration due to the simplifications employed, the modeling approach conducted, and the need for specific patient data to conduct numerical simulations with a significant degree of fidelity. A clear example of these limitations is the non-consideration of bony tissue (neglecting cortical and trabecular structures) that simplified the construction of biological elements in the model; since the 3D model was only focused on foot soft tissues, the model is not adequate to evaluate whole foot structural conditions; along with the utilized boundary conditions where they were based on specific situations, moments, or instants during stance phases of a normal gait, simulating a quasi-static analysis disregarding dynamic considerations; results estimations cannot be directly and precisely compared to experimental data for the simplified assumptions previously stated. Even though similar behavior patterns are provided, clinical assessment by a professional is necessary for any decision-making procedure. Likewise, constant advancements in medical imaging facilitate the development of increasingly sophisticated three-dimensional biological models. This progress allows the incorporation of detailed representations of the complex foot musculature (intrinsic and extrinsic muscles); furthermore, assigning material properties that more accurately reflect biological tissues is required, as only linear elastic, homogeneous, and isotropic properties were assumed for this research work. In addition, the Finite Element model was constructed based on a specific patient approach and not targeted to a vast population; thus, further investigation is needed to be developed in different population groups. In recognition of the manuscript's limitations, the results were primarily intended to provide a qualitative analysis of the biomechanical pressure distribution effects on the plantar region from a mechanical-computational perspective. This approach acknowledges that the results presented may not represent the exact whole-foot behavior but estimate a suitable prediction of the effects generated in the plantar zone.

6. Conclusions

The current research has provided feasible results predicting plantar pressure points during the different stance phases, even under quasi-static considerations disregarding dynamic conditions, which demonstrates the impact of the Finite Element Method as a powerful tool for analyzing the human body. Applying an innovative and unconventional way to evaluate the foot sole when performing a gait cycle provided a valuable medical-validated database for clinicians to deepen their understanding regarding foot structural behavior. The reconstruction of biological three-dimensional models combined with numerical simulations is remarkably successful in being the short-term assistive methodology for medical procedures, such as surgical planning, prescription of orthopedic devices, rehabilitation therapies, and more knowledgeable biomechanical principles for education.

The emerging techniques to design and develop high-performance customized orthopedics focus on 3D-printable materials that are often numerically evaluated before being printed and further used. Likewise, the use of 3D-printing technologies has increasingly been recognized as a standard for orthopedics design and reconstruction due to their high performance, which are advantageous techniques for being time-efficient and affordable compared to traditional procedures. Precisely, the unique patient-specific needs for plantar supports are successfully being achieved by the methods presented in the manuscript, from the 3D patient morphology modeling to numerical simulations that analyze the accuracy of the insole design and cushioning properties assigned to suitably re-distribute excessive pressure points. Thus, all methods described in the current research align with recent advances in foot biomechanics, which aim to revolutionize the footwear and prosthetic lower limb industry, contributing to enhancing rehabilitation treatments and people's life quality through optimized foot orthotics with the primary goal of achieving specific individual needs.

Author Contributions: Conceptualization, J.A.S.-P., G.U.-S., B.R.-Á. and F.C.-H.; methodology, J.A.S.-P., G.U.-S., B.R.-Á. and G.M.U.-C.; validation, J.A.S.-P., G.U.-S., B.R.-Á., G.M.U.-C. and F.J.G.-F.; formal analysis, J.A.S.-P., G.U.-S., B.R.-Á. and A.T.-E.; investigation, J.A.S.-P., G.U.-S., B.R.-Á. and G.M.U.-C.; resources, J.A.S.-P., G.U.-S., B.R.-Á. and J.A.G.-N.; writing—original draft preparation, J.A.S.-P., G.U.-S., B.R.-Á. and M.I.C.-C.; writing—review and editing, J.A.S.-P., G.U.-S., B.R.-Á. and F.C.-H.; visualization, J.A.S.-P., G.U.-S., B.R.-Á. and A.C.-L.; supervision, J.A.S.-P., G.U.-S., B.R.-Á. and F.C.-H.; project administration, J.A.S.-P., G.U.-S., B.R.-Á. and G.M.U.-C. All authors have read and agreed to the published version of the manuscript.

Funding: This research received no external funding.

Institutional Review Board Statement: The study was conducted in accordance with the Declaration of Helsinki, and approved by the Ethics Committee of Biomechanics Group, Instituto Politécnico Nacional, Escuela Superior de Ingeniería Mecánica y Eléctrica, Sección de Estudios de Posgrado e Investigación, Unidad Profesional Adolfo López Mateos (approval number BIOMECH/0012/2023, 14 June 2023).

Informed Consent Statement: Written informed consent has been obtained from the patient(s) to publish this paper.

Data Availability Statement: All data generated or analyzed during this study are included within the article.

Acknowledgments: The authors gratefully acknowledge the Instituto Politécnico Nacional and Consejo Nacional de Humanidades Ciencias y Tecnologías for supporting this research.

Conflicts of Interest: The authors declare no conflict of interest.

Appendix A

Table A1. First case study summary of numerical evaluation results for the heel strike, loading response, and mid-stance phases.

Type of Analysis	Heel Strike Phase		Loading Response Phase		Mid-Stance Phase	
	Maximum	Minimum	Maximum	Minimum	Maximum	Minimum
Total deformation (mm)	6.3416	0	7.1337	0	6.1659	0
Deformation X axis (mm)	0.9612	−0.9616	1.749	−1.2735	3.0399	−1.7385
Deformation Y axis (mm)	6.3411	−0.0761	7.1337	−0.1915	6.1624	−0.9437
Deformation Z axis (mm)	1.0297	−0.8593	1.4182	−1.5603	2.1061	−1.7235
Total elastic strain (mm/mm)	0.6967	8.299×10^{-16}	0.5902	4.39×10^{-16}	0.9464	5.95×10^{-16}
Elastic strain X axis (mm/mm)	0.3455	−0.2559	0.2692	−0.2004	0.4559	−0.2695
Elastic strain Y axis (mm/mm)	0.39	−0.6420	0.1909	−0.4240	0.5435	−0.6249
Elastic strain Z axis (mm/mm)	0.2724	−0.2734	0.3155	−0.1925	0.3726	−0.3106
Nominal stress X axis (MPa)	0.0617	−0.1174	0.0891	−0.1704	0.1152	−0.1162

Table A1. *Cont.*

Type of Analysis	Heel Strike Phase		Loading Response Phase		Mid-Stance Phase	
	Maximum	Minimum	Maximum	Minimum	Maximum	Minimum
Nominal stress Y axis (MPa)	0.0643	−0.1495	0.0659	−0.2107	0.1247	−0.1511
Nominal stress Z axis (MPa)	0.0663	−0.1102	0.0593	−0.1604	0.1442	−0.1217
Shear stress XY plane (MPa)	0.0373	−0.0281	0.0488	−0.0540	0.0466	−0.0634
Shear stress YZ plane (MPa)	0.0343	−0.0258	0.0537	−0.0449	0.0470	−0.0383
Shear stress XZ plane (MPa)	0.0220	−0.0188	0.0331	−0.0208	0.0226	−0.0252
von Mises stress (MPa)	0.1334	0	0.1619	0	0.1289	0
Maximum principal stress (MPa)	0.0730	−0.0830	0.0905	−0.1536	0.1825	−0.1088
Minimum principal stress (MPa)	0.0511	−0.1672	0.0238	−0.2174	0.0713	−0.1653

Table A2. First case study summary of numerical evaluation results for the heel rise and pre-swing phases.

Type of Analysis	Heel Rise		Pre-Swing	
	Maximum	Minimum	Maximum	Minimum
Total deformation (mm)	8.1699	0	9.1625	0
Deformation X axis (mm)	1.6727	−2.177	2.2721	−2.7693
Deformation Y axis (mm)	8.1698	−1.2569	9.1615	−0.7243
Deformation Z axis (mm)	2.0717	−2.6718	1.5841	−2.4929
Total elastic strain (mm/mm)	1.0893	4.26×10^{-16}	1.4249	4.029×10^{-16}
Elastic strain X axis (mm/mm)	0.4747	−0.2871	0.7611	−0.3579
Elastic strain Y axis (mm/mm)	0.2355	−0.7421	0.4636	−1.1273
Elastic strain Z axis (mm/mm)	0.4177	−0.2561	0.5801	−0.5227
Nominal stress X axis (MPa)	0.0952	−0.1973	0.1034	−0.2758
Nominal stress Y axis (MPa)	0.0752	−0.3486	0.1452	−0.4176
Nominal stress Z axis (MPa)	0.1148	−0.2508	0.1210	−0.3123
Shear stress XY plane (MPa)	0.0655	−0.1053	0.0704	−0.1368
Shear stress YZ plane (MPa)	0.0693	−0.0728	0.0896	−0.0909
Shear stress XZ plane (MPa)	0.0366	−0.0488	0.0453	−0.0437
von Mises stress (MPa)	0.2005	0	0.2729	0
Maximum principal stress (MPa)	0.1454	−0.1783	0.1531	−0.2691
Minimum principal stress (MPa)	0.0374	−0.3855	0.1013	−0.4533

Table A3. Second case study summary of numerical evaluation results for the heel strike, loading response, and mid-stance phases.

Type of Analysis	Heel Strike Phase		Loading Response Phase		Mid-Stance Phase	
	Maximum	Minimum	Maximum	Minimum	Maximum	Minimum
Total deformation (mm)	5.0269	0	6.1577	0	4.9285	0
Deformation X axis (mm)	1.4225	−0.5925	1.8206	−0.8742	1.8526	−1.3961
Deformation Y axis (mm)	5.0266	−0.0705	6.1576	−0.1074	4.9284	−0.5991
Deformation Z axis (mm)	0.6477	−0.5966	0.9268	−0.7788	1.2221	−1.3223
Total elastic strain (mm/mm)	0.3596	5.6254×10^{-14}	0.3574	7.1839×10^{-14}	0.7251	9.997×10^{-14}
Elastic strain X axis (mm/mm)	0.1172	−0.1137	0.1698	−0.133	0.3588	−0.2016
Elastic strain Y axis (mm/mm)	0.2019	−0.2402	0.2964	−0.2767	0.3121	−0.5439
Elastic strain Z axis (mm/mm)	0.1603	−0.1478	0.1329	−0.1842	0.2458	−0.3044
Nominal stress X axis (MPa)	0.0257	−0.0571	0.0464	−0.0929	0.0995	−0.3104
Nominal stress Y axis (MPa)	0.019	−0.0591	0.0415	−0.099	0.0888	−0.413
Nominal stress Z axis (MPa)	0.027	−0.0605	0.0439	−0.0983	0.0773	−0.3432
Shear stress XY plane (MPa)	0.0143	−0.0153	0.0187	−0.0188	0.061	−0.0422
Shear stress YZ plane (MPa)	0.0158	−0.0196	0.0146	−0.0141	0.0564	−0.0531

Table A3. Cont.

Type of Analysis	Heel Strike Phase		Loading Response Phase		Mid-Stance Phase	
	Maximum	Minimum	Maximum	Minimum	Maximum	Minimum
Shear stress XZ plane (MPa)	0.0083	−0.0112	0.0102	−0.0116	0.0265	−0.0276
von Mises stress (MPa)	0.0529	0	0.0707	0	0.1333	0
Maximum principal stress (MPa)	0.0424	−0.0536	0.0578	−0.0901	0.1196	−0.3092
Minimum principal stress (MPa)	0.0157	−0.0682	0.0299	−0.1024	0.0632	−0.4185

Table A4. Second case study summary of numerical evaluation results for the heel rise and pre-swing phases.

Type of Analysis	Heel Rise		Pre-Swing	
	Maximum	Minimum	Maximum	Minimum
Total deformation (mm)	7.5367	0	8.4016	0
Deformation X axis (mm)	1.2509	−1.8733	3.0257	−1.8019
Deformation Y axis (mm)	7.5367	−0.9327	8.3979	−0.4156
Deformation Z axis (mm)	1.7482	−2.1883	2.1923	−1.6503
Total elastic strain (mm/mm)	1.0011	4.7186×10^{-16}	1.0424	1.5761×10^{-15}
Elastic strain X axis (mm/mm)	0.4901	−0.2881	0.5395	−0.2877
Elastic strain Y axis (mm/mm)	0.2103	−0.7489	0.4538	−0.9172
Elastic strain Z axis (mm/mm)	0.4304	−0.2245	0.4146	−0.3263
Nominal stress X axis (MPa)	0.0912	−0.1922	0.1105	−0.3156
Nominal stress Y axis (MPa)	0.0757	−0.3103	0.0724	−0.3358
Nominal stress Z axis (MPa)	0.0813	−0.2218	0.0874	−0.3223
Shear stress XY plane (MPa)	0.0732	−0.0897	0.0611	−0.0702
Shear stress YZ plane (MPa)	0.0543	−0.0698	0.0636	−0.1045
Shear stress XZ plane (MPa)	0.0303	−0.0369	0.0417	−0.028
von Mises stress (MPa)	0.168	0	0.1874	0
Maximum principal stress (MPa)	0.14	−0.1638	0.1187	−0.3047
Minimum principal stress (MPa)	0.0642	−0.3242	0.0384	−0.3572

References

1. Lou, C.; Wang, S.; Liang, T.; Pang, C.; Huang, L.; Run, M.; Liu, X. A Graphene-Based Flexible Pressure Sensor with Applications to Plantar Pressure Measurement and Gait Analysis. *Materials* **2017**, *10*, 1068. [CrossRef] [PubMed]
2. Kim, D.; Lewis, C.L.; Gill, S.V. Effects of obesity and foot arch height on gait mechanics: A cross-sectional study. *PLoS ONE* **2021**, *16*, e0260398. [CrossRef] [PubMed]
3. Mei, Q.; Kim, H.K.; Xiang, L.; Shim, V.; Wang, A.; Baker, J.S.; Gu, Y.; Fernandez, J. Toward improved understanding of foot shape, foot posture, and foot biomechanics during running: A narrative review. *Front. Physiol.* **2022**, *13*, 1062598. [CrossRef]
4. Ang, C.K.; Solihin, M.I.; Chan, W.J.; Ong, Y.Y. Study of Plantar Pressure Distribution. *MATEC Web. Conf.* **2018**, *237*, 01016. [CrossRef]
5. Nandikolla, K.V.; Bochen, R.; Meza, S.; Garcia, A. Experimental Gait Analysis to Study Stress Distribution of the Human Foot. *J. Med. Eng.* **2017**, *2017*, 3432074. [CrossRef] [PubMed]
6. Pirker, W.; Katzenschlager, R. Gait disorders in adults and the elderly. *Wien. Klin. Wochenschr.* **2017**, *129*, 81–95. [CrossRef] [PubMed]
7. Cicirelli, G.; Impedovo, D.; Dentamaro, V.; Marani, R.; Pirlo, G.; D’Orazio, T.R. Human Gait Analysis in Neurodegenerative Diseases: A Review. *IEEE J. Biomed. Health Inform.* **2022**, *26*, 229–242. [CrossRef]
8. Stöckel, T.; Jacksteit, R.; Behrens, M.; Skripitz, R.; Bader, R.; Mau-Moeller, A. The mental representation of the human gait in young and older adults. *Front. Psychol.* **2015**, *6*, 943. [CrossRef] [PubMed]
9. Hulleck, A.A.; Menoth-Mohan, D.; Abdallah, N.; El-Rich, M.; Khalaf, K. Present and future of gait assessment in clinical practice: Towards the application of novel trends and technologies. *Front. Med. Technol.* **2022**, *4*, 901331. [CrossRef]
10. Taş, S.; Çetin, A. An investigation of the relationship between plantar pressure distribution and the morphologic and mechanic properties of the intrinsic foot muscles and plantar fascia. *Gait Post.* **2019**, *72*, 217–221. [CrossRef]
11. Rusu, L.; Paun, E.; Marin, M.I.; Hemanth, J.; Rusu, M.R.; Calina, M.L.; Bacanoiu, M.V.; Danoiu, M.; Danciulescu, D. Plantar Pressure and Contact Area Measurement of Foot Abnormalities in Stroke Rehabilitation. *Brain Sci.* **2021**, *11*, 1213. [CrossRef]

12. Abdul Razak, A.H.; Zayegh, A.; Begg, R.K.; Wahab, Y. Foot Plantar Pressure Measurement System: A Review. *Sensors* **2012**, *12*, 9884–9912. [CrossRef] [PubMed]
13. Chen, J.-L.; Dai, Y.-N.; Grimaldi, N.S.; Lin, J.-J.; Hu, B.-Y.; Wu, Y.-F.; Gao, S. Plantar Pressure-Based Insole Gait Monitoring Techniques for Diseases Monitoring and Analysis: A Review. *Adv. Mater. Technol.* **2022**, *7*, 2100566. [CrossRef]
14. Jones, A.D.; Crossland, S.R.; Nixon, J.E.; Siddle, H.J.; Russell, D.A.; Culmer, P.R. STrain Analysis and Mapping of the Plantar Surface (STAMPS): A novel technique of plantar load analysis during gait. *Proc. Inst. Mech. Eng. H* **2023**, *237*, 841–854. [CrossRef] [PubMed]
15. Crossland, S.R.; Siddle, H.J.; Culmer, P.; Brockett, C.L. A plantar surface shear strain methodology utilising Digital Image Correlation. *J. Mech. Behav. Biomed. Mater.* **2022**, *136*, 105482. [CrossRef] [PubMed]
16. Syed, N.; Karvannan, H.; Maiya, A.G.; Binukumar, B.; Prem, V.; Chakravarty, R.D. Plantar pressure distribution among asymptomatic individuals: A cross-sectional study. *Foot Ankle Spec.* **2012**, *5*, 102–106. [CrossRef] [PubMed]
17. Chatwin, K.E.; Abbott, C.A.; Boulton, A.J.M.; Bowling, F.L.; Reeves, N.D. The role of foot pressure measurement in the prediction and prevention of diabetic foot ulceration—A comprehensive review. *Diabetes Metab. Res. Rev.* **2020**, *36*, e3258. [CrossRef] [PubMed]
18. Trejo-Enriquez, A.; Urriolagoitia-Sosa, G.; Romero-Ángeles, B.; García-Laguna, M.Á.; Guzmán-Baeza, M.; Martínez-Reyes, J.; Rojas-Castrejon, Y.Y.; Gallegos-Funes, F.J.; Patiño-Ortiz, J.; Urriolagoitia-Calderón, G.M. Numerical Evaluation Using the Finite Element Method on Frontal Craniocervical Impact Directed at Intervertebral Disc Wear. *Appl. Sci.* **2023**, *13*, 11989. [CrossRef]
19. Maya-Anaya, D.; Urriolagoitia-Sosa, G.; Romero-Ángeles, B.; Martínez-Mondragon, M.; German-Carcano, J.M.; Correa-Corona, M.I.; Trejo-Enriquez, A.; Sánchez-Cervantes, A.; Urriolagoitia-Luna, A.; Urriolagoitia-Calderón, G.M. Numerical Analysis Applying the Finite Element Method by Developing a Complex Three-Dimensional Biomodel of the Biological Tissues of the Elbow Joint Using Computerized Axial Tomography. *Appl. Sci.* **2023**, *13*, 8903. [CrossRef]
20. Cruz-López, S.; Urriolagoitia-Sosa, G.; Romero-Ángeles, B.; Urriolagoitia-Calderón, G.M.; Marquet-Rivera, R.A.; Hernández-Vázquez, R.A.; Mastache-Miranda, O.A.; Vázquez-Feijo, J.A. Biomechanical analysis of the femur bone with the cotyle of the hip prosthesis. *MOJ Appl. Bionics Biomech.* **2023**, *7*, 11–12. [CrossRef]
21. Martínez-Mondragon, M.; Urriolagoitia-Sosa, G.; Romero-Ángeles, B.; Pérez-Partida, J.C.; Cruz-Olivares, I.M.; Urriolagoitia-Calderón, G. Bilinear Numerical Analysis of the Structural Behavior of a Dental Implant Applied as a Biomaterial Carbon Fiber Reinforced Polyether-Ether-Ketone (CFR-PEEK): A Finite Element Analysis. *Dent. Hypoth.* **2023**, *14*, 45–48.
22. Telfer, S.; Erdemir, A.; Woodburn, J.; Cavanagh, P.R. What Has Finite Element Analysis Taught Us about Diabetic Foot Disease and Its Management? A Systematic Review. *PLoS ONE* **2014**, *9*, e109994. [CrossRef] [PubMed]
23. Rai, D.V.; Aggarwal, L.M. The Study of Plantar Pressure Distribution in Normal and Pathological Foot. *Pol. J. Med. Phys. Eng.* **2006**, *12*, 25–34.
24. Ukobitz, D.; Faullant, R. Leveraging 3D Printing Technologies: The Case of Mexico's Footwear Industry. *Res.—Technol. Manag.* **2021**, *64*, 20–30. [CrossRef]
25. Jandova, S.; Mendricky, R. Benefits of 3D Printed and Customized Anatomical Footwear Insoles for Plantar Pressure Distribution. *3D Print. Addit. Manuf.* **2022**, *9*, 547–556. [CrossRef] [PubMed]
26. Ali, M.H.; Trubayev, S.; Shehab, E. 3D Printed Large-Scale Insole and Its Challenges. In Proceedings of the 8th Brunei International Conference on Engineering and Technology 2021, Universiti Teknologi Brunei, Seri Begawan, Brunei Darussalam, 8–10 November 2021.
27. Shaikh, S.; Jamdade, B.; Chanda, A. Effects of Customized 3D-Printed Insoles in Patients with Foot-Related Musculoskeletal Ailments—A Survey-Based Study. *Prosthesis* **2023**, *5*, 550–561. [CrossRef]
28. Chen, R.K.; Jin, Y.-A.; Wensman, J.; Shih, A. Additive manufacturing of custom orthoses and prostheses—A review. *Addit. Manuf.* **2016**, *12*, 77–89. [CrossRef]
29. Wu, S.; Zeng, T.; Liu, Z.; Ma, G.; Xiong, Z.; Zuo, L.; Zhou, Z. 3D Printing Technology for Smart Clothing: A Topic Review. *Materials* **2022**, *15*, 7391. [CrossRef]
30. Kumar, R.; Sarangi, S.K. 3D-Printed Orthosis: A Review on Design Process and Material Selection for Fused Deposition Modeling Process. In *Advances in Materials Processing and Manufacturing Applications*, 1st ed.; Patnaik, A., Kozeschnik, E., Kukshal, V., Eds.; Springer Singapore Publishing: Singapore, 2021; Volume 1, pp. 531–538.
31. Rodriguez-Colon, R.; Nayak, V.V.; Parente, P.E.L.; Leucht, P.; Tovar, N.; Lin, C.C.; Rezzadeh, K.; Hacquebord, J.H.; Coelho, P.G.; Witek, L. The presence of 3D printing in orthopedics: A clinical and material review. *J. Orthop. Res.* **2023**, *41*, 601–613. [CrossRef]
32. Kumar, P.; Rajak, D.K.; Abubakar, M.; Ali, S.G.M.; Hussain, M. 3D Printing Technology for Biomedical Practice: A Review. *J. Mater. Eng. Perform.* **2021**, *30*, 5342–5355. [CrossRef]
33. Gelaziene, E.; Milasienė, D. Influence of the Type of Plastic and Printing Technologies on the Compressive Behavior of 3D-Printed Heel Prototypes. *Materials* **2023**, *16*, 1930. [CrossRef] [PubMed]
34. Teixeira, R.; Coelho, C.; Oliveira, J.; Gomes, J.; Pinto, V.V.; Ferreira, M.J.; Nóbrega, J.M.; Silva, A.F.D.; Carneiro, O.S. Towards Customized Footwear with Improved Comfort. *Materials* **2021**, *14*, 1738. [CrossRef]
35. Rico-Baeza, G.; Pérez-Soto, G.I.; Morales-Hernández, L.A.; Cuan-Urquizo, E.; Camarillo-Gómez, K.A. Additively Manufactured Foot Insoles Using Body-Centered Cubic (BCC) and Triply Periodic Minimal Surface (TPMS) Cellular Structures. *Appl. Sci.* **2023**, *13*, 12665. [CrossRef]

36. Kermavnar, T.; Shannon, A.; O'Sullivan, L.W. The application of additive manufacturing/3D printing in ergonomic aspects of product design: A systematic review. *Appl. Ergon.* **2021**, *97*, 103528. [CrossRef] [PubMed]
37. Walker, K.J.; Przestrzelski, B.T.; Kaluf, B.; Driggers, N.H.; Ballard, W.D., 2nd; Pruett, T.C.; Hoeffner, S.L.; DesJardins, J.D. Novel 3D-printed foot orthoses with variable hardness: A comfort comparison to traditional orthoses. *Med. Eng. Phys.* **2023**, *115*, 103978. [CrossRef] [PubMed]
38. Hudak, Y.F.; Li, J.S.; Cullum, S.; Strzelecki, B.M.; Richburg, C.; Kaufman, G.E.; Abrahamson, D.; Heckman, J.T.; Ripley, B.; Telfer, S.; et al. A novel workflow to fabricate a patient-specific 3D printed accommodative foot orthosis with personalized latticed metamaterial. *Med. Eng. Phys.* **2022**, *104*, 103802. [CrossRef] [PubMed]
39. Lee, Y.C.L.; Lin, G.; Wang, M.J.J. Comparing 3D foot scanning with conventional measurement methods. *J. Foot Ankle Res.* **2014**, *7*, 44. [CrossRef]
40. Sacco, R.; Munoz, M.-A.; Billuart, F.; Lalevée, M.; Beldame, J. Validation of an Automated Optical Scanner for a Comprehensive Anthropometric Analysis of the Foot and Ankle. *Bioengineering* **2023**, *10*, 968. [CrossRef] [PubMed]
41. Silva, R.; Silva, B.; Fernandes, C.; Morouço, P.; Alves, N.; Veloso, A. A Review on 3D Scanners Studies for Producing Customized Orthoses. *Sensors* **2024**, *24*, 1373. [CrossRef]
42. Barrios-Muriel, J.; Romero-Sánchez, F.; Alonso-Sánchez, F.J.; Rodríguez Salgado, D. Advances in Orthotic and Prosthetic Manufacturing: A Technology Review. *Materials* **2020**, *13*, 295. [CrossRef]
43. Farhan, M.; Wang, J.Z.; Bray, P.; Burns, J.; Cheng, T.L. Comparison of 3D scanning versus traditional methods of capturing foot and ankle morphology for the fabrication of orthoses: A systematic review. *J. Foot Ankle Res.* **2021**, *14*, 2. [CrossRef] [PubMed]
44. Rogati, G.; Leardini, A.; Ortolani, M.; Caravaggi, P. Semi-automatic measurements of foot morphological parameters from 3D plantar foot scans. *J. Foot Ankle Res.* **2021**, *14*, 18. [CrossRef] [PubMed]
45. Chhikara, K.; Sidhu, S.S.; Gupta, S.; Saharawat, S.; Kataria, C.; Chanda, A. Development and Effectiveness Testing of a Novel 3D-Printed Multi-Material Orthosis in Nurses with Plantar Foot Pain. *Prosthesis* **2023**, *5*, 73–87. [CrossRef]
46. Hasibuzzaman, M.; Wahab, A.A.; Seng, G.H.; Ramlee, M.H. Three-dimensional printed orthosis in biomedical application: A short review. *J. Phys. Conf. Ser.* **2021**, *2071*, 012025. [CrossRef]
47. Agarwal, R.; Malhotra, S.; Gupta, V.; Jain, V. The application of Three-dimensional printing on foot fractures and deformities: A mini-review. *Ann. 3D Print. Med.* **2022**, *5*, 100046. [CrossRef]
48. Negru, N.; Leba, M.; Rosca, S.; Marica, L.; Ionica, A. A new approach on 3D scanning-printing technologies with medical applications. *IOP Conf. Ser. Mater. Sci. Eng.* **2019**, *572*, 012049. [CrossRef]
49. Brognara, L.; Mafla-España, M.A.; Gil-Molina, I.; Castillo-Verdejo, Y.; Cauli, O. The Effects of 3D Custom Foot Orthotics with Mechanical Plantar Stimulation in Older Individuals with Cognitive Impairment: A Pilot Study. *Brain Sci.* **2022**, *12*, 1669. [CrossRef]
50. Anggoro, P.W.; Tauviquirrahman, M.; Jamari, J.; Bayuseno, A.P.; Bawono, B.; Avelina, M.M. Computer-aided reverse engineering system in the design and production of orthotic insole shoes for patients with diabetes. *Cogent Eng.* **2018**, *5*, 1470916. [CrossRef]
51. Mo, S.; Leung, S.H.S.; Chan, Z.Y.S.; Sze, L.K.Y.; Mok, K.M.; Yung, P.S.H.; Ferber, R.; Cheung, R.T.H. The biomechanical difference between running with traditional and 3D printed orthoses. *J. Sports Sci.* **2019**, *37*, 2191–2197. [CrossRef]
52. Wang, Y.; Jiang, W.; Gan, Y.; Yu, Y.; Dai, K. Clinical Observation of 3D Printing Technology in Insoles for Flexible Flatfoot Patients. *J. Shanghai Jiaotong Univ.* **2021**, *26*, 398–403. [CrossRef]
53. Mueller, J.; Richter, M.; Schaefer, K.; Ganz, J.; Lohscheller, J.; Mueller, S. How to measure children's feet: 3D foot scanning compared with established 2D manual or digital methods. *J. Foot Ankle Res.* **2023**, *16*, 21. [CrossRef]
54. Lin, K.-W.; Chou, L.-W.; Su, Y.-T.; Wei, S.-H.; Chen, C.-S. Biomechanical Effect of 3D-Printed Foot Orthoses in Patients with Knee Osteoarthritis. *Appl. Sci.* **2021**, *11*, 4200. [CrossRef]
55. Shih, K.-S.; Jhou, S.-Y.; Hsu, W.-C.; Hsu, C.-C.; Chen, J.-W.; Yeh, J.-C.; Hung, Y.-C. A Biomechanical Investigation of Athletic Footwear Traction Performance: Integration of Gait Analysis with Computational Simulation. *Appl. Sci.* **2020**, *10*, 1672. [CrossRef]
56. Niu, J.; Liu, J.; Zheng, Y.; Ran, L.; Chang, Z. Are arch-conforming insoles a good fit for diabetic foot? Insole customized design by using finite element analysis. *Hum. Factors Ergon. Manuf.* **2020**, *30*, 303–310. [CrossRef]
57. Zhang, H.; Lin-Lv, M.; Yang, J.; Niu, W.; Cheung, J.C.; Sun, W.; Wong, D.W.; Ni, M. Computational modelling of foot orthosis for midfoot arthritis: A Taguchi approach for design optimization. *Acta Bioeng. Biomech.* **2020**, *22*, 75–83. [PubMed]
58. Serrato-Pedrosa, J.A.; Urriolagoitia-Sosa, G.; Romero-Ángeles, B.; Urriolagoitia-Calderón, G.M.; Cruz-López, S.; Urriolagoitia-Luna, A.; Carbajal-López, D.E.; Guereca-Ibarra, J.R.; Murillo-Aleman, G. Biomechanical Evaluation of Plantar Pressure Distribution towards a Customized 3D Orthotic Device: A Methodological Case Study through a Finite Element Analysis Approach. *Appl. Sci.* **2024**, *14*, 1650. [CrossRef]
59. Jastifer, J.R. Intrinsic muscles of the foot: Anatomy, function, rehabilitation. *Phys. Ther. Sport* **2023**, *61*, 27–36. [CrossRef]
60. Zulkifli, S.S.; Loh, W.P. A state-of-the-art review of foot pressure. *Foot Ankle Surg.* **2020**, *26*, 25–32. [CrossRef] [PubMed]
61. Jones, A.D.; De Siqueira, J.; Nixon, J.E.; Siddle, H.J.; Culmer, P.R.; Russell, D.A. Plantar shear stress in the diabetic foot: A systematic review and meta-analysis. *Diabet. Med.* **2022**, *39*, e14661. [CrossRef]
62. Oliveira, L.B.; Maranhão, D.A.; Cliquet, A.; Dinato, M.C.M.E.; Pagnano, R.G. Reliability of wireless insole baropodometry of normal individual's gait. *Acta Ortop. Bras.* **2021**, *29*, 238–241. [CrossRef]

63. Chevalier, T.L.; Hodgins, H.; Chockalingam, N. Plantar pressure measurements using an in-shoe system and a pressure platform: A comparison. *Gait Posture* **2010**, *31*, 397–399. [CrossRef] [PubMed]
64. Luboz, V.; Perrier, A.; Bucki, M.; Diot, B.; Cannard, F.; Vuillerme, N.; Payan, Y. Influence of the calcaneus shape on the risk of posterior heel ulcer using 3D patient-specific biomechanical modeling. *Ann. Biomed. Eng.* **2015**, *43*, 325–335. [CrossRef] [PubMed]
65. Su, H.; Mo, Z.; Guo, J.; Fan, Y. The effect of arch height and material hardness of personalized insole on correction and tissues of flatfoot. *J. Healthc. Eng.* **2017**, *2017*, 8614341. [CrossRef]
66. Kharazi, M.; Bohm, S.; Theodorakis, C.; Mersmann, F.; Arampatzis, A. Quantifying mechanical loading and elastic strain energy of the human Achilles tendon during walking and running. *Sci. Rep.* **2021**, *11*, 5830. [CrossRef] [PubMed]
67. Bojsen-Møller, F.; Lamoreux, L. Significance of free-dorsiflexion of the toes in walking. *Acta. Orthop. Scand.* **1979**, *50*, 471–479. [CrossRef]
68. Shaulian, H.; Gefen, A.; Wolf, A. Computational modeling of the plantar tissue stresses induced by the clinical practice of off-loading of the diabetic foot. In *The Science, Etiology and Mechanobiology of Diabetes and its Complications*, 1st ed.; Gefen, A., Ed.; Academic Press: London, UK, 2021; Volume 1, p. 38.
69. Chokhandre, S.; Halloran, J.P.; van den Bogert, A.J.; Erdemir, A. A three-dimensional inverse finite element analysis of the heel pad. *J. Biomech. Eng.* **2012**, *134*, 031002. [CrossRef] [PubMed]
70. Strzalkowski, N.D.; Triano, J.J.; Lam, C.K.; Templeton, C.A.; Bent, L.R. Thresholds of skin sensitivity are partially influenced by mechanical properties of the skin on the foot sole. *Physiol. Rep.* **2015**, *3*, e12425. [CrossRef]
71. Zhang, M.; Mak, A.F.T. In vivo friction properties of human skin. *Prosthet. Orthot. Int.* **1999**, *23*, 135–141. [CrossRef] [PubMed]
72. Van Alsenoy, K.; van der Linden, M.L.; Ryu, J.H.; Girard, O.; Al Raisi, L.; Santos, D. Isolated and combined effects of EVA and TPU custom foot orthoses on constant speed, treadmill running kinematics. *Front. Earth Sci.* **2023**, *11*, 1170661. [CrossRef]
73. Zolfagharian, A.; Lakhi, M.; Ranjbar, S.; Bodaghi, M. Custom Shoe Sole Design and Modeling Toward 3D Printing. *Int. J. Bioprint.* **2021**, *7*, 396. [CrossRef]
74. Xie, J.; Zhou, Z.; Luo, T.; Pang, H.; Meng, X.; Zhou, F. Study on Design and Additive Manufacturing of Customized Bionic Sports Sole for the Elderly. *IEEE Access* **2021**, *9*, 69830–69838. [CrossRef]
75. Li, J.; Shu, W.; Yang, Y.; Yan, R. Parametric modeling and performance analysis of a personalized insole based on 3D scanning and selective laser sintering. *Int. J. Comp. Integr. Manuf.* **2020**, *33*, 936–945. [CrossRef]
76. Ravi, T.; Ranganathan, R.; Ramesh, S.P.; Dandotiya, D.S. 3D Printed Personalized Orthotic Inserts Using Photogrammetry and FDM Technology. In *Fused Deposition Modeling Based 3D Printing. Materials Forming, Machining and Tribology*, 1st ed.; Dave, H.K., Davim, J.P., Eds.; Springer International Publishing: Cham, Switzerland, 2021; Volume 1, pp. 349–361.
77. Danko, M.; Sekac, J.; Dzivakova, E.; Zivcak, J.; Hudak, R. 3D Printing of Individual Running Insoles—A Case Study. *Orthop. Res. Rev.* **2023**, *15*, 105–118. [CrossRef] [PubMed]
78. Brognara, L.; Navarro-Flores, E.; Iachemet, L.; Serra-Catalá, N.; Cauli, O. Beneficial Effect of Foot Plantar Stimulation in Gait Parameters in Individuals with Parkinson’s Disease. *Brain Sci.* **2020**, *10*, 69. [CrossRef]
79. Anggoro, P.W.; Bawono, B.; Jamari, J.; Tauviqirrahman, M.; Bayuseno, A.P. Advanced design and manufacturing of custom orthotics insoles based on hybrid Taguchi-response surface method. *Heliyon* **2021**, *7*, e06481. [CrossRef]
80. Yildiz, K.; Medetalibeyoglu, F.; Kaymaz, I.; Ulusoy, G.R. Triad of foot deformities and its conservative treatment: With a 3D customized insole. *Proc. Inst. Mech. Eng. Part. H J. Eng. Med.* **2021**, *235*, 780–791. [CrossRef]
81. Nouman, M.; Chong, D.Y.R.; Srewaradachpisa, S.; Chatpun, S. The Effect of Customized Insole Pads on Plantar Pressure Distribution in a Diabetic Foot with Neuropathy: Material and Design Study Using Finite Element Analysis Approach. *Appl. Sci.* **2023**, *13*, 399. [CrossRef]
82. Nouman, M.; Dissaneewate, T.; Chong, D.Y.R.; Chatpun, S. Effects of thickness and length of custom made insole on plantar pressure for diabetic foot with neuropathy: A finite element approach. *Songklanakarin J. Sci. Technol.* **2021**, *43*, 1677–1684.
83. Tang, L.; Wang, L.; Bao, W.; Zhu, S.; Li, D.; Zhao, N.; Liu, C. Functional gradient structural design of customized diabetic insoles. *Songklanakarin J. Mech. Behav. Biomed. Mater.* **2019**, *94*, 279–287. [CrossRef]
84. Lemmon, D.; Shiang, T.; Hashmi, A.; Ulbrecht, J.S.; Cavanagh, P.R. The effect of insoles in therapeutic footwear—A finite element approach. *J. Biomech.* **1997**, *30*, 615–620. [CrossRef]
85. Rawlings, N. The Way We Stand: A Sequential Case Study on Foot Angle. *J. Biosci. Med.* **2023**, *11*, 79–89. [CrossRef]
86. Ghazali, M.J.; Ren, X.; Rajabi, A.; Zamri, W.F.H.W.; Mohd Mustafah, N.; Ni, J. Finite Element Analysis of Cushioned Diabetic Footwear Using Ethylene Vinyl Acetate Polymer. *Polymers* **2021**, *13*, 2261. [CrossRef]
87. Akrami, M.; Qian, Z.; Zou, Z.; Howard, D.; Nester, C.J.; Ren, L. Subject-specific finite element modelling of the human foot complex during walking: Sensitivity analysis of material properties, boundary and loading conditions. *Biomech. Model Mechanobiol.* **2018**, *17*, 559–576. [CrossRef]
88. Wang, Y.; Li, Z.; Wong, D.W.; Cheng, C.K.; Zhang, M. Finite element analysis of biomechanical effects of total ankle arthroplasty on the foot. *J. Orthop. Translat.* **2017**, *12*, 55–65. [CrossRef] [PubMed]
89. Chen, W.M.; Lee, S.J.; Lee, P.V.S. Plantar pressure relief under the metatarsal heads: Therapeutic insole design using three-dimensional finite element model of the foot. *J. Biomech.* **2015**, *48*, 659–665. [CrossRef] [PubMed]

90. Budhabhatti, S.P.; Erdemir, A.; Petre, M.; Sferra, J.; Donley, B.; Cavanagh, P.R. Finite element modeling of the first ray of the foot: A tool for the design of interventions. *J. Biomech. Eng.* **2007**, *129*, 750–756. [CrossRef]
91. Mo, F.; Li, Y.; Li, J.; Zhou, S.; Yang, Z. A three-dimensional finite element foot-ankle model and its personalisation methods analysis. *Int. J. Mech. Sci.* **2022**, *219*, 107108. [CrossRef]

Disclaimer/Publisher’s Note: The statements, opinions and data contained in all publications are solely those of the individual author(s) and contributor(s) and not of MDPI and/or the editor(s). MDPI and/or the editor(s) disclaim responsibility for any injury to people or property resulting from any ideas, methods, instructions or products referred to in the content.

Article

The Design and Application of an Advanced System for the Diagnosis and Treatment of Flatfoot Based on Infrared Thermography and a Smart-Memory-Alloy-Reinforced Insole

Ali F. Abdulkareem ¹, Auns Q. Al-Neami ¹, Tariq J. Mohammed ² and Hayder R. Al-Omairi ^{3,4,*}

¹ Biomedical Engineering Department, College of Engineering, Al-Nahrain University, Baghdad 64040, Iraq; st.ali.f.abdulkareem@ced.nahrainuniv.edu.iq (A.F.A.); auns.q.hashim@nahrainuniv.edu.iq (A.Q.A.-N.)

² Alkarkh General Hospital, Alkarkh Health Directorate, Iraqi MOH, Baghdad 10011, Iraq; tariqaljupory@gmail.com

³ Department of Biomedical Engineering, University of Technology—Iraq, Baghdad 10066, Iraq

⁴ Applied Neurocognitive Psychology Lab, Carl von Ossietzky Universität Oldenburg, 26129 Oldenburg, Germany

* Correspondence: hayder.r.alomairi@uotechnology.edu.iq

Citation: Abdulkareem, A.F.; Al-Neami, A.Q.; Mohammed, T.J.; Al-Omairi, H.R. The Design and Application of an Advanced System for the Diagnosis and Treatment of Flatfoot Based on Infrared Thermography and a Smart-Memory-Alloy-Reinforced Insole. *Prosthesis* **2024**, *6*, 1491–1509. <https://doi.org/10.3390/prosthesis6060108>

Academic Editors: Arnab Chanda and Marco Ciccio

Received: 30 August 2024

Revised: 24 November 2024

Accepted: 26 November 2024

Published: 9 December 2024

Correction Statement: This article has been republished with a minor change. The change does not affect the scientific content of the article and further details are available within the backmatter of the website version of this article.



Copyright: © 2024 by the authors. Licensee MDPI, Basel, Switzerland. This article is an open access article distributed under the terms and conditions of the Creative Commons Attribution (CC BY) license (<https://creativecommons.org/licenses/by/4.0/>).

Abstract: Background: Flatfoot deformity is a common condition in children and teenagers that may increase the risk of knee, hip, and back pain. Most of the insoles suggested to treat flatfoot symptoms are not designed to adapt to foot temperature during walking, and they are either too soft to provide support or hard enough to be uncomfortable. **Purpose:** This study aims to develop an advanced solution to diagnose and treat flexible flatfoot (FFT) using infrared thermography measurements and a hybrid insole reinforced by nitinol (NiTiCu) smart-memory-alloy wires (SMAWs), this super-elastic alloy can return back to its pre-deformed shape when heated, which helps to reduce the local high-temperature points caused by the uneven pressure of FFT. This approach achieves a more uniform thermal distribution across the foot, which makes the hybrid insole more comfortable. **Methods:** The study involved 16 subjects, divided into two groups of eight flat-footed and eight normal. The procedure includes two parts, namely, designing a prototype insole with SMAW properties based on thermography measurement by using SolidWorks, and evaluating this design using Ansys. Second, a hybrid insole reinforced with SMAWs is customized for flatfoot subjects. The thermography measurement differences between the medial and lateral sides of the metatarsophalangeal line are compared for the normal and flatfoot groups before and after wearing the suggested design. **Results:** The results show that our approach safely diagnosed FFT and significantly improved the thermal distribution in FFT subjects by more than 80% after wearing the suggested design. A paired *t*-test reported significant (*p*-value > 0.001) thermal decreases in the high-temperature points after using the SMAW insole, which was closely approximated to the normal subjects. **Conclusions:** the SMAW-reinforced insole is comfortable and suitable for treating FFT deformity, and infrared thermography is an effective tool to evaluate FFT deformity.

Keywords: flatfoot; pes planus; insoles; and infrared thermography

1. Introduction

Flat feet, or pes planus, represent a prevalent foot deformity characterized by a depressed arch, thereby making the sole partially or completely in contact with the ground and causing the internal rotation of the tibia and femur, as well as an anterior pelvic tilt [1–3]. Flatfoot is a familiar bone deformity that can be diagnosed in childhood, as young as six years old [4]. This deformity is associated with global health concerns, such as lower back pain [5,6]. Also, it affects the kinematics and kinetics of the lower extremities, ground reaction forces, muscle movement, and overall gait, which have been related to various clinical measures, including symptoms (with a focus on pain in particular), radiography,

and quality of life. Typically, flat feet distort the normal gait and usually require therapy to correct them; in severe cases, where the pain becomes unbearable, surgery may be required [7–10]. The shoe, barefoot, and insole groups were significantly different in the kinematics of lower limb joints, as Kulcu et al. found, evaluating immediate changes in gait with the use of bilateral silicone insoles and hypothesizing that silicone insoles would have improved joint kinematics and kinetics [11–13]. Traditional insoles designed to treat flatfoot symptoms often fall short, especially for children. Many conventional options are either too soft, providing inadequate arch support, or too rigid, causing discomfort and restricting natural foot movement. These shortcomings can lead to persistent foot pain and discomfort, especially during activities that require prolonged standing or walking. As a result, children may be less inclined to engage in physical activity, further aggravating their condition. This highlights the need for innovative solutions such as our hybrid insole reinforced with a nitinol smart memory alloy (SMA). By combining comfort with the necessary structural support, our approach aims to effectively mitigate the challenges associated with flatfoot and provide a more suitable option for young patients. Thus, with most traditional insoles, including customized insoles, there are still shortcomings that need to be optimized [13–17]. The majority of flatfoot patients can also experience relief from their symptoms and a delay in the disease's progression when using traditional orthopedic insoles. However, there are still restrictions: while most sarapus exhibit some consistency as a result of the arch collapsing, there are still significant variations in the distribution of plantar pressure amongst sarapus. Orthopedic insoles may even harm lower limbs or exacerbate foot deformities if they are not able to properly fit the wearer's unique foot characteristics [18]. Flat feet can be classified as either flexible or rigid arches, which may or may not reform in non-weight-bearing postures [5]. Flexible flatfoot (FFT) is the most common posture deformity among children [18]. The arch of the FFT subjects appears normal during sitting and toeing, but would collapse while standing, e.g., in the case of weight bearing. However, the arch remains flat in the rigid flatfoot position despite the foot having repositioned [19,20]. Partial or complete collapse of the medial longitudinal arch (MLA) of the foot, together with the following three-dimensional foot deformities: eversion of the hindfoot, adduction, and supination of the forefoot; lateral subluxation of the navicular; and valgus deformity of the heel, are postural deformities associated with flatfoot [3].

Since pediatric flatfoot usually first appears in childhood and can last into adulthood, early identification is crucial. Pediatric patients' formerly supple feet will eventually become more rigid, and it is thought to induce foot tiredness and pain. This could happen in one's early adolescent or early adult years. The hindfoot will unavoidably undergo adaptive modifications that affect how it interacts with the forefoot. As the calcaneus shifts into the valgus and the hindfoot everts, the forefoot must be supinated to maintain plantigrade plantation. There is a greater chance of a gastrocnemius–soleus contracture, because the Achilles tendon shifts laterally with the calcaneus and the axis of stress on the subtalar joint shifts. Rigidity rises as a result of these structural alterations, making therapy more difficult [21–23]. Researchers discovered that the rate of anterior knee discomfort and intermittent back pain was almost twice as high in teenage patients with moderate to severe flatfoot [24].

Currently, most flatfoot assessments focus on the medial longitudinal arch (MLA), using common techniques including traditional arch height, navicular drop [24], footprint index [1,25], and radiographs [26]. However, the arch height can be calculated from the differences between the ground and the highest point of the soft tissue on the medial arch's margin [27]. The navicular drop test has a moderate to good intra-reproducibility of measurement and was originally described as a way to characterize the height change in the navicular bone under weight bearing and non-weight bearing conditions [28]. The footprint index classification is a popular technique that has historically been carried out using an ink-type instrument [29]. Recently, the plantar pressure system or the planter scanning system has been used to measure and determine the footprint [30,31]. Based on X-rays,

researchers have employed the arch index to identify flatfoots; nevertheless, determining the arch type is expensive and time-consuming and also requires a high dose to complete the test, but it is a reliable process [3]. Even though the X-ray test is reliable, the human foot is a complex structure with an intricate skeletal framework (bones) and diverse tissue components (soft tissue). From that perspective, functional and anatomical diagnostics are required at the same time, and due to this complex foot structure, no validated technique can accurately assess the functional and anatomical capabilities of the foot [32]. Some of the techniques used inertial measurement units (IMUs) for walking analysis, because IMUs were developed recently in the medical field, utilized especially in the analysis of movement [33], for example, foot clearance [34].

Modern methods of diagnosing flatfoot require a combination of functional and anatomical diagnostics. For example, infrared thermography has been suggested as a tool to evaluate the anatomical and functional condition of the human foot, such as in cases of Platypodia [32,35]. The objectives of this study are, first, to use infrared thermography to determine the thermal distribution on the medial and lateral sides of the metatarsophalangeal line (MTPL) of the normal subjects and FFT clinically diagnosed subjects to confirm the efficiency of these measurements. Second, to design and test an interactive hybrid insole to treat flatfoot symptoms in children from six to eighteen years old, aiming for final treatment in the future. These insoles incorporated advanced materials of nitinol smart memory alloy (SMA) aimed at mitigating flatfoot deformities in the future, alleviating pain, and enhancing comfort. However, traditional insoles were found to be ineffective in reducing pain, especially in children. In contrast, the hybrid insole with SMA was more comfortable than the traditional insole without SMA. We evaluated the performance of our suggested approach on the empirical data and compared the thermal distribution on the medial and lateral sides of MTPL of the FFT subjects before and after wearing the NiTiCu reinforced insole with normal subjects. The study involved eight clinically diagnosed flatfoot subjects and eight normal subjects, with data used to assess the quantitative and qualitative aspects of our suggested design and application. Statistical analysis, including a paired *t*-test with effect size (Cohen's *D*), was performed after and before wearing the hybrid insole to follow up on the significant differences in the performance of our suggested design and application.

2. Materials and Method

2.1. Subjects

Sixteen subjects participated in our study, divided into two groups (eight normal subjects and eight FFT subjects). The FFT subjects are clinically diagnosed by physical examination [36–38]. The physical examination was used to analyze the foot mechanism of the FFT subjects compared to the normal subjects. The examination was performed during walking; the examiner asked the subject about the source or location of the pain, and assessed the alignment of the foot and ankle, which helps in evaluating the strength of the surrounding ligaments and tendons [38]. Normal subjects had no history of postural stability issues, gait abnormalities, or cognitive impairment in the past 12 months. The IRB of Al-Nahrain University, College of Engineering, Biomedical Engineering Department approved the study protocol under the code (N. BME/24/25/1). Subjects were excluded if they had sustained lower extremity injuries within six months before participation and still experienced pain, had undergone surgery on their hip, knee, or ankle joints, or could not walk or stand due to pain in the lower extremities or back. All of the subjects' information is shown in Table 1.

The age of the subjects who participated in this study was (7–16) years old, which is parallel with the recent studies, such as (7–15) years old [38], and (7–14) years old [39]. Most studies chose a subject of an average age of around 11 years old, similar to our study.

Table 1. Subjects' information.

Subjects' Information	Normal Foot (No. = 8)		FFT (No. = 8)	
	Mean	±Std	Mean	±Std
Age (year)	12.5	1.7728	11.625	3.1139
Weight (kg)	49.75	13.26	48.237	18.722
Height (cm)	155.6	8.484	146.5	15.042
Average shoe size (Euro)	39.25	2.1876	37.125	3.907

2.2. Equipment and Materials

Several pieces of equipment and materials have been used in this study, including:

2.2.1. Processing Computer

The computer used for software design is an HP desktop with an Intel® Core™ (Santa Clara, CA, USA) i7-12700 processor (2.1 GHz up to 4.9 GHz, 25 MB L3 cache, 12 cores, 20 threads), 1 TB hard memory, 64 GB DDR5-3600 MHz RAM (2 × 32 GB), and a NVIDIA® GeForce RTX™ (3050 (Santa Clara, CA, USA) 4 GB GDDR6 dedicated) graphics card.

2.2.2. Nitinol Smart-Memory-Alloy Wires (SMAWs)

In this study, we employed 10 m nitinol smart-memory-alloy wires (NiTiCu-20-5 (SMAWs) AF = 20 °C (Ø = 0.5 mm, Heiko Engelhardt company, Offenburg, Germany) due to their biocompatibility, shape-memory effect, and super-elasticity [40]. The wires used in this study have the following properties, as specified in the manufactured guide: reshaped wire with a transformation temperature of 20 °C and a diameter of 0.5 mm. When cooled to temperatures of approximately 10 °C, the material becomes plastically deformable. Conversely, when heated to temperatures of approximately 20 °C, the material undergoes a phase transformation, whereby it “remembers” its original shape. This material is designated as a shape-memory alloy (SMA) due to its unique ability to undergo shape changes when subjected to specific temperature conditions. At normal ambient temperatures (approximately 20 °C), the alloy exhibits super-elastic behavior. The alloy's copper content (NiTiCu) contributes to narrow hysteresis compared to binary nickel titanium. The wire has a “straight” embossed shape. The material is readily deformable at temperatures below that of a typical room. It can also be easily manipulated in this condition. It is possible to extend the wire by up to 8% without causing any damage. Upon heating above the conversion temperature (for example, by the application of warm water or an electric current), the material returns to its embossed shape and generates significant forces.

2.2.3. Evaluation of the NiTiCu Wires Insole

Testing the nitinol wires and Ethylene Vinyl Acetate (EVA) insole matrix: This step was important to obtain estimated knowledge about the forces of the insole and to obtain information important for the Ansys simulation. Several tests were carried out for both materials as follows: Tensile tests for nitinol wires were performed, while the other material properties were considered from the manufacturer labels. A tensile test, compressibility test, hardness test, and thermal conductivity test for the EVA material were performed, while the other material properties were considered from the manufacturer labels. A tensile test was carried out for both NiTiCu wires and EVA materials; for more details, see Supplementary Materials Figures S1 (a and b for NiTiCu wires) and S2 (a and b for EVA sheet).

The hardness test was carried out manually using a shore harness tester (TH200). For more details, see Supplementary Materials Table S1 and the chart curve in Figure S3, which show the results of an electrical compression machine. The thermal conductivity results are shown in Supplementary Material Table S2.

2.2.4. Polymer Plates from Ethylene Vinyl Acetate (EVA)

The EVA used in this study was evaluated based on several tests, such as the tensile test, compressibility test, hardness test, and thermal conductivity test, to ensure no mechanical errors occur during the customization of our suggested insole. The material properties are shown in Supplementary Materials Table S3.

2.2.5. Infrared Thermography Detector

The infrared thermography detector used in this study was from the sensor technology model (iHA417W) with a detecting range of 8–14 microns. The detector properties are $\leq 25.4 \times 25.4 \times 30.3$ with a 9.1 mm lens, a typical NETD of <40 mk, a detect distance of 0.5 m/5 m; it is lightweight, at 32.2 ± 3 g, and has a superior temperature measurement accuracy of $\leq \pm 0.5$ °C. This detector is registered according to ROHS/REACH standards.

2.2.6. Silicone Rubber

We used a silicone rubber insole with a Poisson's ratio of 0.49 and a Young's modulus 10^4 N/m² as an insole matrix to fix nitinol wire inside it for the SolidWorks premium 2021 SP3 and Ansys 2023 (v231) simulation softwares.

2.3. Experimental Procedure and Study Design

As shown in Figure 1, the first step involved measuring subject characteristics (e.g., weight, shoe size, etc.). Then, we measured the thermal distribution on the medial and lateral sides of both normal and FFT subjects using an IR detector. Please note that a consultant physician uses a physical examination of the foot and on whom it is performed to analyze the foot mechanics. Additionally, we must mention that if the pain is severe, doctors may recommend imaging tests, such as X-rays, CT scans, MRIs, or ultrasounds, to detect the nature and degree of deformity, but this is not the case for the flexible flatfooted subjects who participated in this study. Subjects with normal feet and FFT were asked to walk for 10 min and then stand on one foot for 40 s to ensure a good heat transfer between the insole and feet; in the meantime, their feet were thermally photographed using an IR detector. From these thermal measurements, we calculate the average temperature on the medial and lateral sides of MTPL for each flatfoot subject. Based on these calculations, a foot trace for an individual flatfooted subject was designed with twenty NiTiCu wires spread based on the thermal footprint and inserted into the traces using SolidWorks premium 2021 SP3 software. These designs were imported into Ansys 2023 (v231) software to simulate the effect of the wires, applying a hypothetical force of 500 newtons to represent the subject weight of a 14-year-old child [41] to evaluate insole enhancement. After evaluating the simulation design, we customized the hybrid NiTiCu insole with 12 NiTiCu wires, inserted the insole in their shoe, and asked the subjects with FFT to wear their shoe with the NiTiCu hybrid insole on one foot, walk for 10 min, and repeat the one-foot stand for thermal imaging and temperature measures to compare the average temperature on the medial and lateral sides of MTPL of the foot before and after processing. Size differences between the medial and lateral sides of the foot were evaluated by positioning the feet on a glass board, tracing them, and manually measuring differences. The results indicated that the lateral side of the metatarsophalangeal line is about 10% larger than the medial side. Comfortable foot positioning, while seated, was found to be at an average angle of 25° from the vertical line parallel to the foot.

2.4. Software System Design

In order to minimize temperature variation, the subject places his or her foot in the box while continuous infrared heat monitoring is activated. The person then immediately takes off their shoe after standing on one foot, and a picture slide is taken. If any delay occurs in the thermography procedure, the entire procedure is repeated from the start.

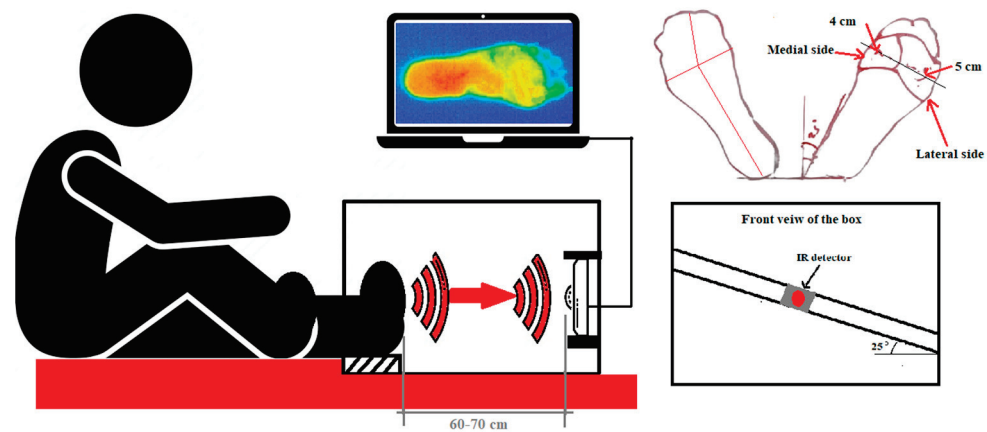


Figure 1. Experimental procedure and study design.

We used SolidWorks Premium 2021 SP3 [30,42,43] and Ansys Workbench 2023 (v231) software to design a custom insole for each subject and initial results evaluation, which have been widely used in recent studies [44,45]. SolidWorks Premium 2021 SP3.0 release software was used to import the foot model of the normal subject to the SolidWorks workbench, then draw a cube larger than that foot model and insert the model in it. By removing the foot from the cube, a foot trace was confirmed, as shown in Figure 2. The extra surrounding area of the cube was removed around the foot trace, and an insole model was confirmed. Afterwards, 20 wires shaped as normal arch, 16 cm in length, were inserted into the model. Finally, the insole model was finished and saved using the IGS file type, so that it would be accepted by the Ansys software.

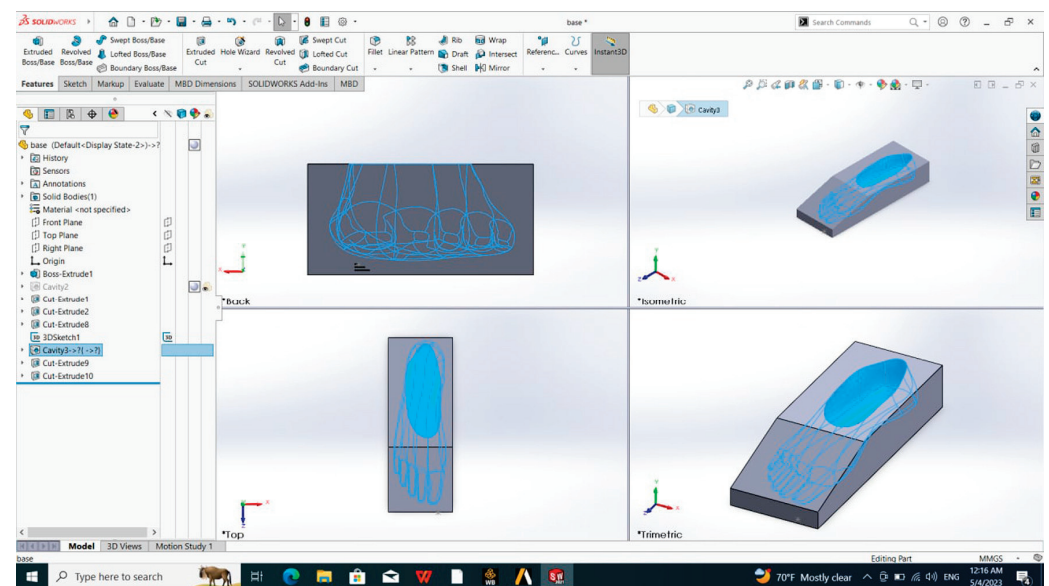


Figure 2. SolidWorks insole trace.

Ansys “release 2023R1 Inc\231” software simulation was carried out by importing the insole model created by SolidWorks in (IGS form) to the Ansys working bench. All of the Ansys analysis is based on the mechanical properties of the EVA material and nitinol wires. It is assumed that the average weight of the subjects in this study was around 50.9 kg, which corresponds to a force of approximately 500 Newton, as they were between the ages of 7 and 18 years old [41]. The wires are assumed to exert a force of 5 newtons at the start of the simulation and a maximum force of 20 newtons at the end of the simulation According to the 0.5 mm diameter NiTiCu force property supplied by the manufacturer for 10 m: If it is heated over the conversion temperature (e.g., in warm water or by an electric current), it

returns to the embossed shape and develops considerable forces. It can heat up to approx. 50 °C at a diameter of 0.5 mm and a weight of 6.5 kg vertically. This corresponds to a force of 65 N, i.e., for 16 cm of wire length used in this simulation, a maximum of 1 N will be assumed for each reshaped wire (i.e., 20 N for 20 wire) in the center of the wires, decaying to zero at both ends of the wires. The forces of the wire decay one Newton per centimeter to the lateral side of the wires, starting from the center. The simulation consists of five steps, from zero force to 20 newtons for 20 wires, to mimic heat transfer from the foot to the proposed insole. It must be mentioned that some references mentioned another NiTi SMA exerting the maximum output force of the SMA micro-coil, which was approximately 720 mN at 105 °C [40,46].

2.5. Hardware System Design

In this study, we modified the traditional EVA insole by inserting 12 of our suggested NiTiCu wires into the medial side of the insole. Each wire was the same length, used to reinforce the insole for the proposed design. Finally, the insole will be glued using silicone to close the incision opening. The NiTiCu wires were reshaped using a graphite template carved by a CNC carving machine. The design of the graphite template was established using SolidWorks, as shown in Figure 3 by tracing a normal human subject's foot medial arch. Then, the template containing 12 NiTiCu wires was heated in an electric oven at 450 °C for 10 min, as recommended by the manufacturer. Figures 4–6 below show the template and the reshaped wires.

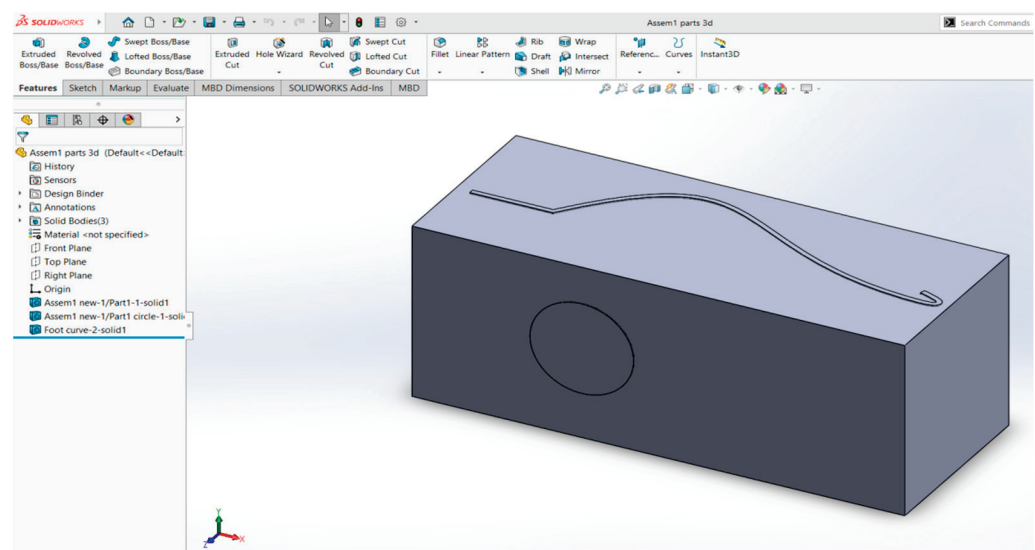


Figure 3. SolidWorks template design.



Figure 4. CNC-carved graphite template with NiTiCu wires fixed inside it, so that it can reshape and take the medial arch foot shape.



Figure 5. Reshaped NiTiCu SMA wires.

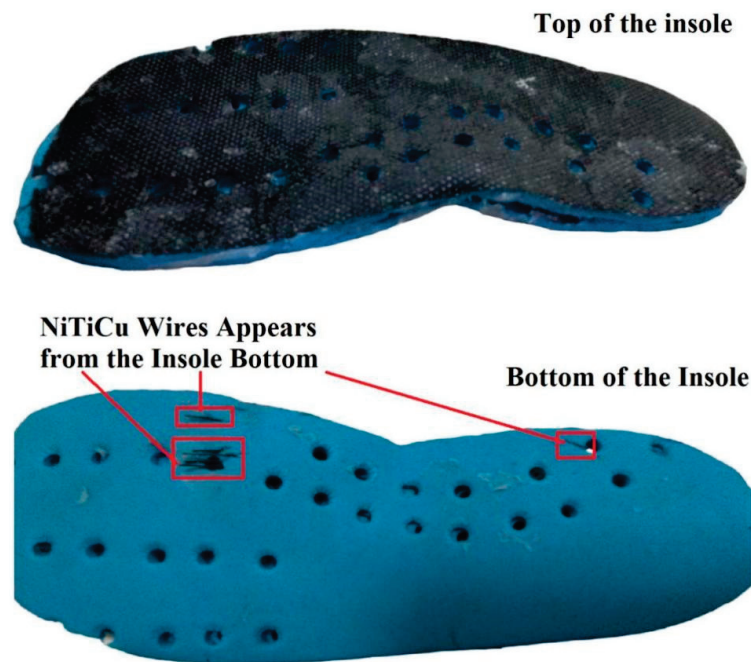


Figure 6. Manufactured insole reinforced by NiTiCu SMA wires.

2.6. SMA Placement Design

Twelve NiTiCu wires of 12 cm length each were inserted in the incision made in the medial side of the EVA insole plate along its length from the center of the insole, spread transversely 5 mm from its medial rim to about 12 mm, i.e., 1 mm between each two adjacent wires. Figure 6 shows the final manufactured NiTiCu SMA wire-reinforced insole used for testing. This design was established to mimic normal foot medial arch action in normal human subjects, so that the pressure forces were redistributed, normalizing the pressure forces on the soles of flatfeet subjects.

2.7. Data Analysis

We use an IR detector to measure the average temperature across the medial and lateral sides of the metatarsophalangeal line for subjects with a normal foot as the first group, subjects with flat feet before wearing the proposed insole as the second group, and subjects with flat feet after wearing the proposed insole as the third group. Then, the difference between the average temperature on the medial and lateral sides is calculated for each subject by subtraction. The results in this investigation targeted only a limited population of flatfoot patients, children with flexible flatfoot without any other complications, so all thermal measurements from all subjects were considered and no results were ignored. After calculating the differences in temperature for all subjects, an average temperature difference for each group was calculated. Finally, a qualitative comparison was made between the thermal measurements of normal subjects and FFT subjects before and after wearing the proposed insole.

Statistically, we applied a paired *t*-test with a bootstrap sample size of $N = 1000$ and calculated the effect size (Cohen's *D*) to investigate the significant thermal differences across

MTPL between normal and flatfoot subjects and between flatfoot subjects before and after wearing the hybrid proposed insole.

Every participant was asked to rate their feelings after using the hybrid insole from 1 to 10, in comparison to how they felt wearing conventional flatfoot therapy insoles and how they felt when they wore no insole at all.

3. Results

3.1. Qualitative Comparison of Normal and Flatfoot Subjects Before and After Testing

In this section, we briefly provide a qualitative comparison of the average temperature across the medial and lateral sides of MTPL of the foot between the normal subjects, and the FFT subjects before and after wearing the NiTiCu insole design. The experimental results are based on two components averaged across subjects: the IR thermographic results and the software results. The results showed that there was an average temperature difference between the medial and lateral sides of the metatarsophalangeal line of 0.016875°C for normal subjects, 1.07125°C for flatfooted children, and 0.2725°C after wearing the hybrid insole, which is closer to normal subjects. The data obtained from the analysis of thermal distribution differences were imported into IBM SPSS Bootstrapping 22 version software, which was then used to calculate the results of the t -test, Cohen's D , and bootstrap. The thermographic results demonstrated a significant (p -value < 0.001 , Cohen's $D = 3.827$) decrease in high-temperature points for the flatfoot subjects after wearing our suggested NiTiCu insole in comparison with the flatfoot subjects' group before wearing the NiTiCu insole. All comparisons are still significant (p -value < 0.001) after the bootstrap test with an $n = 1000$ sample. However, there are significant differences between the normal subjects and FFT subjects before wearing the NiTiCu-reinforced insole, but insignificant differences were reported after wearing the NiTiCu insole, as shown in Figure 7.

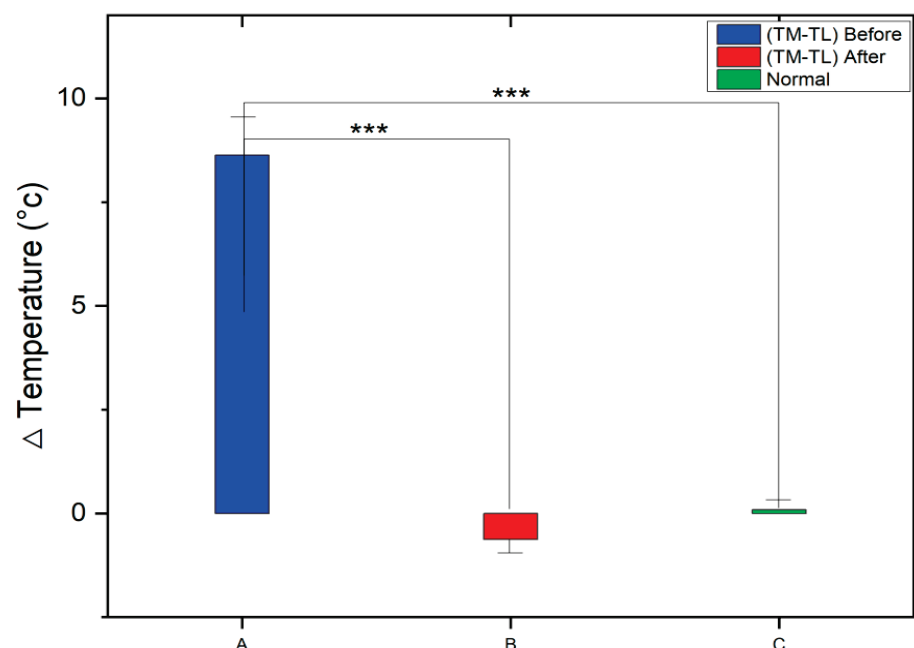


Figure 7. The subjects' results of the temperature differences between the medial and lateral lines. (A) The blue bar represents the flatfoot group before wearing the NiTiCu insole; (B) the red bar represents the flatfoot group after wearing the hybrid insole; and (C) the green bar represents the normal subjects. Three stars (***) indicate a significance level of p -value < 0.001 , which was reported by comparing the flatfoot group before and after wearing the NiTiCu insole, and p -value < 0.001 when comparing the flatfoot group without the NiTiCu insole with normal subjects.

The results demonstrated that the highest difference in average temperature between the medial and lateral lines across the MTPL was 1.31°C before wearing the NiTiCu

insole, decreasing to 0.32 °C after wearing the NiTiCu insole, which is an improvement ratio of 14:1. However, the lowest difference in average temperature between the medial and lateral lines across MTPL was 1.0 °C before wearing the NiTiCu insole, decreasing to 0.75 °C after wearing the NiTiCu insole, which is an improvement ratio of 4:1. The comparison of the normal and subjects with FFT is shown in Table 2 below. There is a significant difference between the normal and FFT subjects before wearing the NiTiCu insole, but there is an insignificant difference between them after wearing the NiTiCu insole, as shown in Tables 2 and 3. In addition, Table 3 shows the effect of the hybrid insole in improving thermal distribution on flatfoot subjects across MTPL to be closer to that of normal subjects, by interactively supporting the medial arch of the foot. Through long-term use, this technique aims to change the bone and muscle structure of the foot in a way that reshapes it closer to the natural foot.

Table 2. The temperature distribution differences on both sides of the metatarsophalangeal line for all eight normal foot subjects for each subject's left and right foot; it also includes each subject's data (age, gender, weight, length, and foot size).

S. No.	Age, Years/Gender	Weight, kg/Length, cm	Shoe Size, EU	Temperature Medial T_M – Lateral T_L , °C for Both R.F./L.F.
SN1	11/Male	55/159	40	L5 – L3 = 33.41 – 33.23 = 0.18 L5 – L6 = 33.66 – 33.56 = 0.06
SN2	14/Male	45/160	42	L5 – L3 = 33.73 – 33.66 = 0.07 L3 – L5 = 33.35 – 33.16 = 0.19
SN3	12/Male	42/145	40	L5 – L3 = 32.1 – 31.93 = 0.17 L3 – L5 = 31.91 – 32.04 = –0.13
SN4	9/Male	53/143	39	L5 – L3 = 31.66 – 31.54 = 0.12 L3 – L5 = 30.48 – 30.06 = –0.12
SN5	14/Female	40/155	38	L5 – L3 = 37.16 – 37.29 = –0.13 L3 – L5 = 31.65 – 31.6 = 0.05
SN6	13/Male	78/169	42	L2 – L1 = 33.23 – 33.29 = –0.06 L2 – L1 = 33.23 – 33.29 = –0.06
SN7	14/Male	50/154	38	L5 – L3 = 29.73 – 29.6 = 0.13 L3 – L5 = 29.41 – 29.73 = –0.32
SN8	13/Female	35/160	37	L5 – L3 = 28.23 – 28.30 = –0.07 L3 – L5 = 28.85 – 28.66 = 0.19
Average Temperature, °C				0.016875 °C

An illustrative example (see Figure 8) was used to demonstrate the average temperature distribution on the medial and lateral sides of MTPL of a FFT subject before and after wearing the NiTiCu insole, as well as for a normal subject, showing how the temperature became approximately equal between the medial and lateral sides of MTPL after wearing the NiTiCu insole. The figure also shows the thermal distribution of a normal subject, demonstrating that the average temperature on the medial line of MTPL is approximately equal compared to the average temperature on the lateral line of MTPL on the left and right foot.

After using our proposed hybrid insole, the FFT subjects rated its comfort on a scale of 1 to 10 based on a questionnaire administered by the examiner. Their responses are shown in Table 4.

Table 3. The temperature distribution differences on both sides of the metatarsophalangeal line before and after wearing the NiTiCu wire-reinforced EVA insole for all eight flatfoot child subjects; it also includes each subject's data (age, gender, weight, length, and foot size).

S. No.	Age, Years/Gender	Weight, kg/Length, cm	Shoe Size, EU	Temperature Medial TM – Lateral TL Before Wearing Insole, °C	Temperature Medial TM – Lateral TL After Wearing Insole, °C
S1	9/Female	39/133	35	$L2M30.54 - L1L29.23 = 1.31$	$L2M30.41 - L1L30.73 = -0.32$
S2	11/Male	27.3/135	34	$L2M27.1 - L1L28.29 = 1.19$	$L1L28.29 - L2M29.6 = -0.31$
S3	7/Male	24.6/126	31	$L5M27.16 - L3L25.91 = 1.25$	$L5M26.48 - L3L27.48 = -1$
S4	15/Female	45/148	36	$L4M20.23 - L2L19.23 = 1$	$L3M22.29 - L5L22.16 = 0.13$
S5	10/Male	71/160	39	$L5M27.41 - L3L26.16 = 1.25$	$L5M25.35 - L3L25.6 = -0.25$
S6	14/Female	45/150	38	$L3M27.04 - L5L26.16 = 0.88$	$L3M27.54 - L5L27.54 = 0$
S7	16/Male	75/172	43	$L4M28.85 - L2L27.85 = 1$	$L4M28.23 - L2L28.96 = -0.75$
S8	11/Male	59/148	41	$L4M31.73 - L5L31.04 = 0.69$	$L3M26.98 - L5L26.66 = 0.32$
Average Temperatures				1.07125	0.28375

Table 4. Rate of FFT subjects' comfortability to the hybrid insole.

S. No.	Age, Years/Gender	Weight, kg/Length, cm	Shoe Size, EU	Temperature Medial TM – Lateral TL After Wearing Insole, °C	Satisfaction Rate
S1	9/Female	39/133	35	$L2M30.41 - L1L30.73 = -0.32$	8
S2	11/Male	27.3/135	34	$L1L28.29 - L2M29.6 = -0.31$	9
S3	7/Male	24.6/126	31	$L5M26.48 - L3L27.48 = -1$	5
S4	15/Female	45/148	36	$L3M22.29 - L5L22.16 = 0.13$	10
S5	10/Male	71/160	39	$L5M25.35 - L3L25.6 = -0.25$	9
S6	14/Female	45/150	38	$L3M27.54 - L5L27.54 = 0$	10
S7	16/Male	75/172	43	$L4M28.23 - L2L28.96 = -0.75$	5
S8	11/Male	59/148	41	$L3M26.98 - L5L26.66 = 0.32$	8

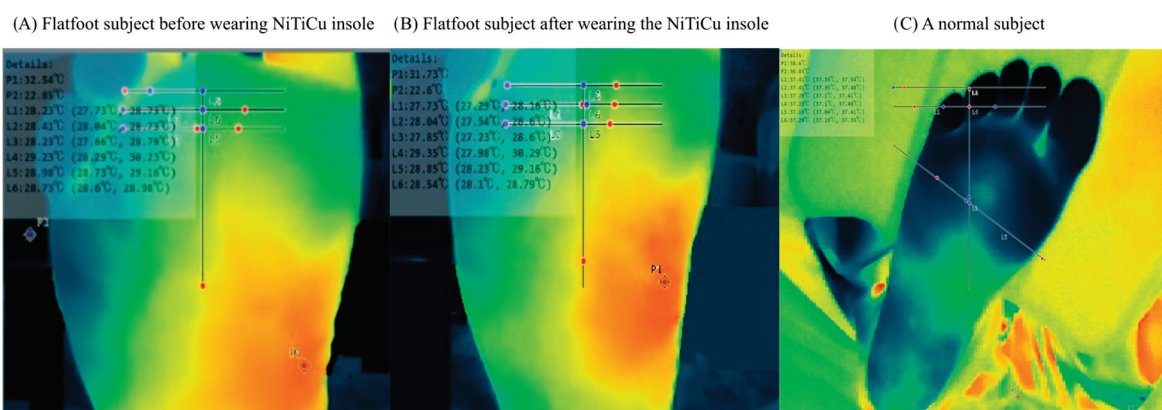


Figure 8. The thermal distribution of a (A) FFT subject before wearing the NiTiCu insole, the average temperature difference between the medial and lateral sides is 1.25 °C; (B) the same flatfoot subject after wearing the NiTiCu insole, the temperature difference between the medial and lateral sides is 0.09 °C; and (C) the temperature difference of a normal subject between the medial and lateral sides is 0.06 °C.

3.2. SolidWorks Results

We used the SolidWorks premium 2021 SP3 to design the suggested insole with and without NiTiCu wires to investigate the effect of the NiTiCu wires on the pressure distribution of the flatfoot subjects. Figure 9 is an example of a flatfoot subject with a weight of 59 kg and a shoe size of 41.

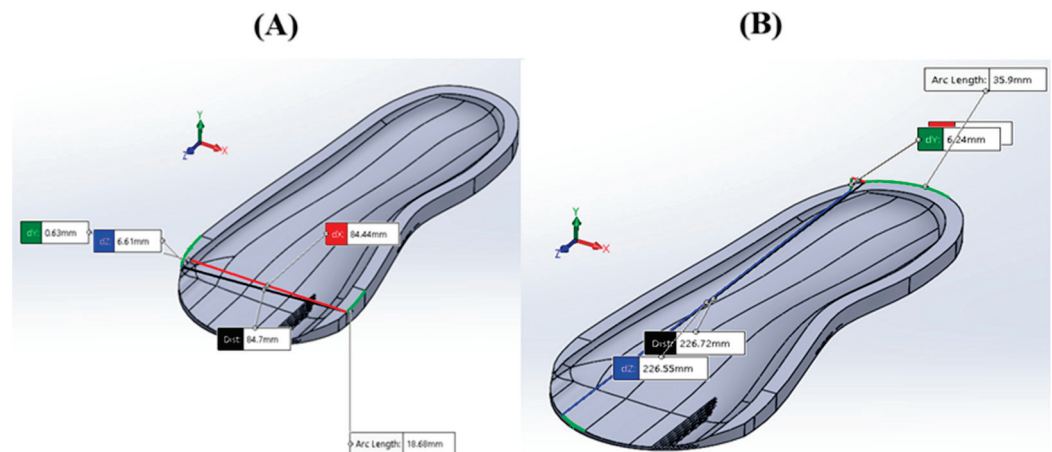


Figure 9. (A) Side and (B) top view of the imaginary insole.

3.3. Ansys Simulation Results

By using Ansys simulation, the results show that there is a suitable effect on the foot, with a total maximum vertically upward deformation of 1.3078 mm in the center of the medial arch of the foot, as shown in Figure 10a,b, and Von-mises equivalent stress of 16.383 MPa, as shown in Figure 11, which gave an estimated value of the efficiency of using SMA nitinol wires in reinforcing the traditional insole.

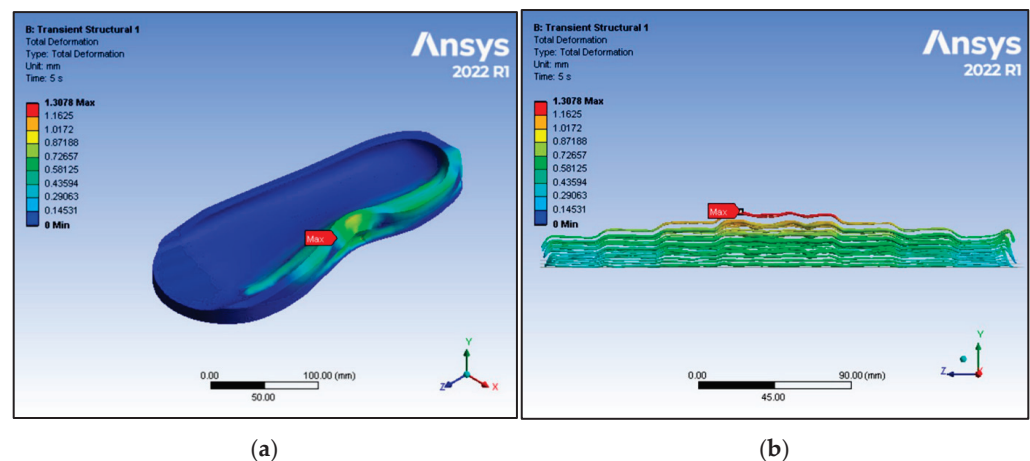


Figure 10. (a,b) show the total upward vertical deformation using Ansys software (max: 1.3078 mm).

To clarify the efficiency in comparison with the traditional insole, an imaginary traditional insole (not reinforced using nitinol SMA wires) was used in the Ansys simulation under the same conditions, and the results show that there was 0.016646 MPa downward equivalent Von-mises stress and a downward deformation for the insole (i.e., the insole compressed under body weight) of 0.061132 mm, as shown in Figures 12 and 13 below.

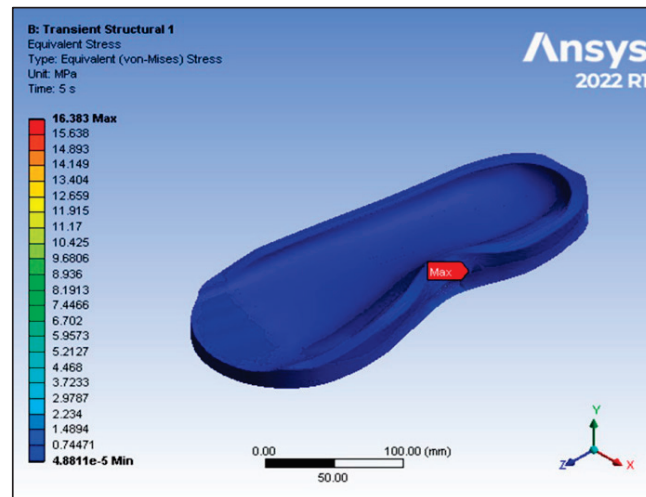


Figure 11. Equivalent upward vertical Von-mises stress (max: 16.383 MPa).

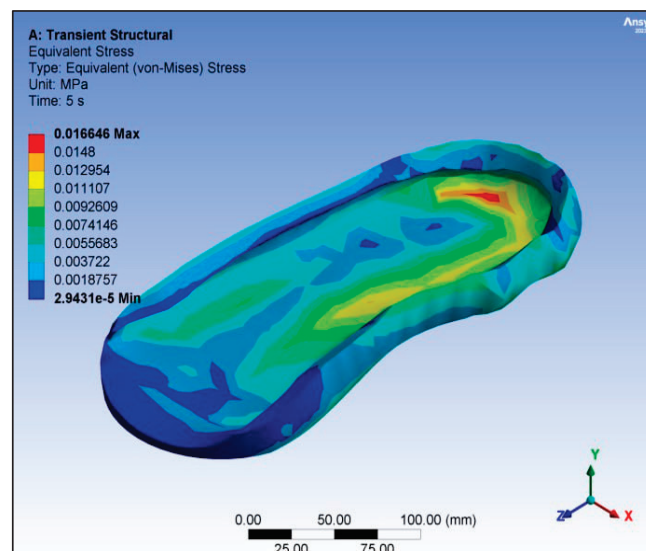


Figure 12. Equivalent downward vertical Von-mises stress (max: 0.016646 MPa).

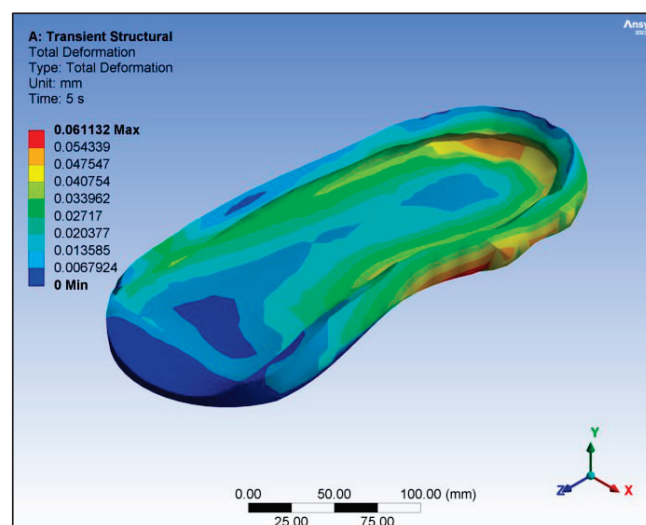


Figure 13. Total downward vertical deformation (max: −0.061132 mm).

4. Discussion

Flatfoot deformity is a widespread condition impacting a lot of people, especially in their childhood. Primarily, flat feet disrupt the natural reflexes of the sole, which impacts posture and gait [47]. Both posture and gait are crucial for balance and perception. When natural posture is affected, it limits the ability to maintain an upright stance, while an altered gait leads to unstable movements. If flat feet are not treated promptly, various complications can arise, including painful stress, muscle weakness, and significant functional disabilities, all of which can severely impact an individual's quality of life [32].

The aim of this study is to develop a model to detect FFT deformity based on thermal technology (IR imaging) by measuring the temperature differences between the medial and lateral sides of the MTPL of the foot, who are then clinically diagnosed by physical examination as flatfooted people and compared with those of normal people. Based on these measurements, we designed a simulation prototype of a hybrid insole to treat this deformity using SolidWorks, and tested this design using Ansys software. According to these simulation results, a hybrid insole reinforced with NiTiCu smart-memory-alloy wires to improve the thermal distribution on the medial and lateral sides of the MTPL of the foot was designed. The innovative design of the SMA-reinforced insoles not only improves comfort and heat distribution for children with FFT, but also offers a personalized treatment solution that can adapt to individual foot dynamics, potentially leading to improved clinical outcomes. By effectively addressing localized high-temperature points and redistributing weight, this approach can significantly reduce associated pain and discomfort, enabling improved mobility and overall quality of life for children. In addition, the integration of infrared thermography as a diagnostic tool enhances the ability to monitor treatment progress and make data-driven decisions, which could ultimately streamline clinical workflows and improve patient management strategies. The results show that our proposed approach improves the thermal balance on the medial and lateral sides and provides a more comfortable insole for the FFT subjects. Figure 7 shows a significant reduction in the high-temperature points on the medial or lateral side after wearing our proposed insole, and there are insignificant differences between the normal subjects and the FFT subjects after treatment.

In this study, nitinol SMA wires formed in the shape of a normal foot medial arch were used to reinforce the insole to mimic normal foot medial arch action in normal human subjects in an interactive pattern relative to foot temperature change during normal activity, so that the pressure forces could be redistributed to normalize the pressure forces on the soles of flatfeet subjects.

In contrast to A. Urakov, D. Nikityuk, A. Kasatkin, and I. Lukoyanov's study, we found that the average temperature differences across MTPL was 0 °C and 0.3 °C larger on the medial side than lateral side [48], for normal subjects and flatfooted subjects, respectively; our approximation finds that the average of the temperature differences across MTPL was 0.016875 °C and 1.07125 °C larger in the medial side than lateral side, for normal subjects and flatfooted subjects, respectively [34]. There could be two possible explanations for the differences in findings between their study and ours. First, they employed an uncontrolled imaging design in which the patient is positioned 1.5 m from the infrared detector without a shield to protect them from ambient infrared radiation. The tiny sample size (only five normal and five flatfooted samples were examined) may be the second explanation. Important data loss could result from either of these causes. The size of the data set was the main factor affecting the overall performance. This is because the images collected for this research are quite small. However, we used a bootstrap test with $N = 1000$ to increase the sample size. After the bootstrap test, the differences were still significant. From the illustrative example in Figure 8, we can clearly see how the high-temperature point on the medial side decreased to be approximately equal to the temperature on the lateral and medial sides and near that of the normal subject, which indicates that our proposed approach provides the best solution to treat the FFT subjects, and according to the survey, the hybrid insole reduced the pain. The SolidWorks insole design was very appropriate

and was close to the real insole shape with 3D measurements, making it suitable for Ansys simulation. The Ansys simulation results show a high deformation effect, which means high lifting forces will affect the patient's foot, making pressure distribution correction applicable, enough to achieve the purpose of the study and treat flatfoot deformity. The Ansys simulation results, which indicate that the forces exerted by the SMA wires can reach up to 20 Newtons, are clinically significant, as they demonstrate the insole's ability to provide adequate support to the medial longitudinal arch during weight-bearing activities, thereby improving stability and comfort for children with flexible flatfoot. In addition, the deformation patterns observed suggest an effective distribution of load across the foot, which is critical for reducing localized high-temperature areas and alleviating pain associated with flatfoot deformities. In a future work, a long-term follow-up of all subjects who participated in this study will be carried out, so that we can determine the effect of the proposed insole on reducing FFT deformity.

Furthermore, our approach offers a comprehensive, low-cost method for both verifying the clinical diagnosis of FFT using non-ionizing noninvasive IR thermography and immediately treating the symptoms of this deformity with an interactive hybrid insole that made use of nitinol SMAW characteristics. The primary constraint of this study is that, in order to obtain the necessary thermal image at the required position at MTPL, the process of thermal imaging for the foot needs to be more appropriately designed. Additionally, the manufacturing process of the hybrid insole takes a long time, because it is necessary to create a mold and use special software for designing customized insoles.

Our method of creating hybrid insoles typically costs between USD 30 and USD 40 for research purposes, which includes fees for materials, molds, and design. Because of the interactive insole's increased comfort and interactive pressure impact, it is considered inexpensive. This can be compared to alternative insole construction techniques, like 3D-printing insoles, which are considered a passive treatment intended to raise the medial midfoot's peak pressure and pressure-time integral, indicating support on the medial longitudinal arch, along with an offloading on the hindfoot and greater ankle dorsiflexion, costing roughly USD 22 [9,47].

On the other hand, a traditional insole is more cost-effective and could be adopted, but its support of the foot is imprecise. Plantar pressure redistribution insoles (PPRIs) are another type of insole, which are individually customized plantar pressure-based insoles that help users change the abnormally distributed pressure on the pelma. They are more adequate than traditional insoles, but they cost more, and they are still considered a passive treatment method [48,49].

One of the commonly used techniques for flatfoot diagnostics is radiographic imaging, or X-ray, but this technique is time-consuming, costly, and carries the risk of radiation exposure; furthermore, this technique does not provide a functional image of the foot [1,50,51]. Another widely used technique is the footprint index, usually using a podoscope, which is correlated with age, gender, and BMI. The indices under investigation are appropriate for identifying adult flatfoot, particularly Clarke's angle, which has a very high diagnostic accuracy for this population [52]. Given that radiography is rather costly and causes biohazards, and the footprint index is not recommended for children, neither of these techniques can offer an interactive functional anatomy diagnosis. However, our approach is cost-effective (it only requires an IR detector to confirm and follow-up the diagnosis for many patients) and provides a functional anatomical thermal image.

This study recommends more significant thermographic design procedures in the future, if possible. It would be significant if a researcher were to find a highly IR-transparent material that can carry the subject's weight, so that the subject stands on that material and is thermally imaged using an IR detector located under this material, i.e., a weight-bearing thermal image. If that is not possible, our approach could be modified to automatically detect the flatfoot deformity using image-processing software that would minimize the processing time as much as possible.

Future investigations should assess the long-term durability of the proposed insole and its sustained effect on the foot's structure and function. Additionally, future studies are required to compare our proposed approach with traditional techniques, such as biomechanical measurements, to evaluate their relative effectiveness.

The significance of the temperature differences between the medial and lateral sides of the foot lies in the clinical relevance of thermal distribution. In a normal foot, there is typically an equilibrium in temperature distribution, reflecting a balance in the load distribution across the foot. However, the high-temperature point is a source of pain in the feet. Moreover, in cases of FFT, the medial side often experiences increased load, leading to higher localized temperatures. These temperature variations are indicative of biomechanical imbalances. By comparing the thermal profiles of flatfoot and normal feet, we can assess the severity of deformity and monitor the effectiveness of interventions, such as the use of corrective insoles, in restoring a more balanced temperature distribution.

One limitation of our approach is that we did not compare our method with traditional biomechanical measurements or other established techniques for flatfoot diagnosis. Although our thermography-based technique is promising, further research is needed to validate its accuracy against these conventional methods.

In addition, while our insole design showed significant improvements in thermal distribution for flatfoot subjects, the long-term durability of the SMA-reinforced insole remains unexplored. Future studies should investigate how the prolonged use of this design affects foot structure and function over time.

In addition, we recommend the investigation of more advanced thermographic designs. For example, the development of a highly IR-transparent material that can support the subject's weight would allow for weight-bearing thermal imaging, providing a more realistic and direct measurement of thermal distribution under weight-bearing conditions. If such a material is not available, an alternative could be to design a foot fixation mechanism that minimizes thermal data loss and does not interfere with the natural foot temperature during imaging. This would ensure more accurate thermal data collection while maintaining accuracy.

5. Conclusions

The current study concludes that by improving thermal distribution on the flatfoot and significantly reducing high-temperature points, our approach provides a comprehensive and novel solution for the diagnosis and treatment of FFT. Using infrared thermography, we effectively measured temperature differences between the medial and lateral sides of the foot to confirm our diagnosis and evaluate treatment efficacy. The customized hybrid insole reinforced with NiTiCu smart-memory-alloy wires (SMAWs) showed significant improvements in comfort and functionality for the flatfoot subjects compared with the normal subjects.

Key Findings and Implications

Our findings suggest that this SMAW-reinforced insole can reduce localized high-temperature points caused by unequal pressure distribution and achieve a more uniform distribution of heat across the foot. This innovative approach not only addresses the immediate symptoms of FFT, but also has the potential to improve long-term outcomes by minimizing discomfort and improving overall foot health. By integrating advanced materials and thermographic technology, our research offers a promising pathway for future applications in the treatment of children's flat feet and highlights the need for personalized solutions in the management of this common condition. A limitation of our study is that our thermographic-based method was not compared with conventional biomechanical measurements or other established methods of flatfoot diagnosis, which necessitates further validation of our approach. In addition, although our SMA-reinforced insole showed significant improvements in thermal distribution, its long-term durability and effects on foot structure and function remain to be investigated. Future research should

also explore advanced thermographic designs, such as the development of a highly IR-transparent material for weight-bearing thermal imaging, or the implementation of a foot fixation mechanism that minimizes the loss of thermal data without altering the natural temperature of the foot.

Supplementary Materials: The following supporting information can be downloaded at: <https://www.mdpi.com/article/10.3390/prosthesis6060108/s1>, Figure S1a: Tensile test results for nitinol SMA wires (Test results values); Figure S1b: Tensile test results for nitinol SMA wires (The ratio between y axis Force and x axis elongation); Figure S2a: Tensile test results for EVA sheet (Load–extension curve); Figure S2b: Tensile test results for EVA sheet (Stress-strain curve); Figure S3: Compressibility curve for EVA; Table S1. Compressibility test results; Table S2. Conductivity test results; Table S3. EVA Mechanical Properties.

Author Contributions: Conceptualization, A.F.A., A.Q.A.-N. and T.J.M.; methodology, A.F.A.; software, A.F.A.; validation, A.F.A., A.Q.A.-N., T.J.M. and H.R.A.-O.; formal analysis, A.F.A. and H.R.A.-O.; investigation, A.F.A.; resources, A.F.A.; data curation, A.F.A., A.Q.A.-N. and H.R.A.-O.; writing—original draft preparation, A.F.A.; writing—review and editing, A.F.A., A.Q.A.-N., T.J.M. and H.R.A.-O.; visualization, A.F.A., A.Q.A.-N. and T.J.M.; supervision, A.Q.A.-N. and T.J.M.; project administration, A.F.A. and A.Q.A.-N.; funding acquisition, A.F.A. All authors have read and agreed to the published version of the manuscript.

Funding: This research received no external funding.

Institutional Review Board Statement: The study was conducted in accordance with the Declaration of Helsinki, and approved by the IRB of the Biomedical engineering department, College of Engineering, Al-Nahrain University under the code (N.BME/24/25/1) (approval date: 15 Jan 2024).

Informed Consent Statement: Informed consent was obtained from all subjects involved in the study. Written informed consent has been obtained from the patient(s) to publish this paper.

Data Availability Statement: The data that support the findings of this study are available from the corresponding author upon reasonable request.

Acknowledgments: We thank the Biomedical, Mechanical, and Prosthetics and Orthotics Engineering departments. We thank the Ministry of Health/Technical Efforts Directorate. We also thank Hussain Faisal and Fadhil Kareem Farhan for their technical support.

Conflicts of Interest: The authors declare no conflicts of interest.

References

1. Hsu, W.-C.; Sugiarto, T.; Chen, J.-W.; Lin, Y.-J. The Design and Application of Simplified Insole-Based Prototypes with Plantar Pressure Measurement for Fast Screening of Flat-Foot. *Sensors* **2018**, *18*, 3617. [CrossRef]
2. Farahpour, N.; Jafarnezhad, A.; Damavandi, M.; Bakhtiari, A.; Allard, P. Gait ground reaction force characteristics of low back pain patients with pronated foot and able-bodied individuals with and without foot pronation. *J. Biomech.* **2016**, *49*, 1705–1710. [CrossRef]
3. Alsaidi, F.A.; Moria, K.M. Flatfeet Severity-Level Detection Based on Alignment Measuring. *Sensors* **2023**, *23*, 8219. [CrossRef]
4. Fawcus, H.B.; WAR Office (UK). *Report on the Health of the Army for the Year 1931*; H.M.S.O.: London, UK, 1933; pp. iv+158.
5. Almutairi, A.F.; Mustafa, A.B.; Saidan, T.B.; Alhizam, S.; Salam, M. The prevalence and factors associated with low back pain among people with flat feet. *Int. J. Gen. Med.* **2021**, *14*, 3677–3685. [CrossRef]
6. Dars, S.; Uden, H.; Banwell, H.A.; Kumar, S. The effectiveness of non-surgical intervention (Foot Orthoses) for paediatric flexible pes planus: A systematic review: Update. *PLoS ONE* **2018**, *13*, e0193060. [CrossRef]
7. Ueki, Y.; Sakuma, E.; Wada, I. Pathology and management of flexible flat foot in children. *J. Orthop. Sci.* **2019**, *24*, 9–13. [CrossRef]
8. Marouvo, J.; Sousa, F.; Fernandes, O.; Castro, M.A.; Paszkiel, S. Gait kinematics analysis of flatfoot adults. *Appl. Sci.* **2021**, *11*, 7077. [CrossRef]
9. Cheng, K.-W.; Peng, Y.; Chen, T.L.-W.; Zhang, G.; Cheung, J.C.-W.; Lam, W.-K.; Wong, D.W.-C.; Zhang, M. A three-dimensional printed foot orthosis for flexible flatfoot: An exploratory biomechanical study on arch support reinforcement and undercut. *Materials* **2021**, *14*, 5297. [CrossRef]
10. Cen, X.; Gao, L.; Yang, M.; Liang, M.; Bíró, I.; Gu, Y. Arch-support induced changes in foot-ankle coordination in young males with flatfoot during unplanned gait termination. *J. Clin. Med.* **2021**, *10*, 5539. [CrossRef]

11. Galafate, D.; Pournajaf, S.; Condoluci, C.; Goffredo, M.; Di Girolamo, G.; Manzia, C.M.; Pellicciari, L.; Franceschini, M.; Galli, M. Bilateral foot orthoses elicit changes in gait kinematics of adolescents with down syndrome with flatfoot. *Int. J. Environ. Res. Public Health* **2020**, *17*, 4994. [CrossRef]
12. Renganathan, G.; Barnamehei, H.; Das, S.; Kurita, Y. Effect of Wearing Running Shoes on Lower Limb Kinematics by Using OpenSim Simulation Software. *Actuators* **2022**, *11*, 152. [CrossRef]
13. Chen, K.C.; Chen, Y.C.; Yeh, C.J.; Hsieh, C.L.; Wang, C.H. The effect of insoles on symptomatic flatfoot in preschool-aged children: A prospective 1-year follow-up study. *Medicine* **2019**, *98*, e17074. [CrossRef]
14. Bednarczyk, E.; Sikora, S.; Kossobudzka-Górska, A.; Jankowski, K.; Hernandez-Rodriguez, Y. Understanding flat feet: An in-depth analysis of orthotic solutions. *J. Orthop. Rep.* **2024**, *3*, 100250. [CrossRef]
15. Evans, A.M.; Rome, K.; Carroll, M.; Hawke, F. Foot orthoses for treating paediatric flat feet. *Cochrane Database Syst. Rev.* **2022**, *2022*, CD006311. [CrossRef]
16. Zhou, X.; Zeng Qi Liao, Z.; Lu, P.; Zou, J.; Li, S.; Huang, G. Application of customized orthopedic insoles in the treatment of flatfoot. *Chin. J. Tissue Eng. Res.* **2022**, *26*, 4587–4592. [CrossRef]
17. Jiang, Y.; Wang, D.; Ying, J.; Chu, P.; Qian, Y.; Chen, W. Design and preliminary validation of individual customized insole for adults with flexible flatfeet based on the plantar pressure redistribution. *Sensors* **2021**, *21*, 1780. [CrossRef]
18. Pfeiffer, M.; Kotz, R.; Ledl, T.; Hauser, G.; Sluga, M. Prevalence of flat foot in preschool-aged children. *Pediatrics* **2006**, *118*, 634–639. [CrossRef]
19. Nikolaidou, M.E.; Boudolos, K.D. A footprint-based approach for the rational classification of foot types in young schoolchildren. *Foot* **2006**, *16*, 82–90. [CrossRef]
20. Boryczka-Trefler, A.; Kalinowska, M.; Szczerbik, E.; Stębowska, J.; Łukaszewska, A.; Syczewska, M. How to Define Pediatric Flatfoot: Comparison of 2 Methods: Foot Posture in Static and Dynamic Conditions in Children 5 to 9 Years Old. *Foot Ankle Spec.* **2023**, *16*, 43–49. [CrossRef]
21. Kane, K. Foot Orthoses for Pediatric Flexible Flatfoot: Evidence and current practices among canadian physical therapists. *Pediatr. Phys. Ther.* **2015**, *27*, 53–59. [CrossRef]
22. Vulcano, E.; Maccario, C.; Myerson, M.S. How to approach the pediatric flatfoot. *World J. Orthop.* **2016**, *7*, 1. [CrossRef]
23. Halabchi, F.; Mazaheri, R.; Mirshahi, M.; Abbasian, L. Pediatric Flexible Flatfoot; Clinical Aspects and Algorithmic Approach. *Iran. J. Pediatr.* **2013**, *23*, 247.
24. Aenumulapalli, A.; Kulkarni, M.M.; Gandotra, A.R. Prevalence of flexible flat foot in adults: A cross-sectional study. *J. Clin. Diagn. Res.* **2017**, *11*, AC17. [CrossRef]
25. Hernandez, A.J.; Kimura, L.K.; Laraya, M.H.F.; Fávaro, E. Calculation of Staheli's plantar arch index and prevalence of flat feet: A study with 100 children aged 5–9 years. *Acta Ortop. Bras.* **2007**, *15*, 68–71. [CrossRef]
26. Chen, C.-H.; Huang, M.-H.; Chen, T.-W.; Weng, M.-C.; Lee, C.-L.; Wang, G.-J. The correlation between selected measurements from footprint and radiograph of flatfoot. *Arch. Phys. Med. Rehabil.* **2006**, *87*, 235–240. [CrossRef]
27. Hawes, M.R.; Nachbauer, W.; Sovak, D.; Nigg, B.M. Footprint parameters as a measure of arch height. *Foot Ankle* **1992**, *13*, 22–26. [CrossRef]
28. Vauhnik, R.; Turk, Z.; Piliš, I.A.; Mičetić-Turk, D. Intra-rater reliability of using the navicular drop test for measuring foot pronation. *Hrvat. Športskomedicinski Vjesn.* **2006**, *21*, 8–11.
29. Queen, R.M.; Mall, N.A.; Hardaker, W.M.; Nunley, J.A. Describing the medial longitudinal arch using footprint indices and a clinical grading system. *Foot Ankle Int.* **2007**, *28*, 456–462. [CrossRef]
30. Shaikh, S.; Jamdade, B.; Chanda, A. Effects of Customized 3D-Printed Insoles in Patients with Foot-Related Musculoskeletal Ailments—A Survey-Based Study. *Prosthesis* **2023**, *5*, 550–561. [CrossRef]
31. Rattanasak, A.; Uthansakul, P.; Uthansakul, M.; Jumphoo, T.; Phapatanaburi, K.; Sindhupakorn, B.; Rooppakhun, S. Real-Time Gait Phase Detection Using Wearable Sensors for Transtibial Prosthesis Based on a kNN Algorithm. *Sensors* **2022**, *22*, 4242. [CrossRef] [PubMed]
32. Urakov, A.; Nikityuk, D.; Kasatkin, A.; Lukoyanov, I. Infrared plantography as a method to evaluate the functional anatomy of the human foot. In Proceedings of the QIRT Council, Gdańsk, Poland, 4–8 July 2016. [CrossRef]
33. Al-Omairi, H.R.; AL-Zubaidi, A.; Fudickar, S.; Hein, A.; Rieger, J.W. Hammerstein–Wiener Motion Artifact Correction for Functional Near-Infrared Spectroscopy: A Novel Inertial Measurement Unit-Based Technique. *Sensors* **2024**, *24*, 3173. [CrossRef] [PubMed]
34. Benoussaad, M.; Sijobert, B.; Mombaur, K.; Coste, C.A. Robust foot clearance estimation based on the integration of foot-mounted IMU acceleration data. *Sensors* **2015**, *16*, 12. [CrossRef]
35. Lorusso, F.; Gehrke, S.A.; Festa, F.; Scarano, A. Wearing Effect of Implant Steel Drills and Tappers for the Preparation of the Bone Osteotomies: An Infrared Thermal Analysis and Energy Dispersive Spectroscopy-Scanning Electron Microscopy (EDS-SEM) Study. *Prosthesis* **2022**, *4*, 679–694. [CrossRef]
36. Raj, R.J.; Ashwini, C.A.; Ajoy, S.M. Flat Foot in 14–16 Years Old Adolescents and its Association with Bmi and Sports Activity. *J. Clin. Diagn. Res.* **2022**, *16*, AC01–AC05. [CrossRef]
37. Atik, A. Flexible flatfootness. *North. Clin. Istanbul.* **2014**, *1*, 57–63. [CrossRef] [PubMed]
38. Gül, Y.; Yaman, S.; Avcı, D.; Çilengir, A.H.; Balaban, M.; Güler, H. A Novel Deep Transfer Learning-Based Approach for Automated Pes Planus Diagnosis Using X-ray Image. *Diagnostics* **2023**, *13*, 1662. [CrossRef] [PubMed]

39. Bobiński, A.; Tomczyk, Ł.; Pelc, M.; Chruścicki, D.A.; Śnietka, B.; Morasiewicz, P. Arthroereisis with a Talar Screw in Symptomatic Flexible Flatfoot in Children. *J. Clin. Med.* **2023**, *12*, 7475. [CrossRef]
40. D'Andrea, D.; Milone, D.; Nicita, F.; Risitano, G.; Santonocito, D. Qualitative and Quantitative Evaluation of Different Types of Orthodontic Brackets and Archwires by Optical Microscopy and X-ray Fluorescence Spectroscopy. *Prosthesis* **2021**, *3*, 342–360. [CrossRef]
41. Oğuzhan, Y.; Kemal, T.; Gökhan, Ç. Evaluate the Physical Fitness Levels of Turkish Primary School Male and Female Children Between 7–14 Ages. *Sci. Mov. Health* **2014**, *14*, 585–593.
42. Bose, D.; Singh, G.; Gupta, S.; Chanda, A. Development of a Novel Customized Insole for Effective Pressure Offloading in Diabetic Patients. *Prosthesis* **2024**, *6*, 341–356. [CrossRef]
43. Chhikara, K.; Sidhu, S.S.; Gupta, S.; Saharawat, S.; Kataria, C.; Chanda, A. Development and Effectiveness Testing of a Novel 3D-Printed Multi-Material Orthosis in Nurses with Plantar Foot Pain. *Prosthesis* **2023**, *5*, 73–87. [CrossRef]
44. K N, C.; Eram, A.; Shetty, N.; Shetty, D.D.; Futane, M.; Keni, L.G. Evaluating Angled Abutments: Three-Dimensional Finite Element Stress Analysis of Anterior Maxillary Implants. *Prosthesis* **2024**, *6*, 315–328. [CrossRef]
45. Juneja, S.; Miranda, G.; Eram, A.; Shetty, N.; K N, C.; Keni, L.G. Investigating the Influence of All-Ceramic Prosthetic Materials on Implants and Their Effect on the Surrounding Bone: A Finite Element Analysis. *Prosthesis* **2024**, *6*, 74–88. [CrossRef]
46. Hamid, Q.Y.; Hasan, W.Z.W.; Hanim, M.A.A.; Nuraini, A.A.; Hamidon, M.N.; Ramli, H.R. Shape memory alloys actuated upper limb devices: A review. *Sens. Actuators Rep.* **2023**, *5*, 100160. [CrossRef]
47. Pan, J.W.; Ho, M.Y.M.; Loh, R.B.C.; Shahril Iskandar, M.N.U.R.; Kong, P.W. Foot Morphology and Running Gait Pattern between the Left and Right Limbs in Recreational Runners. *Phys. Act. Health* **2023**, *7*, 43–52. [CrossRef]
48. Hsu, C.Y.; Wang, C.S.; Lin, K.W.; Chien, M.J.; Wei, S.H.; Chen, C.S. Biomechanical Analysis of the FlatFoot with Different 3D-Printed Insoles on the Lower Extremities. *Bioengineering* **2022**, *9*, 563. [CrossRef]
49. Hoang, N.T.T.; Chen, S.; Chou, L.W. The impact of foot orthoses and exercises on pain and navicular drop for adult flatfoot: A network meta-analysis. *Int. J. Environ. Res. Public Health* **2021**, *18*, 8063. [CrossRef]
50. Kao, E.F.; Lu, C.Y.; Wang, C.Y.; Yeh, W.C.; Hsia, P.K. Fully automated determination of arch angle on weight-bearing foot radiograph. *Comput. Methods Programs Biomed.* **2018**, *154*, 79–88. [CrossRef]
51. Khan, F.; Chevidikunnan, M.F.; Alsobhi, M.G.; Ahmed, I.A.I.; Al-Lehidan, N.S.; Rehan, M.; Alalawi, H.A.; Abduljabbar, A.H. Diagnostic Accuracy of Various Radiological Measurements in the Evaluation and Differentiation of Flatfoot: A Cross-Sectional Study. *Diagnostics* **2022**, *12*, 2288. [CrossRef]
52. Pita-Fernández, S.; González-Martín, C.; Seoane-Pillado, T.; López-Calviño, B.; Pérttega-Díaz, S.; Gil-Guillén, V. Validity of footprint analysis to determine flatfoot using clinical diagnosis as the gold standard in a random sample aged 40 years and older. *J. Epidemiol.* **2015**, *25*, 148–154. [CrossRef]

Disclaimer/Publisher's Note: The statements, opinions and data contained in all publications are solely those of the individual author(s) and contributor(s) and not of MDPI and/or the editor(s). MDPI and/or the editor(s) disclaim responsibility for any injury to people or property resulting from any ideas, methods, instructions or products referred to in the content.

Article

Investigating Material Performance in Artificial Ankle Joints: A Biomechanical Study

Hasan Mhd Nazha ^{1,*}, Muhsen Adrah ², Thaer Osman ², Mohammad Issa ³, Ahmed Imran ⁴, Yicha Zhang ⁵ and Daniel Juhre ¹

¹ Faculty of Mechanical Engineering, Otto von Guericke University Magdeburg, Universitätsplatz 2, 39106 Magdeburg, Germany; daniel.juhre@ovgu.de

² Faculty of Technical Engineering, University of Tartous, Tartous P.O. Box 2147, Syria; mohssenadra@tartous-univ.edu.sy (M.A.); t.osman@tartous-univ.edu.sy (T.O.)

³ Faculty of Biomedical Engineering, Al-Andalus University for Medical Sciences, Tartous P.O. Box 101, Syria; mi11@au.edu.sy

⁴ Department of Biomedical Engineering, Ajman University, Ajman P.O. Box 346, United Arab Emirates; a.imran@ajman.ac.ae

⁵ Mechanical Engineering and Design Department, Université de Technologie de Belfort-Montbéliard, ICB UMR CNRS 6303, 90010 Belfort, France; yicha.zhang@utbm.fr

* Correspondence: hasan.nazha@ovgu.de

Abstract: This study delves into an in-depth examination of the biomechanical characteristics of various materials commonly utilized in the fabrication of artificial ankle joints. Specifically, this research focuses on the design of an ankle joint resembling the salto-talaris type, aiming to comprehensively understand its performance under different loading conditions. Employing advanced finite element analysis techniques, this investigation rigorously evaluates the stresses and displacements experienced by the designed ankle joint when subjected to varying loads. Furthermore, this study endeavors to identify the vibrating frequencies associated with these displacements, offering valuable insights into the dynamic behavior of the ankle joint. Notably, the analysis extends to studying random frequencies across three axes of motion, enabling a comprehensive assessment of directional deformities that may arise during joint function. To validate the effectiveness of the proposed design, a comparative analysis is conducted against the star ankle design, a widely recognized benchmark in ankle joint prosthetics. This comparative approach serves dual purposes: confirming the accuracy of the findings derived from the salto-talaris design and elucidating the relative efficacy of the proposed design in practical application scenarios.

Keywords: biomechanics; artificial ankle joints; finite element analysis; prosthesis

Citation: Nazha, H.M.; Adrah, M.; Osman, T.; Issa, M.; Imran, A.; Zhang, Y.; Juhre, D. Investigating Material Performance in Artificial Ankle Joints: A Biomechanical Study. *Prosthesis* **2024**, *6*, 509–526. <https://doi.org/10.3390/prosthesis6030036>

Academic Editor: Arnab Chanda

Received: 4 April 2024

Revised: 28 April 2024

Accepted: 9 May 2024

Published: 13 May 2024



Copyright: © 2024 by the authors. Licensee MDPI, Basel, Switzerland. This article is an open access article distributed under the terms and conditions of the Creative Commons Attribution (CC BY) license (<https://creativecommons.org/licenses/by/4.0/>).

1. Introduction

The ankle joint serves as a crucial link between the leg and foot, facilitating load transfer that is essential for activities like standing, walking, running, and jumping, crucial for balance and stability [1]. It absorbs external forces' impact during these activities, owing to its robust skeletal, biomechanical, and cartilaginous structural characteristics [1]. Despite the challenges in treating various types of arthritis, collaborative efforts among surgeons, physicians, and researchers have led to the development of treatment modalities, including surgical and non-surgical approaches [2]. However, the limited efficacy of non-surgical treatments in pain alleviation often necessitates surgical interventions, with Total Ankle Replacement being the preferred procedure [2,3].

Moreover, the ankle joint exhibits dynamic mechanical activity beyond passive functions, particularly evident during efforts to increase walking speed [3]. Technological advancements have transformed ankle joint disorder treatment, replacing traditional approaches with artificial joint replacements [4]. Yet initial attempts at ankle joint replacement have faced challenges, including increased problems and difficulties [5].

Current biomechanical studies prioritize developing joints that mimic natural movement, possess extended lifespans, and employ high-quality, biocompatible materials to minimize inflammatory reactions [4]. However, ankle joint replacement is not devoid of drawbacks, with complications such as loosening, infection, anesthesia-related issues, and nerve injury persisting in many patients even years after surgery [6,7]. These challenges underscore the imperative of understanding ankle joint biomechanics to develop artificial joints that optimize mobility while minimizing adverse effects.

Consequently, there is a pressing need for the development of artificial ankle joints with enhanced characteristics or quasi-archetypal designs. Suggestions or designs for ankle joints must consider factors like walking speed and jumping, necessitating an understanding of vibrating frequencies and deformities in multiple directions. Such insights can pave the way for the creation of ankle joints that function more effectively and efficiently [8].

2. Basic Components of the Human Ankle

The ankle essentially consists of three bones: the tibia, fibula, and talus [8,9]. The talus is usually called the ankle bone and its top part is located inside a bowl-like structure that is made of two parts, which are the fibula and the lower part of the tibia. The lower part of the ankle, however, is supported by the calcaneus and generally is called the heel bone. According to these parts, the legs of human beings can move up and down so easily due to the link to these three basic bones that is similar to a joint. In addition to this, there exists a material similar to oil, named the articular cartilage, to present a level that is quasi-void of friction when bones move. The articular cartilage must be quite thin and hard to support the weight of the body. Figure 1a [10] shows the overall structure of the ankle joint. In addition to this, ligaments and tendons are considered significant soft tissues to perform the movement of the ankle; as ligaments play a key role in linking bones, tendons are the soft tissues used to join bones and muscles [11]. Tendons are located on both sides of the ankle joint and avail a capacity to make bones well joined. Tendons also support the ankle joint at the same time, and there are miscellaneous types of tendons that perform different tasks. For example, the Achilles tendon can be used while jumping, running, or walking. Figure 1b elaborates on ligaments and tendons.

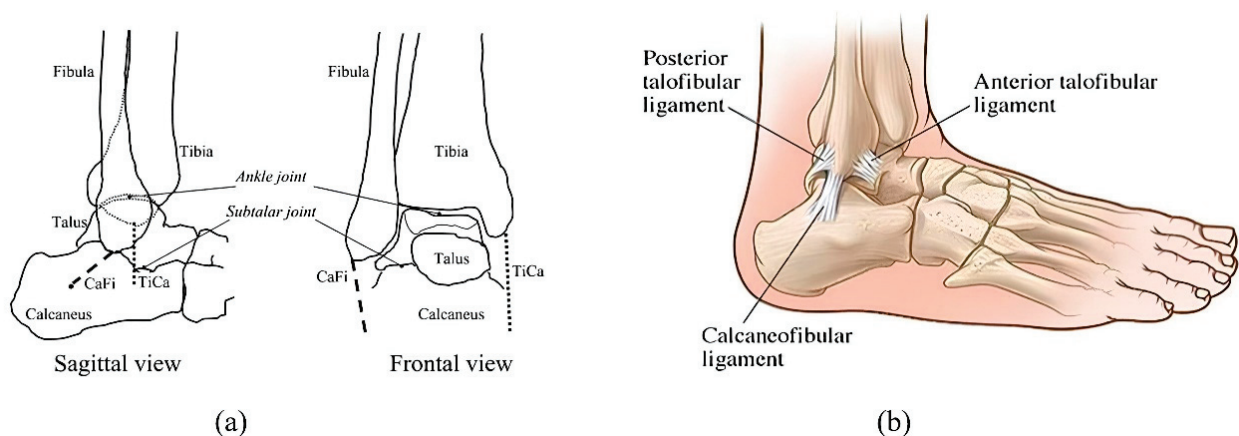


Figure 1. (a) Overall structure of ankle joint; (b) ligaments and tendons.

3. Replacement of the Entire Salto-Talaris Ankle Joint

The artificial salto-talaris joint is one of the most used artificial ankle joints and is considered a complete substitute for the non-constrained ankle, where it can be planted surgically. Generally speaking, the carrier can move freely on more than one surface. Such a design consists of three parts: a leg component (tibia) which is metal and enters inside the shinbone, a metal ankle component (talar) fixed from the bottom to the bones, and finally, a plastic component fixed to the tibia, as is elaborated in Figure 2. According to this, the lower part of the plastic component (carrier) slides over the upper surface of the ankle

component (Talar), and a cylinder with the shinbone component helps fasten the apparatus to the bone.

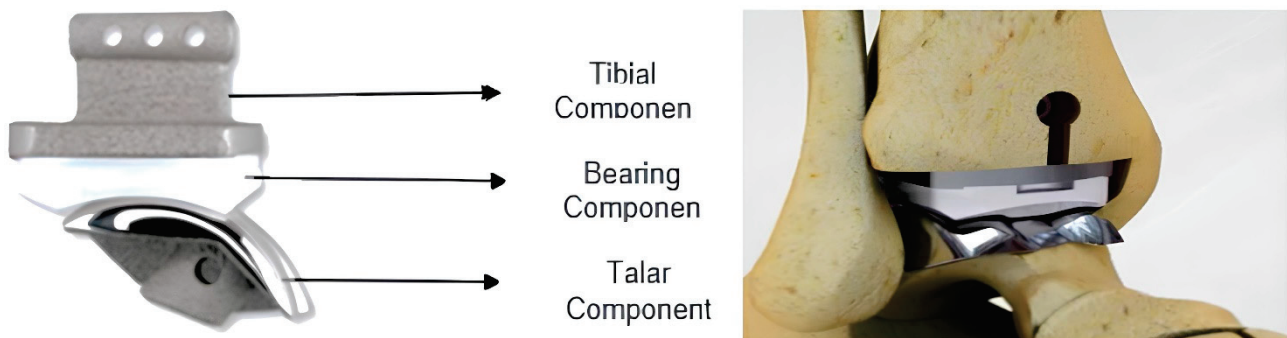


Figure 2. Parts of the artificial ankle joint salto-talaris.

4. Materials and Methods

Based on the aforementioned studies and research, a significant challenge in designing the three-dimensional archetype of an artificial ankle joint lies in selecting a material that exhibits lower stresses, higher resistance to deformity, and lower density. This selection aims to attain desired mechanical properties while also assessing the impact of load distribution along the length of prosthetic limbs on unexpected movement conditions. Furthermore, prioritizing mechanical strength and durability is essential for ensuring safety. Metallic materials, commonly used under load-bearing conditions, may exhibit toxicity and susceptibility to corrosion-induced breakage [12]. To address this, a comparative analysis among five different materials will be conducted during simulated load conditions (ranging from 50 to 100 kg) to evaluate their performance. These materials are as follows:

First: Metal materials:

- Stainless steel (SS316L):

Austenitic chromium–nickel stainless steel is heat-resistant with high corrosion resistance, comparable to chromium–nickel steel when exposed to several kinds of harmful chemicals such as seawater, salt water solutions, and the like.

- Titanium–aluminum–vanadium alloys (Ti-6Al-4V):

Alfa beta titanium alloys have high energy and excellent erosion resistance. They are used in biomedicine. This specification refers to their chemical structure: up to almost 90% titanium, 6%, aluminum, 4% vanadium, 0.25% (maximally) iron, and 0.2% (maximally) oxygen. They possess distinct energy characteristics, a low flexibility factor, and malleability, and are amenable to temperature treatment.

- B-type titanium alloys (Ti-13Nb-13Zr):

These are new titanium alloys developed to suit medical implant applications. These alloys are characterized by low ductility, high energy, excellent hot and cold formability, and high corrosion resistance [13].

- Cobalt–chromium molybdenum alloys (Co-Cr-Mo):

Cobalt–chromium molybdenum alloys consist of 26–30% Cr, 5–7% Mo, and less than 0.35% carbon with some basic cobalt. This alloy can be manufactured by casting, striking, and pressing. Its features include high strength and fatigue resistance, a low to medium elastic modulus, and high abrasion resistance.

Second: Polymeric materials:

- Polyethylene (Ultra-High-Molecular-Weight Polyethylene) (UHMWPE):

This is the polymer material of choice in ankle replacements. Due to a range of features including corrosion resistance and biocompatibility, it remains the gold standard to date.

It has very long polymer chains that tend to transfer the load more effectively toward the polymer backbone by enhancing intermolecular activities [14].

Table 1 reveals the mechanical characteristics of these items [15–17]. On the other hand, the vibration frequency values (frequency [Hz]) are calculated; the random vibration of the three directions (x, y, and z) is also achieved. This is to analyze the findings, identify the appropriate item to implement the artificial ankle joint, and select the archetypal design. The significance of this research stems from studying the biomechanics and its influence on the leg and the ankle to prevent the side effects observed following the surgery; all this is through manipulating the finite element method that concludes with these criteria.

Table 1. Mechanical properties of the SS316L, Ti-6Al-4V, Ti-13Zr, Co-Cr-Mo, and UHMWPE materials.

Material Properties	Co-Cr-Mo	Ti-13Nb-13Zr	UHMWPE	Ti-6Al-4V	SS316L
Density (kg/m ³)	8300	4920	930	4430	7980
Poisson's ratio	0.32	0.32	0.46	0.31	0.3
Young's modulus (GPa)	205	79–84	0.894	110	193
Submission stress (MPa)	660	836–908	21.4	880	205
Maximum tensile strength (MPa)	1100	973–1037	38.6	950	515

4.1. Selecting Materials for Each Element of the Components of an Artificial Ankle

The artificial ankle joint consists of three parts:

1. Tibial Component: Polymeric item (UHMWPE), Ti-6Al-4V alloy, SS316L alloy, Co-Cr-Mo alloys, and Ti-13 Nb-13Zr alloys.
2. Bearing Component: UHMWPE.
3. Talar Component: Polymeric item (UHMWPE), Ti-6Al-4V alloy, SS316L alloy, Co-Cr-Mo alloys, and Ti-13 Nb-13Zr alloys.

4.2. Three-Dimensional Design of the Artificial Salto-Talaris Ankle Joint

The three-dimensional prototype of the artificial ankle joint was drawn via CATIA software (V5R18, Dassault Systèmes, Vélizy-Villacoublay, France). There are three parts to this design. The tibial component consists of an empty tube that is soon inserted into the lower part of the leg; it is fastened from below with the bearing component that looks like a semi-circle bow. One apparent feature is that it moves on all levels; when it slides higher toward the talar, the bow looks concave in order to fix it to the upper part of the ankle, and from above the component, it is possible to fasten the bearing component. These measures are designed as is apparent in Table 2 [16]. Figure 3 elaborates on the three-dimensional archetype of the salto-talaris artificial ankle joint.

Table 2. Measures of design of the artificial ankle joint.

Design components		Tibial component					Bearing component			
Component specifications	Height	Length	Front view	Back view	The length of the hollow cylinder	Cylinder diameter	Height	Length	Front view	Back view
Gauge (mm)	2.5	35	32	28	19	4	8	35	32	28
Design components		Specifications of artificial lower ankle components (talar)								
Component specifications	Height	Length		Width		Cylinder diameter		Curve		
Gauge (mm)	6	38		32		10		29		

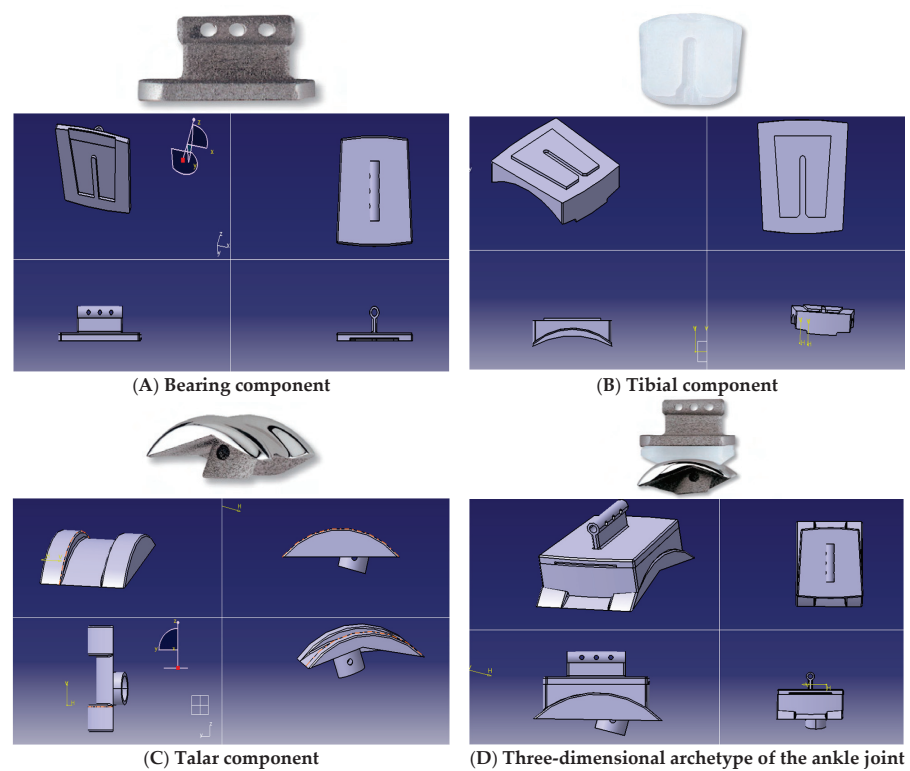


Figure 3. (A–C) Components with three dimensional archetype of the artificial (D) salto-talaris ankle joint.

4.3. FEA of the Salto-Talaris Ankle Joint

Each part of the ankle joint components has to be capable of holding both tensile and compressive loads successively. On the other hand, pressures and deviations are supposed to be within the permissible limits. A perfect contact pair is formulated in our study. However, parts of the components are always bonded to each other. The archetype is exported as an igs file, and such a file can be imported into the environment of Ansys software (v. 19 R1, ANSYS, Inc., Canonsburg, PA, USA) in order to open an archetype. Finally, the archetype was prepared for analysis, where 11,188 elements were structured with 21,829 nodes accordingly. With the help of ANSYS, miscellaneous dimensional conditions are identified in addition to conducting an analysis. Figure 4 elaborates on the finite element archetype of the implant, as well as the dimensional conditions suggested for the archetype prior to analysis.

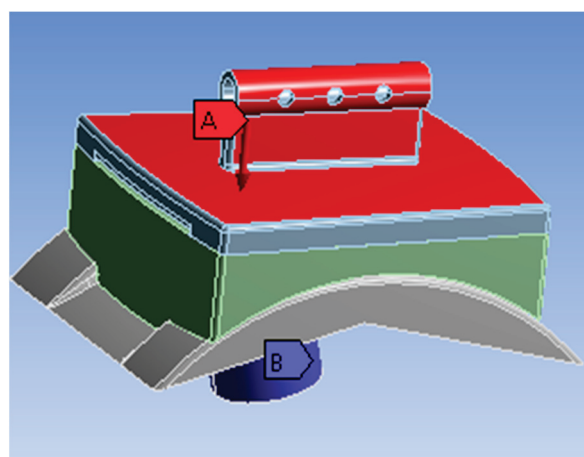


Figure 4. Loads and boundary conditions.

5. Results

5.1. Conditions of Natural Walking

Figures 5 and 6 disclose the results of the displacement and stress compared to von Mises stress under the conditions of natural walking of the five items with the help of the ANSYS software, provided that the patient's weight is 50 kg. It has been observed that the item UHMWPE has the lowest stress value compared to von Mises stress, contrasting other manipulated items when the highest stress reaches 38.968 MPa, whereas the sliding value of this item is the highest, reaching 0.2745 mm. Accordingly, it seems that the UHMWPE item is the best in light of the resulting stresses. We can also observe that Ti-13Nb-13Zr alloys possess a maximum stress reaching 54.043 MPa, and a maximum displacement of 0.020894 mm. Thus, this alloy is considered the best to use following UHMWPE according to the resulting stresses. In terms of displacement values, we notice that the Co-Cr-Mo material has an upper stress of up to 56.476 MPa and a low displacement of 0.016551 mm compared to the rest of the materials, as the results indicate that the biomechanical response intensifies at the front of the artificial ankle joint, which contributes to the pressure observed at the front of the joint. The highest point allows us to improve the pressure location, manipulate the direction, and improve the displacement properties of each material. Other effects of the patient's weights and different loads are elaborated in Table 3 and Figures 7 and 8.

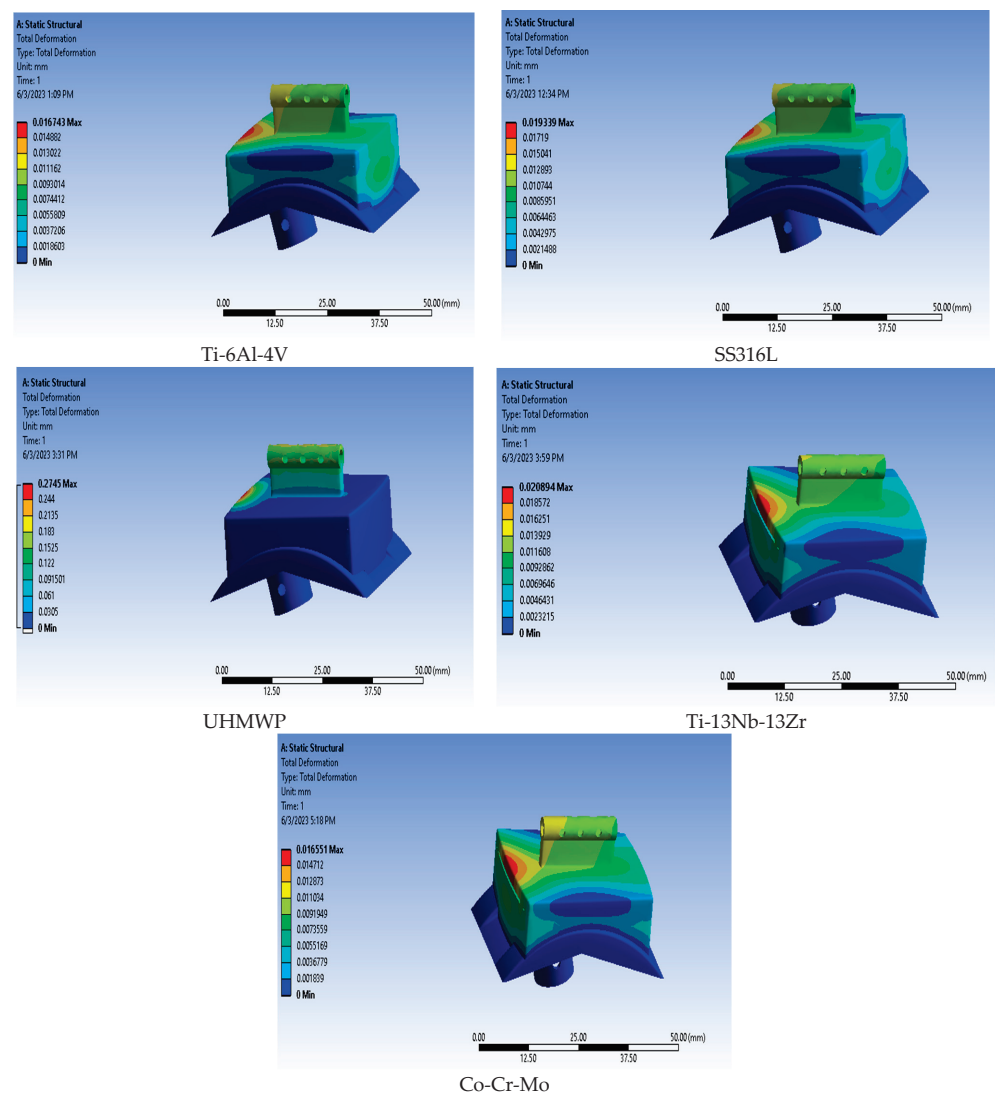


Figure 5. Results of displacement analysis under normal walking conditions.

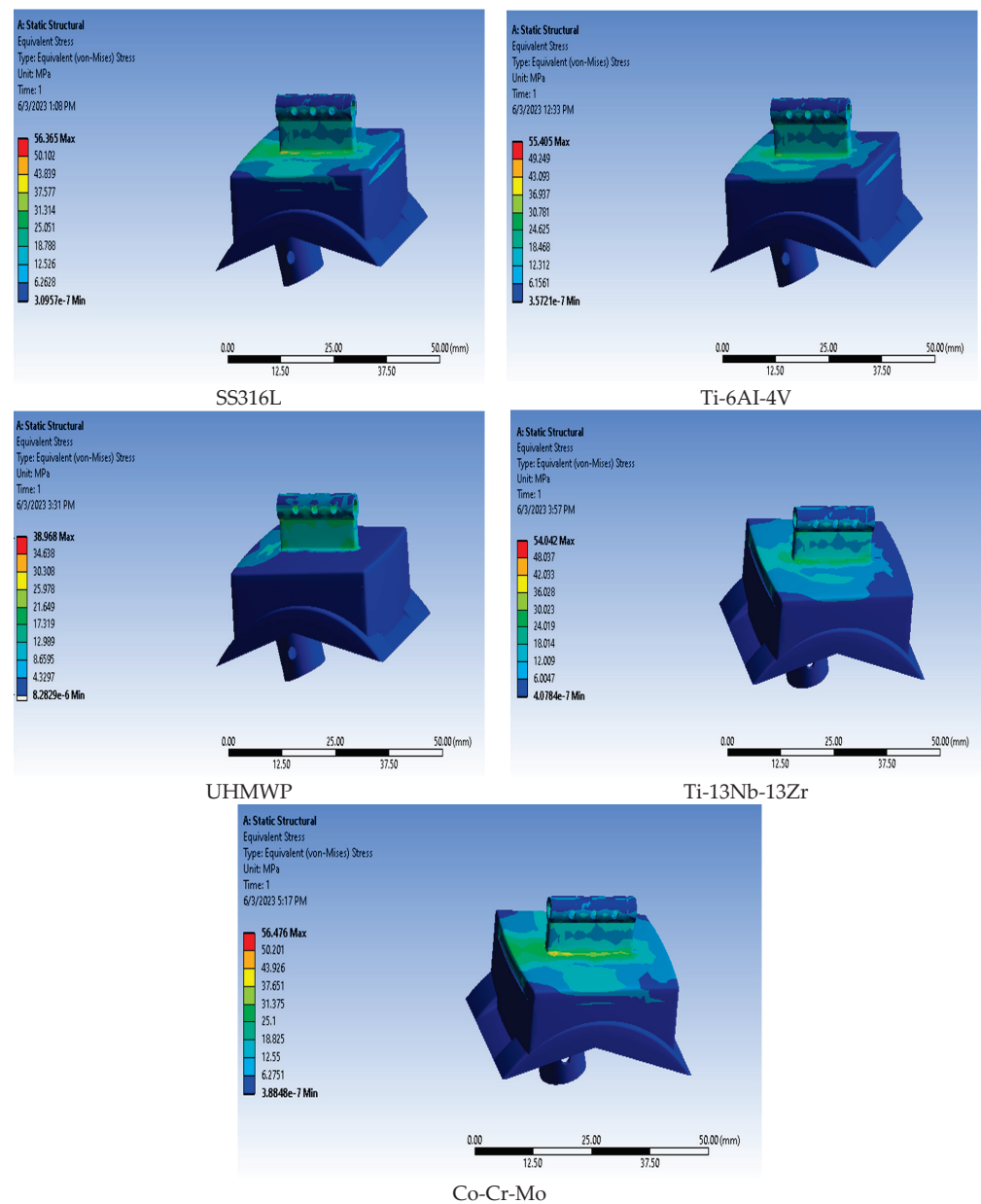


Figure 6. Results of the von Mises stress analysis.

Table 3. Summary of the results of salto-talaris joint under natural walking conditions.

Patient Weight (kg)	Maximum Load (N)	Material	Displacement (Max) mm	Von Mises Stress (Max) MPa
50	2000	SS316L	0.0167	56.365
		Ti-6Al-4V	0.0193	55.405
		UHMWPE	0.2745	38.968
		Ti-13Nb-13Zr	0.0209	54.042
		Co-Cr-Mo	0.0166	56.476
60	2400	SS316L	0.0201	67.638
		Ti-6Al-4V	0.0232	66.486
		UHMWPE	0.3294	46.761
		Ti-13Nb-13Zr	0.0251	64.85
		Co-Cr-Mo	0.0199	67.771

Table 3. Cont.

Patient Weight (kg)	Maximum Load (N)	Material	Displacement (Max) mm	Von Mises Stress (Max) MPa
70	2800	SS316L	0.0234	78.911
		Ti-6Al-4V	0.0271	77.567
		UHMWPE	0.3843	54.555
		Ti-13Nb-13Zr	0.0293	75.659
		Co-Cr-Mo	0.0232	79.066
80	3200	SS316L	0.0268	90.184
		Ti-6Al-4V	0.0309	88.648
		UHMWPE	0.4392	62.348
		Ti-13Nb-13Zr	0.0334	86.467
		Co-Cr-Mo	0.0265	90.361
90	3600	SS316L	0.0268	101.46
		Ti-6Al-4V	0.0348	99.73
		UHMWPE	0.4941	70.142
		Ti-13Nb-13Zr	0.0376	97.276
		Co-Cr-Mo	0.0298	101.66

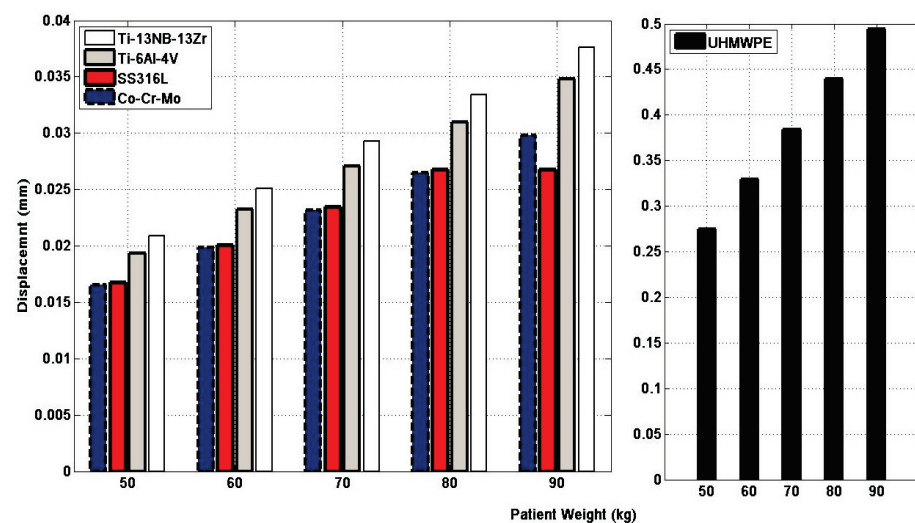


Figure 7. Displacement values for the studied materials under normal walking conditions for the studied materials.

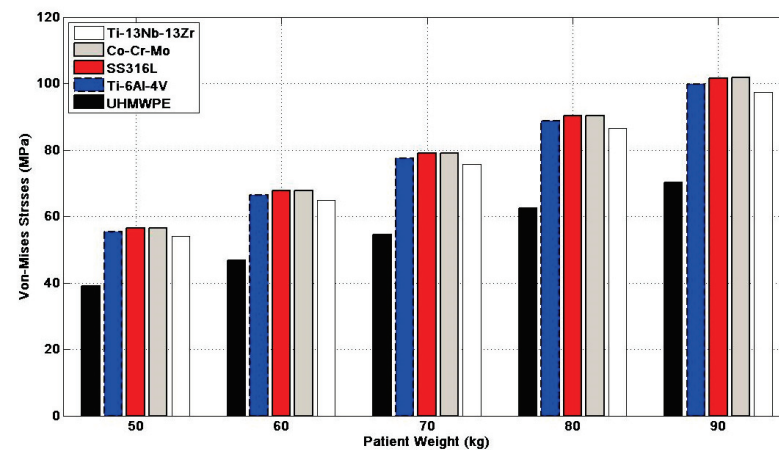


Figure 8. Von Mises stress of the studied materials during normal walking of the materials used in the ankle industry.

5.2. Under the Effect of Loading

Concerning the stress resulting from the artificial ankle joint under the influence of loading, we still need to conduct a lot of analyses to confirm that the ankle joint could meet the expectations of the vast majority, like walking, running, and jumping, since these will lead to miscellaneous stresses upon the ankle joint. Figures 9 and 10 and Table 4 disclose displacement values and von Mises' stress of the researched items within the loading conditions; the results showed that the UHMWPE material had the lowest von Mises stress value by 194.84 MPa, while the displacement value was high by 1.3725 mm at a force of 10,000 N. The Ti-13Nb-13Zr material also showed the lowest stress after the UHMWPE material, and it was found that the Co-Cr-Mo material was better in terms of displacement, but had higher pressures compared to other materials. We could confirm the significance of using UHMWPE items in manufacturing the ankle joint, since it reveals low stress values when compared to other items used with higher values of displacement.

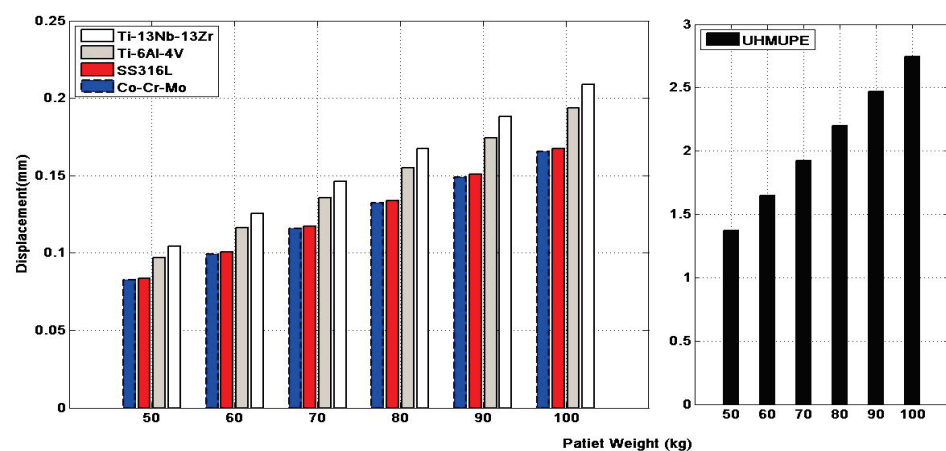


Figure 9. Diagram of displacement of the implanting items under loading conditions.

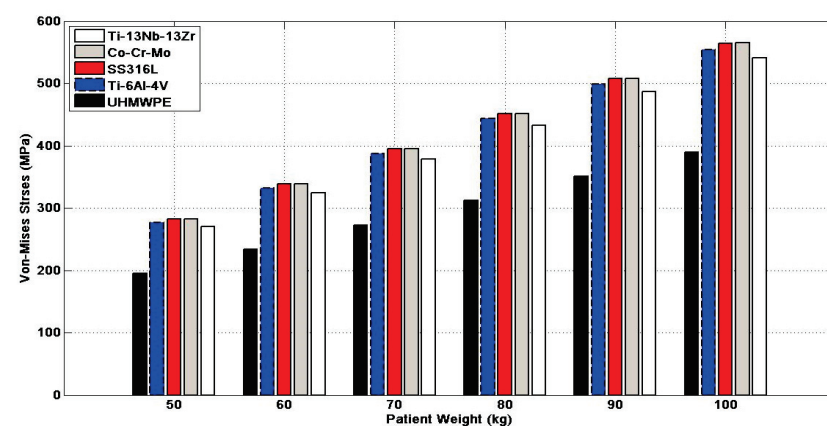


Figure 10. Diagram of von Mises stresses of the implanting items under loading.

Table 4. Results of von Mises stresses and displacement of the items used in manufacturing the ankle joint under loading conditions.

Patient Weight (kg)	Maximum Load (N)	Material	Displacement (Max) mm	Von Mises Stress (Max) MPa
50	10,000	SS316L	0.0837	281.82
		Ti-6Al-4V	0.0967	277.03
		UHMWPE	1.3725	194.84
		Ti-13Nb-13Zr	0.1045	270.21
		Co-Cr-Mo	0.0828	282.38

Table 4. *Cont.*

Patient Weight (kg)	Maximum Load (N)	Material	Displacement (Max) mm	Von Mises Stress (Max) MPa
60	12,000	SS316L	0.1005	338.19
		Ti-6Al-4V	0.1160	332.43
		UHMWPE	1.6470	233.81
		Ti-13Nb-13Zr	0.1254	324.25
		Co-Cr-Mo	0.0993	338.86
70	14,000	SS316L	0.1172	394.55
		Ti-6Al-4V	0.1354	387.84
		UHMWPE	1.9215	272.77
		Ti-13Nb-13Zr	0.1463	378.29
		Co-Cr-Mo	0.1159	395.33
80	16,000	SS316L	0.1339	450.92
		Ti-6Al-4V	0.1547	443.24
		UHMWPE	2.1960	311.74
		Ti-13Nb-13Zr	0.1672	432.34
		Co-Cr-Mo	0.1324	451.81
90	18,000	SS316L	0.1507	507.28
		Ti-6Al-4V	0.1741	498.65
		UHMWPE	2.4705	350.71
		Ti-13Nb-13Zr	0.1880	486.38
		Co-Cr-Mo	0.1490	508.28
100	20,000	SS316L	0.1674	563.65
		Ti-6Al-4V	0.1934	554.05
		UHMWPE	2.7450	389.68
		Ti-13Nb-13Zr	0.2089	540.42
		Co-Cr-Mo	0.1655	564.76

5.3. Analyzing the Vibrating Behaviour

Vibration analysis is meant to study the dynamic characteristics of skeletons under the effect of vibrating stimulus in the ankle joint, where it is fastened exclusively from one side. To complete this study, the boundary conditions used are similar to what has been previously mentioned above. An analysis was conducted to trace the total deformity in six positions. The concluding results of the values of frequency and total deformities are elaborated in Figures 11–15 and in Tables 5–9 of the implanting items in this study. According to these results, it transpires that the frequency values of the item UHMWPE are low compared to other manipulated items: an amount of 155.774 Hz. By contrast, the values of the total deformity of this item are much higher compared to other researched items (16.365 mm). This is due to the low values of the density and flexibility of the UHMWPE compared to other items. From this, we observe that this item is the best to avoid the frequency stimulus.

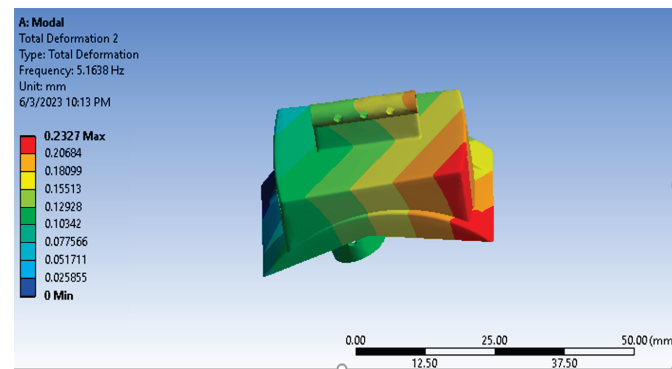


Figure 11. Vibration results of Ti-6Al-4V part.

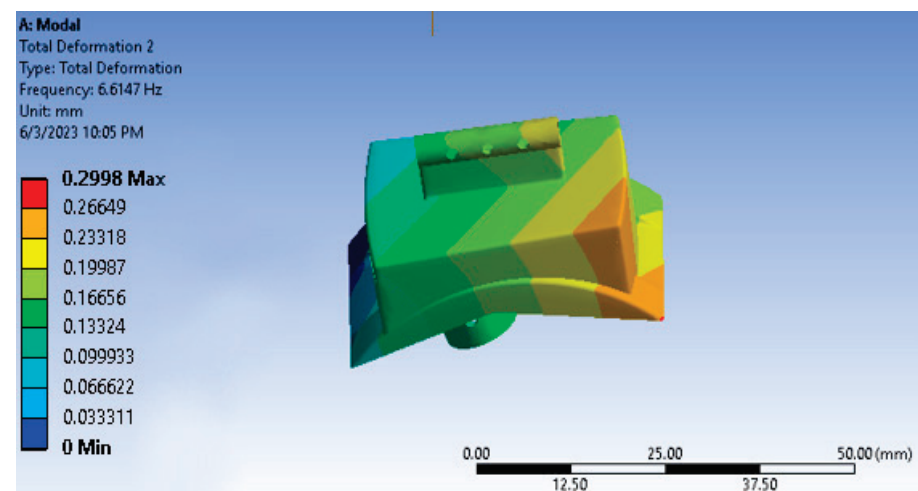


Figure 12. Vibration results of the Ti-13Nb-13Zr part.

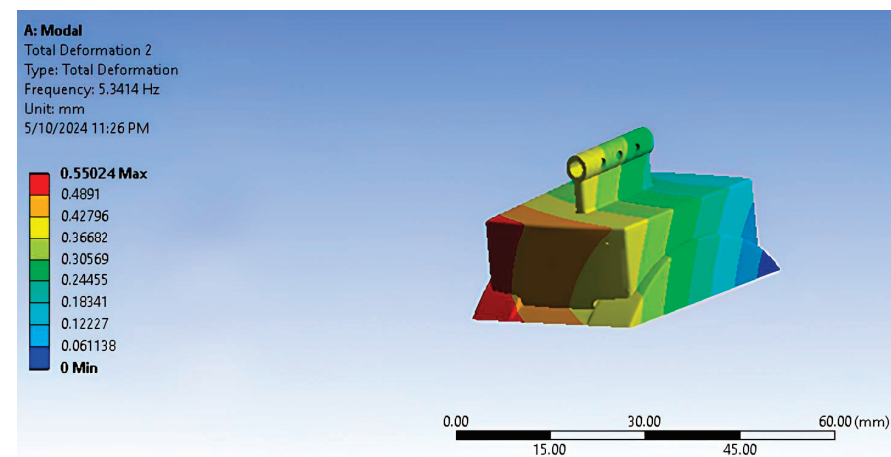


Figure 13. Vibration results of the Co-Cr-Mo part.

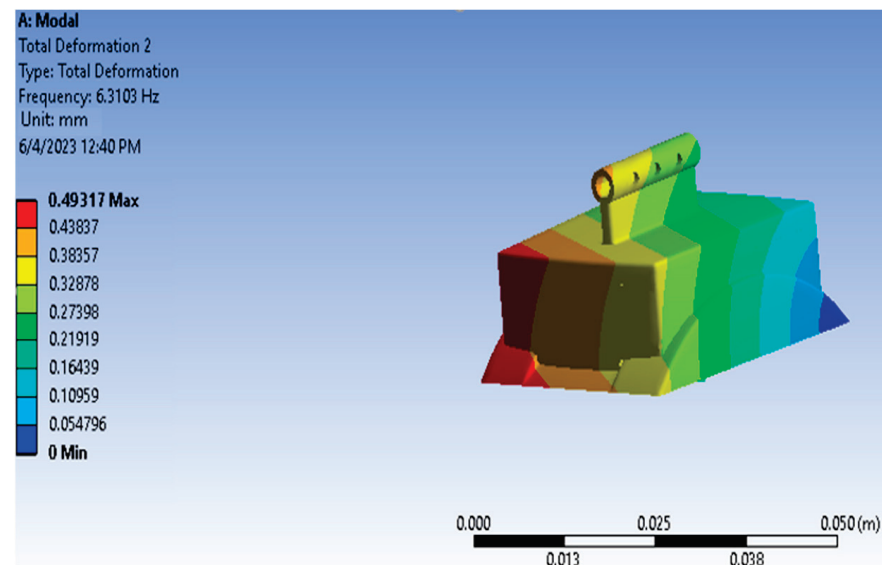


Figure 14. Vibration results of the SS316L part.

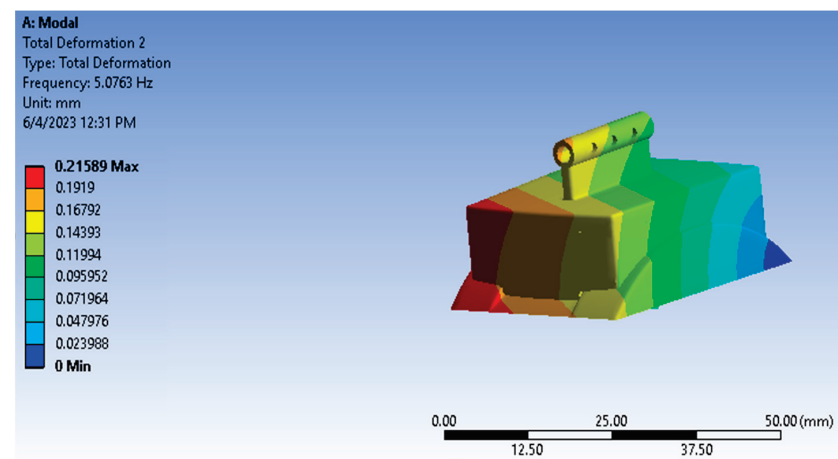


Figure 15. Vibration results of the UHMWPE part.

Table 5. Values of frequency and total deformation of Ti-6Al-4V joint.

Model	Frequency (Hz)	Total Deformation (mm)	Displacement [(mm ²)/Hz]
1	1.254	0.0015	0.002×10^{-3}
2	5.1638	0.2327	0.0105
3	23.354	1.656	0.1174
4	51.35	4.7141	0.4328
5	105.53	8.8925	0.7493
6	170.25	15.235	1.3633

Table 6. Values of frequency and total deformation of Ti-13Nb-13Zr part.

Model	Frequency (Hz)	Total Deformation (mm)	Displacement [(mm ²)/Hz]
1	1.0874	0.0019	0.0003×10^{-2}
2	6.6147	0.2998	0.0136
3	22.7567	1.7638	0.1367
4	50.592	5.3708	0.5702
5	104.6127	7.7898	0.5801
6	165.6927	15.6878	1.4853

Table 7. Values of frequency and total deformation of Co-Cr-Mo part.

Model	Frequency (Hz)	Total Deformation (mm)	Displacement [(mm ²)/Hz]
1	1.354	0.0012	0.0016×10^{-3}
2	5.3414	0.5502	0.0567
3	26.546	1.45	0.0792
4	53.54	3.518	0.2312
5	109.254	9.1456	0.7656
6	177.25	15.0125	1.2715

After concluding with the vibration analysis using ANSYS, random vibration can be simulated, which is the vibration according to three directions (x, y, z). This is an attempt to reach the value of the deformity in these directions. It is also possible to identify the deformity by linking to the aforementioned vibration analysis by recording the displacement values (displacement [mm²]/Hz) and appropriate frequencies. Contrariwise, PSD displacement was selected, and we recorded the results of the analysis, as is apparent in Table 10 and Figure 16, with a probability value of 68.269%. The material UHMWPE is the best in terms of directional deformation according to three directions (x, y, z) compared to other materials; the material Co-Cr-Mo was the best in terms of directional deformation after UHMWPE. As a conclusion, it is still the best item to use under the loading conditions specific to jumping and at high speed in uneven areas (rough places or slopes).

Table 8. Values of frequency and total deformation of SS316L part.

Model	Frequency (Hz)	Total Deformation (mm)	Displacement [(mm ²)/Hz]
1	1.4886	0.008	0.004×10^{-2}
2	6.3103	0.4932	0.0385
3	25.3613	1.52	0.0911
4	52.4403	4.6182	0.4067
5	108.486	9.1120	0.7653
6	175.4403	15.1172	1.3026

Table 9. Values of frequency and total deformation of UHMWPE part.

Model	Frequency (Hz)	Total Deformation (mm)	Displacement [(mm ²)/Hz]
1	1.0206	0.0011	0.0012×10^{-4}
2	5.0763	0.2159	0.0092
3	21.255	1.2699	0.0759
4	49.704	3.7759	0.2868
5	107.274	11.2509	1.1800
6	155.774	16.365	1.7192

Table 10. The final results of the higher directional deformation of each item on the axes x, y, and z when exposed to vibration.

Number	Materials	Directional Deformation (mm)(x)	Directional Deformation (mm)(y)	Directional Deformation (mm)(z)
1	SS316L	1.7727	1.6789	5.7788
2	Ti-6Al-4V	2.3205	2.2412	0.7862
3	UHMWPE	0.8358	0.7360	0.4925
4	Ti-13Nb-13Zr	2.2262	2.1508	0.7661
5	Co-Cr-Mo	1.6165	1.5613	0.5118

5.4. Confirming the Correct Design Analysis

In addition, the ability of the model to restore the original state in the absence of applied forces or loading conditions was verified. The elastic strain method was used

during the analysis using ANSYS, as elastic strain is a very essential factor to measure whether a model is practical or not. The elastic strain is shown in the Figure 17. However, we observe that the maximum elastic strain in this design reaches 4.4484×10^{-2} mm/mm, and that the minimal elastic strain is 2.01×10^{-8} mm/mm. We also observe the non-existence of any red regions in the design of the archetype. This proves that such a design has the capacity to restore its original status [3].

In addition, in order to obtain the optimal design of the artificial ankle joint, this design (salto-talaris) was compared with the star ankle design [15]. To perfectly achieve this, measures and results of the star ankle design were recorded and applied to the salto-talaris design in compliance with forces of 2000 N, 2500 N, 3000 N, and 3500 N. Figure 18 reveals both aforementioned designs. The results of analyzing the von Mises stresses and displacements of the items Ti-6Al-4V and Co-Cr-Mo are elaborated in Figure 19. Whilst the results for the material Ti-6Al-4V for the salto-talaris design showed an amount of 55.405 MPa, for the star ankle design, it showed an amount of 57.952 MPa, and the displacement for the salto-talaris design showed 0.0193 mm, while for the star ankle, it showed 0.0612 mm. However, we can confirm that the values of displacement and higher stress (equivalent to von Mises stress) in designing salto-talaris joints are lower in comparison with the star ankle design of both items [3].

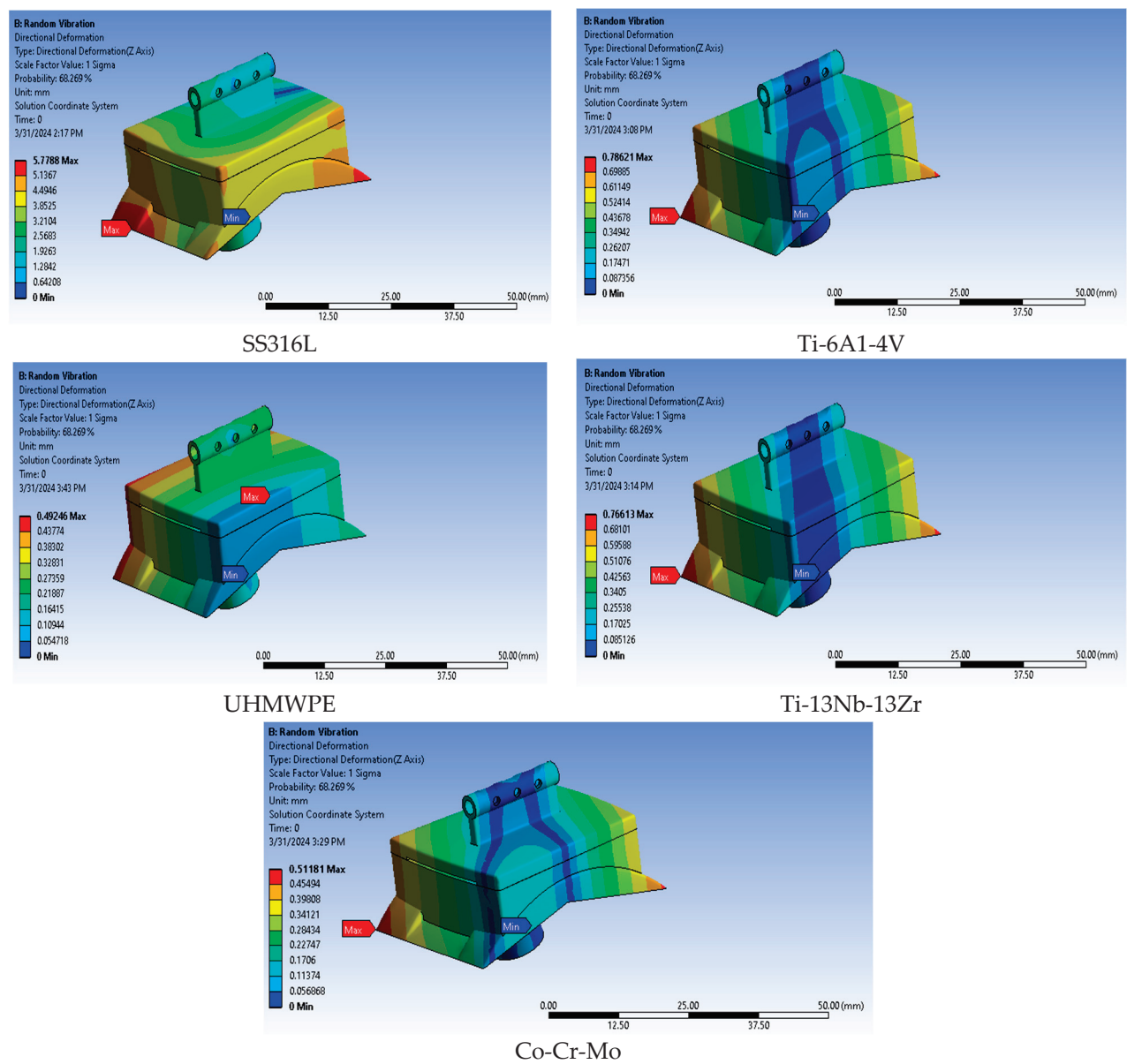


Figure 16. Directional deformation along three (XYZ) axes of the studied materials.

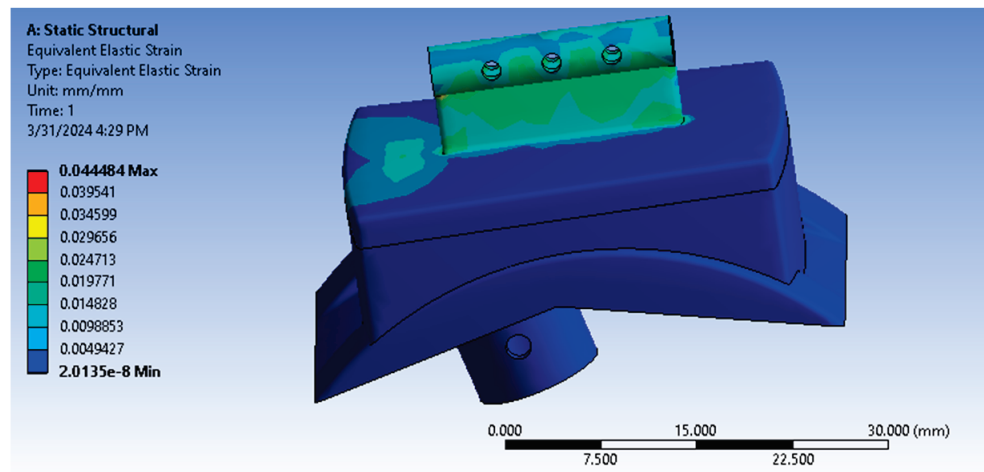


Figure 17. Analysis of the equivalent elastic strains.

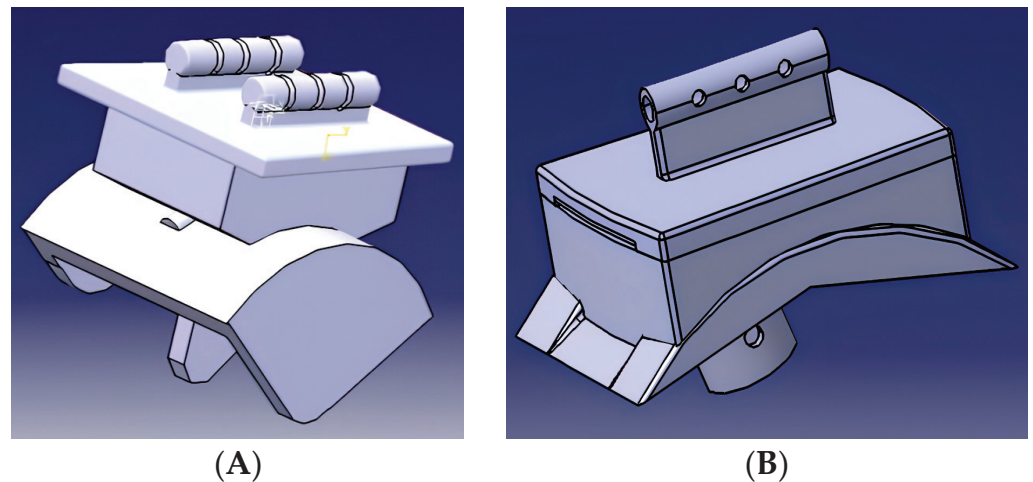


Figure 18. A comparison between designs of the artificial ankle joints: (A) Star Ankle, and (B) Salto-Talaris.

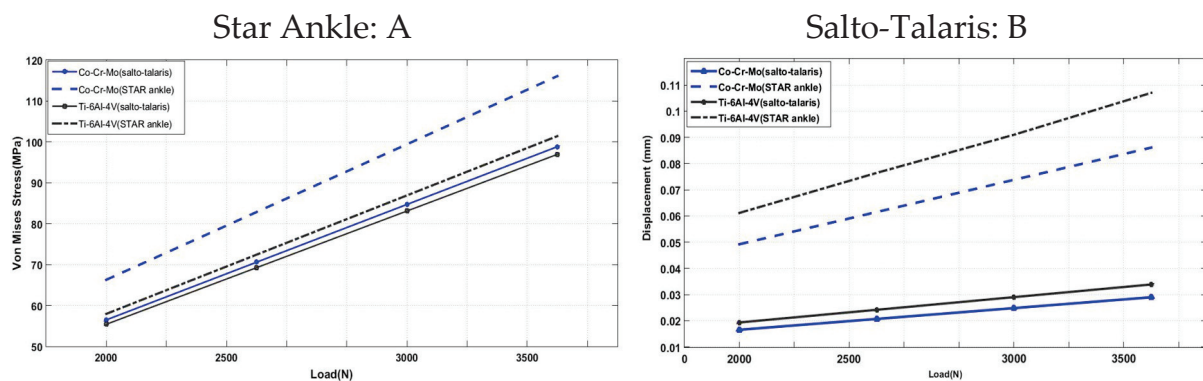


Figure 19. A comparison between values of displacement and maximal stress equivalent to von Mises via the use of the designs of salto-talaris and star ankle.

6. Discussion

The finite element method (FEM) serves as a robust numerical technique that is extensively utilized for intricate numeric analyses under complex conditions and geometries [18]. It finds broad application in assessing ankle and foot models' performance under various loading and material conditions [19], as well as in evaluating the stability of prosthetic ankle joints [20]. Ankle joint designs often feature intricate geometries, posing challenges in deriving analytical solutions for stress distribution and optimal material selection. Total ankle joint replacements have emerged as the preferred treatment for joint failure, aiming to restore range of motion, thus garnering increasing significance. Numerous studies investigate artificial joint performance, spanning both experimental approaches and finite element analyses.

The long-term success or failure of such transplants heavily relies on distributed pressure. Current biomechanical studies aim to develop joints that maintain the natural range of motion and have prolonged lifespans by designing them with ideal shapes and introducing high-quality materials to their manufacture to prevent inflammatory reactions [3]. Similar findings were corroborated by Manvi et al. [15] in their study on designs and material selection. They revealed that implant groups exert higher forces and energy to maintain the implant in the predetermined position of the prosthesis. Their study also highlighted that the top and front of the ankle experience the highest stress, crucial for joint treatment and enhancement. The UHMWPE material emerged as superior in stress resistance, albeit displaying higher displacement values attributed to its structural hierarchy. Jian Yu et al. [17] showed the effect of implant materials for total ankle joint replacement (TAR) in order to

reduce stress on the components of the joint. The materials were compared, showing that the UHMWPE polymeric material is better in terms of stress values, which confirms to us UHMWPE's suitability for joint composition, as well as the validity of our results [17].

Under impact loading, artificial ankle joints typically endure stress levels equal to five times the body's weight during walking [16,19], escalating to approximately ten times during running [21,22], and two to twelve times during jumping. The importance of utilizing UHMWPE elements in ankle joint manufacturing is evident, given their low pressure values compared to other elements, despite exhibiting higher displacement values, facilitating appropriate design and material selection under different loads.

Following vibration analysis using ANSYS, random vibrations in three directions (x, y, z) can be simulated, aiding in designing distortion-resistant joints under varying loading conditions. However, despite its significance, such studies often receive inadequate attention. Elastic strain analysis is pivotal in evaluating design practicality, as evidenced by the absence of red spots, indicating the design's ability to restore its original state. Ștefan-Cătălin Popescu et al. [23] showed that the importance of comparing design and model predictions was compared to loading and displacement conditions, which leads to selecting the best preoperative ankle model and improving the kinematic state in our research. A comparison between the salto-talaris and star ankle designs revealed lower displacement and stress values in the former, affirming its superiority in terms of lesser displacement values and higher equivalent stress. This confirms that the proposed design is the best. This approach offers exciting prospects for improving patient care and optimizing prosthetic joint replacements. We remain optimistic that future research will improve and extend these findings, ultimately improving treatments for individuals with inflammation and joint laxity. In conclusion, the design can be developed in all conditions, including walking, running, jumping, and walking in rough places, which also allows for the selection and development of the appropriate material within these conditions.

This study has several limitations that should be considered for the future optimization of computational resources while maintaining fundamental analysis. The materials selected for comparison may not represent the full range of materials available for artificial ankle joints. Although this research includes different types of metal alloys and one polymeric material, there may be other materials with different properties that could be relevant. Work on developing a new material with low density and high properties is expected in the future. Another limitation of this study is also the lack of inclusion of bone modeling for simplification purposes. While bones are an integral part of the study of biomechanics, their exclusion simplifies the analysis and can be justified depending on the specific focus of the study or the desired level of computational complexity. This choice allows for a comprehensive analysis of stress distribution and biomechanical interactions from all sides, providing a comprehensive view of the effect of the implant on the surrounding bone. This allows us to validate the bone density distributions determined for healthy ankle bones by the bone remodeling model via bone densitometry devices; thereby, bone remodeling results can be analyzed and compared with the true bone density of the specimen.

7. Conclusions

In this research, we introduced significant insights into the design of artificial ankle joints using the CATIA software, aiming to ensure accurate pattern design and enhance reader understanding. Through extensive analyses conducted in ANSYS, leveraging the finite element method (FEM), we have validated the design and compared various materials for ankle joint manufacturing. Furthermore, thorough investigations into the characteristics of skeletons under vibrational stimuli, including random vibrations derived from vibration analysis, have been undertaken.

Based on our conclusive findings, we can now develop an archetype design devoid of directional deformities under diverse load conditions such as running, jumping, or brisk walking on uneven surfaces. Additionally, material selection for joint fabrication can be informed by the stress values and frequency characteristics observed in the joint

structure. Notably, UHMWPE material exhibits lower stress values and offers superior usability compared to other materials, albeit with higher displacement values. Conversely, Ti-13-Nb-13Zr material demonstrates elevated stress levels but with minimal displacement. Meanwhile, Ti-6Al-4V material presents higher stress and displacement values, albeit less than SS316L and Co-Cr-Mo. The opportunity to develop novel materials with lower density and enhanced characteristics, coupled with continued refinement of the design to prioritize human comfort, represents promising avenues for future research endeavors. Addressing these limitations could pave the way for more effective and comfortable artificial ankle joint designs, further advancing the field of biomechanics and joint replacement technology.

Author Contributions: Software, formal analysis, data curation validation, and writing—original draft: H.M.N. and M.A.; conceptualization, methodology, and supervision: T.O.; conceptualization, data curation, and visualization: M.I. and Y.Z.; resources, supervision, and writing—review and editing: A.I. and D.J. All authors have read and agreed to the published version of the manuscript.

Funding: This research received no external funding.

Institutional Review Board Statement: Not applicable.

Informed Consent Statement: Not applicable.

Data Availability Statement: The data that support the findings of this study are available upon reasonable request from the authors.

Conflicts of Interest: The authors declare no conflicts of interest.

References

1. Janice, J.E.; Winter, D.A. Kinetic Analysis of the Lower Limbs During Walking: What Information Can Be Gained from a Three-Dimensional Model? *J. Biomech.* **1995**, *28*, 753–758.
2. Faldini, C.; Mazzotti, A.; Belvedere, C.; Durastanti, G.; Panciera, A.; Geraci, G.; Leardini, A. A New Ligament-Compatible Patient-Specific 3D-Printed Implant and Instrumentation for Total Ankle Arthroplasty: From Biomechanical Studies to Clinical Cases. *J. Orthop. Traumatol.* **2020**, *21*, 16. [CrossRef] [PubMed]
3. Zhao, T.R.; Vahora, M.; Li, Z.J. Computer Aided Artificial Ankle Joints Design. *J. Orthop. Traumatol.* **2018**, *5*, 82–87.
4. Nunley, A.J.; Walton, D. *Ankle Arthrodesis in Case Competencies in Orthopaedic Surgery*; Elsevier: Amsterdam, The Netherlands, 2016.
5. Vickerstaff, J.A.; Miles, A.W.; Cunningham, J.L. A Brief History of Total Ankle Replacement and a Review of the Current Status. *Med. Eng. Phys.* **2007**, *29*, 1056–1064. [CrossRef] [PubMed]
6. Hermus, J.P.S. Complications in Total Ankle Replacement. *Foot Ankle Clin.* **2024**, *29*, 157–163. [CrossRef] [PubMed]
7. Yu, J.; Zhao, D.; Chen, W.M.; Chu, P.; Wang, S.; Zhang, C.; Huang, J.; Ma, X. Finite Element Stress Analysis of the Bearing Component and Bone Resected Surfaces for Total Ankle Replacement with Different Implant Material Combinations Fudan. *BMC Musculoskelet. Disord.* **2022**, *45*, 1783–1789. [CrossRef]
8. Mrcsa, R.K.; Siddique, M.S. Stresses in the Ankle Joint and Total Ankle Replacement Design. *Foot Ankle Surg.* **2011**, *17*, 58–63. [CrossRef]
9. Zhang, Y. Computational Modelling of Biomechanics and Biotribology for an Artificial Ankle Joint. In *Computational Modelling of Biomechanics and Biotribology in the Musculoskeletal System*; Elsevier: Amsterdam, The Netherlands, 2021; pp. 499–515. ISBN 9780128195314.
10. Leardini, A.; Connor, J.O.; Giannini, S. Biomechanics of the Natural, Arthritic, and Replaced Human Ankle Joint, Alberto Leardini. *J. Foot Ankle Res.* **2014**, *7*, 8–20. [CrossRef] [PubMed]
11. Earll, M.; Wayne, J.; Brodrick, C.; Vokshoor, A.; Adelaar, R. Contribution of the Deltoid Ligament to Ankle Joint Contact Characteristics: A Cadaver Study. *Foot Ankle Int.* **1996**, *17*, 317–324. [CrossRef] [PubMed]
12. Li, Y.; Yang, C.; Zhao, H.; Qu, S.; Li, X.; Li, Y. New Developments of Ti-Based Alloys for Biomedical Applications. *Materials* **2014**, *7*, 1709–1800. [CrossRef] [PubMed]
13. Schneider, S.G.; Nunes, C.A.; Rogero, S.O.; Higa, O.Z.; Bressiani, J.C. Mechanical Properties and Cytotoxic Evaluation of the Ti-3Nb-13Zr Alloy. *Biomecânica* **2000**, *8*, 84–87. [CrossRef]
14. Shen, F.-W. Ultrahigh-Molecular-Weight Polyethylene (UHMWPE) in Joint Replacement. In *Biomedical Polymers*; CRC Press: Boca Raton, FL, USA, 2007; ISBN 9781420044515.
15. Manvi, M.; Pradeepa, S.K.; Savadi, R. Finite Element Analysis on Stainless Steel and Titanium Alloy Used as Ankle Joint Replacement Implant Materials. *Int. J. Eng. Dev. Res.* **2016**, *4*, 586–592.
16. Oliveira, D.S.; Rodrigues, S. Biomechanics of the Total Ankle Arthroplasty Stress Analysis and Bone Remodeling. Master's Thesis, Técnico Lisboa, Lisboa, Portugal, 2013; pp. 72–363.

17. Jian, Y.; Dahang, Z.; Chen, W.; Chu, M.; Wang, P. Finite Element Stress Analysis of the Bearing Component and Bone Resected Surfaces for Total Ankle Replacement with Different Implant Material Combinations. *BMC Musculoskelet. Disord.* **2022**, *45*, 70.
18. Nazha, H.M.; Szávai, S.; Juhre, D. An Overview of Mathematical Methods Applied in the Biomechanics of Foot and Ankle–Foot Orthosis Models. *J* **2023**, *7*, 1–18. [CrossRef]
19. Bischoff, J.E.; Dharia, M.; Hertzler, J.S. Evaluation of Total Ankle Arthroplasty Using Highly Crosslinked Ultrahigh Molecular-Weight Polyethylene Subjected to Physiological Loading. *Foot Ankle Int.* **2019**, *40*, 880–887. [CrossRef] [PubMed]
20. Stauffer, R.N.; Chao, E.Y.; Brewster, R.C. Force and Motion Analysis of the Normal, Diseased, and Prosthetic Ankle Joint. *Clin. Orthop. Relat. Res.* **1977**, *127*, 189–196. [CrossRef]
21. Miller, M.C.; Smolinski, P.; Conti, S.; Galik, K. Stresses in Polyethylene Liners in a Semiconstrained Ankle Prosthesis. *J. Biomech. Eng.* **2004**, *126*, 636–640. [CrossRef] [PubMed]
22. Burdett, R.G. Forces Predicted at the Ankle during Running. *Med. Sci. Sports Exerc.* **1982**, *14*, 308–316. [CrossRef] [PubMed]
23. Popescu, Ș.C. Mechanical Analysis of Scandinavian Total Ankle Replacement Prostheses through Finite Element. *Int. J. Mechatron. Appl. Mech.* **2018**, *4*, 27–31.

Disclaimer/Publisher’s Note: The statements, opinions and data contained in all publications are solely those of the individual author(s) and contributor(s) and not of MDPI and/or the editor(s). MDPI and/or the editor(s) disclaim responsibility for any injury to people or property resulting from any ideas, methods, instructions or products referred to in the content.

Article

Simulation-Based Design of a Cam-Driven Hydraulic Prosthetic Ankle

Anna Pace ^{1,2,*}, James Gardiner ³ and David Howard ¹

¹ School of Science, Engineering and Environment, University of Salford, Salford M5 4WT, UK; d.howard@salford.ac.uk

² Soft Robotics for Human Cooperation and Rehabilitation, Istituto Italiano di Tecnologia, 16163 Genoa, Italy

³ Department of Sport and Exercise Sciences, Manchester Metropolitan University, Manchester M15 6BX, UK; james.gardiner@mmu.ac.uk

* Correspondence: anna.pace@iit.it or a.pace1@edu.salford.ac.uk

Abstract: Background/Objectives: A cam-driven hydraulic prosthetic ankle was designed to overcome the weaknesses of commercial prostheses and research prototypes, which largely fail to mimic the energy-recycling behaviour of an intact ankle, resulting in poor walking performance for lower-limb prosthesis users. **Methods:** This novel device exploits miniature hydraulics to capture the negative work performed during stance, prior to push-off, in a hydraulic accumulator, and return positive work during push-off for forward body propulsion. Two cams are used to replicate intact ankle torque profiles based on experimental data. The design process for the new prosthesis used a design programme, implemented in MATLAB, based on a simulation of the main components of the prosthetic ankle. **Results:** In this paper, we present the design programme and explain how it is used to determine the cam profiles required to replicate intact ankle torque, as well as to size the cam follower return springs. Moreover, a constraint-based preliminary design investigation is described, which was conducted to size other key components affecting the device's size, performance, and energy efficiency. Finally, the feasible design alternatives are compared in terms of their energy losses to determine the best design with regard to minimising both energy losses and device size. **Conclusions:** Such a design approach not only documents the design of a particular novel prosthetic ankle, but can also provide a systematic framework for decomposing complex design challenges into a series of sub-problems, providing a more effective alternative to heuristic approaches in prosthetic design.

Academic Editor: Arnab Chanda

Received: 2 December 2024

Revised: 17 January 2025

Accepted: 23 January 2025

Published: 28 January 2025

Citation: Pace, A.; Gardiner, J.; Howard, D. Simulation-Based Design of a Cam-Driven Hydraulic Prosthetic Ankle. *Prosthesis* **2025**, *7*, 14. <https://doi.org/10.3390/prosthesis7010014>

Copyright: © 2025 by the authors. Licensee MDPI, Basel, Switzerland. This article is an open access article distributed under the terms and conditions of the Creative Commons Attribution (CC BY) license (<https://creativecommons.org/licenses/by/4.0/>).

Keywords: prosthetics; prosthetic ankle; prosthetic foot; simulation; computational modelling; design; hydraulics; cam

1. Introduction

Individuals with lower-limb amputations still face daily challenges due to the limited performance of commercial passive (i.e., unpowered) prosthetic feet—whether energy storage and return (ESR) or conventional prostheses [1]—which still falls short of the human foot functionality. In particular, a major problem is that they cannot generate the plantarflexion moment required during push-off for forward propulsion, failing to emulate the missing plantarflexion musculature, leading to a consequent decrease in push-off power generation. Push-off power peak values for passive prostheses are, indeed, generally less than half those measured in healthy subjects, which are usually between 3.5 and 4.5 W/kg [2,3]. As a result, prosthesis users typically exhibit gait asymmetries

due to compensatory strategies, leading to higher energy consumption when compared to healthy subjects [4–7].

Over the last two decades, many research efforts have been made to better replicate the anatomically intact ankle's energy storage and release mechanism and/or its torque-versus-angle curve, through both powered and unpowered designs. A well-known active (i.e., powered) prosthetic foot that has reached the market is the Ottobock Empower, which can actively generate power during push-off. However, although push-off is improved, its energy recycling performance is no better than passive carbon fibre ESR prosthetic feet [8]. In addition, active designs show limitations related to the use of batteries and electric motors, including increased weight, size, and cost, as well as reduced user autonomy [9]. These limitations are compounded by a lower acceptance rate due to the complex control architectures that increase the cognitive load on the user [10].

Active and passive ESR concepts can mainly be classified as clutch-and-spring or hydraulic prostheses [11]. The former are usually complex designs that provide discrete, non-biomimetic control of the ankle joint, and are often large and heavy. Hydraulics is used in commercial prostheses mainly for damping, and for ground and speed adaptation purposes, as seen in the Meridium and Triton Smart Ankles (Ottobock), the Elan (Blatchford), and the Freedom Kinnex 2.0 (Proteor). Some active research designs, including electrohydrostatic or electrically powered hydraulic actuators, can actively power push-off and generate biomimetic ankle torques, but are also often large and heavy [11].

Nevertheless, as opposed to clutch-and-spring concepts, hydraulics is well suited to both providing biomimetic ankle torques and storing and returning energy over the gait cycle by including a hydraulic accumulator. For active devices, this should lead to smaller actuators and batteries. Furthermore, hydraulics is also well suited to miniaturisation (due to high power densities).

Therefore, driven by the desire to improve the quality of life of lower-limb prosthesis users, and aware of the increasing number of people living with a lower-limb amputation, mainly because of vascular diseases [12], we designed a novel prosthetic ankle (Figure 1) that exploits the advantages of hydraulics and uses an accumulator for recycling energy at the ankle joint [11]. In addition, it provides biomimetic ankle joint torques by including two cam-driven rams.



Figure 1. The new hydraulic ankle prosthesis described in [11,13]: a solid model including the main components (cams, rollers, followers, rams) and a foot consisting of two carbon fibre laminates.

Via a gearbox, the prosthetic ankle joint drives a camshaft on which two cams are mounted and, in turn, these drive two miniature hydraulic rams. The “stance cam-ram system” stores the eccentric (negative) work performed during mid-stance (i.e., from foot flat until ankle maximum dorsiflexion) by pumping oil into the accumulator, while the “push-off system” performs concentric (positive) work during push-off (i.e., from ankle

maximum dorsiflexion to maximum plantarflexion) through fluid flowing from the accumulator to the ram, providing forward propulsion. Each ram is connected to a tank during load acceptance (i.e., from heel strike to foot flat) and swing, as well as during the working phase of the other ram (i.e., push-off for the stance cam-ram system, and mid-stance for the push-off cam-ram system). A detailed description of the design can be found in [11,13].

The performance of the new design was assessed using a simulation model, implemented in MATLAB, which simulates the operation of the new device over the whole gait cycle (results reported in [11]). The results show that the prosthesis can replicate the torque of an intact ankle during the working phases of the two cam-ram systems. Moreover, 78% of the total eccentric work stored by the prosthetic ankle during one gait cycle (i.e., the energy input) is returned as concentric work, primarily during push-off; 14% is stored in the accumulator and can power future gait cycles; and 8% is lost. Furthermore, the main components of the system, which were sized using a simulation-based design programme, are physically realistic and the prosthesis matches the size and mass of the missing anatomy [11].

In this paper, we describe in detail the simulation-based design programme, which was implemented in MATLAB. MATLAB is a commercial programming and numeric computing environment widely used in the scientific community due to its computing capabilities for simulation and modelling. Moreover, simulations represent an effective way to virtually test and optimize designs, reducing development time and the costs and risks associated with physical prototyping, although their reliability depends on the model accuracy and the assumptions used. The design programme we present uses the aforementioned simulation model to design the cam profiles, such that they generate the required intact ankle torque profiles, and also the cam follower return springs. We also describe our preliminary design investigation, which used the aforementioned design programme to specify other key components based on two design objectives, namely minimising energy losses and keeping the device size acceptably small.

We believe that such a design programme can provide a systematic framework to decompose complex design challenges into manageable sub-problems, while basing the process on a rigorous analysis of the mechanical design of the system and its dynamics.

2. Materials and Methods

The novelty of the new design lies in the use of a hydraulic accumulator to store and return energy, and cam-driven hydraulic rams to provide biomimetic ankle torques. The two cam profiles are designed to replicate the torque-versus-angle curve of the ankle joint of a healthy subject. This was achieved using a design programme implemented in MATLAB (R2018b, The MathWorks, Inc., Natick, MA, USA), which incorporates a simulation of the whole system over the whole gait cycle based on a detailed mathematical model including all significant sources of energy loss. As well as calculating the two cam profiles, the design programme also sizes the two cam-follower return springs to ensure continuous contact between each cam and the corresponding roller-follower. The design programme was used in a preliminary design investigation and, to simplify the process, the design parameters were classified as primary and secondary independent variables, dependent variables, and constants. This classification enabled a sequential design process whereby the design variables were assigned in order of importance and, at each stage, the subset of feasible designs was reduced until, finally, the best design was identified, which is the one described in [11].

The following subsections describe the simulation-based design programme; the classification of the design parameters; and the preliminary design investigation.

2.1. Simulation-Based Design Programme

The MATLAB design programme uses an iterative approach with three nested loops: an outer loop to size the cam follower return springs; a middle loop to determine the cam profiles; and an inner time-stepping loop to model the states of the valves, the dynamics of the cam-ram systems, and the filling and emptying of the accumulator. In other words, the inner loop simulates the whole system over one gait cycle, and the two outer loops automate two aspects of the design process.

The middle loop converges iteratively to calculate the two cam profiles that enable the system to match the ankle torque versus angle curve of an intact ankle (from in vivo experimental data [14]), during the working phases of the two cam-rams. Iterations are necessary to calculate the two cam profiles because the total camshaft torque (sum of the two cam torques) is determined by the dynamics of the two cam-rams, which are in turn based on velocities and accelerations that depend upon the cam profiles (so there is a circular dependency). In other words, simulation over the gait cycle requires a priori knowledge of the cam profiles. Consequently, an initial estimate of the two cam profiles is used to run the simulation model and calculate the actual camshaft torque curves in the two working phases. The error between the required and the actual (i.e., calculated) torques is, in turn, used in the following iteration to update the cam profiles. The iteration loop is repeated until the error is negligible over the two working phases. Therefore, the calculation of the cam profiles is described below under the two following headings.

2.1.1. Estimating an Initial Cam Profile

The method for estimating an initial cam profile is the same for both cam-ram systems, so it is explained for the stance cam-ram only. The purpose of each cam profile is to define the ratio of piston incremental displacement to cam incremental angle ($\frac{dy}{d\theta_c}$) as a function of cam rotation angle θ_c . All friction terms were neglected for this initial estimate, as well as the torque generated by the non-working cam-ram that is connected to a tank. Therefore, it can be assumed that, during its working phase, the stance cam torque ($T_{cSTANCE}$) equals the required camshaft torque (T_{c_r}), and the work performed by the stance cam is equal to the work performed by the piston on the hydraulic fluid:

$$W = T_{cSTANCE} d\theta_c = T_{c_r} d\theta_c = F_h dy. \quad (1)$$

By rearranging Equation (1), the initial estimate of $\frac{dy}{d\theta_c}$ during the stance cam's working phase is

$$\frac{dy}{d\theta_c} = \frac{T_{c_r}}{F_h} = \frac{T_{c_r}}{(P - P_{atm})A}, \quad (2)$$

where neglecting the piston O-ring friction causes the hydraulic ram force to be the product of the gauge cylinder pressure and piston area ($F_h = (P - P_{atm})A$, with $P = P_{cyl} = P_{acc}$ because all friction terms between the cylinder and accumulator (i.e., pipes, fittings, valve) are neglected, and $P_{acc} = 0.90P_{max}$).

The cam profile is also followed during the non-working phase, i.e., when the ram is connected to a tank. So, for cam angles within the working range, the ratios $\frac{dy}{d\theta_c}$ in the non-working phase are determined by the interpolation of the working phase results. For cam angles outside of the working range, a constant cam radius is required to avoid unnecessary piston displacement in the non-working phase and hence minimise friction losses. For this reason, the ratio $\frac{dy}{d\theta_c}$ is set to zero for cam angles outside the range seen during the working phase.

Consequently, the overall piston displacement (y) is evaluated by cumulatively summing the incremental changes $\Delta y = \frac{dy}{d\theta_c} \Delta\theta_c$, with $y_{min} = 0$ (see Figure 2), and this is used

to calculate the cam profile. Specifically, the profile is obtained by connecting the contact points P between the cam and roller, whose coordinates (x_P, y_P) are evaluated in the cam frame as follows (refer to Figure 3 and Table A1 for the nomenclature, and to [13] for a full explanation):

$$\begin{bmatrix} x_P \\ y_P \end{bmatrix}_{cam} = \begin{bmatrix} \cos\theta_c & \sin\theta_c \\ -\sin\theta_c & \cos\theta_c \end{bmatrix} \begin{bmatrix} e + r\sin\alpha \\ (a + y) - r\cos\alpha \end{bmatrix}. \quad (3)$$

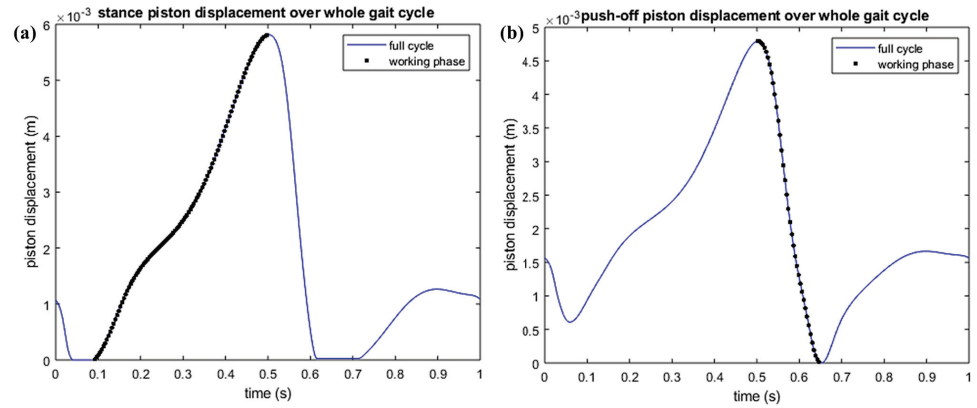


Figure 2. Piston displacement (y) during the working phase (black dots) and over the complete gait cycle (blue solid line) for the stance cam-ram (a) and the push-off cam-ram (b). During the non-working phases, the working phase cam surface is followed within its range of cam angles; outside this range, the piston displacement is constant (flat sections of blue line).

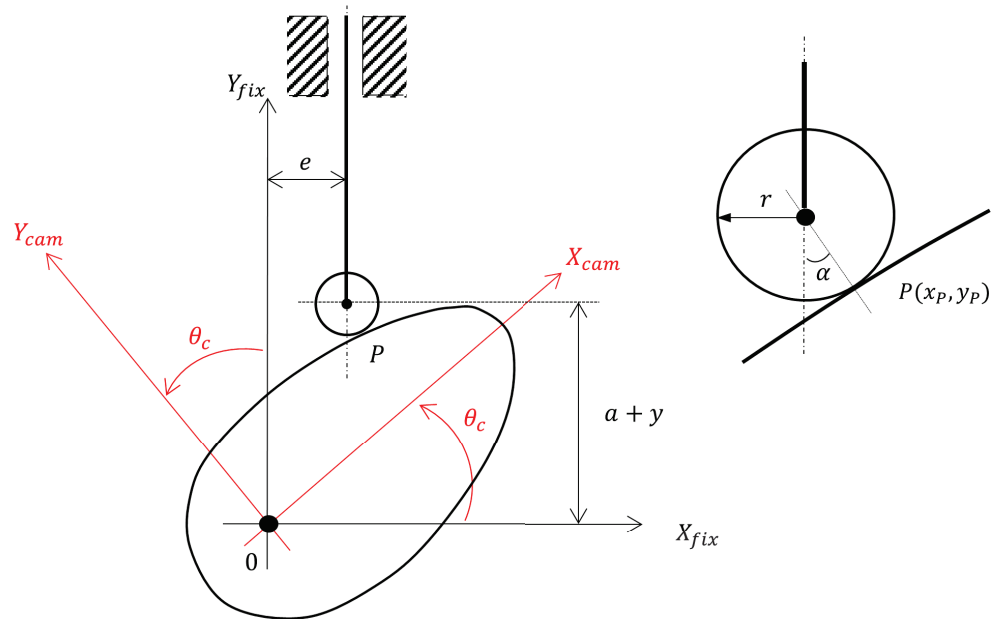


Figure 3. Roller-follower on cam surface with the cam frame (X_{cam}/Y_{cam}) rotated anticlockwise by an angle θ_c relative to the fixed frame (X_{fix}/Y_{fix}). Variable e defines the distance between the centre line of the follower and the centre line of the camshaft, while a describes the starting position of the follower in the vertical direction. On the right-hand side: a magnified view of the roller-follower shows the roller radius r , the cam pressure angle α , and the contact point $P(x_P, y_P)$.

2.1.2. Updating Cam Profiles

The simulation model used to iteratively update the cam profiles simulates the operation of the whole system over one gait cycle, evaluating the changes in energy stored and released in the accumulator, and the total ankle torque in output from the device. Moreover, it includes all the friction terms and the torque generated by the non-working cam-ram that

were previously neglected. Its only input is the ankle angle-versus-time profile obtained from experimental gait data, which is the only variable the user can govern once the new design is established.

For the first iteration, the initial cam profiles drive the simulation model. This allows for an accurate calculation of the actual camshaft torque T_c , which is used to update $\frac{dy}{d\theta_c}$ over the working phases of the cams and, hence, the cam profiles, through a modified version of Equation (2) as follows:

$$\left(\frac{dy}{d\theta_c}\right)_{n+1} = \frac{T_{c_{r_{n+1}}}}{F_{h_{n+1}}} \simeq \frac{T_{c_{r_n}} + T_{c_{error}}}{F_{h_n}} = \left(\frac{dy}{d\theta_c}\right)_n + \frac{T_{c_{error}}}{F_{h_n}}. \quad (4)$$

In other words, $\frac{dy}{d\theta_c}$ for iteration $n + 1$ is equal to the previous $\frac{dy}{d\theta_c}$ for iteration n plus an adjustment corresponding to adding the camshaft torque error $T_{c_{error}} = T_{c_{r_n}} - T_{c_n}$ (i.e., required minus actual camshaft torque). As the iterative algorithm converges, there are diminishing changes to the cam-ram dynamics, and the error approaches zero. F_{h_n} in Equation (4) is the actual ram force including piston O-ring friction. For the second and subsequent iterations, the updated cam profile calculated using Equation (4) is used to drive the simulation model.

2.1.3. Sizing the Follower Return Springs

The outer loop of the design programme specifies the two linear return springs, which are part of the follower assembly and ensure cam–roller contact.

An iterative approach is also necessary in this case: knowledge of the normal forces F_n acting between the cams and the rollers over the gait cycle is necessary to specify the follower return springs, but F_n calculation itself depends on the follower return-spring parameters. In the first iteration, the return springs were omitted, and the simulation model was run to evaluate the normal cam forces without return springs ($F_{n_{NOspring}}$) over the whole gait cycle. These data were used to calculate the minimum return-spring force ($F_{s_{required}}$) at every point in the gait cycle that would make F_n greater than or equal to a minimum positive value ($F_{n_{desired}} = 20 \text{ N}$), which was chosen to guarantee cam operation under only compressive (positive) normal forces between cam and roller. In other words,

$$F_{s_{required}} = F_{n_{desired}} - F_{n_{NOspring}}. \quad (5)$$

A search algorithm was implemented that found the ‘best’ return springs, i.e., those minimising the area included between the linear spring characteristic and the $F_{s_{required}}$ curve. This algorithm is explained in detail in [13]. As explained above, multiple iterations of this method should be used to converge on a solution, with the new values of F_n replacing $F_{n_{NOspring}}$.

2.2. Classification of the Design Parameters

In order to conduct the preliminary design of the main components of the system, firstly, all the design parameters were classified into three categories: *independent* variables, *dependent* variables, and *constants* (see [13] for a complete description).

The independent variables can be further split into *primary* and *secondary*. The former are those that strongly influence the magnitude of the forces acting on the cam-ram components (i.e., cam, roller, follower, and bearings), which in turn determines the selection of these components, specifically their size, so that they can withstand those forces. Furthermore, by determining the forces in the system, these primary independent variables are also expected to directly affect the energy efficiency of the system. Conversely, secondary

independent variables do not have a strong effect on the size of the cam-ram components. Nevertheless, they likely influence energy efficiency and the overall system dimensions.

To minimise the number of primary independent variables and thus simplify the design investigation, we initially identified three primary independent variables: gear ratio, maximum hydraulic pressure in the accumulator, and hydraulic ram bore. The gearbox, placed between the ankle and the camshaft, determines the camshaft torque; a change in its ratio directly affects the forces acting on the cam-ram components. Similarly, the maximum hydraulic pressure and the ram bore determine the hydraulic force acting on the piston and, in turn, the forces acting on the other cam-ram components.

We selected sensible values for these three variables (see Table 1) based on upper or lower limits that we thought provided reasonable constraints on the components' sizes. A minimum gear ratio (GR) of one corresponds to a system without a gearbox and, consequently, zero gearbox losses and a simpler design, which would be a significant advantage. Two higher ratios were included in case a ratio of one leads to overly large forces and, hence, large cam-ram components. The ram bores (D) were chosen to (a) limit the size of the prosthesis by setting a maximum bore of 20 mm and (b) avoid the efficiency penalties associated with smaller hydraulic rams [15–19] by setting a minimum bore of 5 mm. Neubauer et al. [20] used a ram bore of approximately 13 mm in their hydraulic ankle–foot orthosis. They also used pressures around 100 bar demonstrating that this is practically feasible. Industrial hydraulic systems typically operate at pressures of up to 200 bar. Hence, for this application, 100 bar was set as the upper limit of the hydraulic pressure (P_{max}) with two smaller values of 20 bar and 50 bar. By combining these values for the three primary independent variables, 27 possible configurations are obtained for the two cam-ram systems.

Table 1. Sensible values chosen for the three primary independent variables.

Gear Ratio GR	Max Pressure P_{max} (bar)	Ram Bore D (mm)
1	20	5
3	50	10
5	100	20

The secondary independent variables include two that were assumed to be important enough for optimum values to be investigated, namely the lowest position of the follower, a (Figure 3), and the follower offset, e (Figure 3).

Other secondary independent variables were assumed to be of lower importance and/or fairly arbitrary, but sensible values could be chosen based on practical constraints. These include the following:

- Diameter and length of the pipes between the rams and the accumulator, $D_{pipe} = 5$ mm and $L_{pipe} = 50$ mm. These are realistic values, and the associated flow losses were assumed to have a negligible effect on the working phase performances of the cam-rams, during which power flows are large. This assumption was confirmed through a sensitivity study explained in [13].
- An accumulator volume of $V_A = 250$ cc was chosen, which was considered small enough to be integrated within the prosthesis pylon, as envisaged, and large enough to store energy over many gait cycles [11,13].

Finally, some design constraints were defined to guide the preliminary design investigation:

- To limit the overall size of the cam-rams, the total length of the hydraulic rams, when the piston is at the end of its outstroke, should be no more than 150 mm. Given that a

cylinder for pressures up to 100 bar has an instroke length of approximately 100 mm, based on hydraulic cylinder catalogues (HYDAIRA [21] for instance), the maximum stroke was set to $stroke_{max} = 50$ mm.

- To limit the overall size of the cam-rams, the upper limit for both the offset e and the distance a was set to $a_{max} = e_{max} = 50$ mm.
- Considering the above bounds, a maximum roller diameter of $d_{roller_{max}} = 30$ mm was set.
- The maximum cam pressure angle was set to $|\alpha|_{max} = 30^\circ$ because cam design handbooks generally suggest limiting the pressure angle to 30° to avoid high lateral forces and, hence, high follower friction. The same 30° limit was also used by Realmuto et al. [22] in the design of their powered ankle prosthesis.

2.3. Preliminary Design Investigation

A preliminary design investigation was conducted to establish a set of “close to optimal” design parameters, which were then used to simulate the potential performance of the novel design; the results are reported in [11,13]. The following subsections describe the four main stages of this preliminary design investigation.

2.3.1. Determine a Subset of Feasible Designs (Primary Independent Variables)

The first stage of the preliminary design investigation reduced the number of feasible designs (i.e., combinations of primary independent variables) by eliminating designs that are unrealistic in terms of size.

We started by considering a gear ratio of $GR = 1$, i.e., a system without a gearbox. This reduced the number of combinations to be analysed from 27 to 9. For each of the nine combinations used for both cam-ram systems (eighteen cases), the length of the piston stroke was estimated to exclude those combinations with a stroke greater than $stroke_{max} = 50$ mm. Neglecting all losses, the stroke lengths were estimated by considering the negative and the positive ankle work performed during the working phases of the stance and the push-off systems, respectively, and, hence, the corresponding energy to be stored in and released from the accumulator. The total work performed by the hydraulic rams over their working phases is $W = F_{h_{nominal}} \cdot stroke_{nominal}$. Rearranging for piston stroke and assuming a constant accumulator pressure, this gives:

$$stroke_{nominal} = \frac{W}{F_{h_{nominal}}} = \frac{W}{P_{max} A} = \frac{W}{P_{max} \pi \left(\frac{D}{2}\right)^2} \quad (6)$$

The energy stored during the working phase of the stance system amounts to approximately 18.9 J, while the energy released during the working phase of the push-off system amounts to approximately 11.9 J, obtained by numerical integration of the ankle power (data collected by Bari for healthy level walking at a self-selected speed [14]).

2.3.2. Determine the Roller Diameters

The second stage of the preliminary design investigation was to find roller diameters (a dependent variable) that can withstand the cam–roller contact forces. For each feasible design deriving from the previous design stage, the MATLAB simulation model was used to evaluate the maximum value of the normal force ($F_{h_{nominal}}$) acting between the cam and the roller for each of the two working phases, generated by the maximum hydraulic force acting on each ram ($F_{h_{nominal}} = P_{max} \pi \left(\frac{D}{2}\right)^2$). Then, the minimum roller diameter (d_{roller}) able to bear the maximum force was identified considering the quoted maximum dynamic radial loads from catalogues: SKF [23] for rollers with a diameter bigger than 16 mm; IKO [24,25] for rollers with a diameter smaller than 16 mm.

Note that to run the MATLAB simulation model for the first time, the roller diameter was initially set to 26 mm, with this being the largest available in [23] that satisfied the design constraint $d_{roller} \leq 30$ mm. Also, arbitrary initial values for distance a (40 mm) and offset e (15 mm) were used.

The simulation model was then rerun with the identified smaller roller diameter to verify that the resulting maximum normal force did not require further modification of the roller selection. Conversely, if the minimum roller diameter had exceeded the maximum available value (26 mm) that satisfies the constraint $d_{roller} \leq 30$ mm, then this case (i.e., one design used in one working phase) would have been excluded from the next stage of the design process.

2.3.3. Determine the Two Secondary Independent Variables, a and e

In the third stage of the preliminary design investigation, the feasible designs identified in the previous subsections (satisfying $stroke \leq 50$ mm and $d_{roller} \leq 30$ mm) were further analysed to find good values for the two secondary independent variables, distance a and offset e , which affect the working phase performance of the two cam-rams. Specifically, altering a and e changes the geometry shown in Figure 3 and, hence, the cam pressure angle α .

Given the previously defined design constraints, the aim was to find values of a and e which satisfy $a_{max} = e_{max} = 50$ mm and keep the cam pressure angle below 30° during the two cam-ram systems' working phases, while also minimising a and e as far as possible. All simulations in this third stage used the correct roller diameter from the previous step.

The process implemented in MATLAB to identify good values for a and e followed the steps below:

1. The distance a was initially set to its upper limit ($a = a_{max} = 50$ mm to minimise cam pressure angle α , and hence follower friction, because increasing a reduces α [13]).
2. A search was undertaken over the range $0 \leq e \leq 50$ mm to find the optimum value of e minimising cam pressure angle α . Specifically, for each value of e , the MATLAB simulation model was run to find the largest absolute value of cam pressure angle, $\max(|\alpha|)$, during the working phase of the cam-ram (the objective function to be minimised).
3. Depending on the optimum (minimum) value of $\max(|\alpha|)$, there were three options:
 - (a) If $\min(\max(|\alpha|)) \geq 30^\circ$, that combination of primary independent variables was eliminated.
 - (b) If $25^\circ \leq \min(\max(|\alpha|)) < 30^\circ$, that combination was considered acceptable with the current value of a and the optimum value of e .
 - (c) If $\min(\max(|\alpha|)) \ll 30^\circ$, smaller values of the distance a were tried to reduce the size of the cam-ram system. For each new value of a , step 2 was repeated.

2.3.4. Compare Energy Losses

In the fourth and last stage of the preliminary design investigation, for each cam-ram system, the design alternatives deriving from the previous design stage were compared in terms of their energy losses. Power flows were calculated, and then the energy balance over the cam-ram's working phase was obtained by integration (see [13] for details). For each design alternative, four energy terms were considered:

- The *energy input*: from the ankle for the stance system; from the accumulator for the push-off system.
- The *energy output*: the energy stored in the accumulator for the stance system, and the energy output to the ankle for the push-off system.

- The *energy lost* because of friction between cam and roller, in the roller, at the follower guide, and at the cylinder O-ring (gearbox friction is zero because there is no gearbox).
- The *energy stored* in the mechanical components of the system, including strain energy in the parallel torsional spring, and the kinetic and potential energies of the roller and follower.

It should be noted that an early-stage simulation model was used for the preliminary design investigation, which only modelled the friction losses directly associated with the two cam-rams during their working phases. Therefore, losses in the two cam-ram systems during their non-working phases, pipe flow losses, losses in the accumulator because of heat transfer, and the two follower return springs were neglected. However, it was assumed these would have little effect on the selection of cam-ram design parameters.

3. Results

The simulation-based design programme, by simulating the operation of the whole system over one gait cycle, successfully generated cam profiles outputting an ankle torque that closely matches that of an intact ankle, while allowing energy storage and release in the accumulator. Five iterations of the simulation model were used because the residuals (i.e., T_{error}) for the two working phases decreased as the number of iterations increased from one to five, after which they increased slightly up to the eighth iteration and then remained constant. The maximum difference between the required and the actual torque was just under 0.02 Nm in the working phases.

When it came to the size of the follower return springs, it was found that multiple iterations of the search algorithm were unnecessary to converge on a solution. When the spring parameters from the first iteration were included in the simulation model to re-evaluate the normal cam forces, F_n was indeed greater than $F_{n_{desired}}$ over the whole gait cycle, and the smallest value of F_n was just less than 22 N. This was deemed to be sufficiently accurate as the chosen $F_{n_{desired}} = 20$ N was to some extent arbitrary.

Then, by replacing the values of energy stored and released in Equation (6), together with the maximum hydraulic pressure and the ram bore from Table 1, the results shown in Table 2 were obtained. The five bold values correspond to those combinations of primary independent variables with a stroke smaller than $stroke_{max}$, which were therefore carried forward to the next stage of the design process. Interestingly, the same five combinations of the primary independent variables (feasible designs) were carried forward for both cam-ram systems.

Table 2. Nominal stroke length (mm) for the stance piston and the push-off piston (considering a system without a gearbox). Bold values correspond to stroke lengths smaller than the upper limit $stroke_{max} = 50$ mm.

<i>D</i> (mm)	STANCE <i>P</i> _{max} (bar)			PUSH-OFF <i>P</i> _{max} (bar)		
	100	50	20	100	50	20
20	6	12	30	4	8	19
10	24	48	120	15	30	76
5	96	193	481	61	121	303

The roller selection procedure was repeated for each of the five feasible designs for both cam-ram systems (10 cases, as shown in Table 2), and it did not reduce the number of feasible designs (i.e., no minimum roller diameters exceeded the maximum available value of 26 mm, satisfying the constraint $d_{roller} \leq 30$ mm). The minimum roller diameter was 19 mm for one feasible design ($P_{max} = 100$ bar and $D = 20$ mm) and 16 mm for the other four feasible designs. This result applied to both cam-ram systems.

As a result of the third stage of the design process, in which good values for the two secondary independent variables (distance a and offset e) were determined, the number of feasible designs (combinations of primary independent variables) was reduced from five to two as shown in Table 3. For the first of these, three alternative values of the distance a were carried forward to the next stage of the design process. This result applied to both cam-ram systems.

Table 3. Design alternatives remaining after evaluating the roller diameters and the two secondary independent variables a and e for the subset of feasible designs. The design parameters are the same for both cam-ram systems except for the offset e of the 4th design alternative.

Combination (Primary Indep. Variables)	Roller \varnothing (mm)	Distance a (mm)	Offset e (mm)	min (max $ \alpha $) (°)
(1) $GR = 1$ $P_{max} = 100$ bar $D = 20$ mm	19	50	19	17.35, (15.96 for push-off)
(2) $GR = 1$ $P_{max} = 100$ bar $D = 20$ mm	19	40	19	20.83, (19.59 for push-off)
(3) $GR = 1$ $P_{max} = 100$ bar $D = 20$ mm	19	30	19	26.74, (25.27 for push-off)
(4) $GR = 1$ $P_{max} = 50$ bar $D = 20$ mm	16	50	36, (37 for push-off)	29.72, (28.56 for push-off)

Results of the energy analysis conducted in the last stage of the design process showed that, for both cam-ram systems, the third design alternative in Table 3 has the smallest energy losses and also the smallest value of distance a (30 mm), which helps to minimise the size of the cam-ram system. Hence, the recommended design parameters for both cam-ram systems are those shown for the third design alternative in Table 3. The associated energy losses for the stance and the push-off cam-ram systems are shown in Table 4.

Table 4. Energy balance for the two cam-ram systems over their working phases for the third combination of Table 3 ($P_{max} = 100$ bar; $D = 20$ mm; $a = 30$ mm; and $e = 19$ mm).

	STANCE System		PUSH-OFF System	
	Energy (J)	%	Energy (J)	%
<i>Energy input</i>	18.91	100	14.73	100
<i>Energy output</i>	18.25	96.53	11.88	80.65
<i>Energy lost</i>	0.26	1.37	0.29	1.95
<i>Energy stored in the system</i>	0.40	2.10	2.56	17.40

4. Discussion

The simulation-based design programme described in this paper successfully enables the specification of the cam profiles and the follower return springs in the energy storage and return prosthetic ankle presented in [11].

Five iterations are enough for the design programme to determine cam profiles able to generate a prosthetic ankle torque matching that of a healthy subject over the two cam-ram working phases (with an error less than 0.02 Nm). One iteration is enough for the design programme to size return springs that guarantee satisfactory cam–roller contact. The design programme also calculates the magnitude of the forces acting within the two cam-ram

systems, which are used to determine the sizes of the main components so that they can withstand those forces.

The design programme is used to conduct a preliminary design investigation to specify the key components of the prosthesis affecting its size and energy efficiency. Results of this preliminary investigation show that, with no gearbox, the best designs for the two cam-ram systems are the same, including the following: a maximum hydraulic pressure of 100 bar; a ram bore of 20 mm; a roller diameter of 19 mm (a value also used by Realmuto et al. [22] for the cam-roller-follower system in their ankle prosthesis); an offset e of 19 mm; and a distance a of 30 mm. This design minimizes the energy losses while keeping the system dimensions within acceptable limits.

The energy balance results for this design alternative, during the working phases of the two cam-ram systems, are very promising [11]. Specifically, the energy losses do not exceed 2% of the energy input to the system (i.e., from the ankle for the stance system and from the accumulator for the push-off system).

However, the two cam-ram systems were designed to have good performances only in their working phases. As previously mentioned, only the friction losses directly associated with the two cam-rams during their working phases were considered in the early-stage simulation model used for this preliminary design investigation. Therefore, to assess the performance of the final design, all of the previously neglected sources of energy loss were included in the model: losses in the non-working phases in the two cam-ram systems associated with rolling resistance between rollers and cams, bearings, and piston O-rings; flow losses in pipes and discrete components (e.g., inlets, exits, bends, and valves); losses in the accumulator because of heat transfer. When all significant sources of energy dissipation are included, there is an increase in the energy losses of about 6% of the total external energy input at the ankle over the gait cycle (i.e., 8.21%) [11], which can be reduced to 5.83% with small changes to the design, as explained in detail in [11,13]. Nevertheless, even then, the cam-ram performances in their working phases will likely dominate the design decisions, as assumed in this study, given that the power flows are much greater in the working phases.

The simulation results suggest the proposed prosthesis would store and release gait energy more efficiently through the use of hydraulics and an accumulator, leading to a reduction in metabolic energy consumption during walking without the need for external power sources. Furthermore, our semi-active design needs only small batteries for control, not for propulsion, potentially reducing weight and increasing autonomy (range between charges). Conversely, while representing a significant advancement over passive designs by providing active push-off propulsion, existing fully active prosthetic feet, such as the Otto-bock Empower (the only one on the market), rely heavily on battery power, which increases weight, limits autonomy, and increases maintenance requirements. As stated in [11], future work includes physical prototyping and experimental validation with prosthetic users. This is necessary to assess user satisfaction and evaluate individual ankle response through gait analysis. In vivo testing results will either confirm simulation predictions or lead to a further simulation-based optimisation of the cam profiles and other key components for different walking conditions.

Overall, a simulation-based design process represents a cost-effective and sustainable alternative to heuristic approaches in prosthetic design. It enables a comprehensive evaluation of all device components and their role within the system dynamics, supported by a rigorous mathematical model. Integrating simulations of the device's operation into an iterative design process represents an efficient approach to advancing prosthetic technology development.

As well as documenting the design of a particular novel prosthetic ankle, the authors believe this is a useful exemplar of how a complex design problem can be broken down into a series of sub-problems, supported by simulation-based design programs. This includes the classification of design parameters for prioritisation purposes, using iterative simulation to converge on solutions, and following a priority-based sequence of design steps.

Author Contributions: Conceptualisation, A.P., J.G. and D.H.; methodology, A.P., J.G. and D.H.; software, A.P., J.G. and D.H.; validation, A.P., J.G. and D.H.; writing-original draft preparation, A.P., J.G. and D.H.; writing-review and editing, A.P. and D.H.; visualisation, A.P. and D.H.; supervision, D.H. All authors have read and agreed to the published version of the manuscript.

Funding: This work was supported by the University of Salford as part of the Graduate Teaching Studentship Scheme.

Institutional Review Board Statement: Not applicable.

Informed Consent Statement: Not applicable.

Data Availability Statement: The original contributions presented in this study are included in the article. Further inquiries can be directed to the corresponding author.

Conflicts of Interest: The authors declare no conflicts of interest. The funders had no role in the design of the study; in the collection, analyses, or interpretation of data; in the writing of the manuscript; or in the decision to publish the results.

Abbreviations

The following abbreviations are used in this manuscript:

ESR Energy storage and return
GR Gear ratio

Appendix A

Table A1. Nomenclature used in this paper.

a	arbitrary constant defining the starting position of the follower in the vertical (y -axis) direction (m)	P	operating pressure (Pa)
A	ram bore area (oil side) (m ²)	P_{acc}	accumulator pressure (Pa)
D	ram bore (m)	P_{atm}	atmospheric pressure (Pa)
D_{pipe}	pipe diameter (m)	P_{cyl}	cylinder pressure (Pa)
d_{roller}	roller diameter (m)	P_{max}	max accumulator hydraulic pressure (Pa)
e	offset given by the distance between the centre line of the follower and the centre line of the camshaft (m)	r	roller radius (m)
F_h	hydraulic ram force (N)	$stroke$	piston stroke (m)
F_n	normal force acting between the cam and the roller (N)	T_c	actual torque at the camshaft (Nm)
$F_{n_{desired}}$	minimum desired value for the normal force between cam and roller (N)	T_{c_r}	required torque at the camshaft (Nm)
$F_{n_{NOspring}}$	normal force between cam and roller when the two return springs are not included in the system (N)	$T_{c_{STANCE}}$	stance cam torque (Nm)
F_s	return-spring force (N)	V_A	accumulator volume (m ³)
$F_{s_{required}}$	required return-spring force (N)	y	piston linear displacement (m)
W	hydraulic ram work/cam work (J)	k	return-spring constant (N/m)
α	cam pressure angle (rad)	L_{pipe}	pipe length (m)
θ_c	cam angle of rotation (rad)	$P(x_P, y_P)$	contact point (with coordinates) between cam and roller (m)

References

1. Versluys, R.; Beyl, P.; Van Damme, M.; Desomer, A.; Van Ham, R.; Lefeber, D. Prosthetic feet: State-of-the-art review and the importance of mimicking human ankle-foot biomechanics. *Disabil. Rehabil. Assist. Technol.* **2009**, *4*, 65–75. [CrossRef]
2. Perry, J.; Burnfield, J.M.; Newsam, C.J.; Conley, P. Energy expenditure and gait characteristics of a bilateral amputee walking with C-leg prostheses compared with stubby and conventional articulating prostheses. *Arch. Phys. Med. Rehabil.* **2004**, *85*, 1711–1717. [CrossRef] [PubMed]
3. Cherelle, P.; Mathijssen, G.; Wang, Q.; Vanderborght, B.; Lefeber, D. Advances in Propulsive Bionic Feet and Their Actuation Principles. *Adv. Mech. Eng.* **2014**, *6*, 984046. [CrossRef]
4. Segal, A.D.; Zelik, K.E.; Klute, G.K.; Morgenroth, D.C.; Hahn, M.E.; Orendurff, M.S.; Adamczyk, P.G.; Collins, S.H.; Kuo, A.D.; Czerniecki, J.M. The effects of a controlled energy storage and return prototype prosthetic foot on transtibial amputee ambulation. *Hum. Mov. Sci.* **2012**, *31*, 918–931. [CrossRef]
5. Adamczyk, P.G.; Kuo, A.D. Mechanisms of Gait Asymmetry Due to Push-Off Deficiency in Unilateral Amputees. *IEEE Trans. Neural Syst. Rehabil. Eng.* **2015**, *23*, 776–785. [CrossRef] [PubMed]
6. Huang, T.P.; Shorter, K.A.; Adamczyk, P.G.; Kuo, A.D. Mechanical and energetic consequences of reduced ankle plantar-flexion in human walking. *J. Exp. Biol.* **2015**, *218*, 3541–3550. [CrossRef] [PubMed]
7. van Schaik, L.; Geertzen, J.H.B.; Dijkstra, P.U.; Dekker, R. Metabolic costs of activities of daily living in persons with a lower limb amputation: A systematic review and meta-analysis. *PLoS ONE* **2019**, *14*, e0213256. [CrossRef] [PubMed]
8. Herr, H.; Grabowski, A.M. Bionic ankle-foot prosthesis normalizes walking gait for persons with leg amputation. *Proceeding R. Soc. B* **2012**, *279*, 457–464. [CrossRef]
9. Laschowski, B.; McPhee, J.; Andrysek, J. Lower-Limb Prostheses and Exoskeletons With Energy Regeneration: Mechatronic Design and Optimization Review. *J. Mech. Robot.* **2019**, *11*, 040801. [CrossRef]
10. Cimolato, A.; Driessen, J.J.M.; Mattos, L.S.; De Momi, E.; Laffranchi, M.; De Michieli, L. EMG-driven control in lower limb prostheses: A topic-based systematic review. *J. Neuroeng. Rehabil.* **2022**, *19*, 43. [CrossRef] [PubMed]
11. Pace, A.; Gardiner, J.; Kenney, L.; Howard, D. Simulated Performance of an Energy Storage and Return Prosthetic Ankle Based on Cams and Miniature Hydraulics. *IEEE Trans. Med. Robot. Bionics* **2022**, *4*, 230–240. [CrossRef]
12. Ziegler-Graham, K.; MacKenzie, E.J.; Ephraim, P.L.; Travison, T.G.; Brookmeyer, R. Estimating the Prevalence of Limb Loss in the United States: 2005 to 2050. *Arch. Phys. Med. Rehabil.* **2008**, *89*, 422–429. [CrossRef] [PubMed]
13. Pace, A. A Novel Hydraulic Energy-Storage-And-Return Prosthetic Ankle: Design, Modelling and Simulation. Ph.D. Dissertation, University of Salford, Salford, UK, 2020.
14. Bari, A.Z. An Efficient Energy Storage and Return Prosthesis. Ph.D. Dissertation, University of Salford, Salford, UK, 2013.
15. Durfee, K.; Xia, J.; Hsiao-Weckler, E. Tiny Hydraulics for Powered Orthotics. In Proceedings of the IEEE International Conference on Rehabilitation Robotics (ICORR), Rehab Week Zurich, ETH Zurich Science City, Zurich, Switzerland, 29 June–1 July 2011; Volume 279, pp. 903–908.
16. Xia, J.; Braun, K.L.; Durfee, W.K. Small-Scale Hydraulics for Human Assist Devices. In Proceedings of the Design of Medical Devices Conference (DMD), Minneapolis, MN, USA, 12–14 April 2011.
17. Xia, J.; Durfee, W.K. Modeling of Tiny Hydraulic Cylinders. In Proceedings of the 52nd National Conference on Fluid Power, Las Vegas, NV, USA, 23–25 March 2011; pp. 657–662.
18. Xia, J.; Durfee, W.K. *Analysis of Small-Scale Hydraulic Actuation Systems*; University of Minnesota: Minneapolis, MN, USA, 2011.
19. Xia, J.; Durfee, W.K. Experimentally validated models of o-ring seals for tiny hydraulic cylinders. In Proceedings of the Symposium on Fluid Power & Motion Control (FPMC), ASME, Bath, UK, 10–12 September 2014.
20. Neubauer, B.C.; Nath, J.; Durfee, W.K. Design of a Portable Hydraulic Ankle-Foot Orthosis. In Proceedings of the 36th Annual International Conference of the IEEE Engineering in Medicine and Biology Society (EMBC), Chicago, IL, USA, 26–30 August 2014. [CrossRef]
21. HYDAIRA. Hydraulic Cylinders. Available online: <http://www.hydairea.ch/produkte/zu.php?nav=prod&lang=en> (accessed on 15 November 2024).
22. Realmuto, J.; Klute, G.; Devasia, S. Nonlinear Passive Cam-Based Springs for Powered Ankle Prostheses. *J. Med. Devices* **2015**, *9*, 011007. [CrossRef]
23. SKF. *Rolling Bearings*; SKF: Gothenburg, Sweden, 2013.
24. IKO. *Cam Followers & Roller Followers*; IKO, NIPPON THOMPSON CO., LTD.: Tokyo, Japan, 2016.
25. IKO. *Cam Followers*; IKO, NIPPON THOMPSON CO., LTD.: Tokyo, Japan, 2017.

Disclaimer/Publisher’s Note: The statements, opinions and data contained in all publications are solely those of the individual author(s) and contributor(s) and not of MDPI and/or the editor(s). MDPI and/or the editor(s) disclaim responsibility for any injury to people or property resulting from any ideas, methods, instructions or products referred to in the content.

Article

Compensating the Symptomatic Increase in Plantarflexion Torque and Mechanical Work for Dorsiflexion in Patients with Spastic Paresis Using the “Hermes” Ankle–Foot Orthosis

Karen E. Rodriguez Hernandez ^{1,*}, Jurriaan H. de Groot ², Eveline R. M. Grootendorst-Heemskerk ^{2,3}, Frank Baas ⁴, Marjon Stijntjes ², Sven K. Schiemanck ^{2,3}, Frans C. T. van der Helm ¹, Herman van der Kooij ^{1,5} and Winfred Mugge ¹

¹ Department of Biomechanical Engineering, Faculty of Mechanical Engineering, Delft University of Technology, 2628 CD Delft, The Netherlands; w.mugge@tudelft.nl (W.M.)

² Department of Rehabilitation Medicine, Leiden University Medical Centre, 2300 RC Leiden, The Netherlands; j.h.de_groot@lumc.nl (J.H.d.G.)

³ Spaarne Gasthuis Hoofddorp, Spaarnepoort 1, 2134 TM Hoofddorp, The Netherlands

⁴ InteSpring BV, Patrijsweg 24, 2289 EX Rijswijk, The Netherlands

⁵ Department of Biomechanical Engineering, Faculty of Engineering Technology, University of Twente, 7500 AE Enschede, The Netherlands

* Correspondence: k.e.rodriguezhernandez@tudelft.nl

Abstract: Background/Objectives: “Hermes” is an ankle–foot orthosis (AFO) with negative stiffness designed to mechanically compensate the symptomatic increase in plantarflexion (PF) torque (i.e., ankle joint torque resistance to dorsiflexion, DF) in patients with spastic paresis. **Methods:** The effectiveness of “Hermes” was evaluated in twelve patients with chronic unilateral spastic paresis after stroke. Using a robotic ankle manipulator, stiffness at the ankle joint was assessed across three conditions: ankle without Hermes (A), ankle with Hermes applying no torque compensation ($A + H_{0\%}$), and ankle with Hermes tuned to compensate 100% of the patients’ ankle joint stiffness ($A + H_{100\%}$). **Results:** A significant reduction in PF torque was found with Hermes applying compensation ($A + H_{100\%}$) compared to the conditions without Hermes (A) and with Hermes applying no compensation ($A + H_{0\%}$). Furthermore, a significant reduction in positive dorsiflexion work was found with Hermes applying compensation ($A + H_{100\%}$) compared to the condition with Hermes applying no compensation ($A + H_{0\%}$). Hermes did not significantly contribute to additional PF torque or positive work when applying no compensation ($A + H_{0\%}$). **Conclusions:** The reductions in PF torque achieved with Hermes are comparable to those seen with repeated ankle stretching programs and ankle robot training. Thus, Hermes is expected to assist voluntary dorsiflexion and improve walking in patients with spastic paresis.

Keywords: muscle spasticity; orthotic devices; stroke; equinus deformity; ankle work

Academic Editor: Arnab Chanda

Received: 17 November 2024

Revised: 13 January 2025

Accepted: 15 January 2025

Published: 27 January 2025

Citation: Hernandez, K.E.R.; de Groot, J.H.; Grootendorst-Heemskerk, E.R.M.; Baas, F.; Stijntjes, M.; Schiemanck, S.K.; van der Helm, F.C.T.; van der Kooij, H.; Mugge, W. Compensating the Symptomatic Increase in Plantarflexion Torque and Mechanical Work for Dorsiflexion in Patients with Spastic Paresis Using the “Hermes” Ankle–Foot Orthosis. *Prosthesis* **2025**, *7*, 12.

<https://doi.org/10.3390/prosthesis7010012>

10.3390/prosthesis7010012

Copyright: © 2025 by the authors.

Licensee MDPI, Basel, Switzerland.

This article is an open access article distributed under the terms and conditions of the Creative Commons Attribution (CC BY) license

(<https://creativecommons.org/licenses/by/4.0/>).

1. Introduction

The symptomatic increase in ankle stiffness or equinus foot is a prevalent clinical symptom in spastic paresis across a spectrum of neurological diseases, e.g., stroke, cerebral palsy, multiple sclerosis, and spinal cord lesions [1]. Increased ankle stiffness is characterized by increased internal plantarflexion (PF) torque, defined as the torque resistance to dorsiflexion (DF), and a limited range of motion (ROM) that originates from both neural (e.g., contracture and spasticity) and non-neural factors (e.g., muscle shortening), mainly affecting the plantar flexor or triceps surae (TS) muscles [2–4] (see Figure 1). Particularly,

non-neural ankle stiffness originates from plantar flexor muscle tissues [5], here called passive ankle stiffness.

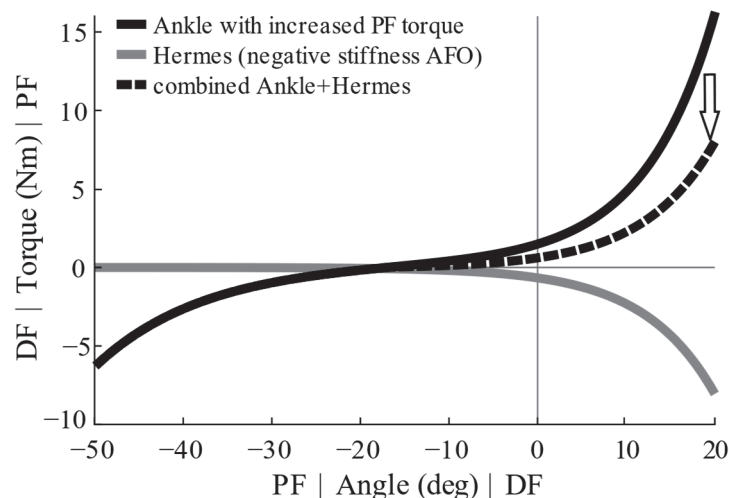


Figure 1. The passive torque-angle characteristic of the ankle is described by a positive (PF) exponential and a negative (DF) exponential (black solid line). The positive torques of the torque-angle characteristic correspond to the internal PF torque. Hermes compensates for the ankle stiffness with an external negative torque (gray line), resulting in a combined Ankle + Hermes torque-angle characteristic and stiffness (black dashed line). Relative to an ankle with increased passive stiffness, this combined Ankle + Hermes torque is aimed to be reduced towards a normal value and potentially allow for a larger ROM (arrow).

Increased ankle stiffness impairs individuals in various activities of daily living, including walking [2,6]. In clinical practice, the management of increased ankle stiffness typically starts with stretching exercises [2,7], which have been shown to decrease ankle stiffness and increase ROM [8,9]. However, the clinical effectiveness of stretching in inducing significant changes in joint mobility, pain, or spasticity in individuals with neurological disease is still a matter of debate [10]. As a result, there remains a challenge in the field of rehabilitation for patients with neurological diseases in reducing increased ankle stiffness to enhance ankle function during daily activities, e.g., gait [2,11].

In a previous study, we demonstrated the concept of mechanically compensating ankle stiffness with Hermes, an ankle-foot orthosis (AFO) that applies negative stiffness to the ankle joint, in patients with chronic stroke [12] (see Figure 1). The negative stiffness of Hermes was adjusted for each patient to compensate different percentages of their ankle stiffness, which was measured using a robotic manipulator. Specifically, Hermes' torque was adjusted based on the torque-angle characteristic of the measured PF torque defined by the ankle stiffness of each patient [12]. By wearing Hermes, the resulting total stiffness of the ankle joint was reduced without limiting the ROM as conventional AFOs tend to do [12]. Traditionally, the indication of AFOs is based on evaluations of the gait pattern in clinical settings [13]. We demonstrated that adding robotic measurements of ankle stiffness hold the potential to improve the customization of ankle-foot orthoses [12,14–17].

Building upon our initial findings [12], the goal of the present study is to validate the effectiveness of Hermes in compensating the ankle stiffness by extending the sample of stroke survivors in the chronic phase. Robotic measurements of the torque at the ankle were conducted. The effectiveness of Hermes in immediately compensating the ankle stiffness was assessed by comparing both the PF torques (i.e., the ankle torque resistance to DF) and positive work (i.e., the positive area under the torque-angle characteristic) with Hermes ($A + H$) and without Hermes (A). Positive work is an equivalent measure of the required

mechanical energy to be exerted by the dorsiflexor muscle (e.g., tibialis anterior, TA) to bring the ankle to the maximum DF angle, for example, during walking. We hypothesized significant PF torque and work reductions in the condition with Hermes compared to that without.

2. Materials and Methods

2.1. *Hermes AFO*

Hermes is a one degree-of-freedom non-powered AFO that consists of orthotic foot and calf parts that are connected by a negative-stiffness mechanism designed by InteSpring BV (Rijswijk, the Netherlands). Negative stiffness arises because, unlike typical ankle-foot orthoses with positive stiffness, Hermes externally applies increasing dorsiflexion torque as the ankle moves towards dorsiflexion [12]. This counteracts the ankle's PF torque, mechanically compensating for the ankle's internal stiffness [12]. The experimental Hermes orthotic brace has a modular design of the foot and calf parts to fit the AFO to the lower legs of patients. The compensation delivered by the negative-stiffness mechanism of Hermes can be adjusted based on the patient-specific torque-angle characteristic of the internal PF torque.

2.2. *Participants*

Patients older than 18 years of age were recruited at the Department of Rehabilitation Medicine at the Leiden University Medical Centre. Inclusion criteria were a history of stroke (>6 months after), unilateral spastic paresis leading to equinus/equinovarus with limited ankle ROM, and an indication of a walking aid, e.g., orthopedic shoes or AFO. Patients were excluded if they were not able to understand the instructions, for example, due to aphasia or cognitive problems, or if they had ankle arthrodesis surgery or were not able to walk short distances (in home). The research protocol was approved by the Leiden-Den Haag-Delft Medical Ethical Committee, CCMO (Centrale Commissie Mensgebonden Onderzoek) trial registration number NL64640.058.19. All patients provided written informed consent prior to the experimental procedure.

2.3. *Experimental Protocol*

All measurements were conducted in a single session and at the same time of day for all patients. A physical medicine and rehabilitation physician assessed the ROM, severity of spasticity (MAS, Modified Ashworth Scale [18] or PRPM, Perceived Resistance to Passive Movement [19]), muscle strength (Medical Research Council [20]) at the ankle joint, and vibration sense at medial and lateral malleoli and at the first metatarsophalangeal (MTP-1) joint (3-point scale [21]). Subsequently, the Hermes orthotic brace was fitted to the patient's affected lower leg by selecting appropriate sizes for the foot and calf orthotic parts (see Figure 2).

Experimental set-up: Following the fitting, we used a robotic ankle manipulator ("Achilles," MOOG Inc., Nieuw Vennep, the Netherlands) to examine the patients' ankle stiffness without and with Hermes.

Patients were seated in front of the ankle manipulator on an adjustable chair with the hip and knee flexed approximately 70 deg and 45 deg, respectively. The patient's foot was attached to the rotational plate of the ankle manipulator using Velcro straps in the condition without Hermes or via the Hermes foot part in the condition with Hermes, as illustrated in Figure 3. The rotations of the ankle manipulator were delimited by the ROM tolerance of the patients as communicated to the experimenter when manually rotating the foot to dorsiflexion and plantarflexion. Before the measurements, the ankle manipulator was calibrated by positioning the patient's ankle at 25 degrees PF and then measuring the

corresponding angle on the ankle manipulator. This calibration allowed for conversion between the manipulator's angle and the patient's ankle's angle.



Figure 2. A photo of a participant wearing Hermes on the left leg. Hermes is composed by calf and foot parts made of prepreg carbon fiber and fabricated by an experienced orthotist.



Figure 3. An example of how a patient was set up at the ankle manipulator for the measurement of the combined Ankle + Hermes PF torque. In this example, Hermes was used on the left leg.

In the Ankle only (A) condition, the ankle's passive ROM (pROM) and the torque over the pROM were measured without Hermes. The pROM, including maximum PF and DF angles, was recorded using the ankle manipulator in a standardized protocol by applying 15 Nm in DF and 7.5 Nm in PF onto the patient's ankle [5,15]. Subsequently, the ankle torque was measured across the pROM while the ankle manipulator applied DF and PF movements, respectively, spanning from the maximum PF angle to the maximum DF angle of the pROM and vice versa. The DF and PF movements followed a ramp-and-hold (RaH) shape with a ramp velocity of $5.0 \text{ deg}\cdot\text{s}^{-1}$, with randomly timed onset and hold periods of

at least 10 s to prevent anticipation [22]. During all measurements, patients were instructed to avoid voluntarily activating any leg muscle or actively resisting the movements of the ankle manipulator. Therefore, the measured torques represent passive contributions.

Due to the viscoelastic properties of muscles, the torque-angle characteristic measured during DF and PF movements exhibits a hysteresis loop, with torque during the DF movement typically being higher than during the PF movement. For the first 5 patients, the patient-specific PF torque to be compensated by Hermes corresponded to the average torque-angle characteristic, obtained by averaging the torques across the DF and PF movements. To address the greater difficulty that patients with spastic paresis experience during DF movement and to potentially improve contrast in the experimental conditions, the patient-specific PF torque to be compensated by Hermes for the remaining 7 patients corresponded to the torque during the DF movement, here referred to as the DF torque-angle characteristic. The positive torque values of these characteristics were input into software developed by InteSpring B.V. to adjust the negative-stiffness mechanism of Hermes (v3.11). The DF stop of Hermes was set at the maximum DF angle of the pROM. This step ensures patient-specific calibration of Hermes as the DF stop dictates the angle at which Hermes delivers its maximum torque (see, for example, Hermes torque at 20 degrees DF in Figure 1).

After completing the Ankle (A) condition, patients proceeded to wear Hermes, which was adjusted to either apply no compensation ($A + H_{0\%}$ condition) or to compensate 100% of the patient-specific PF torque ($A + H_{100\%}$ condition). These Hermes compensation conditions were randomized. The combined Ankle + Hermes PF torques (i.e., in conditions $A + H_{0\%}$, $A + H_{100\%}$) were measured using the ankle manipulator, which applied DF and PF movements with a RaH shape at 5.0 deg.s^{-1} across the pROM measured in the Ankle (A) condition.

2.4. Outcome Measures

The effectiveness of Hermes in compensating the ankle stiffness was assessed by comparing the combined Ankle + Hermes PF torque and positive work across the three conditions, namely A , $A + H_{0\%}$ and $A + H_{100\%}$. For our analysis, we extracted PF torques from the DF torque-angle characteristic at 0 deg., 10 deg. DF, and at the maximum DF angle of each condition (see Figure 4). We selected 0 deg. and 10 deg. DF because these angles encompass the typical DF range during the swing phase of gait, where dorsiflexors generate torque and positive work for foot clearance and heel strike [23]. Additionally, assessing the maximum DF angle allowed us to evaluate the endpoint of the patients' ROM. In total, three torque values per condition were compared for each patient.

The positive work in each of the three experimental conditions was determined as the positive area under the DF torque-angle characteristics. The positive work in each condition was determined within the common ROM shared by the averaged torque-angle characteristics of the three conditions (see Figure 4). Thus, three work values per condition were compared for each patient. See Appendix A for further details on the calculation of positive work.

A repeated-measures one-way ANOVA was used to determine significant differences in positive work and in PF torque in each of the three ankle angles across the three conditions: A , $A + H_{0\%}$ and $A + H_{100\%}$. If the assumption of sphericity was violated, a Greenhouse–Geisser correction was applied. If significant main effects were found, a post hoc analysis was conducted involving multiple pairwise comparisons with Bonferroni correction ($\alpha = 0.05$) to find significant differences between conditions.

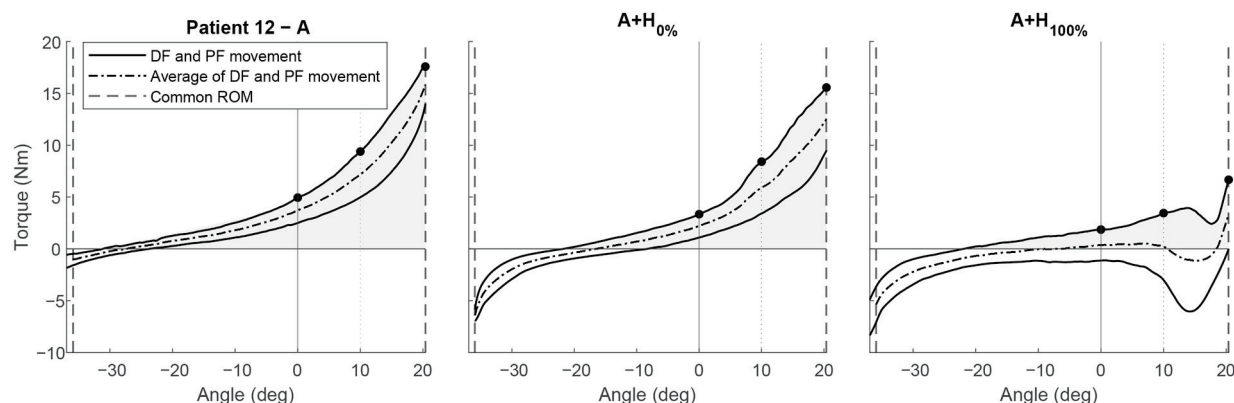


Figure 4. The torque-angle characteristics of Patient 12 measured without (A) and with Hermes ($A + H_{0\%}$ and $A + H_{100\%}$). In the Ankle (A) condition (left panel), the positive torques correspond to the patient-specific PF torque originated from the triceps surae and to be compensated by Hermes. The upper and lower solid lines in each panel denote the hysteresis loop comprising the DF (upper) and PF (lower) torque-angle characteristics. The dashed–dotted lines denote the average of the DF and PF torque-angle characteristic of each condition. The black-filled circles represent the PF torques of the DF torque-angle characteristic at 0 deg. (anatomical ankle angle), 10 deg, and at the max. DF angle used for comparison between patients. The dashed lines and shaded areas, respectively, denote the common ROM shared across conditions for this patient and the areas under the DF torque-angle characteristic (positive work).

3. Results

Twelve patients (eight males) were included in this study. The demographic characteristics and results of the physical evaluation are shown in Table 1. The raw data of four patients, numbered 2–5 in our previous study [12], were re-used for the current study. Note that while the raw data are the same, the outcome measures assessed in this study differ from those of the previous one [12]. All patients, except for Patient 2, underwent treatment with botulinum toxin medication in the calf muscles. Of the initial 12 patients, 10 were included in the group analysis; data from Patient 5 were omitted due to technical issues, and data from Patient 11 were excluded from analysis due to an absence of the limited pROM as measured with the ankle manipulator.

Table 1. Patient characteristics.

Patient Number	1	2	3	4	5	6	7	8	9	10	11	12	
Age (years)	68	51	58	38	65	44	74	58	63	65	42	69	
Gender (F/M)	M	M	F	M	M	F	M	F	M	M	F	M	
Height (cm)	190	180	178	174	180	176	172	168	197	182	168	179	
Weight (Kg)	73	108	78	78	89	75	81	88	98	95	68	79	
Affected side (R/L)	R	R	L	L	R	L	R	R	L	R	R	L	
Stroke type (ischemic (I)/hemorrhagic (H))	I	I	I	H	I	I	H	H	H	I	H	I	
Time since stroke (years)	5	5	8	5	12	16	11	1	2	9	2	7	
Plantarflexor muscle spasticity ¹ (PRPM, MAS for Patients 4 and 5)	0	1	4	0	3	2	3	3	3	3	1	3	
Passive ROM ² (deg.)	DF:	12	18	−2	13	−4	21	25	5	11	17	53	20
	PF:	42	27	37	32	38	49	39	54	47	45	56	48
Vibration sensibility ³	A:	X	X	N	N	N	N	R	R	N	R	R	X
	F:	X	X	N	X	R	R	N	N	N	N	N	R
Botulinum toxin treatment (Y/N)	Y	N	Y	Y	Y	Y	Y	Y	Y	Y	Y	Y	
Walking aids ⁴													

Table 1. Cont.

Patient Number	1	2	3	4	5	6	7	8	9	10	11	12
Orthopedic shoes:	+	+	+	+	-	-	+	+	-	+	+	-
AFO:	-	-	-	+	+	+	+	+	+	-	-	+
Cane:	+	-	+	+	+	-	-	-	+	+	-	+

¹ PRPM: Perceived Resistance to Passive Movement [24]. ² The passive ROM measured with the ankle manipulator in the Ankle (A) condition. Negative values in DF indicate that the ankle did not reach 0 degrees (i.e., anatomical position) and the DF angle is in the PF range. ³ Vibratory sensibility was determined with a Rydel-Seiffer tuning fork placed on the first metatarsophalangeal joint of the foot (F) and the medial and lateral malleoli at the ankle (A) [21]. Sensibility at the ankle was considered to be reduced if the patient had no or reduced sensibility in any or both malleoli, and no sensibility was determined if the patient had no sensibility in both malleoli. ⁴ In addition to the listed walking aids, Patient 8 used a wheelchair for mobility. Abbreviations: DF: dorsiflexion, PF: plantar flexion; X: no sensibility, R: reduced sensibility, N: normal sensibility, AFO: ankle-foot orthosis.

Plantar Flexion Torque and Positive Work

Figure 4 shows an example of the recorded torque-angle characteristics and includes the PF torques and areas under the DF torque-angle characteristic per condition for comparison between patients. The torque-angle characteristics measured from all patients are shown in Appendix B. The maximum DF angle of Patient 8 was <10 deg., and the maximum DF angle of Patient 3 was <0 deg. in the ankle condition (A) (see Table 1). Consequently, the data of these patients were excluded from the statistical test at these angles.

The repeated-measures one-way ANOVAs revealed statistically significant differences at the group level in PF torque between conditions at 0 deg. ($F(2, 16) = 8.031$; $p = 0.005$), 10 deg. ($F(1.208, 8.458) = 10.308$; $p = 0.009$), and max DF ($F(2, 18) = 12.422$; $p < 0.001$). A post hoc analysis indicated that the PF torque with Hermes applying compensation ($A + H_{100\%}$) was significantly lower than both the PF torque with Hermes applying no compensation ($A + H_{0\%}$) and without Hermes (A) at the three assessed angles, i.e., 0 deg., 10 deg., and the max. DF angle (Figure 5). Additionally, no significant differences in PF torque were found between the condition with Hermes applying no compensation ($A + H_{0\%}$), and the condition without Hermes (A). Appendix C provides detailed results of the post hoc analysis.

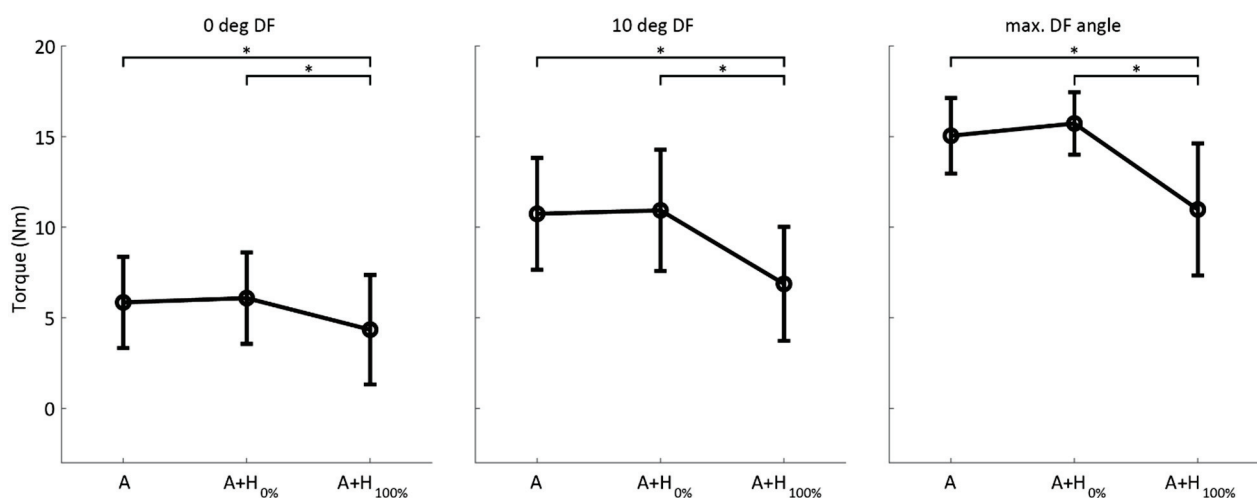


Figure 5. Mean torque values at 0 deg., 10 deg., and maximum DF angle between conditions across all subjects. Error bars represent standard deviations. Post hoc analysis after repeated-measures ANOVAs revealed that significant reductions in PF torque occurred at three assessed angles in the condition with Hermes applying compensation ($A + H_{100\%}$) compared to conditions without Hermes (A) and with Hermes applying no compensation ($A + H_0$). * indicates significant differences ($p \leq 0.05$).

Regarding positive work, the repeated-measures one-way ANOVA showed significant differences between conditions ($F(2, 18) = 5.878$; $p = 0.02$). The post hoc analysis revealed that positive work was significantly reduced when Hermes applied compensation ($A + H_{100\%}$) compared to the condition with Hermes applying no compensation ($A + H_0$) (69 (95% CI, 16 to 121) Nm·deg, $p < 0.05$), but not compared to the condition without Hermes (A) (31 (95% CI, 51 to 114) Nm·deg, $p > 0.05$), as illustrated in Figure 6. Furthermore, positive work in the condition with Hermes applying no compensation ($A + H_0$) was not significantly different from positive work without Hermes (A) ($p > 0.05$).

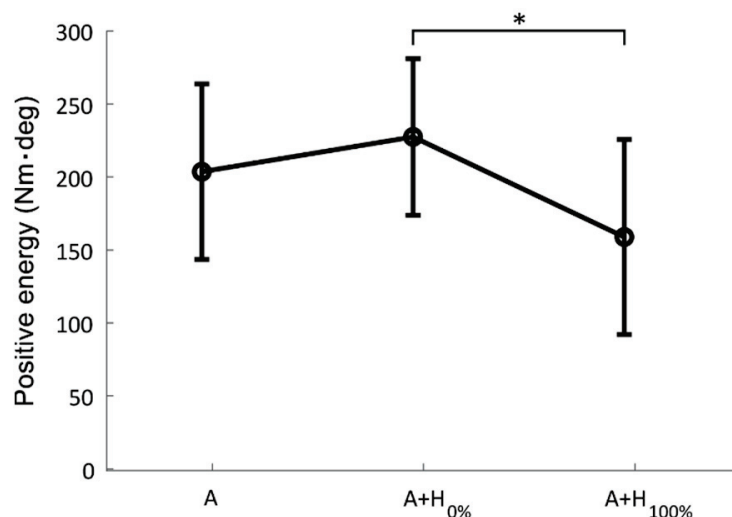


Figure 6. Comparison of mean positive work between conditions across all subjects. Error bars represent standard deviations. Multiple comparisons after repeated-measures ANOVA revealed significant reductions in positive work when Hermes applied compensation ($A + H_{100\%}$) compared to condition without compensation ($A + H_{0\%}$), but not compared to condition without Hermes (A). * indicates significant differences ($p \leq 0.05$).

4. Discussion

In this study, we found that Hermes did not contribute to additional stiffness at the ankle if torque compensation was off. When torque compensation was on, Hermes significantly reduced the PF torque at 0 degrees, 10 degrees, and maximum ankle dorsiflexion. These reductions in PF torque are comparable to the reductions reported after repeated ankle stretching programs [25] and training with an ankle robot in patients with chronic stroke [26]. Furthermore, for most patients in this study, the PF torques in the combined Ankle + Hermes torque-angle characteristic ($A + H_{100\%}$) are comparable to those reported in healthy controls [25], indicating that Hermes is capable of mechanically compensating the increased ankle stiffness in patients with spastic paresis, potentially achieving a clinical level of improvement.

We assume that the PF torque and positive work reductions observed in this study are able to assist voluntary dorsiflexion of the ankle joint, as demonstrated in our previous study [12], and to facilitate walking in patients with spastic paresis. Future research may evaluate the effects of Hermes' assistance during walking and explore the interaction between ankle stiffness compensation and the dynamics of the ankle joint during gait. We anticipate that Hermes may be integrated into clinical studies to manage symptomatic increases in PF torque due to spastic paresis. In the long term, this integration can not only improve ankle control and patient mobility but also potentially reduce costs associated with orthopedic shoes and neuromuscular blockade for addressing spastic paresis.

The significant reduction in positive work demonstrates that Hermes is able to accommodate the patient's passive ROM and reduce the positive work required from the dorsiflexor muscles to dorsiflex the ankle. However, positive work in the condition with Hermes applying compensation ($A + H_{100\%}$) was not significantly lower than positive work in the condition without Hermes (A) as opposed to the results in PF torque.

This lack of significant difference in positive work may be attributed to the inter-patient variability observed in the condition without Hermes, which may originate from differences in ankle stiffness and range of motion among patients. The larger variance in positive work compared to PF torque may also originate from the method of assessing the Hermes' effect. Positive work is determined by considering the entire torque-angle characteristic and provides an indication of the effect of Hermes across the whole range of motion. In contrast, assessing Hermes' effect by assessing the PF torque at specific angles offers insights into Hermes' compensation at precise points along the torque-angle characteristic.

Another limitation is the number of data samples in the group-level analysis. Insufficient data samples may have affected the statistical power to detect differences between conditions. For instance, data from Patients 3 and 8 were absent in some of the statistical tests because these patients were unable to attain 10 degrees DF in the ankle condition (Patient 3 could not reach 0 deg. DF) and therefore also in the Ankle + Hermes conditions. Furthermore, data from Patient 5 were omitted due to technical issues, and data from Patient 11 were excluded from analysis due to an absence of limited pROM as measured with the ankle manipulator. For future studies, a larger group of patients will be essential to validate the findings and generalize them to broader patient populations. Additionally, scaling and/or normalizing methods based on maximum DF torque or positive work could be implemented for more accurate and equitable comparisons across patients, accounting for individual variations in ankle stiffness and ROM.

In addition to slight differences in the results for PF torque and positive work, as explained above, we observed a large variation in the reductions in both PF torque and positive work among patients. This variation is partially because in Patients 6, 7, and 8, we did not observe reductions in PF torque and positive work when in the condition with Hermes applying compensation ($A + H_{100\%}$) compared to the condition without Hermes (A). Furthermore, in our previous study [12], we identified limiting factors contributing to the variability among patients, such as involuntary muscle activation and suboptimal orthotic fit of the modular Hermes orthotic brace. We believe that suboptimal orthotic fit was also a limiting factor in this study that could affect Hermes' ability to compensate ankle stiffness and change torque measurement across the ROM. Custom-made Hermes foot and calf parts, commonly used in clinical practice, are expected to offer a better orthotic fit, potentially reducing misalignment and compensation discrepancies. Another limiting factor in this study that may have led to insufficient torque provided by Hermes is that the setting of the negative stiffness mechanism was not always perfectly guaranteed due to assembly discrepancies. This was particularly observed in Patients 6–8. Future improvements in Hermes may involve the use of more durable mechanism components and a simpler adjustment process. A patient-specific cam and spring will simplify the construction of the negative stiffness mechanism and reduce errors of both assembly and adjustment.

In this study, the appropriate reference for the compensation of PF torque by Hermes was explored, corresponding to either the average torque-angle characteristic or the torque-angle characteristic during DF movement only. Compensating the torque-angle characteristic during DF movement would directly provide the necessary torque to ensure maximal dorsiflexion of the ankle. However, this approach would require the PF muscle to exert more PF work to plantarflex the foot. Conversely, compensating for the average

torque-angle characteristic would ease voluntary PF movement but may be insufficient for achieving the DF angle required for certain activities, such as ascending stairs. We did not observe significant differences between using the two references. We analyzed factor compensation ($A + H_{100\%}$) versus no compensation ($A, A + H_{0\%}$), which justified pooling the results of all patients in the same analysis.

Most patients in this study were undergoing botulinum neurotoxin treatment. This and other treatments, such as stretching, may decrease ankle stiffness. Thus, the treatment may be a covariate that affects the PF torque and positive work outcomes. In this study, botulinum neurotoxin (BoNT) may have reduced the number of =patients who did not achieve 10 degrees and/or 0 degrees DF at baseline such that their outcomes were included in the “PF torque” analysis. Not controlling for individual ankle stiffness may be a limitation in the statistical analysis. However, the number of observations was too low to include additional covariates. In future studies, controlling for baseline ankle stiffness due to BoNT treatment and natural changes will be important.

The optimal Hermes’ compensation for improving ankle function during walking and daily activities is subject to future studies. As Hermes use may also contribute to functional stretching, the initially required compensation may decrease as patients adapt to Hermes. Longitudinal studies are needed to reveal the long-term effects of compensation provided by Hermes.

5. Conclusions

Our results demonstrate that Hermes is able to effectively compensate ankle stiffness, leading to reductions in both the combined Ankle + Hermes PF torque and positive work compared to conditions without Hermes. We believe that the Hermes ankle-foot orthosis can provide a solution for reducing increased ankle stiffness, thereby enhancing ankle function during daily activities and improving walking ability for patients with spastic paresis. Additionally, our findings affirm that robotic measurements of ankle stiffness and combined Ankle + Hermes stiffness are valuable for the precise customization of torque provided by ankle-foot orthoses (precision orthotics). Based on our results, the next step in integrating Hermes into the management of spastic paresis is to evaluate its effects during walking.

Author Contributions: Conceptualization, K.E.R.H., J.H.d.G. and W.M.; methodology, K.E.R.H., J.H.d.G., E.R.M.G.-H., M.S., S.K.S. and W.M.; software, F.B. and E.R.M.G.-H.; resources, F.B., J.H.d.G., M.S. and S.K.S.; formal analysis, K.E.R.H. and E.R.M.G.-H.; data curation, E.R.M.G.-H. and K.E.R.H.; writing—original draft preparation, K.E.R.H.; writing—review and editing, J.H.d.G., M.S., S.K.S., F.C.T.v.d.H., H.v.d.K. and W.M.; supervision, F.C.T.v.d.H., H.v.d.K., J.H.d.G. and W.M.; funding acquisition, F.C.T.v.d.H., J.H.d.G. and W.M.; Clinical trial administration, M.S. and J.H.d.G. All authors have read and agreed to the published version of the manuscript.

Funding: This research was funded by Stichting voor de Technische Wetenschappen (STW) and currently known as NWO-TTW Grant 14904STW – Stiffness as Needed and Health~Holland (LSHM 21005 – Precision Orthotics).

Institutional Review Board Statement: This research was conducted in accordance with the Declaration of Helsinki and was approved by the Leiden-Den Haag-Delft Medical Ethical Committee, CCMO (Centrale Commissie Mensgebonden Onderzoek) trial registration number NL64640.058.19. The research protocol was approved on 19 December 2019, and an update was then approved on 29 September 2022.

Informed Consent Statement: Informed consent was obtained from all subjects involved in this study. Written informed consent has been obtained from the patient(s) to publish this paper.

Data Availability Statement: The data presented in this study related to the plantarflexion torque and positive work are available in the 4TU. ResearchData repository (DOI: 10.4121/fab1a54d-3e68-4d6f-8d94-161c16539760). The participants data supporting this study is restricted to the research safety commission, a designated monitor from the Leiden University Medical Center (LUMC), and national and international supervisory authorities, such as the Dutch Healthcare and Youth Inspectorate (IGJ).

Acknowledgments: We thank Yvette Kerkum, Niels Passchier, Lysanne de Jong, and Peter de Groot from OIM Orthopedie for their collaboration in the design and manufacturing of the Hermes orthotic braces, and we thank Rogier Barents for his collaboration on the design and manufacturing of the negative-stiffness mechanism for Hermes.

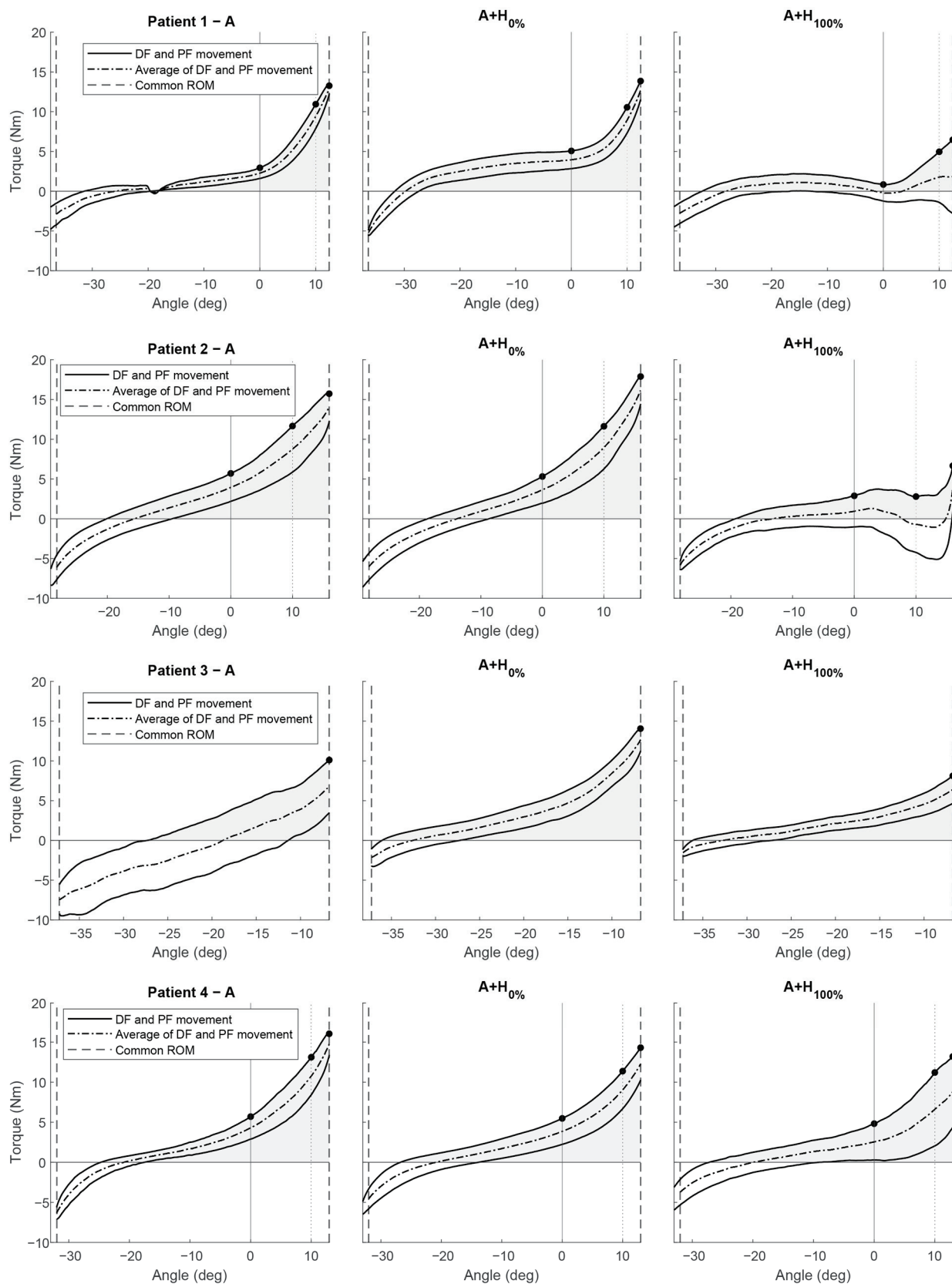
Conflicts of Interest: Frank Baas is affiliated with InteSpring that markets the mechanism utilized in the Hermes ankle-foot-orthosis. All the other authors declare no conflicts of interest. The funders had no role in the design of the study; in the collection, analyses, or interpretation of data; in the writing of the manuscript; or in the decision to publish the results.

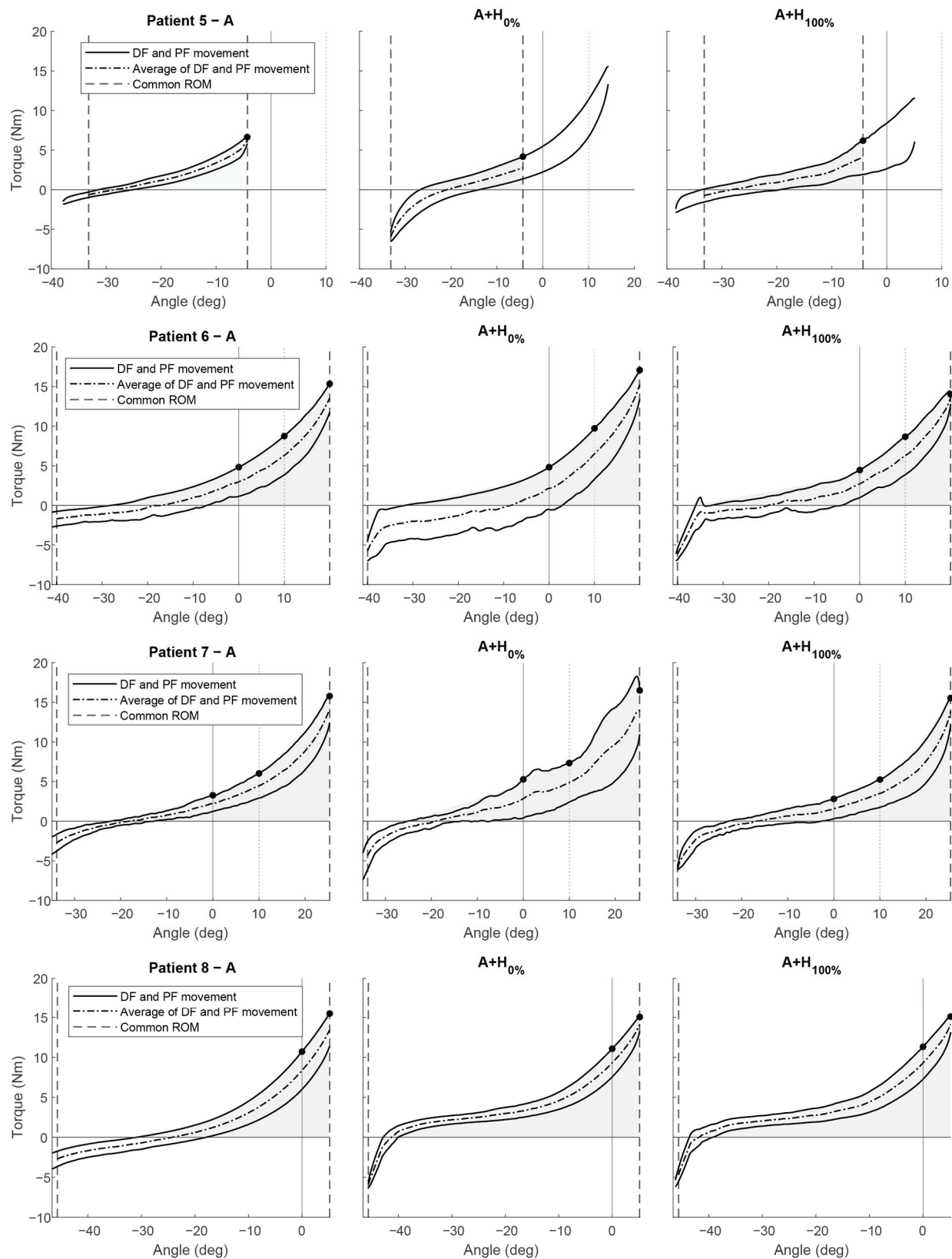
Appendix A. Calculation of Positive Work

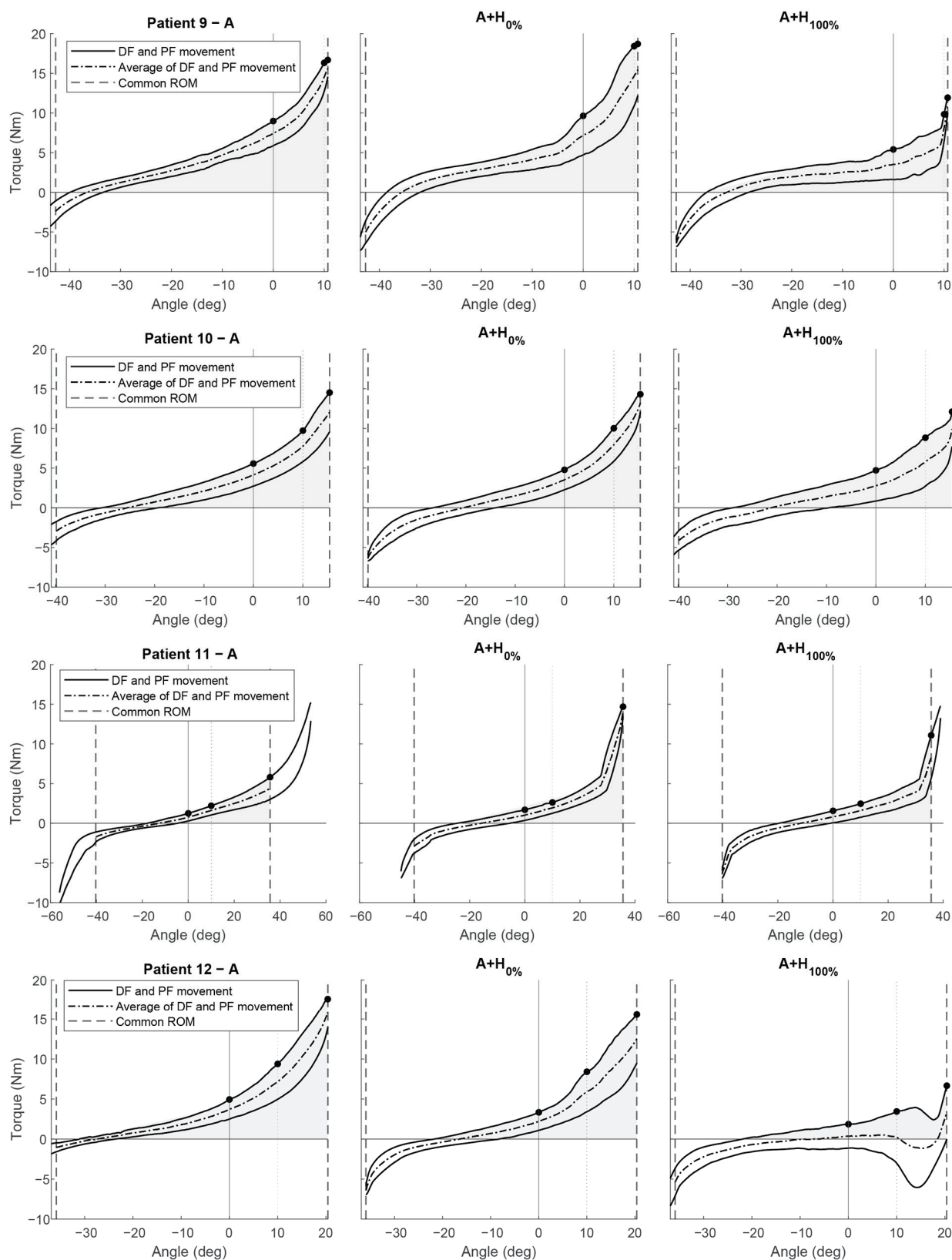
Since the patient's leg was removed from the ankle manipulator between conditions to put on or adjust Hermes, the calibration angle of the ankle manipulator could vary by several degrees between conditions. This variation was allowed to maintain consistent patient posture (i.e., similar hip, knee, and ankle angles before the start of each condition) but resulted in small differences in the passive ROM between conditions for some patients. To account for these small ROM differences and ensure a fair comparison of positive work, the common ROM shared by the averaged torque-angle characteristics across the three conditions was considered the passive ROM for determining the positive work. This common ROM refers to the angles where torque measurements were available for all three conditions.

Appendix B. Torque-Angle Characteristics Measured from All Analyzed Patients

The following figures show the torque-angle characteristics measured without (A) and with Hermes ($A + H_{0\%}$ and $A + H_{100\%}$) for all patients. Solid lines denote the hysteresis loop of the torque measured during the DF and PF movements applied by the ankle manipulator. The dashed-dotted lines denote the average torque of the measured DF and PF movements from the hysteresis loop. The black-filled circles represent the torque values at 0 deg., 10 deg., and max. DF angle for comparison between patients. The dashed lines denote the common ROM across conditions for each patient, while the shaded areas indicate the positive work, calculated as the areas under the torque-angle characteristic.







Appendix C. Post Hoc Analysis

After the repeated-measures ANOVAs, post hoc analyses were conducted to compare the PF torque between conditions (A , $A + H_{0\%}$, and $A + H_{100\%}$) at 0 deg and 10 deg, and at the max. DF angle. Table A1 shows the differences in PF torque (in Nm) along with the 95% confidence intervals for each comparison. Significant reductions in PF torque were

observed in the condition with Hermes applying compensation ($A + H_{100\%}$) compared to both the baseline (A) and when Hermes applied no compensation ($A + H_{0\%}$) across all tested angles ($p < 0.05$).

Table A1. Post hoc analysis.

Angle	Comparison	Difference in Torque (Nm)	95% Confidence Interval	p Value
0°	$A + H_{100\%}$ vs. A	1.5	0.06 to 2.9	0.041
	$A + H_{100\%}$ vs. $A + H_{0\%}$	1.7	0.03 to 3.5	0.046
10° DF	$A + H_{100\%}$ vs. A	3.9	0.2 to 7.5	0.040
	$A + H_{100\%}$ vs. $A + H_{0\%}$	4.1	0.3 to 7.9	0.037
Max. DF Angle	$A + H_{100\%}$ vs. A	4.1	0.6 to 7.5	0.021
	$A + H_{100\%}$ vs. $A + H_{0\%}$	4.8	1.2 to 8.3	0.010

References

- Dietz, V.; Sinkjaer, T. Spastic movement disorder: Impaired reflex function and altered muscle mechanics. *Lancet Neurol.* **2007**, *6*, 725–733. [CrossRef] [PubMed]
- Nonnekens, J.; Benda, N.; van Duijnhoven, H.; Lem, F.; Keijsers, N.; Louwerens, J.W.K.; Pieterse, A.; Renzenbrink, B.; Weerdesteyn, V.; Buurke, J.; et al. Management of Gait Impairments in Chronic Unilateral Upper Motor Neuron Lesions. *JAMA Neurol.* **2018**, *75*, 751. [CrossRef]
- Lieber, R.L.; Steinman, S.; Barash, I.A.; Chambers, H. Structural and functional changes in spastic skeletal muscle. *Muscle Nerve* **2004**, *29*, 615–627. [CrossRef] [PubMed]
- Bar-On, L.; Desloovere, K.; Molenaers, G.; Harlaar, J.; Kindt, T.; Aertbeliën, E. Identification of the neural component of torque during manually-applied spasticity assessments in children with cerebral palsy. *Gait Posture* **2014**, *40*, 346–351. [CrossRef] [PubMed]
- De Gooijer-Van De Groep, K.L.; De Vlugt, E.; de Groot, J.H.; van der Heijden-Maessen, H.C.; Wielheesen, D.H.; van Wijlen-Hempel, R.M.S.; Arendzen, J.; Meskers, C.G. Differentiation between non-neural and neural contributors to ankle joint stiffness in cerebral palsy. *J. Neuroeng. Rehabil.* **2013**, *10*, 81. [CrossRef]
- Gao, F.; Grant, T.H.; Roth, E.J.; Zhang, L.-Q. Changes in Passive Mechanical Properties of the Gastrocnemius Muscle at the Muscle Fascicle and Joint Levels in Stroke Survivors. *Arch. Phys. Med. Rehabil.* **2009**, *90*, 819–826. [CrossRef]
- Bowers, D.; Fheodoroff, K.; Khan, P.; Harriss, J.P.; Dashtipour, K.; Bahroo, L.; Lee, M.; Zakharov, D.; Balcaitene, J.; Evidente, V. Spastic Paresis and Rehabilitation—The Patient Journey. *Eur. Neurol. Rev.* **2016**, *11*, 87. [CrossRef]
- Bovend'Eerd, T.J.; Newman, M.; Barker, K.; Dawes, H.; Minelli, C.; Wade, D.T. The Effects of Stretching in Spasticity: A Systematic Review. *Arch. Phys. Med. Rehabil.* **2008**, *89*, 1395–1406. [CrossRef]
- Bressel, E.; McNair, P.J. The effect of prolonged static and cyclic stretching on ankle joint stiffness, torque relaxation, and gait in people with stroke. *Phys. Ther.* **2002**, *82*, 880–887. [CrossRef]
- Katalinic, O.M.; Harvey, L.A.; Herbert, R.D. Effectiveness of stretch for the treatment and prevention of contractures in people with neurological conditions: A systematic review. *Phys. Ther.* **2011**, *91*, 11–24. [CrossRef]
- Geertsens, S.S.; Kirk, H.; Lorentzen, J.; Jorsal, M.; Johansson, C.B.; Nielsen, J.B. Impaired gait function in adults with cerebral palsy is associated with reduced rapid force generation and increased passive stiffness. *Clin. Neurophysiol.* **2015**, *126*, 2320–2329. [CrossRef]
- Rodriguez Hernandez, K.E.; De Groot, J.H.; Baas, F.; Stijntjes, M.; Grootendorst-Heemskerk, E.R.M.; Schiemanck, S.K.; Van Der Helm, F.C.T.; Van Der Kooij, H.; Mugge, W. Ankle-Foot-Orthosis “Hermes” Compensates Pathological Ankle Stiffness of Chronic Stroke—A Proof of Concept. *IEEE Trans. Neural Syst. Rehabil. Eng.* **2023**, *31*, 3535–3544. [CrossRef] [PubMed]
- Bregman, D.J.J.; Rozumalski, A.; Koops, D.; de Groot, V.; Schwartz, M.; Harlaar, J. A new method for evaluating ankle foot orthosis characteristics: BRUCE. *Gait Posture* **2009**, *30*, 144–149. [CrossRef] [PubMed]
- Klomp, A.; Van der Krogt, J.; Meskers, C.G.; de Groot, J.H.; De Vlugt, E.; van der Helm, F.C.T.; Arendzen, J. Design of a Concise and Comprehensive Protocol for Post Stroke Neuromechanical Assessment. *J. Bioeng. Biomed. Sci.* **2012**, *S1*, 008. [CrossRef]
- Sloot, L.H.; van der Krogt, M.M.; van Eesbeek, S.; de Groot, J.; Buizer, A.I.; Meskers, C.; Becher, J.G.; de Vlugt, E.; Harlaar, J. The validity and reliability of modelled neural and tissue properties of the ankle muscles in children with cerebral palsy. *Gait Posture* **2015**, *42*, 7–15. [CrossRef] [PubMed]
- Meskers, C.G.; de Groot, J.H.; de Vlugt, E.; Schouten, A.C. NeuroControl of movement: System identification approach for clinical benefit. *Front. Integr. Neurosci.* **2015**, *9*, 48. [CrossRef]

17. Rodriguez, K.; De Groot, J.; Baas, F.; Stijntjes, M.; Van Der Helm, F.; Van Der Kooij, H.; Mugge, W. Passive ankle joint stiffness compensation by a novel Ankle-Foot-Orthosis. In Proceedings of the 2018 7th IEEE International Conference on Biomedical Robotics and Biomechatronics (Biorob), Enschede, The Netherlands, 26–29 August 2018; Volume 2018-August, pp. 517–522.
18. Bohannon, R.W.; Smith, M.B. Interrater reliability of a modified Ashworth scale of muscle spasticity. *Phys. Ther.* **1987**, *67*, 206–207. [CrossRef] [PubMed]
19. Fleuren, J.F.M.; Buurke, J.H.; Geurts, A.C.H. Clinical Management of Spasticity and Contractures in Stroke. In *Neurological Rehabilitation*; Rehabilitation Science in Practice Series; CRC Press/Taylor & Francis Group: Boca Raton, FL, USA, 2018; pp. 101–134.
20. Compston, A. Aids to the investigation of peripheral nerve injuries. Medical Research Council: Nerve Injuries Research Committee. His Majesty's Stationery Office: 1942; pp. 48 (iii) and 74 figures and 7 diagrams; with aids to the examination of the peripheral nervous system. By Michael O'Brien for the Guarantors of *Brain*. Saunders Elsevier: 2010; pp. [8] 64 and 94 Figures. *Brain* **2010**, *133*, 2838–2844. [CrossRef] [PubMed]
21. Martina, I.S.J.; Van Koningsveld, R.; Schmitz, P.I.M.; Van Der Meché, F.G.A.; Van Doorn, P.A. Measuring vibration threshold with a graduated tuning fork in normal aging and in patients with polyneuropathy. *J. Neurol. Neurosurg. Psychiatry* **1998**, *65*, 743–747. [CrossRef]
22. de Gooijer-van de Groep, K.L. *Identification of Neural and Non-Neural Contributors to Joint Stiffness in Upper Motor Neuron Disease*; Leiden University Medical Center: Leiden, The Netherlands, 2019.
23. Brockett, C.L.; Chapman, G.J. Biomechanics of the ankle. *Orthop. Trauma* **2016**, *30*, 232–238. [CrossRef] [PubMed]
24. Evaluatie van Spasticiteit—Richtlijndatabase. Available online: https://richtlijndatabase.nl/richtlijn/cerebrale_en_of_spinale_spasticiteit/evaluatie_van_spasticiteit.html (accessed on 8 September 2021).
25. Gao, F.; Ren, Y.; Roth, E.J.; Harvey, R.; Zhang, L.-Q.Q. Effects of repeated ankle stretching on calf muscle-tendon and ankle biomechanical properties in stroke survivors. *Clin. Biomech.* **2011**, *26*, 516–522. [CrossRef]
26. Roy, A.; Forrester, L.W.; Macko, R.F.; Krebs, H.I. Changes in passive ankle stiffness and its effects on gait function in people with chronic stroke. *J. Rehabil. Res. Dev.* **2013**, *50*, 555–572. [CrossRef] [PubMed]

Disclaimer/Publisher's Note: The statements, opinions and data contained in all publications are solely those of the individual author(s) and contributor(s) and not of MDPI and/or the editor(s). MDPI and/or the editor(s) disclaim responsibility for any injury to people or property resulting from any ideas, methods, instructions or products referred to in the content.

Article

Parametric Design of an Advanced Multi-Axial Energy-Storing-and-Releasing Ankle–Foot Prosthesis

Marco Leopaldi ^{1,2}, Tommaso Maria Brugo ^{1,*}, Johnnidel Tabucol ¹ and Andrea Zucchelli ¹

¹ Department of Industrial Engineering, University of Bologna, 40131 Bologna, Italy; marco.leopaldi@unibo.it (M.L.); johnnidel.tabucol2@unibo.it (J.T.); a.zucchelli@unibo.it (A.Z.)

² Interdepartmental Centre for Industrial Research in Advanced Mechanical Engineering Applications and Materials Technology, University of Bologna, 40131 Bologna, Italy

* Correspondence: tommasomaria.brugo@unibo.it; Tel.: +39-349-254-5001

Abstract: The ankle joint is pivotal in prosthetic feet, especially in Energy-Storing-and-Releasing feet, favoured by individuals with moderate to high mobility (K3/K4) due to their energy efficiency and simple construction. ESR feet, mainly designed for sagittal-plane motion, often exhibit high stiffness in other planes, leading to difficulties in adapting to varied ground conditions, potentially causing discomfort or pain. This study aims to present a systematic methodology for modifying the ankle joint's stiffness properties across its three motion planes, tailored to individual user preferences, and to decouple the sagittal-plane behaviour from the frontal and transverse ones. To integrate the multi-axial ankle inside the MyFlex- η , the designing of experiments using finite element analysis was conducted to explore the impact of geometric parameters on the joint's properties with respect to design constraints and to reach the defined stiffness targets on the three ankle's motion planes. A prototype of the multi-axial ankle joint was then manufactured and tested under FEA-derived load conditions to validate the final configuration chosen. Composite elastic elements and complementary parts of the MyFlex- η , incorporating the multi-axial ankle joint, were developed, and the prosthesis was biomechanically tested according to lower limb prosthesis ISO standards and guidelines from literature and the American Orthotic and Prosthetic Association (AOPA). Experimental tests showed strong alignment with numerical predictions. Moreover, implementing the multi-axial ankle significantly increased frontal-plane compliance by 414% with respect to the same prosthesis with only one degree of freedom on the sagittal plane without affecting the main plane of locomotion performance.

Keywords: multi-axial ankle joint; lower-limb prosthesis; prosthetic foot; energy-storing-and-releasing prosthesis; finite element analysis (FEA); design of experiments (DOE); regression analysis; biomechanics

Citation: Leopaldi, M.; Brugo, T.M.; Tabucol, J.; Zucchelli, A. Parametric Design of an Advanced Multi-Axial Energy-Storing-and-Releasing Ankle–Foot Prosthesis. *Prosthesis* **2024**, *6*, 726–743.

<https://doi.org/10.3390/prosthesis6040051>

Academic Editor: Arnab Chanda

Received: 10 April 2024

Revised: 31 May 2024

Accepted: 7 June 2024

Published: 24 June 2024



Copyright: © 2024 by the authors. Licensee MDPI, Basel, Switzerland. This article is an open access article distributed under the terms and conditions of the Creative Commons Attribution (CC BY) license (<https://creativecommons.org/licenses/by/4.0/>).

1. Introduction

Currently, Energy-Storing-and-Releasing (ESR) feet are the most widespread foot prostheses, particularly for individuals with lower-limb amputations exhibiting ambulatory level K3 (active individuals not restricted to low-cadence walking, unlike K2-ambulatory-level amputees) and K4 (sports activities individuals). ESR feet are simple and energy-efficient devices made of composite elastic elements in carbon and/or glass-fiber-reinforced plastic (CFRP/GFRP). They store elastic energy in the mid-stance phase and release it during the push-off phase, partially reducing the metabolic energy cost of the gait [1]. Certain ESR feet incorporate an ankle joint to provide wider range of motion (ROM) and enhance ankle power in the sagittal plane while concurrently alleviating contralateral limb load [2], offering a smoother rollover and easier ambulation on stairs and ramps [3]. Most ESR feet on the market offer only the sagittal-plane degree of freedom (DOF), a limitation that may pose challenges in adapting the user to diverse ground conditions and may lead to gait asymmetry, which may increase torsional stress on the stump [4], gait instability [5], discomfort or pain [6] and skin breakdown [7]. Daily activities, such as turning steps and

side-stepping, require complex ankle–foot behaviour [8,9], as well as walking on uneven terrain and incline roads [10]. A foot prosthesis with a multi-axial ankle joint that offers more than one DOF could promote adaptability and stability on various terrains and in various activities [11–15].

Multi-axial ankle joints have been integrated both into solid ankle-cushioned heel (SACH) and bionic feet. However, SACH feet are suitable for hypo-mobile users (K1/K2 ambulation levels) and basic activities. Some bionic feet, despite offering powered non-sagittal-plane ROMs [9,12,16–20], have limitations related to battery autonomy and weight. Furthermore, multi-axial bionic feet are not currently commercialized.

Various methods have also been investigated to introduce multi-axiality inside advanced ESR feet. Split geometries (composite elastic elements partially cut along their longitudinal direction) improve cross-sloped walking with respect to the continuous carbon forefoot (optimized in width and lamination sequence) [21]. However, genuine foot twisting remains unattainable since the adaptation to inclined terrain relies solely on toe shifting, resulting in elevated lateral forces and inversion/eversion moments on the user's stump. Ankle joints featuring a frontal-plane DOF might enhance frontal-plane adaptability and reduce loads, according to static and dynamic tests with machines [15,22,23]; however, clinical investigations with human patients are necessary to validate these findings. Concerning commercial prostheses, the Triton Side Flex by Ottobock integrates a torsion bar to decouple frontal- and sagittal-plane behaviours, offering inversion and eversion compliance compatible with *American Orthotic and Prosthetic Association* guidelines (AOPA, www.aopanet.org (accessed on 4 May 2021)) [15]. However, the ROM and ankle power in the sagittal plane are limited due to the absence of an ankle joint that enables sagittal-plane rotation [2], binding transverse foot behaviour to the composite blades' torsional stiffness. The Talux foot by Ossur uses a urethane layer between composite elastic elements to provide fluid, natural walking motion on various terrains. Unfortunately, Talux is suitable only for users of low to moderate activity level (K2/K3), and, nowadays, is no longer commercialized. The XTEND Foot employs a specific combination of GFRP and CFRP, but its continuous forefoot nature restricts plane motions to the geometries and lamination sequences of the elastic elements. Ultimately, external modules (such as the Ossur torsion shock adapter or Ottobock torsion adapter) can be incorporated between the pylon and feet and has been demonstrated to be capable of reducing the perceived effort when walking and enhancing turning activities and ambulation on uneven terrain [3].

Despite these advancements, according to the authors' current knowledge, ESR feet for K3/K4 users with multi-axial ankle joints with independent stiffness and biomechanical attributes in the frontal and transverse planes are not currently available. Recognizing the inherent variability in human walking patterns [24,25], the ability to tailor the prosthesis's behaviour in different motion planes to accommodate individual user preferences is crucial [26]. Furthermore, Xu et al. investigate the relationship between the initial contact angle of the ankle with the ground and the ankle's ROM in relation to lower-limb injury risk during single-leg landings. They propose an optimized landing strategy aimed at reducing injury risk. The results suggest that increasing the ankle's ROM and initial contact angle enhances joint energy dissipation and reduces impact loads on the joints, thereby decreasing the risk of lower-limb injuries, including anterior cruciate ligament injuries [27].

Therefore, the authors aimed to address the diverse habits and preferences of users by introducing a methodology for designing a multi-axial ankle joint, allowing for the modification of ankle joint properties. The MyFlex- η (Figure 1a) foot is presented as a case study to validate the methodology. MyFlex- η was designed and built upon MyFlex- δ (Figure 1b), an ESR foot prosthesis with a CFRP spherical ankle joint proposed by Tabucol et al. [28]. The spherical ankle joint of MyFlex- δ managed rotations in all motion planes, with sagittal motion primarily depending on the flexural behaviour of the elastic elements. Foot motion in the frontal and transverse planes was also governed by the torsional stiffness of the composite blades, which depended on blade geometries and lamination sequences. Washers were in fact assembled at link extremities, modifying the spherical uniball joint

connections into cylindrical ones to avoid instability. Additionally, after prolonged use, the spherical ankle seat and joint tended to wear out, generating carbon dust and resulting in interaction between the parts.

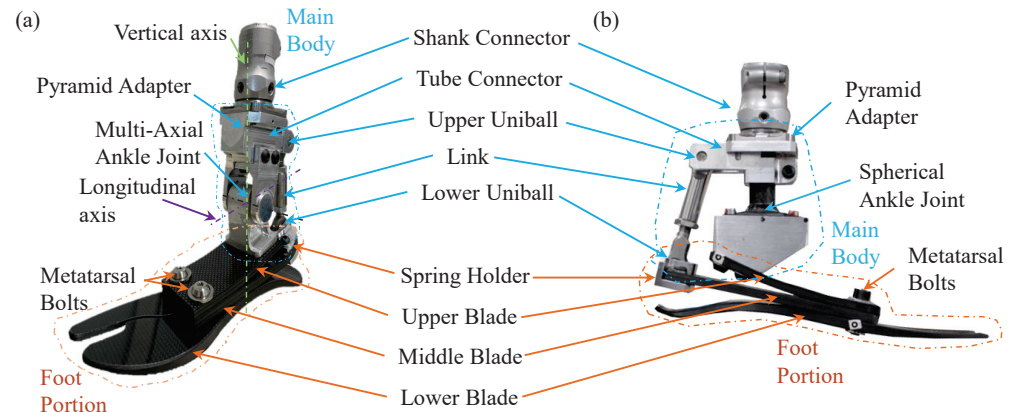


Figure 1. Differences between the MyFlex- η prototype and its predecessor, MyFlex- δ [28]. (a) MyFlex- η features an independent stiffness multi-axial ankle, whereas (b) MyFlex- δ is characterized by a CFRP spherical ankle joint.

Thus, MyFlex- η was introduced with the scope to improve the multi-axiality of MyFlex- δ by integrating an elastomeric multi-axial ankle (Figure 2) that enables independent adjustments of stiffness and biomechanical attributes in the frontal and transverse planes but maintains MyFlex- δ 's stiffness and biomechanical characteristics in the sagittal one.

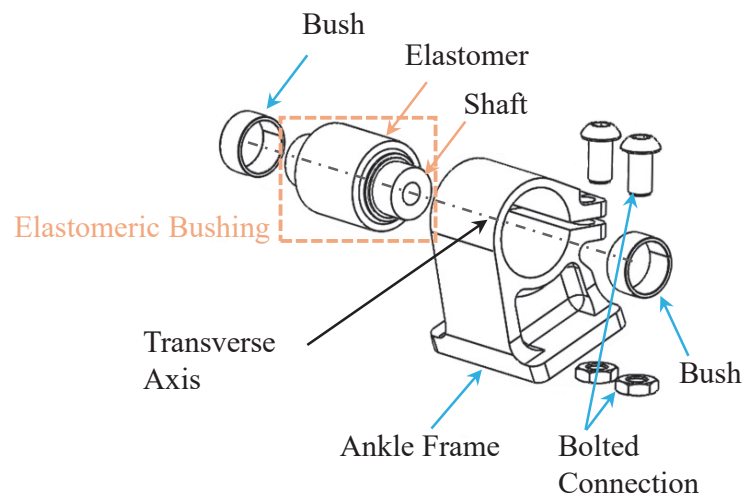


Figure 2. Expanded view of the MyFlex- η multi-axial ankle sub-assembly.

2. Materials and Methods

2.1. Concept Design

MyFlex- η (Figure 1a), representing an evolution of MyFlex- δ (Figure 1b), comprises two primary sub-assemblies: the foot portion and the main body. The first consists of three CFRP leaf springs (upper, middle, and lower blades), interconnected by two metatarsal bolted joints, and a spring holder secured with the same joint onto the middle blade. The latter includes the novel multi-axial ankle joint, and the tube connector is linked to the shank via a pyramid adapter. These sub-assemblies are assembled through two screws connecting the ankle frame to the upper blade and through the two uni-ball at the link extremities, which create two spherical joints with the tube connector and the spring holder. The design of the multi-axial ankle joint was inspired by an anti-vibration bushing commonly used in automotive suspension systems. Typically, it consists of two concentric

hollow metal cylinders connected by an elastomeric insert ring. The elastomer may either be bonded to both cylinders or attached to the inner cylinder and pre-compressed by the outer one, with the chosen manufacturing technique influencing the bushing's stiffness characteristics. In MyFlex- η , the elastomer is melted onto the shaft and secured within the ankle frame (serving as the outer hollow cylinder), screwing two bolted connections (Figure 2). This ankle frame configuration was chosen based on the results obtained from the design of experiments (DOE) presented in Section 2.2. By adjusting bolts' screwing, the pre-compression applied to the elastomer can be modified, leading to joint stiffnesses adjustments in the three planes of motion.

Referring to Figure 3, this design construction allows the equivalent stiffness generated by the torsional stiffness of the leaf spring in series with the bushing's conical stiffness to govern the prosthesis' frontal-plane motion. Conical stiffness is determined as the ratio between the conical load and elastomeric bushing conical rotation applied and calculated around the longitudinal axis (Figure 3d). This stiffness also manages the transverse foot rotation, where conical load and bushing rotation are applied and calculated around the vertical axis (Figure 3c).

The hinge connections between the shaft and the tube connector's arms enable the control of the foot's sagittal stiffness exclusively through the flexural stiffness of the composite blades, ensuring that no torsional load is applied on the bushing (Figure 3e). Radial stiffness (Figure 3b), defined as the ratio between the vertical load (or radial load) generated during the gait cycle and the vertical displacement (or radial displacement) of the transverse axis, manages foot shock absorption and can modify prosthesis sagittal ROM (as described in Section 2.4). Conversely, axial stiffness (Figure 3a), equal to the ratio between the axial load and the axial displacement of the vertical axis applied along the transverse axis, was set to a specific value to avoid possible ankle misalignment that could have posed risks for the user during gait (as discussed in Section 2.2).

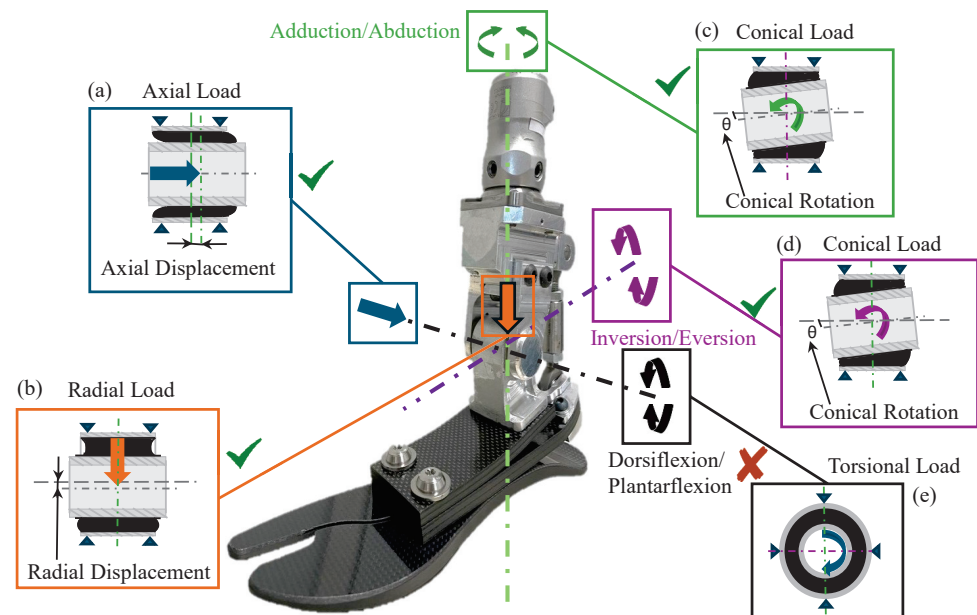


Figure 3. Sectional views of the multi-axial ankle joint, accompanied by schematic representations of applicable load conditions. (a) Radial load; (b) conical load around the longitudinal axis; (c) conical load around the vertical axis; (d) axial load; (e) torsional load; schematic representation of which elastomeric bushing stiffness manages ankle motions.

2.2. Design of Experiments of the Multi-Axial Ankle

The feasibility of incorporating an elastomeric bushing within the main body of MyFlex- η was investigated through a DOE using finite element (FE) analysis (FEA) with ANSYS Workbench 2023. To streamline the computational efficiency, a half-bushing model

(Figure 4a) was imported from a CAD environment, exploiting load and geometry symmetry, and linear material conditions were assumed instead of hyper-elastic properties.

Poisson's ratio and density for the elastomer were, respectively, set to 0.49 g/cm³ (semi-not-compressible solid) and 1.12 g/cm³.

The A.N. Gent equation (Equation (1)) was employed to establish a correlation between the Shore A hardness (ShA) of the hyper-elastic material and the Young's Modulus as follows:

$$E = \frac{0.0981(56 + 7.62336\text{ShA})}{0.137505(254 - 2.54\text{ShA})} \quad (1)$$

The trapezoidal section of the elastomer, along with its 1 mm thick filleted extensions on both sides, was deliberately engineered to alleviate the initial stress generated at the bonding interface with the shaft during the pre-compression phase and to extend the bonding surface.

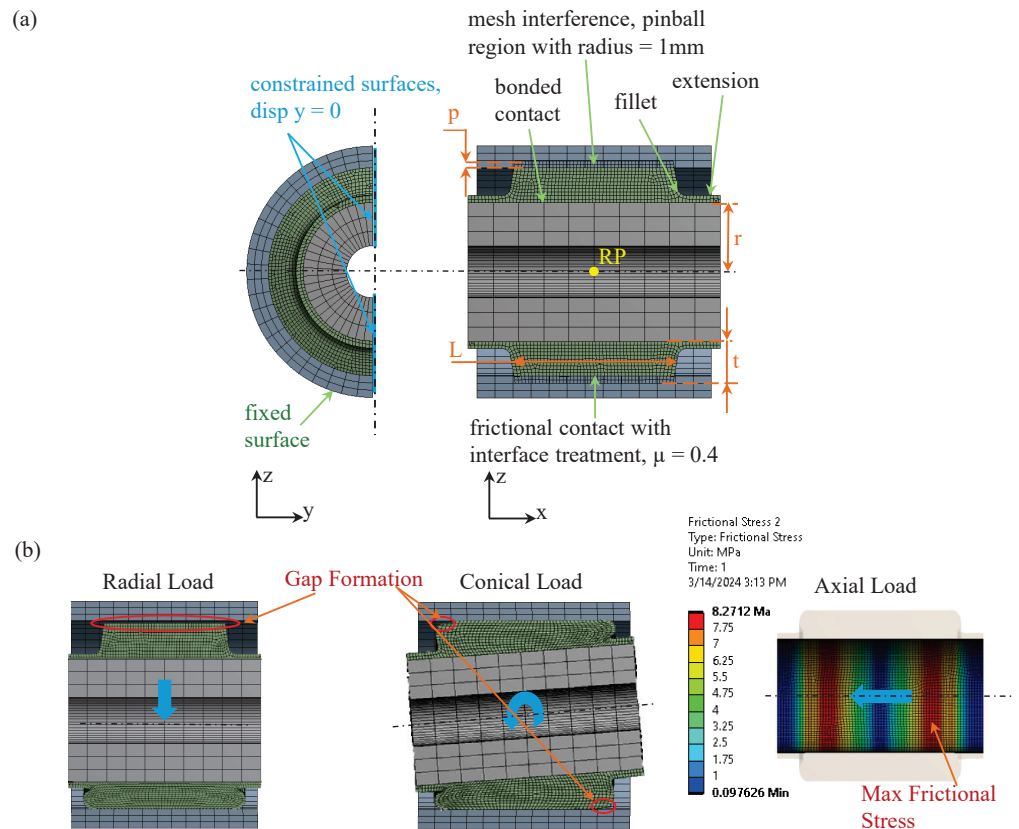


Figure 4. Finite element (FE) modelling of the elastomeric bushing for DOE. (a) Parameters, contact, mesh, and constraints. (b) Critical outputs, obtained from the analysis, monitored to select the optimal configuration of the bushing to integrate within the ankle of the prosthesis.

The pre-compression was modelled as the interference between the external radius of the elastomer and the internal radius of the external hollow cylinder and applied through a frictional contact (pure penalty formulation and friction coefficient = 0.4), with a ramped effect in the interface treatment of geometry modification. Consequently, a bonded connection was established between the elastomer and the shaft (Augmented Lagrange formulation). The outer surface of the external hollow cylinder was fixed to represent the constraint with the ankle frame. Symmetry was simulated by constraining the displacement of the bushing's sectioned areas along the y-direction. All components were modelled using quadratic displacement behaviour 3D elements with 20 nodes (SOLID 186). Working conditions were replicated by applying loads in the centre-of-gravity point of the shaft

by using a rigid remote point (RP). A mesh convergence test was conducted to minimize stress error. The internal and external bushing cylinders were discretized with a coarse mesh, whereas a finer mesh was employed for the elastomer, given its significantly higher compliance than the metal cylinders (approximately four orders of magnitude).

Non-linear simulations were conducted under static structural conditions using a direct solver, with the elastomer's pre-compression and load application simulated in the first and second steps, respectively. Then, 5° of rotation around the y-axis (RP_{y-rot}), 1 mm of displacement along the z-axis (RP_{z-disp}), and 1 mm of displacement along the x-axis (RP_{x-disp}) were applied at the remote point, separately. Conical (K_{con}), radial (K_{rad}), and axial (K_{ax}) stiffness were determined as the ratios between displacements and fixed support reaction moments and forces according to the following equations (Equations (2)–(4)):

$$K_{con} = \frac{M_y}{RP_{y-rot}} \left(\frac{Nm}{o} \right) \quad (2)$$

$$K_{rad} = \frac{F_z}{RP_{z-disp}} \left(\frac{N}{mm} \right) \quad (3)$$

$$K_{ax} = \frac{F_x}{RP_{x-disp}} \left(\frac{N}{mm} \right) \quad (4)$$

The bushing's parameters (Figure 4a) were systematically varied to evaluate their impact on its mechanical properties. Maximum geometric parameter values were constrained by functional requirements to match human ankle dimensions and ensure the compatibility of the main body with the foot cosmetic cover. Minimum geometrical parameter values were defined based on the loads extrapolated from MyFlex- δ simulations carried out considering the ultimate static test strength condition for a P5 category prosthesis (according to [29], www.iso.org (accessed on 15 June 2021)). Five values for each parameter were explored within predefined limits (Table 1).

The undesirable positioning of the centre of pressure (COP) during gait, attributed to ankle misalignment, poses a risk of reduced user confidence or even falls [30–32]. Therefore, constraints were applied to avoid ankle misalignment with respect to the vertical axis of the prosthesis, arising from excessive axial displacement and material strength limitations: gap formation between the elastomer and the outer hollow cylinder, resulting from conical and radial loading (Figure 4b), was limited to zero; the frictional stress (FS) at the bonding interface between the elastomer and the shaft was kept below the permissible value of 9.4 MPa (determined from the validation of the FE model with experimental displacing force tests) to prevent elastomer detachment from the shaft (Figure 4b). Furthermore, considering the axial reaction force generated in the ankle experienced from the cross-slope simulations conducted on MyFlex- δ under the aforementioned load conditions, ankle stiffness was confined within a range of 1200 to 1600 (N/mm) to ensure axial displacement remained below 1 mm.

Table 1. DOE parameters: pre-compression (p), internal radius (r), Young's Modulus (E), thickness (t), medium length between short and long edges of the elastomer trapezoidal section (L). The chosen parameters' values define the DOE design space.

Parameter	Units	Values
Pre-compression (p)	mm	0.5, 0.6, 0.7, 0.8, 0.9
Radius (r)	mm	6, 7, 9, 11, 12
Young's Modulus (E)	MPa	8, 12, 16, 20, 24
Thickness (t)	mm	3, 3.5, 4.5, 5.5, 6
Length (L)	mm	12, 14, 18, 22, 24

A regression analysis was employed to fit the results carried out from a total of 9375 simulations (computational time of 15 min for each simulation, using four micropro-

cessor cores) and investigate the relationships between parameter variation with the output and constraints. The regression coefficients (β_i) of the response surface (Equation (5)) were determined using the least squares method knowing the outputs (Y_i) obtained from FEAs and the matrix of the five levels of the independent parameters [33] as follows:

$$Y_i = \beta_0 + \beta_1 p + \beta_2 r + \beta_3 E + \beta_4 t + \beta_5 L + \beta_6 p^2 + \beta_7 r^2 + \beta_8 E^2 + \beta_9 t^2 + \beta_{10} L^2 + \beta_{11} pr + \beta_{12} pE + \beta_{13} pt + \beta_{14} pL + \beta_{15} rE + \beta_{16} rt + \beta_{17} rL + \beta_{18} Et + \beta_{19} EL + \beta_{20} tL \quad (5)$$

Fitted response surface vectors (Y_{fit}) were computed, and non-significant regression coefficients by the analysis of p_{values} associated with each parameter and Pareto charts were excluded. Subsequently, the adjusted coefficients of multiple determination R^2 , assessing the model's reliability, were found to be 0.9905, 0.9945, and 0.9994, respectively, for conical, radial, and axial stiffness. For simplicity, response surface vectors were reported only for stiffness outputs, as follows (all other vectors with the complete sensitivity analysis are provided in the Supplementary Material):

$$K_{con} = 3.16 + 2.09p - 0.31r - 0.47E + 1.18t - 0.71L + 0.32t^2 + 0.03L^2 + 0.04rE - 0.13rt + 0.05rL - 0.1Et + 0.05EL - 0.16tL \quad (6)$$

$$K_{rad} = -8150 + 4622.5p + 28.1r + 72.9E - 367t + 506.9 + 821.8t^2 + 66.8rE - 281.3rt + 68.8rL - 249.4Et + 60.1EL - 250tL \quad (7)$$

$$K_{ax} = -138.6 + 79.1p + 1.6r + 2.9E - 14.3t + 5.6L + 41.9t^2 + 7.8rE - 19rt + 4.7rL - 17.5Et + 5.1EL + 10.6tL \quad (8)$$

The bar charts in Figure 5 illustrate the parameters' contributions to the bushing properties. Concerning stiffnesses, the elastomer length (L) had the greatest impact on the conical stiffness, and elastomer thickness (t) predominantly influenced radial stiffness, while the Young's Modulus mainly affected the axial stiffness. Based on the contribution percentages and regression coefficient signs, an increase in L resulted in a differential increase in stiffnesses, whereas an increase in thickness led to a reduction in stiffnesses, along with a beneficial effect on the stresses developed in the elastomer.

With a clear perspective of parameter sensitivity, the bushing configuration was selected with the aim of replicating the sagittal stiffness and biomechanical behaviour of MyFlex- δ , while also enhancing its adaptation to cross-slopes. Radial stiffness was set to be greater than 9000 (N/mm), since 2D ISO 10328 cyclic simulations (ISO 10328, www.iso.org) performed on MyFlex- η (Section 2.4) revealed the prosthesis ROM increased with bushing radial compliance. Differently, conical stiffness was chosen to obtain a foot frontal rotation greater than 8 degrees, as recommended by AOPA guidelines (AOPA, www.aopanet.org), considering that an ESR foot with a split keel can reach almost 2.5/4.5 degrees [15,23]. In conclusion, due to the high strength constraints identified in the DOE and the fused deposition modelling (FDM) technology adopted to manufacture the elastomeric ring, the Filaflex 82A filament by RECREUS was chosen. The final geometric configuration, determined by considering the Filaflex Young's Modulus strength of 22 MPa and 45 MPa, respectively (www.recreus.com/filaments/9-filaflex-82a.html (accessed on 23 April 2022)), comprised the following parameters and mechanical properties: $p = 0.8$ mm, $r = 8$ mm, $E = 22$ MPa, $t = 5$ mm, $L = 19$ mm, $K_{con} = 5.19$ (Nm/o), $K_{rad} = 10,609$ (N/mm), and $K_{ax} = 1614.3$ (N/mm).

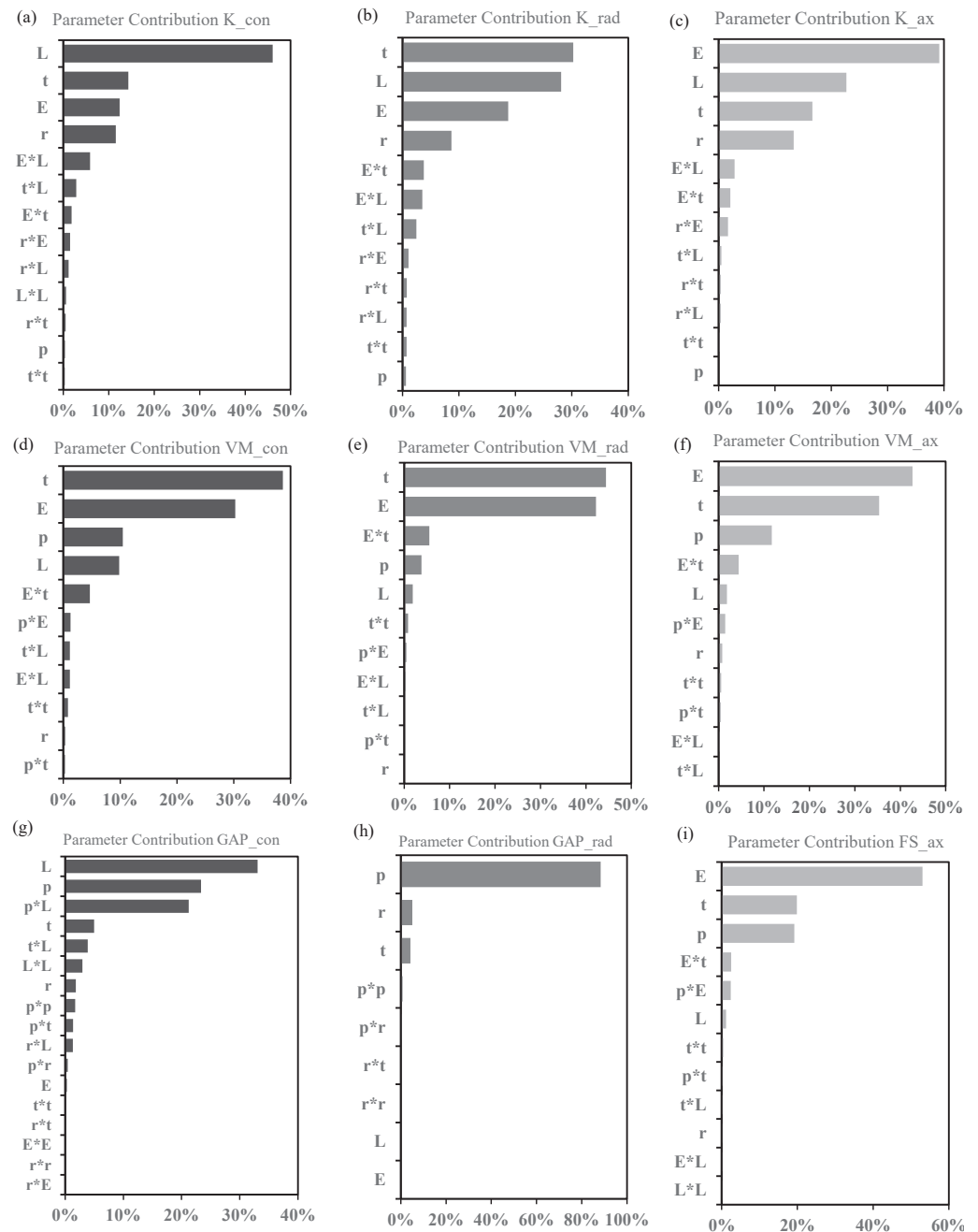


Figure 5. Parameters' contributions resulting from the sensitivity analysis: (a) conical stiffness (b), radial stiffness (c), axial stiffness (d), equivalent von Mises stress due to conical load (e), equivalent von Mises stress due to radial load (f), equivalent von Mises Stress due to axial load (g), gap formation due to conical load (h), gap formation due to radial load (i), frictional stress at shaft bonding interface due to axial load. L = elastomer length, t = elastomer thickness, E = Young's Modulus, p = pre-compression.

2.3. ISO 10328 and Cross-Slope Adaptation Test Simulations

Once the bushing configuration was defined, the methodology proposed by Tabu-col et al. [34] was adopted to finalize the design of the entire foot prosthesis.

The 2D blade geometries of MyFlex- η mirrored those of MyFlex- δ , since one of the authors' aims was to enable independent adjustments of stiffness and biomechanical attributes in the frontal and transverse planes and keep the same sagittal stiffness of MyFlex- δ . Consequently, 3D finite element analysis (FEA) was directly employed to determine

the stacking sequences of the middle and upper blades (with the lower blade provided by Ossur). Specifically, the ISO 10328 static test (Figure 6a) and a static cross-slope adaptation test (Figure 6b) were replicated in ANSYS Workbench to achieve the desired stiffness category and strength objectives. In the ISO 10328 static tests, the forefoot and heel were independently compressed by applying vertical displacement to a platform, inclined at 15° backward for the plantarflexion test and 20° forward for the dorsiflexion test relative to the ground, which was free to move longitudinally. In a cross-slope adaptation test, the platform loads the entire sole with an inclination on the frontal plane of +9.3° for inversion and −9.3° for eversion.

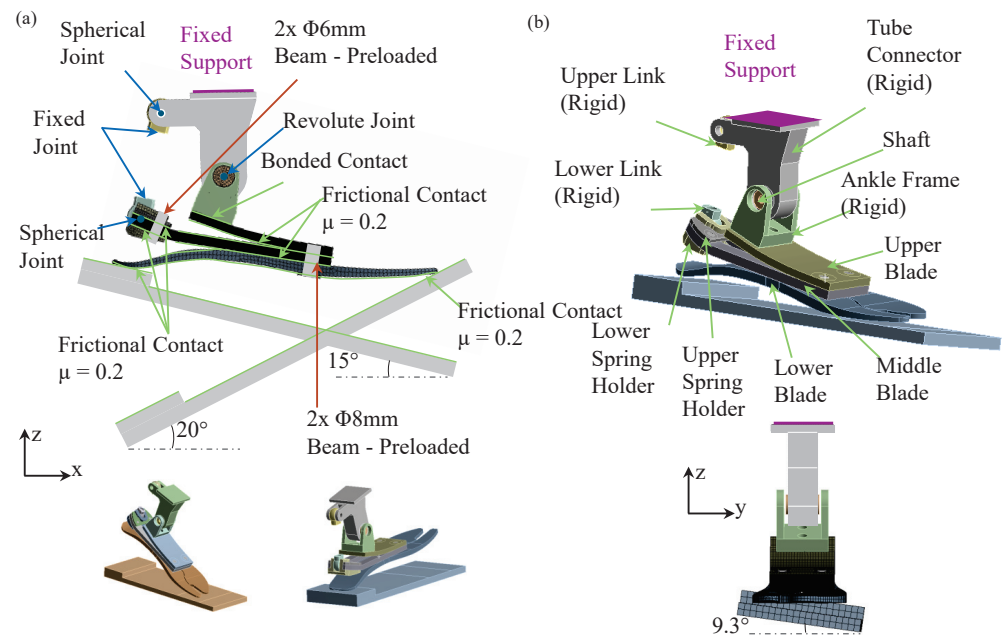


Figure 6. MyFlex- η 3D FE models. (a) ISO 10328 static test. (b) Cross-slope test (inversion test illustrated). Elastomeric bushing contacts defined in the DOE were replicated in these models. Pure penalty formulation law was used for all contacts. Preloaded beam joints (BEAM3, ANSYS) were used for the bolted connections. A fixed body-to-body joint connected the upper and lower link parts to replicate the link connector. Spherical body-to-body joints modelled the kinematic spherical joint between the upper uniball of the link and tube connector, as well as between the lower uniball of the link and spring holder. A revolute body-to-body joint modelled the hinge joint formed between the shaft and ankle frame. Composite blades were modelled with a solid element (SOLID185) for each ply through the thickness using Ansys ACP, while all other parts were discretized directly with solid elements. The ankle frame, tube connector, and both lower and upper links parts were modelled as rigid bodies to mitigate computational costs.

Upon the definition of the stacking sequence (5 simulations required, each with a computational cost of 8 h, utilizing 8-core processors), an ankle frame and tube connector were designed through different 3D FE models. Such FE models were built replicating critical load schemes defined by reaction forces generated within MyFlex- η FE simulations. Parts were designed considering a safety factor of 2 and a fatigue strength of the aluminium 7075-T6 (160 MPa). Foot prosthesis models were also used to perform simulations considering a rigid elastomer to understand the multi-axial bushing's contribution to foot static stiffness behaviour.

2.4. Functionality Verification

Two-dimensional FEA was exclusively used to verify the influence of the bushing's radial compliance on the prosthesis ROM. A 2D FE model replicating a single gait cycle, as outlined in ISO 10328, was consequently built (Figure 7a). The simulations were conducted

by applying, through the inclined platforms, the same ground reaction forces (GRFs) (calculated considering a user body weight (BW) of 100 kg, Figure 7b) at the heel and forefoot of the prosthesis. The elastic elements of the foot portion were assumed to have identical flexural stiffness, while variations in the elastomer material properties were explored. These variations involved transitioning from a rigid configuration to elastomer with different Young's Modulus values (E), calculated using Equation (1) for shore hardness values of 65, 75, and 85 ShA. The overall rotation of the foot was subsequently calculated as the variation in the inclination of the orange line defined by the H-M markers with respect to the horizontal black line.

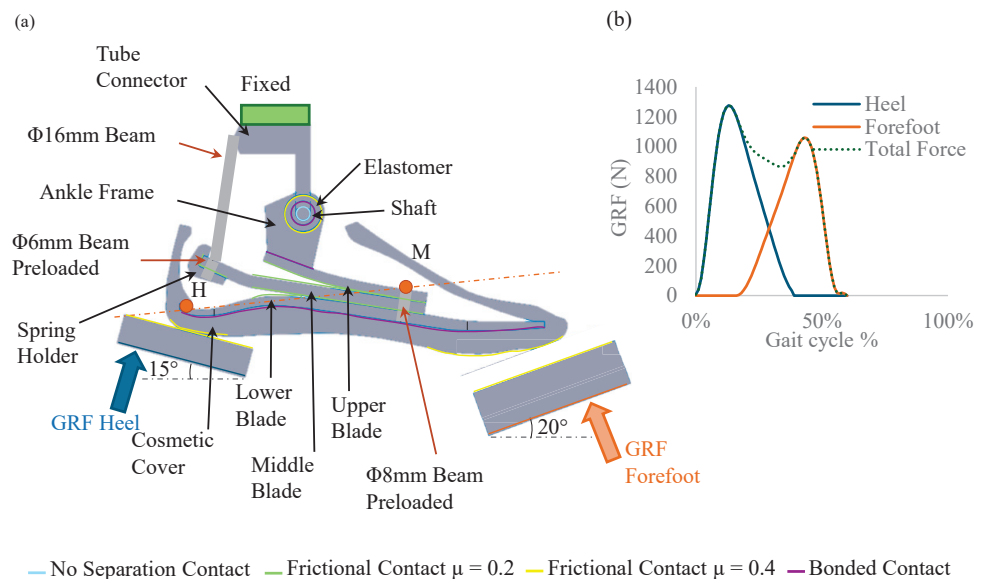


Figure 7. MyFlex- η 2D FE model. (a) ISO 10328 cyclic test. (b) Ground reaction forces applied at the heel and forefoot. Elastomeric bushing contacts defined in the DOE were replicated in this model. A cosmetic cover in low-density polyethylene (LDPE) was employed in the 2D CAD model, as suggested by the standard guidelines, and bonded on the lower blade. No separation contact was used to replicate the hinge joint formed between the shaft and tube connector. Pure penalty formulation law was used for all contacts. Preloaded beam joints (BEAM3, ANSYS) were used for the bolted connections. A body-to-body beam joint (BEAM3, ANSYS) connected the tube connector and the spring holder to replicate the link connector. All parts were modelled with a plane element (PLANE182).

Each of the four simulations necessitated 5 min of computational time, leveraging 8-core processors. The analysis of foot sagittal rotation (Figure 8) unveiled a notable fluctuation in the maximum dorsiflexion angle for bushings with higher compliance, whereas plantarflexion remained largely consistent across all configurations. As previously referenced in Section 2.2, this analysis was conducted to establish a constraint on the radial stiffness of the bushing, aiming to emulate the sagittal biomechanical characteristics, i.e., ROM, of MyFlex- δ .

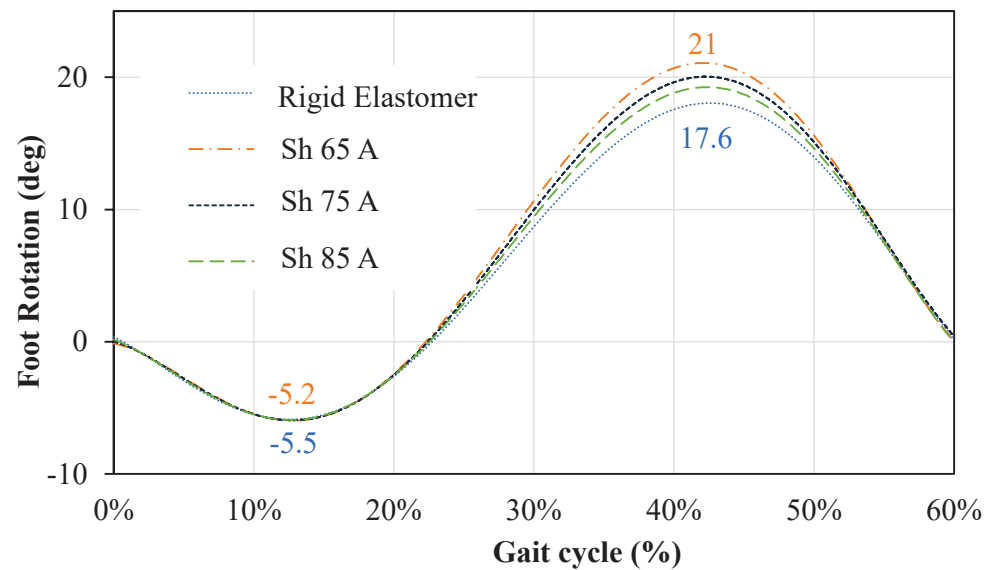


Figure 8. MyFlex- η 2D FEA: ISO 10328 cyclic test results related to the stance phase.

2.5. Testing Method

The designed elastomeric bushing was manufactured (Figure 9a) together with three distinct test setups. The selection of these test setups was guided by the need to evaluate the elastomeric bushing's stiffness and strength under radial, conical, and axial loading conditions, as predicted by FEA. These specific loads represent the forces the bushing would encounter during use of the prosthetic foot. Referring to the bushing, the elastomeric part was firstly 3D printed in two halves and then mounted on the shaft. All the parts were assembled inside a mould and placed in an oven at 200 °C for 15 min to melt the elastomers on the shaft. Subsequently, the bushing was pre-compressed inside an ankle frame interfaced with a load cell (Figure 9b) through the bolted connections (Figure 2), adhering to the DOE results. In the radial test (Figure 9b), the hollow shaft of the bushing was compressed by two parallel supports connected to the piston of a hydraulic press machine (INSTRON 8033, 825 University Ave, Norwood, MA, USA). In the conical test (Figure 9c), a lever was inserted into the hollow shaft and loaded at a specific distance to primarily induce a bending effect. In the axial test, the ankle joint was positioned on top of a holed plate (Figure 9d), and its internal shaft was subjected to axial loading using a pin. To ensure accuracy and repeatability, tests were conducted three times for each loading condition by controlling the displacement of the piston and measuring the reaction force using a load cell mounted on top of the machine. This precise control and measurement ensured that the applied loads and resulting displacements were accurately recorded. The testing equipment, including load cells and displacement sensors, were regularly calibrated to ensure their accuracy, minimizing measurement errors and ensuring the reliability of the data collected.

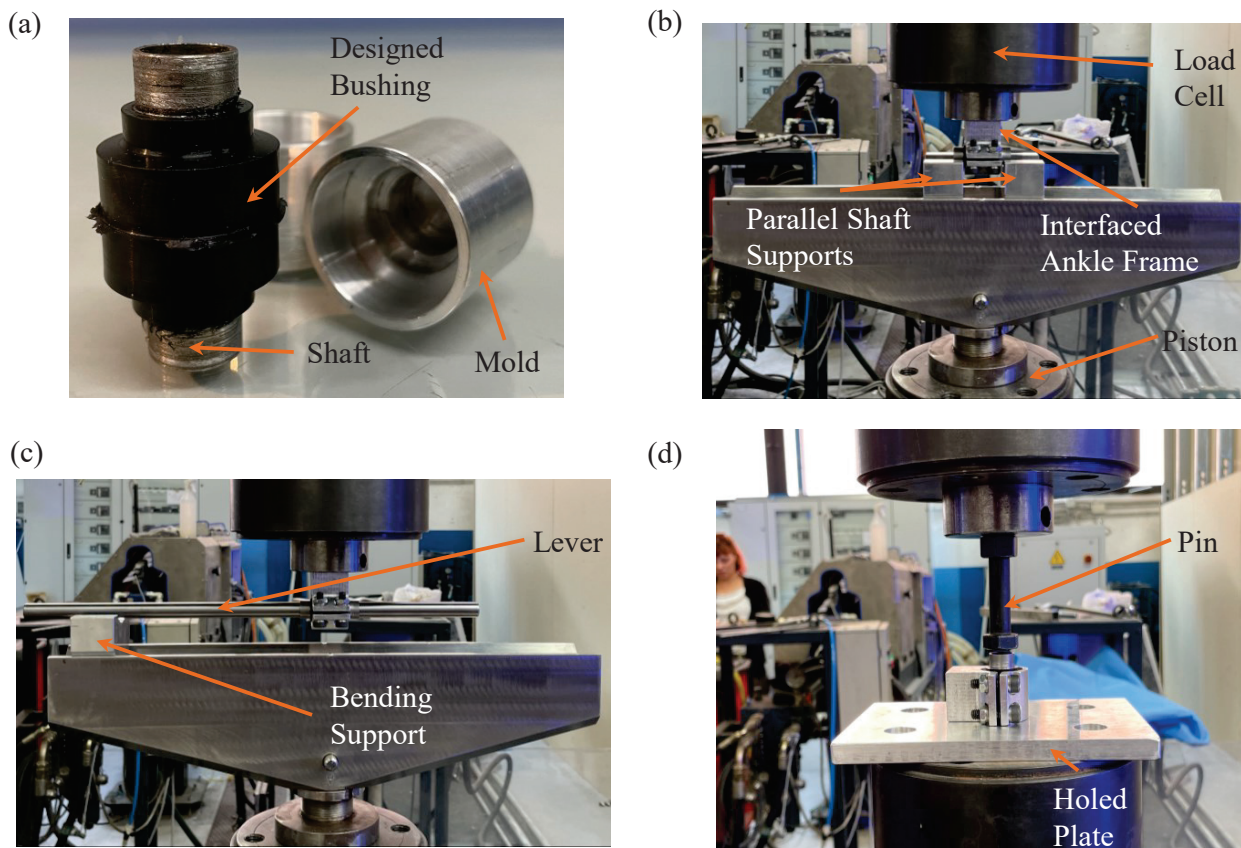


Figure 9. (a) Manufactured bushing. (c) Conical setup for conical stiffness characterization, (d) axial setup for axial stiffness characterization. All the setup parts were manufactured in aluminium 7075, apart from the lever, which was realized in C40 steel.

Furthermore, it was considered that errors due to the compliance of the setup were negligible, as materials with stiffnesses four orders of magnitude greater than that of the elastomer were used to manufacture the bushing.

A MyFlex- η prototype was then manufactured and characterized through equivalent ISO 10328 and cross-slope adaptation test setups. Experimental curves depicting the relationship between the reaction force measured by the load cell and vertical platform displacement for the ISO 10328 (Figure 10a) tests were plotted and compared with the results obtained from 3D FEAs. Concerning the cross-slope adaptation tests, markers were positioned on the foot prosthesis keel to evaluate frontal foot rotations in relation with the load measured by the load cell (Figure 10b).

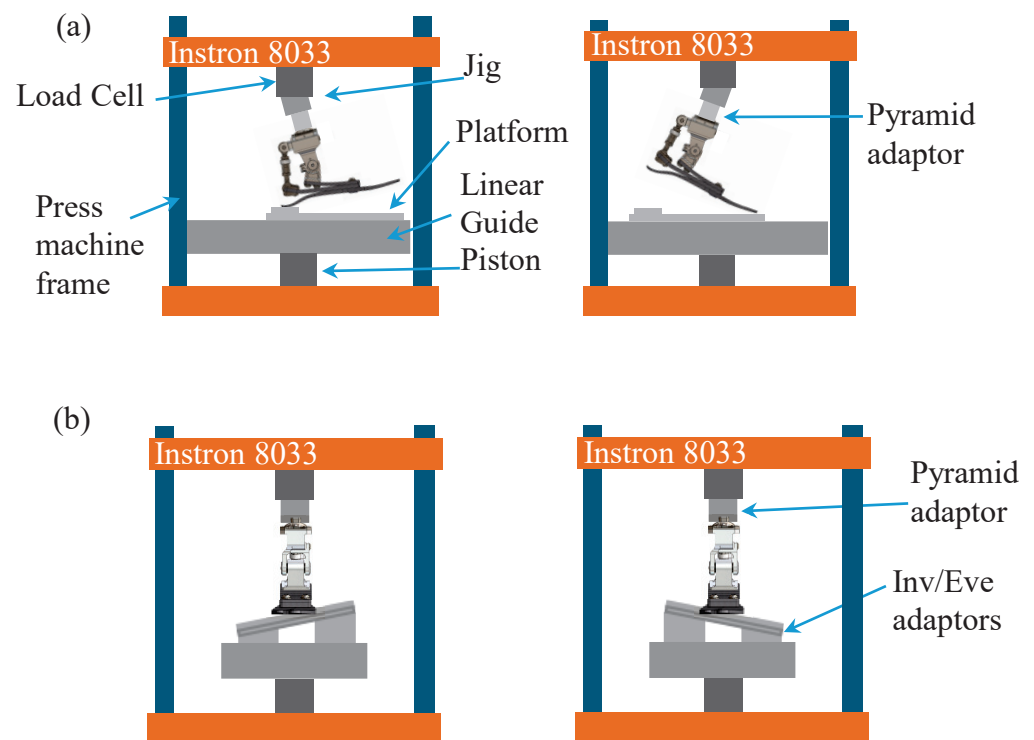


Figure 10. MyFlex- η mechanical test setup characterization. (a) ISO 10328 sagittal equivalent static test setup: the foot fixed on the load cell assembled on top of the hydraulic press machine was compressed by a piston that pushed a platform upward, which was free to move along the foot in a longitudinal direction thanks to a linear guide. Two different jigs were interposed between the prototype and the top of the machine in consideration of foot inclinations described in the standard. (b) Cross-slope adaptation test setup: inclined inversion and eversion adaptors were used to assemble the platform on the piston, providing the required frontal plane slope for frontal plane tests. The foot was directly mounted on the load cell with its longitudinal axis parallel to the ground to assess the ankle rotation.

3. Results

The test results, both for the bushing and the entire prosthesis, were compared with the corresponding results from FEAs to verify the numerical models' reliability. For the bushing radial and axial cases, the reaction force measured by the load cell was plotted against the imposed displacement of the piston (Figure 11a). Meanwhile, in the conical test, the bending moment was plotted against the conical rotation (Figure 11b).

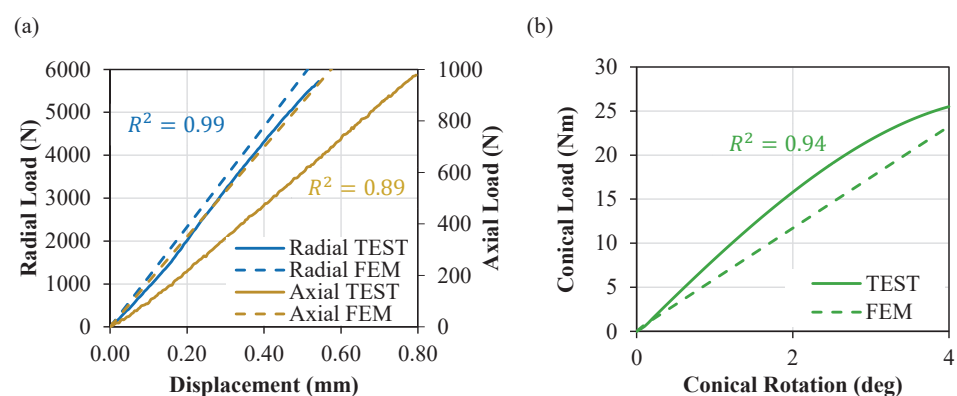


Figure 11. Bushing experimental test vs. FEA results: (a) radial and axial load test; (b) conical load test.

The coefficient of multiple determination was calculated for each loading condition. The observed mismatch, primarily highlighted in the conical and axial stiffness curves ($R_{\text{con}}^2 = 0.94$, $R_{\text{rad}}^2 = 0.99$ and $R_{\text{ax}}^2 = 0.89$), can be attributed to the elastomer linear material properties used and rigid adhesive contact modelling between the elastomer and shaft. Nevertheless, no gap formation was observed during the radial and conical test, and no detachment was obtained at the bonding interface under critical axial loading conditions. The final bushing stiffnesses and standard deviation obtained were $K_{\text{con}} = 6.22$ (Nm/o) with std = 0.15 (Nm/o), $K_{\text{rad}} = 10,201$ (N/mm) with std = 725 (N/mm), and $K_{\text{ax}} = 1167.5$ (N/mm) with std = 97 (N/mm).

Prosthesis experimental test curves exhibited notable similarity to the numerical simulations (Figure 12), particularly in relation to the ISO 10328 static test conducted (Figure 12a). Moreover, no discernible disparities were observed between the 3D FEA NB curves, which represented the foot configuration simulated with a rigid elastomer and those associated with the multi-axial foot configuration. Further experimentation with a rigid elastomer integrated within the ankle was deemed unnecessary to corroborate the minimal influence of elastomer compliance on the stiffness characteristics of the prosthesis, given the satisfactory correspondence achieved for the bushing under radial load conditions.

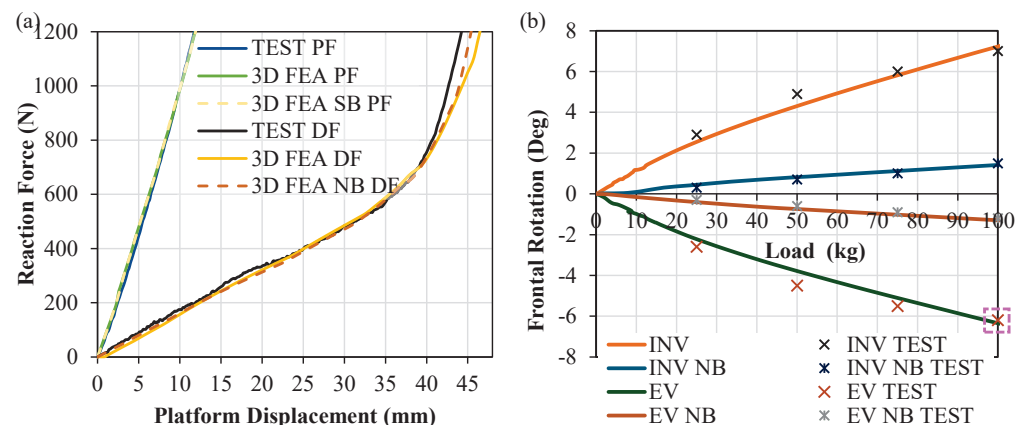


Figure 12. Foot prosthesis experimental test compared with FEA results. (a) ISO 10328 static test curves: PF = plantarflexion test; DF = dorsiflexion test; NB = no bushing; (b) Cross-slope adaptation test: experimental test rotation calculated at 25, 50, 75, and 100% of load application compared with FEA curves. INV = inversion; EV = eversion; NB = no bushing.

Conversely, the bushing incorporation resulted in an increase of 414% in the prosthesis' frontal-plane compliance. Specifically, comparing the overall rotation of the prosthesis' keel by analyzing marker displacement, the prosthesis tested with and without the bushing demonstrated a frontal rotation of 7.2 degrees and 1.4 degrees, respectively (Figure 12b). The discrepancy observed in the conical stiffness of the bushing (Figure 9b), attributed to the elastomer linear properties, was also evident in the initial part of the torsional stiffness curves of the foot. Nevertheless, the maximum errors observed between FEA and the experimental results remained below 10% under a load application of 100 kg (Figure 13).

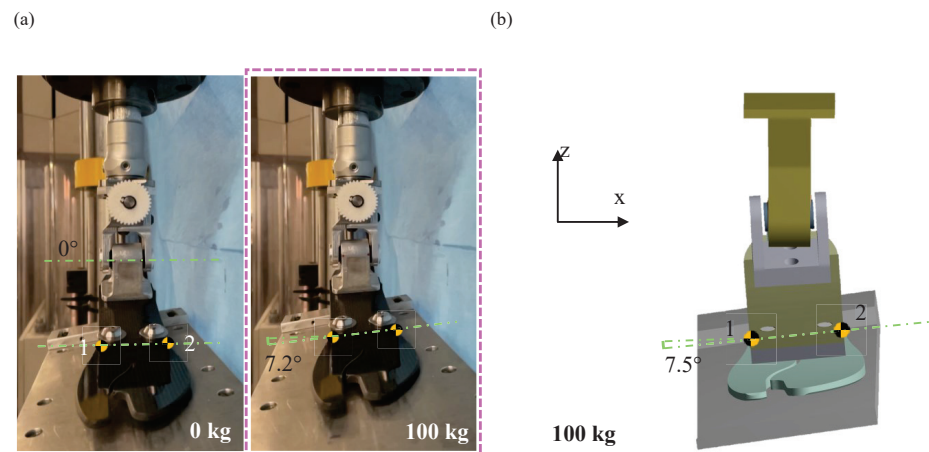


Figure 13. Foot prosthesis cross-slope adaptation static test compared with FEA result: (a) experimental eversion test evaluated at 0 and 100% of load application. (b) FE eversion test at 100% of load application.

4. Discussion

Advantages linked with integrating a single DOF joint on each ankle's motion plane of the prosthesis were observed in previous research [2,3] in terms of enhanced ROM and better adaptation on uneven terrain with a consequent reduction in lateral forces applied on the user stump. Commercial ESR prostheses, in fact, include different features to improve multi-axiality in an attempt to reach such benefits. Continuous forefoot feet, for example, are assembled with elastic elements realized with a lamination sequence that comprises both CFRP or GFRP or a present partial cut along their longitudinal axes (split geometries) to improve torsional compliance in the frontal plane. External modules can be mounted between the foot and shank to improve shock absorption and reduce torsional stress due to excessive frontal and transverse foot stiffnesses. Moreover, the Triton Side Flex includes an ankle joint realized with a torsion bar with its axis placed along the longitudinal axis of the prosthesis to improve cross-slope adaptation, reaching frontal plane rotation greater than 8 degrees. However, a lack of ESR foot prostheses that integrate an ankle with three DOFs is evident.

This study presents the development of an ESR foot, MyFlex- η , featuring a novel multi-axial ankle joint, based on an elastomeric bushing. The primary objective of this research was to introduce a methodology for designing a customizable multi-axial ankle capable of independently adjusting stiffness across the three ankle motion planes. An FEA DOE was employed, and the elastomeric bushing geometric and material parameters were varied to reach the stiffness and strength targets in all ankle motion planes defined considering ISO standards and AOPA and literature guidelines. The MyFlex- η foot presented as a case study in this paper was designed and built upon MyFlex- δ , an ESR foot prosthesis with a CFRP spherical ankle joint, with the scope to improve its multi-axiality but maintain its stiffness and biomechanical behaviour on the main plane of locomotion. In particular, the bushing's conical stiffness was designed to manage ankle motion in frontal and transverse planes instead of using an external shock absorber [3], thereby also reducing stump stresses [15,22,23]. Experimental tests performed on the elastomeric bushing generally demonstrate the reliability of the numerical models used and confirm the efficacy of the methodology used to design the multi-axial ankle. The final bushing experimental stiffnesses and standard deviations obtained were equal to $K_{\text{con}} = 6.22$ (Nm/o) with std = 0.15 (Nm/o), $K_{\text{rad}} = 10,201$ (N/mm) with std = 725 (N/mm), and $K_{\text{ax}} = 1167.5$ (N/mm) with std = 97 (N/mm). Meanwhile, the coefficients of multiple determination calculated between experimental and numerical results

for each loading condition were equal to $R_{\text{con}}^2 = 0.94$, $R_{\text{rad}}^2 = 0.99$ and $R_{\text{ax}}^2 = 0.89$. To further enhance the methodology, reduce the error obtained in axial loading conditions and better predict the conical bushing behaviour, future iterations could explore utilizing viscous–elastic material properties and modelling adhesive contact between the elastomer and shaft, albeit at the cost of increased computational complexity. Nonetheless, the proposed methodology can be readily applied to modify both the geometry and materials, allowing for tailored adjustments of the ankle stiffness according to specific user needs. Additionally, different materials could be combined to independently adjust the conical stiffness in the frontal and transverse planes. In conclusion, the results comparing the biomechanical behaviour of MyFlex- η and MyFlex- δ in the sagittal plane and the cross-slope adaptation test are presented in Table 2. As observed, the ROM in the sagittal plane is approximately the same, while performances of MyFlex- η have been improved by 43–44% in cross-slope adaptation motions with respect to MyFlex- δ .

Table 2. Main plane of locomotion (sagittal plane), according to ISO 10328, and cross-slope adaptation tests’ comparison between MyFlex- η and MyFlex- δ . D = dorsiflexion, P = plantarflexion, I = inversion, E = eversion.

Prosthesis	Sagittal Plane	Cross-Slope Adaptation
MyFlex- η	D 19 / P 9	I 7.2 / E 6.8
MyFlex- δ	D 20 / P 7	I 4.1 / E 3.8

5. Conclusions

In this study, a systematic methodology for designing a customizable multi-axial ankle utilizing an elastomeric bushing was proposed by the authors. A multi-variable regression model was employed to analyse the outputs obtained from DOE conducted through non-linear numerical simulations, aiming to predict bushing stiffnesses across the three ankle planes of motion. Subsequently, FEAs were conducted to develop an ESR prosthetic foot incorporating the novel multi-axial ankle. Experimental tests demonstrated good agreement with numerical simulation predictions, although refinements to the FE model could enhance reliability. Importantly, the implementation of the multi-axial ankle resulted in a substantial 414% increase in frontal-plane compliance when compared to results obtained with the same prosthesis with only one DOF on the sagittal plane. Overall, the DOE also underscored the influence of elastomer pre-compression, the sole parameter adjustable in real time, and the inter-relationship between parameters on bushing properties. Consequently, by designing an elastomeric ring combining various elastomer materials and adjusting pre-compression in real time via bolted connections, users could have the flexibility to tailor the multi-axial behaviour of the foot according to their requirements. These promising mechanical outcomes hold the potential to enhance user comfort and warrant validation through future clinical investigations. Additionally, employing FEM and mechanical tests to replicate dynamic loading conditions on the frontal plane [35] (www.iso.org, 30 May 2021) could provide valuable insights into ground reaction forces and moments transmitted to the user’s stump [22,23]. However, while computerized simulations offer advantages for preliminary studies, further human investigations remain imperative for assessing clinical significance.

Supplementary Materials: Supplementary file “DOE regression analysis” can be downloaded at: <https://www.mdpi.com/article/10.3390/prosthesis6040051/s1>; file includes Finite Element Analysis Design of Experiments results and regression analysis. All the other datas are contained within the article.

Author Contributions: Conceptualization, M.L. and T.M.B.; methodology, M.L., T.M.B. and J.T.; validation, M.L. and T.M.B.; formal analysis, M.L.; investigation, M.L., T.M.B. and J.T.; data curation, M.L.; writing—original draft preparation, M.L.; writing—review and editing, M.L., T.M.B. and J.T.; visualization, M.L. and T.M.B.; supervision, T.M.B.; project administration, A.Z.; funding acquisition, A.Z. All authors have read and agreed to the published version of the manuscript.

Funding: This work was supported by the European Union’s Horizon 2020 Research and Innovation Programme—“MyLeg” (No. 780871, 2018).

Institutional Review Board Statement: Not Applicable.

Informed Consent Statement: Not Applicable.

Data Availability Statement: Results of Finite Element Analysis Design of Experiments presented in the Section 2.2 “Design of Experiments of the Multi-Axial Ankle” are included in the Supplementary Materials.

Acknowledgments: The authors want to thank Marcello Pauletti and Alexandru Sorin Iacob (MSc students at the University of Bologna) for their contributions to the manufacturing and testing of MyFlex- η . The authors want also to thank Stefano Monti and Roberto Budini (DIN Technicians at the University of Bologna) for their fundamental contributions to the realization of the prototypes. The first author extends sincere thanks, with a special mention to his brother, Andrea Leopaldi, for being a continual source of inspiration and strength in daily life.

Conflicts of Interest: The authors declare no conflicts of interest. The funders had no role in the design of the study; in the collection, analyses, or interpretation of data; in the writing of the manuscript, or in the decision to publish the results.

References

1. Klute, G.K.; Kallfelz, C.F.; Czerniecki, J.M. Mechanical properties of prosthetic limbs: Adapting to the patient. *J. Rehabil. Res. Dev.* **2001**, *38*, 299–307.
2. Heitzmann, D.W.W.; Salami, F.; De Asha, A.R.; Block, J.; Putz, C.; Wolf, S.I.; Alimusaj, M. Benefits of an increased prosthetic ankle range of motion for individuals with a trans-tibial amputation walking with a new prosthetic foot. *Gait Posture* **2018**, *64*, 174–180. [CrossRef]
3. Su, P.; Gard, S.A.; Lipschutz, R.D.; Kuiken, T.A. The effects of increased prosthetic ankle motion on the gait of persons with bilateral transtibial amputations. *NIH Am. J. Phys. Med. Rehabil.* **2010**, *89*, 34–47. [CrossRef]
4. Hendershot, B.D.; Wolf, E.J. Three-dimensional joint reaction forces and moments at the low back during over-ground walking in persons with unilateral lower-extremity amputation. *Clin. Biomech.* **2014**, *29*, 235–242. [CrossRef]
5. Iosa, M.; Paradisi, F.; Brunelli, S.; Delussu, A.S.; Pellegrini, R.; Zenardi, D.; Paolucci, S.; Traballese, M. Assessment of gait stability, harmony, and symmetry in subjects with lower-limb amputation evaluated by trunk accelerations. *J. Rehabil. Res. Dev.* **2014**, *51*, 623–634. [CrossRef]
6. Lee, W.C.; Zhang, M.; Mak, A.F. Regional differences in pain threshold and tolerance of the transtibial residual limb: Including the effects of age and interface material. *Arch. Phys. Med. Rehabil.* **2005**, *86*, 641–649. [CrossRef]
7. Highsmith, M.J.; Kahle, J.T.; Klenow, T.D.; Andrews, C.R.; Lewis, K.L.; Bradley, R.C.; Ward, J.M.; Orriola, J.J.; Highsmith, J.T. Interventions to manage residual limb ulceration due to prosthetic use in individuals with lower extremity amputation: A systematic review of the literature. *Technol. Innov.* **2017**, *18*, 115–123. [CrossRef]
8. Glaister, B.C.; Bernatz, G.C.; Klute, G.K.; Orendurff, M.S. Video task analysis of turning during activities of daily living. *Gait Posture* **2007**, *25*, 289–294. [CrossRef]
9. Ficanha, E.M.; Rastgaar, M. Preliminary design and evaluation of a multi-axis ankle-foot prosthesis. In Proceedings of the 5th IEEE RAS/EMBS International Conference on Biomedical Robotics and Biomechatronics IEEE, Sao Paulo, Brazil, 12–15 August 2014; pp. 1033–1038.
10. Dixon, P.C.; Pearsall, D.J. Gait Dynamics on a Cross-Slope Walking Surface. *J. Appl. Biomech.* **2010**, *26*, 17–25. [CrossRef]
11. Damavandi, M.; Dixon, P.C.; Pearsall, D.J. Kinematic adaptations of the hindfoot, forefoot, and hallux during cross-slope walking. *Gait Posture* **2010**, *32*, 411–415. [CrossRef]
12. Madusanka, D.G.K.; Wijayasingha, L.N.S.; Sanjeevan, K.; Ahamed, M.A.R.; Edirisooriya, J.C.W.; Gopura, R.A.R.C. A 3DOF transtibial robotic prosthetic limb. In Proceedings of the 7th International Conference on Information and Automation for Sustainability, Colombo, Sri Lanka, 22–24 December 2014; IEEE: Piscataway, NJ, USA, 2014; pp. 1–6.
13. Brockett, C.L.; Chapman, G.J. Biomechanics of the ankle. *Orthop. Trauma* **2016**, *30*, 232–238. [CrossRef]
14. Moriguchi, C.; Sato, T.; Gil Coury, H. Ankle movements during normal gait evaluated by flexible electrogoniometer. *Rev. Bras. Fisioter.* **2007**, *11*, 205–211. [CrossRef]
15. Ernst, M.; Altenburg, B.; Schmalz, T. Characterizing adaptations of prosthetic feet in the frontal plane. *Prosthetics Orthot. Int.* **2020**, *44*, 225–233. [CrossRef]

16. Agboola-Dobson, A.; Wei, G.; Ren, L. Biologically Inspired Design and Development of a Variable Stiffness Powered Ankle-Foot Prosthesis. *J. Mech. Robot.* **2019**, *11*, 1–15. [CrossRef]
17. Bellman, R.D.; Holgate, M.A.; Sugar, T.G. SPARKy 3: Design of an active robotic ankle prosthesis with two actuated degrees of freedom using regenerative kinetics. In Proceedings of the 2nd Biennial IEEE/RAS-EMBS International Conference on Biomedical Robotics and Biomechanics (BioRob.), Scottsdale, AZ, USA, 19–22 October 2008; pp. 511–516.
18. Masum, H.; Bhaumik, S.; Ray, R. Conceptual Design of a Powered Ankle-foot Prosthesis for Walking with Inversion and Eversion. *Procedia Technol.* **2014**, *14*, 228–235. [CrossRef]
19. Rad, N.F.; Yousefi-Koma, A.; Tajdari, F.; Ayati, M. Design of a novel three degrees of freedom ankle prosthesis inspired by human anatomy. In Proceedings of the 4th RSI International Conference on Robotics and Mechatronics (ICRoM), Tehran, Iran, 26–28 October 2016; pp. 428–432.
20. Tsung-Han Hsieh, B.A. Design and Control of a Two-Degree-of-Freedom Powered Ankle-Foot Prosthesis. Master's Thesis, Massachusetts Institutes of Technology, Cambridge, MA, USA, September 2019.
21. Maitland, M.E.; Allyn, K.J.; Ficanha, E.; Colvin, J.M.; Wernke, M.M. Finite Element Simulation of Prosthetic Foot Adaptation to Mediolateral-Angled Cross-Slopes. *JPO J. Prosthetics Orthot.* **2020**, *32*, 236–244. [CrossRef]
22. Maitland, M.E.; Allyn, K.J.; Ficanha, E.M.; Colvin, J.M.; Wernke, M.M. Finite Element Simulation of Frontal Plane Adaptation Using Full-Foot, Split-Toe, and Cam-Linkage Designs in Prosthetic Feet. *J. Prosthetics Orthot.* **2022**, *34*, 14–21. [CrossRef]
23. Wernke, M.M.; Ficanha, E.M.; Thomas, Z.; Maitland, M.E.; Allyn, K.J.; Albury, A.; Colvin, J. Mechanical testing of frontal plane adaptability of commercially available prosthetic feet. *J. Rehabil. Assist. Technol. Eng.* **2022**, *9*, 20556683221123330. [CrossRef]
24. Fukuchi, C.A.; Fukuchi, R.K.; Duarte, M. A public dataset of overground and treadmill walking kinematics and kinetics in healthy individuals. *PeerJ* **2018**, *6*, e4640. [CrossRef]
25. James Mahoney, M.E.; Stapleton, D.B.; Renner, K.; Puccinelli, A.; Vardaxis, V. Evaluation of the subtalar joint during gait using 3-D motion analysis: Does the STJ achieve neutral position? *Foot Ankle Online J.* **2019**, *12*, 157–163.
26. Fogelberg, D.J.; Allyn, K.J.; Smersh, M.; Maitland, M.E. What People Want in a Prosthetic Foot: A Focus Group Study. *JPO J. Prosthetics Orthot.* **2016**, *28*, 145–151. [CrossRef] [PubMed]
27. Xu, D.; Zhou, H.; Quan, W.; Ma, X.; Chon, T.E.; Fernandez, J.; Gusztav, F.; Kovács, A.; Baker, J. S.; Gu, Y. New Insights Optimize Landing Strategies to Reduce Lower Limb Injury Risk. *Cyborg Bionic Syst.* **2024**, *5*, 0126. [CrossRef] [PubMed]
28. Tabucol, J.; Kooiman, V.G.M.; Leopaldi, M.; Brugo, T.M.; Leijendekkers, R.A.; Tagliabue, G.; Raveendranathan, V.; Sotgiu, E.; Benincasa, P.; Oddsson, M.; et al. The Functionality Verification through Pilot Human Subject Testing of MyFlex-δ: An ESR Foot Prosthesis with Spherical Ankle Joint. *Appl. Sci.* **2022**, *12*, 4575. [CrossRef]
29. ISO. Available online: <https://www.iso.org/standard/38708.html> (accessed on 15 June 2021).
30. Oliveira, L.F.; Simpson, D.M.; Nadal, J. Calculation of area of stabilometric signals using principal component analysis. *Physiol. Meas.* **1996**, *17*, 305–312. [CrossRef] [PubMed]
31. Pillet, H.; Bonnet, X.; Lavaste, F.; Skalli, W. Evaluation of force plate-less estimation of the trajectory of the centre of pressure during gait. Comparison of two anthropometric models. *Gait Posture* **2010**, *31*, 147–152. [CrossRef] [PubMed]
32. Popovic, M.R.; Pappas, I.P.I.; Nakazawa, K.; Keller, T.; Morari, M.; Dietz, V. Stability criterion for controlling standing in able-bodied subjects. *J. Biomech.* **2000**, *33*, 1359–1368. [CrossRef]
33. Montgomery, D.C. *Design and Analysis of Experiments*, 9th ed.; Wiley: Hoboken, NJ, USA, 2017.
34. Tabucol, J.; Brugo, T.M.; Povolito, M.; Leopaldi, M.; Oddsson, M.; Carloni, R.; Zucchelli, A. Structural fea-based design and functionality verification methodology of energy-storing-and-releasing prosthetic feet. *Appl. Sci.* **2022**, *12*, 97. [CrossRef]
35. ISO. Available online: <https://www.iso.org/standard/69821.html> (accessed on 30 May 2021).

Disclaimer/Publisher's Note: The statements, opinions and data contained in all publications are solely those of the individual author(s) and contributor(s) and not of MDPI and/or the editor(s). MDPI and/or the editor(s) disclaim responsibility for any injury to people or property resulting from any ideas, methods, instructions or products referred to in the content.

Article

Non-Backdrivable Wedge Cam Mechanism for a Semi-Active Two-Axis Prosthetic Ankle

Michael J. Greene ¹, Ivan Fischman Ekman Simões ², Preston R. Lewis ³, Kieran M. Nichols ⁴
and Peter G. Adamczyk ^{4,*}

¹ PA Consulting Group, San Francisco, CA 94110, USA

² Department of Mechanical Engineering, Virginia Polytechnic Institute and State University, Blacksburg, VA 24060, USA

³ Medical College of Wisconsin, Milwaukee, WI 53226, USA

⁴ Department of Mechanical Engineering, University of Wisconsin–Madison, Madison, WI 53706, USA; knichols4@wisc.edu

* Correspondence: peter.adamczyk@wisc.edu

Abstract: Frontal plane ankle motion is important for balance in walking but is seldom controlled in robotic prostheses. This article describes the design, control and performance of a semi-active two-degree-of-freedom robotic prosthetic ankle. The mechanism uses a non-backdrivable wedge cam system based on rotating inclined planes, allowing actuation only during swing phases for low power, light weight and compactness. We present details of the mechanism and its kinematic and mechatronic control, and a benchtop investigation of the system's speed and accuracy in ankle angle control. The two-axis ankle achieves angular reorientation movements spanning ± 10 deg in any direction in less than 0.9 s. It achieves a plantarflexion/dorsiflexion error of 0.35 ± 0.27 deg and an inversion/eversion error of 0.29 ± 0.25 deg. Backdriven motion during walking tests is negligible. Strengths of the design include self-locking behavior for low power and simple kinematic control. Two-axis ankle angle control could enable applications such as balance augmentation, turning assistance, and wearable perturbation training.

Keywords: prosthesis; ankle; non-backdrivable; inversion; plantarflexion; sagittal; frontal; two-axis; semi-active

Citation: Greene, M.J.; Fischman Ekman Simões, I.; Lewis, P.R.; Nichols, K.M.; Adamczyk, P.G. Non-Backdrivable Wedge Cam Mechanism for a Semi-Active Two-Axis Prosthetic Ankle. *Prosthesis* **2024**, *6*, 683–707. <https://doi.org/10.3390/prosthesis6030049>

Academic Editor: Arnab Chanda

Received: 6 May 2024

Revised: 4 June 2024

Accepted: 11 June 2024

Published: 19 June 2024



Copyright: © 2024 by the authors. Licensee MDPI, Basel, Switzerland. This article is an open access article distributed under the terms and conditions of the Creative Commons Attribution (CC BY) license (<https://creativecommons.org/licenses/by/4.0/>).

1. Introduction

Humans are less stable in the lateral direction than the anteroposterior direction during gait [1]. This instability is especially problematic for persons with amputation (PWA) of the lower limb, who lack control of the ankle in the frontal plane [2]. Existing commercially available prostheses address this problem only partially through passive mechanical compliance, such as split forefoot structural keels (e.g., [3,4]) or ankle bumpers, allowing for elastic inversion and eversion motion (e.g., [5]). This compliance remains inferior to the natural ankle's behavior, which can adapt its frontal angle to uneven ground and can even be used to actively correct balance perturbations through ankle inversion/eversion (IV/EV) control [6–9].

A few research prostheses have attempted to improve this shortcoming. Three include powered IV/EV control: one based on pure IV/EV angle control through an ankle module mounted above a standard prosthesis [10]; one that includes IV/EV under powered two-axis control using a cable system [11]; and one with fully powered two-axis control [12]. These mechanisms are effective in modulating IV/EV angle, but their height, mass and power consumption present challenges in deployment. An alternative approach is to accomplish a portion of the natural ankle's IV/EV function using a semi-active device—one that adjusts the passive properties of the prosthesis without supplying human-scale power to the movement. Semi-active approaches are popular in commercial prostheses with

sagittal plane adaptation, such as the robotic Össur *Proprio Foot*, [13], and hydraulic ankles such as Ottobock *Meridium* [14] and Triton *Smart Ankle* [15], Fillauer *Raize* [16], Proteor *Kinnex* [17], Endolite *Élan* [18], and College Park *Odyssey* [19,20]. Two such semi-active devices have been reported in research for frontal ankle motion: one that allows for free frontal motion during landing, then locks with a clutch to provide firm support [21], and one that controls frontal ankle stiffness through a variable-spring mechanism [22].

The aim of this paper is to describe the mechanics, design, control and performance of a non-backdrivable wedge cam mechanism for two-axis angle control, and its application to a novel semi-active ankle module called the Two-Axis 'Daptive Ankle (TADA) [23] that controls the ankle angle in both sagittal and frontal planes (Figure 1). Rather than adapting passively to different surfaces, the TADA mechatronically controls both plantarflexion/dorsiflexion (PF/DF) and IV/EV ankle angles. The inspiration for this concept is the natural ankle's ability to move in both directions, accomplished in the body by articulations at the talocrural and talocalcaneal joints. The TADA combines these movements into two-axis movement about a single joint center, exploiting the self-locking properties of the wedge cam mechanism to maximize torque holding capacity while minimizing the system's height and weight. Example intended use cases include matching ground slopes in arbitrary orientations; lifting or lowering the toes for stairs; inverting or everting the foot for turns [24,25]; and augmenting foot placement control with ground-matching IV/EV motion to enhance lateral balance [7,8].

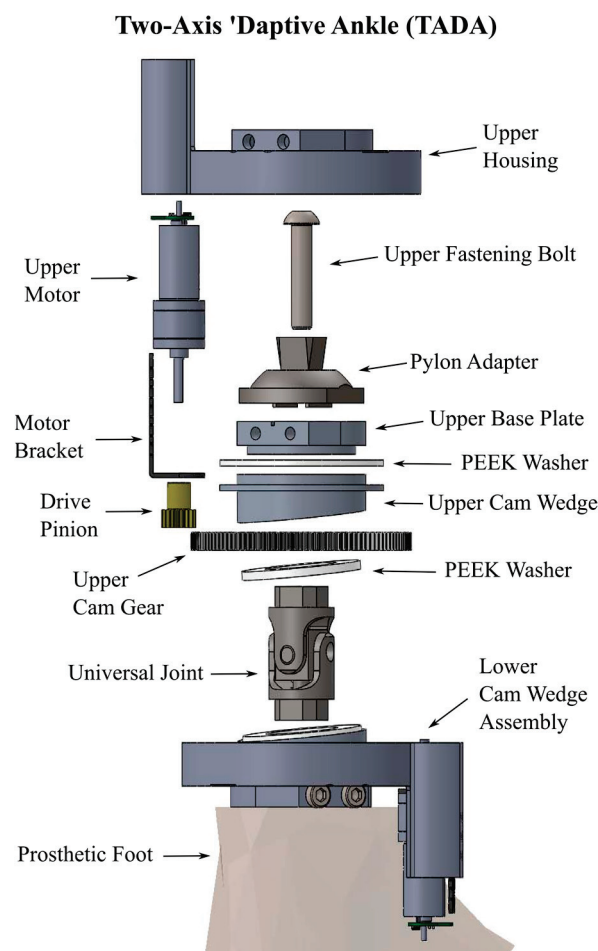


Figure 1. The TADA mechanism (upper half exploded) is made up of two angled wedge cams stacked on top of each other. By rotating the cams about the vertical axis, the ankle can achieve angles between zero and ten degrees in the frontal plane, sagittal plane or a combination of the two.

2. Materials and Methods

2.1. Mechanism Design Concept

The TADA aims to balance the convenience of passive ankles and the performance of powered ankles to add substantial function while minimizing added mass, height and power demand. Rather than actively powering ankle movements during stance phase [10–12], the TADA reorients the ankle during swing phases when the foot is off the ground. By adjusting the PF/DF and IV/EV angles, the TADA can alter the ankle moment experienced throughout the subsequent stance phase, thereby influencing whole-stride gait metrics such as the dynamic mean ankle moment arm [26]. The TADA is controlled based on readings from a foot-mounted inertial measurement unit (IMU) that allows reconstruction of foot movement to determine gait and some environmental conditions [27,28]. The TADA will then move to adapt to these conditions and/or to initiate or augment the body's response.

The TADA is based on a non-backdrivable wedge cam mechanism that can be driven by two small motors when unloaded but cannot move and is not backdriven when external loads (i.e., ankle moments) are applied. The mechanism consists of two stacked, cylindrical wedge-shaped cams that rotate about their cylindrical axes under the control of low-power DC motors. The mating faces of the wedge cams are cut at an angle of $\beta = 5$ deg with respect to the perpendicular cross-section of the cylinder. Rotation of the wedge cams changes the orientations of the two mating faces, and thereby also reorients the foot beneath. An internal universal joint (two-axis rotational joint) holds the stack together, supports axial and shear forces and prevents rotation of the distal prosthesis about the vertical axis. Each motor and pinion is mounted together with one of the wedge cams by a bracket and housing that ensure the motor and pinion stay in contact with the wedge cam's external gear all throughout the gait cycle. The mechanism is shown in Figure 1. The system can achieve angles of ± 10 deg in any combination of PF/DF and IV/EV. Critical design parameters are given in Table 1. Assembly images and videos of the movement are available in the Supplementary Materials.

Table 1. Dimensions for TADA components.

Parameter	Value
Universal joint—outer diameter	25.4 mm
Universal joint—radius to base of shear pin	8.40 mm
Wedge cam—outer diameter	50.0 mm
Wedge cam—inner diameter	42.0 mm
Wedge cam washer—outer diameter	46.0 mm
Wedge cam—face angle	5 degrees
Wedge cam—height at center of face	15.5 mm
Wedge cam—gear pitch diameter	70.0 mm
Wedge cam—number of teeth	120
Motor pinion gear—number of teeth	17

2.2. Strength Analysis of the TADA Mechanism

We designed the ankle for a hypothetical user with unilateral lower limb amputation with a body mass of $m = 100$ kg, foot length of 0.27 m (the most common prosthesis size), and a K2 Medicare Functional Classification Level (the most common level, indicating community ambulation but not highly dynamic activity). For this hypothetical case, we assumed the activity of interest was walking, and, therefore, we used design loads of 1.2 body weight (rounded to 1200 N) in the vertical direction and 0.2 body weight in the anterior and lateral directions (rounded to 200 N each) [29,30]. For structural analysis, we assumed a worst case in which the upper base plate is held fixed while all three of these loads are applied simultaneously at a ground contact point near the ball of the foot: roughly 55% of foot length (0.15 m) anterior from the ankle and 0.10 m below the ankle joint center (center of the U-joint). This assumption approximated loads in the late stance phase of

walking, shortly before toe push-off. We analyzed a neutral ankle angle configuration, neglecting the minor effects of changing cam wedge angles on contact loads. It is worth noting that these strength analyses were purely theoretical; the mechanism did not undergo rigorous destructibility nor durability testing beyond use in walking tests.

The critical components that determine the strength of the mechanism are the pins in the central universal joint and the surfaces of the wedge cams. The wedge cam is subjected to compressive stress on one side at a time to support the ankle joint moment arising from the ground contact force. To analyze the stress on the wedge cam, we computed a moment balance of the sagittal applied force about the ankle, neglecting the small inversion/eversion moment produced by the lateral force. Thus, a 1200 N vertical load together with a 200 N anterior load creates a 200 Nm plantarflexion torque T_{ank} supported by the ankle. To analyze the load on the U-joint, we assumed well-aligned contact between the wedge cams, implying by Hooke's law that the cam surface stress varies linearly in proportion to the distance from the ankle joint, up to the wedge cam radius r . In that case, the resultant reaction force through the wedge cam face has a moment arm of $\pi r/4$ about the ankle joint (0.0172 m), leading to a contact force magnitude of 11,600 N.

The peak contact stress depends on the radial width t of the wedge cam washer that is supported by the cam wall: $\sigma_{\text{max}} = 2T_{\text{ank}} / (\pi r^2 t \cos \beta)$. For the TADA as built, $t = 0.002$ m and $r = 0.022$ m (midpoint radius of the portion of the washer supported by the wedge cam wall), so the maximum stress is estimated to be $\sigma_{\text{max}} \approx 132$ MPa. For the PEEK material used at this interface, the permissible static surface pressure is 150 MPa or higher, so the estimated stress is within this strength limit. A more conservative (worse-case) estimate is to assume small-region contact at the nominal radius of the wedge cam. In this case, the moment balance about the ankle yields a smaller contact force of 9100 N due to the greater moment arm (0.022 m). But the smaller contact region (estimated at 0.015 m tangential by 0.002 m radial) yields an estimated stress of 300 MPa, which would be well above the material limit. Therefore, strength requirements suggest that the system needs to be well-aligned to distribute the contact stress as in the nominal case. These same stress conditions apply to the other PEEK washers between the wedge cams and the base plates. In use, none of the PEEK washers experienced damage, suggesting that the conservative approach may overestimate the stress and the true stress is likely between the two estimates given.

The U-joint supports forces and moments in all directions except the two rotational degrees of freedom: it supports axial tension to balance the compressive stress on the wedge cam; shear forces to prevent translation of the foot; and axial torque to prevent the foot from undergoing internal/external rotation. To analyze the load on the U-joint, we used the applied forces and the cam reaction force estimated above using the linear stress distribution on the cam surface. Both the tensile and the torsional loads on the U-joint are physically supported by nearly pure shear forces in the pins of the U-joint, in two orthogonal directions (anteroposterior, mediolateral). The estimated tensile load on the U-joint due to the 1200 N vertical forefoot load and the ankle joint moment is 10,400 N, or 5200 N vertical shear force per pin. The estimated horizontal components of shear in the pins include contributions from both direct-acting mediolateral and anteroposterior forces and the torsion produced by the mediolateral force on the ball of the foot. With a radius to the base of each pin of 0.0084 m, static equilibrium analysis yields horizontal shear forces of 3500 N in two pins and 3700 N in the other two pins. The resultant of vertical and horizontal shear force (maximum 6350 N) can be used directly with a maximum shear stress criterion to design the pin components in a custom U-joint; it is equivalent to a pure torque of 54 Nm on the U-joint. The U-joint used in the TADA was instead chosen as an off-the-shelf component (1-inch (0.0254 m) diameter steel U-joint, McMaster-Carr, Atlanta, GA, USA) to exceed this strength, as determined by its maximum torque rating (344 Nm).

Final design parameters for the TADA as built are shown in Table 1. According to the analysis above, the ideal (close contact) case has a safety factor of roughly 1.14 on the PEEK material and 6.4 on the U-joint. These safety factors allow for imperfect device alignment and/or more dynamic activities.

2.3. Ankle Kinematic Control

Kinematic and inverse kinematic laws for controlling ankle angle through wedge cam angular position are derived using a serial-chain manipulator approach. Reference frames (Figure 2) are placed on the upper base plate at its bottom face (frame 0; axes x_0, y_0, z_0 , attached rigidly to the prosthetic pylon/shank); the upper wedge cam on its top orthogonal face (frame 1) and bottom inclined face (frame 2); the lower wedge cam on its top inclined face (frame 3) and bottom orthogonal face (frame 4); and the lower base plate on its top face (frame 5; attached rigidly to the foot). The upper and lower wedge cams are driven to rotate about the z_0/z_1 axis and the z_4/z_5 axis, respectively, and the wedge faces are cut at a fixed angle β (here 5 degrees) about the y_1/y_2 and y_3/y_4 axes.

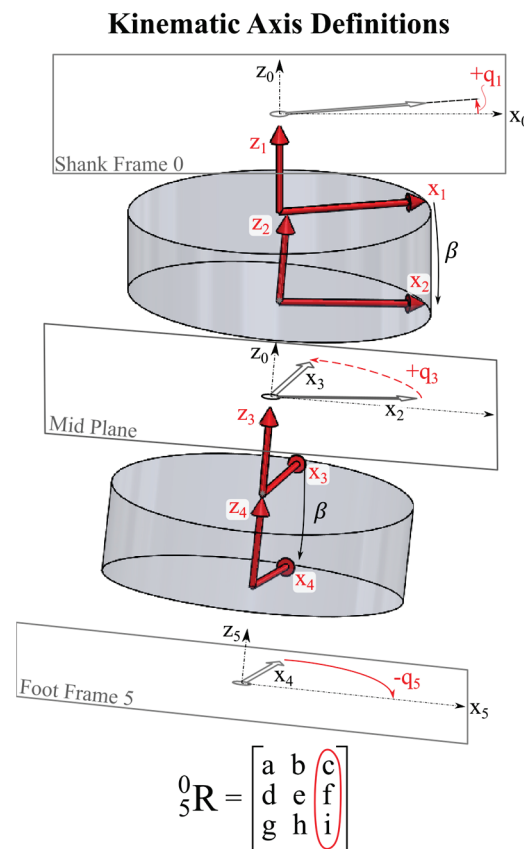


Figure 2. CAD model of TADA, displaying reference frames 0 to 5 used to derive kinematic control laws. Each rotation is positive when the distal component rotates about its respective $+z$ axis relative to the proximal component, according to the right-hand-rule. All components distal to a given rotation are assumed to move with the rotating part for analysis; the final rotation q_5 is used to enforce the constraint that the toes point forward (1). The matrix ${}^0_5\mathbf{R}$ built from these rotations is used to deduce the control parameters, notably the last column $[c \ f \ i]^T$, which represents the axis z_5 in frame 0 (see Figure 3).

The individual rotations are subject to the constraint that the toes point forward, and they have a complex relationship to final PF/DF and IV/EV angles. They can be described by a sequence of rotations relative to the tibial pylon axes (frame 0): first a controlled rotation q_1 of the first wedge about z_1 ; then a fixed rotation of angle β about axis y_2 ; then a rotation q_3 of the second wedge about axis z_3 ; then a fixed rotation β about axis y_4 ; then a final controlled rotation of the foot itself by an angle q_5 about axis z_5 . This final rotation keeps the foot facing forward, a constraint which is enforced physically by the U-joint and described mathematically below (see Equations (4)–(8)). The composition of all these rotations yields a complicated rotation matrix ${}^0_5\mathbf{R}$ expressing the orientation of

frame 5 in coordinates of frame 0 (see Appendix A). This rotation matrix can be used to solve for the rotations necessary to achieve a desired foot orientation. In this approach, the desired PF/DF and IV/EV angles are used to compute a desired rotation matrix (R_{PFIV} ; see Appendix A), and terms are matched to the equivalent rotation matrix 0_5R to determine the required wedge cam rotation angles q_i . These equations are complex and require numerical solution.

However, given the constraints of the U-joint and wedge cams, we chose to parameterize the ankle angle control to be based on two inputs of (a) the magnitude of the tilt angle, θ , and (b) the “downward direction” relative to the pylon, α (see Figure 3). θ represents the tilt magnitude (0–10 deg) of the foot’s z_5 axis from the pylon’s z_0 axis. α represents the direction of the projection of the foot’s z_5 axis on the x_0 - y_0 plane, measured as an angle from the x_0 axis (–180 to 180 deg). This formulation represents the 3D orientation of the foot more intuitively, especially for tasks such as matching a world-frame ground incline (in which the incline’s magnitude and direction are known, but PF/IV angles are not obvious).

Downward Direction Control

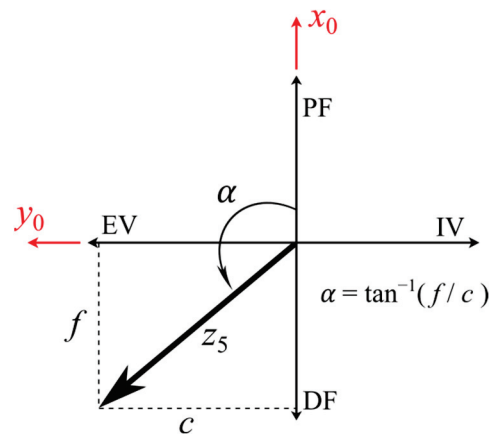


Figure 3. Projection of desired z_5 axis of the foot frame into the leg fixed frame (frame number 0) determines a “downward” direction defined by angle α . For example, setting α to 135 degrees yields an equal combination of DF and EV. f and c refer to elements of the desired rotation matrix 0_5R , see Figure 2.

The (θ, α) pair can be used to create an axis–angle formulation of the rotation matrix (R_{ax_ang} ; see Appendix A) that can be matched numerically to 0_5R as above. Alternatively, a closed-form relationship can be derived. In the rotation matrix 0_5R , the third column represents the unit vector z_5 (the surface normal to the foot’s top face) expressed in the pylon reference frame (frame 0): ${}^0z_5 = [c, f, i]^T$ (see Figure 2). The last element i is the projection of z_5 onto the z_0 axis: simply the cosine of the overall foot inclination angle θ . To control foot inclination angles (ranging 0 to 2β), the last element i is compared to the symbolic rotation matrix 0_5R (Appendix A):

$$i = \cos(\theta) = \cos^2(\beta) - \cos(q_3) \sin^2(\beta). \quad (1)$$

Thus, the relative rotation angle between the upper and lower wedge cams, q_3 , can be computed in closed form and simplified:

$$q_3 = \cos^{-1} \left(\frac{\cos^2(\beta) - \cos(\theta)}{\sin^2(\beta)} \right) = 2 \cos^{-1} \left(\frac{\sin\left(\frac{\theta}{2}\right)}{\sin(\beta)} \right). \quad (2)$$

The first two elements of 0z_5 (c, f) are the projection of z_5 (the foot frame “up” axis) into the (x_0, y_0) plane; this projection can be viewed as a direction vector indicating which part

of the foot is intended to point most downward relative to the pylon. This vector direction is defined by the vector's angle α from the $+x_0$ axis (Figure 3). This direction can be deduced from the target rotation matrix if PF/DF and IV/EV angles are specified, or directly as a downward direction vector if this is known, e.g., from the slope of a known ground surface relative to the leg. The angle α is computed from the four-quadrant arctangent:

$$\alpha = \tan^{-1}(f/c). \quad (3)$$

For the maximum inclination angle ($\theta = 2\beta$) in any direction, α is the angle at which the thickest parts of the wedge cams are aligned on top of each other, pushing that side of the prosthesis downward and lifting the opposite side. In this case, $q_1 = -q_5 = \alpha$ and $q_3 = 0$. In the current control algorithm, $\alpha = \{0, 180\}$ degrees correspond to pure PF/DF, while $\alpha = \{-90, 90\}$ degrees correspond to pure IV/EV (Figure 3).

For the “neutral” configuration ($\theta = 0$), q_3 is 180 deg and q_1 and q_5 are each 90 deg from α (Figure 4). In this case, the equal and opposite face inclines cancel to hold the mechanism in the shape of a cylinder. It can be observed that the neutral configuration is not unique; it exists with equivalent effect for all α .

Neutral Pose

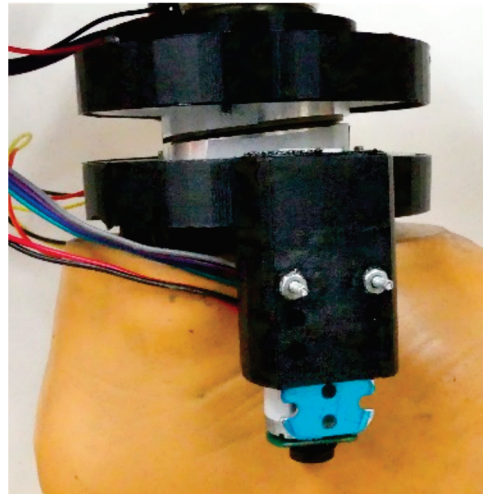


Figure 4. The TADA ankle device in neutral position. Neutral PF/DF and IV/EV angles are achieved by aligning the top and bottom wedge cams in opposite orientations so their respective face angles cancel. This pose is not unique; the two cams may be rotated together without changing foot orientation.

For intermediate angles ($0 < \theta \leq 2\beta$), the upper and lower wedge cams are controlled to rotation angles q_1 and q_5 by separate motors. These angles are determined by the downward direction α and the rotation q_3 between the wedge cams, which are each an equal rotation from α in opposite directions. This relationship is captured by two equations:

$$q_1 = \alpha - \tan^{-1}\left(\frac{\tan\left(\frac{q_3}{2}\right)}{\cos(\beta)}\right), \quad (4)$$

$$q_5 = -\left(\alpha + \tan^{-1}\left(\frac{\tan\left(\frac{q_3}{2}\right)}{\cos(\beta)}\right)\right). \quad (5)$$

The second terms in (4) and (5) account for the face angle β , which distorts the effects of target rotations at the inclined face (q_3) on the actuated rotations at the orthogonal

faces (q_1 and q_5). Because β is a small angle, simplified equations are adequate for more intuitive control:

$$q_1 \approx \alpha - q_3/2. \quad (6)$$

$$q_5 \approx -(\alpha + q_3/2). \quad (7)$$

These simplified equations are accurate within 0.11 degrees of cam rotation for the current design ($\beta = 5$ deg), leading to negligible ankle angle error. They also imply an intuitive relationship among the three rotations that describes conceptually how q_5 acts to turn the toes forward after rotations q_1 and q_3 :

$$q_1 + q_3 + q_5 \approx 0. \quad (8)$$

Note that q_3 in (2) results from the inverse cosine function, and hence has both positive and negative solutions; the sign determines which wedge cam turns clockwise and which counterclockwise from the downward direction angle α , but the effects are equivalent. Also note that q_5 is specified as a positive rotation of the foot relative to the lower wedge cam about axis z_5 (see Figure 2), but is actually implemented by driving the lower wedge cam to an angle $-q_5$ relative to the lower base plate/foot, where the motor is grounded. This relationship addresses the seemingly counterintuitive sign of q_5 in (7). Finally, it is important to note that despite the U-joint's action of resisting axial rotation, the multiaxial movement still allows the x -axis of the foot frame (x_5) to deviate slightly from the sagittal plane. With a face angle of 5 deg, the maximum deviation is 0.43 deg, occurring when the downward direction angle α is in the set $\{\pm 45, \pm 135\}$ deg.

2.4. Nonbackdrivability of the Wedge Cam Mechanism

The wedge cam mechanism uses friction to prevent the cams from backdriving during stance phase. This is a critical component of the semi-active design: it allows for the use of small motors and transmission components because they do not support large external moments from body weight. The inclined surface between the two wedge cams experiences a compressive load distributed over one side of the contact area, which forms a couple with the tensile load in the universal joint to support the ankle moment (Figure 5A). The compressive load on the wedges, acting at an inclined angle (Figure 5B), creates a twisting moment on each wedge, which is held in balance by friction on both the angled face and the orthogonal face (Figure 5C). The worst case is neutral PF/DF (downward direction angle $\alpha \in \{0, 180\}$ degrees with the two wedges' x_1 and x_3 axes toward the left and right) with a large vertical force applied at the forefoot to create a large ankle moment M_{ankle} . In this case, the contact stress on the inclined face between the two wedge cams creates a backdriving twist moment M_{back} on each:

$$M_{\text{back}} = M_{\text{ankle}} \tan(\beta). \quad (9)$$

Fortunately, this twist moment is countered by the moment capacity of friction on both the upper and lower surfaces. Analysis of these balancing moments under a Coulomb friction model reveals a relationship between the surface friction coefficient and the incline angle of the wedge cams:

$$\tan(\beta) \leq \frac{2\mu}{1 - \mu^2}. \quad (10)$$

This relationship indicates that a friction coefficient as low as 0.05 is sufficient to ensure locking at a face inclination angle of up to 5.7° . The true friction coefficient is expected to be higher ($\mu \approx 0.1$ for the PEEK plastic used at the interface, allowing angles up to 11.4°); therefore, the current face angle of 5.0° is well within the safe, non-backdrivable range. Friction also opposes rotation of the wedges by the motors during swing phases, but since the normal force is very low in that case, it is easily overcome by small motors. Detailed analysis of the friction locking mechanism is presented in Appendix B.

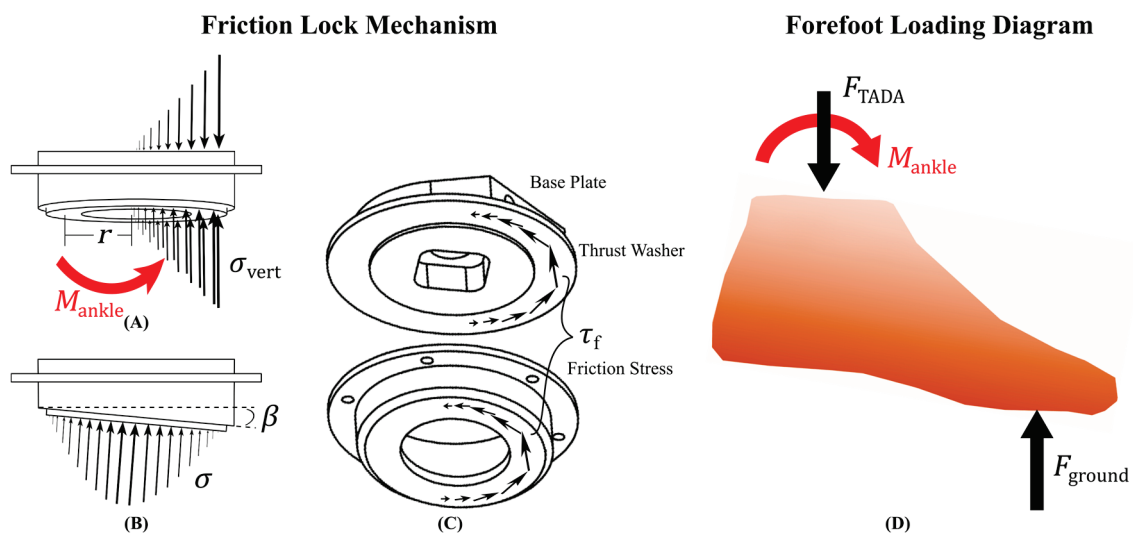


Figure 5. Stresses on the upper wedge cam in the worst-case loading scenario for backdriving of the rotational mechanism: vertical loading on the forefoot (denoted here by M_{ankle}), with the wedge cams' x -axes oriented in the frontal plane. (A) Side view of the upper wedge cam showing the distribution of vertical-direction stresses σ_{vert} . Only the front half of the wedge cam is loaded, compressed from below by the lower wedge cam and from above by the upper base plate. The toes are pointing to the right in this view. (B) Front view showing sinusoidal distribution of the normal reaction stress σ on the inclined face. The toes are pointed out of the page in this view. (C) Friction stress capacity τ_f is determined by the coefficient of friction and the normal stresses. Friction from both surfaces prevents backdriving of the mechanism by the inclined normal stress. (D) Sagittal view of the free body diagram of the prosthetic foot. The force of the ground on the foot (F_{GROUND}) acts on the forefoot to create counteracting reactions F_{TADA} and M_{ankle} at the ankle joint.

2.5. Control of the Ankle Mechanism

2.5.1. Sensing and Actuation for TADA Control

Small brushed DC gear motors (31:1 Metal Gearmotor 20Dx41L mm 12V CB; Pololu Corp., Las Vegas, NV, USA; mass 44 g each) are mounted in the upper and lower housings to actuate the two wedge cams. Each motor has an acetal pinion gear (17 teeth) mounted on its output shaft, which drives a spur gear (120 teeth) mounted on the wedge cam to rotate it during swing phases (SDP/SI, Hicksville, NY, USA). Each motor includes a rotational quadrature encoder for position control (375 counts per revolution of the pinion). The gearmotors have nominal stall torque of 0.24 Nm at 1.6 A drive current, and no-load speed of 47 rad/s (450 RPM) at 12 V applied voltage; assuming no friction, this no-load speed would cause the wedge cam to rotate at 6.66 rad/s. With the maximum required angular reorientation being $\pm\pi$ radians (± 180 deg), this movement speed yields a movement time estimate of 0.47 s. In reality, the friction at the interfaces restricts this motion, and we expect the motor to run near its peak power speed (roughly half the no-load speed). This condition predicts wedge cam movement times of roughly 0.9 s for ± 180 deg reorientation.

The motors are controlled by a Raspberry Pi 3B embedded computer, together with a dual H-bridge motor control board (MAX14870; Pololu Corp., Las Vegas, NV, USA), a dedicated 8-bit microcontroller for encoder counting and analog sensor reading (Alamode; Wyolum, Reston, VA, USA), and two analog bipolar Hall effect sensors to read permanent magnets installed on the rotating wedge cams to set the “home” position (DRV5053, Texas Instruments, Dallas, TX, USA). An inertial measurement unit (IMU; 3 Space; Yost Engineering, Portsmouth, OH, USA) is mounted on the foot to distinguish stance and swing phases in the gait cycle and to reconstruct foot trajectory [27] to support control decisions [28]. The embedded computer is programmed in Python (for logic and motor control) and the microcontroller in C (for sensor management).

The rotation of the wedge cams is controlled using a shifted bang–bang control law for the motors (Figure 6). Bang–bang control means that the motor receives either full voltage (maximum allowed PWM duty cycle, forward or backward) when its position is outside a deadband surrounding the target position, or no voltage at all (in this case, short-circuit braking mode) [31]. This style of control is chosen because the friction-based mechanism prevents smaller inputs (lower PWM duty cycle) from moving the wedge cams at all. More traditional algorithms like proportional control would continually apply an ineffectual small current to the motors when near but not perfectly at the target position, wasting battery power and heating the motors. The shifted bang–bang controller adds a direction-based component to the normal bang–bang scheme: the deadband is shifted toward the side from which the angle is approaching, so that the command is set to zero earlier (Figure 6) and rotation stops closer to the target. The parameters are the width and shift of the deadband and the amplitude of the active signal. Shifted bang–bang control reduced overshoot, improved positioning accuracy and eliminated residual power consumption relative to other control schemes tested (results are shown in Figures 7 and 8).

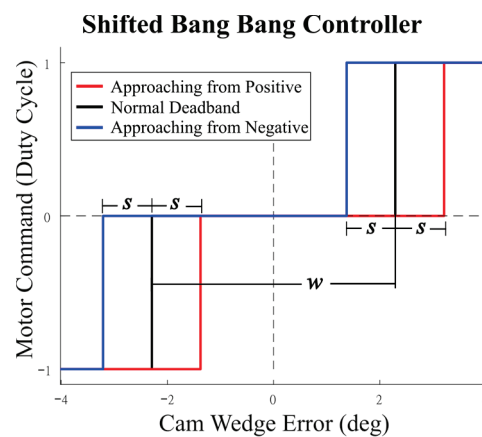


Figure 6. Shifted bang–bang control law (blue and red), compared to standard bang–bang control (black). Shifting the deadband based on the approach direction reduced overshoot. The deadband is parametrized by width w and shift s in units of angle.

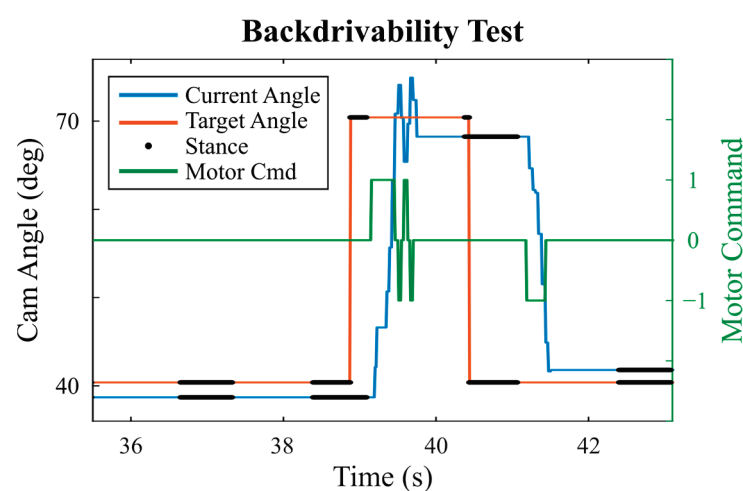


Figure 7. Example of cam movement during swing phases and non-backdrivability during stance phases. The target angle (red) can change anytime, but the cam angle (blue) moves only when actuated by the motor (green, right axis) during swing phases. The cam angle does not change when the ankle bears body weight during stance phases (black). For motor commands, ± 1 indicates maximal commands, and 0 is off.

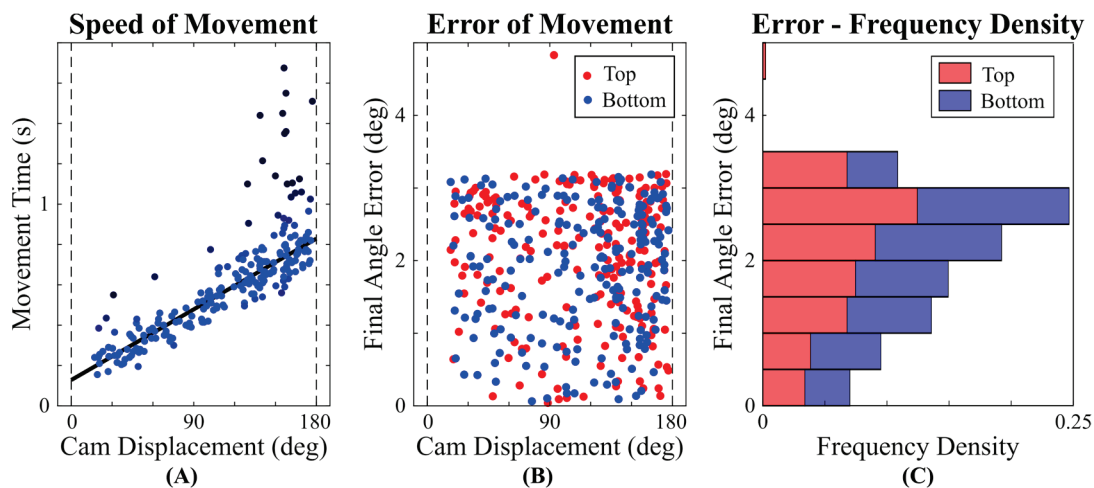


Figure 8. (A) A weighted least-squares fit suggests a linear relationship between wedge cam displacement and movement time ($t = 0.0039 \Delta\theta_{\text{top}} + 0.1282$). Darker color indicates outliers with low weighting. (B) Error of movement displays that all but one of the wedge cam displacements have final errors below 3.2 degrees. Outliers in both plots indicate instances when the mechanism was briefly stuck. (C) Frequency density of observed final wedge cam angle errors.

2.5.2. Performance Optimization

There are two numerical indeterminacies in solving for the required wedge cam orientation angles, which provide some freedom to optimize performance based on the specific circumstances of every angle adjustment. First, q_3 could be either positive or negative due to the inverse cosine function used to define it. The difference determines which wedge cam is more clockwise than the other, but the two solutions produce equivalent ankle angles. Therefore, we include logic to choose the sign of q_3 that minimizes the movement time from the prior orientation setting, i.e., the choice that results in less excursion of the two wedge cams. Second, the “downward” direction α is indeterminate whenever the desired inclination angle is 0. This neutral ankle pose is achieved by any combination of wedge cam orientations that are 180 degrees apart (Figure 4). Therefore, when returning to neutral, we include logic that moves directly toward the “nearest neutral” from the prior setting, by maintaining the last α value and setting q_3 to 180 degrees.

2.5.3. Safety Precautions to Eliminate Unnecessary Motions of the TADA

Certain safety precautions are also necessary during the movement. For large changes in ankle pose, the intermediate ankle angles that occur during the movement of the wedge cams can sometimes be very different from either the new or the old setting; the ankle may look like it is drawing a circle with the toes as it moves. When these intermediate poses include plantarflexion, the toes could contact the ground and trip the user. Therefore, we implement an interpolation method that eliminates this undesired “toe circumduction” phenomenon by interpolating the total motion into many small steps and issuing commands for all the intermediate steps at a rate both motors can achieve. First we determine the angle through which each wedge cam must rotate, and estimate the total movement time based on the typical movement speed. Then we interpolate both cams’ angle changes into n pieces at 10 Hz spanning the estimated movement time. Finally, we issue the interpolated commands to both motors at 10 Hz to maintain synchrony. This interpolation method successfully eliminates the hazardous toe movements.

2.5.4. Performance Testing of the Accuracy and Backdrivability of the TADA

To test the backdrivability of the TADA under external loads, we performed walking trials on the TADA with a standard low-profile prosthesis (Seattle Natural Foot; Trulife, Dublin, Ireland) using a prosthesis simulator boot on the right leg of an unimpaired user (a

member of the research team) and a contralateral lift shoe [32]. An experimenter manually commanded the TADA to alternate between a specific inclined posture and a neutral posture several times within each one-minute walking trial. We performed a trial for each of the nine angle settings: 5 and 10 deg settings in each of PF, DF, IV and EV, and a neutral-only trial. We recorded data from the onboard prosthesis controller at 84 Hz (observed controller frequency). These controller data included the angular position of the top and bottom wedge cams, their respective target angles, and the top and bottom motor commands. We also recorded the angular velocity of the foot from the attached IMU. We quantified backdrivability as the total range of motion of the top and bottom wedge cams during stance periods within each trial (results in Figure 7).

To validate the design and control approach, we tested ankle angle control performance with an external motion capture system for reference. We attached the TADA to a mounting frame and attached a standard foot prosthesis to the TADA. We commanded the prosthesis to move to 48 poses five times each in a random order (240 total random movements), with a dwell time of 2.5 s at each orientation (see Figure 9, the command poses are the white circles with red outlines). We measured foot motion using optical motion capture (12-camera Optitrack Prime 13 system; NaturalPoint, Corvallis, OR, USA), with five reflective markers attached to the foot prosthesis and five attached to the mounting frame.

We calculated the performance of the wedge cams in reorienting quickly and accurately (results in Figure 8). We calculated the angular displacement of each wedge cam movement from its starting pose to each new target, and used motion capture data to measure the time from the first ankle movement (2 deg/s threshold) to the first arrival within 0.1 deg of the final pose (excluding fine settling adjustments). We plotted movement time vs. displacement and performed a recursive weighted least squares fit to determine a linear relationship between them (MATLAB R2021a *fitlm* function with robust fitting), to inspect the typical and worst-case movement times. We also recorded the error of the final wedge cam orientations relative to their commanded orientations. We plotted error vs. displacement to inspect the accuracy achieved by the shifted bang–bang controller. We further plotted a frequency density histogram of movement errors to observe the distribution of final wedge cam orientation errors. We calculated whether the distributions were Gaussian using Kolmogorov–Smirnov and Anderson–Darling normality tests (MATLAB R2021a functions *kstest* and *adtest*).

We analyzed the motion of the prosthesis using inverse kinematics software (Visual3D v6.01.25; C-Motion, Germantown, MD, USA) and custom scripts in MATLAB R2021a. To match observed movements to commanded movements despite potential misalignment during assembly, we created a functional ankle reference frame from the functional sagittal and frontal axes of the prosthetic ankle movement. First we defined a functional joint center (FJC) using a subset of the 240 random movements, analyzed with the Gillette method built into Visual3D [33,34]. Next, we found the functional sagittal axis using only PF/DF movements, and the functional frontal axis using only IV/EV movements. The two functional axes are orthogonal and intersect at the FJC.

We used the inverse kinematic model to compute the PF/DF and IV/EV angles about these functional joint axes from the stationary posture following each of the 240 movements. We compared the commanded and measured angles of the prosthesis. We computed the mean and standard deviation of the five repetitions at each pose to characterize repeatability (results in Figure 9A).

Finally, we characterized backlash in the kinematic mechanism for a subset of commanded poses. We commanded several poses (−10, −6.67, −3.33, 0, 3.33, 6.67, and 10 degrees of pure PF and pure IV) and manually rotated the prosthesis in a clockwise motion within the backlash limits in both directions. We recorded the maximum deviation in each direction as an indication of how tightly the prosthesis maintains each posture (results in Figure 9B).

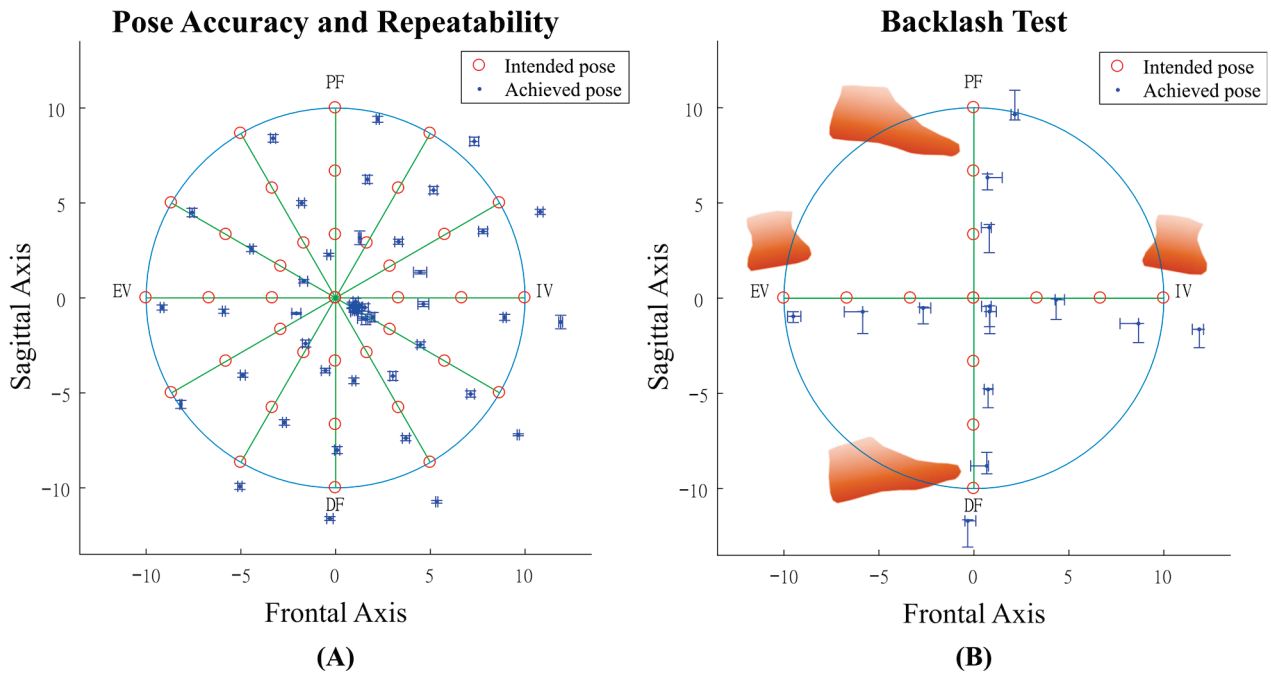


Figure 9. (A) Accuracy and variability test of ankle angles achieved over 240 randomized movements to 48 poses. Radial lines indicate different values for downward direction α . Red circles ○ indicate different values for foot inclination angle θ . Blue dots ● indicate the mean of the achieved configuration of the prosthetic foot when targeting each configuration. Standard deviations of foot angle in both sagittal and frontal planes are shown in both tests. Results show error in most configurations including the various “neutral” settings ($\theta = 0$). However, each configuration has high repeatability with little deviation. (B) Ankle backlash test shows that in any configuration, the prosthetic foot is free to deviate slightly from the desired configuration by no more than 1.56 degrees in the sagittal plane and no more than 0.98 degrees in the frontal plane. The configuration with maximum ankle backlash in the PF/DF direction was PF 10 degrees, and in the IV/EV direction, it was EV 6.67 degrees. Inset graphics illustrate the extremes of motion (maximal PF, DF, IV, EV) through sagittal and posterior views, assuming a right foot.

2.5.5. Accuracy Optimization

Initial testing of the TADA’s ankle kinematic performance showed that there must be some inaccuracy in the geometry of the parts or their alignment, as there was imperfect matching of poses achieved to those commanded (see Figure 9A). However, the system’s repeatability allows it to be calibrated to pre-correct for this distortion. Using the results of the initial tests (shown in Figure 9A), we implemented a two-dimensional interpolation to map the intended physical configuration into adjusted commands for direction and inclination based on the initial results. We used *scatteredInterpolant* objects in MATLAB R2021a to perform linear two-dimensional interpolation among scattered (rather than gridded) input data using a triangulation algorithm [35]. We built two interpolating functions—one for α and one for θ —using the observed PF and IV angles as reference coordinates (independent variables; blue dots in Figure 9A) and the original commanded values of α and θ as function values (dependent variables; red circles in Figure 9A). We then used the target PF and IV angles (red circles) to look up adjusted α and θ commands to compensate for the original errors (Figure 10A). Some adjusted commands fell outside the meaningful range; we remedied this by limiting the adjusted θ to a maximum of 10 degrees (2β). The resulting corrections were programmed into the controller to ensure optimal accuracy in later pose commands. Results of this correction are shown in Figure 10B.

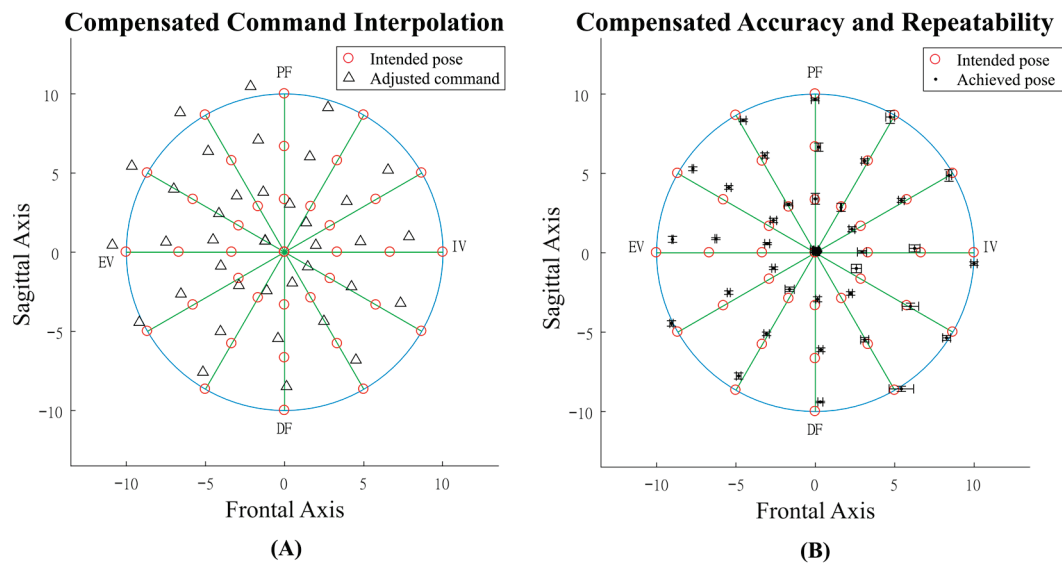


Figure 10. (A) Adjusted commands to improve accuracy, derived from interpolation (MATLAB *scatteredInterpolant*) of raw positioning results displayed in Figure 9A. The black triangles Δ represent compensated commands that should be given to the controller to better zero the device and hence reach desired positions (red circles \circ) with reduced orientation errors. (B) These corrections successfully helped to reduce the final positioning error (black dots and standard deviation bars) of the prosthetic ankle over the random 240-configuration test. Part B reprinted with permission from [23].

3. Results

Benchtop and walking trials indicated that the TADA functioned as designed. The mechanism successfully repositioned to all commands in both tests, and held its position until commanded to a new one. No component failure occurred, and no material damage was observed.

Backdriving of the mechanism under body weight in walking was negligible. Figure 7 shows an excerpt of cam movement data from a walking trial with periodic switches between an inclined angle (5 deg EV) and neutral. The wedge cam moves only when actuated by the motor during swing phases, and not when supporting the body-weight loads applied during stance. In total, across nine backdrivability test trials, only 64 samples showed any angle change out of a total of 27,044 samples during stance phases (0.24% of samples), and these few movements were very small and occurred at the beginning of the stance phases when the cam was settling after an actuated movement. The motors did not activate to hold the cams in place during stance.

Figure 8 shows that the ankle can move into any desired position in less than 0.9 s on average (Figure 8A), with movement time proportional to the angle of change for each wedge cam, as expected for motors running at near-constant speed. The regression line predicts movement of 90 degrees in 0.48 s and 180 degrees in 0.83 s. All but one of the movements resulted in wedge cam orientation errors less than 3.2 deg (Figure 8B). This is equivalent to ankle angle error magnitude less than 0.6 deg. The wedge cam orientation errors' frequency density histogram (Figure 8C) showed a skewed distribution with a peak in the 2.5–3 degrees error bin. The distribution was determined to be non-Gaussian using both statistical tests ($p < 0.0005$). Several outliers were present, indicating movements that took unexpectedly long times to reach their target poses (Figure 8A).

Figure 9A shows that angles throughout the target of 10 degrees inclination in any direction are achievable by the TADA mechanism. The foot angles measured by motion capture show errors between the achieved foot orientations (blue dots) and the commands (red circles). The worst mean error was 0.79 ± 0.50 deg in PF/DF and 1.25 ± 0.56 deg in IV/EV. The maximum orientation error magnitude was 3.49 deg (2.28 deg in PF/DF and 2.64 deg in IV/EV), with errors generally biased toward dorsiflexion in the sagittal plane

and toward inversion in the frontal plane. The result angles show low variability in the achieved configurations (PF/DF ± 0.15 deg s.d., IV/EV ± 0.15 deg s.d.).

Figure 9B shows that backlash in the mechanism was modest but present in all configurations. Maximum backlash averaged 1.09 ± 0.29 deg (mean \pm s.d.; max 1.56 deg excess dorsiflexion) in the sagittal plane (PF/DF) and 0.64 ± 0.20 deg (max 0.98 deg excess inversion) in the frontal plane (IV/EV) across all conditions shown. The configuration with maximum ankle backlash in the PD/DF direction was PF 10 degrees, and in the IV/EV direction, it was EV 6.67 degrees

Figure 10A shows the remapping of intended ankle poses to adjusted commands. Adjusted commands outside the 10-degree circle were projected radially onto it (by limiting θ to 10 deg). The adjusted commands successfully brought the measured configuration into alignment with the intended poses (Figure 10B). The final positioning error when using the adjusted commands was 0.35 ± 0.27 deg in PF/DF and 0.29 ± 0.25 deg in IV/EV, with worst-case errors of 1.23 deg for PF/DF and 1.79 deg for IV/EV. Backlash was not affected by this change.

4. Discussion

The results show that the TADA design is successful in achieving non-backdrivability as intended. The observation of negligible backdriven motion in the wedge cams despite large time-varying external loads experienced in walking (Figure 7) demonstrates that the friction-based wedge cam design is able to support high external loads while successfully isolating the small motors from them. Therefore, the non-backdrivability is a critical contributor to system compactness and weight savings: the TADA uses small actuators because these neither drive nor withstand body-weight forces. Non-backdrivability also provides a fail-safe benefit: it enables the TADA to remain in its most recent pose if it is powered off.

The results also show that the TADA was successful in achieving two-axis motion of the ankle. Movement time (Figure 8) of 0.48 s for a 90-degree cam movement and 0.83 for 180-degree movement were approximately as predicted from the powertrain design. These movement times indicate the ability to move the ankle from an extreme pose (± 10 deg) to neutral or vice-versa within roughly one swing phase of gait (~ 0.5 s). Therefore, full reversal of ankle angle—such as when turning around on a slope—can be accomplished in two strides. Full turns in walking generally take at least two strides to accomplish, so this movement speed is appropriate for a gradual adaptation strategy, as proposed for a previous semi-active prosthesis [28]. The presence of longer-duration movements—likely due to friction or momentary “sticking”—suggests the need to further optimize the drive train for reliability. A goal for the next revision of this prosthesis is to reduce variability in movement time and achieve all movements in one swing phase—a reduction in movement time that is likely achievable with only modest increases in motor size and quality. Such higher-speed movement would ensure robustness, and if reduced further, would also enable more dynamic adaptations such as lifting the toes during swing phases.

The semi-active design includes several unusual features which proved successful in achieving two-axis control with low system mass. The combination of a non-backdrivable friction-lock wedge cam system with shifted bang–bang control minimizes the power used for actuation. The motors run at full power for short periods of time, and then rest and consume no power at all while the friction lock holds position. Friction computations suggest that the wedge cam face angle could be increased to roughly 10 degrees while retaining this locking property, which may enable further increases in range-of-motion (theoretically exceeding ± 20 deg). The TADA has a build height of only 50 mm and a mass of 550 g excluding the controller and battery; it may be possible to reduce these specifications further with design optimization. The semi-active design means the additional battery and control electronics can also be relatively small and lightweight.

Angles throughout the achievable range of PF/DF and IV/EV were achieved with high precision and repeatability. But, the absolute positioning accuracy under nominal

commands was not as good as intended (see Figure 9A). Several factors could contribute to this inaccuracy, including different mechanical loads, such as the gravitational moment due to prosthesis weight; misalignment between the universal joint and the wedge cams; or manufacturing or assembly inaccuracy in the wedge cam face angles. The total angular excursion in each direction exceeded the 10 degrees (2β) that should be achievable (Figure 9A). The excess motion suggests that some level of manufacturing inaccuracy contributes, such as a 6 deg face angle β instead of the intended 5 deg angle. The imperfect isolation of PF/DF and IV/EV (Figure 9A) further suggests some misalignment in the nominal pose, which may be a consequence of imperfect zeroing of the wedge cam rotation angles or of limitations in the definition of PF/DF and IV/EV directions during motion capture. The system registers the absolute position at startup by rotating each wedge cam a full revolution and detecting a small embedded magnet with a hall effect magnetic sensor on the housing. The zero position is defined by an offset from the magnet's position, which is set visually by the experimenter. Both detection of the magnet and the visual determination of offset could have introduced error in the final zero position.

Whatever the underlying reasons for the pose error, the simple correction mapping used to adjust commands was successful in reducing mean error by 55% in PF/DF and 76% in IV/EV, and reducing the worst-case error by 46% and 32%, respectively. Future versions will improve the initial accuracy further by building in features such as limit switches for better zeroing and/or absolute position encoders for continuous direct configuration measurement. Pre-correction of any remaining misalignment can be built into the controller following a calibration test similar to that used here.

The kinematic planning algorithm based on the downward direction and inclination angle greatly simplified the control calculations and made them more practical. The simple formulas in (3)–(8) are much easier than comparing the rotation matrix itself against its counterpart based on separate PF/DF and IV/EV angles (see Appendix A). Another practical advantage is apparent in the use case of adapting to the terrain angle: if the ground slope can be measured (e.g., through a pylon camera [36,37] or kinematic sensors [38]), it will likely be measured in a pylon reference frame, which will natively define inclination θ and downward direction α .

In steady-state level walking, the TADA is intended to set ankle angles that are equivalent to a prosthetist's ideal alignment of the prosthesis, and essentially leave the ankle fixed in that position as long as the motion continues. In this way, the user can exploit the mechanics of the foot module attached below the TADA as intended by its manufacturers. Within each stride, the load path through the TADA changes from initial contact at the heel to final contact at the toe. Early in ground contact, the ground reaction force acts to force the ankle into plantarflexion, and this external force is counteracted by compressive contact forces at the posterior edge of the wedge cams. Through mid-stance, the ground reaction force advances toward the toe while also shifting mediolaterally under the foot; at each instant, a different point around the circumference of the wedge cam mechanism supports the external ankle moment. Finally, in late contact to toe-off, the mechanism experiences loads similar to the worst-case scenario analyzed above, with the wedge cams supporting the highest loads at their anterior edge. Throughout the movement, the wedge cams never move because the TADA's non-backdrivable mechanism enables "set-it-and-forget-it" use in this case; the system consumes minimal power and requires no active control (only quiescent sensing and state monitoring).

Beyond steady-state level walking, the availability of two-axis controlled movement enables several interesting use cases that may yield biomechanical benefits. The most obvious is adaptation to terrain: the TADA module could be integrated with sensing such as an ankle load cell [39] to detect and match the slope of the ground. Once the slope is detected, local movements like turns or repeated paths could be tracked in real-time with an embedded inertial sensor [27,28,40,41] and used to preemptively adapt the TADA to the known ground slope under the upcoming footfall. Another application is to augment balance during locomotion, such as enhancing lateral balance [1] and steering [42]. In

this usage, the TADA could sense changes in foot placement or movement direction and preemptively move to augment them. A third use case could be perturbation training, in which the TADA would create small disturbances to the ankle angle to lightly disturb the user [43]. Practicing with this mode could train a prosthesis user to be more stable on uneven terrain even without the TADA's assistance. Finally, the TADA could be used to deliberately make changes to the ground contact conditions in order to influence a person's movement. For example, a DF perturbation could facilitate acceleration [44] or an IV/EV perturbation could facilitate a turn. These functions could eventually be coupled with a brain-machine interface to enable feed-forward control of the prosthesis.

A consideration for translating the TADA to commercialization is how to scale it for larger or smaller users. As a standalone ankle module, the TADA can be used with prosthetic feet of different sizes and, therefore, it need not be scaled finely for small increments. However, a few sizes may be envisioned, such as small/pediatric, medium, and large. The key mechanical design parameters must be chosen to respect stress limits on the key components—the mating surfaces of the wedge cams and the pins in the universal joint. The worst-case stress on these parts is driven by the multiaxial ankle moment, which depends on body mass m and foot length l (assumed proportional to body height h). Assuming a constant body mass index (m/h^2), foot length scales with $m^{1/2}$ and therefore ankle moment scales with $m^{3/2}$. For constant stress, the stress-bearing area of the critical pieces must remain proportional to this load such that area also scales with $m^{3/2}$. A proportional scale-up of the TADA's geometry then yields length dimensions scaled by $m^{3/4}$ (square root of area) and device mass scaled by $m^{9/4}$ (cube of length). Thus, a small/pediatric TADA with a 70 kg weight limit is expected to have a mass of 290 g and a build height of 38 mm, and a large TADA with a 125 kg weight limit is expected to have a mass of 910 g and a height of 63 mm. These rough estimates can be used to gauge whether simple scaling is adequate, or whether a redesign for users of different sizes might be necessary. It should be noted that an “oversized” TADA will still function for a smaller user if it can be fitted to the body; there is no lower limit to the loads that work with the mechanism, only an upper limit for strength.

Finally, the wedge cam drive mechanism may not be limited to use in two-axis ankle motion, but could be used in other multi-axis robotic concepts. Unactuated versions of the wedge cam design are prevalent in ductwork to allow rigid pipes to articulate to variable angles; the actuated version could be used for repositionable tentacles or support structures, perhaps with higher wedge angles in cases that allow for higher friction. Alternatively, the semi-active mechanism described here could be converted into a fully-powered mechanism for multiple applications if the friction interfaces in the wedge cam stack were instead supported by bearings and the system was powered by stronger motors.

Limitations

The main limitation of the TADA concept is its design as an inherently semi-active device. Without the ability to articulate under body-weight loads, responsive control of stance phases cannot be achieved. This limitation prevents the TADA from mimicking some features of natural ankle control, such as responsive control of ankle inversion/eversion moment during a stance phase in response to a perturbation [7,8]. Such a response would require an active prosthesis [11,12]. However, the compactness, low mass and low power consumption of the semi-active mechanism stand as the benefits gleaned from trading away this function, while still gaining the ability to adapt to two-axis slopes. Future brain-machine interfaces and pylon-embedded sensors may narrow this performance gap by improving the predictive capabilities of controllers for semi-active mechanisms like the TADA.

One challenge for application of the TADA is the height of the prosthetic foot attached beneath it. The final height of the ankle above the ground is important for the kinematics of foot movement: an ankle near ground level accomplishes nearly pure rotation of the plantar surface, whereas an ankle much higher also causes this surface to translate substantially as

a result of the rotation. In the current assembly, the TADA is attached on top of a standard-height foot, so the TADA ankle center is at roughly the same height as a natural ankle. Therefore, we expect the effects of articulation to match closely the natural ankle's effects (see Figure 1). However, we expect the TADA to be most beneficial when the motions are closest to pure rotation, i.e., when the ankle is mounted on a very low-profile prosthesis. This case would allow for intentional control of the ground contact angle without large shifts in the location of the plantar surface. A future design challenge may be to design a foot prosthesis to achieve such a low center of rotation by incorporating TADA-like mechanisms inside the foot module.

The greatest limitation of the mechanism design itself is the backlash or “slop” in the angle setting. In the current realization, this backlash has a magnitude of roughly one degree, meaning that the ankle can move this amount even when the mechanism is holding a configuration. This backlash is a consequence of the formally over-constrained mechanism: perfect operation requires the centers of the wedge cam faces to coincide with the rotational center of the internal two-axis universal joint. Due to manufacturing tolerances, this can never be perfectly achieved, so the mechanism must be built with a little room for error. In the current device, this backlash is minimized by adding thin shims during installation of the universal joint to ensure the mechanism does not bind. However, the wedge cams incorporate PEEK plastic inserts as the interface surfaces, and the tolerance and dimensional stability of these parts may be inadequate. In future revisions, we will consider replacing the plastic components in favor of metal-on-metal interfaces with tighter tolerances, and we will design a more convenient adjustment mechanism to perform fine alignment of the joints to minimize this backlash.

The imperfect kinematic performance under nominal commands, and, therefore, the need to calibrate and adjust the commands, is an inconvenience that should be improved. As discussed above, it could arise from several imperfections including manufacturing tolerances, initial alignment of the wedge cams, and even axis definitions in the motion capture system. A critical improvement for future versions will be to tighten geometric tolerances and eliminate the alignment steps, to greatly reduce uncertainty about the movement directions. Another improvement would be to incorporate precise absolute angle measurement for the wedge cams, in place of the initial alignment procedure and incremental tracking currently used.

Another challenge is the balance of friction vs. motor power. The semi-active design concept aims to achieve light weight, which promotes smaller motors, but the presence of an intentional friction pathway resists all motion and demands larger motors to overcome it. Substantial effort during tuning was dedicated to achieving a feasible motor size and power settings. Certain configurations are the most taxing; specifically, any move from plantarflexion to dorsiflexion requires the motors to overcome both friction and the gravitational moment of the prosthesis' weight. This problem was ultimately overcome with a slight increase in motor voltage. Future revisions will use better motors and optimize the choice of battery and control electronics to further guard against these problems. These changes are also expected to improve actuation speed and reduce noise.

Because friction plays such an important role in this mechanism, it is important to consider how stably it can be defined. As designed, the TADA requires a friction coefficient of at least 0.05 to ensure non-backdrivability in the wedge cams, and the upper limit interacts with the motor power requirements as described above. The current design was chosen because the PEEK plastic contact has relatively well-characterized friction properties within this range ($\mu = 0.1$) without any need for lubrication. In future work, one goal is to change this material for one with better dimensional stability and tolerance, but this again leads to the challenge of selecting materials and potentially lubricant. In general, it seems likely that either lubricant-free operation or the use of a solid lubricant or lubricant-impregnated solid material would be desirable, to prevent any need for adding lubricant through maintenance. Careful shielding and additional testing in harsh use cases

such as dusty or wet conditions will be necessary to verify that this critical property is preserved in any future mechanism.

Finally, the packaging and form factor of the TADA limit its direct conversion to a final version. Revisions to the housing and component layout are needed for improved compactness and robustness. The protective housings should be nested and enclosed with a rubber seal, the electronics and batteries should be embedded, and the motors should be switched to right-angle drive or offset behind the tibial pylon to reduce height and fit within a standard shoe. The Raspberry Pi 3B was chosen for its ease of implementation as opposed to an embedded controller. It includes a GUI, is flexible, and is very versatile in its functionalities. Some of the limitations of using this single board computer include latency due to use of Python programming and presence of an operating system, and high power consumption. This can be observed by the fact that the highest attainable sampling frequency was 84 Hz. In future work, an embedded controller would be more suitable since it is more compact in size and offers better energy efficiency. With such a controller, real-time reconstruction could be utilized. These and other improvements will improve the practicality of future versions of the TADA.

5. Conclusions

The non-backdrivable, semi-active wedge cam mechanism of the Two-Axis ‘Daptable Ankle (TADA) successfully and repeatably achieves control of the ankle angle in two directions with low weight and power consumption. Orientation control in this mechanism has a simple and intuitive form for easy implementation. Shifted bang–bang motor control achieves maximal-speed movement with no-power rest conditions and adequate accuracy. Some backlash is necessary to prevent binding in the mechanism, but this can be improved with better machining tolerances. Upcoming work will include application testing to determine the effects of two-axis ankle control on walking in persons with amputation, including adaptation to slopes and speeds, augmentation of balance and steering, and perturbation training to promote robust balance.

Supplementary Materials: The following supporting information can be downloaded at: <https://www.mdpi.com/article/10.3390/prosthesis6030049/s1>, Figure S1: Kinematic Relationships; Figure S2: Supplemental Views of TADA.

Author Contributions: Conceptualization, M.J.G., I.F.E.S. and P.G.A.; methodology, M.J.G. and P.G.A.; software, M.J.G.; validation, M.J.G. and P.G.A.; formal analysis, M.J.G. and P.G.A.; investigation, M.J.G. and P.G.A.; resources, P.G.A.; data curation, M.J.G.; writing—original draft preparation, M.J.G., I.F.E.S., P.R.L., K.M.N. and P.G.A.; writing—review and editing, M.J.G., I.F.E.S., P.R.L., K.M.N. and P.G.A.; visualization, P.G.A.; supervision, P.G.A.; project administration, P.G.A.; funding acquisition, P.G.A. All authors have read and agreed to the published version of the manuscript.

Funding: This work was supported in part by the US National Science Foundation (grant number HRD-1612530), the US Department of Defense (grant number W81XWH2010884) and by the University of Wisconsin-Madison Office of the Vice Chancellor for Research and Graduate Education with funding from the Wisconsin Alumni Research Foundation.

Institutional Review Board Statement: The study was conducted according to the guidelines of the Declaration of Helsinki, and approved by the Institutional Review Board (or Ethics Committee) of The University of Wisconsin (protocol 2017-0678, approved 8 January 2018).

Informed Consent Statement: Not applicable.

Data Availability Statement: Data are contained within the article.

Acknowledgments: The authors thank Bryan Blaise and Rebecca Roembke for contributions to the manufacturing, testing and maintenance of the TADA.

Conflicts of Interest: Authors P.G.A. and I.F.E.S. are inventors on a patent covering the technology described in this manuscript. Author P.G.A. was a part owner of Intelligent Prosthetic Systems, LLC. The remaining authors declare that the research was conducted in the absence of any commercial or financial relationships that could be construed as a potential conflict of interest.

Appendix A

Below are the rotation matrices used to represent the movements of the TADA prosthetic ankle (see Ankle Design section). Each matrix converts a column vector expressed in the frame indicated by the lower left subscript into its equivalent vector expressed in the frame indicated by the upper left superscript. Each step of the manipulation is described following the relevant matrix:

$${}^0_1R = \begin{bmatrix} \cos(q_1) & -\sin(q_1) & 0 \\ \sin(q_1) & \cos(q_1) & 0 \\ 0 & 0 & 1 \end{bmatrix}, \quad (A1)$$

rotation of upper wedge cam, controlled by motor 1.

$${}^1_2R = \begin{bmatrix} \cos(q_2) & 0 & \sin(q_2) \\ 0 & 1 & 0 \\ -\sin(q_2) & 0 & \cos(q_2) \end{bmatrix}, \quad (A2)$$

inclination of the upper wedge cam face; $q_2 = \beta = \frac{\pi}{36}$.

$${}^2_3R = \begin{bmatrix} \cos(q_3) & -\sin(q_3) & 0 \\ \sin(q_3) & \cos(q_3) & 0 \\ 0 & 0 & 1 \end{bmatrix}, \quad (A3)$$

rotation of lower wedge cam relative to upper wedge cam (conceptual only; it is a consequence of q_1 and q_5 in (1)).

$${}^3_4R = \begin{bmatrix} \cos(q_4) & 0 & \sin(q_4) \\ 0 & 1 & 0 \\ -\sin(q_4) & 0 & \cos(q_4) \end{bmatrix}, \quad (A4)$$

inclination of the lower wedge cam face; $q_4 = \beta = \frac{\pi}{36}$.

$${}^4_5R = \begin{bmatrix} \sin(q_5) & -\sin(q_5) & 0 \\ \sin(q_5) & \cos(q_5) & 0 \\ 0 & 0 & 1 \end{bmatrix}, \quad (A5)$$

theoretical rotation of the foot back into a toes-forward orientation; controlled in practice through rotation of the lower wedge cam, controlled by motor 2.

The composition of sequential rotations makes the final rotation matrix 0_5R expressing foot-fixed reference frame 5 in coordinates of leg-fixed reference frame 0:

$${}^0_5R = {}^0_1R {}^1_2R {}^2_3R {}^3_4R {}^4_5R = \begin{bmatrix} a & b & c \\ d & e & f \\ g & h & i \end{bmatrix}. \quad (A6)$$

Individual elements of 0_5R are:

$$\begin{aligned} a &= -\cos(q_5)\#5 - \sin(q_5)\#3 \\ b &= \sin(q_5)\#5 - \cos(q_5)\#3 \\ c &= \cos(q_1) \cos(q_4) \sin(q_2) - \sin(q_4)\#7 \\ d &= \cos(q_5)\#4 + \sin(q_5)\#2 \\ e &= \cos(q_5)\#2 - \sin(q_5)\#4 \\ f &= \sin(q_4)\#6 + \cos(q_4) \sin(q_1) \sin(q_2) \\ g &= \sin(q_2) \sin(q_3) \sin(q_5) - \cos(q_5)\#1 \\ h &= \sin(q_5)\#1 + \cos(q_5) \sin(q_2) \sin(q_3) \\ i &= \cos(q_2) \cos(q_4) - \cos(q_3) \sin(q_2) \sin(q_4) \end{aligned} \quad (A7)$$

The numbered arguments in these expressions are:

$$\begin{aligned}
 \#1 &= \cos(q_2) \sin(q_4) + \cos(q_3) \cos(q_4) \sin(q_2) \\
 \#2 &= \cos(q_1) \cos(q_3) - \cos(q_2) \sin(q_1) \sin(q_3) \\
 \#3 &= \cos(q_3) \sin(q_1) + \cos(q_1) \cos(q_2) \sin(q_3) \\
 \#4 &= \cos(q_4) \#6 - \sin(q_1) \sin(q_2) \sin(q_4) \\
 \#5 &= \cos(q_4) \#7 + \cos(q_1) \sin(q_2) \sin(q_4) \\
 \#6 &= \cos(q_1) \sin(q_3) + \cos(q_2) \cos(q_3) \sin(q_1) \\
 \#7 &= \sin(q_1) \sin(q_3) - \cos(q_1) \cos(q_2) \cos(q_3)
 \end{aligned} \tag{A8}$$

The matrix 0_5R is equivalent to a rotation matrix specified directly by a pitch–roll or roll–pitch Euler angle sequence of body-fixed rotations. For a pitch–roll sequence (first plantarflexion θ_{PF} about a leftward-pointing mediolateral y -axis, then inversion θ_{IV} (assuming the right foot) about a forward-pointing anteroposterior x -axis), the matrix is derived in two steps:

$$R_{PF} = \begin{bmatrix} \cos(\theta_{PF}) & 0 & \sin(\theta_{PF}) \\ 0 & 1 & 0 \\ -\sin(\theta_{PF}) & 0 & \cos(\theta_{PF}) \end{bmatrix} \tag{A9}$$

$$R_{IV} = \begin{bmatrix} 1 & 0 & 0 \\ 0 & \cos(\theta_{IV}) & -\sin(\theta_{IV}) \\ 0 & \sin(\theta_{IV}) & \cos(\theta_{IV}) \end{bmatrix} \tag{A10}$$

$$R_{PF_IV} = R_{PF}R_{IV} = {}^0_5R = \begin{bmatrix} \cos(\theta_{PF}) & \sin(\theta_{IV}) \sin(\theta_{PF}) & \cos(\theta_{IV}) \sin(\theta_{PF}) \\ 0 & \cos(\theta_{IV}) & -\sin(\theta_{IV}) \\ -\sin(\theta_{PF}) & \sin(\theta_{IV}) \cos(\theta_{PF}) & \cos(\theta_{IV}) \cos(\theta_{PF}) \end{bmatrix}. \tag{A11}$$

Individual rotations can be solved for numerically to obtain q_1 , q_3 , and q_5 that match the 0_5R and R_{PF_IV} matrices. A similar matrix can be derived from a roll–pitch rotation sequence or using pylon-fixed rotation axes. In any of these cases, derivation through Euler angles results in some distortion of the movement relative to the intended direction-and-angle control (e.g., see the zero value in R_{PF_IV} that may not be zero in 0_5R). This occurs because two sequential pitch–roll or roll–pitch rotations are incomplete for describing a three-dimensional rotation as implemented by the TADA; a third rotation such as yaw would be necessary. The degree of distortion can be evaluated by including that third rotation and determining its required value, similar to the error evaluation associated with Equation (8) above. Practically, the conclusion is that a simple two-rotation Euler sequence is not recommended.

The matrix 0_5R is also equivalent to a rotation matrix specified directly by the (θ, α) pair, which can be transformed into an axis–angle formulation. For a rotation of θ about unit axis $\hat{\omega} = [\omega_x, \omega_y, \omega_z]$, a rotation matrix can be built using Rodrigues' formula [45]:

$$R_{ax_ang} = \begin{bmatrix} C + \omega_x^2 \bar{C} & \omega_x \omega_y \bar{C} - \omega_z S & \omega_x \omega_z \bar{C} + \omega_y S \\ \omega_x \omega_y \bar{C} + \omega_z S & C + \omega_y^2 \bar{C} & \omega_y \omega_z \bar{C} - \omega_x S \\ \omega_x \omega_z \bar{C} - \omega_y S & \omega_y \omega_z \bar{C} + \omega_x S & C + \omega_z^2 \bar{C} \end{bmatrix}. \tag{A12}$$

where $C = \cos \theta$, $\bar{C} = (1 - \cos \theta)$ and $S = \sin \theta$ for compactness. The rotation axis $\hat{\omega}$ is in the plane orthogonal to the TADA's upper surface; $\hat{\omega}$ is rotated 90 deg relative to the direction vector α ; and $\omega_z = 0$. Individual rotations can be solved for by numerical solution for q_1 , q_3 , q_5 that match the 0_5R and R_{ax_ang} matrices.

Appendix B

This section provides an analysis of the backdriving rotational moment and friction holding moment in the wedge cam mechanism. For simplicity, we assume Coulomb friction and a point–load contact model. Forces are localized at the contact point farthest away

from the joint center toward the applied load, which is in fact the location of contact in the real mechanism due to backlash in the wedge cams. The result is identical to using a distributed load model (Figure 5). Figure A1 shows the upper wedge cam under loading at the forefoot (see Figure 5).

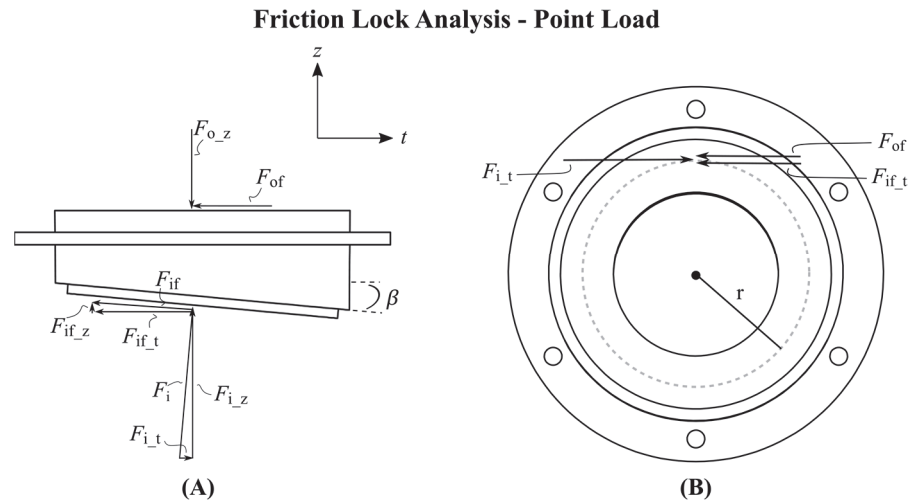


Figure A1. Diagram of applied static loads and friction holding forces to prevent backdriving in the wedge cam mechanism: (A) front view (toes pointing out of the page); (B) bottom view (toes pointing up). The analysis assumes localized loading at the point farthest from the joint axis. The result is equivalent to the distributed load case (Figure 4).

The causal load is applied to the inclined face in the z -direction, F_{i_z} , to support the ankle moment M_{ankle} (see Figure 5):

$$F_{i_z} = M_{\text{ankle}}/r. \quad (\text{A13})$$

This applied load elicits a reaction force normal to the inclined surface, F_i , which also has a component in a direction tangential to the circumference of the wedge cam, F_{i_t} , due to the surface inclination:

$$F_{i_z} = F_i \cos(\beta), \quad (\text{A14})$$

$$F_{i_t} = F_i \sin(\beta) = F_{i_z} \tan(\beta). \quad (\text{A15})$$

The tangential component of the normal force, F_{i_t} , tends to backdrive the wedge cam with moment M_{back} due to its action at a distance r from the rotation axis (related to (9)):

$$M_{\text{back}} = r F_{i_t}. \quad (\text{A16})$$

This rotational moment is opposed by friction on both the top and bottom surfaces of the wedge cam. The normal reaction force F_i establishes the capacity for a friction force on the inclined surface, F_{if_cap} , approximated by a coefficient of Coulomb friction, μ . To analyze the holding limit, we assume incipient slip, such that the actual friction force F_{if} equals this limit:

$$F_{if} = F_{if_cap} = \mu F_i. \quad (\text{A17})$$

The friction force capacity also has components in the z and t directions, F_{if_z} and F_{if_t} :

$$F_{if_t} = F_{if} \cos(\beta) = \mu F_i \cos(\beta). \quad (\text{A18})$$

$$F_{if_z} = F_{if} \sin(\beta) = \mu F_i \sin(\beta). \quad (\text{A19})$$

On the upper, orthogonal face of the wedge cam, a normal force F_{o_z} opposes all the z-direction forces on the inclined surface, and establishes a similar friction force:

$$F_{o_z} = F_{i_z} + F_{if_z} \quad (A20)$$

$$F_{of} = \mu F_{o_z}. \quad (A21)$$

All the tangential friction forces act with moment arm r about the rotational axis. To achieve static equilibrium, the holding moment from the friction forces must balance the backdriving moment from the normal force:

$$r(F_{if_t} + F_{of}) = M_{back}. \quad (A22)$$

Substituting (A13) through (A21) into (A22) yields an estimate of the friction coefficient necessary to prevent backdriving of a wedge cam with a given angle β :

$$\mu \geq \frac{1 - \cos(\beta)}{\sin(\beta)}. \quad (A23)$$

Rearrangement of (A23) also yields an estimate of the maximum wedge cam angle β that can be held by a material interface with a given friction coefficient μ (identical to (10)):

$$\tan(\beta) \leq \frac{2\mu}{1 - \mu^2}. \quad (A24)$$

For a desired wedge cam angle $\beta = 5$ degrees, Equation (A23) gives a required friction coefficient $\mu \geq 0.044$. For a designed friction coefficient of 0.1 based on the materials at the interface (PEEK plastic and aluminum), the maximum wedge cam angle estimated from Equation (A24) is 11.42 degrees. By both calculations, the estimated safety factor of the TADA as designed is roughly 2.25.

References

1. Bauby, C.E.; Kuo, A.D. Active Control of Lateral Balance in Human Walking. *J. Biomech.* **2000**, *33*, 1433–1440. [CrossRef]
2. Hof, A.L.; van Bockel, R.M.; Schoppen, T.; Postema, K. Control of Lateral Balance in Walking: Experimental Findings in Normal Subjects and above-Knee Amputees. *Gait Posture* **2007**, *25*, 250–258. [CrossRef]
3. Vari-Flex. Available online: <https://www.ossur.com/prosthetic-solutions/products/dynamic-solutions/vari-flex> (accessed on 12 February 2019).
4. Lindhe Xtend. Available online: <https://www.lindhextend.com/products/prosthetic-foot-amputee> (accessed on 17 December 2018).
5. Multiflex Pyramid Ankle. Available online: <http://www.endolite.com/products/multiflex-pyramid-ankle> (accessed on 8 June 2018).
6. Vlutters, M.; van Asseldonk, E.H.F.; van der Kooij, H. Reduced Center of Pressure Modulation Elicits Foot Placement Adjustments, but No Additional Trunk Motion during Anteroposterior-Perturbed Walking. *J. Biomech.* **2018**, *68*, 93–98. [CrossRef]
7. Reimann, H.; Fietrow, T.; Jeka, J.J. Strategies for the Control of Balance during Locomotion. *Kinesiol. Rev.* **2018**, *7*, 18–25. [CrossRef]
8. Reimann, H.; Fietrow, T.D.; Thompson, E.D.; Agada, P.; McFadyen, B.J.; Jeka, J.J. Complementary Mechanisms for Upright Balance during Walking. *PLoS ONE* **2017**, *12*, e0172215. [CrossRef]
9. Reimann, H.; Fietrow, T.; Thompson, E.D.; Jeka, J.J. Neural Control of Balance during Walking. *Front. Physiol.* **2018**, *9*, 1271. [CrossRef]
10. Panzenbeck, J.T.; Klute, G.K. A Powered Inverting and Everting Prosthetic Foot for Balance Assistance in Lower Limb Amputees. *JPO J. Prosthet. Orthot.* **2012**, *24*, 175. [CrossRef]
11. Ficanha, E.M.; Rastgaar, M.; Kaufman, K.R. A Two-Axis Cable-Driven Ankle-Foot Mechanism. *Robot. Biomim.* **2014**, *1*, 17. [CrossRef]
12. Clites, T.R.; Carty, M.J.; Ullauri, J.B.; Carney, M.E.; Mooney, L.M.; Duval, J.-F.; Srinivasan, S.S.; Herr, H.M. Proprioception from a Neurally Controlled Lower-Extremity Prosthesis. *Sci. Transl. Med.* **2018**, *10*, eaap8373. [CrossRef]
13. Össur Proprio Foot. Available online: <http://www.ossur.com/prosthetic-solutions/bionic-technology/proprio-foot> (accessed on 13 September 2014).
14. Meridium. Available online: <https://www.ottobockus.com/prosthetics/lower-limb-prosthetics/solution-overview/meridium/> (accessed on 12 May 2018).

15. Triton Smart Ankle. Available online: <https://www.ottobockus.com/prosthetics/lower-limb-prosthetics/solution-overview/triton-smart-ankle/> (accessed on 19 June 2018).
16. Raize. Available online: <http://fillauer.com/Lower-Extremity-Prosthetics/feet/raize.html> (accessed on 19 June 2018).
17. Kinnex. Available online: <http://www.freedom-innovations.com/kinnex/> (accessed on 10 July 2018).
18. Endolite Elan. Available online: <http://www.endolite.com/products/elan> (accessed on 22 August 2016).
19. OdysseyK2. Available online: <https://www.college-park.com/odysseyk2> (accessed on 19 June 2018).
20. OdysseyK3. Available online: <https://www.college-park.com/odysseyk3> (accessed on 19 June 2018).
21. Yeates, K.H.; Segal, A.D.; Neptune, R.R.; Klute, G.K. A Coronally Clutching Ankle to Improve Amputee Balance on Coronally Uneven and Unpredictable Terrain. *J. Med. Devices* **2018**, *12*, 031001–031012. [CrossRef]
22. Gorges, J.J. Controlled Coronal Stiffness Prosthetic Ankle for Improving Balance on Uneven Terrain. Ph.D. Dissertation, University of Washington, Seattle, WA, USA, 2013.
23. Adamczyk, P.G. Chapter 9—Semi-Active Prostheses for Low-Power Gait Adaptation. In *Powered Prostheses*; Dallali, H., Demircan, E., Rastgaar, M., Eds.; Academic Press: Cambridge, MA, USA, 2020; pp. 201–259. ISBN 978-0-12-817450-0.
24. Segal, A.D.; Orendurff, M.S.; Czerniecki, J.M.; Schoen, J.; Klute, G.K. Comparison of Transtibial Amputee and Non-Amputee Biomechanics during a Common Turning Task. *Gait Posture* **2011**, *33*, 41–47. [CrossRef]
25. Taylor, M.J.D.; Dabnichki, P.; Strike, S.C. A Three-Dimensional Biomechanical Comparison between Turning Strategies during the Stance Phase of Walking. *Hum. Mov. Sci.* **2005**, *24*, 558–573. [CrossRef]
26. Adamczyk, P.G. Ankle Control in Walking and Running: Speed- and Gait-Related Changes in Dynamic Mean Ankle Moment Arm. *J. Biomech. Eng.* **2020**, *142*, 071007–071015. [CrossRef]
27. Rebula, J.R.; Ojeda, L.V.; Adamczyk, P.G.; Kuo, A.D. Measurement of Foot Placement and Its Variability with Inertial Sensors. *Gait Posture* **2013**, *38*, 974–980. [CrossRef]
28. Glanzer, E.M.; Adamczyk, P.G. Design and Validation of a Semi-Active Variable Stiffness Foot Prosthesis. *IEEE Trans. Neural Syst. Rehabil. Eng.* **2018**, *26*, 2351–2359. [CrossRef]
29. Donelan, J.M.; Kram, R.; Kuo, A.D. Mechanical and Metabolic Determinants of the Preferred Step Width in Human Walking. *Proc. R. Soc. Lond. B* **2001**, *268*, 1985–1992. [CrossRef]
30. Donelan, J.M.; Kram, R.; Kuo, A.D. Mechanical Work for Step-to-Step Transitions Is a Major Determinant of the Metabolic Cost of Human Walking. *J. Exp. Biol.* **2002**, *205*, 3717–3727. [CrossRef]
31. Ellis, G. Chapter 12—Nonlinear Behavior and Time Variation. In *Control System Design Guide*, 4th ed.; Ellis, G., Ed.; Butterworth-Heinemann: Boston, UK, 2012; pp. 235–260. ISBN 978-0-12-385920-4.
32. Collins, S.H.; Kuo, A.D. Recycling Energy to Restore Impaired Ankle Function during Human Walking. *PLoS ONE* **2010**, *5*, e9307. [CrossRef]
33. Schwartz, M.H.; Rozumalski, A. A New Method for Estimating Joint Parameters from Motion Data. *J. Biomech.* **2005**, *38*, 107–116. [CrossRef]
34. Functional Joints—Visual3D Wiki Documentation. Available online: http://www.c-motion.com/v3dwiki/index.php?title=Functional_Joints (accessed on 15 February 2019).
35. Amidror, I. Scattered Data Interpolation Methods for Electronic Imaging Systems: A Survey. *J. Electron. Imaging* **2002**, *11*, 157–176. [CrossRef]
36. Krausz, N.E.; Lenzi, T.; Hargrove, L.J. Depth Sensing for Improved Control of Lower Limb Prostheses. *IEEE Trans. Biomed. Eng.* **2015**, *62*, 2576–2587. [CrossRef]
37. Kleiner, B.; Ziegenspeck, N.; Stolyarov, R.; Herr, H.; Schneider, U.; Verl, A. A Radar-Based Terrain Mapping Approach for Stair Detection Towards Enhanced Prosthetic Foot Control. In Proceedings of the 2018 7th IEEE International Conference on Biomedical Robotics and Biomechatronics (Biorob), Enschede, The Netherlands, 26–29 August 2018; pp. 105–110.
38. Shell, C.E.; Klute, G.K.; Neptune, R.R. Identifying Classifier Input Signals to Predict a Cross-Slope during Transtibial Amputee Walking. *PLoS ONE* **2018**, *13*, e0192950. [CrossRef]
39. Europa+. Available online: <http://orthocareinnovations.com/europa/> (accessed on 2 August 2018).
40. Nichols, K.M.; Adamczyk, P.G. Sensitivity of Lower-Limb Joint Mechanics to Prosthetic Forefoot Stiffness with a Variable Stiffness Foot in Level-Ground Walking. *J. Biomech.* **2023**, *147*, 111436. [CrossRef]
41. Adamczyk, P.G.; Harper, S.E.; Reiter, A.J.; Roembke, R.A.; Wang, Y.; Nichols, K.M.; Thelen, D.G. Wearable Sensing for Understanding and Influencing Human Movement in Ecological Contexts. *Curr. Opin. Biomed. Eng.* **2023**, *28*, 100492. [CrossRef]
42. Rebula, J.R.; Ojeda, L.V.; Adamczyk, P.G.; Kuo, A.D. The Stabilizing Properties of Foot Yaw in Human Walking. *J. Biomech.* **2017**, *53*, 1–8. [CrossRef]
43. Sheehan, R.C.; Rábago, C.A.; Rylander, J.H.; Dingwell, J.B.; Wilken, J.M. Use of Perturbation-Based Gait Training in a Virtual Environment to Address Mediolateral Instability in an Individual With Unilateral Transfemoral Amputation. *Phys. Ther.* **2016**, *96*, 1896–1904. [CrossRef]

44. Orendurff, M.S.; Bernatz, G.C.; Schoen, J.A.; Klute, G.K. Kinetic Mechanisms to Alter Walking Speed. *Gait Posture* **2008**, *27*, 603–610. [CrossRef]
45. Weisstein, E.W. Rodrigues' Rotation Formula. Available online: <https://mathworld.wolfram.com/RodriguesRotationFormula.html> (accessed on 1 October 2020).

Disclaimer/Publisher's Note: The statements, opinions and data contained in all publications are solely those of the individual author(s) and contributor(s) and not of MDPI and/or the editor(s). MDPI and/or the editor(s) disclaim responsibility for any injury to people or property resulting from any ideas, methods, instructions or products referred to in the content.

Article

User-Centered Design Framework for Personalized Ankle–Foot Orthoses

Peter Dabnichki ^{1,*} and Toh Yen Pang ²¹ Mechanical, Manufacturing and Mechatronic Engineering, School of Engineering, STEM College, RMIT University, Melbourne, VIC 3000, Australia² Biomedical Engineering, School of Engineering, STEM College, RMIT University, Melbourne, VIC 3000, Australia; tohyen.pang@rmit.edu.au

* Correspondence: peter.dabnichki@rmit.edu.au

Abstract: Background/Objectives: Integrated design and simulation solutions enable the manufacturing of advanced personalized orthotics that improve patients gait characteristics and balance. The success of such a rehabilitation approach is highly dependent on compliance, i.e., users wearing the orthosis consistently. Specifically, for most young children, functionality is secondary to appearance and peer perception. However, the starting point of the traditional design approach is to address functionality and then try to make the appearance more palatable to the wearer. As a result, compliance is a common issue, resulting in slow and uneven rehabilitation progress. **Methods:** This work proposes a method that inverts this traditional approach and devises an attractive light design that can be adapted to ensure structural soundness. **Results/Conclusions:** The broader framework is called the user-centered design process. The main advantage is in the flexibility of the added manufacturing approach, allowing for a personalized design that is attractive to the user, promoting higher compliance.



Academic Editor: Arnab Chanda

Received: 11 December 2024

Revised: 14 January 2025

Accepted: 15 January 2025

Published: 23 January 2025

Citation: Dabnichki, P.; Pang, T.Y. User-Centered Design Framework for Personalized Ankle–Foot Orthoses. *Prosthesis* **2025**, *7*, 11. <https://doi.org/10.3390/prosthesis7010011>

Correction Statement: This article has been republished with a minor change. The change does not affect the scientific content of the article and further details are available within the backmatter of the website version of this article.

Copyright: © 2025 by the authors. Licensee MDPI, Basel, Switzerland. This article is an open access article distributed under the terms and conditions of the Creative Commons Attribution (CC BY) license (<https://creativecommons.org/licenses/by/4.0/>).

Keywords: orthotics; additive manufacturing; personalized design; ankle–foot orthoses

1. Introduction

Ankle–foot orthoses (AFOs) are essential devices in pediatric rehabilitation, particularly for children with conditions such as cerebral palsy, foot drop, or neuromuscular impairments [1–4]. These devices aid in enhancing mobility, preventing deformities, and improving overall gait. However, adherence to prescribed AFO use among children and adolescents remains a persistent challenge [5]. In a comprehensive study, Bertini et al. [6] reported that 22% of prescribed orthotic devices were never used and 27% were discontinued after initial use, highlighting a critical gap in their effective utilization.

The recommendation for the continuous use of AFOs for an average of 7 h per day, except for periods dedicated to hygiene purposes, is believed to optimize the benefits associated with gait improvement and the alleviation of linked to foot disorders [7]. However, scientific studies have reported that between 6% and 80% of AFO users wear their orthotic devices less frequently than once a month [8,9]. For instance, Ejm [9] reported that 1 out of 15 AFOs were not used at all, suggesting that approximately 6.67% of users do not wear their orthotic devices. Myers et al. [7] documented that their participants wore their AFO for an average of 4.8 to 4.9 days per week. Key factors influencing non-compliance include the following:

1. *Discomfort and pain:* Common complications with orthotic devices, such as foot calluses and ulcerations (13%), contribute to emotional distress and reduced tolerability among

users. Bertini et al. [6] discovered that AFO users frequently reported symptoms of depression and physical and general fatigue, with emotional distress being the reason for 17% of abandonment of the orthoses altogether. AFO users complained mostly of skin reddening (52%) and moderate to severe pain (41%), highlighting the need for improved design approaches to reduce such adverse effects. Comfort is essential, as devices that can be worn comfortably for extended periods tend to achieve higher compliance rates; this is dependent on appropriate fitting and the use of non-irritating materials [10,11].

2. *Psychosocial factors*: These include the perception of the device, cosmetic concerns, and peer perceptions adolescents [12]. Peer influence and social acceptance can affect adherence, especially among adolescents, who may feel self-conscious about wearing orthotic devices [12,13]. Okçu et al. [14] emphasized that effective patient education and addressing device comfort can enhance compliance and overall satisfaction.
3. *Functional limitations*: Poor integration with footwear, bulkiness, and difficulty in donning or doffing AFOs further discourage their consistent use. The weight of the device is crucial; lighter orthoses are preferred due to their reduced bulk, making them easier to wear for prolonged periods [11,15,16]. Ease of use is another factor that supports compliance. Orthoses that are easy to put on, take off, and adjust independently are more likely to be used regularly [17,18]. Durability contributes positively to user satisfaction as well, with robust devices that maintain their functionality over time requiring fewer repairs or replacements [19]. In addition, Bertini et al. [6] reported that muscle weakness, particularly in foot dorsiflexion and plantarflexion, affects the tolerability and effectiveness of AFOs. Later, Mohammadi et al. [5] introduced the first AFO with modular artificial muscles, but their preliminary results addressing users' comfort were inconclusive.

Esthetic considerations also affect user experience, especially for highly visible orthoses, like those designed for the upper and lower limbs. Designs that are discreet or visually appealing tend to enhance user confidence and compliance [11,20]. A previous study reported that esthetic preferences vary by age: younger children prefer vibrant and customizable design features (e.g., colors, graphic designs such as Superman and unicorns, texture, etc.), while older children prefer discreet and visually inconspicuous options [16]. In addition, the ease of integration of users' shoes with AFOs, esthetic enhancements (e.g., lights, colors), and sleek designs have shown promise in improving engagement, particularly among older children [16,21]. Cosmetic concerns, preferences over function, and negative experiences with homemade or off-the-shelf versions also impact compliance and satisfaction levels among patients [22].

The traditional method of creating AFOs involves negative molding of a cast, or the direct molding of thermoplastics to an individual's leg [23]. These manufacturing approaches often compromise comfort and fit, and significantly reduce the possibility of any creative freedom [2]. Additive manufacturing (AM) has emerged as a promising solution. AM offers a significant advancement in customization that improves biomechanical function, comfort, and esthetics [24–27]. Unlike traditional manufacturing, AM enables the following:

1. *Precision fit*: The use of 3D scanning enables precise modeling of a child's anatomy, allowing the AFO to conform to the shape and size of the user and ensuring a better fit [3], addressing the specific requirements of each user [28,29] and reducing the risk of complications such as pressure sores [6,27].
2. *Selection of lightweight and durable structures*: AM facilitates the creation of complex, lightweight geometries that improve wearability without compromising strength

3. *Incorporating complex geometries and functional features:* AM enables the incorporation of complex geometries and functional features that would be difficult or impossible to achieve with traditional manufacturing methods [2].

These findings underscore the complex interplay between physiological comfort, psychological well-being, and therapeutic adherence in pediatric orthotic intervention. Comfort and fit are dominant issues; traditional rigid AFOs often lead to discomfort, impacting motivation to wear them [30]. Despite these challenges, some studies suggest that improved designs and personalized support could enhance adherence rates. However, the variability in usage highlights the need for tailored interventions to address individual user needs and contexts [31]. In this work, we set a framework for functionality that follows one proposed by an earlier study [32]. The guiding principles we formulated are as follows:

- User acceptance and esthetic preferences
- Comfort and wearability
- Injury prevention.

These guiding rules aim to address age-group-specific objectives and overcome key challenges affecting compliance with a rehabilitation routine that necessarily includes prolonged and consistent wearing of the prescribed orthotics. Hence, the purpose of this study is to develop and validate a systematic framework—enabling the design of personalized orthotics for young children—that integrates the abovementioned principles.

Current approaches to AFO design often emphasize functionality at the expense of child acceptance and comfort, leading to reduced compliance and compromised treatment outcomes. Our methodology uniquely addresses this challenge by incorporating the child's esthetic preferences during the initial design stage, while ensuring that biomechanical requirements are met through engineering validation. This holistic approach advances pediatric orthotic design by concurrently considering the child's visual preferences, physical comfort, and safety requirements, thereby creating AFOs that children are more likely to wear consistently and effectively. The process should also incorporate the selection of appropriate additive manufacturing materials, following the procedure developed by [33,34]. In summary, the aim is to establish a robust process for a personalized design, with a starting point of visually acceptable design for the user, while meeting all structural and biomechanical requirements.

2. Materials and Methods

2.1. Outline of the User-Centered Design Process

This study used a user-centered design process, adapted from established engineering design principles, to develop and evaluate an innovative AFO design (Figure 1). The process started by identifying the limitations inherent in existing AFOs, such as discomfort, restricted mobility, and insufficient individualization. Background research was undertaken to assess current AFO designs, materials, and manufacturing techniques, as well as the specific requirements of individuals with conditions necessitating the use of AFOs (e.g., foot drop, cerebral palsy).

Specific design criteria were established, encompassing comfort, range of motion, ease of donning and doffing, and durability. Collaborative brainstorming sessions yielded numerous AFO design concepts, integrating advanced materials and fabrication methods, including additive manufacturing. These concepts were systematically evaluated against the pre-defined criteria in order to select the optimal design. A prototype AFO was subsequently fabricated, incorporating features such as adjustable stiffness and a personalized fit. The prototype underwent rigorous testing and iterative redesign, guided by biomechanical

analysis and user feedback. This iterative process persisted until the AFO fulfilled the pre-defined requirements for functionality, comfort, and user satisfaction.

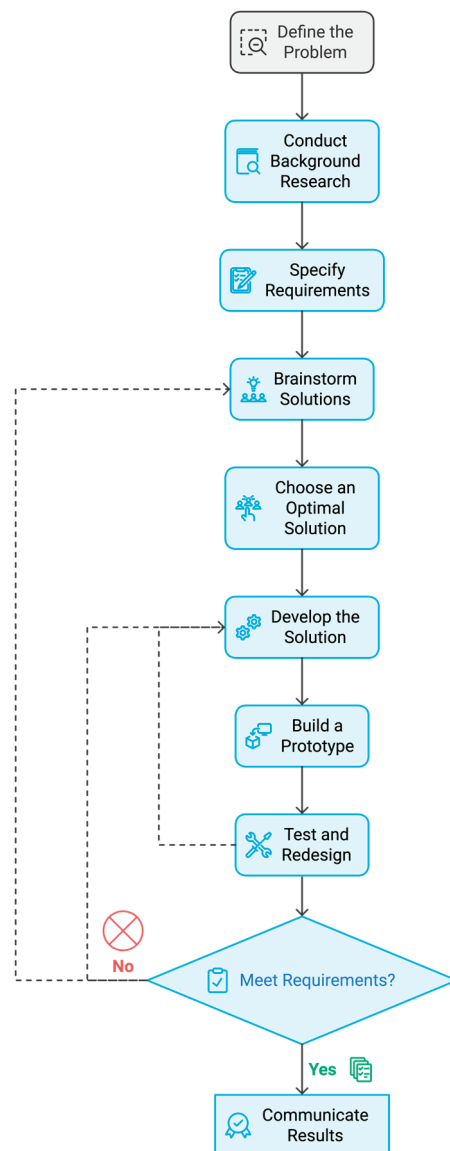


Figure 1. An overview of the user-centered design process, adapted from established engineering design principles.

2.2. Define the Problem

In this phase, we systematically addressed key challenges and limitations associated with current pediatric AFOs by conducting background research. We then identified specific user needs and translated them into actionable design requirements.

Although AFOs can enhance gait stability and decrease energy expenditure, patient compliance is significantly influenced by factors such as the severity of the disease, the degree of customization, and the perceived benefits of the device. Research has consistently indicated suboptimal compliance rates among patients, with reported abandonment rates of 31% and complication rates of 69% associated with AFO use [6].

Current AFO designs are limited by materials, structure, and esthetic requirements. For example, thermoplastic materials often lack breathability, leading to excessive sweating and discomfort, especially in extreme temperatures [16]. Structural rigidity around the malleoli and other areas can cause pressure sores, superficial skin irritation, and reduced

mobility. The bulky design of many AFOs restricts footwear options and exacerbates difficulties in fitting both the AFO and accompanying shoes. Esthetic considerations are frequently overlooked, leaving users, particularly older children, feeling self-conscious and reluctant to wear the devices in public [16]. Furthermore, the process of acquiring an AFO often involves delays, fabrication errors, and inconsistent practitioner approaches, frustrating both users and caregivers [16].

These limitations necessitate further investigation to develop user-centered, functional, and esthetically pleasing designs while improving service delivery, to enhance user satisfaction and adherence to AFOs.

2.3. Specify the Requirements

The design requirements for the AFO were established to balance user preferences with functional and safety standards, thereby providing a solution that is child-friendly and easy to use. Customization was emphasized, necessitating a 90% accuracy in fitting assessments conducted by trained orthotists to ensure a tailored fit to individual limb morphology.

Safety was a principal concern, with adherence to ISO 10328 standards and a minimum safety factor of 2.0 established in load-bearing capacity tests [35]. Mobility was enhanced through lightweight construction, with a maximum weight limit of 900 g, and gait support was assured by facilitating smooth transitions between swing and stride phases.

Comfort and ventilation were addressed by requiring users to walk pain-free for a duration of 30 min, alongside the incorporation of strategically placed ventilation channels, which achieved an optimal breathability. Skin protection was ensured through the use of smooth edges and hypoallergenic materials to reduce the risk of irritation.

Ease of use was prioritized, enabling caregivers to apply or remove the AFO within one minute and complete maintenance in under five minutes. Functional capabilities included moderate resistance to prevent foot-slap in 85% of users, unrestricted ankle rotation up to 45 degrees, and drop-foot prevention via 90-degree leg support during swing phases [36]. Compatibility with 80% of children's shoe sizes was considered, and the design process ensured that the AFO could be manufactured and delivered within a short turnaround time frame, preferably three days after measurement [37].

2.4. Brainstorming Solutions

The ideation phase emphasized user-centered design principles, with a particular focus on pediatric empowerment through creative engagement. The conceptual development process yielded several design solutions, demonstrating playful, child-friendly designs inspired by familiar shapes and characters, such as the “Monkey AFO”. The Monkey AFO uses its arms as functional straps, offering both esthetic appeal and practical utility, while its curved body ensures comfort and fit around the leg (Figure 2).



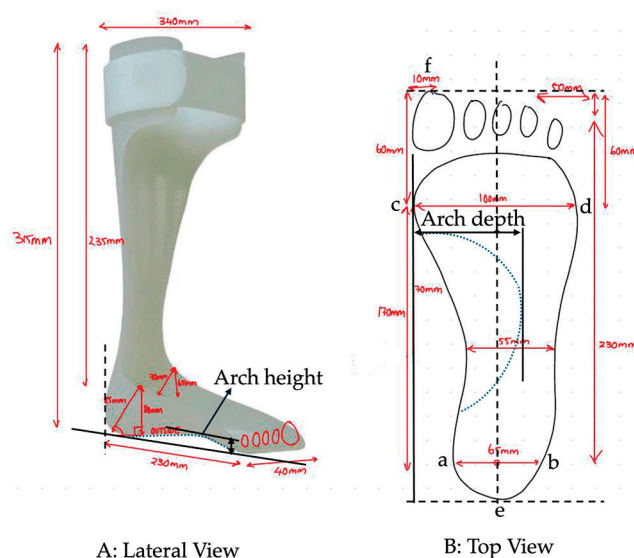
Figure 2. Example of design ideations of ankle–foot orthoses that support the ankle and foot.

Additionally, color palettes and patterns inspired by children's interests, such as TV shows, toys, and nature, were incorporated into other designs (e.g., SpongeBob and snake-inspired designs). These visuals illustrate how themes and bright colors such as yellows, brown, pink, orange, and blues are used to evoke empowerment, self-expression, and engagement among young users. The focus during this stage was to generate a wide range of ideas, setting aside feasibility considerations to encourage innovation. Some concepts were comprehensive designs, while others were collections of features and ideas to be refined in the next stage.

2.5. Develop the Solution

2.5.1. Anthropometric Measurement of the Foot

The initial step of the development of a design solution involved conducting anthropometric measurements of the foot and leg. These measurements were obtained by collecting sample measurements of participants' feet and legs (Figure 3). The measurement of arch length was based on [33,34].



Measurement	Point 1	Point 2
Malleolus width	a Medial Malleolus medial border	b Lateral Malleolus lateral border
MTP Width	c 1 st MTP medial border	d 5 th MTP lateral border
Foot Length	e Rear Line or Heel border	f Longest toe or hallux border

Figure 3. Anthropometric measurement of foot and ankle: (A): lateral view, (B) top view, and table: definition of the foot variables.

Anthropometric measurements were conducted using standardized tools to ensure accuracy and consistency. Lengths were measured using a flexible, non-elastic tape measure (precision ± 1 mm) and a digital caliper (precision ± 0.01 mm) for finer measurements. Circumferences and diameters were measured exclusively with a flexible tape measure, following measurement guidelines for anthropometric research [29,38,39].

To minimize potential errors in anthropometric measurements, we employed the following approach: Two independent researchers conducted each measurement three times under controlled conditions. The average value of these six measurements (three from each researcher) was used as the final value for each parameter. This approach ensured consistency and reliability, reducing the influence of individual variability or transient

errors. By incorporating this method, we aimed to minimize measurement error and enhance the accuracy of the data, ensuring their reliability for informing the final design.

2.5.2. Computer-Aided Design (CAD)

The CAD process began with extensive sketching to define the overall design concept. These sketches served as a visual exploration tool for various design features, such as the shape, structure, and functional components of the AFO. This step included considerations for edge contours, overall height, base shape, and strap configurations.

CATIA software v5 was used for design development (Figure 4), and parametric models were also used to facilitate flexibility in the design process. This approach enabled the adjustment of key parameters, such as dimensions, curves, and attachment points, to accommodate user-specific needs or esthetic variations. Consequently, this approach ensured that the model could be easily customized and iterated upon.

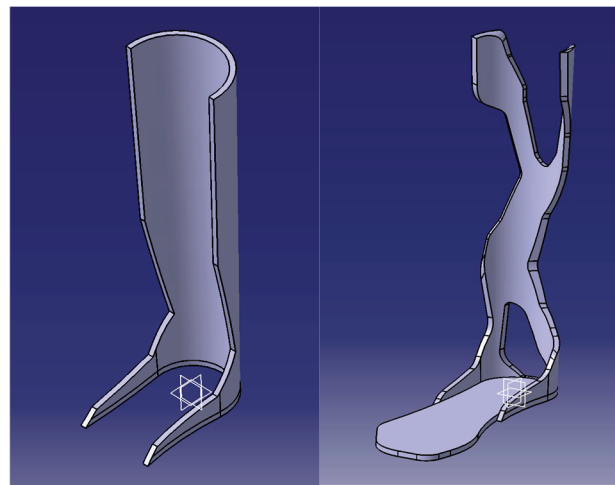


Figure 4. Custom design of ankle-foot orthosis using CATIA software.

2.5.3. Finite Element Analysis of the Proposed Design Solution

The finite element analysis (FEA) of the AFO design was conducted using Fusion 360 software to evaluate the structural performance under simulated loading conditions (Figure 5).



Figure 5. Finite element modeling and analysis of ankle-foot orthosis.

- **Model Preparation**

The AFO design model was imported into Fusion 360 for pre-processing. To facilitate mesh generation, the model underwent remeshing using the Quad Remesher extension by Exoside. This tool enabled the generation of a high-quality quadrilateral mesh, thereby ensuring uniform element distribution and an accurate representation of complex geometries. The target quadrilateral count was iteratively adjusted to achieve an optimal balance between computational efficiency and detail. The quality of the elements was verified to ensure all elements met the standard criteria for aspect ratio and skewness.

- **Boundary Conditions and Loading**

The boundary conditions were applied to simulate realistic usage scenarios. The upper boundary of the ankle portion was constrained in all planes, representing the connection point where the AFO interfaces with the user's leg. A static load corresponding to a child's body weight (15–20 kg) was applied uniformly across the base of the AFO to simulate the typical force exerted during use. The load range was selected based on a normal child's weight data.

- **Material Selection**

Three commonly utilized materials for AFO fabrication were evaluated to compare their mechanical performance:

1. Nylon (Polyamide 12—PA12), a widely used material in Selective Laser Sintering (SLS) 3D printing. PA12 is known for its high strength, elasticity, low density, and good chemical resistance, making it a versatile material for orthotic applications. The low cost of Nylon PA12, combined with its compatibility with SLS technology, makes it cost-effective for the production of multiple orthoses tailored to diverse user needs. Nylon is recyclable, further supporting environmentally sustainable practices (Figure S1).
 2. Polypropylene (PP), a semi-rigid, lightweight thermoplastic selected for its durability and flexibility. While PP is soft, making it comfortable for users, its raw materials are expensive.
 3. High-Density Polyethylene (HDPE), known for its strength, durability, and resistance to chemicals and moisture. HDPE is frequently used in 3D printing for applications requiring high durability. While the material costs of HDPE are relatively cheap, the manufacturing is considered time-consuming and expensive.
- Material properties such as Young's modulus, Poisson's ratio, and density were assigned based on the published literature and material data sheets (Figures S1 and S2).
 - Mesh Generation: To ensure accurate simulation results, the model was meshed using a quadrilateral mesh generated by the Quad Remesher. The mesh was refined in critical stress-concentration areas, such as the ankle and base regions, while maintaining coarser elements in less critical zones to optimize computational resources.
 - The results were analyzed to compare the performance of the three materials. Stress distribution plots, deformation visualizations, and factor of safety (FoS) metrics were documented for each material to identify the most suitable option for AFO fabrication. The analysis also informed potential design improvements to address stress concentration areas or excessive deformation.

2.6. Build a Prototype

The final design was fabricated using an additive manufacturing processes (i.e., as 3D printing) with Nylon PA12 material (Figure 6). This methodology enables the modification

of traditional designs to yield a final functional prototype that is both esthetically pleasing and effective.



Figure 6. Three-dimensional-printed prototype of the custom-designed ankle–foot orthosis.

2.7. Test and Redesign

The 3D-printed AFO underwent user testing involving individuals that were representative of the intended population (Figure 7).



Figure 7. Physical testing and evaluation of ankle–foot orthosis.

The research team wore the AFO prototype for a pre-defined duration, during which key activities, such as standing, walking, ascending and descending stairs, and engagement in light physical activity, were observed. The AFO was fitted by the participants themselves or with assistance from carers to evaluate the ease of application and removal. The prototype was evaluated based on the following criteria:

- **Comfort:** Users reported the absence of pain, irritation, or overheating during use.
- **Usability:** Ease of putting on and removing the AFO, and whether the straps provided adequate support.
- **Mobility:** Users' ability to walk, climb stairs, and engage in daily activities without significant hindrance.

- Durability: Observations of the prototype's ability to withstand use without visible deformation or wear.
- Esthetics: Users' feedback on the appearance of the AFO and whether it was perceived as empowering or appealing.

3. Results and Discussion

The methodology employed in this study was designed to systematically address the limitations of existing AFOs through a user-centered design and engineering approach (Figure 1). Current AFOs, as a rule, prioritize functionality while neglecting user comfort, esthetics, and adaptability, resulting in challenges such as poor compliance, discomfort, and diminished user satisfaction. By synthesizing insights garnered from user feedback, esthetic research, and engineering analysis, this study sought to create AFO designs that enhance both functional performance and the emotional well-being of users (Figure 2).

3.1. Design Considerations

During the design process for this AFO, once anthropometric data were collected (Figure 3), they could be easily integrated into CAD software to develop custom AFO designs tailored to individual users (Figure 4).

We used the 'extrude' approach to modify the support's thickness to the desired height and then shape it by cutting away material to create a tree-like form. This approach met the esthetic design requirement, aiming to empower the user. Additionally, we used a filleting tool to create soft, rounded edges, ensuring comfort by preventing pinching or sharp transitions against the skin. The design also effectively distributed torque from the support down to the base by gradually connecting the two components. The current study prioritized user empowerment in the design by incorporating visually engaging elements that promote compliance and self-expression. Existing AFOs often adopt a closed "boot" design that restricts airflow and contributes to overheating. Our designs integrated strategically placed ventilation features to improve breathability and overall comfort. Our designs also allowed for the AFO to remain integrated within a shoe, facilitating streamlined usability. The use of CAD-based approaches enables easy adjustments and iterative refinement, rendering the manufacturing process more flexible and efficient.

3.2. Customization

One of the key decisions in our design approach was the selection of anthropometric measurement methods over advanced 3D scanning technologies, as has been suggested previously [28,29]. While 3D scanning offers precision and automation, it is often inaccessible in remote Australian areas and developing regions such as Loas, the Pacific Islands, and parts of Africa, where such advanced technology may not be readily available.

The reliance on anthropometric measurement techniques makes this approach highly adaptable to regions where 3D scanning equipment is not feasible. Using standard tools such as tape measures and calipers, users or healthcare providers can collect precise measurements of the foot and leg by following established guidelines for anthropometric research. These guidelines ensure consistency and reproducibility in measurement collection, even when conducted by individuals with minimal technical expertise. This makes the methodology suitable for communities with limited access to healthcare infrastructure or advanced manufacturing technologies. This approach addresses the gap between advanced healthcare technology and the needs of remote or resource-limited communities, enabling a global impact on mobility and quality of life.

However, in urban or resource-rich environments, 3D scanning could play a complementary role by improving the accuracy of anatomical data capture, reducing fabrication

errors, and expediting the production process. The ability to produce detailed 3D models of limb morphology could also enhance the integration of advanced manufacturing techniques, such as additive manufacturing, for creating more precise and bespoke designs. While our approach focuses on providing low-cost, scalable solutions for underserved regions, the potential for hybrid systems combining anthropometry and 3D scanning in diverse healthcare settings warrants further exploration in future work.

3.3. Engineering Evaluation

FEA simulations were performed on the AFO designs to assess their performance under static loading conditions, and provided critical insights into the feasibility of our designs under the loading conditions. The results demonstrated that the proposed design (Figure 5) displayed moderate deformation (12 mm) and low stress levels (1.8 MPa), with acceptable safety factors (FoS = 15) for Nylon material.

The FEA demonstrated the importance of material selection in balancing strength, flexibility, and weight (400 g). Nylon consistently outperformed other materials, showing the lowest deformation and highest safety factors across all designs. This material's properties align well with the requirements of lightweight yet durable AFOs.

The manufacturing flexibility provided by CAD modeling and the use of 3D printing technologies, allowed for rapid prototyping and iterative refinement (Figure 6). This approach reduced the time and cost associated with traditional molding methods while enabling the creation of customizable designs tailored to individual users.

3.4. User Evaluation

Physical testing was performed by using the printed AFOs on group members (Figure 7), with a focus on user experience, particularly in terms of comfort and fit. The physical testing of the prototypes revealed several enhancements in comparison to existing AFOs:

- **Comfort and Fit:** Discomfort was observed around the calf connection. This was primarily due to the unrounded edges of the 3D-printed material. This sharp geometry created localized pressure points, leading to skin irritation and discomfort during wear. This issue highlights a design oversight rather than a material flaw, as simple modifications like rounding edges with a fillet could mitigate these effects. These findings highlighted the importance of incorporating ergonomic design principles into AFO development, particularly for pediatric users, whose skin is more sensitive to pressure and friction. Modifying the material's flexibility and further refining the edge geometry would likely alleviate these concerns.
- **Flexibility and Stiffness:** The prototypes provided adequate alignment support; however, they exhibited excessive stiffness, which impeded natural gait and resulted in discomfort during prolonged use. The rigidity observed in the design was directly attributed to the selection of material and the structural design, which aimed at providing stability and maintaining foot alignment. However, this stiffness restricted natural movement around the ankle, inhibiting gait dynamics and contributing to an unnatural walking experience. While stiffness is beneficial for alignment and stability, excessive rigidity can impede compliance by causing fatigue and discomfort during extended use. In practical terms, future iterations could focus on modifications to the 3D-printed materials, such as using hybrid materials or layered structures to introduce localized flexibility around the ankle. Additionally, design modifications, including integrating hinges or segmented components, could be potential solutions to enhance range of motion without compromising support.

- **Ease of Use:** The integration of adjustable straps and compatibility with standard footwear significantly enhanced usability. This feature enables children to independently don and doff the AFO, which is essential for promoting compliance and fostering autonomy.
- **Esthetic and Psychological Impact:** A survey-based methodology to evaluate the psychological impact of esthetic designs was developed to evaluate the relationship between AFO designs and perceived empowerment using a five-Likert rating scale, ranging from “Children will not feel empowered wearing this AFO” (1) to “Children will feel extremely empowered wearing this AFO” (5). This survey was only conducted internally with project team members, due to resource limitations and time constraints. This approach allowed us to validate the framework, refine the survey structure, and ensure consistency in the rating process. The visual appeal of the designs was positively received by the intended users, aligning with the objective of creating a device that fosters empowerment and self-expression. The actual design was an initial prototype that could be adapted to the body surface to increase the functional comfort. We refrained from using a composite structure with soft pads on the interfaces in order to keep the cost down. Adding appropriate foam pads would address the comfort issue, but a less costly option is also possible.

3.5. Material Selection

Material selection is a critical aspect of designing pediatric AFOs, requiring comfort, durability, cost, and environmental sustainability to be balanced. Our evaluation focused on three candidate materials—Nylon PA12, Polypropylene (PP), and High-Density Polyethylene (HDPE)—to determine the most suitable option for our design.

In addition to superior mechanical and chemical properties for medical applications like AFOs, the smooth surface finish and elasticity of Nylon PA12 could reduce pressure points and irritation. It can be treated or padded for enhanced skin comfort, making it suitable for prolonged wear. The low cost and recyclability of Nylon PA12 make it sustainable for the production of multiple orthoses tailored to diverse user needs.

It was observed that the semi-crystalline structure of PP caused significant warping during cooling, complicating its use in 3D printing. The high material and production costs of PP also limit its feasibility for pediatric AFOs. Similarly, HDPE is prone to warping and exhibited poor adhesion during 3D printing, necessitating precise temperature control and pre-treatment.

Among the three materials, Nylon PA12 was selected as the optimal choice for pediatric AFOs due to its balance of mechanical performance, skin comfort, cost-effectiveness, and sustainable production, with minimal material waste.

3.6. Implications and Future Directions

The results reveal the importance of adopting a holistic approach to AFO design, integrating engineering performance, user comfort, and esthetics. While the prototypes address many of the limitations of current AFOs, further optimization is required, particularly in reducing stiffness and addressing fit-related discomfort. The initial evaluation of our AFO design focused on short-term metrics, such as comfort, ease of use and immediate user satisfaction.

We acknowledge the importance of long-term testing for a comprehensive evaluation of the performance, durability and impact on therapeutic outcomes of AFOs. To achieve this, future studies could also benefit from advanced user testing, including long-term wear trials and motion analysis, to assess the functional and psychological impacts of the designs. To ensure structural integrity, particularly in high-stress regions like the ankle and

heel, repeated load-bearing evaluations and material fatigue analyses to ensure structural fatigue analysis should be considered. Periodic surveys with users should be conducted to evaluate prolonged skin comfort, ease of use, and esthetic satisfaction, thereby determining any changes in user preferences and device functionality. Furthermore, gait analyses using a motion capture system such as the Vicon system, force plate technology, and gait analysis software should be considered to monitor potential improvements in spatial-temporal parameters such as step length, stride symmetry and cadence. Additionally, muscle strength, particularly in foot dorsiflexion and plantarflexion, should be evaluated to monitor improvements in functional mobility. These tools and methodologies will provide objective metrics to determine whether the AFO supports natural gait patterns and contributes to improved therapeutic outcomes.

The anthropometric approach empowers users and carers to participate actively in the design process. By providing simple tools and instructions, individuals can measure their foot and leg dimensions accurately and send these data to a designer. To ensure accuracy and reproducibility, future work should focus on developing standardized, easy-to-follow protocols for anthropometric measurements that are tailored to AFO design. Training materials, such as instructional videos or illustrated guides, could be created to assist users and healthcare providers in collecting reliable data. Furthermore, future iterations of this methodology could integrate emerging technologies, such as mobile-phone-based 3D scanning. This would provide a bridge between low-tech and high-tech solutions, expanding applicability as technology becomes more widespread in underserved regions.

This study demonstrates the potential for modern design and manufacturing techniques to create AFOs that not only improve mobility and alignment, but also empower users through comfort, usability, and self-expression. By prioritizing user-centered design principles, AFOs can shift from being solely function-focused devices to holistic solutions that enhance both physical and emotional well-being.

In this study, we only incorporated a survey-based methodology to validate the framework, refine the survey structure, and ensure consistency in the rating process. However, as the survey did not involve external participants, future studies will be required to extend this methodology to include children and their caregivers, ensuring more comprehensive and generalizable results. Future work should also incorporate established questionnaires, such as the Pediatric Quality of Life Inventory (PedsQL) or the Self-Perception Profile for Children (SPPC), to evaluate psychological outcomes more robustly. These tools will allow for a deeper understanding of how esthetic design impacts user confidence, social acceptance, and compliance with prescribed use.

Although this study demonstrated the utility of materials such as Nylon 6 for 3D-printed AFOs, future research should explore alternative materials that have already been obtained following the procedure presented by Hu et al. [33] and Hu et al. [34], and manufacturing methods that balance cost, durability, and user comfort. Developing low-cost 3D printing solutions that are tailored for use in developing regions could further enhance the scalability of this approach.

4. Conclusions

This study highlights the importance of a user-centered design in enhancing adherence to and satisfaction with AFOs. By systematically addressing key factors such as comfort, functionality, esthetics, weight, ease of use, and customization, we propose design solutions that are tailored to the diverse needs and preferences of users. Our research has established a framework for functionality, informed by prior studies, that focuses on principles such as user acceptance, comfort, wearability, and injury prevention. Incorporating user feedback

was found to be a key strategy to address persistent issues, including poor fit, skin irritation, and psychological discomfort, which often lead to device rejection or inconsistent use.

The project also explored the potential of additive manufacturing to create more comfortable and engaging AFOs for children. This approach sought to mitigate non-compliance caused by discomfort and unappealing designs, while advancing functionality and esthetic appeal. Our methodology encompassed concept development, prototyping, testing, and iterative refinement. Beyond meeting functional requirements, these solutions must also address esthetic and psychological factors to enhance the overall user experience.

Future studies should expand on these findings by exploring advanced manufacturing methods, such as additive manufacturing, and integrating emerging technologies, such as smart materials, to further personalize and optimize AFO performance. By fostering both theoretical and practical advancements in AFO design, we hope to contribute to a significant change in rehabilitation technology that prioritizes user satisfaction and clinical effectiveness.

Supplementary Materials: The following supporting information can be downloaded at: <https://www.mdpi.com/article/10.3390/prosthesis7010011/s1>, Figure S1: Nylon PA2200 Material Data Sheet., Figure S2: High-Density Polyethylene material data sheet.

Author Contributions: Methodology, P.D.; validation, P.D.; formal analysis, T.Y.P.; writing—original draft preparation, T.Y.P.; writing—review and editing, P.D.; project administration, P.D.; All authors have read and agreed to the published version of the manuscript.

Funding: This research received no external funding.

Institutional Review Board Statement: Ethical review and approval were waived for this study, due to the study being conducted solely within the research team and not involving external participants. As such, ethics approval is not required. All team members have been fully informed of the study's purpose, scope, and the nature of the activities involved. No identities were disclosed and no records have been kept.

Informed Consent Statement: Informed consent was obtained from all subjects involved in the study.

Data Availability Statement: All data generated or analyzed during this study are included in this published article.

Acknowledgments: The authors acknowledge the contributions of Ethan Hayess, Reece Pellow, and Isabella Ashby to the project.

Conflicts of Interest: The authors declare no conflicts of interest.

References

1. Gomes, H.R.C.; De Sampaio, C.P.; Fabris, S.; Vicentin, J. *Development of Ankle-Foot Type Pediatric Orthosis by Using 3D Printing*; Federal University of Santa Catarina: Florianópolis, Brazil, 2023; pp. 94–106. [CrossRef]
2. Kariuki, L.W.; Ikua, B.W.; Karanja, S.K.; Ng'Ang'A, S.P. A Digital and Additive Manufacturing Approach for the Fabrication of Custom Orthoses. In Proceedings of the 2023 IEEE AFRICON, Nairobi, Kenya, 20–22 September 2023; pp. 1–4. Available online: https://journals.scholarsportal.info/details/21530033/v2023inone/1_adaamaftfoco.xml (accessed on 14 January 2025).
3. Peng, C.; Tran, P.; Lator, S.; Tirosh, O.; Rutz, E. Tuning the mechanical responses of 3D-printed ankle-foot orthoses: A numerical study. *Int. J. Bioprinting* **2024**, *10*, 3390. [CrossRef]
4. Yeh, C.-H.; Lin, K.-R.; Su, F.-C.; Hsu, H.-Y.; Kuo, L.-C.; Lin, C.-C. Optimizing 3D printed ankle-foot orthoses for patients with stroke: Importance of effective elastic modulus and finite element simulation. *Heliyon* **2024**, *10*, e26926. [CrossRef]
5. Mohammadi, V.; Tajdani, M.; Masaei, M.; Ghalehney, S.M.; Lee, S.C.K.; Behboodi, A. DE-AFO: A Robotic Ankle Foot Orthosis for Children with Cerebral Palsy Powered by Dielectric Elastomer Artificial Muscle. *Sensors* **2024**, *24*, 3787. [CrossRef]
6. Bertini, A.; Manganelli, F.; Fabrizi, G.M.; Schenone, A.; Santoro, L.; Cavallaro, T.; Tagliapietra, M.; Grandis, M.; Previtali, S.C.; Falzone, Y.M.; et al. Use, tolerability, benefits and side effects of orthotic devices in Charcot-Marie-Tooth disease. *J. Neurol. Neurosurg. Psychiatry* **2023**, *95*, 434–441. [CrossRef] [PubMed]

7. Myers, S.; Dinkel, D.; Hassan, M.; Despiegelaere, H.; Johanning, J.; Pipinos, I. Examining Ankle Foot Orthosis Wear Time in Patients with Peripheral Artery Disease. *Innov. Aging* **2020**, *4*, 211. [CrossRef]
8. Swinnen, E.; Kerckhofs, E. Compliance of patients wearing an orthotic device or orthopedic shoes: A systematic review. *J. Bodyw. Mov. Ther.* **2015**, *19*, 759–770. [CrossRef]
9. Holtkamp, F.C.; Wouters, E.J.M.; van Hoof, J.; van Zaalen, Y.; Verkerk, M. Use of and Satisfaction with Ankle Foot Orthoses. *Clin. Res. Foot Ankle* **2015**, *3*, 167. [CrossRef]
10. Bashir, A.Z.; Dinkel, D.M.; Pipinos, I.I.; Johanning, J.M.; Myers, S.A. Patient Compliance with Wearing Lower Limb Assistive Devices: A Scoping Review. *J. Manip. Physiol. Ther.* **2022**, *45*, 114–126. [CrossRef]
11. Baghbanbashi, A.; Farahmand, B.; Azadinia, F.; Jalali, M. Evaluation of User's Satisfaction with Orthotic and Prosthetic Devices and Services in Orthotics and Prosthetics Center of Iran University of Medical Sciences. *Can. Prosthet. Orthot. J.* **2022**, *5*, 37981. [CrossRef] [PubMed]
12. Faux-Nightingale, A.; Kelemen, M.; Stewart, C. Ankle-foot orthosis adherence in children and adolescents with cerebral palsy: A scoping review. *Prosthet. Orthot. Int.* **2022**, *46*, 351–356. [CrossRef]
13. Gray, M.M.; Bradnock, G.; Gray, H.L. An Analysis of the Qualitative Factors which Influence. *Prim. Dent. Care* **2000**, *7*, 157–161. [CrossRef] [PubMed]
14. Okçu, M.; Tuncay, F.; Koçak, F.A.; Doğru, Y.G.; Güngör, Z.K.; Kaya, S.S. Factors Affecting Compliance with Lower and Upper Extremity Orthoses in Patients with Disability Due to Neurological Diseases. *J. Phys. Med. Rehabil. Sci.* **2022**, *25*, 240–247. [CrossRef]
15. Zhou, C.; Yang, Z.; Li, K.; Ye, X. Research and Development of Ankle-Foot Orthoses: A Review. *Sensors* **2022**, *22*, 6596. [CrossRef] [PubMed]
16. Lahoud, D.; Teng, C.H.; Nusem, E.; Burns, J.; Wrigley, C.; Cheng, T.L. Content analysis of child user and carer perspectives of ankle-foot orthoses. *Prosthet. Orthot. Int.* **2020**, *45*, 12–19. [CrossRef] [PubMed]
17. Li, W.; Baddour, N.; Lemaire, E. A Novel Quick Release Mechanism for Ankle Foot Orthosis Struts. *Can. Prosthet. Orthot. J.* **2022**, *5*, 38802. [CrossRef] [PubMed]
18. Russell Esposito, E. Chapter 41-Ankle-Foot Orthoses and Rocker Bottom Shoes. In *Foot and Ankle Biomechanics*; Ledoux, W.R., Telfer, S., Eds.; Academic Press: Cambridge, MA, USA, 2023; pp. 647–659.
19. Mohaddis, M.; Maqsood, S.A.; Ago, E.; Singh, S.; Naim, Z.; Prasad, S. Enhancing Functional Rehabilitation Through Orthotic Interventions for Foot and Ankle Conditions: A Narrative Review. *Cureus* **2023**, *15*, e49103. [CrossRef]
20. Ghoseiri, K.; Bahramian, H. User satisfaction with orthotic and prosthetic devices and services of a single clinic. *Disabil. Rehabil.* **2011**, *34*, 1328–1332. [CrossRef]
21. Civil, D.A. Design and Development of a Soft Pediatric Support Garment for Ankle-Foot Orthoses Wearers. Master's Thesis, University of Delaware, Newark, DE, USA, 2019.
22. Smitham, P.; Molvik, H.; Smith, K.; Attard, J.; Cullen, N.; Singh, D.; Goldberg, A. A review of orthotic design, patient compliance and satisfaction in an NHS outpatient service. *Orthop. Proc.* **2012**, *94*, 78.
23. Rogati, G.; Caravaggi, P.; Leardini, A. Design principles, manufacturing and evaluation techniques of custom dynamic ankle-foot orthoses: A review study. *J. Foot Ankle Res.* **2022**, *15*, 38. [CrossRef] [PubMed]
24. Banga, H.K.; Kalra, P.; Belokar, R.M.; Kumar, R. Customized design and additive manufacturing of kids' ankle foot orthosis. *Rapid Prototyp. J.* **2020**, *26*, 1677–1685. [CrossRef]
25. Walbran, M.; Turner, K.; McDaid, A. Customized 3D printed ankle-foot orthosis with adaptable carbon fibre composite spring joint. *Cogent Eng.* **2016**, *3*, 1227022. [CrossRef]
26. Banga, H.K.; Kumar, P.; Kumar, H. Utilization of Additive Manufacturing in Orthotics and Prosthetic Devices Development. *IOP Conf. Series Mater. Sci. Eng.* **2021**, *1033*, 012083. [CrossRef]
27. Chen, R.K.; Jin, Y.-A.; Wensman, J.; Shih, A. Additive manufacturing of custom orthoses and prostheses—A review. *Addit. Manuf.* **2016**, *12*, 77–89. [CrossRef]
28. Silva, R.; Morouço, P.; Lains, J.; Amorim, P.; Alves, N.; Veloso, A. Innovative Design and Development of Personalized Ankle-Foot Orthoses for Stroke Survivors with Equinovarus Foot: Protocol for a Feasibility and Comparative Trial. *JMIR Res. Protoc.* **2023**, *13*, e52365. [CrossRef] [PubMed]
29. Griffin, L.; Sokolowski, S.; Lee, H.; Seifert, E. Methods and Tools for 3D Measurement of Hands and Feet. In *Proceedings of the Advances in Interdisciplinary Practice in Industrial Design*, Orlando, FL, USA, 21–27 July 2018; Springer: Cham, Germany, 2019; pp. 49–58.
30. Bayón, C. Moving forward: The importance of tailored orthotic management in children with cerebral palsy. *Dev. Med. Child Neurol.* **2023**, *66*, 8–9. [CrossRef]
31. Dinkel, D.; Hassan, M.; Rech, J.P.; De Spiegelaere, H.; Johanning, J.; Pipinos, I.; Myers, S. Assessing wear time and perceptions of wearing an ankle foot orthosis in patients with peripheral artery disease. *PM&R* **2022**, *15*, 493–500. [CrossRef]
32. Dabnichki, P. Biomechanical testing and sport equipment design. *Sports Eng.* **1999**, *1*, 93–105. [CrossRef]

33. Hu, C.-W.; Dabnichki, P.; Baca, A.; Nguyen, C.T.; Pang, T.Y. Preventive strategy of flatfoot deformity using fully automated procedure. *Med. Eng. Phys.* **2021**, *95*, 15–24. [CrossRef] [PubMed]
34. Hu, C.-W.; Nguyen, C.T.; Hölbling, D.; Pang, T.Y.; Baca, A.; Dabnichki, P. A novel 3D printed personalised insole for improvement of flat foot arch compression and recoil—preliminary study. *Proc. Inst. Mech. Eng. Part L J. Mater. Des. Appl.* **2022**, *237*, 329–342. [CrossRef]
35. Jensen, J.S.; Treichl, H.B. Mechanical testing of prosthetic feet utilized in low-income countries according to ISO-10328 standard. *Prosthet. Orthot. Int.* **2007**, *31*, 177–206. [CrossRef] [PubMed]
36. Xia, H.; Kwon, J.; Pathak, P.; Ahn, J. Design of A Multi-Functional Soft Ankle Exoskeleton for Foot-Drop Prevention, Propulsion Assistance, and Inversion/Eversion Stabilization. In Proceedings of the 2020 8th IEEE RAS/EMBS International Conference for Biomedical Robotics and Biomechatronics (BioRob), New York, NY, USA, 29 November–1 December 2020; pp. 118–123. [CrossRef]
37. Patel, P.; Gohil, P. Custom orthotics development process based on additive manufacturing. *Mater. Today Proc.* **2022**, *59*, A52–A63. [CrossRef]
38. Isman, R.E.; Inman, V.T. *Anthropometric Studies of the Human Foot and Ankle*; Bulletin of Prosthetics Research. 1969. Available online: <https://www.rehab.research.va.gov/jour/69/6/1/97.pdf> (accessed on 14 January 2025).
39. O'Meara, D.; Vanwanseele, B.; Hunt, A.; Smith, R. The reliability and validity of a three-camera foot image system for obtaining foot anthropometrics. *J. Appl. Biomech.* **2010**, *26*, 349–356. [CrossRef] [PubMed]

Disclaimer/Publisher's Note: The statements, opinions and data contained in all publications are solely those of the individual author(s) and contributor(s) and not of MDPI and/or the editor(s). MDPI and/or the editor(s) disclaim responsibility for any injury to people or property resulting from any ideas, methods, instructions or products referred to in the content.

Article

Friction Optimization of Talc Powder-Reinforced Elastomers for Prosthetic Foot Application

Muhammad Khafidh ^{1,*}, Donny Suryawan ¹, Lilis Kistriyani ², Muhammad Naufal ¹ and Rifky Ismail ^{3,4}

¹ Department of Mechanical Engineering, Universitas Islam Indonesia, Sleman, Yogyakarta 55584, Indonesia

² Department of Chemical Engineering, Universitas Islam Indonesia, Sleman, Yogyakarta 55584, Indonesia

³ Department of Mechanical Engineering, Universitas Diponegoro, Semarang 50275, Indonesia

⁴ Center for Biomechanics, Biomaterials, Biomechatronics, and Biosignal Processing (CBIOM3S), Universitas Diponegoro, Semarang 50275, Indonesia

* Correspondence: khafidh@uii.ac.id

Abstract: Patients with lower limb amputation usually use prosthetic feet. Elastomeric material is an important part of prosthetic feet since it can determine their safety and lifetime. The elastomeric material should have high friction for safety, and at the same time it should have low wear for a longer lifetime. This research is aimed to study the optimum formulation of talc-powder-reinforced silicone elastomer to obtain high friction during sliding contact. The Taguchi orthogonal array L9 formula is used to achieve the aforementioned goal. The experiments use multiple parameters, namely, the type of silicone, the type of surface texture, the amount of catalyst, and the amount of talc powder. The results show that the combination of RTV 683, a smooth texture, 4% of catalyst, and 60% of talc powder is the most optimum composition to obtain the highest frictional force. It has a higher friction force in comparison with the imported products, and, at the same time, it has comparable wear with the imported products. The hardness of the optimized materials is comparable with the imported products. However, the tensile and tear strengths of the optimized materials need to be improved.

Keywords: silicone elastomer; Taguchi method; prosthetic feet; friction

Citation: Khafidh, M.; Suryawan, D.; Kistriyani, L.; Naufal, M.; Ismail, R. Friction Optimization of Talc Powder-Reinforced Elastomers for Prosthetic Foot Application. *Prosthesis* **2023**, *5*, 88–99. <https://doi.org/10.3390/prosthesis5010007>

Academic Editors: Arnab Chanda and Marco Cicciù

Received: 25 October 2022

Revised: 28 December 2022

Accepted: 9 January 2023

Published: 12 January 2023



Copyright: © 2023 by the authors. Licensee MDPI, Basel, Switzerland. This article is an open access article distributed under the terms and conditions of the Creative Commons Attribution (CC BY) license (<https://creativecommons.org/licenses/by/4.0/>).

1. Introduction

Major amputations are suffered by almost 38 million people worldwide, out of which 85% of people are lower-limb amputated [1]. In Indonesia, more than 8.5% of the population suffered from disabilities, which increased by approximately 2.45% from 2012. People with lower limb amputations will have difficulty walking [2] and reduce mobility [3]. The popular solution for patients with lower limb amputation is lower limb prostheses. The main parts of lower limb prostheses are a socket, shank (also known as phylon), and a prosthetic feet. The prosthetic foot is one of the most important parts since it can determine the lifetime of the product.

Different types of prosthetic feet have been developed in past few decades, such as the solid ankle cushion heel (SACH) prosthetic foot, the single-axis-design prosthetic foot, the multiple-axis (multiaxial)-design prosthetic foot, and the microprocessor foot. SACH is a popular type that is used in Indonesia and other developing countries because it offers a lower price than other types of prosthetic feet. The SACH is also simpler than other prosthetic feet due to the absence of mechanical articulation [4]. The local product of SACH that is available on the Indonesian market can be seen in Figure 1.

The prosthetic foot is a crucial part in determining the lifetime of the lower limb prosthesis. The prosthetic foot will have a longer life if the foot materials have high wear resistance. On the other hand, the prosthetic foot should have high friction to avoid slips. Therefore, material selection of the prosthetic foot is of importance. Elastomeric materials are widely used in prosthetic feet because they can fulfill the requirements [5]. Several types of elastomeric materials have been studied to be used in prosthetic feet, such as natural

rubber [6], ethyl-vinyl-acetate [7], polyurethane [8], silicone [9], and the combination of polyurethane and neoprene [10].



Figure 1. Local product of SACH in Indonesia market.

Silicone elastomers were used in several medical devices due to their advantageous properties, such as being soft and flexible, highly chemically resistant, and having good biocompatibility [11,12]. Some examples of those elastomeric materials are PDMS and ecoflex [13]. The medical devices that are made of silicone are maxillofacial prosthetic material [7], implant to medialization laryngoplasty [14], finger joints [15], breast implants [16], and catheters [17]. However, in some applications, silicone elastomers cannot fulfill all of the requirements due to their low tensile and tear strengths. Therefore, several studies were conducted to improve the mechanical properties of silicone materials, such as by adding fillers to the silicone [18,19].

The study of prosthetic feet was conducted in several aspects, such as structure [20], cyclic foot (fatigue) [6], and dorsiflexion [21]. While the elastomeric materials of the foot were studied in the aspect of mechanical properties, such as tensile strength, tear strength, and hardness [21]. Although several aspects of prosthetic feet have been studied, the study of the tribological aspects, such as friction and wear, of the elastomeric materials is still limited in the literature. The study of the tribological aspects of prosthetic feet is important due to their influence on the lifetime and safety of the products.

In the present study, an elastomeric material based on silicone elastomer reinforced by talc powder was investigated in the tribological aspect. The Taguchi method was used to find an optimum parameter for tribological characteristics. The Taguchi method is very effective and efficient for an experiment that uses many variables. It can reduce the number of samples and the test. So, it saves time and cost. Many researchers use the Taguchi method to find the optimum parameter value or composition [22–24]. The Taguchi method uses several basic formulas to calculate the optimum result. The formula is called the S/N ratio (signal to noise ratio). There are three characteristics of the S/N ratio. There are normal-is-better, larger-is-better, and smaller-is-better. The normal-is-better is used when a specified value is most desired. Equation (1) shows the S/N ratio formula for normal-is-better. The larger-is-better and the smaller-is-better equation are used when the largest or smallest value is the most desired. Equations (2) and (3) show the S/N ratio formula for larger-is-better and smaller-is-better, respectively.

$$SN_t = 10 \log \left(\frac{y^2}{s^2} \right) \quad (1)$$

$$SN_L = -10 \log \left(\frac{1}{n} \sum_{i=1}^n \frac{1}{y_i^2} \right) \quad (2)$$

$$SN_s = -10 \log \left(\frac{1}{n} \sum_{i=1}^n y_i^2 \right) \quad (3)$$

where n is the number of replicas and y is the test result. In the present study, the main material characteristic to be achieved is high friction. Four parameters were varied to achieve the goal. Moreover, the wear mass and mechanical properties of the silicone were investigated.

2. Materials and Methods

The present study uses four independent variables: the type of silicone elastomer, the surface texture, the percentage of catalyst, and the percentage of talc powder. The type of silicone elastomer and the amount of catalyst will significantly influence the mechanical and tribological properties of the elastomer. Therefore, the selection of silicone and the percentage of the catalyst are important. The talc powders were added to the silicone elastomer to improve the mechanical and tribological properties of the silicone elastomer. While the surface textures were varied to obtain high friction. Each variable is varied by three levels, as shown in Table 1. The number of the test run is derived from the variables and the levels following the Taguchi orthogonal array L9 formula. The details of the test run can be seen in Table 2. The materials were made based on the composition shown in Table 2. Three tests were conducted for each run number to check the repeatability.

Table 1. The control factors and their levels.

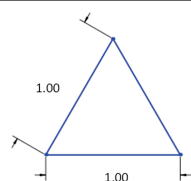
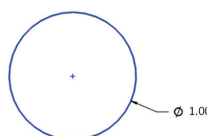
Control Factors		Levels		
		1	2	3
A	Silicone type	RTV 683	RTV M4503	RTV 48
B	Texture	Smooth	Triangle	Circle
C	Catalyst	2%	3%	4%
D	Talc	60%	80%	100%

Table 2. The composition of the run number based on Taguchi orthogonal array L9.

Run Number	Control Factor			
	Silicone Type	Texture	Catalyst	Talc
1	RTV 683	Smooth	2%	60%
2	RTV 683	Triangle	3%	80%
3	RTV 683	Circle	4%	100%
4	RTV 48	Smooth	3%	100%
5	RTV 48	Triangle	4%	60%
6	RTV 48	Circle	2%	80%
7	M4503	Smooth	4%	80%
8	M4503	Triangle	2%	100%
9	M4503	Circle	3%	60%

The textured surface of the testing sample consists of three types. The first one is a smooth surface, a flat surface without texture. The other two are an equilateral triangle and a circle. The geometric shape and size of the triangle and circle are shown in Table 3.

Table 3. The textured geometry.

Texture	Geometry
Triangle	
Circle	

A pin-on-disc tribometer is used to investigate the tribological characteristics of the materials. The sliding contact occurs between a silicone pin and a smooth tile. The silicone pin was manufactured with three different textures at the end of the tip. The arithmetic roughness of the tile is $0.045\ \mu\text{m}$. The pin and the disc used in this study are shown in Figure 2. The load of 7 N was used in the sliding contact experiments; it is based on the force distribution of the $54\ \text{cm}^2$ cross-section foot during mid-foot loading [25]. The angular speed of the disc is 20 rpm, and the radius of the wear track is 20 mm, resulting in a linear speed of 42 mm/s. The tests were conducted at ambient temperature. The tribometer tests were stopped once the sliding distance reached 200 m (~80 min). The tensile, tear, and hardness tests of the silicone elastomers were conducted by following the ISO 37:2015, ISO 34-1: 2015, and ISO 7619-1: 2010, respectively.

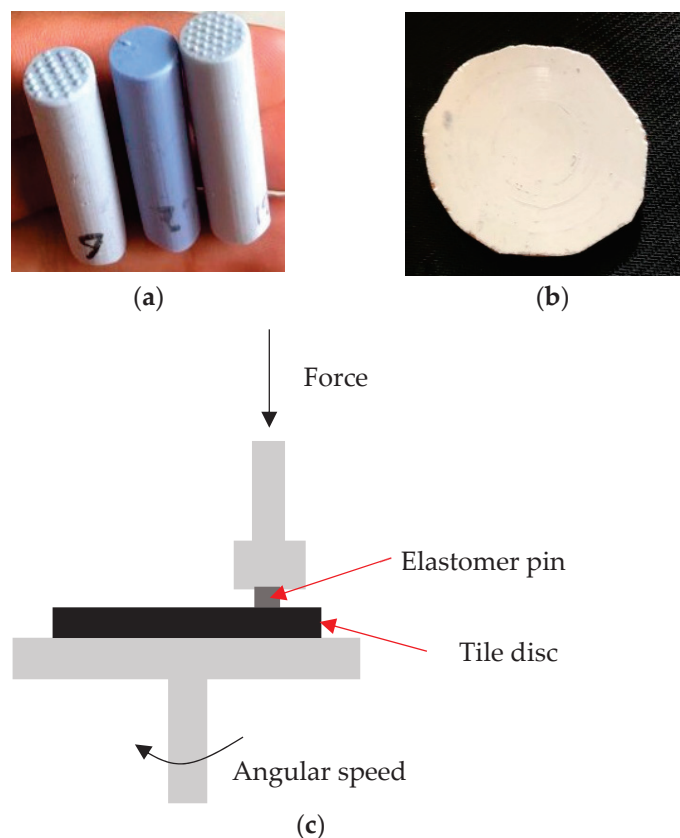


Figure 2. The contacting materials (a) several silicone pins with various textures, (b) the tile disc, and (c) pin-on-disc tribometer, schematically.

3. Results and Discussions

Figure 3 shows the result of the tribometer test. It can be seen that at a certain sliding distance, the friction force reaches a constant value. In the present study, the value of the friction force is determined when the friction force reaches a steady-state phase.

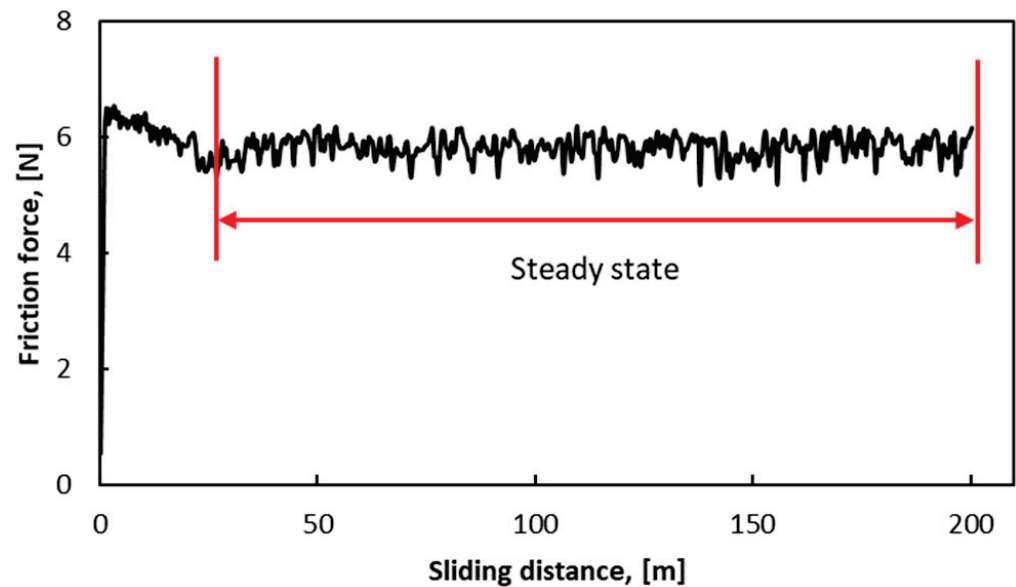


Figure 3. Friction force as a function of sliding friction, the red line shows a steady state phase.

Table 4 shows the result of the sliding friction test for each run number. The friction force is determined when the signal reaches a steady state phase. The experiment was repeated three times for each run number. The result of frictional force was used to calculate the S/N ratio. The S/N ratio was calculated by using the larger is better equation (Equation (2)) since the purpose of the optimization is to have a higher friction force. The higher the friction force, the safer the prosthetic feet. The average S/N ratio for all run numbers is 13.92; see Table 4.

Table 4. The frictional force and S/N calculation.

Run Number	Frictional Force (N)				Calculation	
	1	2	3	Mean	Variance	S/N Larger Better
1	5.41	6.20	6.06	5.89	0.18	15.36
2	4.70	4.99	5.03	4.91	0.03	13.80
3	5.16	6.31	5.24	5.57	0.41	14.81
4	5.56	5.78	5.83	5.72	0.02	15.15
5	5.79	5.41	6.74	5.98	0.47	15.42
6	3.92	3.95	3.46	3.78	0.07	11.49
7	5.75	4.71	5.30	5.25	0.27	14.32
8	4.53	3.91	4.43	4.29	0.11	12.60
9	4.24	3.95	4.27	4.15	0.03	12.35
Average of S/N						13.92

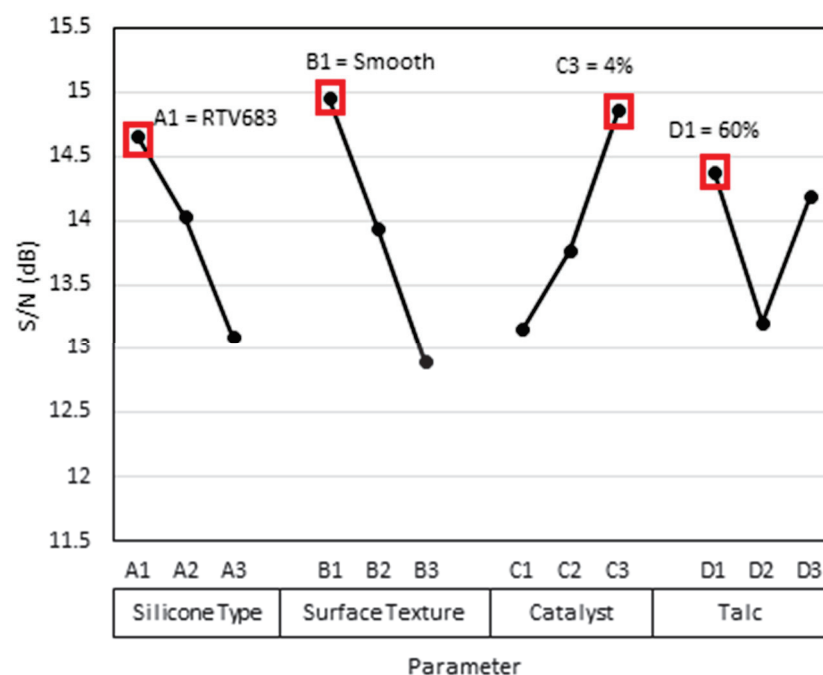
After calculating the S/N ratio, the results are grouped by the parameters and their levels. Where A is the type of silicone, B is the surface texture, C is the percentage of catalyst, and D is the percentage of talc powder. The number label is the level of each parameter. For example, the code A1 means RTV683, A2 means RTV M4503, and so on. Table 5 shows the grouping result of the S/N ratio and the mean of the frictional force.

Table 5. The average S/N ratio for the frictional force.

	S/N Ratio	Mean [N]
A1	14.66	5.46
A2	14.02	5.16
A3	13.09	4.56
B1	14.94	5.62
B2	13.94	5.06
B3	12.89	4.50
C1	13.15	4.65
C2	13.77	4.93
C3	14.85	5.60
D1	14.38	5.34
D2	13.20	4.64
D3	14.19	5.20

Figure 4 shows the plotting results of Table 5. The combination of the highest value of each control factor is a prediction of the optimum composition. Therefore, combining the RTV 683, a smooth texture, 4% of catalyst, and 60% of talc powder may achieve the highest friction force. Generally, the friction force of the contacting materials depends on adhesive friction and hysteresis friction [26]. In the previous research, the friction of elastomeric materials is significantly influenced by the adhesive component, while the hysteresis component plays a minor role [27]. The smooth texture of the elastomer will result in a larger real contact area between surfaces [28]. For adhesive friction, the larger the real contact area, the higher the friction force. The smallest amount of talc powder (60%) was found to be the best composition to obtain the highest friction force. A small amount of filler, such as talc powder, will result in low mechanical properties. As a result, a larger real contact area will be found on the contacting surface since the elastomer will fill the cavity of the tile roughness. The $\frac{S}{N}$ ratio of the optimum composition was calculated by the following Equation:

$$P_{opt} = \frac{1}{n} \sum_{i=1}^n \left(\frac{S}{N} \right)_k - (n-1) \left(\frac{\bar{S}}{N} \right) \quad (4)$$

**Figure 4.** The $\frac{S}{N}$ ratio graph for frictional force in the smooth tile.

The P_{opt} is the $\frac{S}{N}$ ratio prediction of the optimum composition; $\frac{1}{n} \sum_{i=1}^n \left(\frac{S}{N} \right)_k$ is the mean-of-signal-to-noise ratio for the evaluated process parameters; n is the number of process parameters, which is equal to 4; and $\bar{\frac{S}{N}}$ is the mean of signal-to-noise ratio for all of the process parameters. The calculated P_{opt} in the present study is 17.06, as can be seen in Table 6. The prediction of the friction force value for the optimum composition material can be calculated by the inversion of Equation (2), and the result is 7.07 N.

Table 6. Prediction of optimum $\frac{S}{N}$ ratio.

Parameter	S/N
A1	14.66
B1	14.94
C3	14.85
D1	14.38
P_{opt}	17.06

Since the optimum composition (A1, B1, C3, and D1) is outside of the run number composition (see Table 2), it has to be validated by additional experiments. The samples with the optimum composition were produced and tested. The validation experiment is shown in Table 7. The result shows that the average friction force (6.75 N) is near the prediction results (~7 N). The improvement of the friction force is 33.40% in comparison with the average friction force of all run numbers.

Table 7. The validation results.

Number of Tests	Friction Force (N)
1	6.72
2	6.80
3	6.73
Average	6.75

The results of multifactor optimization show that the combination of RTV 683, a smooth texture, 4% of catalyst, and 60% of talc powder is the most optimum composition to obtain the highest frictional force. This optimized material was compared to the existing products, namely, imported product A and imported product B. The tribometer tests of the imported products were conducted by using the same operating conditions as the optimized material. The comparison of the friction force is shown in Figure 5. It can be seen that the optimized material has a higher friction force compared to the other products. This high friction will improve the safety of the product since it can avoid the slip during the usage of prosthetic feet.

The important parameter for prosthetic foot material is not only high friction but also low wear. The low wear of material will affect the lifetime of the product. The lower the wear, the longer the lifetime. The high friction will be obtained by the weak mechanical properties, but at the same time, it will result in high wear. A similar case was found in the tire product [29]. Achieving both goals is very challenging since they are a contradiction. Therefore, optimization is needed to compromise both goals. The comparison of wear mass between the imported products and the optimized material can be seen in Figure 6. It shows that the imported product B has the lowest wear, while the wear of optimized material is slightly higher than the imported product A. The wear mass of the optimized material is still higher than that of the imported products. However, the value is comparable to the imported product A when the standard deviation is considered. The result of the friction force of imported product A is lower than that of the optimized material, see Figure 5.

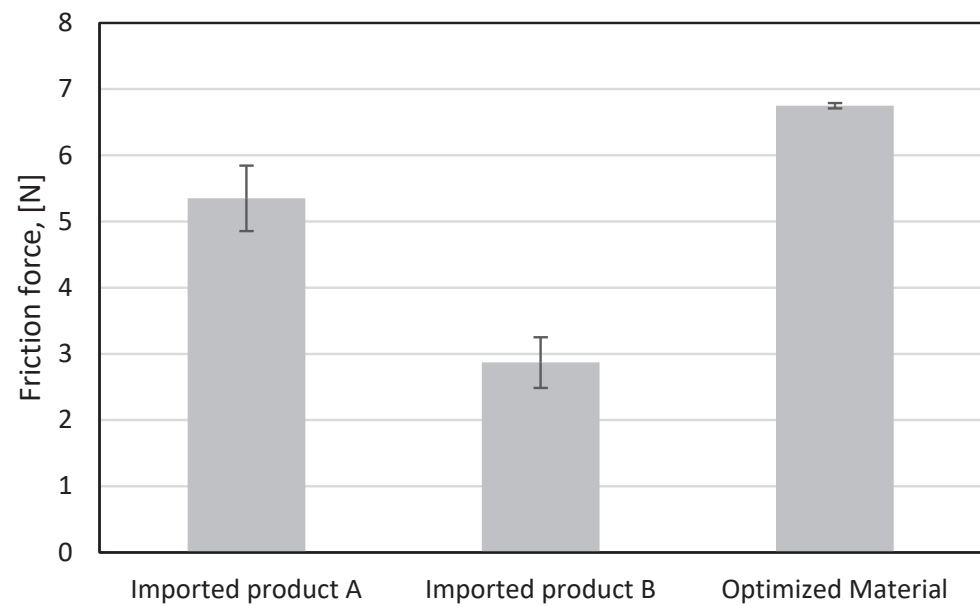


Figure 5. The comparison of friction force between the imported products and the optimized material.

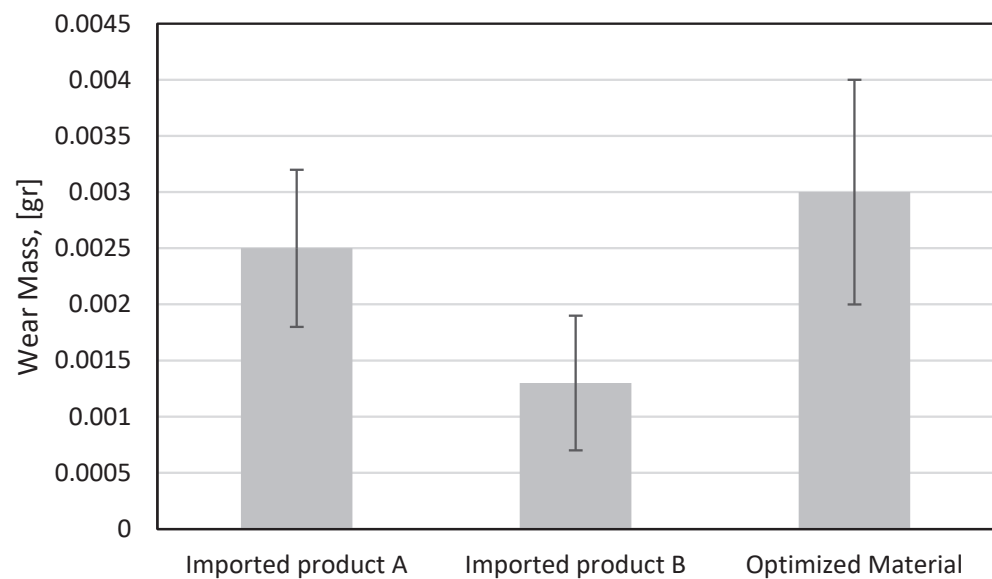


Figure 6. The comparison of wear mass between the imported products and the optimized material.

The pin on the disc tribometer tests shows that the optimum composition has better characteristics for the frictional force, but the wear mass is still worse than the imported products as the benchmark. Furthermore, the mechanical characteristics of the optimized material are still lower than the imported product. Figure 7 shows the comparison of the tensile strength test between the imported products and the optimized material. The tensile strength of the optimized material is only around half that of the imported product A. The reinforcement of talc powder without any coating on the talc surface will result in a weak bond between the talc powder and the silicone elastomers. A previous study indicates that the use of silane coating on the filler will improve those bonds, and as a result, the mechanical properties of the composites will improve [30]. The use of the silane coating on the talc surface will be conducted in a future study.

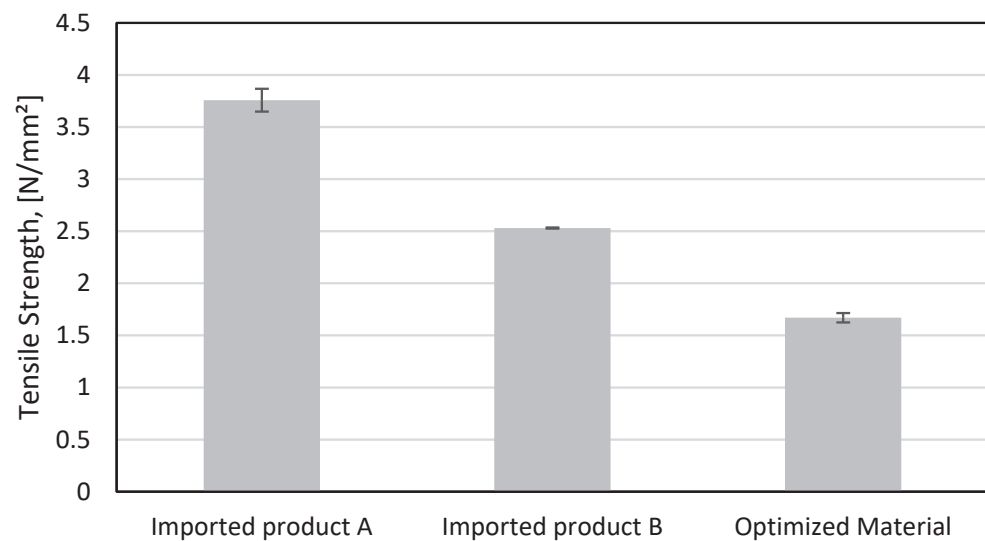


Figure 7. The comparison of tensile strength between the imported products and the optimized material.

Another mechanical characteristic is tear strength. This characteristic is important to avoid tears when a prosthetic foot comes into contact with a sharp material. Figure 8 shows the result of the tear strength of the imported products and the optimized material. It shows that the tear strength of the optimized material is lower than that of the imported products. The tear strength of the optimized material is only approximately a quarter smaller than that of the imported products. For future study, the use of long filler, such as fiber, needs to be investigated to improve the tear strength. Some studies reported that fiber could improve the tear strength of the composites [31,32].

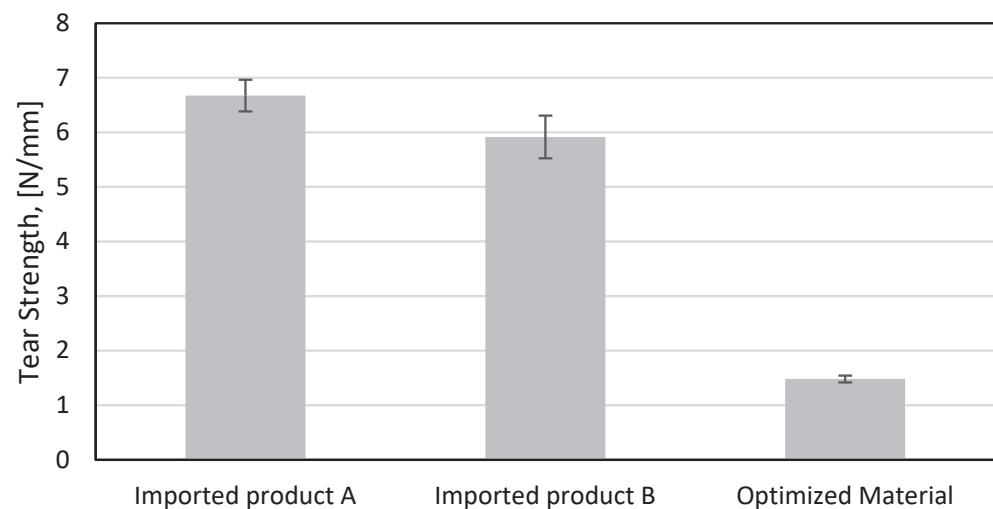


Figure 8. The comparison of tear strength between the imported products and the optimized material.

Figure 9 shows that the optimized material has a similar hardness to the imported product B, but it is lower than the imported product A. Overall, some mechanical characteristics of the optimized material are inferior to the imported products. Therefore, some research needs to be conducted to improve the mechanical properties of the material, and at the same time, the material has high friction and low wear. A coating process on the talc surface and the use of long filler, such as fibers, in the material is an alternative way to achieve the aforementioned goals.

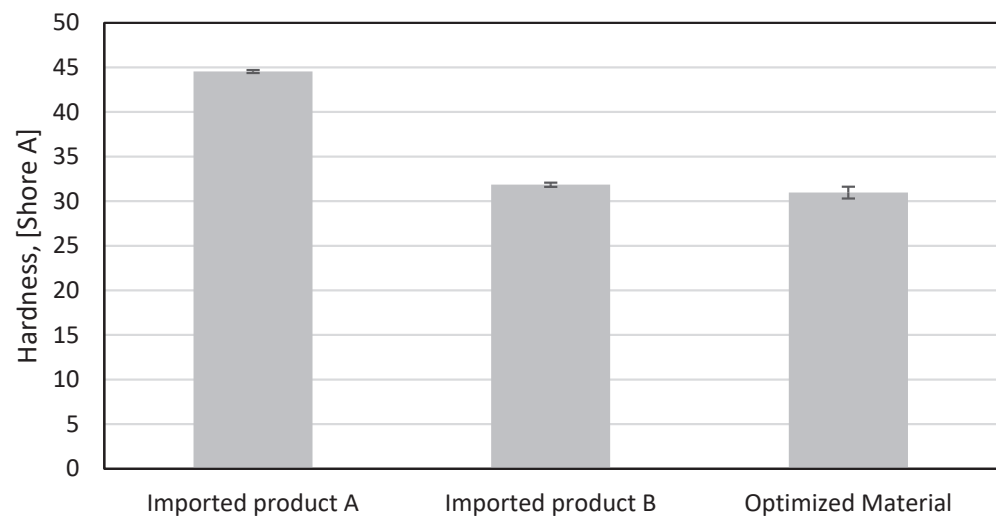


Figure 9. The comparison of hardness between the imported products and the optimized material.

4. Conclusions

In this work, silicone elastomer-reinforced talc powder for prosthetic feet was studied. The main goal of the present study is to obtain an optimum formulation that has high friction force. The Taguchi orthogonal array L9 formula was used to obtain the optimum formulation of silicone elastomer. The key conclusions can be drawn as follows:

- The combination of RTV 683, a smooth texture, 4% of catalyst, and 60% of talc powder is the most optimum composition.
- The friction force of the optimized material is 6.75 N. The improvement of the friction force is 33.40% in comparison with the average friction force of all the run numbers.
- The friction force of the optimized material is higher than the imported products.
- The tensile and tear strengths of the optimized material are lower than the imported products.
- The low tensile and tear strengths can be caused by the weak bond between talc powder and silicone rubber. In future works, a coating of talc powder will be conducted to improve the bond between talc powder and silicone rubber. Moreover, a relatively long filler, such as fibers, will be used to improve the tensile and tear strengths of the composites.

Author Contributions: Conceptualization, M.K., L.K. and D.S.; methodology, M.K.; validation, M.N. and M.K.; investigation, M.N.; data curation, M.N. and D.S.; writing—original draft preparation, D.S. and M.K.; writing—review and editing, M.K. and R.I.; supervision, R.I.; and funding acquisition, M.K. All authors have read and agreed to the published version of the manuscript.

Funding: This research was funded by the Ministry of Education, Culture, Research, and Technology, Republic of Indonesia, grant number 071/E5/PG.02.00.PT/2022.

Institutional Review Board Statement: Not applicable.

Informed Consent Statement: Not applicable.

Data Availability Statement: Not applicable.

Conflicts of Interest: The authors declare no conflict of interest.

References

1. Chauhan, P.; Singh, A.K.; Raghuwanshi, N.K. The state of art review on prosthetic feet and its significance to imitate the biomechanics of human ankle-foot. *Mater. Today Proc.* **2022**, *62*, 6364–6370. [CrossRef]
2. Waters, R.L.; Mulroy, S. The energy expenditure of normal and pathologic gait. *Gait Posture* **1999**, *9*, 207–231. [CrossRef] [PubMed]
3. Stepien, J.M.; Cavenett, S.; Taylor, L.; Crotty, M. Activity Levels Among Lower-Limb Amputees: Self-Report Versus Step Activity Monitor. *Arch. Phys. Med. Rehabil.* **2007**, *88*, 896–900. [CrossRef] [PubMed]
4. Staros, A. The SACH (solid-ankle cushion-heel) foot. *Ortho. Pros. Appl. J.* **1957**, *11*, 23–31.
5. Nishi, T. Rubber wear mechanism discussion based on the relationship between the wear resistance and the tear resistance with consideration of the strain rate effect. *Wear* **2019**, *426–427*, 37–48. [CrossRef]
6. Sasaki, K.; Pinitlertsakun, J.; Rattanakoch, J.; Sukthomya, S.; Guerra, G.; Latt, T.; De Silva, N.; Kanagarandnam, B.; Suntharalingam, S. The development and testing of a modified natural rubber CR solid ankle–cushion heel prosthetic foot for developing countries. *J. Rehabil. Assist. Technol. Eng.* **2017**, *4*, 2055668317712978. [CrossRef]
7. Andreopoulos, A.G.; Evangelatou, M.; Tarantili, P.A. Properties of maxillofacial silicone elastomers reinforced with silica powder. *J. Biomater. Appl.* **1998**, *13*, 66–73. [CrossRef]
8. Jensen, J.S.; Nilsen, R.; Thanh, N.H.; Saldana, A.; Hartz, C. Clinical field testing of polyurethane feet for trans-tibial amputees in tropical low-income countries. *Prosthet. Orthot. Int.* **2006**, *30*, 182–194. [CrossRef]
9. Kulkarni, J.; Curran, B.; Ebdon-Parry, M.; Harrison, D. Total contact silicone partial foot prostheses for partial foot amputations. *Foot* **1995**, *5*, 32–35. [CrossRef]
10. Ramli, W.S.W.; Zin, M.I.I.M.; Desa, M.S.Z.M.; Ramli, A. “Return-To-Work”: Application of New Materials to Develop the Durable and Low Cost of Solid Ankle Cushion Heel (SACH) Prosthetic Foot. In *Human-Centered Technology for a Better Tomorrow*; Springer: Singapore, 2022; pp. 475–483.
11. Zare, M.; Ghomi, E.R.; Venkatraman, P.D.; Ramakrishna, S. Silicone-based biomaterials for biomedical applications: Antimicrobial strategies and 3D printing technologies. *J. Appl. Polym. Sci.* **2021**, *138*, 50969. [CrossRef]
12. Colas, A.; Curtis, J. 7-Silicones. In *Handbook of Polymer Applications in Medicine and Medical Devices*; Modjarrad, K., Ebnesajjad, S., Eds.; William Andrew Publishing: Oxford, UK, 2013; pp. 131–143. [CrossRef]
13. Mariello, M.; Fachechi, L.; Guido, F.; De Vittorio, M. Conformal, Ultra-thin Skin-Contact-Actuated Hybrid Piezo/Triboelectric Wearable Sensor Based on AlN and Parylene-Encapsulated Elastomeric Blend. *Adv. Funct. Mater.* **2021**, *31*, 2101047. [CrossRef]
14. Ustundag, E.; Boyaci, Z.; Keskin, G.; Kaur, A.; Ozkarakas, H. Soft Tissue Response of the Larynx to Silicone, Gore-Tex, and Irradiated Cartilage Implants. *Laryngoscope* **2005**, *115*, 1009–1014. [CrossRef] [PubMed]
15. Swanson, A. Finger joint replacement by silicone rubber implants and the concept of implant fixation by encapsulation. *J. Ann. Rheum. Dis.* **1969**, *28* (Suppl. S5), 47.
16. Herdman, R.; Ernster, V.; Bondurant, S. *Safety of Silicone Breast Implants*; National Academy of Sciences: Washington, DC, USA, 2000.
17. Curtis, J.; Colas, A. Chapter II.5.18—Medical Applications of Silicones. In *Biomaterials Science*, 3rd ed.; Ratner, B.D., Hoffman, A.S., Schoen, F.J., Lemons, J.E., Eds.; Academic Press: Cambridge, MA, USA, 2013; pp. 1106–1116. [CrossRef]
18. He, Q.; Li, A.; Zhang, Y.; Liu, S.; Guo, Y.; Kong, L. A study on mechanical and tribological properties of silicone rubber reinforced with white carbon black. *Tribol.-Mater. Surf. Interfaces* **2018**, *12*, 9–16. [CrossRef]
19. Silva, V.P.; Gonçalves, M.C.; Yoshida, I.V.P. Biogenic silica short fibers as alternative reinforcing fillers of silicone rubbers. *J. Appl. Polym. Sci.* **2006**, *101*, 290–299. [CrossRef]
20. Naseri, A.; Moghaddam, M.M.; Grimmer, M.; Sharbafi, M.A. Passive hydraulic prosthetic foot to improve the push-off during walking. *Mech. Mach. Theory* **2022**, *172*, 104777. [CrossRef]
21. Yousif, L.E.; Resan, K.K.; Fenjan, R.M. Temperature Effect on Mechanical Characteristics of A New Design Prosthetic Foot. *Int. J. Mech. Eng. Technol.* **2018**, *9*, 1431–1447.
22. Mitra, A.C.; Jawarkar, M.; Soni, T.; Kiranchand, G.R. Implementation of Taguchi Method for Robust Suspension Design. *Procedia Eng.* **2016**, *144*, 77–84. [CrossRef]
23. Mohsin, I.; He, K.; Li, Z.; Zhang, F.; Du, R. Optimization of the Polishing Efficiency and Torque by Using Taguchi Method and ANOVA in Robotic Polishing. *Appl. Sci.* **2020**, *10*, 824. [CrossRef]
24. Abd Maleque, M.; Harina, L.; Bello, K.; Azwan, M.; Rahman, M.M. Tribological properties of surface modified Ti-6Al-4V alloy under lubricated condition using Taguchi approach. *J. Tribol.* **2018**, *17*, 15–28.
25. Lidstone, D.E.; DeBerardinis, J.; Dufek, J.S.; Trabia, M.B. Electronic measurement of plantar contact area during walking using an adaptive thresholding method for Medilogic® pressure-measuring insoles. *Foot* **2019**, *39*, 1–10. [CrossRef] [PubMed]
26. Moore, D.F. *The Friction and Lubrication of Elastomers*; Pergamon: Oxford, UK, 1972; Volume 9.
27. Khafidh, M.; Schipper, D.J.; Masen, M.A. The Formation of a Modified Surface Layer on Elastomeric Materials. *Tribol. Lett.* **2019**, *67*, 27. [CrossRef] [PubMed]
28. Mokhtari, M.; Schipper, D.J.; Tolpekina, T.V. On the Friction of Carbon Black- and Silica-Reinforced BR and S-SBR Elastomers. *Tribol. Lett.* **2014**, *54*, 297–308. [CrossRef]
29. Weng, P.; Tang, Z.; Guo, B. Solving “magic triangle” of tread rubber composites with phosphonium-modified petroleum resin. *Polymer* **2020**, *190*, 122244. [CrossRef]
30. Liu, K.; Stadlbauer, W.; Zitzenbacher, G.; Paulik, C.; Burgstaller, C. Effects of surface modification of talc on mechanical properties of polypropylene/talc composites. *AIP Conf. Proc.* **2016**, *1713*, 120008. [CrossRef]

31. Jacob, M.; Thomas, S.; Varughese, K.T. Mechanical properties of sisal/oil palm hybrid fiber reinforced natural rubber composites. *Compos. Sci. Technol.* **2004**, *64*, 955–965. [CrossRef]
32. Kalapakdee, A.; Amornsakchai, T. Mechanical properties of preferentially aligned short pineapple leaf fiber reinforced thermoplastic elastomer: Effects of fiber content and matrix orientation. *Polym. Test.* **2014**, *37*, 36–44. [CrossRef]

Disclaimer/Publisher’s Note: The statements, opinions and data contained in all publications are solely those of the individual author(s) and contributor(s) and not of MDPI and/or the editor(s). MDPI and/or the editor(s) disclaim responsibility for any injury to people or property resulting from any ideas, methods, instructions or products referred to in the content.



Article

Morton's Extension on Hallux Rigidus Pathology

Rubén Sánchez-Gómez ^{1,2,*}, Juan Manuel López-Alcorocho ³, Almudena Núñez-Fernández ¹, María Luz González Fernández ¹, Carlos Martínez-Sebastián ⁴, Ismael Ortuño-Soriano ¹, Ignacio Zaragoza-García ^{1,5} and Álvaro Gómez-Carrión ¹

¹ Faculty of Nursing, Physiotherapy and Podiatry, Universidad Complutense de Madrid, 28040 Madrid, Spain

² Instituto de Investigación Sanitaria Hospital Clínico San Carlos (IdISSC), 28040 Madrid, Spain

³ Research Unit of Clínica CEMTRO, 28035 Madrid, Spain

⁴ Department Nursing and Podiatry, University of Malaga, 29016 Málaga, Spain

⁵ Instituto de Investigación Sanitaria imas12, Grupo Invecuid, 28041 Madrid, Spain

* Correspondence: rusanc02@ucm.es

Abstract: Study design, case-control study: Background, Morton's extension (ME) is a kind of orthotic that has been used as a conservative treatment of painful hallux rigidus (HR) osteoarthritis, but only their effects on first metatarsophalangeal joint (MPJ) mobility and position in healthy subjects have been studied, but not on its applied pulled tension forces neither in subjects with HR. Objectives: This study sought to understand how ME's orthotics with three different thicknesses could influence the kinematic first MPJ by measuring hallux dorsiflexion using Jack's test and a digital algometer with a rigid strip anchored to the iron hook's extremity and comparing subjects with healthy first MPJ mobility to those with HR. We aimed to clarify whether tension values were different between healthy and HR subjects. Methods: Fifty-eight subjects were selected, of whom thirty were included in the case group according to HR criteria and twenty-eight were included in the control group. A digital algometer (FPX[®] 25, Wagner Instruments[®], Greenwich, CT, USA) was used to assess the pulled tension values (kgf) of the first MPJ during Jack's test. Results: The pulled tension values were highly reliable (ICC > 0.963). There were no statistically significant differences between the pulled tension values for the different ME conditions in the case ($p = 0.969$) or control ($p = 0.718$) groups. However, as it's expected, there were statistically significant differences comparing all pulled tension values between case and control group subjects ($p < 0.001$). Conclusions: Different ME's thicknesses had no influence on the pulled effort applied during the dorsiflexion Jack's test between the healthy and HR groups; therefore, it can be prescribed without joint-care danger. In addition, it is proven that there is greater resistance to performing Jack's test in the HR group than in the healthy group, regardless of ME's orthotics. Furthermore, it is shown that the digital algometer device is a valid tool to detect the first MPJ restriction and is more reliable than other tests.

Keywords: algometer; hallux rigidus; metatarsal bones; metatarsophalangeal joint

Citation: Sánchez-Gómez, R.; López-Alcorocho, J.M.; Núñez-Fernández, A.; González Fernández, M.L.; Martínez-Sebastián, C.; Ortuño-Soriano, I.; Zaragoza-García, I.; Gómez-Carrión, Á. Morton's Extension on Hallux Rigidus Pathology. *Prosthesis* **2023**, *5*, 251–263. <https://doi.org/10.3390/prosthesis5010019>

Academic Editor: Arnab Chanda

Received: 19 January 2023

Revised: 10 February 2023

Accepted: 16 February 2023

Published: 21 February 2023



Copyright: © 2023 by the authors. Licensee MDPI, Basel, Switzerland. This article is an open access article distributed under the terms and conditions of the Creative Commons Attribution (CC BY) license (<https://creativecommons.org/licenses/by/4.0/>).

1. Introduction

The limitation of the first metatarsophalangeal joint (MPJ) can be classified as functional hallux limitus or hallux rigidus [1] (HR) depending on the level of this limitation, reaching null movement on the last stage; this one, also called osteoarthritis, is a pathological condition referred to by other authors as hallux flexus [2] or hallux equinus [3] too. HR is the most common presentation with pain of the first MPJ, with an incidence of ~2.5% in people older than 50 years of age [4]. The main symptoms are pain with an active or passive load under manual dorsal and plantar mobilization of the first MPJ or during the heel off-phase of the gait cycle, or pain related to impingement of the medial branch of the superficial peroneal nerve from the dorsal osteophyte, as well as cartilage destruction and restricted joint mobility [5]. HR could disturb the normal gait cycle and thus affect other structures of the body, such as the knee, ankle, lower back, and hip [6]. Understanding gait

as the different phases of the human displacement on the floor, which are divided into the phase of first contact, phase of full contact, phase of propulsion, and phase of push-off [7]. If this pathological status is not addressed, surgery will eventually be required to improve the symptoms and restore mobility [8].

Although most literature reviews have shown that non-surgical interventions cannot stop the degenerative progress of HR in the first MPJ [9], non-surgical management of symptomatic HR has been suggested as an early-stage (0–2) palliative solution [10]. Non-steroidal anti-inflammatory drugs, ultrasound therapy, shoe modifications, hallux strapping, and rigid insoles have been identified as the best options to reduce clinical pain [10–12], with a 60% success rate [13]. These rigid insoles with a modification on the first ray, which was also described as Morton's extension (ME) [6,13], have been used in orthopedics to treat restrictive pathologies like symptomatic HR. MEs are rectangular pieces of semi-rigid material (of varying thicknesses) that are placed under the insoles around the first MPJ. Morton [14] was the first author to argue for first-ray alteration as an etiology of overload disease under the second metatarsal bone, but it was Ebisui [14] and Kelso [15] who detected the relationship between the first-ray dorsiflexed position in the sagittal plane and the first MPJ's restrictive dorsiflexion motion and Dananberg [16] who related its biomechanical consequences.

The Windlass mechanism has been described as a spring system formed by a cable that is attached to a fat plantar pad and calcaneus bone on one end and the proximal phalanx of the hallux base and the first metatarsal head on the other. This cable is the plantar aponeurosis and—under normal conditions—stabilizes the medial arch of the foot during the gait cycle. The Windlass mechanism also rises and shortens the medial arch through the first MPJ's dorsiflexion during the heel-off phase of the gait cycle [17]. When the first MPJ's mobility is restricted by soft tissue structures or bone alterations [18,19], this windlass mechanism is altered, thereby affecting the normal propulsion of the body. One of these bone alterations is metatarsus primus elevatus [20,21], where the first metatarsal bone takes an elevated position in the sagittal plane relative to the second metatarsal bone and to the floor. In this way, simulated restriction of the first MPJ's dorsiflexion with a 4- or 8-mm acrylic platform under the first ray (e.g., a ME) was already demonstrated, using a classical goniometer, in healthy participants [22]. However, it remains unclear if the first MPJ, in a metatarsus primus elevatus position induced by ME, would have the same reducing effects in subjects with the first MPJ restriction pathology (subjects with HR).

Nowadays, mobility assessment of the first MPJ is one of the most common methods to assess the biomechanical function of the foot, although a few more complicated kinematic parameters can also be useful [23]. Given this, Jack's test describes a passive, static, weight-bearing resting position (WRP) to assess the dorsiflexion mobility of the first MPJ, thereby simulating the push-off phase of the gait cycle by executing a simulated Windlass mechanism [17], pulling the hallux in the dorsal direction passively until the movement stops [24,25].

There are a few ingenious studies that assess the mobility [26–28] and the reliability [29,30] of the first MPJ grades of motion on non-WRP in healthy subjects but not with HR pathology or on WRP, a condition consistent with reality [31]. In addition, the pressure needed to reach the motion but not the pull tension necessary to perform the manual Jack test has been assessed, which is the most common maneuver in daily clinical practice. Furthermore, if the clinicians use ME to treat HR, it would be advisable to know the kinematic repercussions on the joint under different ME thicknesses.

On the other hand, it is remarkable to know that a lot of musculoskeletal pathologies do not show any mobility and/or visual restrictions, cause biomechanical forces moments do not always have kinematics behavior but also kinetics effects [32,33] and so that that's why it is hypothesized that tension values can represent better than mobility values what occurs inside the joint.

Therefore, the principal purpose of this research was to know the effects of three different ME insoles on the pulled tension values that were required to perform simulated

dorsiflexion of the first MPJ, executing a validated [34] Jack's test, in subjects with normal and restricted ranges of motion of the first MPJ (i.e., HR). Secondary to this study, we sought to compare the tension values of healthy and HR subjects during Jack's test without any ME insoles. Knowing these force-inside-joint alterations, the ME insoles could be recommended to avoid overload inside the joint.

Due to their regular shape and the fact that healthy first MPJs have shown normal values of dorsiflexion grades during the final phase of the dynamic gait [35] and arthrosis first MPJs with osteoarthritis surfaces damage have shown important limitations of mobility [36], it was thought that the tension values needed to develop the dorsiflexion grades needed to perform the Jack test were greater for HR subjects than healthy participants. Hence, the hypothesis of the present study was that there was a difference in tension values between subjects with HR and healthy subjects in dorsiflexion mobility of the first MPJ during Jack's test with or without any of the ME insoles.

2. Methods

2.1. Study Design

A case-control study was carried out between January 2021 and March 2021, following the Strengthening the Reporting of Observational Studies in Epidemiology (STROBE) requirements [37]. This research was approved by the Institutional Review Board of the Hospital Universitario Nuestra Señora de Valme affiliated with the authors in October 2020, ref number f7f4a6567676d7ba7163bce0d15e7f98c9f33355; the digital algometer used in the present research is non-dangerous and non-invasive. All legal permissions were obtained. All the participants had informed consent and data protection act forms to be signed by them if they were in agreement with the study. The standards of the Helsinki Declaration regarding human experimentation were respected; the experiments were performed in accordance with relevant guidelines and regulations or adhered' to the "Declaration of Helsinki 1964".

2.2. Participants

The research case group associated with HR consisted of participants, men and women, between 35 and 45 years old, who met the following inclusion criteria: (1) restricted first MPJ-assisted dorsal mobility, according to a validated active range of motion with the subject in a non-weight-bearing test, below 10 degrees of dorsal flexion to consider hallux rigidus [1]; (2) restricted non-weight-bearing-assisted plantarflexion of the first MPJ under 35° [38]; (3) pain during active and passive plantarflexion and dorsiflexion of the first MPJ [39]; (4) no trauma or injury in the lower limbs and feet for 1 year ago; (5) normal range of motion in the subtalar joint (30°), midtarsal joint (15° along the longitudinal axis), and ankle joint (at least 20° of dorsiflexion with the knee fully extended) [19] according to classical maneuvers [19] and (6) age between 30 and 60 years old. Subjects were excluded if they were under the effects of any drugs or had any hypermobility condition (e.g., ligamentous hyperlaxity). The control group consisted of healthy, age-matched subjects with a neutral foot posture index (between 0 and +5 points) according to validated tool criteria [40].

2.3. Measurement Procedures, Instruments, and Variables

To set the first metatarsal bone in the dorsiflexion position, flat insoles were selected in 30° shore-A material with ME thicknesses of 2, 4, and 8 mm [22] and made (Termofeet SL, Madrid, Spain) in 45° shore-A hardness of ethylene-vinyl acetate (EVA) (Figure 1), adjusted to the size of the subject's feet, and incorporated randomly into the right foot for each measurement and for each subject. The ME was a rectangular piece of EVA that was also placed inside the insoles under the area of the first MPJ. The proximal edge of the piece was located in the anatomical neck of the first metatarsal bone, and the distal edge was located in the middle of the proximal phalanx of the hallux. Three measurements were

made for each condition to determine consistency. To avoid any imbalance, the same flat insole in the contralateral foot was placed.



Figure 1. Flat insoles with Morton's extension of 2, 4, and 8 mm.

To assess the effects of the three ME thicknesses on the first MPJ, a digital algometer tested previously [41] (FPX[®] 25, Wagner Instruments[®], Greenwich, CT, USA) with a rigid strip anchored to the iron hook's extremity was used. This device had a 10×0.01 kgf (kilogram-force) capacity/graduation and an accuracy of 0.3% of the full scale. Previous studies have reported good reliability and validity for this device (intra-rater reliability: 0.895, 95% CI = 0.846–0.928; SEM = 2.36; MDC = 6.55) [42]. In the static WRP, the proximal phalanx of the hallux was pulled to its maximal dorsal position until the foot showed supination movement, which was evaluated through the Helbing sign axis [19,43] as the change in the Helbing lines, drawn before, verifying the supination movement of the rearfoot with a digital goniometer Preciva[®] (Winkelmesser, Munich, Germany), during the performance of the hallux traction. This technique was developed by an experienced clinician (RS-G), transmitting the tension needed to perform Jack's test [25] through the rigid strip anchored to the algometer (Figure 2). To avoid bias, the verticality of the thrust was maintained to avoid the change in direction of the dorsal vector and always at the same height. The order between the WRP and ME's placing and between ME's thickness conditions was simple and randomized (Figure 3).



Figure 2. Digital algometer pulling hallux with Morton's extension flat insole.

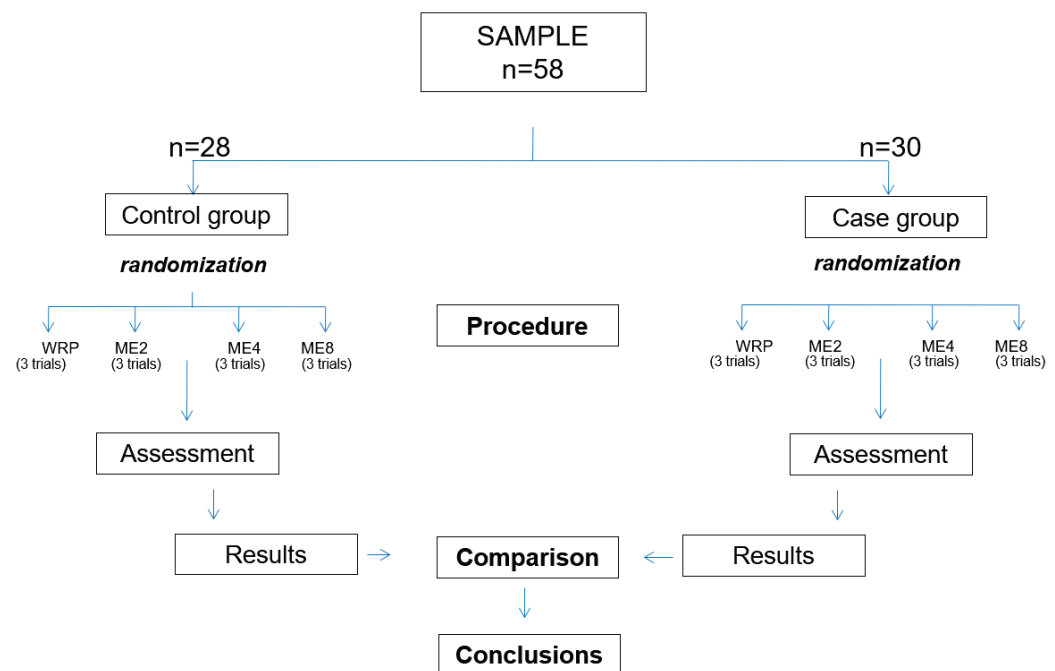


Figure 3. Work chart of the procedure. Abbreviations: CASES GROUP = participants with hallux rigidus; CONTROL GROUP = healthy participants, without hallux rigidus; ME = Morton’s extension insoles; WRP = weight-bearing resting position (without insoles).

2.4. Sample Size

The sample size was calculated using software from the Epidemiology Unit of Biostatistics (www.fisterra.com, accessed on 20 May 2021) to detect differences in the kgf applied to the first MPJ during Jack’s test between the case and control groups and between the different MEs. Previous measures in healthy subjects have shown that the mean strength with the 8 mm insole was 3.2 ± 0.7 kgf (mean \pm SD) (personal observations). In another similar study, ten healthy subjects were recruited [22]. According to these data, we needed to include at least 46 subjects (23 in the control group and 23 in the case group) to detect a difference in the mean strength of 0.7 kgf using Student’s t-test for independent samples with 80% power, in a bilateral contrast, and $\alpha = 0.05$. Considering that some subjects could be lost to follow-up, we established a final sample of 60 subjects (30 per group).

2.5. Statistical Methods

To validate the reliability across the measurement trials, the 25 intra-class correlation coefficients (ICCs) were evaluated according to the specifications of Landis and Koch: coefficients less than 0.20 represent a slight agreement; between 0.20 and 0.40, fair reliability; between 0.41 and 0.60, moderate reliability; between 0.61 and 0.80, substantial reliability; and between 0.81 and 1.00, almost perfect reliability. Coefficients of 0.90 or larger reflect sufficient reliability, given that reliability coefficients exceeding 0.90 increase the likelihood that a measure is also reasonably valid [43].

All the continuous data were studied for normality using the Kolmogorov–Smirnov test; normal distributions were noted for p -values > 0.05 . Independent Student’s t-tests were used to determine if there were significant differences between the case and control groups under the WRP and the three continuous variables used in the study. Similarly, ANOVA was used to test if there were significant differences in the applied tension values between the different conditions. Tukey’s test was used for post hoc comparisons. The Spearman rank correlation coefficient was used to determine the correlation between the thickness of the ME insoles and the effect on the pulled applied tension. We present each descriptive summary as the mean \pm SD. For all the analyses, we considered p -values < 0.05 .

(within a 95% confidence interval) as statistically significant. We analyzed the data using SPSS software, version 19.0 (SPSS Science, Chicago, IL, USA).

3. Results

A total of 58 subjects (34 females and 24 males) participated in the study; 28 subjects were recruited to the control group and 30 subjects were included in the case group (Figure 4).

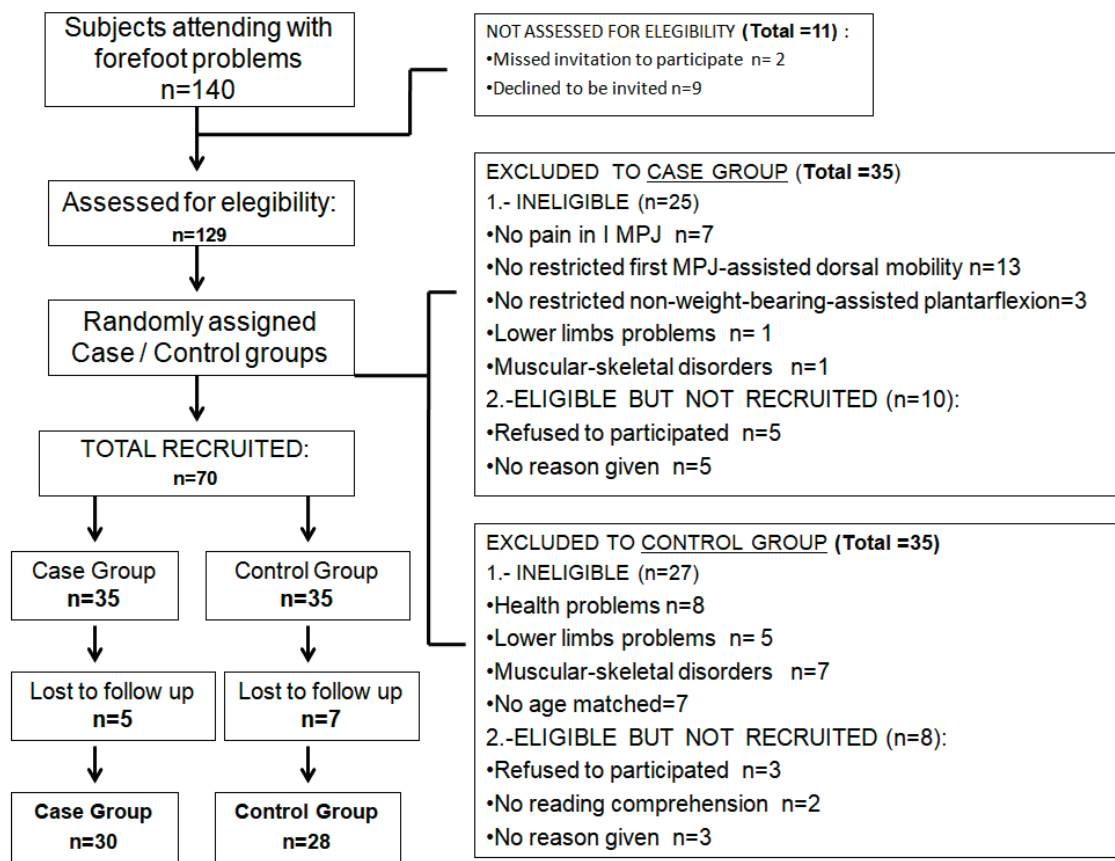


Figure 4. Flow chart. Representation of participants' recruitment. IMPJ = first metatarsophalangeal joint; n = population.

The sociodemographic characteristics of the case and control groups are shown in Table 1. The homogeneity of the four measured physical characteristics [weight, height, foot size, and body mass index (BMI)] guaranteed the applicability of the results to the sample. The distribution was normal ($p > 0.05$).

The reliability of the variables followed perfect ICC criteria and ranged from 0.963 to 0.989 (Table 2). According to our obtained values (Table 2), the control group required almost 1 kgf less effort than the case group to move the MPJ dorsally under the 4 mm ME [4.122 ± 0.162 kgf in the case group vs. 3.325 ± 0.139 kgf in the control group under WRP ($p < 0.001$); 4.211 ± 0.116 kgf in the case group vs. 3.538 ± 0.123 kgf in the control group under a 4 mm ME ($p < 0.001$)]. The differences were smaller for the 2 mm ME: 4.139 ± 0.142 kgf in the case group vs. 3.421 ± 0.133 kgf in the control group ($p < 0.001$) (Figure 5). Nevertheless, in the case group, the WRP and the different ME insoles had similar pulled tension values, which ranged from 4.122 ± 0.16 kgf in the WRP to 4.211 ± 0.116 kgf in the 4 mm ME condition (not statistically significantly different, $p > 0.05$); the differences were smaller with the 2 and 8 mm MEs (4.139 ± 0.142 kgf with a 2 mm ME and 4.179 ± 0.126 kgf with an 8 mm ME) (Table 2). For the controls, the WRP and different ME insole conditions showed similar pulled tension values, which ranged

from 3.325 ± 0.139 kgf in the WRP to 3.538 ± 0.123 kgf with the 4 mm-thick ME; the 8-mm-thick ME (3.465 ± 0.134 kgf) and 2 mm-thick ME (3.421 ± 0.133 kgf) values were quite similar (Table 2) ($p > 0.05$). These data are shown in Figure 5, where it is possible to see the differences in tension values between the groups.

Table 1. Descriptive socio-demographics data of cases and control healthy group subjects.

	Total Population $n = 58$	CASES GROUP HR Participants $n = 30$	CONTROL GROUP Healthy Participants $n = 28$	
Variable	Mean \pm SD (95% CI)	Mean \pm SD (95% CI)	Mean \pm SD (95% CI)	p -Value
Age (years)	40.62 ± 1.12 (40.98–40.33)	42.53 ± 5.72 (44.57–40.48)	38.57 ± 1.12 (38.98–38.15)	0.9
Weight (kg)	67.44 ± 9.98 (70–64.87)	66.6 ± 9.37 (69.95–63.24)	68.35 ± 10.7 (72.31–64.38)	<0.001
Height (cm)	167.77 ± 10.01 (170.34–165.19)	167.53 ± 7.72 (170.29–164.76)	164 ± 12.14 (168.49–159.5)	<0.001
Foot Size (Es)	40.2 ± 1.9 (40.50–39.89)	38.2 ± 2.10 (38.95–37.44)	40.3 ± 0.35 (40.42–40.17)	<0.001
BMI (kg/m^2)	21.48 ± 1.47 (21.85–21.1)	20.2 ± 1.74 (20.82–19.57)	22.95 ± 2.58 (23.90–21.99)	<0.001

Abbreviations: N = sample size; CASES GROUP = participants with hallux rigidus; CONTROL GROUP = healthy participants, without hallux rigidus; SD = Standard Deviation; CI = confidence interval; p -value = level of significance; $p < 0.05$ (with a 95% confidence interval) was considered statistically significant; Es = number according to European mode size; BMI = body mass index.

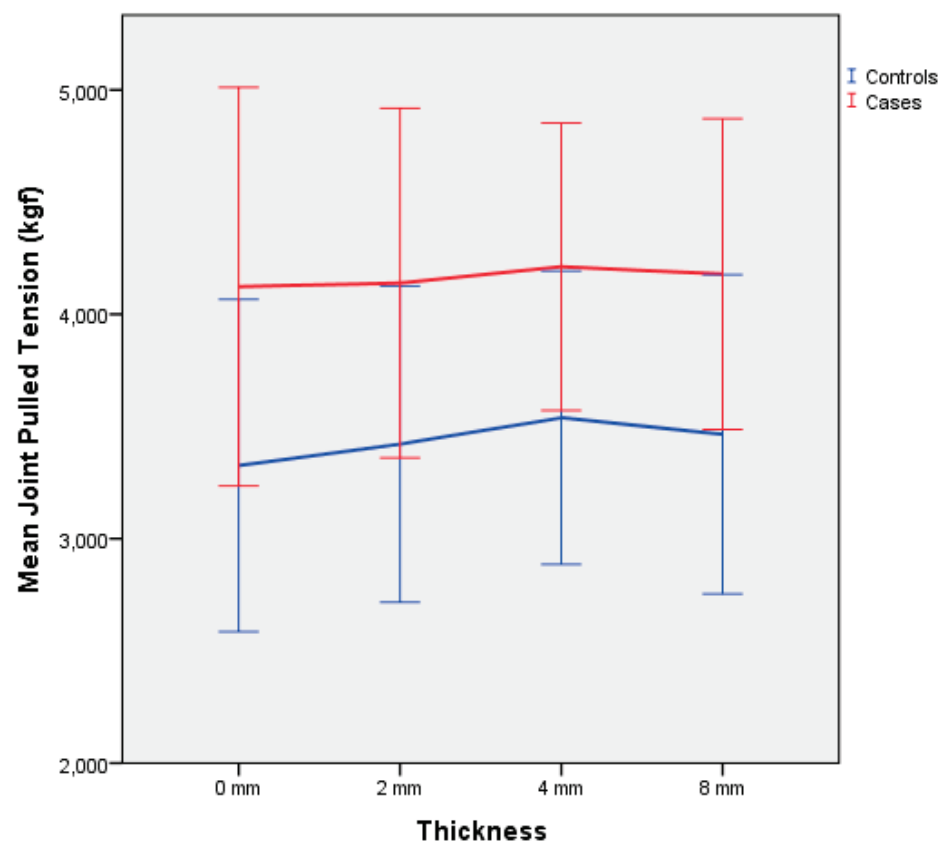


Figure 5. Difference in pulled joint tension applied (kgf) between the case group and the control group. Mean + SD data between cases (red lines) and control (blue lines) groups. The highest values of cases in the Hallux rigidus group showed a clear difference.

Table 2. Mean values and reliability of pulled tension for measurements of first MPJ under each Morton's extensions insoles thickness between cases and control groups.

Thickness ME Variable	CASES GROUP <i>n</i> = 30		CONTROL GROUP <i>n</i> = 28		<i>p</i> -Value
	Mean (kgf) ± SD (95% CI)	ICC 95% IC (Li-Ls)	Mean (kgf) ± SD (95% CI)	ICC 95% IC (Li-Ls)	
I MPJ WRP	4.122 ± 0.162 (3.79–4.45)	0.989 (0.98–0.994)	3.325 ± 0.139 (3.03–3.61)	0.971 (0.948–0.98)	<0.001
ME 2 mm	4.139 ± 0.142 (3.84–4.43)	0.97 (0.94–0.985)	3.421 ± 0.133 (3.14–3.69)	0.963 (0.928–0.982)	<0.001
ME 4 mm	4.211 ± 0.116 (3.97–4.45)	0.969 (0.943–0.984)	3.538 ± 0.123 (3.28–3.79)	0.94 (0.88–0.97)	<0.001
ME 8 mm	4.179 ± 0.126 (3.92–4.43)	0.972 (0.939–0.987)	3.465 ± 0.134 (3.18–3.74)	0.971 (0.94–0.986)	<0.001
WRP vs. ME2 <i>p</i> -value	1	-	0.956	-	-
WRP vs. ME4 <i>p</i> -value	0.969	-	0.669	-	-
WRP vs. ME8 <i>p</i> -value	0.992	-	0.879	-	-
ME2 vs. ME4 <i>p</i> -value	0.983	-	0.924	-	-
ME2 vs. ME8 <i>p</i> -value	0.997	-	0.996	-	-
ME4 vs. ME8 <i>p</i> -value	0.998	-	0.98	-	-

Abbreviations: CASES GROUP = participants with hallux rigidus; CONTROL GROUP = healthy participants, without hallux rigidus; SD = standard deviation; CI = confidence interval; ICC = intraclass correlation coefficient; Li = inferior limit; Ls = superior limit; IMPJ = first metatarsophalangeal joint; ME = Morton's extension insoles; mm = millimeters; *p*-value = level of significance; *p* < 0.05 (with a 95% confidence interval) was considered statistically significant. WRP = weight-bearing resting position (without insoles).

Spearman's rho correlations between the ME thickness and the amount of pulled joint tension were not statistically significant for either group (case, *p* = 0.715; control, *p* = 0.481) (Figure 6).

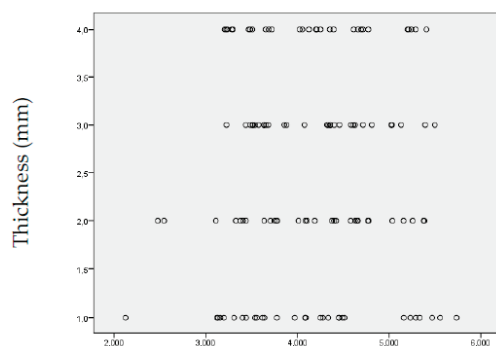
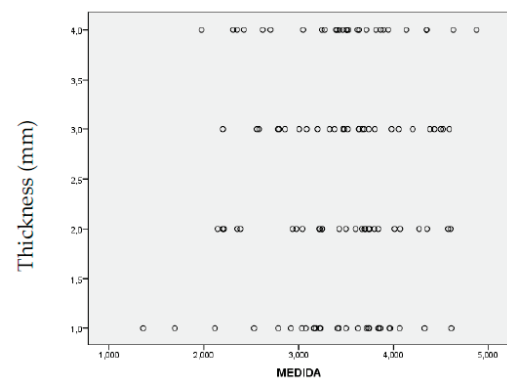
**(A)** Cases. Joint pulled tension (kgf)**(B)** Control. Joint pulled tension (kgf)

Figure 6. The correlation between Morton's extension insoles thickness (mm) and pulled joint tension applied (kgf). **(A)** = Cases group; hallux rigidus participants. **(B)** = control group; healthy participants. Spearman's rho = level of significance; *p* < 0.05 (with a 95% confidence interval) was considered statistically significant; kgf = kilogram force.

4. Discussion

The main goal of the present research was to study the behavior of the first MPJ under the effects of three different kinds of ME orthoses on healthy subjects versus HR subjects in WRP, recording values of pulled tension with a digital algometer; a secondary goal was to compare the pulled tension values between healthy and HR subjects without any ME orthoses. Rigid MEs have been used as a conservative treatment for the first stages of HR [10,44], and their effects have been studied with respect to the position [22,45] and pressure [46] of the first ray on healthy subjects; this is the first research that studies the pulled tension forces applied in HR subjects on WRP, as Moisan et al. [28] proposed.

First MPJ is a rolling structure regulated by the rotational equilibrium theory described before [47], in which kinetic and kinematic forces are present in the different phases of the human gait. Taking into account that this study is not about the first MPJ's mobility or position, nor is it about pressure values, but instead about kinetics inside the first MPJ, and considering that MEs have a direct implication on this rolling mechanism [48], it was essential to know the effects of that kind of orthosis on the first MPJ tension forces.

It is known that the thicker the MEs were placed, the wider the dorsal gap formed over the first MPJ as a result of the distance generated between the joint's bone surfaces and the more difficult it was to roll the proximal phalanx of the hallux over the head of the first metatarsal bone [21,22,49], so Jack's test performed with pulled tension would show higher values as much thickness beneath the first MPJ was placed. Surprisingly, our results showed that it did not matter how much thicker the MEs were, because the values of the tension applied did not increase statistically significantly, in contrast with those studies that argued that the dorsal first MPJ's mobility was influenced by the position of the first ray [14,15,22] cause were smaller as much thickness acrylic platform were placed below of it [22]. It was a highlight result because it emphasized the idea that (unseen) kinetics is more important than (visible) kinematics and that the forces inside the joint may not always have the measurable motion representation but have internal implications, in line with discoveries reached by other authors [50–53].

The hypothesis proposed at the beginning of the present study could not be confirmed according to the results because there was no statistically significant difference between the applied pulled tension in Jack's test for the case or control groups, regardless of the ME thickness. Moreover, the differences that were detected were small. In our study, the pulling force applied on the first MPJ during the measurements did not show any proportional correlation with the ME thickness, as opposed to the results of Roukis et al. [22], who showed a 19.3% incremental restriction on the first MPJ's mobility in proportion to 4 mm first-ray simulated dorsiflexion. The data revealed that, regardless of the external ME's restrictions, the pulling force needed to perform Jack's test was the same after reaching the joint stop movement through the thickness of the ME.

On the other hand, it is mandatory to consider the variations of the first ray function when some pieces are placed beneath it, and how these variations are poorly correlated with the real dorsiflexion angle during gait [54,55]. For example, the total amount of dorsal mobility of the first ray in WRP, with the ground reactions forces acting under the foot, was set at 4.9 mm [56], which is lower than that achieved with the foot in resting non-weight bearing position; this is due to the increased tension on the plantar aponeurosis related to the windlass mechanism [17,57], as it has been shown previously by the intrinsic correlation between first MPJ, the rearfoot supination and the triceps surae activation [58,59]. The ME thicknesses used in the present experiment were 2, 4, and 8 mm [22]. In our results, the 4 mm ME orthotic produced the greatest tension effort on the first MPJ, which could be linked as a rough comparison with the mobility results of Grady [56], but without any statistical significance.

The "artificial dorsal-opening" of the first MPJ got through the ME's effects placed under the first MPJ and could be used to avoid pain inside the joint, pushing away the phalanx and metatarsal dorsal surfaces during the push-off phase; however, it has been shown that these MEs had no effects on the kinetic data because the exerted tension was

enough to produce the needed dorsiflexion of the first MPJ before to achieve the “stop” point determined by supination of the rearfoot. Further dynamic research is now needed to clarify if the present data could be applied to functional gait and if our kinetics results would be similar to the results of examining the kinematics variables under similar conditions.

Nevertheless, according to our data, the authors could hypothesize that the case group had more difficulty achieving peak mobility in Jack’s test than the control group, as shown by the greater force values applied, regardless of the ME’s thickness. As expected, this is in accordance with the field’s current knowledge about the mobility of the first MPJ [16,22,48]. Grebing et al. [56] detected a decrease in the first-ray simulated dorsiflexion when comparing healthy versus first MPJ arthrodesis subjects, which explains the increase in pulled force we observed in the HR group compared to the healthy control group.

There are controlling orthoses for hyper-pronated feet [60], and these have been shown to restore the mobility of first MPJs with restricted dynamic mobility (named functional hallux limitus) at the 5-month follow-up. It is also possible to improve this mobility in real time using cut-out orthoses [61]. Nevertheless, the objective of the present research was to assess the tension values of the ME on a totally restricted first MPJ, not just dynamic-functional restriction. Moreover, Reina et al. [62] showed no statistical difference in the X-ray of first-second intermetatarsal angles and HAV-angle values between custom-made foot orthoses and no orthoses in subjects with HAV, indicating that kinematics data are not always related to kinetics values, which is in line with our results.

The first MPJ dorsiflexion resistance test or similar has already been proven in healthy subjects, showing the ICC intra-rater reliability of 0.77 ($p < 0.001$) [28], 0.814 ($p = 0.784$) [29], and 0.568 [26] in contrast to the 0.989 ($p < 0.001$) obtained in this research. Then, the authors proposed the digital algometer as a valid tool to detect HR in healthy subjects.

Limitations

The present device had a 10×0.01 kgf capacity/graduation and an accuracy of 0.3% of the full scale; furthermore, the small effect sizes throughout the results between the WRP and MEs inside each control and case group are in line with another comparative kinetic and kinematic study with small effect sizes between the case and control groups [63]. Therefore, the reported values should be considered with caution.

This is a novel force–kinetic study related to pulled tension and did not focus on the first MPJ’s mobility or position; therefore, further investigations are needed to be able to make comparisons with these results. Moreover, further dynamics measurements will be required to verify the ME effects discovered in the present simulated research. In addition, future research with X-ray assessments to correlate the elevation of the first metatarsal bone with ME and how it changes the forces of dorsiflexion could be interesting. There is no reliable method for determining the final position of the proximal phalanx of the hallux during Jack’s test.

5. Conclusions

The orthopedic use of rigid ME as a palliative treatment for HR has been studied regarding mobility, but not force–kinetic effects. In the present study, the authors showed that with the use of different MEs, the tension values detected during the simulated toe-off phase of the gait cycle (i.e., Jack’s test) in healthy individuals and subjects with HR had no correlation with the ME’s thickness. Although we were able to confirm that performing Jack’s test in individuals with HR required higher kgf tension values than in healthy individuals, the data showed that the prescription of bigger MEs did not affect tension forces inside the first MPJ, and thus its prescription can be made free of joint damage. In addition, the digital algometer is a valid tool to detect HR pathology versus healthy subjects.

Future research will be needed to assess the kinetic and force effects of ME on the shoes to check the first MPJ’s behavior.

6. Clinical Relevance

This is the first study that assesses the first MPJ motion using tension force values with a valid tool as a digital algometer to discriminate HR pathology versus healthy subjects with a high level of accuracy and reliability. In addition, it has been proven that subjects with HR store more tension forces inside the first MPJ during the simulated push-off phase of gait (i.e., Jack's test) than healthy subjects, proving the etiology of joint disruption caused by kinetics and not only by kinematics and therefore alerting clinicians to consider both biomechanical forces when applying their orthopedic treatments.

Author Contributions: Conceptualization, R.S.-G., Á.G.-C. and M.L.G.F.; methodology, C.M.-S., J.M.L.-A., A.N.-F. and I.O.-S.; software, I.Z.-G. and J.M.L.-A.; validation, I.Z.-G., A.N.-F. and J.M.L.-A.; formal analysis, Á.G.-C. and C.M.-S.; investigation, R.S.-G.; resources, M.L.G.F.; data curation, R.S.-G.; writing—original draft preparation, R.S.-G., J.M.L.-A., M.L.G.F., A.N.-F., C.M.-S., Á.G.-C., I.O.-S. and I.Z.-G.; writing—review and editing, R.S.-G. and Á.G.-C.; visualization, I.O.-S.; supervision, I.Z.-G.; project administration, I.Z.-G. and I.O.-S.; funding acquisition, no needed. All authors have read and agreed to the published version of the manuscript.

Funding: This research received no external funding.

Institutional Review Board Statement: The study was conducted in accordance with the Declaration of Helsinki, and approved by the Institutional Review Board of Hospital Universitario Nuestra Señora de Valme (code f7f4a656767d7ba7163bce0d15e7f98c9f33355, 27 October 2020) for studies involving humans.

Informed Consent Statement: “Informed consent was obtained from all subjects involved in the study.” “Written informed consent has been obtained from the patient(s) to publish this paper”.

Data Availability Statement: The datasets used and/or analyzed during the current study available from the corresponding author on reasonable request.

Conflicts of Interest: The authors declare no conflict of interest.

References

1. Stuck, R.M.; Moore, J.W.; Patwardhan, A.G.; Sartori, M. Forces under the hallux rigidus foot with surgical and orthotic intervention. *J. Am. Podiatr. Med. Assoc.* **1988**, *78*, 465–468. [PubMed]
2. Cotterill, J.M. Stiffness of the Great Toe in Adolescents. *Br. Med. J.* **1887**, *1*, 1158. [CrossRef] [PubMed]
3. Rzonca, E.; Levitz, S.; Lue, B. Hallux equinus. The stages of hallux limitus and hallux rigidus. *J. Am. Podiatr. Med. Assoc.* **1984**, *74*, 390–393. [CrossRef]
4. Colò, G.; Fusini, F.; Samaila, E.M.; Rava, A.; Felli, L.; Alessio-Mazzola, M.; Magnan, B. The efficacy of shoe modifications and foot orthoses in treating patients with hallux rigidus: A comprehensive review of literature. *Acta Biomed.* **2020**, *91*, e2020016.
5. Caravelli, S.; Mosca, M.; Massimi, S.; Pungetti, C.; Russo, A.; Fuiano, M.; Catanese, G.; Zaffagnini, S. A comprehensive and narrative review of historical aspects and management of low-grade hallux rigidus: Conservative and surgical possibilities. *Musculoskelet. Surg.* **2018**, *102*, 201–211. [CrossRef]
6. Dananberg, H.J. Gait style as an etiology to chronic postural pain. Part I. Functional hallux limitus. *J. Am. Podiatr. Med. Assoc.* **1993**, *83*, 433–441.
7. Jamari, J.; Ammarullah, M.I.; Santoso, G.; Sugiharto, S.; Supriyono, T.; Permana, M.S.; Winarni, T.I.; van der Heide, E. Adopted walking condition for computational simulation approach on bearing of hip joint prosthesis: Review over the past 30 years. *Heliyon* **2022**, *8*, e12050. [CrossRef]
8. Coughlin, M.J.; Shurnas, P.S. Hallux Rigidus. *J. Bone Joint. Surg.* **2004**, *86 Pt 2*, 119–130. [CrossRef]
9. Drago, J.J.; Oloff, L.; Jacobs, A.M. A comprehensive review of hallux limitus. *J. Foot Surg.* **1984**, *23*, 213–220.
10. Shurnas, P.S. Hallux Rigidus: Etiology, Biomechanics, and Nonoperative Treatment. *Foot Ankle Clin.* **2009**, *14*, 1–8. [CrossRef]
11. Gould, N. Hallux rigidus: Cheilotomy or implant? *Foot Ankle* **1981**, *1*, 315–320. [CrossRef] [PubMed]
12. Smith, R.W.; Katchis, S.D.; Ayson, L.C. Outcomes in Hallux Rigidus Patients Treated Nonoperatively: A Long-Term Follow-Up Study. *Foot Ankle Int.* **2000**, *21*, 906–913. [CrossRef]
13. Grady, J.F.; Axe, T.M.; Zager, E.J.; Sheldon, L.A. A Retrospective Analysis of 772 Patients with Hallux Limitus. *J. Am. Podiatr. Med. Assoc.* **2002**, *92*, 102–108. [CrossRef] [PubMed]
14. Ebisui, J.M. The first ray axis and the first metatarsophalangeal joint: An anatomical and pathomechanical study. *J. Am. Podiatr. Med. Assoc.* **1968**, *58*, 160–168. [CrossRef]
15. Kelso, S.F.; Richie, D.H.; Cohen, I.R.; Weed, J.H.; Root, M. Direction and range of motion of the first ray. *J. Am. Podiatr. Med. Assoc.* **1982**, *72*, 600–605. [CrossRef]

16. Dananberg, H.J. Functional hallux limitus and its relationship to gait efficiency. *J. Am. Podiatr. Med. Assoc.* **1986**, *76*, 648–652. [CrossRef]
17. Hicks, J. The mechanics of the foot. II. The plantar aponeurosis and the arch. *J. Anat.* **1954**, *88*, 25–30.
18. Lyritis, G. Developmental disorders of the proximal epiphysis of the hallux. *Skelet. Radiol.* **1983**, *10*, 250–254. [CrossRef]
19. Root, M.L.; Orien, W.P. *Normal and Abnormal Function of the Foot*; Corp, C.B., Ed.; Clinical Biomechanics Corp.: Los Angeles, CA, USA, 1977; Volume II.
20. Lambrinudi, C. Metatarsus Primus Elevatus. *Proc. R. Soc. Med.* **1938**, *31*, 1273. [CrossRef]
21. Ohara, K.; Tanaka, Y.; Taniguchi, A.; Kurokawa, H.; Kumai, T.; Yamada, H. Is metatarsus primus elevatus truly observed in hallux rigidus? Radiographic study using mapping methods. *J. Orthop. Sci.* **2018**, *24*, 312–319. [CrossRef] [PubMed]
22. Roukis, T.; Scherer, P.; Anderson, C. Position of the first ray and motion of the first metatarsophalangeal joint. *J. Am. Podiatr. Med. Assoc.* **1996**, *86*, 538–546. [CrossRef]
23. Kim, H.K.; Mirjalili, S.A.; Fernandez, J. Gait kinetics, kinematics, spatiotemporal and foot plantar pressure alteration in response to long-distance running: Systematic review. *Hum. Mov. Sci.* **2018**, *57*, 342–356. [CrossRef] [PubMed]
24. Downey, M. Tarsal coalitions. A surgical classification. *J. Am. Podiatr. Med. Assoc.* **1991**, *81*, 187–197.
25. Jack, E.A. Naviculo-cuneiform fusion in the treatment of flat foot. *J. Bone Jt. Surg.* **1953**, *35-B*, 75–82. [CrossRef]
26. Heng, M.L.; Chua, Y.K.; Pek, H.K.; Krishnasamy, P.; Kong, P.W. A novel method of measuring passive quasi-stiffness in the first metatarsophalangeal joint. *J. Foot Ankle Res.* **2016**, *9*, 41. [CrossRef] [PubMed]
27. Molyneux, P.; Bowen, C.; Ellis, R.; Rome, K.; Jackson, A.; Carroll, M. Ultrasound Imaging Acquisition Procedures for Evaluating the First Metatarsophalangeal Joint: A Scoping Review. *Ultrasound Med. Biol.* **2021**, *48*, 397–405. [CrossRef] [PubMed]
28. Moisan, G.; McBride, S.; Isabelle, P.; Chicoine, D.; Walha, R. Intrarater and interrater reliability of the first metatarsophalangeal joint dorsiflexion resistance test. *Musculoskelet. Care* **2022**, *14*, 1–6. Available online: <https://pubmed.ncbi.nlm.nih.gov/35833706/> (accessed on 7 February 2023). [CrossRef]
29. Leow, Y.; Kong, P.W.; Liu, Y.; Pan, J.W.; Fong, D.T.; Chan, C.C.; Heng, M.L. Test-retest reliability of a clinical foot assessment device for measuring first metatarsophalangeal joint quasi-stiffness. *Foot* **2020**, *45*, 101742. [CrossRef]
30. Curran, S.; Jones, A. Intrarater and interrater reliability of first metatarsophalangeal joint dorsiflexion: Goniometry versus visual estimation. *J. Foot Ankle Res.* **2010**, *3*, P5. [CrossRef]
31. Mens, M.; Bouman, C.; Dobbe, J.; Bus, S.; Nieuwdorp, M.; Maas, M.; Wellenberg, R.; Streekstra, G. Metatarsophalangeal and interphalangeal joint angle measurements on weight-bearing CT images. *Foot Ankle Surg.* **2023**, *23*, S1268–7731. Available online: <https://pubmed.ncbi.nlm.nih.gov/36641368/> (accessed on 9 February 2023). [CrossRef]
32. Desmyttere, G.; Hajizadeh, M.; Bleau, J.; Begon, M. Effect of Foot Orthosis Design on Lower Limb Joint Kinematics and Kinetics during Walking in Flexible pes Planovalgus: A Systematic Review and Meta-Analysis. In *Clinical Biomechanics*; Elsevier Ltd.: Amsterdam, The Netherlands, 2018; Volume 59, pp. 117–129. Available online: <https://pubmed.ncbi.nlm.nih.gov/30227277/> (accessed on 20 May 2021).
33. Kirby, K.A. The medial heel skive technique. Improving pronation control in foot orthoses. *J. Am. Podiatr. Med. Assoc.* **1992**, *82*, 177–188. [CrossRef] [PubMed]
34. Sánchez-Gómez, R.; Becerro-de-Bengoa-Vallejo, R.; Losa-Iglesias, M.E.; Calvo-Lobo, C.; Navarro-Flores, E.; Palomo-López, P.; Romero-Morales, C.; López-López, D. Reliability Study of Diagnostic Tests for Functional Hallux Limitus. *Foot Ankle Int.* **2020**, *41*, 457–462. [CrossRef] [PubMed]
35. Dananberg, H.J. The Kinetic Wedge. *J. Am. Podiatr. Med. Assoc.* **1988**, *78*, 98–99. [CrossRef] [PubMed]
36. Ho, B.; Baumhauer, J. Hallux rigidus. *EFORT Open Rev.* **2017**, *2*, 13–20. [CrossRef] [PubMed]
37. Vandembroucke, J.P.; von Elm, E.; Altman, D.G.; Gøtzsche, P.C.; Mulrow, C.D.; Pocock, S.J.; Poole, C.; Schlesselman, J.; Egger, M. Strengthening the Reporting of Observational Studies in Epidemiology (STROBE): Explanation and elaboration. *Int. J. Surg.* **2014**, *12*, 1500–1524. [CrossRef]
38. Shereff, M.J.; Bejjani, F.J.; Kummer, F.J. Kinematics of the first metatarsophalangeal joint. *J. Bone Jt. Surg.* **1986**, *68*, 392–398. [CrossRef]
39. Mann, R.A.; Coughlin, M.J.; Duvries, H.L. Hallux rigidus: A review of the literature and a method of treatment. *Clin. Orthop. Relat. Res.* **1979**, *142*, 57–63. [CrossRef]
40. Redmond, A.C.; Crosbie, J.; Ouvrier, R.A. Development and validation of a novel rating system for scoring standing foot posture: The Foot Posture Index. *Clin. Biomech.* **2006**, *21*, 89–98. [CrossRef]
41. Sarcevic, Z.Z.; Tepavcevic, A.P. Association between abductor hallucis abductory force and navicular drop index, a predictive correlational study. *J. Pediatr. Orthop. B* **2020**, *30*, 484–487. [CrossRef]
42. Kelly-Martin, R.; Doughty, L.; Garkavi, M.; Wasserman, J.B. Reliability of modified adherometer and digital pressure algometer in measuring normal abdominal tissue and C-section scars. *J. Bodyw. Mov. Ther.* **2018**, *22*, 972–979. [CrossRef]
43. Portney, L.; Watkins, M. Foundations of Clinical Research: Applications to Practice. In *Survey of Ophthalmology*, 3rd ed.; Hall, P.P., Ed.; Prentice Hall Health: Upper Saddle River, NJ, USA, 2009; Volume 47, 598p.
44. Park, C.H.; Chang, M.C. Forefoot disorders and conservative treatment. *Yeungnam Univ. J. Med.* **2019**, *36*, 92–98. [CrossRef] [PubMed]
45. Kunnasegaran, R.; Thevendran, G. Hallux Rigidus Nonoperative Treatment and Orthotics. In *Foot and Ankle Clinics*; W.B. Saunders: Philadelphia, PA, USA, 2015; Volume 20, pp. 401–412.

46. Rambarran, K.K. Reduce Relative Plantar Pressure—Search Results—PubMed. Available online: <https://pubmed.ncbi.nlm.nih.gov/?term=Rambarran+KK%2C+reduce+relative+plantar+pressure> (accessed on 10 February 2023).
47. Kirby, K.A. Subtalar Joint Axis Location and Rotational Equilibrium Theory of Foot Function. *J. Am. Podiatr. Med. Assoc.* **2001**, *91*, 465–487. [CrossRef] [PubMed]
48. van Gheluwe, B.; Dananberg, H.J.; Hagman, F.; Vanstaen, K. Effects of hallux limitus on plantar foot pressure and foot kinematics during walking. *J. Am. Podiatr. Med. Assoc.* **2006**, *96*, 428–436. [CrossRef]
49. Horton, G.A.; Park, Y.-W.; Myerson, M.S. Role of Metatarsus Primus Elevatus in the Pathogenesis of Hallux Rigidus. *Foot Ankle Int.* **1999**, *20*, 777–780. [CrossRef]
50. Fuller, E.A. Center of pressure and its theoretical relationship to foot pathology. *J. Am. Podiatr. Med. Assoc.* **1999**, *89*, 278–291. [CrossRef]
51. Huerta, J.P.; Moreno, J.M.R.; Kirby, K.A. Static Response of Maximally Pronated and Nonmaximally Pronated Feet to Frontal Plane Wedging of Foot Orthoses. *J. Am. Podiatr. Med. Assoc.* **2009**, *99*, 13–19. [CrossRef] [PubMed]
52. Mills, K.; Blanch, P.; Chapman, A.R.; McPoil, T.G.; Vicenzino, B. Foot orthoses and gait: A systematic review and meta-analysis of literature pertaining to potential mechanisms. *Br. J. Sport. Med.* **2009**, *44*, 1035–1046. [CrossRef]
53. Nigg, B.M. The Role of Impact Forces and Foot Pronation: A New Paradigm. *Clin. J. Sport Med.* **2001**, *11*, 2–9. [CrossRef]
54. Gatt, A.; Mifsud, T.; Chockalingam, N. Severity of pronation and classification of first metatarsophalangeal joint dorsiflexion increases the validity of the Hubscher Manoeuvre for the diagnosis of functional hallux limitus. *Foot* **2014**, *24*, 62–65. [CrossRef]
55. Halstead, J.; Redmond, A.C. Weight-Bearing Passive Dorsiflexion of the Hallux in Standing Is Not Related to Hallux Dorsiflexion During Walking. *J. Orthop. Sport. Phys. Ther.* **2006**, *36*, 550–556. [CrossRef]
56. Grebing, B.R.; Coughlin, M.J. The Effect of Ankle Position on the Exam for First Ray Mobility. *Foot Ankle Int.* **2004**, *25*, 467–475. [CrossRef] [PubMed]
57. Durrant, M.N.; Siepert, K.K. Role of soft tissue structures as an etiology of hallux limitus. *J. Am. Podiatr. Med. Assoc.* **1993**, *83*, 173–180. [CrossRef] [PubMed]
58. Maceira, E.; Monteagudo, M. Functional Hallux Rigidus and the Achilles-Calcaneus-Plantar System. *Foot Ankle Clin.* **2014**, *19*, 669–699. [CrossRef] [PubMed]
59. Sánchez-Gómez, R.; Romero-Morales, C.; Gómez-Carrión, Á.; De-La-Cruz-Torres, B.; Zaragoza-García, I.; Anttila, P.; Kantola, M.; Ortuño-Soriano, I. Effects of Novel Inverted Rocker Orthoses for First Metatarsophalangeal Joint on Gastrocnemius Muscle Electromyographic Activity during Running: A Cross-Sectional Pilot Study. *Sensors* **2020**, *20*, 3205. [CrossRef]
60. Munuera, P.V.; Domínguez, G.; Palomo, I.C.; Lafuente, G. Effects of rearfoot-controlling orthotic treatment on dorsiflexion of the hallux in feet with abnormal subtalar pronation: A preliminary report. *J. Am. Podiatr. Med. Assoc.* **2006**, *96*, 283–289. [CrossRef]
61. Becerro de Bengoa Vallejo, R.; Gomez, R.S.; Losa Iglesias, M.E. Clinical improvement in functional hallux limitus using a cut-out orthosis. *Prosthet. Orthot. Int.* **2016**, *40*, 215–223. [CrossRef]
62. Reina, M.; Lafuente, G.; Munuera, P.V. Effect of custom-made foot orthoses in female hallux valgus after one-year follow up. *Prosthet. Orthot. Int.* **2012**, *37*, 113–119. [CrossRef]
63. Sung, P.S.; Zipple, J.T.; Andraka, J.M.; Danial, P. The kinetic and kinematic stability measures in healthy adult subjects with and without flat foot. *Foot* **2017**, *30*, 21–26. [CrossRef]

Disclaimer/Publisher’s Note: The statements, opinions and data contained in all publications are solely those of the individual author(s) and contributor(s) and not of MDPI and/or the editor(s). MDPI and/or the editor(s) disclaim responsibility for any injury to people or property resulting from any ideas, methods, instructions or products referred to in the content.

Article

Design Analysis of Prosthetic Unilateral Transtibial Lower Limb with Gait Coordination

Susmita Das ^{1,2,*}, Dalia Nandi ² and Biswarup Neogi ³

¹ Electronics and Instrumentation Engineering Department, Narula Institute of Technology, Kolkata 700109, West Bengal, India

² Electronics & Communication Engineering Department, Indian Institute of Information Technology, Kalyani 741235, Nadia, India; dalia@iiitkalyani.ac.in

³ JIS College of Engineering, Electronics and Communication Engineering, Kalyani 741235, Nadia, India; biswarupneogi@gmail.com

* Correspondence: susmitad2011@gmail.com; Tel.: +91-8017205403

Abstract: People with lower limb amputations struggle through difficulties during locomotion in their daily activities. People with transtibial amputations take support from prosthetic legs for systematic movement. During motion, they experience some mobility issues while using general prosthetic limbs regarding gait pattern. The design of a prosthetic-controlled lower limb with gait synchronization for physically disabled persons is the main goal of the present research work, which can provide an improved walking experience. The design and performance analysis of prosthetic lower limbs for people with transtibial amputations is performed in the present paper. The designed rehabilitation system shows synchronization between the normal and the prosthetic limbs achieved with gait coordination. The dynamics of the lower extremities in different postural activities are used for design purpose utilizing Euler–Lagrange motion theory. The artificial motion of the knee and the ankle joints function through the angular movement of the servo motors according to the movements of the rotary encoders placed on the sound limb joints. The range of motion of both the sound and prosthetic limbs are compared for different steps during a gait cycle. The prosthetic electronic system design of the artificial lower limb is able to show the gait style of human being with body kinesics. The nonlinear domain stability analysis of the designed prosthetic limb is presented through the Lyapunov method. A PIDF2 controller tuning process is implemented for the designed limb's performance improvement. The designed prosthetic system is beneficial for people with unilateral transtibial amputations with a great societal impact.

Citation: Das, S.; Nandi, D.; Neogi, B. Design Analysis of Prosthetic Unilateral Transtibial Lower Limb with Gait Coordination. *Prosthesis* **2023**, *5*, 575–586. <https://doi.org/10.3390/prosthesis5020040>

Academic Editor: Arnab Chanda

Received: 18 April 2023

Revised: 27 May 2023

Accepted: 1 June 2023

Published: 15 June 2023



Copyright: © 2023 by the authors. Licensee MDPI, Basel, Switzerland. This article is an open access article distributed under the terms and conditions of the Creative Commons Attribution (CC BY) license (<https://creativecommons.org/licenses/by/4.0/>).

Keywords: people with transtibial amputations; prosthetic limb; servo motor; gait coordination; nonlinear control

1. Introduction

People who have undergone amputations and have one normal lower limb can control the synchronized movement of a prosthetic leg attached to the residual part of the amputated limb to experience normal walking pattern. According to the range of motion of a normal leg, an artificial leg moves as per the prosthetic arrangement to provide a humanoid stride for motion. The hardware design of the artificial system includes the movement signal acquired from the existing limb of a person with an amputation to replicate the leg movement. The total constructional design works as a humanoid robotic leg with a prosthetic attachment and rehabilitation features for people with transtibial amputations. The full setup is controlled by networking and programming logic to obtain a balanced and symmetrical walking style. A person with a unilateral transtibial amputation can retrieve their previous capability to walk with a rehabilitation process. A controller-based exoskeleton design operation is described for the clinical outcome for people who have undergone amputation [1]. Single actuator-powered lower limb prosthesis design with

kinematics is described in [2]. An elaborate review work is presented regarding system design of lower extremity prosthetic system in [3]. Recent advancements to lower limb exoskeleton design are considered in [4]. The mechanical human motion with functionality is described in [5]. The robotic motion planning, control and mechanics have been described in [6]. Lower limb joint prosthesis-oriented design has been shown in [7]. Rehabilitation related to the bounded control method for joint movements has been presented in [8]. A power-assisted active interface has been presented in [9]. Artificial human ankle movement has been implemented in [10]. A review of lower limb rehabilitation design has been presented in [11]. Leg motion experiments with knee flexion analysis have been performed in [12]. Joint rehabilitation-oriented lower limb design has been implemented in [13,14]. Human movement data acquisition was performed in [15,16]. In the recent research, prosthetic system design for people with transtibial amputations has been presented with mechanical structure [17,18]. The most unexplored part is electronic system design for gait synchronization between the normal limb and the prosthetic limb with body gesture. Until now, mechanical exoskeletons and prosthetic models have been designed for people with lower limb amputations to be capable of performing the daily tasks. The gait synchronization of the artificial limb with and the healthy limb utilizing kinesiological analysis is the goal of the current work along with the natural body movement. According to the gait pattern of the normal limb of a person with an amputation, the artificial limb's movement is the main unexplored job for forward movement process. The Range of Motion (RoM) implementation with proper functionality for the unilateral transtibial amputated leg is a matter that has not been executed in previous research works until now. The theory of Lyapunov stability is a standard theory for non-linear systems and one of the most important mathematical tools in the analysis of non-linear systems in robotic design [19] which has been applied in the present work.

2. Methodology

Building a controlled prosthetic lower limb with gait synchronization for people who have undergone amputation is the most challenging job. Human factors related to knowledge are reflected through this present work [20]. The lower extremity solution gives artificial movement of the residual leg of an amputated person according to the gait style of the existing or normal leg. This method depicts the function of prosthetic model for artificial lower limbs with the joint movement signals of human legs.

2.1. Technological System Design

In Figure 1, the schematic diagram of a gait-synchronized artificial limb design process is presented [21]. Initially, the output voltages of the joints (knee and ankle) in the normal leg were acquired using rotary encoders. The rotary encoders were attached at the knee and ankle joints to observe the angular movement value during motion, as shown in Figure 2. The data were recorded for different muscular activities related to lower limb movement for a complete gait cycle [22]. Motor movements for an artificial limb were processed using the different angular movements during gait, replicating those of the normal leg. Mobility with synchronization in walking patterns is a novelty of this work.

Rotary encoders of the normal right limb knee joint and ankle joint were denoted as $R.E_{knee}$ and $R.E_{ankle}$, respectively. Servo motors of the prosthetic left limb knee joint and ankle joint were denoted as M_{knee} and M_{ankle} . The normal right limb of people who have undergone amputation as the transmitter was denoted as NL_{Tx} and the prosthetic left limb of a person with an amputation as the receiver was denoted as PL_{Rx} . In the present study, goniometers are used for measuring the angular movements at ankle and knee joints of normal and prosthetic limbs.

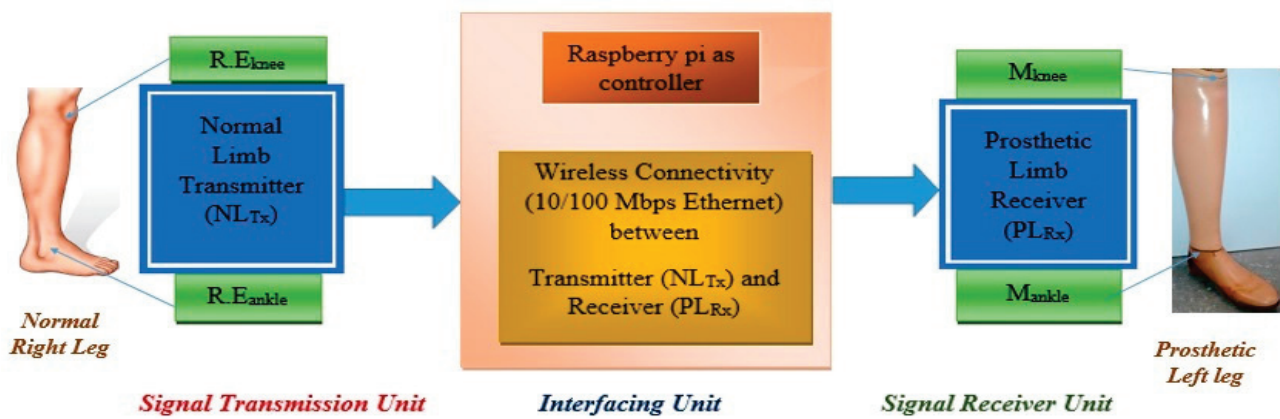


Figure 1. Schematic Design of Gait-Synchronized Prosthetic Limb with Normal Limb.

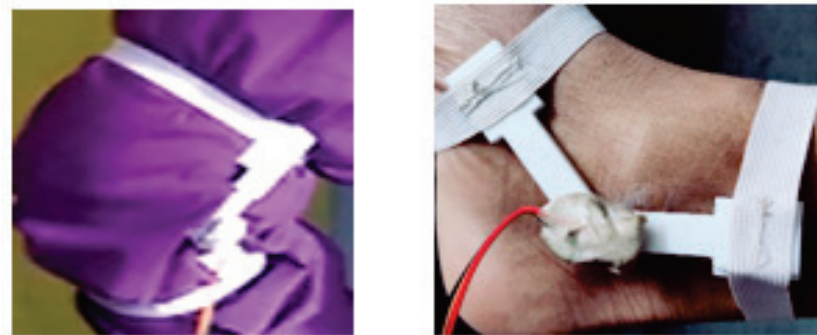


Figure 2. Pictorial Representation of Rotary Encoder connected at knee and ankle joints.

2.2. Embedded System Implementation of an Artificial Lower Limb

The artificial leg model is considered to represent the design of the electronic prosthetic system presented in Figure 1. The joint movement signal was given through rotary encoders attached at the knee and ankle joints of a normal limb with a predefined range of motion to be implemented on the artificial model [23,24]. Here, according to the existing limb movement, the artificial leg moved with proper gait style in the prosthetic system design. Raspberry pi 3b+, Arduino Nano, Node MCU, 16 channel Servo driver (PCA 9685), Servo motor MG 995 were needed to implement the prosthetic system with portability. Raspberry pi 3b+ controlled the whole system as the main controller, and Arduino Nano was used to implement the movement of the limb as per the output of the rotary encoders. PCA 9685 drove the servo motors (MG 995) placed at two different joints of the leg model. These were used to perform the movements of the joints to help the amputee person to walk with gait synchronization. The wireless connection maintained the serial communication with a 9600 BAUD (Bits of Actual Usable Data) rate. The system was made portable using a 12 volt lithium ion battery with better power usage compared with the other types. This operated at a higher voltage than other rechargeable batteries with lower rates of charge loss.

The comparison between sound limb and artificial lower limb with respect to gait functionality is shown to present the prosthetic system's performance. The model is beneficial for people who have undergone amputation to experience a normal walking style. To solve the challenging part of facing any posture change in the progression, inverse kinematics was applied, which is explained in detail in Section 3.1.

2.3. Gait Synchronization Process

Stance and swing phases are two stages of a human gait cycle. The initial step where the contact of the foot starts from the ground, followed by consecutive steps, represents stance phase. In total, 60% of gait cycle includes stance zone and almost 40% of gait cycle involves swing phase. The swing phase shows the support of a single leg where the foot is

not connected to the ground. The most important seven steps to complete the gait cycle of a human being are heel strike, foot flat, midstance, push off, acceleration, mid-swing and deceleration. The initial four steps are included in the stance phase and the rest of the steps are involved in the swing phase. The movement angles with respect to the ground were measured with a goniometer to show Range of Motion (RoM) of normal limb and prosthetic limb of a person with a unilateral transtibial amputation. The RoM of the knee joint of the normal limb ranged from 0 degrees to 150 degrees for flexion and 120 degrees to 0 degrees for extension. The RoM of the ankle joint of the normal limb was from 0 degrees to 40 degrees for plantar flexion and 0 degrees to 20 degrees for dorsiflexion. The RoM of the knee joint of the designed prosthetic limb was from 120 to 180 degrees. The RoM of the ankle joint of the designed prosthetic limb was from 0 to 56 degrees [17]. In Figure 3, the pictorial representation of the normal and the designed prosthetic lower limb design are shown.

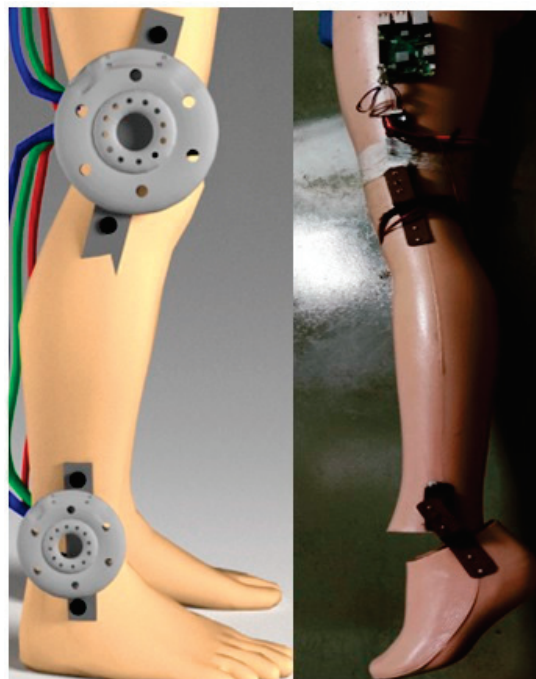


Figure 3. Pictorial Representation of Right Normal Limb and Left Prosthetic Limb.

3. Results and Discussion

The gait performance analysis with respect to the seven steps of the normal and the designed prosthetic limb is shown in Figures 4 and 5. The knee and ankle joint movements of the prosthetic limb show a balanced condition all the steps of a single gait cycle. In each and every step of one gait, the angular motion of the joints and the corresponding output voltage values were compared with the normal limb's movement to represent the differences in gait pattern for a body balancing feature creation using synchronization. In Table 1, the gait angular output variation of the normal and prosthetic limb are presented. The angular measurements are taken using Goniometer connected at the joints. It was observed that the prosthetic limb was capable of performing the synchronized gait pattern for people with transtibial amputations with a balanced condition of body kinesics.

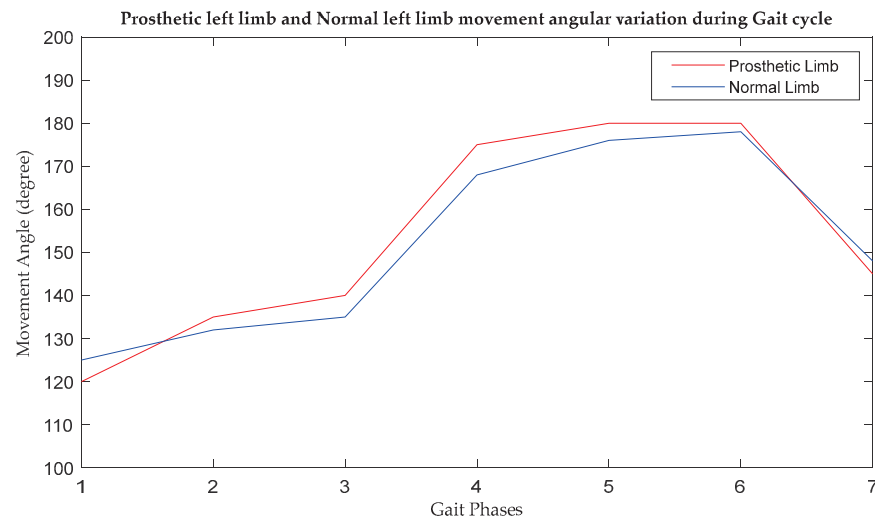


Figure 4. Graphical presentation of the Prosthetic left limb and Normal left limb movement of Knee joint during Gait cycle.

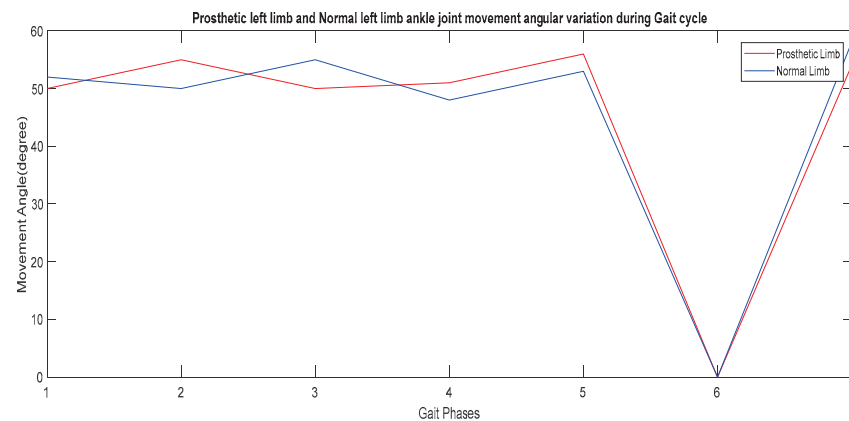


Figure 5. Graphical presentation of the Prosthetic left limb and Normal left limb movement of Ankle joint during Gait cycle.

Table 1. Gait angle variation in the normal right limb (rotary encoder), the prosthetic left limb (Servo motor) and the normal left limb.

SL. No.	Gait Phases	Movement Angle of the Normal Right Limb (Degree)		Movement Angle of the Prosthetic Left Limb (Degree)		Movement Angle in the Normal Left Limb (Degree)		Angular Deviation between Prosthetic Left Limb and Normal Left Limb (Degree)	
		Knee Joint (R.E _{knee})	Ankle Joint (R.E _{ankle})	Knee Joint (M _{knee})	Ankle Joint (M _{ankle})	Knee Joint	Ankle Joint	Knee Joint	Ankle Joint
1	Heel strike	180	20	120	50	125	52	5	2
2	Foot flat	170	0	135	55	132	50	3	5
3	Midstance	180	2	140	50	135	55	5	5
4	Push off	125	54	175	51	168	48	7	3
5	Acceleration	140	51	180	56	176	53	4	3
6	Mid-swing	125	50	180	0	178	0	2	0
7	Deceleration	180	18	145	54	148	58	3	4

From Figures 4 and 5 it has been clearly observed that the movement angle variations for knee and ankle joints of the prosthetic limb is closely followed by the normal limb

movement. The changes in the 6th gait phase due to ankle movement is justified as per feet position on the ground as shown in Figure 5.

In Table 2, the gait output voltage variation in the rotary encoder placed on the normal limb joints and the servo motors placed in the prosthetic limb are presented. The voltage variations obtained from the prosthetic limb is almost similar to that of the normal limb for all the gait phases. It is observed that the prosthetic limb is capable to perform the synchronized gait pattern for people with transtibial amputations with changed value of potential outcome due to changes in the angular measurement.

Table 2. Gait output voltage variation in the Normal right limb (rotary encoder), the prosthetic left limb (Servo motor) and the Normal left limb.

Sl. No.	Gait Phases	Movement Output of the Normal Right Limb (Volt)		Movement Output of the Prosthetic Left Limb (Volt)		Movement Output in the Normal Left Limb (Volt)		Output Deviation between Prosthetic Left Limb and Normal Left Limb (Volt)	
		Knee Joint (R.E _{knee})	Ankle Joint (R.E _{ankle})	Knee Joint (M _{knee})	Ankle Joint (M _{ankle})	Knee Joint	Ankle Joint	Knee Joint	Ankle Joint
1	Heelstrike	5.1	5.1	5.5	5.3	5.7	5.0	0.2	0.3
2	Footflat	5.0	5.2	5.1	5.1	5.0	5.5	0.1	0.4
3	Midstance	4.9	6.2	5.2	5.1	5.4	5.3	0.2	0.2
4	Pushoff	4.9	4.9	5.3	5.2	5.2	5.2	0.1	0.0
5	Acceleration	4.9	4.1	5.4	5.4	5.4	5.2	0.0	0.2
6	Mid-swing	4.8	4.2	5.6	5.2	5.3	5.3	0.3	0.1
7	Deceleration	4.9	4.2	5.5	5.3	5.4	5.3	0.3	0.2

The knee and ankle joint movements of the prosthetic limb show a balanced condition during walking or the steps in a single gait cycle. In each and every step, the angular motion and output voltage values were compared with the normal limb's movement to represent the difference. For all the gait phases, the voltage deviation was much less, such as below 0.5.

Mathematical model generation is required to present the behavioral characteristics of the designed system, as shown in Figure 6. The stability improvement of the designed lower limb prosthesis is essential for balanced walking.

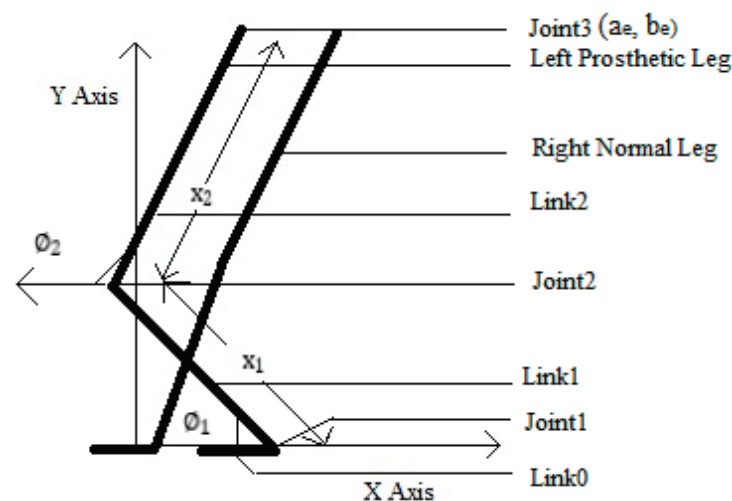


Figure 6. Schematic normal and prosthetic lower extremities with length and angular variations.

The postures of sitting and standing were observed for designing the most suitable system for people with lower limb activity challenges. Two specific cases of angular limb motions and lengths of upper and lower links of the lower extremity are shown in Table 3.

Table 3. Measurements of upper and lower links of a designed lower limb for two specific cases of limb motions with respect to the ground.

SL. No.	Posture Condition of Limb	Length of Lower Link	Length of Upper Link	Angle of Lower Link	Angle of Lower Link
		x_1 (Inches)	x_2 (Inches)	φ_1 (Degrees)	φ_2 (Degrees)
01	Sitting	16	18	52	22
02	Standing	16	18	87	89

3.1. The Sitting Condition as Case I (17.5 Inches from the Floor)

Measurements were acquired from the lower limb utilizing standard measuring apparatuses such as a ruler and a goniometer to measure the angular variation considering a schematic structure of a normal and prosthetic lower limb system, as shown in Figure 6. In this schematic diagram, a human lower limb is shown. Three joints and three links are presented in the diagram. The first (joint 1), second (joint 2) and third joints (joint 3) represent the ankle joint, the knee joint and the hip joint, respectively. The hip joint is connected to the upper half of the body. The first link (link 0) represents the feet, the second link (link 1) represents the lower half of the leg and the third link (link 2) represents the upper half of the leg. The coordinate [6] of the hip joint is (a_e, b_e) and the joint displacements in angular forms are $(\varnothing_1, \varnothing_2)$, as given by the kinematic [7,8] Equations (1) and (2), as given below.

$$a_e(\varnothing_1, \varnothing_2) = x_1 \cos \varnothing_1 + x_2 \cos(\varnothing_1 + \varnothing_2) \quad (1)$$

$$b_e(\varnothing_1, \varnothing_2) = x_1 \sin \varnothing_1 + x_2 \sin(\varnothing_1 + \varnothing_2) \quad (2)$$

The acquired measurements of the designed lower limb are given below:

x_1 = lower link length between knee and ankle joints = 16 inches;

x_2 = upper link length between knee and hip joint = 18 inches;

a_e = angle between the lower link and x axis for joint 1 = 52° ;

b_e = angle between the lower link and x axis for joint 2 = 22° .

After putting the measurement from Table 3 in Equations (1) and (2), Equations (3) and (4) are achieved. For the conditions sitting and standing, the mathematical model presents the information of the coordinate of the hip joint in Equations (3) and (4) as shown below.

$$a_e(\varnothing_1, \varnothing_2) = 0.4831 \quad (3)$$

$$b_e(\varnothing_1, \varnothing_2) = -1.9466 \quad (4)$$

The hip joint coordinate is (0.4831, -1.9466) as per Equations (3) and (4). This mathematical analysis regarding the motions of the knee and ankle joints at the sitting condition and the resultant condition is the necessary output. The outcome is achieved from the total derivatives of the earlier-mentioned kinematic Equations (1) and (2):

(a_e, b_e) is the variable of both $(\varnothing_1, \varnothing_2)$. Therefore, the incorporation of two partial derivatives are utilized in the total process of calculation. The vector form of the position coordinate and angular variations is shown in Equation (5).

Using the method described in [12], J is obtained as a 2×2 matrix as given below.

$$J = \begin{bmatrix} -33.5186 & -17.7326 \\ 0.4831 & 3.0909 \end{bmatrix} \quad (5)$$

where J = linear velocity of the system.

3.2. The Standing Condition as Case II

The acquired measurements of the designed lower limb were $x_1 = 16$ inches, $x_2 = 18$ inches; $\theta_1 = 87^\circ$; and $\theta_2 = 89^\circ$ for standing.

Similarly, J (linear velocity) [12] is a 2×2 matrix as shown in Equation (6), given by

$$J = \begin{bmatrix} -11.8755 & -1.2735 \\ 27.0708 & 17.9548 \end{bmatrix} \quad (6)$$

The matrix gives mathematical expression of the partial derivatives of the functions $a_e(\theta_1, \theta_2)$, $b_e(\theta_1, \theta_2)$ related to the joint displacements regarding angular changes as (θ_1, θ_2) in Equations (5) and (6). The matrix J presents the Jacobian Matrix.

3.3. Characteristic Equation Generation of Designed Prosthetic Limb from Jacobian Matrix

The obtained characteristic polynomial for case I can be obtained using the matrix method described in [12] from the Jacobian Matrix as given in Equation (5).

The achieved polynomial is as given below [12]:

$$f_1(t) = t^2 + 30.4277t + 112.1692 \quad (7)$$

In case II, in a similar way, the characteristic polynomial can be obtained using the Jacobian matrix given in Equation (6):

The achieved polynomial is as given below

$$f_2(t) = t^2 - 29.8303t + 178.7476 \quad (8)$$

The achieved characteristic equations of the designed system show the nonlinear presentation of the designed artificial leg.

The closed loop transfer function of the designed prosthetic limb is given below

$$G_{CLP} = \frac{9.904e27s^2 + 3.013e29s + 1.111e30}{1.981e28s^2 - 5.916e27s + 2.881e30} \quad (9)$$

The closed loop transfer function of the normal limb as developed by the authors is given below [12]

$$G_{CLN} = \frac{2.815e14s^2 + 7.216e15s + 2.602e16}{5.629e14s^2 - 1.256e16s + 3.109e16} \quad (10)$$

3.4. Lyapunov Stability Analysis of Designed Prosthetic Lower Limb

The Lyapunov stability [20] analysis is proposed for the nonlinear system stability analysis of the designed prosthetic limb, as mentioned in Equation (9).

$$\text{Since } e(s)G_c(s) \cdot G_p(s) = Y(s) \quad (11)$$

and $r(s) - y(s) = e(s)$, and assuming $r(s) = 0$, it can be stated that $y(s) = -e(s)$.

In this instance, $r(s)$ = reference input, $y(s)$ = system output and $e(s)$ = error value, $G_c(s)$ = controller transfer function and $G_p(s)$ = process transfer function. Now, the mathematical model is shown in Equation (12) according to Equation (11).

$$e(s)(9.904e27s^2 + 3.013e29s + 1.111e30) = -e(s)(1.981e28s^2 - 5.916e27s + 2.881e30) \quad (12)$$

Using Inverse Laplace Transform, the transfer function is shown in Equation (13)

$$(9.904e27\ddot{e} + 3.013e29\dot{e} + 1.111e30e) = 0 \quad (13)$$

Now, taking the scalar positive definite function, which is given by

$$V(x) = \frac{1}{2}S_1 \cdot x_1^2 + \frac{1}{2}S_2 \cdot x_2^2 + \frac{1}{2}S_3 \cdot x_3^2 \quad (14)$$

where $S_1 > 0, S_2 > 0$.

Now, taking the derivative with respect to time, t , yields

$$\dot{V}(x) = S_1 \cdot x_1 \cdot x_2 + x_2 \cdot x_3 (S_2 - b_1 \cdot S_3) - x_3 \cdot (a_1 \cdot S_3 \cdot x_3 + c_1 \cdot S_3 \cdot x_1) \quad (15)$$

For the positive definite function V , another positive definite function U is needed such that $\dot{V}(x) = -U(x)$. Now, the coefficients are taken in such a manner that $\dot{V}(x) = -U(x)$. Therefore, it is taken as

$$(S_2 - b_1 \cdot S_3) = 0 \quad (16)$$

$$S_1 = 0 \quad (17)$$

Now, substituting Equations (16) and (17) in Equation (15) and also $\dot{V}(x) = 0$, $V(x) \rightarrow \infty$ as $x \rightarrow \infty$ and $\dot{V}(x) = 0$ are obtained. A way of showing that $\dot{V}(x)$ being negative semi-definite is sufficient for asymptotic stability is to show that the x axis is not a trajectory of the system. For $\dot{x}_1 = \dot{x}_2 = 0$ and $\dot{x}_2 = \dot{x}_3 = 0$, it is shown that $x_1 = m$ (constant). The equilibrium state at the origin of the system is asymptotically stable. Therefore, the mentioned system in this work is asymptotically stable. The overall control law design and development of the efficient system for artificial lower limbs is the main focus of the work.

In Figure 7 from Equations (9) and (10) in Section 3.3 the output of the normal limb compared with that of the designed prosthetic limb is shown, where the normal limb system is mentioned as sys with a red line and the prosthetic limb system is mentioned as sys1 with a yellow line.

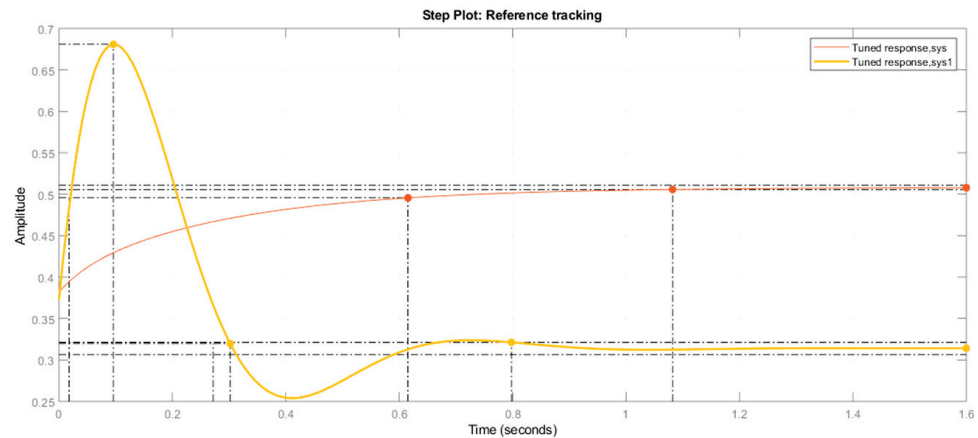


Figure 7. Graphical Presentation of Designed Normal Limb (sys) and Prosthetic Lower Limb (sys1) without tuning.

The system stability improvement was performed through a PIDF2 controller. In Figure 8, the output of the normal limb compared with that of the designed prosthetic limb, where the normal limb system is mentioned as sys with a red line and the prosthetic limb system is mentioned as sys1 with a yellow line.

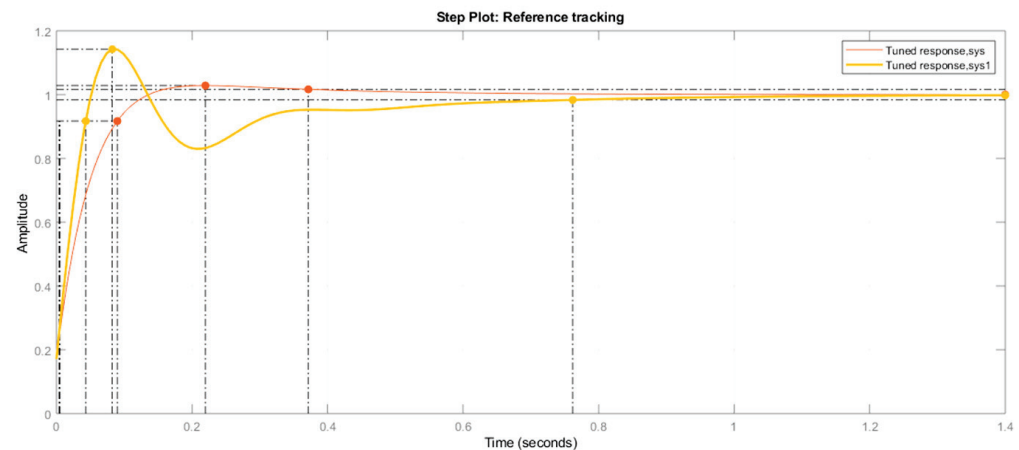


Figure 8. Graphical Presentation of Normal Limb (sys) and Designed Prosthetic Lower Limb (sys1), with PIDF2 (2 Degrees of Freedom type) Controller with tuning.

According to Table 4, the rise time has changed in the tuned condition of the designed prosthetic lower limb system. The settling time is decreased in the designed limb's dynamic characteristics, which indicates that after tuning stabilized output is obtained within a comparatively shorter period of time. The overshoot was decreased in the designed prosthetic limb where better stability was achieved, as a minimum time was needed to reach the required output. The peak value had a notable difference in between two mentioned systems such as the designed and the tuned systems. The change in the response time was recognizable after the PIDF2 type controller application on this 2DoF system. The proportional constant was lesser after tuning the designed system. This type of controller is suitable to use in this nonlinear system stability analysis as the system behavior is non-deterministic. After observing the graphical presentations and the characteristics values in Figures 7 and 8, the PIDF2 controller showed suitable nonlinear system stability with the dynamic characteristics of the designed prosthetic lower limb.

Table 4. Performance and Robustness Parameters of the Normal and the Designed Prosthetic Lower Limb using a PIDF2 Controller.

Tuning Condition	Rise Time (Seconds)	Settling Time (Seconds)	Overshoot (%)	Peak	Proportional Constant (K_p)	Integral Constant (T_i)	Derivative Constant (K_d)	Response Time (Seconds)	Transient Behavior
Without tuning	0.0302	0.798	117	0.681	1.1864	NA	NA	0.3515	0.6
With tuning	0.0393	0.762	14.2	1.14	0.41239	0.0084228	0	0.05571	0.6

4. Conclusions and Future Scopes

The locomotion control of the artificial lower limb movement of the gait cycle of a human being with the help of a kinesiological joint movement signal has been implemented in the present work. Gait synchronization of the prosthetic limb with sound lower limb movement has been performed. The Range of Motion (RoM) analysis for the artificial limb movement was made for the gait pattern implementation compared with the normal limb's motion features. The angular output of the designed prosthetic and normal knee joints differed in a range from 2 to 7 degrees and that of the ankle joints from 0 to 5 degrees. The voltage output of the built prosthetic and normal knee joints differed in a range from 0.1 to 0.3 volts and that of the ankle joints from 0.2 to 0.4 volts. The obstacle handling was incorporated with the artificial lower limb with body balancing attributes. The kinematic artificial system design and mathematical model generation is the most unexplored method utilized in this model design. The nonlinear stability analysis of the designed prosthetic limb was performed using a Lyapunov stability method suitable for system behavioral analysis, and

asymptotic stability was achieved. The use of PIDF2 controller improved the stability of the designed artificial limb system with proper adjustment of the tuning parameters.

A system design with better Degrees of Freedom is the future challenge. Analysis of leg types with different body weights and, according to that, servo motor movement analysis for robot-legs can be explored. The obstruction avoidance capability during motion can be added as special feature of this unilateral transtibial lower limb.

Author Contributions: Conceptualization, S.D. and B.N.; methodology, S.D. and D.N.; software, S.D.; validation, S.D.; formal analysis, S.D.; investigation, S.D.; resources, S.D.; data curation, S.D.; writing—original draft preparation, S.D.; writing—review and editing, S.D. and D.N.; visualization, S.D.; supervision, D.N. and B.N.; project administration, B.N.; funding acquisition, S.D. All authors have read and agreed to the published version of the manuscript.

Funding: This research received no external funding.

Institutional Review Board Statement: Not applicable.

Informed Consent Statement: Not applicable.

Data Availability Statement: Not applicable.

Acknowledgments: The authors are thankful for the support of the Indian Institute of Information Technology Kalyani.

Conflicts of Interest: The authors declare no conflict of interest.

References

1. de Miguel-Fernández, J.; Lobo-Prat, J.; Prinsen, E.; Font-Llagunes, J.M.; Marchal-Crespo, L. Control strategies used in lower limb exoskeletons for gait rehabilitation after brain injury: A systematic review and analysis of clinical effectiveness. *J. Neuroeng. Rehabil.* **2023**, *20*, 23. [CrossRef] [PubMed]
2. Tran, M.; Gabert, L.; Hood, S.; Lenzi, T. A lightweight robotic leg prosthesis replicating the biomechanics of the knee, ankle, and toe joint. *Sci. Robot.* **2022**, *7*, eabo3996. [CrossRef] [PubMed]
3. Yu, C.; Ye, J.; Jia, J.; Zhao, X.; Chen, Z.; Chen, J. Design, Synthesis, and Experiment of Foot-Driven Lower Limb Rehabilitation Mechanisms. *J. Mech. Robot.* **2021**, *14*, 021001. [CrossRef]
4. Asif, M.; Tiwana, M.I.; Khan, U.S.; Qureshi, W.S.; Iqbal, J.; Rashid, N.; Naseer, N. Advancements, Trends and Future Prospects of Lower Limb Prosthesis. *IEEE Access* **2021**, *9*, 85956–85977. [CrossRef]
5. Penzlin, B.; Bergmann, L.; Li, Y.; Ji, L.; Leonhardt, S.; Ngo, C. Design and First Operation of an Active Lower Limb Exoskeleton with Parallel Elastic Actuation. *Actuators* **2021**, *10*, 75. [CrossRef]
6. Azizi, M.R.; Rastegarpanah, A.; Stolkin, R. Motion Planning and Control of an Omnidirectional Mobile Robot in Dynamic Environments. *Robotics* **2021**, *10*, 48. [CrossRef]
7. Zhang, Y.; Wang, E.; Wang, M.; Liu, S.; Ge, W. Design and Experimental Research of Knee Joint Prosthesis Based on Gait Acquisition Technology. *Biomimetics* **2021**, *6*, 28. [CrossRef] [PubMed]
8. Das, S.; Nandi, D.; Neogi, B. A Gait Synchronized and Body Kinesics Controlled Prosthetic System for Lower Extremity Amputation. Patent 202131050624A, 16 June 2022.
9. Abu-Dakka, F.J.; Valera, A.; Escalera, J.A.; Abderrahim, M.; Page, A.; Mata, V. Passive Exercise Adaptation for Ankle Rehabilitation Based on Learning Control Framework. *Sensors* **2020**, *20*, 6215. [CrossRef] [PubMed]
10. Park, K.; Ahn, H.-J.; Lee, K.-H.; Lee, C.-H. Development and Performance Verification of a Motorized Prosthetic Leg for Stair Walking. *Appl. Bionics Biomech.* **2020**, *2020*, 8872362. [CrossRef] [PubMed]
11. Das, S.; Das, D.N.; Neogi, B. Design Approach for Artificial Human Ankle Movement. In Proceedings of the 2019 Devices for Integrated Circuit (DevIC), Kalyani, India, 23–24 March 2019; pp. 404–407. [CrossRef]
12. Shi, D.; Zhang, W.; Zhang, W.; Ding, X. A Review on Lower Limb Rehabilitation Exoskeleton Robots. *Chin. J. Mech. Eng.* **2019**, *32*, 74. [CrossRef]
13. Zahedi, M.S.; Stech, N.; Moser, D.; Sykes, A.J. Lower Limb Prosthesis with Knee Flexion Control During Descent of A Downward Incline. US Patent 10,285,827, 14 May 2019.
14. Das, S.; Das, D.N.; Neogi, B. Lower Limb Movement Analysis for Exoskeleton Design. In Proceedings of the 2019 IEEE Region 10 Symposium (TENSYP), Kolkata, India, 7–9 June 2019; pp. 759–764. [CrossRef]
15. Du, Y.; Wang, H.; Qiu, S.; Yao, W.; Xie, P.; Chen, X. An Advanced Adaptive Control of Lower Limb Rehabilitation Robot. *Front. Robot. AI* **2018**, *5*, 116. [CrossRef] [PubMed]
16. Fairley, J.; Warder, H.; Coutts, J. Modular Lower Limb Prosthesis System. US Patent App. 15/947,444, 11 October 2018.

17. Maddison, R.; Gemming, L.; Monedero, J.; Bolger, L.; Belton, S.; Issartel, J.; Marsh, S.; Direito, A.; Solenhill, M.; Zhao, J.; et al. Quantifying Human Movement Using the Moven Smartphone App: Validation and Field Study. *JMIR Mhealth Uhealth* **2017**, *5*, e122. [CrossRef] [PubMed]
18. Cherelle, P.; Grosu, V.; Flynn, L.; Junius, K.; Moltedo, M.; Vanderborght, B.; Lefeber, D. The Ankle Mimicking Prosthetic Foot 3—Locking mechanisms, actuator design, control and experiments with an amputee. *Robot. Multibody Mech. Dep. Mech. Eng. Vrije Univ. Bruss. Belg. Flanders Make Bel-Gium Robot. Auton. Syst.* **2017**, *91*, 327–336. [CrossRef]
19. Mortazavi, F.; Nadian-Ghomsheh, A. Stability of Kinect for range of motion analysis in static stretching exercises. *PLoS ONE* **2018**, *13*, e0200992. [CrossRef] [PubMed]
20. Piazza, C.; Della Santina, C.; Gasparri, G.M.; Catalano, M.G.; Grioli, G.; Garabini, M.; Bicchi, A. Toward an adaptive foot for natural walking. In Proceedings of the 16th IEEE-RAS International Conference on Humanoid Robots, Cancun, Mexico, 15–17 November 2016; pp. 1204–1210.
21. Koller, J.R.; Jacobs, D.A.; Ferris, D.P.; Remy, C.D. Learning to walk with an adaptive gain proportional myoelectric controller for a robotic ankle exoskeleton. *J. Neuroeng. Rehabil.* **2015**, *12*, 97. [CrossRef] [PubMed]
22. Liu, Z.; Huang, D.; Xing, Y.; Zhang, C.; Wu, Z.; Ji, X. New Trends in Non-linear Control Systems and Applications. *Abstr. Appl. Anal.* **2015**, *2015*, 637632. [CrossRef]
23. Kawakami, T.; Hosoda, K. Bipedal walking with oblique mid-foot joint in foot. In Proceedings of the IEEE International Conference on Robotics and Biomimetics, Zhuhai, China, 6–9 December 2015; pp. 535–540.
24. Khansari-Zadeh, S.M.; Billard, A. Learning Control Lyapunov Function to Ensure Stability of Dynamical System-based Robot Reaching Motions. *Robot. Auton. Syst.* **2014**, *62*, 752–765. [CrossRef]

Disclaimer/Publisher’s Note: The statements, opinions and data contained in all publications are solely those of the individual author(s) and contributor(s) and not of MDPI and/or the editor(s). MDPI and/or the editor(s) disclaim responsibility for any injury to people or property resulting from any ideas, methods, instructions or products referred to in the content.

Article

EMG and IMU Data Fusion for Locomotion Mode Classification in Transtibial Amputees

Omar A. Gonzales-Huisa ¹, Gonzalo Oshiro ², Victoria E. Abarca ³, Jorge G. Chavez-Echajaya ⁴ and Dante A. Elias ^{3,*}

¹ Faculty of Science and Engineering, Electronic Engineering, Pontificia Universidad Católica del Perú, Lima 15088, Peru; gonzales.omar@pucp.edu.pe

² Faculty of Science and Engineering, Mechatronics Engineering, Pontificia Universidad Católica del Perú, Lima 15088, Peru; gonzalo.oshiro@pucp.edu.pe

³ Biomechanics and Applied Robotics Research Laboratory, Pontificia Universidad Católica del Perú, Lima 15088, Peru; victoria.abarca@pucp.edu.pe

⁴ Faculty of Science and Engineering, Biomedical Engineering, Pontificia Universidad Católica del Perú, Lima 15088, Peru; jorge.chaveze@pucp.edu.pe

* Correspondence: delias@pucp.pe

Abstract: Despite recent advancements in prosthetic technology, lower-limb amputees often remain limited to passive prostheses, which leads to an asymmetric gait and increased energy expenditure. Developing active prostheses with effective control systems is important to improve mobility for these individuals. This study presents a machine-learning-based approach to classify five distinct locomotion tasks: ground-level walking (GWL), ramp ascent (RPA), ramp descent (RPD), stairs ascent (SSA), and stairs descent (SSD). The dataset comprises fused electromyographic (EMG) and inertial measurement unit (IMU) signals from twenty non-amputated and five transtibial amputated participants. EMG sensors were strategically positioned on the thigh muscles, while IMU sensors were placed on various leg segments. The performance of two classification algorithms, support vector machine (SVM) and long short-term memory (LSTM), were evaluated on segmented data. The results indicate that SVM models outperform LSTM models in accuracy, precision, and F1 score in the individual evaluation of amputee and non-amputee datasets for 80–20 and 50–50 data distributions. In the 80–20 distribution, an accuracy of 95.46% and 95.35% was obtained with SVM for non-amputees and amputees, respectively. An accuracy of 93.33% and 93.30% was obtained for non-amputees and amputees by using LSTM, respectively. LSTM models show more robustness and inter-population generalizability than SVM models when applying domain-adaptation techniques. Furthermore, the average classification latency for SVM and LSTM models was 19.84 ms and 37.07 ms, respectively, within acceptable limits for real-time applications. This study contributes to the field by comprehensively comparing SVM and LSTM classifiers for locomotion tasks, laying the foundation for the future development of real-time control systems for active transtibial prostheses.

Citation: Gonzales-Huisa, O.A.; Oshiro, G.; Abarca, V.E.; Chavez-Echajaya, J.G.; Elias, D.A. EMG and IMU Data Fusion for Locomotion Mode Classification in Transtibial Amputees. *Prosthesis* **2023**, *5*, 1232–1256. <https://doi.org/10.3390/prosthesis5040085>

Academic Editor: Arnab Chanda

Received: 20 October 2023

Revised: 15 November 2023

Accepted: 16 November 2023

Published: 21 November 2023

Keywords: electromyography; inertial sensor; long short-term memory; support vector machine; transtibial prosthesis



Copyright: © 2023 by the authors. Licensee MDPI, Basel, Switzerland. This article is an open access article distributed under the terms and conditions of the Creative Commons Attribution (CC BY) license (<https://creativecommons.org/licenses/by/4.0/>).

1. Introduction

The number of patients undergoing amputations is increasing annually in the Western world, with 90% of these cases related to lower-limb amputations [1] (p. 5). In the United States, it is estimated that over 185,000 individuals experience some form of amputation each year [2], with more than 150,000 of these cases involving lower-limb amputations [3]. Lower-limb amputations are a significant cause of locomotor [4] and functional difficulty for the individual, leading to physical, psychological, family, and personal impacts [5]. Additionally, it has been observed that in transtibial amputees, the loss of ankle power

generation increases metabolic energy costs by 20–30% [6]. This situation raises the risk of musculoskeletal problems and falls [7].

Despite advances in prosthetic technology in recent years, many people with lower-limb amputations are limited to passive prostheses that result in asymmetric gait and require more significant energy expenditure from the user [6,8]. The incapacity of passive prostheses to generate energy limits the abilities of both transfemoral and transtibial amputees to move appropriately during daily activities [9]. Tasks such as ascending ramps or climbing stairs require net-positive power outputs that are not entirely achievable with passive prostheses [10].

In order to address these challenges, the development of active prosthetics has become one of the primary objectives [8,10]. These prosthetics must be able to deliver the appropriate power and mechanical torque, potentially assisting amputees in various locomotion activities, not limited exclusively to level walking [9]. Developing a control system that allows a transtibial prosthesis to replicate the walking abilities of a healthy individual and adapt naturally to different terrains remains a significant challenge [11]. For some commercially available active lower-limb prostheses, amputees need to instruct their motion intention to the prosthesis through buttons or by executing a non-natural movement [12]. Therefore, it is necessary to develop control systems containing algorithms that can automatically detect a user's movement intention during various locomotion activities to manage an active transtibial prosthesis [13,14].

The commonly used sensors for movement intention recognition are electromyography (EMG) sensors or inertial measurement units (IMU) [4]. EMG sensors have the potential to achieve a high range of voluntary control over the prosthesis and represent the earliest signal that can be extracted during motor activities [15]. On the other hand, using IMU sensors allows for identifying the gait cycle phase in conjunction with other mechanical sensors like contact switches or load cells [11,12,15]. Some studies have fused the data provided by both types of sensors, as seen in the case of Barberi et al. [15], who developed a locomotion task classification algorithm for transfemoral prosthesis comparing support vector machine (SVM) algorithms with a linear or second-order polynomial kernel. Four EMG sensors located in the muscles of the amputated leg, three IMU sensors, and contact switches for data collection were used to achieve an accuracy greater than 94%. Zhou et al. [16] fused data from three EMG signals and one IMU inertial signal to develop an ankle-movement-recognition system on non-amputees. Different algorithms were compared in this study, with SVM being the traditional algorithm with the best performance and bi-directional long short-term memory (BiLSTM) being the algorithm with the overall best performance at 99.8%. Meng et al. [17] collected EMG and inertial signals from ten non-amputee subjects to train classification algorithms for seven locomotion activities. They performed a fusion of EMG and IMU data and tested it on four classification algorithms: support vector machine (SVM), K-nearest neighbor (KNN), artificial neural network (ANN), and linear discriminant analysis (LDA). The fusion of the EMG signals improved the accuracy of steady-state locomotion-activity recognition by using SVM from 90% (using only acceleration data) to 98% (using the data fusion of EMG + IMU). Hu et al. [18] propose using their dataset to develop control strategies for motion-intention recognition by using EMG and IMU data-fusion techniques focused on machine learning classification. Given the ongoing introduction of new sensors, the fusion of technologies for motion recognition is a hotspot in the field of prosthetic-control research [16].

The existing literature includes studies that evaluate ankle movements in transtibial amputees by using EMG sensors placed on muscles of the leg segment (such as the tibialis anterior and gastrocnemius) [19,20]. However, the majority of transtibial amputees, especially in developing countries, use a socket-suspended prosthesis [21,22]. This socket type makes it challenging to position EMG sensors and increases the risk of displacement by constant friction [6]. Additionally, comparative studies involving SVM and LSTM have been found, but the participants evaluated are people without any mobility impairment or locomotion disorder [7,16,17].

This study illustrates the influence of integrating EMG and IMU signal data on classifying five locomotion tasks among individuals with and without transtibial amputations. The evaluated locomotion activities include walking on a flat surface, an incline/decline ramp, and ascending/descending stairs. A comparison between two classification models, support vector machine (SVM) and long short-term memory (LSTM), both of which have shown optimal results in previous research, is presented [6,7,14–17]. The significant contributions of this work are as follows:

- The fusion of two critical signals, EMG and IMU, significantly enhanced locomotion task classification.
- A comprehensive comparison between two powerful classification models, SVM and LSTM, tailored explicitly for transtibial amputees across a spectrum of locomotion activities.
- A methodology to identify the most representative muscles on the thigh in the gait cycle of individuals with transtibial amputations who use prosthetic sockets on the residual limb was elaborated.
- The use of domain-adaptation techniques to enhance the developed models' adaptability and robustness, ensuring the models' reliability and effectiveness across diverse locomotion patterns.

2. Materials and Methods

2.1. Experiment Setup

This study was conducted at the Biomechanics and Applied Robotics Laboratory at the Pontificia Universidad Católica del Perú. It was approved by the Ethics Committee for Research in Life Sciences and Technologies of the same institution (approval number 073-2023-CEICVyT/PUCP). A total of 5 male participants with transtibial amputations (Group A) and 24 participants without amputations (12 males and 12 females, Group B) were recruited for this study. Group A had an average age of 38.6 ± 16.36 years, weight of 76.00 ± 11.64 kg, and height of 172.04 ± 6.24 cm. Table 1 shows more detailed background information for this group. Group B had an average age of 22.125 ± 2.51 years, weight of 62.56 ± 11.39 kg, and height of 164.92 ± 9.34 cm. All the participants provided written informed consent before the experiment.

Table 1. Transtibial amputee subjects' characteristics (age, height, weight, amputated side, years since amputation, and current prosthesis).

Participant	Age (Years)	Height (cm)	Weight (kg)	Amputated Side	Year since Amputation	Current Prosthesis
Amputee 01	58	167	66	Right	17 years/2006	Transtibial prosthesis with acrylic sock-type socket with liner and rigid foot
Amputee 02	50	167	79	Left	5 years/2018	Transtibial plastic socket type prosthesis without liner and articulated foot
Amputee 03	24	170	70	Right	1.5 years/2022	Transtibial fiberglass prosthesis with resin, socket type with liner and articulated foot
Amputee 04	20	174	70	Right	2 years/2021	Transtibial carbon fiber socket-type prosthesis with liner and rigid foot
Amputee 05	41	182	95	Right	12 years/2011	Transtibial carbon fiber socket-type prosthesis with liner and rigid foot

Selection criteria were established to ensure that participants in both groups met the requirements for this study. For Group A, the inclusion criteria included a minimum stump length of 12.7 cm, possession of a well-maintained transtibial prosthesis, the ability to walk independently, and a non-congenital amputation. For Group B, the inclusion criteria included regular physical activity to facilitate the identification of evaluated muscles and the absence of any motor or pathological limitation significantly affecting their gait. A licensed occupational therapist provided support in validating the selection criteria. All participants underwent an evaluation to confirm that they met the selection criteria. These criteria were established to ensure that the study results were valid and reliable and that the participants represented the target population.

EMG signals were captured from four muscles in the right thigh, as shown in Table 2 and Figure 1: rectus femoris (RF), biceps femoris (BF), tensor fascia latae (TF), and adductor longus (AL). In addition, IMU signals were captured from the sensor placed on the rectus femoris (RF), the tibia (TB), and the instep on the foot (FT) [15]. The sensors were placed on the muscles through palpation while participants performed specific muscle activation movements, as detailed in Table 2. A set of six Trigno Avanti wireless non-invasive surface sensors from DELSYS was used for this purpose [23].

Table 2. Movements for muscle detection during EMG sensor positioning.

Muscle	Movement
Rectus femoris (RF)	With the hip slightly flexed, perform knee extension movements.
Biceps femoris (BF)	With the hip slightly extended, perform knee flexion movements, bringing the heel towards the gluteus.
Tensor fasciae latae (TF)	Perform hip abduction movements from a natural position.
Adductor Longus (AL)	With the feet at hip level, rest the inside edge of the foot against the floor.

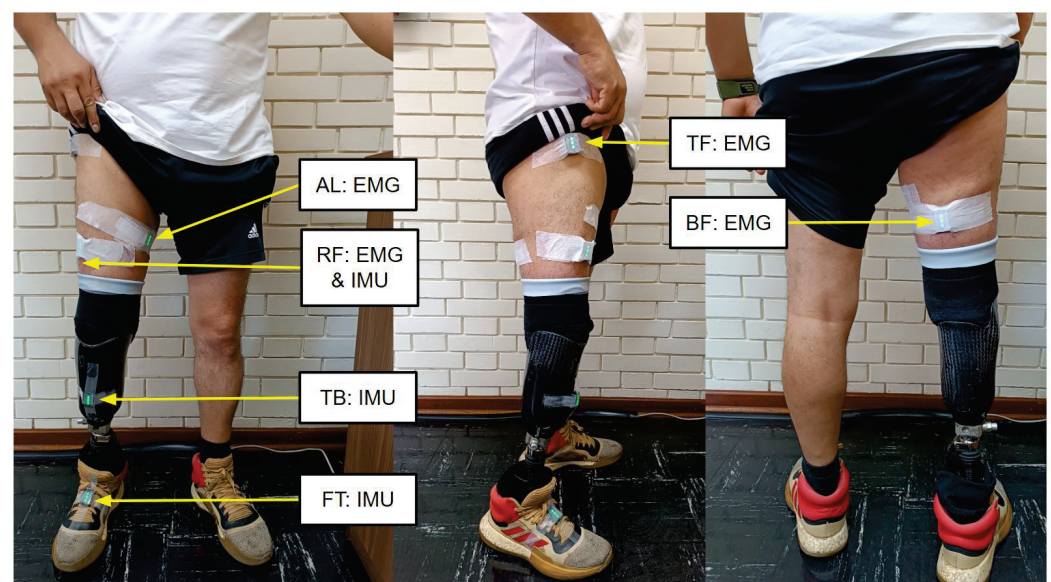


Figure 1. Experiment setup for data collection. The participant wore a set of sensors. EMG electrodes were placed on four muscles—rectus femoris (RF), biceps femoris (BF), tensor fascia latae (TF), and adductor longus (AL). Inertial sensors were placed on the rectus femoris (RF), tibia (TB), and the foot (FT).

2.2. Experimental Protocol and Tests

Before starting data collection, the sensors were positioned and the participants were instructed to perform short walks to verify the correct capture of the signals by the sensors. Once the proper functioning of the sensors was confirmed, data collection proceeded. Five

locomotion activities were addressed in this study, namely ground-level walking (GLW), ramp ascent (RPA), ramp descent (RPD), stairs ascent (SSA), and stairs descent (SSD). Activities were performed in three different common-use environments. A six-meter ramp with a 7° slope was designated as the first environment for up/down walking activities. A 10 m flat surface was selected as the second environment for ground-level walking. Finally, 11 steps, each 16 cm high, were designated as the third environment for the stair ascent and descent trials. It should be noted that the environments comply with the A.120 standard of the Ministry of Housing, Construction and Sanitation of the Peruvian government [24]. Each activity was repeated ten times, totaling 50 tests per participant. The participants completed each test at a walking speed that was comfortable for them. A participant undergoing data-collection trials is shown in Figure 2.

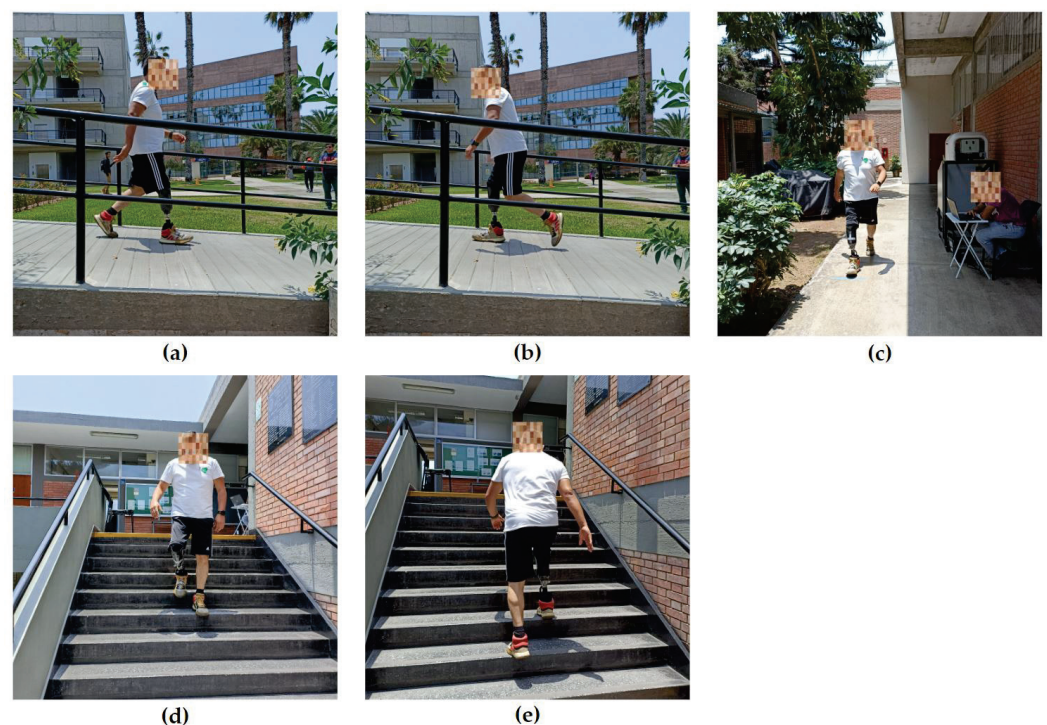


Figure 2. Participant undergoing data-collection trials. (a) Ramp ascent; (b) ramp descent; (c) ground-level walking; (d) stair ascent; (e) stair descent.

2.3. Data Processing

The raw EMG signals were collected at a sampling frequency of 1259 Hz, capturing a range of ± 5.5 mV and using a band-pass filter of 20–450 Hz. The inertial signals were collected at a sampling rate of 148 Hz, with an accelerometer range of ± 16 g and a gyroscope range of ± 2000 dps. All the sensors were configured as EMG+IMU in the data-acquisition EMGWorks Acquisition software version 4.8.0, developed by Delsys, to capture both electromyographic and inertial signals. Figure 3 shows an example of the EMG signals captured during the stair descent of a participant with a transtibial amputation, and Figure 4 shows an example of the EMG signals captured from the same participant during ramp descent.

The Delsys File Utility tool converts the acquired signals from .hpf to .mat format. A MATLAB-R2021a code was developed on a 2x Nvidia GeForce RTX 2080, Intel(R) Core(TM) i7-9700K Processor, and a 64.0 GB RAM computer to organize the raw data from each trial per participant in a way that allows the EMG and IMU information to be visualized by the sensor. Also, the columns not used in the algorithm's training were removed. Each trial per participant contains 16 features, including the EMG signals from the sensors located in the BF, TF, RF, and AL and the inertial signals from the sensors located in the RF, tibia, and foot.

The features from each trial per participant were converted to .csv format for further use in algorithm training. Simultaneously, the EMGWorks Analysis software version 4, developed by Delsys, manually sets each trial's start and end times, ensuring the participant performs the evaluated activity during the segmented time interval.

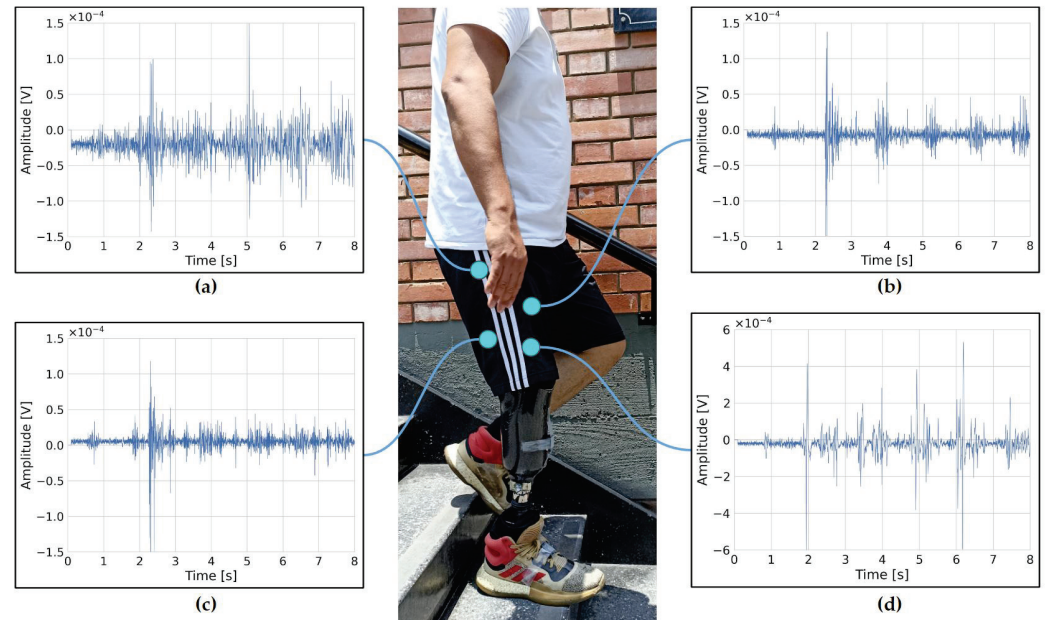


Figure 3. EMG signals of the four muscles evaluated from a transtibial amputation participant while performing the stairs descent task (SSD). (a) Raw EMG signal corresponding to the tensor fasciae latae (TF) muscle. (b) Raw EMG signal corresponding to the adductor longus (AL) muscle. (c) Raw EMG signal corresponding to the biceps femoris (BF) muscle. (d) Raw EMG signal corresponding to the rectus femoris muscle (RF).

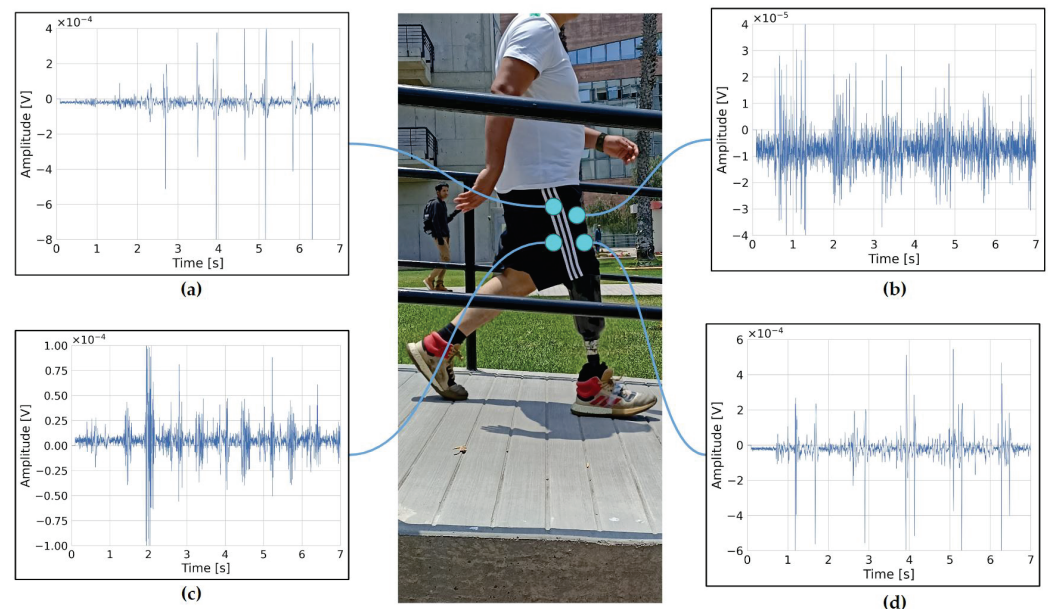


Figure 4. EMG signals of the four muscles evaluated from a participant with a transtibial amputation while performing the task of ramp descending (RPD). (a) Raw EMG signal corresponding to the tensor fasciae latae (TF) muscle. (b) Raw EMG signal corresponding to the adductor longus (AL) muscle. (c) Raw EMG signal corresponding to the biceps femoris (BF) muscle. (d) Raw EMG signal corresponding to the rectus femoris muscle (RF).

A peak-detection algorithm in Python processes the Z-axis acceleration data from the sensor located on the tibia to identify walking cycles within the segmented time interval. Literature-provided data show that the average duration between gait cycles varies between 0.8 and 1.6 s [14], a time-frame set as a constraint for peak detection as shown in Figure 5.

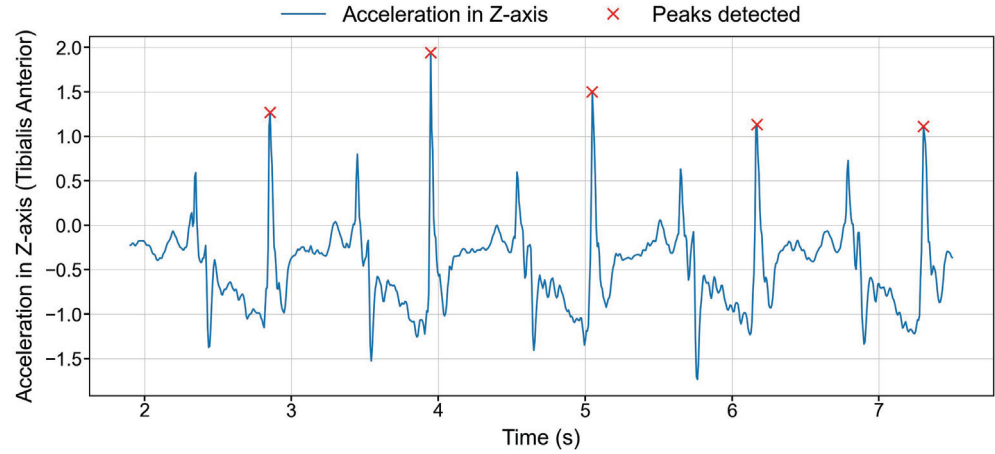


Figure 5. Graph of the Z-axis acceleration from the sensor corresponding to the tibia after being processed by the peak-detection algorithm. The interval between two consecutive 'x' marks corresponds to one gait cycle.

Identifying the gait cycles in each trial allows for segmenting the EMG and IMU data. The EMG and IMU datasets are segmented separately due to their different sampling frequencies. Four features are extracted from the EMG signals, including the mean absolute value (MAV), root mean square (RMS), standard deviation (SD), and waveform length (WL) [25]. The literature review demonstrates the importance of these features in a time-domain analysis [6,15–17,25,26]. In the case of inertial signals, only the MAV is extracted [4,15]. The feature-extracted EMG and IMU description was quantified by Equations (1)–(4):

$$\text{Mean Absolute Value (MAV)} = \frac{1}{N} \sum_{i=1}^N x(t_i) \quad (1)$$

$$\text{Root Mean Square (RMS)} = \sqrt{\frac{1}{N} \sum_{i=1}^N x(t_i)^2} \quad (2)$$

$$\text{Standard Deviation (SD)} = \sqrt{\frac{\sum_{i=1}^N (x_i - \bar{x})^2}{N}} \quad (3)$$

$$\text{Waveform Length (WL)} = \sum_{i=2}^N |x(t_i) - x(t_{i-1})| \quad (4)$$

A shorter EMG window length becomes fundamental for reducing the computational burden overall in tasks where the interaction between the human and the machine requires a real-time actuation [27]. Even though the EMG and IMU signals were sampled with different frequencies, by using a fixed window length of 80 ms [17,27,28] and overlapping of 40 ms for feature extraction, the same amount of data is finally obtained for both signals. These new signals are a low-frequency representation of the original signals. For example, for the RMS calculation, since a data point is obtained every 80 ms, after evaluating the entire trial timeline, the same amount of RMS data will be accepted for both EMG and IMU signals. Figure 6 depicts an example of sequence extractions.

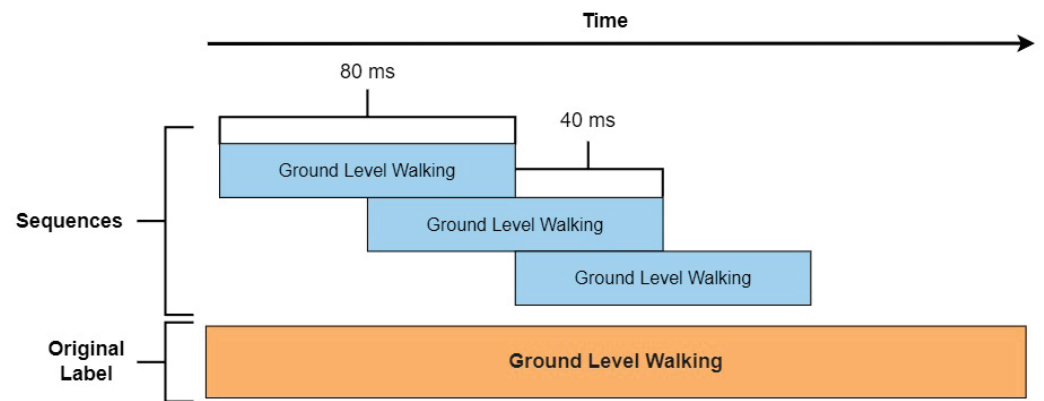


Figure 6. Example of sequence extraction. The gait cycle is represented in orange, and the blue sequences represent data segments of ground-level walking.

2.4. System Architecture

Two algorithms were employed: support vector machine (SVM) and long short-term memory (LSTM). SVM is a classical machine learning algorithm based on hyperplane separation in a higher-dimensional space, which renders it effective for non-linear classification problems. This algorithm has been employed in various studies for its low computational cost and high efficiency [6,14–17]. In this study, an SVM with an RBF kernel is employed. On the other hand, LSTM is a recurrent neural network algorithm whose primary concept involves regulating cell states by using input, forget, and output gates [16]. The architecture for LSTM in this study comprises an input layer followed by a bi-directional LSTM layer with 144 units, succeeded by a Dropout layer with a rate of 0.4. Subsequently, a second bi-directional LSTM layer with 72 units is implemented, followed by a Dropout layer with a rate of 0.4. Next, a dense layer with a ReLU activation function and 16 units is included, followed by a Softmax layer with five outputs for classification. The process followed by the LSTM algorithm is detailed in Figure 7.

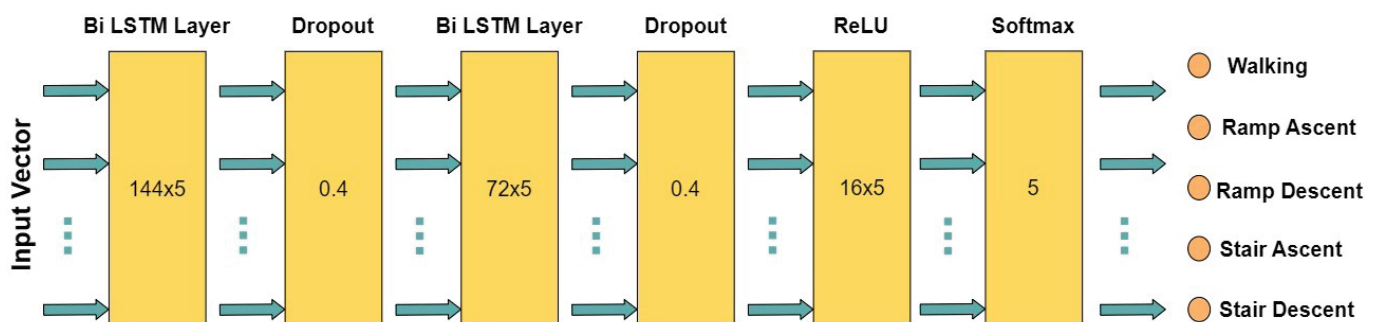


Figure 7. Architecture of the process performed by the LSTM algorithm, separated into layers.

2.5. Data Analysis: Performance Metrics

The proposed classifier model was evaluated by using accuracy, precision (P), recall (R), and the F1 score. *Accuracy* represents the proportion of accurate predictions out of the total predictions made. *Precision (P)* quantifies the proportion of true positives (T_p) that were indeed correct about the total positive predictions, minimizing false positives (F_p). *Recall* quantifies the proportion of true-positive (T_p) cases that the model accurately identified. This metric ensures that any true-positive case is inadvertently overlooked. The *F1 score* represents the proportion between precision (P) and recall (R). It is used for evaluating the algorithm's performance, and its application helps mitigate substantial

imbalances between false positives (Fp) and false negatives (Fn). The performance metrics were quantified by Equations (5)–(8):

$$Accuracy = \frac{Tp + Tn}{Tp + Tn + Fp + Fn} \quad (5)$$

$$Precision = \frac{Tp}{Tp + Fp} \quad (6)$$

$$Recall = \frac{Tp}{Tp + Fn} \quad (7)$$

$$F1\ score = \frac{2PR}{P + R} \quad (8)$$

2.6. Hyperparameters

The primary hyperparameters used during the training of the SVM and LSTM models are described in this subsection. The computer setup is a 2x Nvidia GeForce RTX 2080, Intel(R) Core(TM) i7-9700K Processor, and 64.0 GB RAM.

2.6.1. Selection Methodology

The RandomizedSearchCV and GridSearchCV methodologies were used to acquire the optimal values for the hyperparameters. RandomizedSearchCV randomly groups hyperparameters from a large set and iterates them ten times for training and performance evaluations. The optimal combination of hyperparameters is selected by using five-fold cross-validation. A more specific range of values for the hyperparameters can be chosen due to the outputs of this methodology.

The GridSearchCV methodology exhaustively explores all possible combinations of the reduced set of hyperparameters. Three-fold cross-validation systematically examines each combination for training and validation, ultimately identifying the combination with the best performance.

2.6.2. Hyperparameters Selected for SVM

The kernel in SVM is a mathematical function that transforms data from their original domain to a higher-dimensional feature space. Three prominent kernel types were evaluated: linear, polynomial, and RBF. Among them, the radial basis function (RBF) kernel demonstrated superior performance within the algorithm. Another critical component of the SVM model is the C-SVM, a regularization parameter that dictates the permissible extent of training errors. In this implementation, the C-SVM was set to a value of 10.

2.6.3. Hyperparameters Selected for LSTM

For the LSTM model, several hyperparameters were meticulously selected to optimize its performance. The learning rate was set at 0.001 to ensure efficient convergence towards the global minimum and to prevent the model from getting stuck in local minima. The Adaptive Moment Estimation (Adam) optimizer was employed to adapt the model's weights during training. The loss function used was categorical cross-entropy, which quantifies the difference between the model's predictions and the actual training values, thereby serving as a performance metric during training. Regarding training epochs, the data were presented 200 times to the model. Early stopping criteria were also implemented; training would cease if the loss function in the validation data did not improve by a margin of 0.001 over ten consecutive epochs. The ModelCheckpoint feature was also used to preserve the model states that demonstrated superior performance throughout the training process.

2.7. Domain-Adaptation Techniques

In locomotion classification tasks, domain adaptation is vital to ensure robust models for cross-subject generalization. The core objective is to minimize performance gaps when applying a model to new subjects not encountered during training. This necessity arises from the inherent variability in human biomechanics, where individuals exhibit unique movement patterns and characteristics. Consequently, the challenge lies in ensuring that the trained model, which has learned from a specific dataset, can seamlessly extend its predictive capabilities to individuals not encountered during the training phase. Therefore, domain adaptation enhances the model's adaptability and minimizes performance disparities when confronted with diverse subjects. This is essential for the practical deployment of locomotion classification systems in real-world scenarios where encountering new subjects is inevitable.

Several domain-adaptation techniques are employed to address the challenges of cross-subject variability in locomotion classification. One prominent approach is transfer learning, where models are initially pre-trained on data from multiple subjects and subsequently fine tuned on a smaller dataset from a subject not included in the initial training set. This enables the model to leverage knowledge from diverse subjects while refining its predictive capabilities for the target subject. Another effective strategy involves feature-alignment techniques like correlation alignment (CORAL). This method aligns feature distributions across subjects, ensuring a harmonized representation of locomotion characteristics and minimizing discrepancies in the model's performance when applied to new individuals.

2.8. Statistical Analysis

Statistical analysis was performed by using an analysis of variance (ANOVA) to contrast the metrics obtained, such as the accuracy, precision, and F1 score, on the results. Performing this analysis is crucial to determine whether there is a significant difference when comparing the performance of the classification models used (SVM and LSTM) and the different groups of participants (amputees and non-amputees). However, the drawback lies in the fact that an ANOVA only indicates the presence of at least one distinct group when it detects a significant difference without specifying which one. Tukey's honest significant difference (HSD) post hoc methodology was applied after the ANOVA to identify the most significant mean differences between the groups to obtain a more detailed comparison.

The statistical analysis was carried out in several steps. In the data-preparation phase, separate groups were created for the SVM and LSTM models according to their performance metrics. Before the ANOVA application, assumption checks, including normality and the homogeneity of variances, were performed by using the Shapiro–Wilk test for normality and Levene's test for the homogeneity of variances in the assumption-verification stage. The ANOVA test was implemented for each performance metric (accuracy, precision, and F1 score) to identify the possible statistically significant differences between the two models. If the ANOVA detected significant differences, Tukey's honest significant difference (Tukey's HSD) post hoc test for paired comparisons was performed to determine which specific pairs of models showed significant differences.

2.9. Experimental Steps

An exhaustive set of experiments tailored to each dataset was conducted to evaluate the efficacy of the proposed classification models. The experiments were designed to address various aspects of model generalization and performance. Below are the specific experimental configurations:

1. Train and test the algorithm on each subject within the non-amputee dataset, meaning the model is trained on 80% of the data from each non-amputee subject and then validated on the remaining 20% of the data from the same subject.
2. Train and test on each subject within the amputee data set, using the 80–20 data distribution, similar to the previous item.

3. Train and test the algorithm on each subject within the non-amputee dataset, meaning the model is trained on 50% of the data from each non-amputee subject and then validated on the remaining 50% of the data from the same subject.
4. Train and test on each subject within the amputee data set, using the 50–50 data distribution, similar to the previous item.
5. Train and test on the non-amputee dataset on a subject-independent basis, meaning the models are trained by using the data from all subjects except one in the non-amputee dataset.
6. Train and test on the amputee dataset with a subject-independent basis following the same paradigm as the previous step.
7. Test the effect of training with non-amputee data and testing on a single amputee subject.
8. Test the effect of training with non-amputee data and testing on the entire amputee dataset.
9. Evaluate the classification latency assessment of the system.

3. Results

This section systematically presents the findings from the experimental configurations delineated in Section 2. A granular analysis was performed, segregating the results based on two primary criteria: the source of the data—either from the non-amputee or the amputee cohorts—and the type of classification model employed—support vector machine (SVM) or long short-term memory (LSTM). This nuanced approach facilitates a comprehensive understanding of the relative performance and adaptability of the proposed models.

3.1. Within-Subject Evaluation for Non-Amputee and Amputee Datasets

Each model—SVM and LSTM—was trained and tested intra-subject in two experimental scenarios. In the first scenario, for each subject, 80% of the available data were devoted to model training, while the remaining 20% were reserved for evaluation. In the second scenario, for each subject, 50% of the available data were allocated to model training, while the other 50% were reserved for evaluation. This experiment was conducted for both amputee and non-amputee datasets, with twenty non-amputee subjects and five amputee subjects. Four of the twenty-four non-amputee subjects initially evaluated were excluded due to irregularities identified during the data-review process.

The accuracy, precision, and F1 score were calculated for each model by five-fold cross-validation to ensure robustness and reliability. Table 3 shows the summary corresponding to the first distribution, 80–20. On the other hand, Table 4 shows the summary corresponding to the second distribution, 50–50.

The results corroborate that the SVM model tends to outperform the LSTM model across all the evaluated metrics—accuracy, precision, and F1 score—for both the amputee and non-amputee datasets. Likewise, the SVM is still shown to be superior at first glance in all the metrics evaluated in both the 80–20 and 50–50 distributions. Specifically, in the 80–20 distribution, the average accuracy of the SVM model on the amputee dataset was approximately 96.68%, compared to 93.39% for the LSTM model. Similar trends were observed with the non-amputee dataset, where the SVM model yielded an average accuracy of approximately 98.84%, in contrast to 93.36% for the LSTM model. Similarly, in the 50–50 distribution, the mean accuracy of the SVM model in the amputee dataset was approximately 95.35%, as opposed to 93.30% for the LSTM model. The mean accuracy of the SVM model on the non-amputee dataset was 95.46%, in contrast to 93.33% for the LSTM model. However, it was observed that the mean of the SVM metrics decreased and the standard deviation increased in the 50–50 distribution compared to the 80–20 distribution. This did not happen with the LSTM metrics, maintaining similar values in both distributions.

To enhance comprehension, Figure 8 illustrates bar plots representing the average performance metrics—accuracy, precision, and F1 score—across the two datasets, following the first 80–20 distribution. Figure 8a is dedicated to the non-amputee group, while

Figure 8b presents the results for the amputee group. Similarly, Figure 9 illustrates bar charts similar to those in Figure 8 but corresponding to the second 50–50 distribution.

Table 3. Summary of performance metrics for within-subject evaluation on amputee and non-amputee datasets using SVM and LSTM models and using the 80–20 data distribution.

Subject	Support Vector Machine			Long Short-Term Memory		
	Accuracy (%)	Precision (%)	F1 Score (%)	Accuracy (%)	Precision (%)	F1 Score (%)
Non-Amputee 01	99.20 ± 0.252	99.21 ± 0.240	99.21 ± 0.244	98.48 ± 0.202	98.39 ± 0.259	98.38 ± 0.187
Non-Amputee 02	97.70 ± 0.837	97.60 ± 0.760	97.22 ± 1.036	93.73 ± 0.518	92.91 ± 0.690	92.43 ± 0.587
Non-Amputee 03	97.94 ± 0.813	97.92 ± 0.898	97.92 ± 0.850	95.41 ± 0.538	95.48 ± 0.503	95.41 ± 0.524
Non-Amputee 04	96.82 ± 0.815	96.56 ± 0.919	96.46 ± 0.934	91.40 ± 0.732	91.11 ± 0.715	90.89 ± 0.791
Non-Amputee 05	97.02 ± 1.078	97.09 ± 1.018	97.00 ± 1.037	92.18 ± 0.911	92.31 ± 1.155	92.13 ± 0.916
Non-Amputee 06	94.63 ± 0.253	94.57 ± 0.282	94.34 ± 0.265	90.47 ± 0.945	90.50 ± 0.879	90.15 ± 1.010
Non-Amputee 07	97.69 ± 0.606	97.87 ± 0.501	97.70 ± 0.639	97.03 ± 0.279	96.94 ± 0.356	96.96 ± 0.278
Non-Amputee 08	96.76 ± 0.799	96.67 ± 0.863	96.11 ± 1.016	89.67 ± 0.493	88.00 ± 0.944	87.62 ± 0.719
Non-Amputee 09	96.40 ± 0.741	96.27 ± 0.782	96.18 ± 0.785	94.72 ± 0.482	94.40 ± 0.476	94.29 ± 0.529
Non-Amputee 10	96.41 ± 0.730	96.28 ± 0.719	95.94 ± 0.833	93.14 ± 0.676	93.10 ± 0.420	92.10 ± 0.821
Non-Amputee 11	96.01 ± 0.427	95.55 ± 0.512	95.34 ± 0.415	90.79 ± 0.520	90.37 ± 0.849	89.62 ± 0.480
Non-Amputee 12	97.90 ± 0.914	97.86 ± 0.869	97.51 ± 1.184	94.36 ± 0.660	93.35 ± 0.828	93.33 ± 0.889
Non-Amputee 13	95.97 ± 0.759	96.00 ± 0.743	95.73 ± 0.766	92.34 ± 0.463	91.63 ± 0.466	91.35 ± 0.609
Non-Amputee 14	97.51 ± 0.309	97.49 ± 0.325	97.37 ± 0.351	95.71 ± 0.696	95.27 ± 0.725	95.09 ± 0.795
Non-Amputee 15	96.62 ± 0.684	96.46 ± 0.745	96.40 ± 0.757	92.05 ± 0.588	91.94 ± 0.802	91.70 ± 0.585
Non-Amputee 16	96.77 ± 1.206	97.00 ± 1.156	96.68 ± 1.285	93.00 ± 0.846	93.30 ± 0.719	92.82 ± 0.930
Non-Amputee 17	95.11 ± 0.883	94.82 ± 0.843	94.66 ± 0.939	91.64 ± 0.605	90.49 ± 0.844	90.72 ± 0.719
Non-Amputee 18	96.17 ± 0.605	96.09 ± 0.627	95.65 ± 0.721	93.30 ± 0.470	93.41 ± 0.474	92.15 ± 0.629
Non-Amputee 19	97.34 ± 0.538	97.23 ± 0.578	96.79 ± 0.709	92.91 ± 0.358	92.36 ± 0.481	91.42 ± 0.401
Non-Amputee 20	96.90 ± 0.340	96.80 ± 0.388	96.71 ± 0.352	94.80 ± 0.434	94.87 ± 0.517	94.47 ± 0.454
Non-Amputee Average	98.84 ± 0.679	96.77 ± 0.688	96.55 ± 0.756	93.36 ± 0.571	93.01 ± 0.655	92.65 ± 0.643
Amputee 01	95.47 ± 0.869	95.46 ± 0.901	95.19 ± 0.985	91.38 ± 0.301	91.16 ± 0.445	90.87 ± 0.367
Amputee 02	95.31 ± 0.722	95.39 ± 0.700	95.31 ± 0.662	91.31 ± 0.494	91.25 ± 0.485	91.03 ± 0.436
Amputee 03	96.83 ± 0.532	97.18 ± 0.559	96.70 ± 0.591	94.33 ± 0.470	94.03 ± 0.629	93.96 ± 0.512
Amputee 04	97.05 ± 0.465	97.13 ± 0.506	96.98 ± 0.479	94.22 ± 0.299	94.36 ± 0.286	94.03 ± 0.315
Amputee 05	98.72 ± 0.447	98.67 ± 0.429	98.57 ± 0.436	95.69 ± 0.418	95.51 ± 0.414	95.47 ± 0.463
Amputee Average	96.68 ± 0.607	96.77 ± 0.619	96.55 ± 0.631	93.39 ± 0.396	93.26 ± 0.452	93.07 ± 0.419

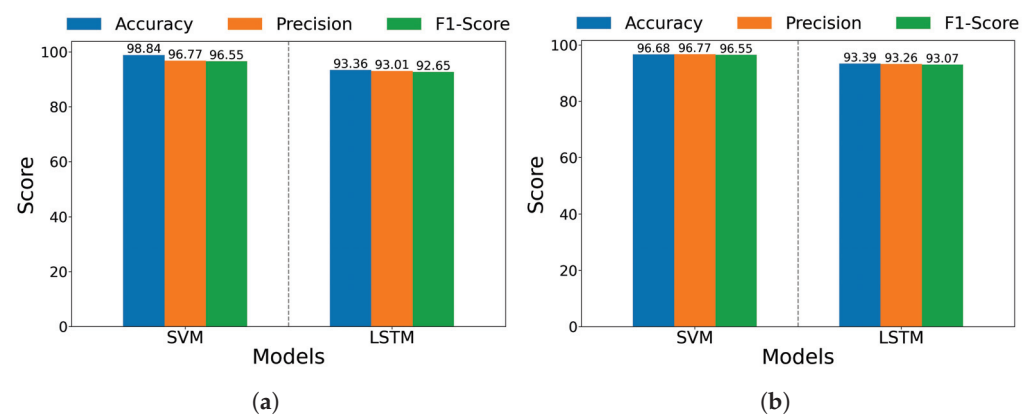
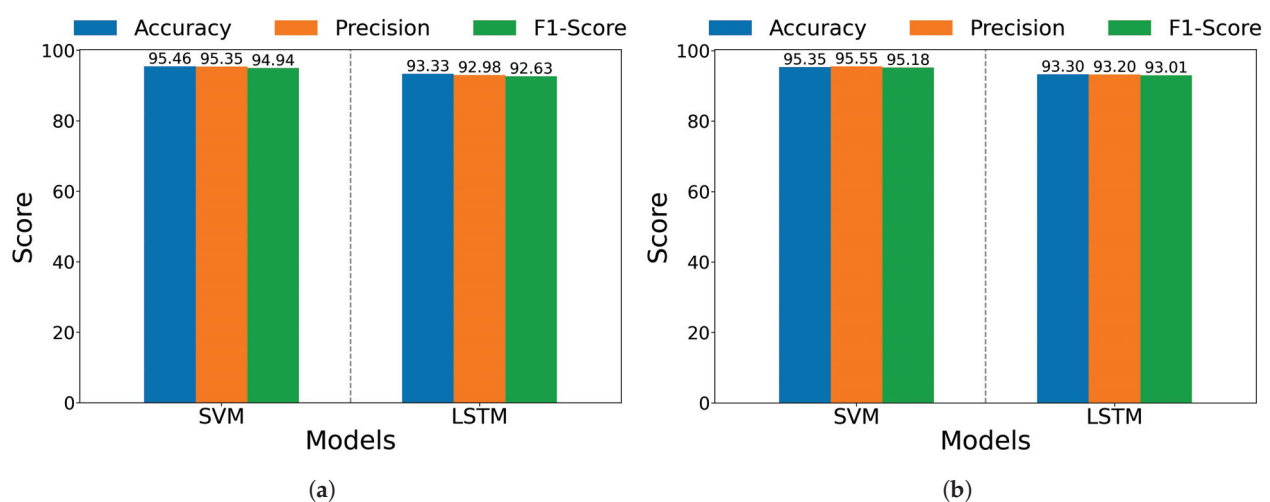


Figure 8. Bar plots for the average of performance metrics by using SVM and LSTM models in the 80–20 data distribution: (a) within-subject evaluation on non-amputee dataset, (b) within-subject evaluation on amputee dataset.

Table 4. Summary of performance metrics for within-subject evaluation on amputee and non-amputee datasets using SVM and LSTM models and using the 50–50 data distribution.

Subject	Support Vector Machine			Long Short-Term Memory		
	Accuracy (%)	Precision (%)	F1 Score (%)	Accuracy (%)	Precision (%)	F1 Score (%)
Non-Amputee 01	98.93 ± 0.423	98.96 ± 0.419	98.93 ± 0.433	98.17 ± 0.319	98.03 ± 0.336	98.04 ± 0.342
Non-Amputee 02	96.88 ± 0.673	96.64 ± 0.671	96.18 ± 0.733	93.66 ± 0.462	93.21 ± 0.478	92.32 ± 0.610
Non-Amputee 03	97.48 ± 1.428	97.49 ± 1.386	97.42 ± 1.459	95.37 ± 0.702	95.44 ± 0.640	95.36 ± 0.683
Non-Amputee 04	94.70 ± 1.371	94.24 ± 1.503	94.07 ± 1.493	91.91 ± 0.178	91.70 ± 0.258	91.41 ± 0.188
Non-Amputee 05	96.04 ± 0.781	96.20 ± 0.714	95.90 ± 0.818	91.94 ± 0.285	92.16 ± 0.370	91.91 ± 0.285
Non-Amputee 06	91.69 ± 1.379	91.69 ± 1.481	91.21 ± 1.364	89.93 ± 0.470	89.94 ± 0.647	89.57 ± 0.481
Non-Amputee 07	96.48 ± 0.812	96.78 ± 0.894	96.42 ± 0.928	96.63 ± 0.398	96.53 ± 0.400	96.56 ± 0.399
Non-Amputee 08	94.44 ± 1.223	94.20 ± 1.164	93.13 ± 1.640	88.57 ± 0.612	87.52 ± 0.664	85.99 ± 0.961
Non-Amputee 09	95.32 ± 0.935	95.17 ± 0.892	94.97 ± 1.025	94.91 ± 0.161	94.68 ± 0.117	94.47 ± 0.190
Non-Amputee 10	95.24 ± 0.734	95.05 ± 0.632	94.53 ± 0.799	93.83 ± 0.783	93.58 ± 0.660	92.95 ± 0.919
Non-Amputee 11	93.48 ± 1.463	92.90 ± 2.043	92.34 ± 1.828	91.31 ± 0.752	90.61 ± 0.744	90.20 ± 0.876
Non-Amputee 12	97.25 ± 1.248	97.09 ± 1.317	96.65 ± 1.567	95.40 ± 0.744	94.89 ± 0.762	94.72 ± 0.933
Non-Amputee 13	94.36 ± 1.058	94.14 ± 1.294	93.76 ± 1.266	92.52 ± 0.421	91.99 ± 0.320	91.70 ± 0.498
Non-Amputee 14	95.93 ± 0.683	95.90 ± 0.694	95.62 ± 0.765	95.65 ± 0.528	95.21 ± 0.500	95.11 ± 0.512
Non-Amputee 15	95.73 ± 0.861	95.47 ± 0.890	95.42 ± 0.920	91.89 ± 0.774	91.69 ± 0.951	91.60 ± 0.868
Non-Amputee 16	94.65 ± 1.318	94.87 ± 1.256	94.30 ± 1.510	92.98 ± 0.969	92.98 ± 1.183	92.86 ± 0.950
Non-Amputee 17	94.19 ± 1.239	94.20 ± 1.291	93.56 ± 1.493	91.01 ± 0.542	89.75 ± 0.701	89.92 ± 0.604
Non-Amputee 18	94.82 ± 0.712	94.72 ± 0.865	94.05 ± 0.757	93.39 ± 0.321	93.03 ± 0.430	92.11 ± 0.271
Non-Amputee 19	95.88 ± 0.579	95.74 ± 0.659	95.00 ± 0.688	92.63 ± 0.725	91.75 ± 0.752	91.23 ± 0.757
Non-Amputee 20	95.80 ± 0.967	95.60 ± 1.025	95.42 ± 1.049	94.94 ± 0.641	94.98 ± 0.596	94.61 ± 0.702
Non-Amputee Average	95.46 ± 0.994	95.35 ± 1.055	94.94 ± 1.127	93.33 ± 0.539	92.98 ± 0.575	92.63 ± 0.601
Amputee 01	93.85 ± 2.275	94.07 ± 2.150	93.50 ± 2.489	91.41 ± 0.929	91.21 ± 1.024	90.98 ± 1.010
Amputee 02	93.58 ± 1.121	93.77 ± 1.228	93.70 ± 1.048	90.82 ± 0.618	90.89 ± 0.687	90.59 ± 0.632
Amputee 03	95.84 ± 1.300	96.34 ± 1.016	95.52 ± 1.486	94.47 ± 0.249	94.17 ± 0.326	94.06 ± 0.278
Amputee 04	95.82 ± 0.264	95.96 ± 0.346	95.72 ± 0.265	94.18 ± 0.641	94.25 ± 0.789	94.04 ± 0.689
Amputee 05	97.67 ± 1.058	97.61 ± 1.075	97.45 ± 1.107	95.63 ± 0.530	95.48 ± 0.543	95.37 ± 0.531
Amputee Average	95.35 ± 1.204	95.55 ± 1.163	95.18 ± 1.279	93.30 ± 0.593	93.20 ± 0.674	93.01 ± 0.628

**Figure 9.** Bar plots for the average of performance metrics by using SVM and LSTM models in the 50–50 data distribution: (a) within-subject evaluation on non-amputee dataset, (b) within-subject evaluation on amputee dataset.

Before conducting the principal analysis, the normality of the data and the homogeneity of variances, which are crucial prerequisites for ANOVAs, were assessed. The Shapiro–Wilk test confirmed the normality of the performance metrics (accuracy, precision,

and F1 score) for both the SVM and LSTM models across different scenarios ($p > 0.05$ in all cases), suggesting that the data were normally distributed. Additionally, Levene's test for the homogeneity of variances showed no significant differences between the groups ($p > 0.05$ for all metrics), satisfying the assumption of the homogeneity of variances.

A two-way ANOVA was conducted to investigate the effects of the 'Model Type' (SVM vs. LSTM) and 'Training/Testing Split' (80–20 vs. 50–50) on the performance metrics. The analysis revealed that the 'Model Type' significantly affected the accuracy ($F(1, 116) = 54.61, p < 0.0001$), precision ($F(1, 116) = 62.55, p < 0.0001$), and F1 score ($F(1, 116) = 54.14, p < 0.0001$). However, the 'Training/Testing Split' and the interaction between the 'Model Type' and 'Training/Testing Split' did not significantly affect these metrics ($p > 0.05$ for all).

Following the significant findings from the ANOVA, Tukey's HSD post hoc test was conducted to determine specific pairwise differences between the SVM and LSTM models. The results indicated significant differences in all the performance metrics, further substantiating the superior performance of the SVM model over the LSTM model in this context.

3.2. Cross-Subject Evaluation on Non-Amputee Dataset and Amputee Dataset

To evaluate the generalizability of the support vector machine (SVM) and long short-term memory (LSTM) models, a leave-one-out cross-validation (LOOCV) methodology was utilized. Each iteration of this approach's model training and testing cycle excludes one subject. The training set contains the remaining subjects, with 20% of the data used as a validation set. Figure 10 offers a schematic representation of this data-partitioning strategy.

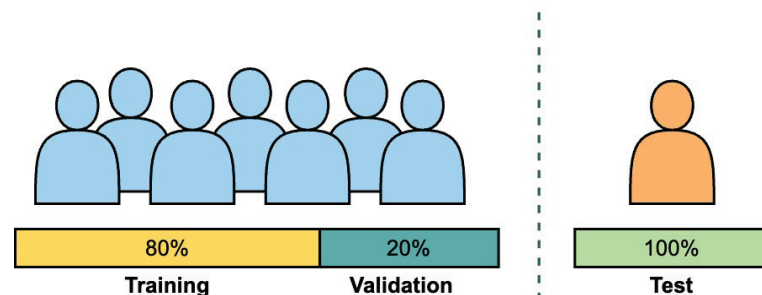


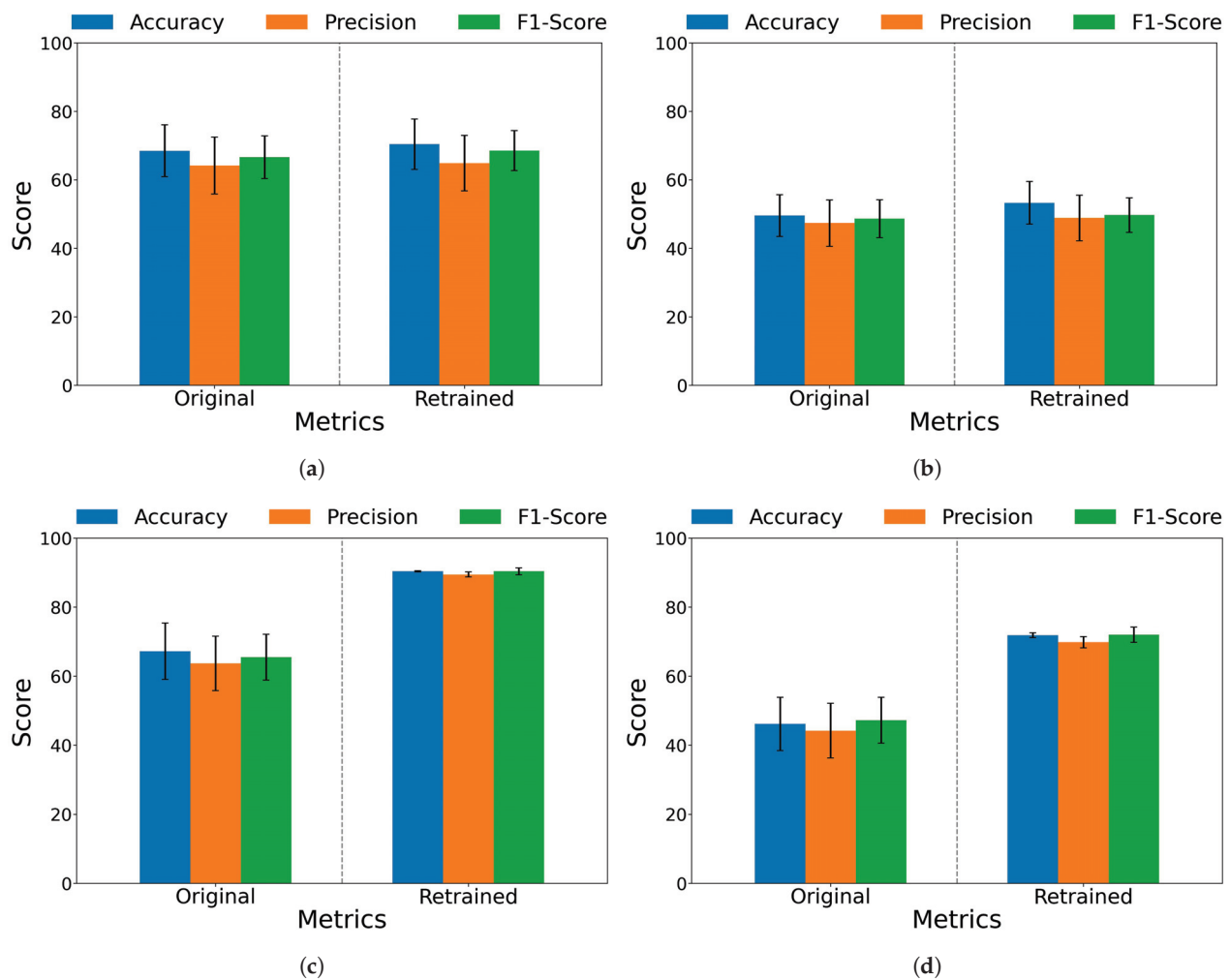
Figure 10. Schematic representation of data partitioning in LOOCV strategy.

After the initial evaluation, the model is subjected to domain-adaptation techniques. The correlation alignment (CORAL) method was used for models involving SVM. The transfer learning technique was used for LSTM models. This iterative procedure was carried out until each subject was singularly excluded from the training set and used for testing. Performance metrics were calculated before and after applying domain-adaptation techniques for the amputee and non-amputee datasets. Notably, domain-adaptation techniques led to significant enhancements, particularly in the LSTM model. For example, while the accuracy of the SVM model improved from 49.52% to 53.22%, the accuracy of the LSTM model improved from 46.16% to 71.86% with the amputee dataset.

Figure 11 further illustrates the comparative performance of the models before and after the application of domain-adaptation techniques. These metrics and other performance measures are comprehensively detailed in Table 5.

Table 5. Average performance metrics of SVM and LSTM models before and after applying domain-adaptation techniques on amputee and non-amputee datasets.

Group Subject		Support Vector Machine			Long Short-Term Memory		
		Accuracy(%)	Precision (%)	F1 Score (%)	Accuracy(%)	Precision (%)	F1 Score (%)
Amputee Group	Before	49.52 ± 6.06	47.33 ± 6.75	48.61 ± 5.48	46.16 ± 7.69	44.21 ± 7.92	47.22 ± 6.63
	After	53.22 ± 6.22	48.84 ± 6.65	49.68 ± 5.02	71.86 ± 0.67	69.83 ± 1.61	72.00 ± 2.19
Non-amputee Group	Before	68.45 ± 7.59	64.13 ± 8.33	66.57 ± 6.26	67.22 ± 8.16	63.67 ± 7.90	65.52 ± 6.64
	After	70.37 ± 7.38	64.83 ± 8.10	68.52 ± 5.94	90.37 ± 0.18	89.45 ± 0.75	90.36 ± 1.03

**Figure 11.** Comparative performance metrics of SVM and LSTM models before and after applying domain-adaptation techniques across non-amputee and amputee datasets. (a) SVM performance on non-amputee dataset. (b) SVM performance on amputee dataset. (c) LSTM performance on non-amputee dataset. (d) LSTM performance on amputee dataset.

After the comparative performance analysis, Figure 12 provides confusion matrices for the SVM and LSTM models after applying their corresponding domain-adaptation technique. These matrices are shown for both the non-amputee and amputee datasets. Including the confusion matrices allows for a more nuanced interpretation of the classification performance, specifically detailing true positives, true negatives, false positives, and false negatives.

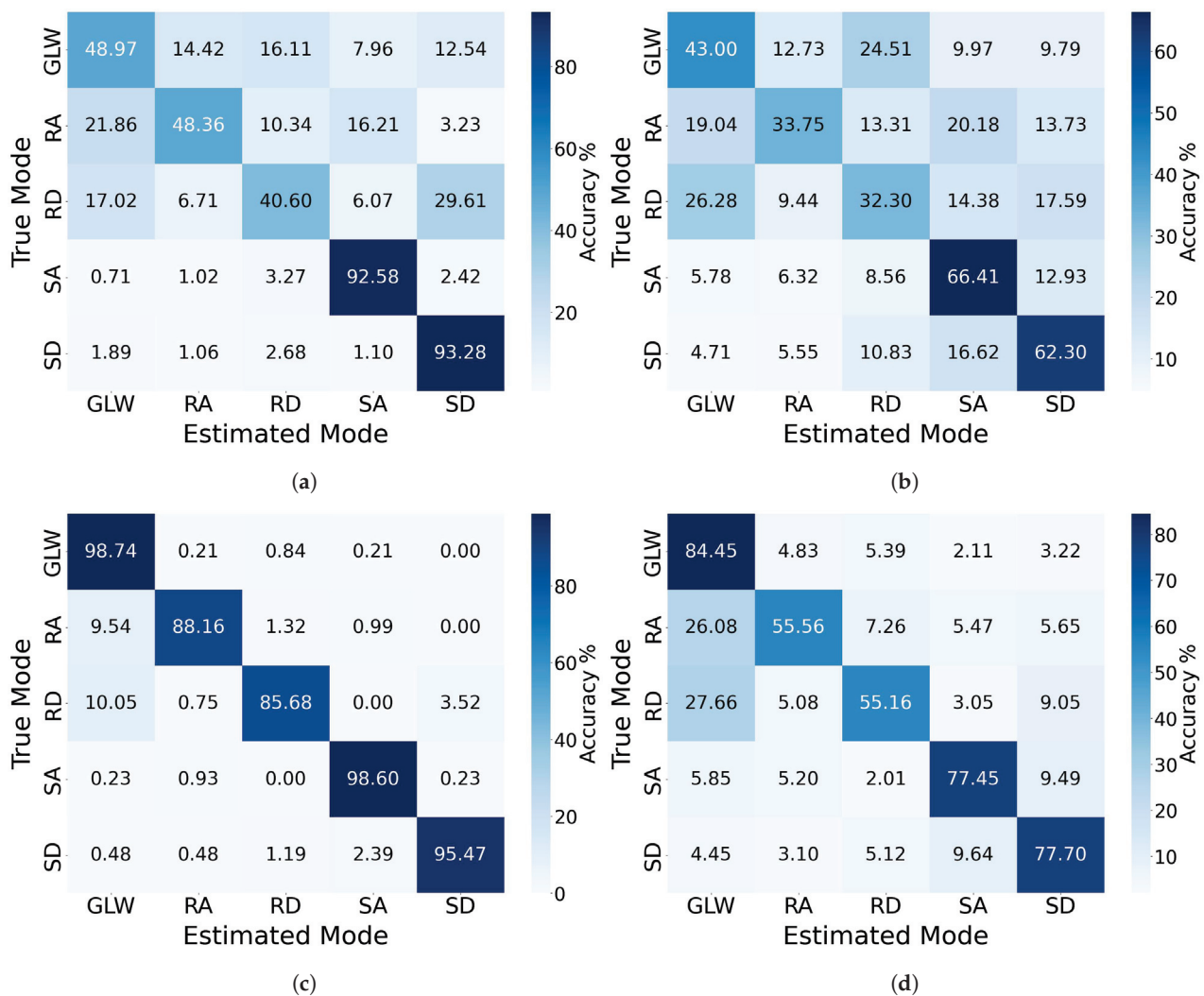


Figure 12. Confusion matrices of SVM and LSTM models with domain-adaptation techniques across non-amputee and amputee datasets. (a) SVM model on the non-amputee dataset, (b) SVM model on the amputee dataset, (c) LSTM model on the non-amputee dataset, and (d) LSTM model on the amputee dataset.

A repeated-measures ANOVA was employed to analyze the effects of the model type (SVM vs. LSTM), domain-adaptation status (before vs. after), and subject type (amputee vs. healthy) on the performance metrics: accuracy, precision, and F1 score. The analysis revealed several key findings. For accuracy, the effects of the model type were significant ($F(1, 16) = 6.51, p = 0.0214$), as well as the effects of domain adaptation ($F(1, 16) = 13.96, p = 0.0018$) and subject type ($F(1, 16) = 41.35, p < 0.0001$). There was also a significant interaction between model type and domain adaptation ($F(1, 16) = 14.69, p = 0.0015$). Similar patterns were observed for the precision and F1 score, with significant effects for model type (precision: $F(1, 16) = 14.10, p = 0.0017$; F1 score: $F(1, 16) = 8.46, p = 0.0103$), domain adaptation (precision: $F(1, 16) = 23.56, p < 0.0002$; F1 score: $F(1, 16) = 14.89, p = 0.0014$), and subject type (precision: $F(1, 16) = 60.02, p < 0.0001$; F1 score: $F(1, 16) = 37.41, p < 0.0001$). The interaction effects between model type and domain adaptation were also significant across these metrics.

From this experiment, it can be concluded that the LSTM model emerged as particularly robust, displaying superior performance metrics with lower variability after the application of domain-adaptation techniques. The results underscore the potential of LSTM models in this application and indicate avenues for future research, especially concerning the amputee dataset.

3.3. Inter-Population Generalizability

The objective of this experiment is to assess the ability of the classifiers to generalize across populations. The 20 non-amputee subjects were divided into two subgroups: 15 for model training and 5 for testing. Two different test scenarios were considered, one with a single amputee subject and the other test with all five amputee subjects.

After the initial testing phase, each model was subjected to domain-adaptation techniques. The correlation alignment (CORAL) technique was used for the SVM models, and the transfer learning technique was used for the LSTM models. These techniques were applied to explore their effects on generalizability across populations.

In the first scenario summarized in Table 6, the initial F1 scores of the SVM and LSTM models were 42.73% and 45.86%, respectively. After applying domain-adaptation techniques, the SVM model obtained a slight performance improvement, raising its F1 score to 45.32%. However, the LSTM model obtained a substantial performance improvement, raising its F1 score to 72.75%.

Table 6. Performance metrics of SVM and LSTM models using a 15-subject non-amputee training set, with and without domain-adaptation techniques on a single amputee subject.

	Support Vector Machine			Long Short-Term Memory		
	Accuracy (%)	Precision (%)	F1 Score (%)	Accuracy (%)	Precision (%)	F1 Score (%)
Before	43.14	43.04	42.73	45.86	45.81	45.68
After	45.71	45.83	45.32	73.07	76.16	72.75

As summarized in Table 7, the initial F1 scores of the SVM and LSTM models in the second scenario were 43.07% and 44.30%, respectively. After applying domain-adaptation techniques, the SVM model obtained a slight performance improvement, raising its F1 score to 44.02%. However, the LSTM model improved substantially, raising its F1 score to 69.30%.

Table 7. Performance metrics of SVM and LSTM models using a 15-subject non-amputee training set, with and without domain-adaptation techniques on multiple amputee subjects.

	Support Vector Machine			Long Short-Term Memory		
	Accuracy (%)	Precision (%)	F1 Score (%)	Accuracy (%)	Precision (%)	F1 Score (%)
Before	43.60	43.82	43.07	45.21	46.38	44.30
After	44.23	43.94	44.02	70.57	71.81	69.30

After applying domain-adaptation techniques, the results obtained in the second scenario, in general, showed that the techniques slightly decreased their performance on all metrics compared to the results for the first scenario. The LSTM models consistently demonstrated a higher accuracy than the SVM models, with a relatively high difference of at least 25 points. These results suggest that the LSTM model is more robust and has a higher capacity for inter-population generalizability.

Although both models experienced improvements in their performance after the application of domain-adaptation techniques, the metrics obtained did not reach the expected level. This limitation could be attributed to the complexity of the dataset, which incorporates approximately 50 features per sample. These numerous and diverse features imply that the signals are inherently different, making it difficult for a preset algorithm to adapt efficiently to a new individual or amputee. In this context, the intrinsic complexity of the dataset emerges as a significant challenge, hindering the ability of models to achieve an optimal performance in adapting to specific situations.

3.4. Classification Latency Assessment

One of the critical factors in real-time classification tasks is the system's response time, often called the "classification latency". The latency was evaluated for both the SVM and LSTM models, encompassing the amputee and healthy-subject datasets. Table 8 summarizes the average classification latency for the SVM and LSTM models. The average latency for the SVM model was 19.84 ms, while it was 37.07 ms for the LSTM model. These latency times are well within the overlapping window time of 40 ms and acceptable limits for real-time applications of 300 ms [14], thereby demonstrating the practicality of the proposed models for real-world implementations.

Table 8. Classification running time of SVM and LSTM models.

Model	Average Latency (ms)
Support Vector Machine	19.84
Long Short-Term Memory	37.07

4. Discussion

4.1. Locomotion Modes

Undertaking a chronological exploration of the presented studies, several salient points emerge, as shown in Table 9.

Table 9. Comparison between this research and previous research regarding classification of locomotion modes acquired with EMG and IMU signals.

Author/Year	Muscle	Locomotion Modes	Participants	Accuracy
Miller et al., 2013 [6]	Tibialis anterior, medial gastrocnemius, vastus lateralis, biceps femoris	Ground-level walking, ramp ascent, ramp descent, stairs ascent, stairs descent	5 non-amputees, 5 transtibial amputees	94.7%, 97.9%
Meng et al., 2021 [17]	Rectus femoris, vastus lateralis, biceps femoris, semitendinosus, tibialis anterior, medial gastrocnemius, lateral gastrocnemius	Ground-level walking, ramp ascent, ramp descent, stairs ascent, stairs descent, standing, sitting	10 non-amputees	98.0%
Barberi et al., 2023 [15]	Adductor longus, rectus femoris, biceps femoris, tensor fasciae latae	Ground-level walking, ramp ascent, ramp descent, stairs ascent, stairs descent	13 transfemoral amputees	94.0%
Present study	Adductor longus, rectus femoris, biceps femoris, tensor fasciae latae	Ground-level walking, ramp ascent, ramp descent, stairs ascent, stairs descent	20 non-amputees, 5 transtibial amputees	98.8%, 96.7%

Commencing with Miller et al.'s research in 2013 [6], there is an evident reliance on a blend of muscles from the upper and lower extremities for electromyography (EMG) data acquisition. Predominantly, the tibialis anterior and the medial gastrocnemius were pivotal muscles in their investigation. Notably, their cohort included an amalgamation of non-amputees and transtibial amputees, and the range of locomotion modes spanned from rudimentary ground-level walking to the more complex tasks of stair navigation. Yet, in the face of this heterogeneity, the research yielded substantial accuracy rates of 94.7% for non-amputees and 97.9% for transtibial amputees.

The subsequent year, 2021, saw Meng et al. [17] embark on an extensive muscle-selection protocol, garnering data from seven muscles. Their inclusion criteria for muscles ensured representation from both the upper- and lower-leg regions. What distinguished their study was the incorporation of static postures, notably standing and sitting, alongside other locomotion modes. With this exhaustive approach, they secured an accuracy pinnacle of 98% among the non-amputee cohort.

Transitioning to Barberi et al.'s 2023 study [15], there was a palpable shift towards an emphasis on proximal muscles of the thigh, incorporating muscles such as the adductor longus and the rectus femoris. Solely focusing on transfemoral amputees, their endeavors culminated in a respectable accuracy rate of 94%. Our current study, however, echoing a similar muscle preference, cast a broader net regarding participant inclusion, embracing both non-amputees and transtibial amputees. The accuracy metrics remain commendable, standing at 98.8% for non-amputees and 96.7% for transtibial amputees.

4.2. *Relevance of Electromyography (EMG), Inertial Measurement Units (IMU), and Data Fusion*

Electromyography (EMG) can detect the intention of movement even before the physical action occurs. EMG signals have demonstrated their significance in predicting human movement intent [29], offering valuable insight into pre-action planning. In parallel, inertial measurement units (IMU) provide the ability to segment data; identify gait cycles; and potentially, in future work, identify specific phases within the gait cycle [30]. IMU data segmentation and analysis contribute to a more complete understanding of motion patterns and gait dynamics. Notably, given the individual variations in gait patterns among participants, a typical pattern was discovered in the Z acceleration of the tibia and foot. This specific pattern enabled us to identify the gait cycles and played a pivotal role in effectively segmenting the data.

The combination of the EMG and IMU signals approach leverages the strengths of each sensor, leading to the more appropriate and precise classification of locomotion tasks. Data fusion enhances the overall performance of locomotion task classification [31], offering a comprehensive perspective on human movement intent and gait dynamics. This integrated approach allows for a deeper understanding of the complexities of locomotion, potentially advancing research and practical applications. A noteworthy aspect is that the fusion of EMG and IMU data in this study enhanced the model's performance and contributed to its robustness across different locomotion tasks. Combining these two data types captures a broader spectrum of biomechanical and physiological characteristics, thereby improving the classifier's ability to distinguish between complex locomotion tasks. This is especially evident in the results, where enhanced performance metrics were observed compared to studies that utilized either EMG or IMU data in isolation.

4.3. *Sensors Positioning*

Four thigh muscles were selected for data collection—rectus femoris, biceps femoris, adductor, and tensor fasciae latae—for the strategic placement of EMG sensors. The experimental positioning identified critical factors impacting the quality of EMG signals. The presence of vellus hair on the thigh posed a challenge by impeding sensor adherence to the skin, inducing relative movement between the sensor and the user's muscle. Another factor that positively influenced the signal quality was the alignment of the sensors with the orientation of muscle fibers, resulting in a notably sharper signal and better tolerance to noise [32].

Muscle selection was guided by the practicality of the sensor application, considering that in developing countries, most individuals with transtibial amputations use sockets that cover a significant portion of the stump, including the knee region. The raw EMG data analysis revealed myoelectric variations among muscles during locomotion tasks, highlighting the rectus femoris as a critical flexor muscle with greater amplitude. Furthermore, depending on the intended locomotion activity, the signals acquired by EMG exhibited variations in amplitude and latency attributed to the effort and duration required for each activity. For instance, the activity of stairs descent displayed greater amplitude in its EMG signals than ramp descent, serving as a distinguishing factor between these two activities.

4.4. *Architectures of the Algorithms*

The growing development of machine learning has encouraged various studies to take the opportunity to develop more suitable algorithms for the lower-limb prosthesis control

system. The studies presented in Table 10 used machine learning to classify aspects related to the control of lower-limb prosthesis.

Table 10. Comparison between this research and previous research regarding the architecture of algorithms using different machine learning methods.

Author/Year	Dataset	Data Acquisition	Architectures of the Algorithms	Machine Learning Method	Accuracy
Bruinsma et al., 2021 [33]	Transfemoral amputee	IMU	RNNs + 4 × GRU + 2 × dense layers	LDA	93.0%
			RNNs + 4 × LSTM + 2 × dense layers	LDA	90.0%
Zhou et al., 2021 [16]	Ankle-foot motion	EMG + IMU	BiLSTM layer + dense layer + Softmax	BiLSTM	99.8%
				SVM	90.4%
				ANN	94.7%
				Decision tree (DT)	74.5%
				Naive Bayes (NB)	82.5%
Mazon et al., 2022 [14]	Transfemoral amputee	IMU	2 × ReLU + Dropout + 2 × dense layer + Softmax	LSTM	95.0%
Putri et al., 2023 [34]	Transtibial amputee	EMG	Hidden	ANN	96.0%
Present study	Transtibial amputees	EMG + IMU	Lineal kernel, 2nd order poly kernel	SVM	98.8%
			BiLSTM + Dropout + BiLSTM + Dropout + ReLU + Softmax	LSTM	93.4%

The research by Bruinsma et al. [33] in 2021 encompasses a dataset from one osseointegrated transfemoral amputee for the acquisition of only inertial data (IMU). What distinguished their study was the use of the machine learning method LDA with three deep neural network architectures in their research (CNNs, RNNs, and CRNNs). The analysis showed an accuracy rate of 90% for LSTM and 93% for the GRU. Among the multiple architectures analyzed, the best performance was the GRU (Gated Recurrent Unit) in combination with RNNs (recurrent neural networks).

Zhou et al. [16], months later, conducted tests with different machine learning algorithms to classify ankle movements. The algorithms used included Naive Bayes (NB), decision tree (DT), artificial neural networks (ANNs), support vector machine (SVM), and bi-directional long short-term memory (BiLSTM). Their dataset consisted of EMG and inertial signals from three non-amputee subjects. Their study confirmed the effectiveness of the SVM and BiLSTM algorithms, achieving accuracies of 90.8% and 99.8%, respectively.

In the following year, 2022, Mazon et al. [14] focused on classifying locomotion modes, obtaining data from one osseointegrated transfemoral amputee by using only inertial data. They focused on using two types of architecture: a convolutional neural network and convolutional recurrent neural network CNN-(LSTM/GRU). Noteworthy, they achieved a peak accuracy of 95% with a system composed of CNN-LSTM networks, which can correctly classify data for the transfemoral amputee subject.

Moving on to Putri et al.'s [34] study in 2023, there was a palpable shift, solely focusing on using an ANN (artificial neural network) as a machine learning method. They used EMGs for data acquisition with a respectable precision rate of 96%. However, the architecture used for development was still being determined.

The studies presented above used different algorithms, among which SVM and LSTM stand out. However, these algorithms have been used to classify ankle movements, gait

cycle phases, or locomotion activities in non-amputees. In contrast to past studies, in this research, the two most prominent algorithms, SVM and LSTM, are used to classify locomotion activities in both non-amputees and transtibial amputees by using EMG and IMU data fusion. In addition, the generalizability of both algorithms was explored to evaluate the ability to classify amputee locomotion tasks with algorithms trained on non-amputee data.

4.5. Dataset Composition and Its Implications

One of the significant strengths of this study lies in the composition of the dataset, which includes data from twenty non-amputated individuals and five transtibial amputees. This diverse dataset enabled a multi-faceted evaluation in three critical dimensions: a within-subject evaluation, cross-subject evaluation within each dataset, and inter-dataset evaluation.

The inclusion of a reasonable number of subjects in both the amputee and non-amputee cohorts allowed for a rigorous assessment of the performance of the models on an intra-subject basis, in addition to facilitating a cross-subject analysis, thereby addressing the generalizability of the classifiers within the same population. The juxtaposition of the amputee and non-amputee data made it feasible to conduct experiments scrutinizing the model's adaptability across different populations. This is critical in real-world applications where a model trained on one demographic must often be generalized to another. Such a comprehensive analysis was only possible with a more diverse or smaller dataset.

A significant focal point of this study was to assess the generalizability of models trained on non-amputee data when applied to amputee subjects. The results affirm that while the models can adapt to new data types through retraining, the performance remains suboptimal compared to that achieved on non-amputee subjects. This draws attention to the need to develop specialized algorithms or incorporate additional features to enhance model adaptability across heterogeneous populations.

4.6. Domain-Adaptation in SVM and LSTM Models

Domain-adaptation techniques were implemented for SVM and LSTM models to enhance the classification of locomotion tasks in transtibial amputees by using EMG and IMU data. For the SVM models, the CORAL method was applied to align the feature distributions of the source and target domains by matching their covariances. This approach, however, yielded mixed results in terms of performance metrics, prompting the consideration of alternative methods like coupled SVMs for a more nuanced approach to non-linear discrepancies in the data. On the other hand, transfer learning was applied with LSTM models, demonstrating a significant increase in the performance metrics and a reduction in their standard deviation. This highlights the effectiveness of transfer learning in capturing the temporal and complex patterns in the data, which may need to be fully addressed by the CORAL method in SVM models.

Incorporating transfer learning with LSTM models in this study was instrumental in addressing the challenges posed by the locomotion data's high-dimensional and non-linear nature. Unlike CORAL's relatively modest impact on SVM model performance, transfer learning in LSTMs showed a robust improvement in classification accuracy and consistency, underscoring its suitability for complex data types. This comparative effectiveness emphasizes the need for a multifaceted approach to domain adaptation, where different techniques are optimized for specific model architectures and data characteristics. The findings suggest that while methods like CORAL can offer computational efficiency in SVM models, integrating transfer learning with LSTM models provides a more comprehensive solution for enhancing the classification of locomotion tasks in transtibial amputees, warranting further exploration in future studies.

4.7. Limitations and Future Outlook

This study has made noteworthy contributions to the classification of locomotion tasks for both transtibial amputees and non-amputees. However, addressing the computational aspects associated with the LSTM and SVM models is crucial. While the SVM model showed a better generalization performance, the computational expenses of extracting features from EMG and IMU signals for real-time operation in embedded systems should be addressed. Although both models achieved classification times under 40 ms—matching the overlapping window duration—this does not account for the time required for feature extraction. Optimizing feature extraction and classification algorithms for a lower computational overhead will be essential for real-world deployments.

Likewise, concerning hardware aspects, it was observed that four EMG sensors and three IMU sensors were sufficient to collect representative data, enabling the differentiation of five locomotion tasks. Noteworthy, the sensors used in data collection, DELSYS Trigno Avanti, are high-end. For future research, exploring the possibility of using low-cost sensors for prosthetic control could make them more accessible, especially in developing countries.

Regarding prosthetic sensor placement, the need for expert intervention and the potential user discomfort associated with locating and attaching sensors for each use present practical challenges. Future endeavors should explore cost-effective sensor solutions with an efficient and user-friendly configuration.

Moreover, prospective research should focus on integrating EMG sensors into customized prosthetic sockets in predetermined positions. This integrated sensor design implemented with the classification algorithm in the control system of a lower-limb prosthesis based on data fusion (EMG + IMU) would have the potential to detect movement intentions more swiftly and accurately without requiring sensor adaptations by experts or causing discomfort for users. This approach enhances the user experience and offers a promising avenue for future investigations in prosthetic technology.

From a clinical standpoint, the utility of the proposed models hinges on their ability to generalize well to real-world, diverse patient populations. Future work should focus on clinically validating these models in various settings and possibly integrating them into prosthetic devices to assess their utility in real-time, dynamic environments.

5. Conclusions

This paper presents a methodology for data acquisition through EMG and IMU sensors, testing both non-amputees and transtibial amputees. A marked differentiator was identified in the raw EMG data from the four thigh muscles tested, allowing for the successful classification of five locomotion tasks. A comparative analysis between the SVM and LSTM models for task classification revealed that the fusion of EMG and IMU signals substantially improved the classification accuracy, supporting the efficacy of multimodal data in locomotion task recognition.

The results of the first comparison highlighted a superior performance of the SVM model in task classification in individual assessments of transtibial amputee and non-amputee subjects. However, after implementing domain-adaptation techniques, subsequent comparisons revealed that the LSTM model exhibits greater robustness and a better intra-population and inter-population generalization ability. Both models demonstrated acceptable latency times, meeting the established real-time requirements, thus highlighting their potential application in embedded systems and real-time environments.

For future research, it is suggested to focus efforts towards integrating EMG and IMU sensors directly into the prosthetic socket, thus enabling their functionality in a more integrated manner. The effective generalization of classification models becomes crucial in this context as it facilitates successfully incorporating these devices in dynamic and real-time environments, thus enhancing their practical utility and clinical applicability.

Author Contributions: Conceptualization, V.E.A., G.O., O.A.G.-H. and D.A.E.; methodology, V.E.A., G.O. and O.A.G.-H.; software, O.A.G.-H.; validation, V.E.A., G.O., O.A.G.-H., D.A.E. and J.G.C.-E.; formal analysis, O.A.G.-H.; investigation, G.O., J.G.C.-E. and V.E.A.; resources, V.E.A. and D.A.E.; data curation, G.O.; writing—original draft preparation, G.O., O.A.G.-H., J.G.C.-E. and V.E.A.; writing—review and editing, G.O., O.A.G.-H., J.G.C.-E., V.E.A. and D.A.E.; visualization, G.O., O.A.G.-H. and J.G.C.-E.; supervision, V.E.A. and D.A.E.; project administration, V.E.A. and D.A.E.; funding acquisition, D.A.E. All authors have read and agreed to the published version of the manuscript.

Funding: This research was funded by “Programa Piloto de proyectos de Investigación en áreas transversales en el Departamento de Ingeniería de la Pontificia Universidad Católica del Perú”, grant number FGR-2023.

Institutional Review Board Statement: This study was conducted in accordance with the Declaration of Helsinki and was approved by the Ethics Committee for Research in Life Sciences and Technologies of Pontificia Universidad Católica del Perú (protocol code: N°073-2023-CEICVt/PUCP; date of approval: 21 August 2023).

Informed Consent Statement: Informed consent was obtained from all the subjects involved in this study.

Data Availability Statement: Data are contained within the article.

Conflicts of Interest: The authors declare no conflict of interest.

Abbreviations

The following abbreviations are used in this manuscript:

ANOVA	Analysis of variance
AL	Adductor longus
BF	Biceps femoris
Bi-LSTM	Bi-directional long short-term memory
CORAL	Correlation alignment
EMG	Electromyographic
FT	Foot
GLW	Ground-level walking
HSD	Honest significant difference
IMU	Inertial measurement unit
LOOCV	Leave-one-out cross-validation
LSTM	Long short-term memory
RBF	Radial basis function
RPA	Ramp ascent
RPD	Ramp descent
RF	Rectus femoris
SSA	Stairs ascent
SSD	Stairs descent
SVM	Support vector machine
TF	Tensor fasciae latae
TB	Tibia

References

1. Vázquez, E. *Los Amputados y su Rehabilitación. Un Reto Para el Estado*; Intersistemas: Ciudad de México (CDMX), Mexico, 2016; p. 5.
2. Ziegler-Graham, K.; MacKenzie, E.J.; Ephraim, P.L.; Travison, T.G.; Brookmeyer, R. Estimating the prevalence of limb loss in the united states: 2005 to 2050. *Arch. Phys. Med. Rehabil.* **2008**, *89*, 422–429. [CrossRef]
3. Molina, C.S.; Faulk, J. *Lower Extremity Amputation*; StatPearls Publishing: Treasure Island, FL, USA, 2022.
4. Su, B.-Y.; Wang, J.; Liu, S.-Q.; Sheng, M.; Jiang, J.; Xiang, K. A CNN-based method for intent recognition using inertial measurement units and intelligent lower limb prosthesis. *IEEE Trans. Neural Syst. Rehabil. Eng.* **2019**, *27*, 1032–1042. [CrossRef]
5. Farro, L.; Tapia, R.; Bautista, L.; Montalvo, R.; Iriartem, H. Características clínicas y demográficas del paciente amputado. *Rev. Med. Hered.* **2012**, *23*, 240–243. [CrossRef]
6. Miller, J.D.; Beazer, M.S.; Hahn, M.E. Myoelectric walking mode classification for transtibial amputees. *IEEE Trans. Biomed. Eng.* **2013**, *60*, 2745–2750. [CrossRef]

7. Sherrat, F.; Plummer, A.; Iravani, P. Understanding LSTM network behaviour of IMU-based locomotion mode recognition for applications in prostheses and wearables. *Sensors* **2021**, *21*, 1264. [CrossRef]
8. Brantley, J.A.; Luu, T.P.; Nakagome, S.; Contreras-Vidal, J.L. Prediction of lower-limb joint kinematics from surface EMG during overground locomotion. In Proceedings of the 2017 IEEE International Conference on Systems, Man, and Cybernetics (SMC), Banff, AB, Canada, 5–8 October 2017.
9. Bhakta, K.; Camargo, J.; Young, A.J. Control and experimental validation of a powered knee and ankle prosthetic device. In Proceedings of the ASME 2018 Dynamic Systems and Control Conference, Atlanta, GA, USA, 30 September–3 October 2018.
10. Simon, A.M.; Finucane, S.B.; Ikeda, A.J.; Cotton, R.J.; Hargrove, L.J. Powered knee and ankle prosthesis use with a K2 level ambulator: A case report. *Front. Rehabil. Sci.* **2023**, *4*, 1203545. [CrossRef]
11. Pi, M. Gait control of robotic leg prosthesis based on motion predictive system. In Proceedings of the International Conference on Advanced Robotics and Mechatronics, Shenzhen, China, 18–21 December 2020.
12. Zhang, K.; Xiong, C.; Zhang, W.; Liu, H.; Lai, D.; Rong, Y.; Fu, C. Environmental features recognition for lower limb prostheses toward predictive walking. *IEEE Trans. Neural Syst. Rehabil. Eng.* **2019**, *27*, 465–476. [CrossRef]
13. Stolyarov, R.; Carney, M.; Herr, H. Accurate heuristic terrain prediction in powered lower-limb prostheses using onboard sensors. *IEEE Trans. Biomed. Eng.* **2021**, *68*, 384–392. [CrossRef]
14. Mazón, D.M.; Groefsema, M.; Lambert, R.B.; Carloni, R. IMU-based classification of locomotion modes, transitions, and gait phases with convolutional recurrent neural networks. *Sensors* **2022**, *22*, 8871. [CrossRef]
15. Barberi, F.; Iberite, F.; Anselmino, E.; Randi, P.; Sacchetti, R.; Gruppioni, E.; Mazzoni, A.; Micera, S. Early decoding of walking tasks with minimal set of EMG channels. *J. Neural Eng.* **2023**, *20*, 026038. [CrossRef]
16. Zhou, C.; Yang, L.; Liao, H.; Liang, B.; Ye, X. Ankle foot motion recognition based on wireless wearable sEMG and acceleration sensors for smart AFO. *Sens. Actuator A Phys.* **2021**, *331*, 113025. [CrossRef]
17. Meng, L.; Pang, J.; Wang, Z.; Xu, R.; Ming, D. The role of surface electromyography in data fusion with inertial sensors to enhance locomotion recognition and prediction. *Sensors* **2021**, *331*, 6291. [CrossRef]
18. Hu, B.; Rouse, E.; Hargrove, L. Benchmark Datasets for bilateral lower-limb neuromechanical signals from wearable sensors during unassisted locomotion in able-bodied individuals. *Front. Robot. AI* **2018**, *5*, 14. [CrossRef]
19. Fleming, A.; Huang, S.; Huang, H. Proportional myoelectric control of a virtual inverted pendulum using residual antagonistic muscles: Toward voluntary postural control. *IEEE Trans. Neural Syst. Rehabil. Eng.* **2019**, *27*, 1473–1482. [CrossRef]
20. Huang, S.; Huang, H. Voluntary control of residual antagonistic muscles in transtibial amputees: Reciprocal activation, coactivation, and implications for direct neural control of powered lower limb prostheses. *IEEE Trans. Neural Syst. Rehabil. Eng.* **2019**, *27*, 85–95. [CrossRef]
21. Turner, S.; McGregor, A.H. Perceived effect of socket fit on major lower limb prosthetic rehabilitation: A clinician and amputee perspective. *Arch. Rehabil. Res. Clin. Transl.* **2020**, *2*, 100059. [CrossRef]
22. Safari, M.R.; Meier, M.R. Systematic review of effects of current transtibial prosthetic socket designs—Part 1: Qualitative outcomes. *J. Rehabil. Res. Dev.* **2015**, *52*, 491–508. [CrossRef]
23. Trigno Avanti Sensor. Available online: <https://delsys.com/trigno-avanti/> (accessed on 11 October 2023).
24. Ministerio de Vivienda, Construcción y Saneamiento del Gobierno Peruano. Accesibilidad Para Personas con Discapacidad y de las Personas Adultas Mayores. Available online: https://www.mimp.gob.pe/adultomayor/archivos/Norma_A_120.pdf (accessed on 11 October 2023).
25. Nazmi, N.; Abdul Rahman, M.A.; Yamamoto, S.-I.; Ahmad, S.A. Walking gait event detection based on electromyography signals using artificial neural network. *Biomed. Signal Process. Control* **2018**, *47*, 334–343. [CrossRef]
26. Toledo-Pérez, D.C.; Rodríguez, J.; Gómez, R.A.; Martínez, J.F.; Carrasco, J.A. Feature selection algorithms to reduce processing time in classification with SVMs. In Proceedings of the XVII International Engineering Congress, Queretaro, Mexico, 14–18 June 2021.
27. Trigini, A.; Scattolini, M.; Mengarelli, A.; Fioretti, S.; Morettini, M.; Burattini, L.; Verdini, F. Role of the Window Length for Myoelectric Pattern Recognition in Detecting User Intent of Motion. In Proceedings of the 2022 IEEE International Symposium on Medical Measurements and Applications (MeMeA), Messina, Italy, 22–24 June 2022.
28. Trigini, A.; Al-Timemy, A.; Verdini, F.; Fioretti, S.; Morettini, M.; Burattini, L.; Mengarelli, A. Decoding transient sEMG data for intent motion recognition in transhumeral amputees. *Biomed. Signal Process. Control* **2023**, *85*, 104936. [CrossRef]
29. Kopke, J.V.; Ellis, M.D.; Hargrove, L.J. Determining User Intent of Partly Dynamic Shoulder Tasks in Individuals with Chronic Stroke Using Pattern Recognition. *IEEE Trans. Neural Syst. Rehabil. Eng.* **2019**, *28*, 350–358. [CrossRef]
30. Sarshar, M.; Polturi, S.; Schega, L. Gait Phase Estimation by Using LSTM in IMU-Based Gait Analysis—Proof of Concept. *Sensors* **2021**, *21*, 5749. [CrossRef]
31. Camargo, J.; Flanagan, W.; Csomay-Shanklin, N.; Kanwar, B.; Young, A. A Machine Learning Strategy for Locomotion Classification and Parameter Estimation Using Fusion of Wearable Sensors. *IEEE Trans. Biomed. Eng.* **2021**, *68*, 350–358. [CrossRef]
32. Huang, H.; Zhou, P.; Li, G.; Kuiken, T.A. An Analysis of EMG Electrode Configuration for Targeted Muscle Reinnervation Based Neural Machine Interface. *IEEE Trans. Neural Syst. Rehabil. Eng.* **2008**, *16*, 37–45. [CrossRef]

33. Bruinsma, J.; Carloni, R. IMU-based deep neural network: Prediction of locomotor and transition intentions of an osseointegrated transfemoral amputee. *IEEE Trans. Neural Syst. Rehabil. Eng.* **2021**, *29*, 1079–1088. [CrossRef]
34. Putri, F.T.; Caesarendra, W.; Królczyk, G.; Glowacz, A.; Prawibowo, H.; Ismail, R.; Indrawati, R.T. Human walking gait classification utilizing an artificial neural network for the ergonomics study of lower limb prosthetics. *Prosthesis* **2023**, *5*, 647–665. [CrossRef]

Disclaimer/Publisher’s Note: The statements, opinions and data contained in all publications are solely those of the individual author(s) and contributor(s) and not of MDPI and/or the editor(s). MDPI and/or the editor(s) disclaim responsibility for any injury to people or property resulting from any ideas, methods, instructions or products referred to in the content.

MDPI AG
St. Alban-Anlage 66
4052 Basel
Switzerland
www.mdpi.com

Prosthesis Editorial Office
E-mail: prosthesis@mdpi.com
www.mdpi.com/journal/prosthesis



Disclaimer/Publisher's Note: The title and front matter of this reprint are at the discretion of the Guest Editor. The publisher is not responsible for their content or any associated concerns. The statements, opinions and data contained in all individual articles are solely those of the individual Editor and contributors and not of MDPI. MDPI disclaims responsibility for any injury to people or property resulting from any ideas, methods, instructions or products referred to in the content.



Academic Open
Access Publishing

mdpi.com

ISBN 978-3-7258-4082-3